HYDRODYNAMIC FORCE COEFFICIENTS FOR RECTANGULAR CYLINDERS IN WAVES AND CURRENTS

VENGATESAN VENUGOPAL, B.Tech., M.Tech.,

SUBMITTED AS A THESIS
FOR THE DEGREE OF DOCTOR OF PHILOSOPHY
IN ENGINEERING

DEPARTMENT OF NAVAL ARCHITECTURE AND OCEAN ENGINEERING
UNIVERSITY OF GLASGOW

MAY 2002

DECLARATION

Except where reference is made to the work of others, this thesis is believed to be original and has not been submitted for any other degree

DEDICATION

To my Parents,
To my mother-in-law, Mrs.Vijaya Pattabiraman
and
To my daughter, Shvetha

CONTENTS

ACKNOWLEGEMENTS

The author immensely happy to express deep sense of gratitude and thanks to Dr.K.S.Varyani, Senior Lecturer, Department of Naval Architecture and Ocean Engineering, Glasgow University, for his invaluable supervision, guidance and continuous support during the entire period of this study, which can never be expressed in words.

The author wishes to express his sincere gratitude to Prof. N.D.P. Barltrop, Head of the Department of Naval Architecture and Ocean Engineering, Glasgow University, for his interest, kind encouragement and for the time spent on technical discussions to make this study successful. His insightful guidance and advice have made substantial differences in this work.

The author would also like to thank Dr.P.K.Das, Reader, for his interest and encouragement.

Special thanks to Mr D.Sinclair, Chief Technician, Mr.D. Percival, Senior Technical Programmer, Mr.G.Dunning, Mr.D.Nicolson, Mr. B.Reilly, Mr. F.Sweeney, Mr.W.Wright for their assistance and continuous help during the experiments.

The author expands his thanks to Mrs. T.Will and Mrs. Maurren for their help and to Mr.Y.T.Chai for his excellent friendship.

The author would like to specially thank his wife Mrs. Kamali Vengatesan for her ever lasting encouragement and great support during difficult moments. The author would also wish to thank his sister-in-law, Miss Sucharita for her encouragement, help and moral supports.

NOTATION

a	Wave amplitude
A	Cross-sectional area of the cylinder
A_n	Wave amplitude of nth component
AR	Aspect ratio = D/B
B	Breadth of cylinder normal to wave crests
C_D	Drag coefficient
C_{DX}	Drag coefficient in horizontal direction
C_{DY}	Drag coefficient in vertical direction
C_{Frms}	Root mean square in-line force coefficient
C_{Fmax}	Maximum in-line force coefficient
C_L	Lift coefficient
$C_{L(n)}$	Lift coefficient for nth harmonic
C_{Lmax}	Maximum lift coefficient
C_{Lrms}	Root mean square lift coefficient
C_M	Inertia coefficient
C_{MX}	Inertia coefficient in horizontal direction
C_{MY}	Inertia coefficient in vertical direction
C_W	Wave celerity
d	Water depth
D	Width of cylinder parallel to wave crests
e_f	Error of force
$\overline{E}$	Mean square error
f_e	Estimated force
F_H	In-line wave force per unit length
F_X	Wave force in horizontal direction

F_Y	Wave force in vertical direction
F_{Xmax}	Maximum in-line force
F_{Xrms}	Root mean square in-line force
F_{Lmax}	Maximum transverse force
F_{Lrms}	Root mean square transverse force
g	Acceleration due to gravity
G	Green function
h	Depth of submergence of the cylinder
H	Wave height
H_n	Wave height associated with nth component
H_s	Significant wave height
k	Wave number
k_n	Wave number associated with nth component
KC	Keulegan - Carpenter number
L	Wave length
p	Dynamic pressure
Re	Reynolds number
$S_{FF}(\omega)$	Spectral density of wave force
$S_{uu}(\omega)$	Spectral density of in-line velocity
$S_{\dot{u}\dot{u}}(\omega)$	Spectral density of in-line acceleration
$S_{\eta}(\omega)$	Wave spectral density
T	Wave period
T_a	Apparent wave period
T_z	Mean zero crossing period
u, U	Horizontal water particle velocity
U_C	Current velocity
U_m, U_{max}	Maximum horizontal water particle velocity
U_{rms}	Root mean square horizontal particle velocity
$\dot{u}, \dot{U}$	Horizontal water particle acceleration

w	Vertical water particle velocity
$\dot{w}$	Vertical water particle acceleration
β	Frequency parameter (= *Re/KC*)
$\psi(n)$	Phase angle for *n*th harmonic
ϕ	Velocity potential
ε_n	Phase associated with nth component
η	Instantaneous water surface elevation
ω	Angular wave frequency
ω_O	Peak frequency
ω_n	Angular wave frequency of the n^{th} Fourier component
∂	Partial sign
ν	Kinematic viscosity of water
ρ	Mass density of water
γ	Peak enhancement factor
σ	Standard deviation or source strength
$X(f)$	Fourier transform

LIST OF FIGURES

LISTS OF PHOTOS

LIST OF TABLES

SUMMARY

The research into hydrodynamic loading on ocean structures is concentrated mostly on circular cross section members and relatively limited work has been carried out on wave loading on rectangular sections, particularly in waves and currents. This research work is therefore carried out focussing on the evaluation of hydrodynamic force coefficients for sharp edged rectangular cylinders of various cross-sections (aspect ratios), subjected to waves and currents. Three cylinders with three different cross-sections are constructed and tested vertically, as surface piercing and horizontally, as fully submerged with the cylinder axis parallel to the wave crests.

The aspect ratios considered for this investigation are 1.0, 1/2, 2/1, 3/4 and 4/3. The length of each cylinder is 2000mm. The sectional loadings are measured on a 100mm section, which is located at the mid-length of the cylinder. The forces are measured using a force measuring system, which consists of load cells, capable of measuring wave and current forces. The in-line & transverse forces (for vertical cylinders) and horizontal & vertical forces (for horizontal cylinders) have been measured. For horizontal cylinder, to study the effect of depth of variation on submergence of the cylinder, the tests are carried out for two depths of submergence.

The experiments are carried out at the Hydrodynamic Laboratory, Department of Naval Architecture and Ocean Engineering, University of Glasgow. The tests are carried out in a water depth of 2.2m with regular and random waves for low Keulegan-Carpenter (KC) number up to 4.5 and the Reynolds number varied from 6.397×10^3 to 1.18×10^5. The combined wave and current effect has been produced by towing the cylinders in regular waves, along and opposite to the wave direction at speeds of ± 0.1 m/s, ± 0.2 m/s and ± 0.3 m/s. Based on Morison's equation, the relationship between inertia and drag coefficients are evaluated and are presented as a function of KC number for various values of frequency parameter, β.

For the vertical cylinders, the drag coefficients decrease and inertia coefficients increase with increase in KC number up to the range of KC tested for all the

cylinders. For the horizontally submerged cylinders, the drag coefficients showed a similar trend to vertical cylinders, whereas the inertia coefficients decrease with increase in KC number for all the cylinders. This reduction in inertia force is attributed to the presence of a circulating flow [Chaplin (1984)] around the cylinders. The random wave results are consistent with regular wave results and the measured and computed force spectrum compares quite well.

While computing the force coefficients in the case of combined waves and currents, only the wave particle velocity is used, as the inclusion of current velocity tends to produce unreliable drag force coefficients. For vertical cylinders, the drag and the inertia coefficients in combined waves and currents are lower than the drag and the inertia coefficients obtained in waves alone. For horizontal cylinders the drag coefficients are larger than those obtained for waves alone and the inertia coefficients are smaller than those measured in waves alone.

The Morison's equation with computed drag and inertia coefficients has been found to predict the measured forces well for smaller KC numbers. However, the comparison between measured and computed positive peak forces indicate that the computed forces are underestimated. It is suggested that if the wave particle kinematics are directly measured, this discrepancy between measured and computed forces might well be reduced.

Wave excitation forces are also reported in non-dimensional forms in the diffraction regime, using 3D-Green function method. Wave induced pressure distribution around the cylinder in regular waves have been measured and are reported as normalised pressures. Wave run-up on the cylinder surfaces has been measured and simple empirical formulae are presented for run-up calculations on the cylinder surfaces. The results of this investigation show that the cylinder aspect ratio plays major role on hydrodynamic force coefficients, dynamic pressure distribution and on wave run-up on cylinder surfaces.

CHAPTER 1
INTRODUCTION

1.1 General

A large variety of marine structures are used by the offshore industry for exploration and production of oil and gas. The move by the oil industry from shallow water conditions to moderate and deeper water has resulted in the development of a variety of new and innovative platform concepts. These include floating structures such as Tension Leg Platforms (TLP) and Semi-submersible Floating Production Systems (FPS). New generations of the above offshore structures, whose columns and pontoons are of square/rectangular cross-section geometry, are emerging. The construction cost with these sections may be considerably less than the conventional one with rounded or circular members. Rectangular sections have some advantages over the circular cylinders. The circular sections are usually much more expensive to build and to join together at nodes. The research into hydrodynamic wave-current loading on ocean structures has concentrated mostly on circular cross-section members and relatively limited work has been carried out on wave loading on other cross-sections such as rectangular section.

Compared to the traditional steel-piled jackets installed in mature producing areas, design of these new platform concepts raises a number of issues in the kinematics and loading area that may not have been as significant as for conventional structures. Recent studies have shown that significant differences in loads can be calculated by different designers even for conventional structures in mature areas, depending on the assumptions made and design codes used. Design codes have been developed to ensure the adequacy of these structures and historical experience has demonstrated their reliability. The primary objective of the structural design is to fulfil some functional and economical criteria for the platform that support the topside facilities for oil operations. It is essential that the structure have a high reliability against

failure. Human lives and enormous investments are at risk when the structure is exposed to tremendous forces from wind, waves and current during a storm. The industries have, during the years, devoted much effort to improve design criteria, calculation procedures and construction to refine the balance between economical investment and structural safety.

1.2 Objectives of the Study

The very complex sea-state makes fluid loading prediction on offshore structures a very complex problem. In order to achieve a better understanding of the fluid mechanics associated with these flows, laboratory and field studies are essential. The literature survey, given in Chapter-2, indicates that in the past, not many investigations have been conducted on wave loading on rectangular cylinders compared to circular cylinders. Among the few research works carried out on square or rectangular cylinders, the different researchers have reported different results and conclusions and this may lead to difficulties in applying these results to the design of offshore structures. Moreover, experiments and investigations in laboratories and most of the published works correspond to small-scale experiments, usually carried out at Reynolds number too low to be a representative of real conditions. Information thus obtained cannot usually be confidently extrapolated to real sea conditions.

In addition to this, experiments that were performed on circular cylinders in harmonic oscillatory flow have conclusively shown that drag and inertia coefficients in oscillatory flow are dependent on both Reynolds and *KC* numbers. Although rectangular cylinders are expected to be less Reynolds number dependent, some doubt must be attached to coefficients derived from small-scale, low Reynolds number experiments. In order to simultaneously attain the high Reynolds number and high *KC* numbers, conditions as seen in extreme storm waves, it is necessary to conduct experiments at much larger scales. Therefore, in the present investigation, large cylinder dimensions were chosen and the experiments were conducted for Reynolds numbers up to 1.18×10^5 and frequency parameter up to 69235. The main

objective of the work is to evaluate in more detail than has been attained by earlier researchers on rectangular cylinders:

(i) the effect of random waves on the force coefficients of the cylinder
(ii) the effect of co-existing waves and current forces on the cylinder
(iii) the effect of depth variation on submergence of the cylinder (in the case of horizontal cylinders)
(iv) wave induced pressures and
(v) wave run-up on the cylinder

The primary objective of the present study is to evaluate the hydrodynamic force coefficients for rectangular cylinders in waves and currents. The hydrodynamic loading from waves and currents on vertically and horizontally mounted rectangular cylinders of various aspect ratios are measured. Drag, inertia and lift coefficients, root mean square coefficients for in-line and lift forces for vertical cylinders and root mean square coefficients for horizontal and vertical forces for horizontal cylinders are derived and presented as a functions of Keulegan-Carpenter numbers. Diffraction forces are also calculated using 3D-Green function method and are compared with experimental results. Results of the measured wave run up on cylinder surfaces and wave induced dynamic pressures at a section of the cylinder due to waves are also reported.

The objectives of the present study are listed in more detail below. It is hoped that this work will form new sources of information on the hydrodynamic behaviour of rectangular cylinders subjected to waves and currents.

Two configurations are selected for the present study:

1. *Cylinder mounted vertically as surface piercing and*
2. *Cylinder placed horizontally submerged with axis parallel to the wave crest*

The cylinders tested are: a square cylinder and two rectangular cylinders. The tests are conducted at low *KC* numbers in the inertia-dominated regime, where measurements of in-line and transverse forces are made. The objectives are:

- *To carry out experimental investigations on the rectangular cylinders with different aspect ratio for regular waves*

Regular waves are generated in the wave tank with different combinations of wave height and wave period. Linear wave theory is employed to calculate the wave particle kinematics and the resulting forces. Morison's formula is then used in conjunction with linear wave theory to evaluate drag and inertia coefficients. Root mean square force coefficients and lift force coefficients are also calculated for all the cylinders. No velocity measurements are made but linear theory is expected to provide good velocity and acceleration estimate in the range of waves tested and symmetry of the zero current forces suggest that no significant unintentional current are generated along with the waves.

- *To investigate the forces on the cylinders due to random waves*

For regular waves, the hydrodynamic force coefficients are determined from accurate laboratory experiments and their dependence on the relevant governing parameters (*Re* & *KC* numbers) is determined. However, the applicability of such results to the more general case of random waves remains uncertain and it was therefore necessary to derive drag and inertia coefficients separately for random waves. In the present investigations, two different spectra namely Pierson-Moskowitz (PM) and JONSWAP (JS) with different significant wave heights and peak periods are used to generate random waves and forces.

- *To study the effect of following and opposing current in regular waves*

One of the major design elements in offshore engineering is the prediction of loading on members of offshore structures subject to wave and current action. The contribution of the load on offshore structures from ocean current is very significant. Hence, research related to determination of wave-current interaction is important. In

this work, the interactions between waves and currents on wave forces are studied. The current effect is produced by towing the cylinder in waves for various speeds. The cylinder is towed in regular waves for following (positive current) sea and head sea (negative current) to produce co-existing wave-current effect.

- *To study the wave induced pressures on a cylinder section*

In the past only a few works have been reported on the wave forces acting on square/rectangular cylinder. Research on wave induced dynamic pressures has not been reported for these cylinders. The wave induced dynamic pressures are measured in a section, around the cylinder in waves and the measured pressures are reported as non-dimensional pressures with wave-flow parameters. These results are used only to help to understand the flow pattern around the cylinders.

- *To study the wave run-up on cylinder surface*

The run-up (local) amplification of the incident wave amplitude around a vertical cylinder can, if severe enough, cause considerable structural damage to the deck and the various appendages beneath the deck. Severe run-up may lead to wave overtopping of the structure or create wave uplift forces on the underside of the structure. Sometimes, the run-up amplitude is more than twice the incident crest amplitude and in random seas as some large individual waves result two times the significant wave heights. In the past, the wave run-up measurements were made only for circular cylinders. In the present investigation, the wave run-up on the square and rectangular cylinders is measured on the front and side surfaces of the cylinder and new simple empirical formulae are developed based on the measurements.

- *To study the Wave forces on the cylinder in the diffraction regime*

The reason for introducing this objective is to evaluate numerically, the wave diffraction forces and the related force coefficients for rectangular cylinders for different aspect ratios.

1.3 Structure of the Thesis

This thesis has been divided into seven chapters:

- *Chapter 1* - Explains the objectives of the study.
- *Chapter 2* - Presents a review of the literature, which has relevance to hydrodynamic loads on cylindrical offshore structures.
- *Chapter 3* - Describes the cylinder model and experimental set-up used for the force and pressure measurements on the cylinder.
- *Chapter 4* - Explains the theoretical backgrounds on the force formulation for regular and random waves, co-existing waves and currents.
- *Chapter 5* - Illustrates the data analysis methods used for the determination of force coefficients for regular, random waves and co-existing waves and currents.
- *Chapter 6* - Devoted to discussions of the results and findings obtained for different flow conditions.
- *Chapter 7*- Describes the overall conclusions of this study with recommendations for future work.

CHAPTER 2

LITERATURE REVIEW

2.1 General

The literature of hydrodynamic loads on cylinders is reviewed in this chapter. A brief description on the wave force regime is given. The literature available on the loading due to steady flow, periodic flow and waves & currents in relation to circular and rectangular cylinders are discussed.

2.2 Force Formulation

Hydrodynamic force formulations on offshore structures are complicated by the many factors involved, such as the non-linear relation between water particle kinematics and water surface displacements, the turbulent flow process about a structural member, the natural variability of wave forces and the possibility of resonance between waves and structures. Five principal categories of factors important in computing hydrodynamic loading on offshore platforms composed of small diameter members are discussed with respect to their relations with the extreme and nominal loading categories (Bea and Lai, 1978);

1. Nature of the problem
2. Oceanographic conditions (methods used to describe wave heights, periods, directional spreading and currents)
3. Wave and current kinematics (descriptions of water particle velocity-acceleration magnitudes, time history and directional characteristics in free-surface and subsurface regimes, and interactions of waves and currents)
4. Platform-wave-current interactions (close-spaced and inclined members, fouling, free surface effects, element forces and integrated result on platform system)

5. Force models (models used to translate kinematics to pressures including drag, lift and inertia as described by models such as those developed by Morison et al.(1950)).

Investigations in the past years have found it necessary to abandon any rigorous mathematical approach and take up something simpler for making any reasonable predictions of forces on offshore structures. The semi-empirical force model developed by Morison et al. (1950) has been the most widely used method since its first introduction. This approach depends upon knowledge of water particle kinematics and empirically determined coefficients, namely the drag coefficient, C_D and inertia coefficient, C_M.

Further problems in the prediction of loads on offshore structure arise because of cylinder orientation and variation of flow conditions along the length of the cylinder. In waves, the incident flow is usually orbital with the type of orbit depending on the ratio of the wavelength to the water depth; the orbit typically being near circular for deep-water waves. A vertical cylinder will therefore be subjected to different flow conditions including a span wise velocity component if it is long enough. A horizontal cylinder on the other hand may have the same incident flow along its span but the wake interaction would be different to that of a vertical cylinder; unless the orbit is flat. For the vertical cylinder, regardless of the orbit, the wake will be swept back against the cylinder; but for the horizontal cylinder the wake will in general follow the orbital path. Depending on the orbit, the vortices shed from the previous half cycle on a horizontal cylinder may be swept far enough away from the cylinder, so that when the flow reverses they may not significantly affect the forces on the cylinder. The horizontal and vertical cylinders in waves therefore represent two different flow situations. For cylinders inclined and yawed, the situation is even more complex, with wake interactions that are totally different to either of the two cases mentioned above.

2.3 Wave Force Regimes

After substantial research, both the designer and researcher still face considerable problems in the prediction of loads on offshore structures. These problems arise for a number of reasons, but probably the most fundamental of all is a lack of understanding of the fluid mechanics associated with these complex unsteady flows generated in the sea. A brief description of the commonly used fluid loading regimes and the prediction methods used therein will help to illustrate some typical problems. These regimes may be broadly classified under the headings of pure reflection, diffraction, inertia and drag as illustrated in Fig.2.1. The regime will depend on two parameters relating to the size of the structure and to the flow conditions. The first of these parameters is the ratio of the diameter of the body *(D)* to the wave length *(L)* of the wave; which serves as a measure of the disturbance of the incident wave. The second is the Keulegan and Carpenter number *(KC)*, which by definition is U_mT/D; where, U_m = Amplitude of the orbital velocity, T = wave period and D is the diameter of the body. This was first introduced by Keulegan and Carpenter (1958), who used it to correlate their force data. The Keulegan and Carpenter number may be viewed as a parameter, which compares the path length of an orbiting fluid particle, with the body diameter and gives an indication of the flow development. It thus gives a measure of the relative importance of drag and inertia forces. There are no distinct boundaries separating these loading regimes and quite often structure experiences loads of different types. However within certain ranges of flow conditions one type of loading may prevail over another.

Pure reflection of waves occur when $D/L > 1$, and is of more significance in the design of coastal structures such as sea walls and breakwaters rather than in the design of offshore structures.

Diffraction forces arise when $D/L > 0.2$; then, the presence of the body causes significant scattering of the incident wave and this effect must be taken into account in the calculation of the loads. In this analysis, viscous effects and hence drag are

usually neglected. In a typical analysis the structure is represented mathematically by a series of grids or elements, over which there are a distribution of sources, the nature of which depends on the type of structure and sea conditions. The velocity potential obtained from this source distribution must satisfy the boundary conditions on the body, at the sea surface, at the seabed and at large distances from the body. Further, the velocity potential includes a contribution due to the undisturbed incident wave (i.e. in the absence of the body), which gives rise to the Froude-Krylov force. The remaining part is the disturbance potential, which includes the effect of wave scattering, and a part, which includes the local flow disturbance, caused by the body, giving rise to the added mass effect. Considerable progress has been made in the diffraction analysis technique, and programs are now available which calculate the loads on and response of both fixed and floating structures.

The diffraction analysis technique can also be used to calculate inertia coefficients of bodies of arbitrary cross-sectional shapes. When the body is no longer large compared with the wave length, wave scattering may be neglected, and in the absence of the body, the pressure gradient due to the undisturbed flow, and hence the acceleration may be assumed uniform over the body. The calculated force is then all inertial from which the inertia coefficient may be obtained.

Inertial loads are dominant when $D/L < 0.2$, and KC less than about 15, then the above assumptions are justified. These loads are composed of two parts, the Froude-Krylov force (F_K) and an added mass effect. The Froude-Krylov force is the force that the fluid would exert on the body, had the presence of the body not disturbed the flow, i.e. due to the pressure gradient of the undisturbed flow, which maintains the fluid acceleration in the absence of the body. The predominance of inertia over drag at small values of KC, leads to prediction methods, which usually neglect viscous effects. However Graham (1978) has shown that for sharp edged bodies this assumption may not be justified, due to the formation of vortices. Graham also states that the effect of the growing vortices may be significant even in the diffraction regime. Here he showed that at low KC, the vortex induced drag component of the

force is related to the internal angle of the shedding edge of the body and to KC. For KC less than about 5, viscous forces, i.e. drag arising from separation and vortex formation, though significant for sharp edged bodies, not as important as inertial forces. As KC increases, these effects become more important, vortex formation and shedding occurs and this leads to asymmetry in the flow, which generates lift and torque on the body. In the region $5<KC<25$ both inertia and drag are important and for this reason, it is commonly referred to as the drag/inertia regime. As KC increases above 25, the flow approaches a quasi-steady situation, and inertial effects are less important.

2.4 Cylinder in Steady Flow

Typically, offshore platforms comprise complex assemblies of circular cylinders and rectangular blocks. The flow over such bodies in isolation depends upon the relative dimension, length/breadth (aspect ratio) and the velocity profiles of the fluid. The main feature of a flow past a body is the phenomenon of flow separation from the body surface and the resulting formation of a large wake behind the body. The presence of the wake alters the flow and the pressure distribution on the body resulting in deficit pressure downstream and excess pressure upstream. This difference of pressure between the front and the back of the body gives rise to a force called the pressure drag. Vortices form in the flow around the cylinder causing fluctuating forces both inline with and transverse to the flow direction. The vortices are shed alternatively from either side of a fixed cylinder producing an oscillating force across the stream, called the lift force.

A flow may be laminar or turbulent. A laminar flow is associated with low Reynolds numbers and turbulent flow with high Reynolds number. At quite modest Reynolds numbers shear layer becomes turbulent immediately after separation and for higher Reynolds numbers the flow pattern and drag coefficient are in general sensibly constant. This statement applies to circular cylinder and the same holds good for rectangular cylinders as well. Bearman and Trueman (1971) conducted experiments

on rectangular cylinders in the range of Reynolds number $2x10^4$ to $7x10^4$and their results are similar to those obtained by Nakaguchi et al.(1967) with Reynolds number of $6x10^4$. They reported that sharp-edged separation would be free of any Reynolds number effects at these comparatively high Reynolds numbers. A number of other researchers [Bostock & Mair (1972); Re = $2x10^4$-$7x10^5$, Courchesne & Laneville (1982); Re = $4x10^4$-$1x10^5$] have chosen this range of Reynolds number for rectangular cylinders as the drag coefficients are free from Reynolds number effect.

2.4.1 Circular Cylinder

The purpose of reviewing the flow behaviour around circular cylinders is to assist the understanding of the effects of vortex shedding on the consequential effects on transverse forces. For smooth or slightly rough cylinders, the basic effect of Reynolds numbers is important as shown in Fig. 2.2. With increasing Reynolds number, the position of the separation point, associated with transition from laminar to turbulent flow moves progressively forward. In the sub-critical region the laminar boundary layer separates ahead of the 90° position and this leads to large wake width and high drag. In the critical region, there is still a separation of the laminar boundary layer but this is followed by turbulent mixing and flow re-attachment. Further round the cylinder, at about 120°, the flow separates but the wake width is reduced and the drag is low. In the post-critical region, the boundary layer is turbulent ahead of the separation and the wake width increases, leading to an increase in drag to the post-critical level. Further increase in Reynolds number leads to changing boundary layer thickness and some variation of C_D in the post-critical plateau, but the changes are now far less marked than the critical region. Surface roughness moves forward the position of transition to turbulent boundary layer and of flow separation with consequent increase in drag. The vortex shedding becomes stronger as Reynolds number is increased to the post-critical region.

The flow patterns associated with different flow regimes are also sketched in Fig. 2.2. At sub-critical Reynolds numbers the flow separates from the surface as a laminar

boundary layer at position LS. The shear layer marks the boundary of the separated wake flow. At some distance, downstream the flow in the shear layer becomes unstable and transition from laminar to turbulent flow occurs. As the Reynolds number increases transition occurs progressively nearer to the separation point. Eventually, in the critical flow regime, transition occurs so close to separation that the increased efficiency of momentum transfer enables the previously separated layer to re-attach and flow along the cylinder surface once more. The flow re-attaches as a turbulent boundary layer is able to remain attached to point TS. With further increase in Reynolds number, transition from laminar to turbulent flow occurs in the attached laminar boundary layer and the separation bubbles disappear. The separation points, TS, move gradually forward. At very high Reynolds numbers the situation stabilises, transition occurs towards the front stagnation point and C_D becomes constant and independent of Reynolds number. The variation of flow patterns around a smooth circular cylinder with Reynolds numbers was investigated using wind tunnel measurements and flow visualisations by many researchers, among the pioneers were Delany and Sorensen (1953), Roshko (1961), Roshko and Fiszdon (1969). Roshko and Fiszdon (1969) have shown that when the Reynolds number lies between 1 and 50, the entire flow is steady and laminar. In the range of Reynolds numbers from about 50 and 200, the flow still retains its laminar character but the near wake became unstable and oscillates periodically. At Reynolds numbers below 1500, turbulence sets in and spread downstream.

In the region between about 1500 and $2x10^5$, the transition and turbulence gradually moves upstream along the free shear layers and the wake became increasingly irregular. When the transition coincides with the separation point at Reynolds number of about $5x10^5$, there is a laminar separation, which is then followed by reattachment to the cylinder, and then a turbulent separation occurs resulting in a narrower wake. This results in a large fall in the drag coefficient, phenomenon known as 'drag crisis'. The transition in the drag coefficient between Reynolds numbers of about $5x10^5$ and $7x10^5$ is interpreted as the transition of the separated boundary layer to a turbulent state, the formation of a separation bubble, reattachment of a rapidly

spreading turbulent free shear layer, and finally separation of the turbulent boundary layer at a position further downstream from the first point of laminar separation.

The reduction of the wake size as a consequence of the retreat of the separation points results in a smaller form drag. The subsequent increase in the drag coefficient between Reynolds numbers of about 10^6 and 10^7 is then interpreted to be a consequence of the transition to a turbulence state of the attached portion of the boundary layer. At very high Reynolds numbers several orders of magnitude larger than 10^7, drastic changes are not likely to occur in the boundary layers and the drag coefficient is not expected to be too much affected.

2.4.2 Rectangular Cylinder

The detailed information regarding forces and flows around rectangular cylinders in a uniform flow is of special interest and of great importance for engineering applications. The forces and pressures acting on bluff bodies, such as rectangular cylinders, in a steady flow and resulting wake and flow patterns are studied by many investigators (Taneda (1959), Taneda (1963), Nakaguchi, Hashimoto and Muto (1968), Bostock and Mair (1972), Otsuki et al. (1974), Laneville et al (1975), Nakamura and Mizota (1975), Courchesne and Laneville (1979), Okajima (1982), Okajima, Mizota and Tanida (1983), Kwok(1983) and Davies et al.(1984)).

When the Reynolds number is sufficiently large, a complicated turbulent vortex system is formed behind bluff bodies placed in a flow field. This vortex system plays an important role in determining the hydrodynamic forces acting on bluff bodies. At extremely low Reynolds numbers, the separation of flow around smooth rectangular cylinders is known to occur at the trailing edges rather than the leading edges where the separation is indiscernible owing to immediate reattachment. As the Reynolds number increases, the flow separation at the leading edges will develop and the steady reattachment becomes impossible. At sufficiently high Reynolds numbers a complicated vortex system is formed behind the bodies. This vortex system

determines the hydrodynamic (or aerodynamic) forces acting on these bluff bodies. In steady flow, the character of the vortices shed immediately behind the cylinder and in the wake further downstream is strongly dependent on the Reynolds number; more explanation for this statement is given below with reference to the work by Okajima (1982). This The shedding frequency, f_o is given in the dimensionless form, $S = f_oD/V$, called Strouhal number, where, D is the body diameter (or size) and V is the velocity of the ambient flow. The Strouhal number characterises the periodic behaviour shown by the fluctuation of the flow in the wake behind the cylinder. Roshko (1955) reported that for bodies having the same frontal area, e.g. a circular cylinder, a 90^0 wedge and a flat plate, the bluffer the body tends to be, the larger was the wake created behind it and this resulted in higher drag force. Delany and Sorensen (1953), investigated the effect of the aspect ratio at rather large Reynolds numbers between $1.1x10^3$ and $2.3x10^6$, found that as the aspect ratio (height to width ratio, d/D) increased from 0.5 to 2, the drag coefficient decreased from 2.2 to 1.4. They also measured the effect of corner radius and found that the drag coefficient of sharp edged cylinders reduced significantly when the corners were rounded. For example for a square cylinder with $r/D = 0.167$ (where, r is the corner radius), they reported, a drag coefficient of 1.2 at Reynolds number of $2x10^5$ compared with a value of 2.0 found with a sharp edged square cylinder.

Okajima conducted experiments on rectangular cylinders with different width to height ratios (B/H = 1, 2, 3 and 4) in wind tunnel and also in water tank and found that at certain range of Reynolds number the flow pattern changes with a sudden discontinuity in Strouhal number if plotted against Reynolds number. The range of Reynolds number obtained in wind tunnel varies between 200- $2x10^4$ and in water tank is about 300. Okajima reported the following:

1. Square cylinder [B/H=1, Fig. 2.3(a)]: In the range of Reynolds number (Re) between 10^2 and $2x10^4$, the Strouhal number (S) for square cylinder show slight change and it takes a value of 0.13 for high values of Reynolds number

between 10^4 and $2x10^4$, which is in close agreement with data by Nakaguchi et al. (1968).

2. Recatngular cylinder [*B/H*=2, Fig. 2.3(b)]: A discontinuity in the Strouhal number curve at *Re* = 500 is seen and this is linked with sharp peaks observed at two predominant frequencies in the power spectrum of the fluctuating velocity in the wake of the cylinder. At Reynolds number below this value, Strouhal number increases with increase in *Re*, reaching a value of 0.18 at *Re* = 500. Then a sharp decrease in the Strouhal number occur and this is related with sudden changes in the flow patterns. For *Re*>600, the lower frequency component becomes dominant with increase in Strouhal number. For *Re*>$5x10^3$, Strouhal number remains almost constant at 0.08-0.09.

3. Rectangular cylinder [*B/H* = 3, Fig.2.3(c)]: At *Re* < 1000, the wake velocity oscillates sinusoidally with a single sharp peak in the power spectrum. For *Re* from 10^3 to $3x10^3$, the spectrum has more than one peak associated with complicated changes in the flow patterns. At *Re* =1000, one small peak occur in the lower frequency range in addition to the dominant peak in the spectrum and the Strouhal number at this stage is 0.16. At *Re*=1220, two different kinds of signal of quite different amplitude and frequency, appeared alternatively in the same record. One had a regular shape (known as mode-I) with small amplitude and high frequency (S = 0.16) and are intermittently replaced by the other waves with larger amplitude and lower frequency (known as mode-II). Mode- II waves are irregular in shape and resolved into two dominant peaks with S = 0.06 and 0.12. Therefore, it is evident that in this region of *Re*, three distinct values of Strouhal number are obtained for one value of Reynolds number. A further gradual increase of Reynolds number in this region leads to the disappearance of mode-I accompanied by the development of mode-II and at high Reynolds numbers, mode-II remains dominant and the value of Struohal number reaches 0.16 to 0.17.

4. Rectangular cylinder [B/H = 4, Fig. 2.3(d)]: In this case the Strouhal number is almost independent of Reynolds numbers. The velocity signals are regular in shape resulting a single sharp peak in the spectrum.

Vickery (1966) measured the fluctuating lift and drag on a long square cylinder. The measurements include the correlation of lift along the cylinder and the distribution of fluctuating pressure on a cross section. Vickery noted that the presence of a large scale turbulence in the stream had a marked influence on the magnitude of both the steady and the fluctuating forces and reported that the changes with turbulence include an increase in wake pressure and a reduction in fluctuating lift of about 50%. The magnitude of the fluctuating lift was found to be considerably greater than that of a circular cross-section and the span wise correlation was much stronger.

Bearman and Trueman (1972) measured the base pressure coefficient, drag coefficient and Strouhal number of rectangular cylinders and confirmed that the drag coefficient rises to nearly 3.0 when the depth of the section is just over half width. They observed a maximum value of drag coefficient of 2.94 for aspect ratio (d/h, h being normal to the flow) = 0.62. They argued that for small values of aspect ratios, the effect of the body downstream of separation is to reduce the size of the separated wake cavity, thus leading to a decrease in base pressure and an increase in drag. In the case of higher values of aspect ratios ($d/h > 0.6$), they suggested that the vortices are forced to form further downstream because of the influence of the trailing edge corners, thus resulting in a reduction of drag. Therefore, the further the vortices are persuaded to form away from the body the higher the base pressure and hence lower the drag.

Laneville and Williams (1979) performed tests to investigate the effect of intensity and large scale turbulence on the drag coefficient of two-dimensional rectangular cylinder and found that the effect of large scale turbulence is not significant while the effect of turbulence intensity is important. It was also reported that the drag coefficients for a given 2D rectangular cylinder is reduced as the intensity of

turbulence increases, for cylinders with aspect ratio (*H/D, D* is the dimension normal to the flow) of 0.63 or greater. For cylinders with $0.5<H/D<0.63$, the drag coefficient for a given cylinder increases to a relative maximum as the intensity of turbulence increases, and then decreases. In another study by Laneville and Yong (1983) the square-section cylinder was extremely sensitive to upstream turbulence level and showed that a free stream turbulence level of 10% can reduce the drag coefficient from 2.2 to about 1.5. The presence of free stream turbulence seems to accelerate the growth of the separated shear layers to such an extent that some reattachment, or at least some interference between the shear layers and the rear edges takes place, and thus results in a drag coefficient smaller that that for smooth flow.

Obasaju (1983) studied the changes that take place in the flow around a square section cylinder for different angle of incidence from 0° to 45°. it was observed that as the incidence is increased from 0°, the Strouhal number at first decreased slightly and then increased sharply to a maximum at 13.5° incidence, which is the incidence where re-attachement of the shear layer is expected to commence. Sub-harmonic peaks were found in pressure and velocity spectra at 5° and 10° incidence and it was suggested that they may have been caused by an interaction between the vortex and trailing edge corner. Thus, the foregoing discusions provides some idea about the flow pattern and forces on a rectangular cylinder subjected to steady flow.

2.5 Cylinder in Periodic Flow/Waves

2.5.1 Circular Cylinder

Most of the published literature on hydrodynamic interactions with the cylinder of various shapes were focused on the variation of C_D and C_M with the non dimensional flow parameters, namely Reynolds number, Re (= $U_{max}D/\nu$; U_{max} = *Maximum horizontal particle velocity,* D = *Diameter of the cylinder,* ν = *Kinematic viscosity*) and Keulegan- Carpenter number, KC (= $U_{max}T/D$; T = *wave period*). Extensive effort has been made in the past for obtaining prototype and laboratory values of the

force coefficients connected with the Morison's equation. Tests were performed in different flow conditions, e.g. accelerating flow, planar oscillating flow, simulated waves, laboratory waves, and sea waves.

Keulegan and Carpenter (1958) used Morison's equation to represent the force. Here forces were measured on several flat plates and circular cylinders, placed at the node of a standing wave. By comparing Morison's equation with Fourier series solution for C_M and C_D, the time dependent values of these coefficients were obtained. However, they used only the first term of these series and obtained constant values, averaged over the cycle for the drag and inertia coefficients, which they found, correlated well with the parameter now called the Keulegan – Carpenter number. Other measured quantities, namely the maximum force and the phase of the maximum force also correlated well with KC. The predicted force, obtained by substituting the calculated values of C_M and C_D in Morison's equation agreed fairly well with the measured force on the circular cylinder, except in the vicinity of KC about 15. In general the agreement on plates was not so good. One of the most surprising results that was reported by Keulegan and Carpenter, is that no correlation with Reynolds number was obtained, neither for the flat plates nor the circular cylinders.

Subsequent re-plotting of Keulegan and Carpenter's data both by Sarpkaya (1976a) and by Garrison, Field and May (1977) showed some dependence on both drag and inertia coefficients on Reynolds numbers. This lack of Reynolds number dependence was also overlooked earlier by Sarpkaya (1975). A probable reason for this was that the apparatus used both by Keulegan and Carpenter and by the above mentioned authors did not allow a systematic variation of Reynolds number, as changing KC resulted in a corresponding change in Reynolds number. However, for any given body size at the same relative oscillation frequency, the ratio of the Reynolds number to KC is constant. This constant termed β by Sarpkaya and is defined as $D^2/\gamma T$, where D = diameter of the body, γ = kinematic viscosity, T = period of oscillation. This parameter therefore gives a measure of the importance of Reynolds number. By

plotting Keulegan and Carpenter's data for different β values, Sarpkaya was able to observe trends with Reynolds number.

Sarpkaya (1976a, 1976b) carried out extensive measurements of both in-line and transverse forces on smooth and rough circular cylinders at high Reynolds numbers in a rather large U-tube water tunnel. These results showed significant influence of Reynolds number on both the in-line and transverse force. For smooth circular cylinders and for $Re < 10^5$, drag coefficient was found to be higher than the steady flow value and inertia coefficient lower than the potential flow value of 2.0. For $Re > 10^5$ and $KC > 20$, the value of drag coefficient was found similar to the post supercritical steady flow value of 0.68. For $KC = 20$ and $Re > 10^5$, inertia coefficient was found to have a value of 1.75. It was found that C_M, C_D and C_L were dependent on the KC and Reynolds numbers and the roughness of the cylinders. The frequency parameter, β was introduced to eliminate the maximum water particle velocity appearing on both Reynolds number and KC numbers and correlated all the data with the KC number for fixed values of β. It is a convenient parameter for period flows since, for a given model size and fluid, the frequency parameter depends only on the flow frequency, whereas the Reynolds number depends on both the flow frequency and amplitude of oscillation. Sarpkaya (1976b) also reported that for Reynolds numbers less than 2×10^4 these coefficients do not vary appreciably with Reynolds number and this explains why this dependence was overlooked in previous studies by Keulegan and Carpenter (1958). Sarpkaya also observed that when Keulegan and Carpenter's data was re-plotted for different β values, C_M appeared to decrease with increasing β.

The effect of transverse or lift forces on circular cylinders, both in steady flow and in unsteady motion is well recognised. In a study of lift forces on vertical piles in waves, Bidde (1971) observed that these forces could sometimes be as much as 60 % of the longitudinal force. Here however, there was a substantial gap between end of the pile and the test bed, thus leading to some 3-dimentional end effects, which may reduce the lift.

Isaacson and Maull (1976) also measured transverse forces on vertical cylinders in waves. This work was similar to Bidde's work, but root mean square and maximum values showed a peak at *KC* around 10. Spectral analysis showed that in this range of *KC* number, the dominant lift frequency was twice the wave frequency. They also explained the lift generation in terms of vortex patterns.

Sarpkaya (1975) also measured lift on circular cylinders, but in a harmonically oscillating flow. They observed that the maximum lift force could sometimes even exceed the maximum in-line force. They found good correlation of the maximum lift force with *KC*. However, the lift curve also showed peaks at $KC = 10$ and 17 and a trough at around $KC = 15$. These results also exhibited remarkably little scatter, except in the region of *KC* between 20 and 25. These tests were conducted for Reynolds number up to 5×10^4 and no Reynolds number dependence was observed in this work. However, in the later studies [Sarpkaya (1976a, 1976b)], it was reported that the force coefficients are in fact functions of Reynolds numbers. It is also to be noted that except the work done in 1975, in the rest of his works, Sarpkaya demonstrated that the force coefficients are dependent on the Reynolds number.

Sarpkaya (1976a, 1976b) extended the Reynolds number range to about 10^6 and tested both smooth and rough cylinders in an oscillatory flow. Results presented show that the lift force on smooth cylinders was dependent on *Re* number for $Re > 2 \times 10^4$, and on *KC*, reaching a single peak at *KC* between 10 and 15. As the Reynolds numbers increased the lift dropped and at around $Re \approx 10^6$ it was almost constant at about 0.2. The lift frequency and Strouhal numbers were also dependent on *KC* and *Re* numbers.

Both in-line and transverse forces were also measured by Maull and Milliner (1978) on a circular cylinder in a sinusoidal flow generated in U-tube water tunnel. An alternative method of describing the in-line force in terms of the root mean square

(*rms*) of the measured force was presented. Good correlation between the *rms* force coefficient and *KC* was achieved.

The effect of water particle orbital ellipticity was investigated by Maull and Norman (1979). They reported that the orbital ellipiticity influences the values of the coefficients of drag, inertia and transverse forces and their variations with parameters *KC* and *Re* numbers. Chakrabarti (1980) measured the wave forces on vertical circular cylinders in shallow water conditions and found that the drag and inertia coefficients agreed well with those of Sarpkaya. However, for *KC* number to about 300, Sarpkaya's measurements had led to higher forces than those measured on structures in deep water waves.

Chaplin (1984a) measured forces on a submerged horizontal cylinder with cylinder axis parallel to the wave crests and discussed about the non-linear contributions to the loading on the cylinder in details. The author reported that the dominant non-linear contribution to the loading is at the third order in the wave amplitude and its magnitude was found to be one-half that of inertia force for *KC* approaching 2.0 and the author suggested that the third order force is associated with circulation generated by steady streaming in the oscillatory boundary layer on the cylinder.

Chaplin (1988b) studied the loading on a series of smooth circular cylinders in elliptical orbital flow by driving the cylinder around elliptical paths through water at Reynolds number in the range of 70,000 to 222,000 and *KC* numbers between 6 and 20, with ellipticities between zero and unity. The author found that the rms force coefficient, drag coefficient and inertia coefficient are diminishing with increasing ellipticity. As the ellipticity (say, E) of the flow was increased, inertia coefficient was found to decrease, typically from 1.8 at $E = 0$ to about 0.8 or less around $E = 0.9$. The drag coefficient was also found to decrease as E increased. The author suggested that the fall in C_M from its planar oscillatory flow ($E = 0$) value to about unity for circular orbital flow ($E = 1.0$) was due to the generation of circulation around the cylinder which induced a lift force acting in the opposite direction to the inertia force. The

author compared the measurements on horizontal and vertical cylinders in waves in similar conditions and suggested that the effect of ellipticity is stronger in oscillatory uniform flow than in waves.

Chaplin (1988c) conducted experiments on a 0.5 m diameter smooth horizontal cylinder at depths of submergence of 1.5m, 2.5m and 3.25 m from the flume bed in a water depth of 5.0m. The tests were conducted at Reynolds number around 1.0×10^5 at low *KC* numbers below 7. It was observed that the loading on the horizontal cylinder in waves is influenced by circulation (a steady vortex motion around the cylinder). The measurements also revealed non-linear loading on the cylinder and substantial reduction in inertia coefficients and the author concluded that this reduction is caused by circulation around the cylinder.

Hayashi and Chaplin (1989) investigated the characteristics of lift forces acting on a rigid vertical cylinder in regular waves, covering Reynolds numbers in the range of 1200 to 9000 and *KC* numbers in the range of 7 to 37. They discussed on the relationship between the effective lift coefficients for the first four harmonics and the characteristic *KC* number for three values of wave depth parameters (kd = 0.735, 1.01 and 1.79). The authors concluded that the fundamental frequency component of the lift coefficient dominates for *KC* less than about 7. The second frequency component dominates for the range of *KC* between about 7 and 20. The third frequency component dominates for *KC* between 16 and 25. They reported that the second frequency component of the lift coefficient takes higher values compared with other frequency component lift coefficients and the second frequency component results in peak values for all wave depth parameters at about *KC* between 8 and 20 and this result again confirms the works reported by Isaacson and Maull (1976). Yu and Miso (1989) analysed transverse forces acting on a circular pile in regular and irregular waves. The authors reported that the resultant of inline and transverse forces in regular waves is 40% larger than the inline force and in irregular waves, the resultant force is 18% larger than the inline force.

Koterayama and Nakamura (1992) carried out field tests on a surface piercing vertical circular cylinder of 0.5m diameter over a two year period to obtain drag and inertia coefficients using an ocean research platform in a water depth of 15m. The Authors defined the Keulegan Carpenter number, $K_C^{1/3}$ by the diameter of the cylinder and the significant orbital displacement $H_{1/3}$ of that at still water surface. The values of C_D in the range of $K_C^{1/3} > 10$ are larger than those of laboratory experiments at Reynolds number (Re = 5 x 10^6). The values of C_D and C_M, when plotted with $K_C^{1/3}$, are found to be 0.9 and 1.3 respectively. The authors compared their results with the laboratory measurements of Kasahara et al (1987) for the corresponding Reynolds and KC numbers and found that the C_D and C_M were 0.6 and 1.6 respectively. They also reported that when the directional spreading of the wave is taken into consideration, the time series of orbital motion contributing to the wave force would decrease and the values of drag and inertia coefficients become larger by 5 to 6% and the effect of breaking waves in wind increases the wave force by 10%. A good discussion on the force coefficients for rough cylinders was also presented by the authors and they reported that C_D and C_M of a rough cylinder are larger than those of a smooth cylinder. The authors also reported that the values of C_D and C_M, from least squares fit of a complete force time series, are well arranged as a function of $K_C^{1/3}$, but those defined by least squares fit on wave-by-wave basis result in wide scatter. Further, the authors confirmed that the ocean wave forces on a surface piercing cylinder can be represented by Morison's Formula with an accuracy of 90% and the remaining10% is attributed to the breaking wave forces in wind waves.

Other notable contributions on the forces on circular cylinders are by Ramberg and Niedzwecki (1979), Pearcey (1979), Bearman et al.(1979), Chaplin (1984b), Chaplin(1985), Heideman and Sarpkaya (1985), Chaplin(1988a), Bearman (1988), Davies et al. (1990), Li and Ye (1990) and Burrows et al.(1997).

2.5.2 Rectangular Cylinder

Semi-submersible drilling rigs and Tension Leg platforms with rectangular cross-section members are emerging. The incentive for the new designs is the reduced

capital cost from the flat plate construction. The good performance in waves is mainly caused by the reduction of the wave forces due to the deep submergence of the main buoyancy chambers. The geometry of the above structures is determined such that the wave force cancellation effect occurs at the most advantageous frequency, which arises because the instantaneous upward wave force caused by the vertical columns can be cancelled out by the downward wave force on horizontal members. To determine the geometry, the accurate predictions of the hydrodynamic forces acting on the members of the unit are required. A very limited literature is available for rectangular cylinder in waves.

Sharp edged cylindrical bodies, such as square sections, rectangular sections and flat plates develop wider wake and shed vortices in oscillatory flow even at very low KC values. As a result of this they experience larger drag coefficients than circular cylinders. Bearman et al.(1979) conducted experiments in a U-tube water tunnel on flat plates, circular, square and diamond cross section (flow is normal to the diagonal of the square section) cylinders to obtain C_D & C_M and found that the variation of C_M with KC showed different behaviour for different sections (Fig.2.4). At low KC numbers ($KC \leq 10$), the values of C_D for flat, square and diamond sections were generally found to be decreasing with increasing KC compared with circular cylinders for which the drag coefficient increases with increase in KC up to $KC \leq 10$. The authors found that at small KC numbers, C_D for a circular cylinder approached zero whereas, for flat plates it attained a very high value following an asymptotic trend similar to that found by Keulegan and Carpenter (1958). Beyond the range of KC equal to 10 to 15, the curves for circular, flat and diamond sections show a similar trend. The square cylinder showed the highest value of C_M compared with other sections. Bearman et al. (1979) also measured a force coefficient derived from Morison equation in terms of non-dimensionalised root mean square force during a cycle. The variation of this force coefficient with the KC number showed the same behaviour for all the body shapes. At small KC numbers the force coefficient has a high value and then decreases gradually as the KC number increases before becoming

constant. The flat plates and square cylinder have the largest value of the force coefficient, particularly at low *KC* numbers.

Graham (1978,1980) derived theoretical expressions for inertia and drag coefficients for square and diamond cylinders due to the forces induced by separation and vortex shedding from sharp edged bodies in oscillatory flow at low Keulegan-Carpenter numbers and compared with experimental results. The theory was based on the assumption that at low *KC* numbers, vortices were not convected by the oscillatory flow far from their point of origin. The author found that the theoretical values of the different body shapes did agree with the trends of the measured data for *KC* numbers less than 10. But the agreement deteriorated for *KC* numbers over 10.

Singh (1979) carried out experiments with circular, square and a diamond cylinder and three flat plates in a planar oscillatory flow. From flow visualisation he observed similar flow patterns on the sections with the exception of square cylinder which resulted in the in-line force being similar on these sections. Large vortices were formed for *KC* numbers 10 and 25. For *KC* numbers less than 5, the pattern on all the sections was more or less symmetrical, and on the flat plate, diamond section weak vortices were observed which resulted in a drag force still important in low *KC* numbers. On the circular cylinders the flow remained attached over most of its surface and on the square section the flow separated on the front face and weak re-circulation was observed on the upper and lower surfaces. Singh (1979) concluded that of the four sections, the flat plates experienced the largest forces and the circular cylinder would be the best shape for the design purpose as it experienced the smallest in-line forces. Comparing the results of circular cylinder with previous result, inertia and drag coefficients obtained by Singh (1979), revealed considerable amount of disagreement particularly when comparison is made to Sarpkaya's data for *KC* numbers 10 and 20. Singh (1979) found no obvious explanation for this difference and suggested that this might be due to different data analysis technique and to the manner in which the oscillations in the U-tube were produced. Again large discrepancies in C_M and particularly C_D throughout the *KC* number range were found

for flat plates when Singh (1979) compared his results with those of Keulegan and Carpenter (1958). The C_D and C_M measured by Singh (1979) were found to be lower than those measured by Keulegan and Carpenter. The largest discrepancy was found for C_D at low KC numbers where the drag coefficient measured by Keulegan and Carpenter was considerably larger than that measured by Singh (1979).

Tanaka et al. (1982) carried out experiments with rectangular cylinders oscillating horizontally in still water to measure drag and added mass coefficients. The aspect ratios and corner radius of the cylinders were systematically varied for various angles of flow attack to determine the effects on C_A and C_D. For a square cylinder Tanaka et al. (1982) found no significant dependence of C_A and C_D on Re number (the range considered was up to $10x10^4$). However, a dependence on the KC number was found to exist for all cylinders. On the effect of corner radii, C_A and C_D were found to decrease for increasing corner radii. For cylinders with small corner radius C_D decreased rapidly as KC number increased in the region of low KC numbers, and became constant for higher KC numbers. As the corner radius become smaller, the decrease of C_D was more gradual. On the effect of aspect ratio C_A and C_D, were found to increase as aspect ratio reduced below 1.0.

Bearman et al. (1984) carried out experiments in a U-tube water tunnel generating planar oscillatory flow. The cylinders investigated were square and diamond cylinders and the aim of the work was to investigate the effects of the corner radius on the hydrodynamic forces. The tests were conducted with KC number varying from 1 to 100 and the Re number in the range of 200 to $2x10^4$. For both the square and diamond cylinders, it was found that at low KC number, drag coefficients decreased with increasing corner radius(r/D, the corner radius equal to 0, for sharp edged section and equal to 0.5 for a circular section, see Fig. 2.5) . The reduction of C_D caused by the rounding of corners was more marked at low KC numbers. At high KC, the square section is more sensitive to changing the corner radius than the diamond. The drag of the square cylinder with $r/D = 0.265$ drops to as low as one-third of the value for sharp edged cylinder when KC is higher than about 80 and the

drag of this section is about half the value for a circular cylinder when KC is above 10. The values of drag coefficients measured in oscillatory flow at high KC decreased more rapidly with increasing corner radius than the values measured in steady flow at sub-critical Reynolds numbers. The authors concluded that there is an optimum corner radius $0.265 < r/D < 0.5$ giving minimum drag force. The authors also suggested that the drag coefficient is more sensitive to corner radius in oscillatory flow because of turbulence in the ambient flow which causes the flow separation to be delayed and to occur further downstream, resulting in a larger reduction in drag coefficient. Regarding the inertia coefficients, the circular and diamond cylinders show a minimum value of C_M when KC lies between 10 and 13, whereas, the square section shows less variation with KC. For $KC \geq 13$, values of inertia coefficients for a diamond cylinder decrease with increasing corner radius, but the data for the square cylinders exhibit an opposite trend.

Bearman et al. (1985) carried out experiments at low KC numbers in a U-tube on circular, square and diamond cylinder and a flat plate horizontally mounted. They also conducted an inviscid theoretical analysis to compare the theoretical values of inertia C_M and drag C_D coefficients with those obtained experimentally. This theory is claimed to be valid for KC numbers less than 3. The authors found that in the case of the flat plate, the theoretical predictions of inertia and drag coefficients are good. However, in the case of the square and diamond cylinder, the theory over predicted the magnitude of the drag coefficients by about 20% through the measured drag coefficients followed the predicted trends. The prediction of the inertia coefficient was reasonable in the case of the square cylinder, but less in the case of the diamond cylinder. When the KC number exceeded 3, the measured drag coefficients for all three sharp-edged cylinders are found to vary similarly with the KC number, suggesting that all the cylinders may have a similar vortex shedding pattern.

Ikeda et al. (1988a) carried out experiments on cylinders of different shapes horizontally submerged in regular waves at low KC numbers. The cylinders investigated were a circular cylinder, a square cylinder and a diamond cylinder and a

flat plate. For a flat plate, Ikeda et al. found that C_M and C_D measured in waves are lower that those measured in oscillatory flow (Tanaka et al. (1980)). When the KC number is very small, the variation of C_D with the KC number shows a different pattern for different geometrical shapes. From flow visualisations, the authors observed that the behaviour of vortices around the plate is very different from that of plane oscillatory flow. The authors also pointed out that the behaviour of vortex shedding in regular waves is different from that of oscillatory flow. A circulating flow around the plate was also observed in regular waves but not as strong as the flow around circular cylinders. The authors suggested that the decrease of inertia coefficient with increasing KC numbers was due to circulation. For a square cylinder, C_M decreased rapidly with increasing KC numbers, similar to the case of a circular cylinder, and reached a minimum value at about $KC = 4.5$, and then increased. From flow visualisation of a square cylinder, a strong circulation was observed as in the case of a circular cylinder. In the case of a circular cylinder, two anti-clockwise vortices released in one wave cycle were observed, but in the case of the square cylinder, four vortices one at each corner were observed. The diamond cylinder in waves had different C_M and C_D coefficients from that of a square cylinder with KC number and also they were different from those measured in oscillatory flow (Bearman et al.(1984)). The two extreme cases found are the circular cylinder and the flat plate. In the case of a circular cylinder C_D approaches zero as KC approaches zero, for a flat plate C_D approach '∞' as KC approaches zero. The reason for this is that sharp-edged cylinder sheds vortices in oscillatory flow even at very low KC numbers, and it is believed that the large values of C_D coefficient are associated with the behaviour of the vortices.

Ikeda et al. (1988b) investigated experimentally the viscous forces acting on a lower hull (a rectangular cylinder with rounded corner with aspect ratio = 0.533) horizontally submerged with its axis parallel to the wave crest and found that at low KC numbers, the inertia coefficients decrease rapidly with increasing KC number and it has been concluded that this decrease in inertia force is due to Magnus effect (a lift

force effect produced by a circulating flow). Another notable contribution to wave loads on vertical rectangular cylinder was made by Hamel Derouich (1992).

Chaplin and Retzler (1992) carried out experimental and numerical studies on horizontal cylinders of circular and pontoon sections to investigate non-linear loading beneath waves. The experiments were carried out in a wave flume of 0.5 m water depth. The tests have been carried out for four wave frequencies, 0.8 Hz, 1.0 Hz, 1.2 Hz and 1.3 Hz. Calculated added mass coefficients in horizontal and vertical directions are plotted against KC numbers. Separate KC numbers are defined in horizontal and vertical directions and the maximum KC number obtained is about 3.0. A reduction in added mass coefficients for both the cylinders is observed with KC number. For stationary cylinder, they concluded that while the reduction in added mass coefficient for a circular cylinder is proportional to the square of the KC number, for the pontoon section this reduction is simply proportional to KC numbers. Experiments were also carried out on cylinders moving in circular orbit. Using Navier-Stokes solution the forces on the cylinders were computed and the resulting inertia coefficients are compared with experimental values. They suggested a relationship between inertia coefficients and KC number of the form, $C_M = C_{mo} - R(KC)^2$, in which C_{mo} is the potential flow value and under laminar conditions, the value R is found to be in the range 0.3 to 0.6 for circular cylinder and 0.2 to 0.5 for the pontoon section. The limiting value of KC was less than 1.5 for circular cylinder and about and 1.1 for pontoon section. Also, different R values are given for different flow conditions.

Arai (1993) measured the wave forces on a rectangular cylinder and examined the drag and inertia coefficients up to KC number around 5 (refer Fig. 2.6). The tests were conducted with a rectangular cylinder of aspect ratio = 0.533 for two depths of submergence (h/B = 1.05 and 2.10, where h = depth to the centre of the model from still water level and B = width of the cylinder). The mean flow pattern around the cylinder model is explained by flow visualisation study. The model chosen by Arai (1993) has rectangular corners. The frequency parameter (β) obtained through the

tests ranged from 750 to 6470. Arai (1993) concluded that vertical inertia coefficients decrease as *KC* number increases beyond about 1.0 and the drag force is only affected by varying the model depth. Arai (1995) made another study at low *KC* numbers on a circular (diameter = 45mm), square (45x45 mm) and rectangular cylinder (depth = 24mm and width = 45mm) and found that the inertia coefficients for all the cylinders decrease with increasing *KC*. The author found that the circulation of the flow for all the cylinders is almost same and is proportional to the square of the *KC* number.

Koterayama and Hu (1995) studied the wave forces on a horizontal circular and rectangular cylinder in regular waves experimentally and numerically, for low *KC* numbers ($KC < 6$). The aspect ratio (cylinder width divided by cylinder height) selected is equal to 1.625 and the rectangular model has a radius of round corner, $r/B = 0.125$, where '*r*' is the radius of the round corner. They reported that the force coefficients for a rectangular cylinder are much more complicated than the circular cylinder because of the flow separation. At small *KC* numbers, C_D and C_M values are significantly larger than that of a circular cylinder. The numerical force coefficients calculated for regular waves by Koterayama and Hu (1995) are not identical to the experimental force coefficients obtained by them.

2.5.3 Rectangular Cylinder in Diffraction Regime

Numerous numbers of works have been carried out on various shapes of structural elements in the diffraction regime to investigate the forces and motions. In relation to the literature review, only few of them are given below which will have direct reference to the rectangular cylinders.

Isaacson et al. (1979) conducted experiments on large square cylinders for various cylinder orientations with respect to wave propagation and the results are reported in terms of force coefficients with diffraction parameter. It was found that over the

range of diffraction parameter, *kb*, the maximum force corresponds to an angle of incidence, $\alpha = 45^{o}$.

Shankar et al (1983) used finite element method for the formulation of linear diffraction problem to analyse the wave forces, moments and wave pattern for a large bottom supported vertical cylinders of square and rectangular sections for various angles of wave incidence. The author observed that the normalised horizontal force increases as *kb* (wave number multiplied by the side parallel to wave crest) increases up to a certain value and the further increase *kb* results decrease in the force. This is due to the reason that increases in *kb* results in significant scattering and hence forces are higher till a peak is reached. However, as *kb* increases further, the dynamic effect of the wave reduces leading to reduction in the force. In the case of rectangular cylinders it was observed that for a particular value of *kb*, the horizontal force is maximum when the broader side of cylinder is normal to the wave and minimum force was noted when the shorter side faces the wave. As regards to the effect of relative water depth (*d/L*), it is found that the horizontal force increases with increase in *d/L*. However, when deep-water condition is reached the increase in water depth does not have significant change in the force.

Rahman (1987) formulated a practical method to predict second order wave loads on large offshore structures extending Lighthill's (1979) techniques for deeper water waves to shallow water waves. The author has developed expressions for total horizontal force and overturning moment for the circular and square cylinders and compared the theory with the experimental results.

2.6 Cylinder in Waves and Currents

2.6.1 Circular Cylinder

The interaction of waves and currents and the resulting influence on the responses are important considerations for offshore structure design. When the current is present

along with the waves, the current is often considered to be steady, and its effect on response is linearly superimposed on the effect of waves. In the presence of current, the wave height and wave length experience modification. If the current is in the direction of wave propagation, the wave slope decreases and its length increase. On the other hand, if the current opposes the wave, the wave slope increases in magnitude and the wave length shortens. These changes are due to the interaction between the waves and current.

Moe and Verley (1980) conducted experiments on circular cylinders in a steady flow and evaluated drag, C_{dc} and inertia coefficients, C_{mc} assuming that the two term Morison equation applies to the coexisting flow field. The experiments showed that the current caused profound changes in both drag and inertia coefficients. The authors concluded that, in general, C_{dc} decreases and C_{mc} increases for corresponding KC and Re numbers.

Koterayama (1984) investigated the wave forces on a circular cylinder moving with a constant velocity in regular waves and reported that the wave force coefficients depend mainly on the reduced velocity ($U_C\,T/D$). Sarpkaya and Storm (1985) carried out experiments with smooth and sand roughened cylinders moving with a constant velocity in a sinusoidally oscillating flow to determine the drag and inertia coefficients, and to examine the effect of wake biasing on the modified Morison equation. In this study, the various flow parameters such as relative cylinder velocity, Reynolds number and KC number were varied systematically. The variation of these coefficients is governed by Keulegan-Carpenter number, Reynolds number, relative roughness and the reduced velocity. The results indicated that the drag coefficients decrease with increase in relative current and the inertia coefficients increases for a given Reynolds and KC number and the effect of wake biasing on the force coefficients is most pronounced in the drag-inertia dominated regime. It was also reported that for $KC > 30$, the effect of current on the force coefficients is negligible.

Teng and Li (1990) estimated force coefficients for an inclined circular cylinder for combined wave and current. The force coefficients are estimated based on a new cross spectrum approach, which the authors call the revised cross spectrum approach. This method utilizes the phase shift of water particle velocity and acceleration to derive C_D and C_M. In this method the force coefficients are considered as constant, and not as a function of frequency, avoiding the conflict with the linearisation in spectral analysis. The authors claim that the results from the revised cross spectrum method are stable and are less affected by division number (corresponding parts of measured and predicted cross spectrum) along the cylinder than the results from other methods. From the experiments they found that the results for following and for opposing currents are different. The resulting coefficients for the following currents are larger than those of opposing currents.

Ikeda et al. (1990) studied the effect of steady motion of a circular cylinder on the reduction of wave forces. The cylinder was moving in following and head seas. The motion of the cylinder is varied to obtain the ratio, U/U_W (U is the current speed, U_W is the wave velocity) from zero (no current) to ± 1. The experimental results showed that the inertia forces acting on the cylinder are significantly affected by the constant speed of the cylinder and the inertia coefficients were depending on the direction of motions. The inertia force of a moving cylinder with constant speed decreased with increase in KC number, however, the reduction was found to be smaller than that of a fixed cylinder at zero speed. At $KC = 1.5$, the inertia coefficients decrease by about 25% in the entire range of U/U_W. At $KC = 2.5$, the value of the inertia coefficient for $U/U_W = -0.3$ (the following sea) is fairly large compared to other ranges of constant speed. The values of inertia coefficients in this region are lower than half of the potential flow value and this suggests that the viscous effect on the inertia coefficient decrease.

Chaplin and Subbiah(1996) describe the experimental arrangements by which forces and pressures on a horizontal cylinder are measured in waves and coexisting waves and currents for KC up to about 50. Two sets of cylinders with diameter 0.21m and

0.5m were tested. The effects of a current were simulated by means of the towing carriage up to a speed of 1m/s in either direction with waves. The authors collected data by driving the carriage through waves with speeds of 0.25 m/s, 0.5 m/s and 1.0 m/s in both opposite and along the wave directions. The force coefficients were computed on a wave-by-wave basis and it was observed that over most of the Keulegan Carpenter number range, mean drag coefficients are about 0.5 and inertia coefficients are around 1.5 and 1.0 for the horizontal and vertical directions respectively. They found that the presence of current does not have much effect on the mean drag coefficients. The inertia coefficients reported showed much scatter in waves and currents, especially, in the vertical direction. The authors used constant values of drag and inertia coefficients (C_D = 0.6 & C_M = 1.2) in the Morison equation to examine the accuracy in the prediction of forces. The authors found that the correlation between measured and predicted forces in the horizontal direction was extremely good, whereas, in the vertical direction the Morison formula tends to under estimate the measured peak forces by a margin of the order of 20% and this is linked with self induced circulation. In another study by Chaplin and Subbiah (1997) where laboratory measurements were carried out on forces and pressures on smooth and rough horizontal cylinders of diameters 0.21m and 0.5m in the presence of currents. They confirmed that drag and inertia coefficients obtained from measurements in individual waves are very unstable with respect to Keulegan Carpenter number and found the prediction of horizontal forces using Morison equation is more accurate. They also concluded that drag and inertia coefficients are constant for both cylinders over a wide range of waves and current conditions and they are substantially free from Reynolds number effect.

A review on the drag and inertia coefficients data has also been published in Marine Research Review11(1997). This work has been carried out on vertical circular cylinders in current superposed on regular waves. It was reported that both drag and inertia coefficients take identical values for positive and negative currents. The inertia coefficients, when a current is present, are noticeably different from the zero current case and it is much lower than the inertia coefficients obtained in waves alone, as *KC*

tends to zero. For example, inertia coefficients at KC about 4.0, for a cylinder of diameter equal to 500mm and for a current of + 1.0 m/s is around 0.7. At the same value of KC, for zero current, the inertia coefficient for a circular cylinder is around 2.0 [Sarpkaya and Isaacson (1981)].

2.6.2 Rectangular Cylinder

There is not much literature available for rectangular cylinder subjected to combination of waves and currents. Chaplin and Retzler (1993) described experimental and numerical predictions of flow and forces around horizontal circular cylinder and pontoon section in waves with and without currents at KC numbers below 2. They reported a similar behaviour for both these sections. In an extreme case, in the presence of a current of 1.8 times the speed of the undisturbed oscillatory flow, the inertia coefficient for the vertical oscillatory loading was reduced from its potential flow value by 50%. Current has large influence on inertia coefficients in the vertical direction: the inertia coefficients increase with increase in the following currents and decrease with increase in opposite current compared to the waves alone. Li and He (1995) carried out experiments on square cylinders of 40mm x 40mm and 60mm x 60mm, subjected to waves and currents and correlated the hydrodynamic coefficients with KC number for regular and random waves. The cylinder was also tested with a surface oriented to 45° to the wave. They concluded that drag coefficients obtained for random waves are smaller than those of regular waves. On the effect of changing the wave direction, they reported that, when $KC<18$, drag coefficients for a normally incident wave is greater than that of a diagonally incident wave, but when $KC>18$, C_D values for a diagonally incident wave is larger than that of a normally incident wave. C_M for a normally incident wave is bigger than that of a diagonally incident wave and it gradually decreases with increasing KC, where as, C_M for diagonal incident waves decreases first and reaches a minimum value at $KC = 18$ and then increases rapidly for higher values of KC number. In this study, the effect of current on the force coefficients is not explicitly discussed.

The force coefficients reported in the past for square cylinders [example: Bearman et al.(1979, 1984), Graham (1978), Singh(1979) and Tanaka et al (1982)] corresponds to the experiments performed either in a U-tube set-up or cylinder oscillating in still water. In the first case, the cylinder was held fixed and the fluid oscillated harmonically and in the second case the cylinder oscillated harmonically in still water with a given frequency and amplitude. In both the cases the flow is one-dimensional; whereas, when tests are conduced in a wave flume or basin, the flow is two-dimensional such that the free stream velocity field varies in both horizontal and vertical directions, and the generated waves are not necessarily sinusoidal. Further the development of the boundary layer and separation points are different between planer motion and wave motion and therefore the pressure distribution around the body will be different in both the methods and this yield differences in measured forces. For example, for a circular cylinder, Chakrabarti (1990) showed a comparison between his test results in waves with Sarpakaya (1976) results from planar motions, corresponding to a β value of 1085 as shown in Fig. 2.7 and this indicate a clear difference between planer tests and wave motion tests at this range of β. If the same were applied to a square or rectangular cylinder, then one would realise the significance and needs of the tests to be conducted in waves and unfortunately there have not been many test data are available for these cylinders in wavy flow and therefore the present work is undertaken.

The previous works on square/rectangular cylinders were mostly conducted at low Reynolds number. Among the very few results available for sharp edged rectangular cylinders, those reported by Arai (1993) are corresponding to a frequency parameter (β) from 750 to 6470. Although, sharp edged square cylinders are known to be less sensitive to Reynolds numbers effects in steady flow (refer Fig.2.8), it would be interesting to examine the effects in wavy flow on what would be the change in the force coefficients if the cylinders are tested for higher (β) values and this is experimented with the present model.

It is evident from the literature that the force coefficients in random waves can be different from the one obtained through regular waves. Although, the Morison's equation is commonly used for predicting wave forces in regular and irregular waves, the values of drag and inertia coefficients obtained for irregular wave forces are not necessarily the same as those determined from regular waves, especially at low *KC* numbers [Davies et al. (1990) and Li and He (1995)]. On the other hand, it is also expected that these force coefficients will depend on the shape of the spectrum. Hence, for these reasons it will be most appropriate to estimate force coefficients directly from random wave force measurements and this is carried out in the present work.

It is also inferred from the literature that the combined actions of waves superposed on currents are known to result different drag and inertia coefficients for circular cylinder compared to the force coefficients in waves alone. From the results reported by Chaplin and Retzler (1993), this is indeed true for a square cylinder (pontoon) with rounded corners. However, from the literature, it is apparent that except for the square cylinder, other rectangular sections, as considered in this study, does not seem to have any data in combined wave and currents and therefore this is another part to be looked into in detail.

It is understood from the literature that the wave run-up may lead to wave overtopping of the structure or create wave uplift forces on the underside of the structure. Previous researchers made run-up calculations only for circular cylinders and to the knowledge of the author none of the information is available on any of the experiments that were performed in waves to calculate the wave run-up for rectangular cylinders. Further, the wave run-up pattern for a rectangular cylinder might be different from the circular cylinder as they have flat vertical surfaces exposed to the wave crests and therefore it is essential to examine the run-up on square and rectangular cylinders.

More importantly, the influence on the force coefficients by varying the cross sectional area has not been reported in waves and also in combined waves & currents and hence this study will concentrate on this aspect. It is evident from the foregoing literature review that more laboratory investigations remain to be carried out for a better understanding and quantification of the wave and current forces on rectangular cylinders.

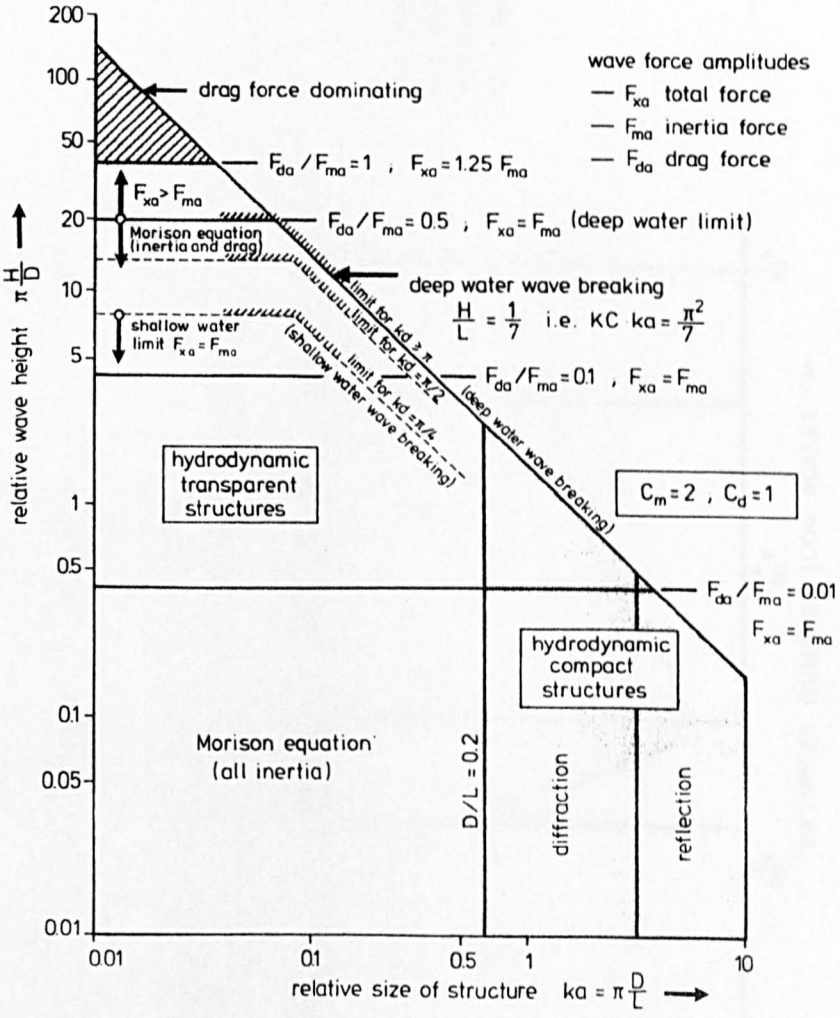

Fig.2.1 Loading regimes of horizontal forces on a vertical cylinder [Clauss et al., (1992)]

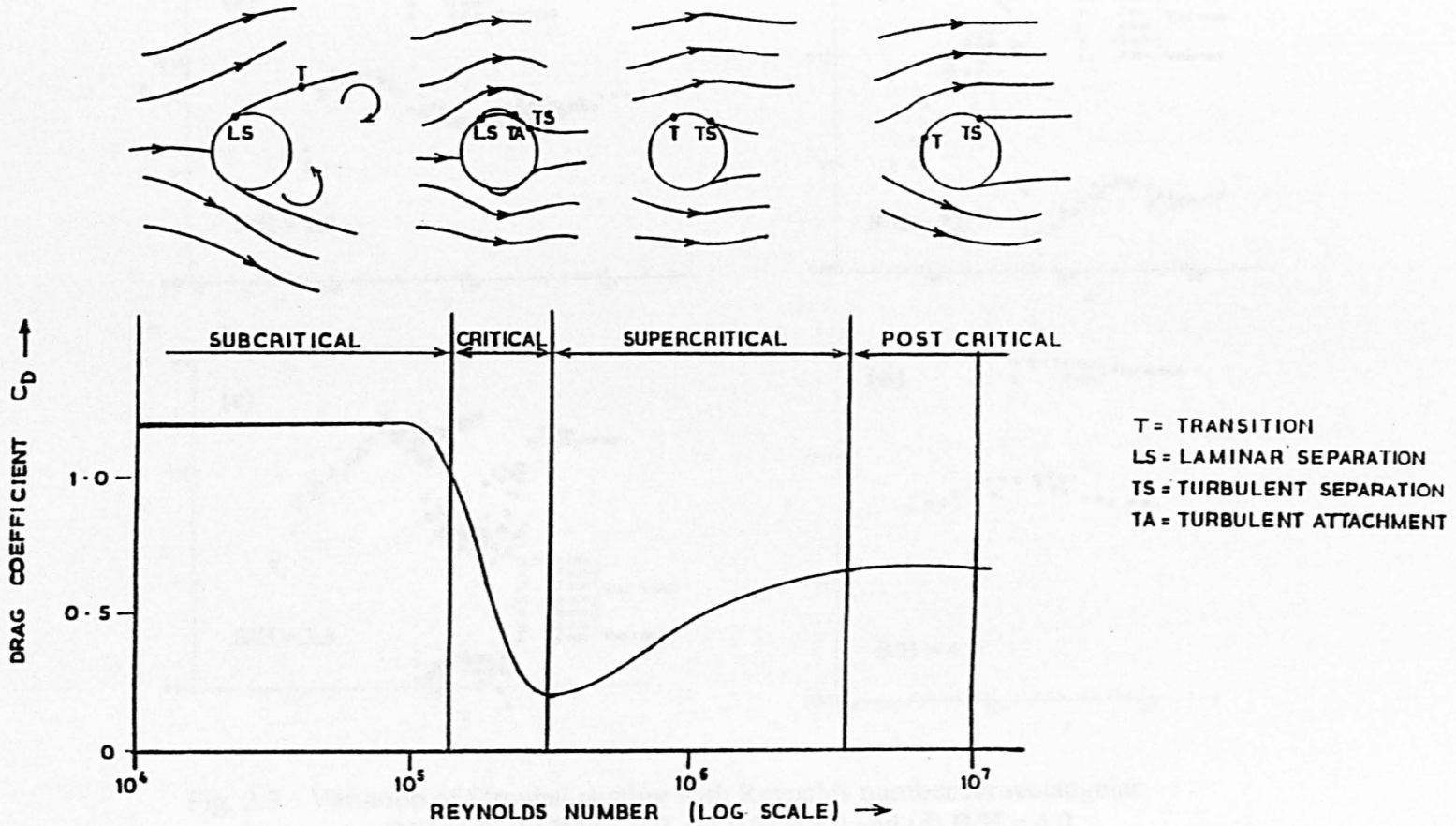

Fig. 2.2. Two dimensional flow over circular cylinder [Scruton (1981)]

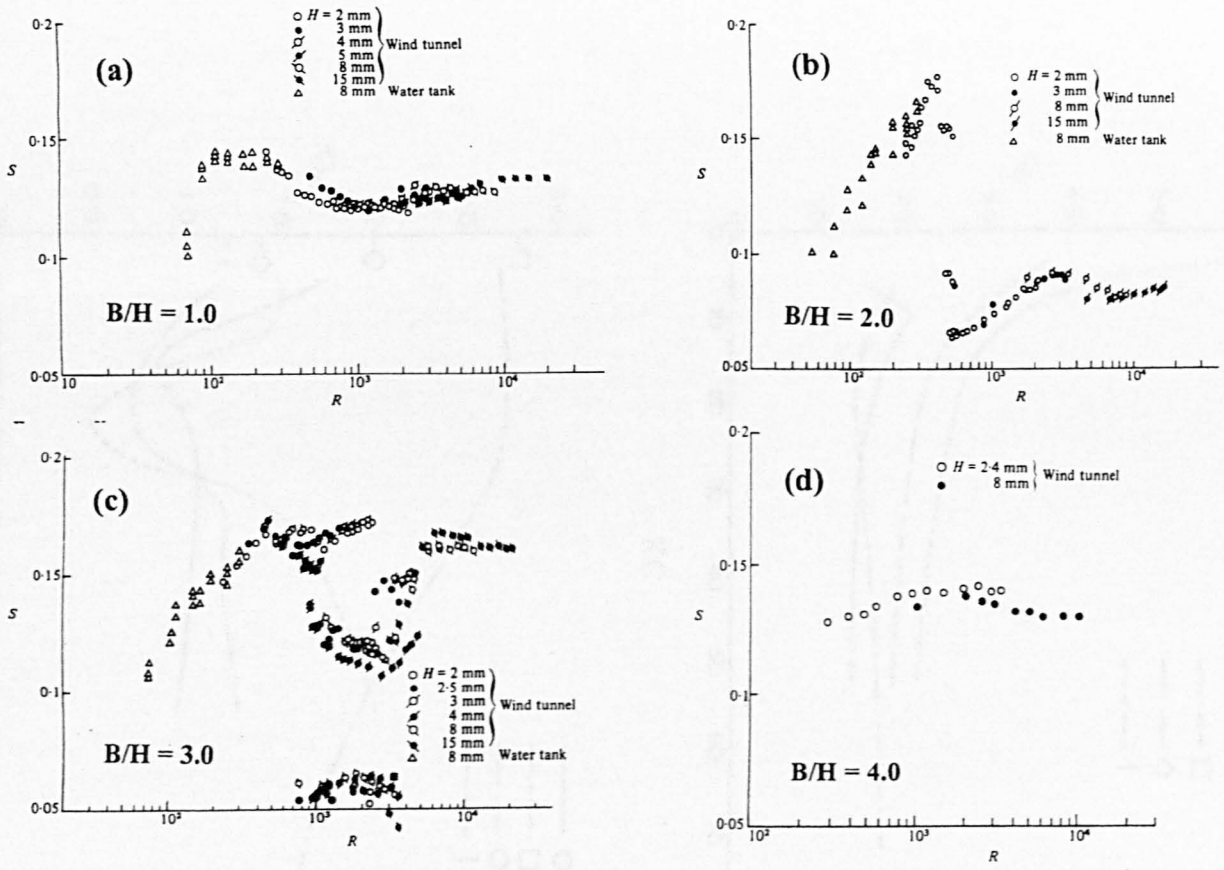

Fig. 2.3 Variation of Strouhal number with Reynolds number for rectangular cylinders; (a) B/H=1.0, (b) B/H = 2.0, (c) B/H = 3.0 and (d) B/H = 4.0

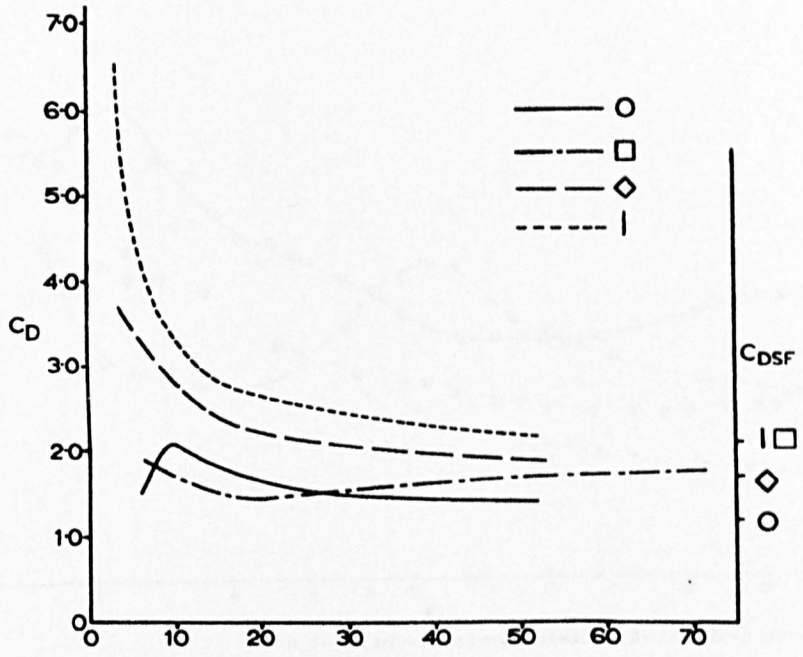

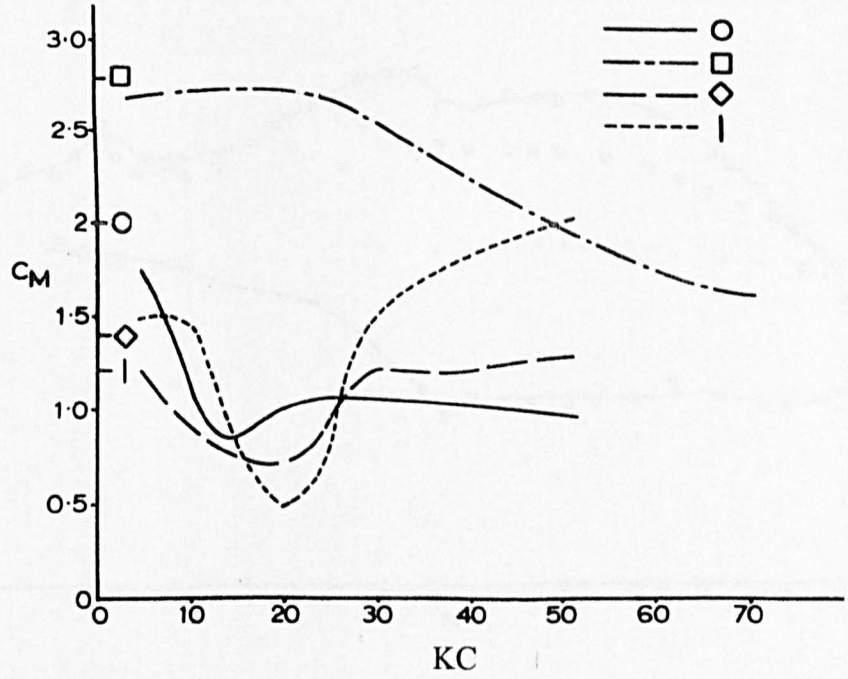

Fig. 2.4 Drag and inertia coefficients for various shapes [Bearman et al., (1979)]

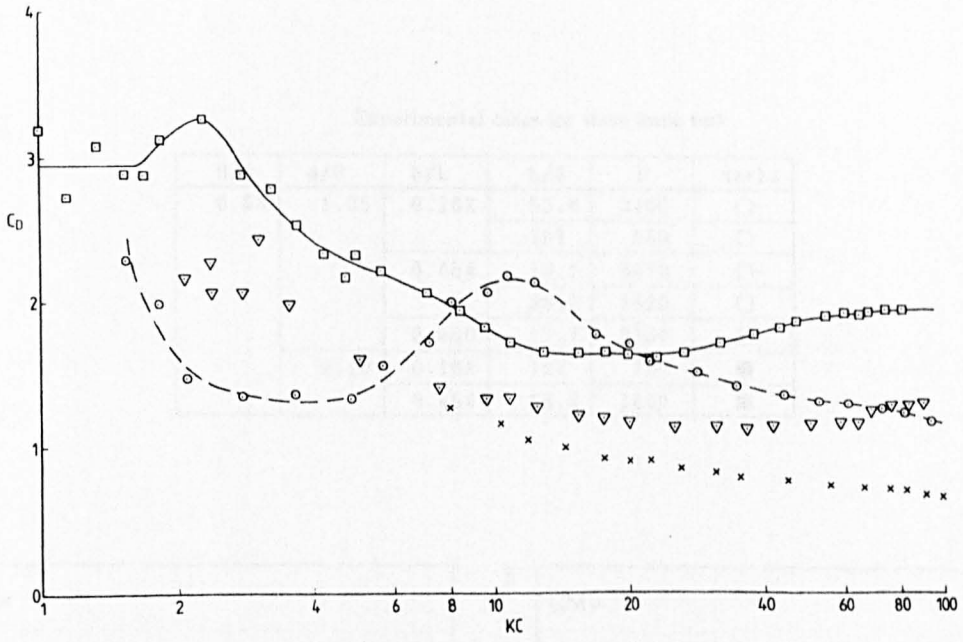

□, $\beta = 213$, $r/D = 0$ (sharp-edged cylinder): ▽, $\beta = 172$, $r/D = 0.132$; ×, $\beta = 172$, $r/D = 0.265$; ○, $\beta = 196$, $r/D = 0.5$ (circular cylinder)

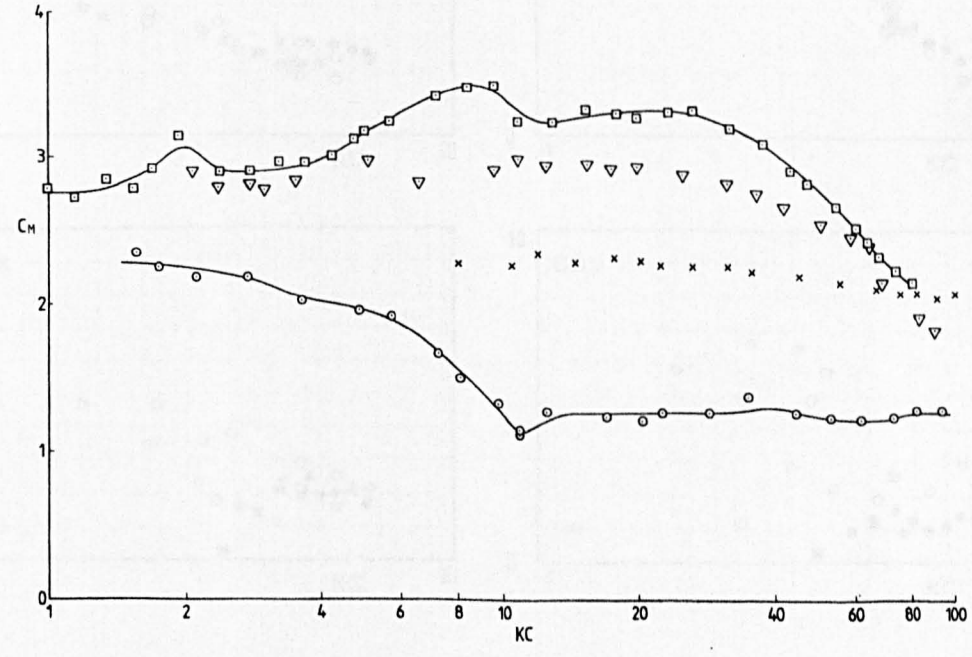

Fig. 2.5 Drag and inertia coefficients of a square cylinder [Bearman et al., (1984)]

Experimental cases for wave force test

H/B	d/B	h/L	L/B	β	marks
0.53	1.05	0.162	53.4	3400	○
			107	850	○
		0.454	19.1	6470	□
			38.2	1620	□
		0.980	17.7	2380	⊟
	2.10	0.162	107	750	●
		0.454	38.2	1430	■

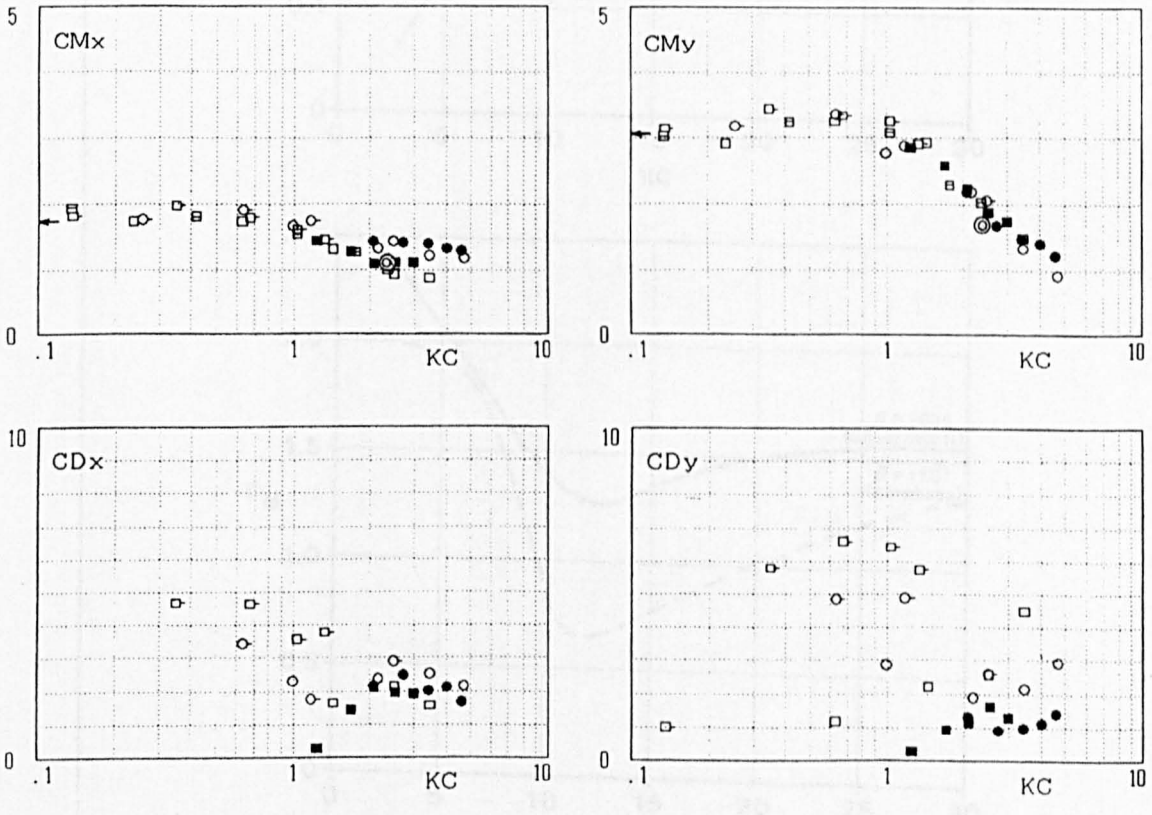

Fig. 2.6 Drag and inertia coefficients of a rectangular cylinder [Arai (1993)]

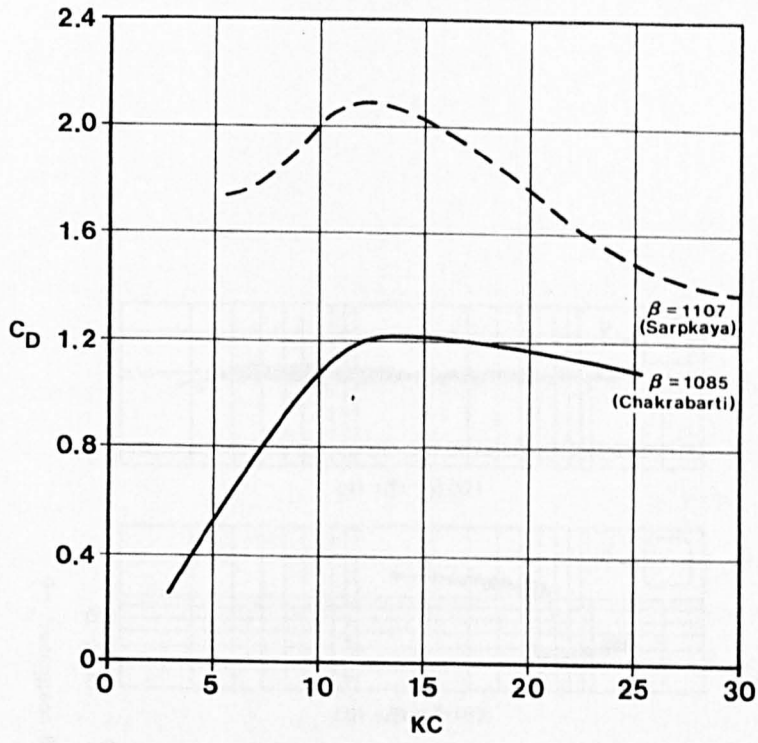

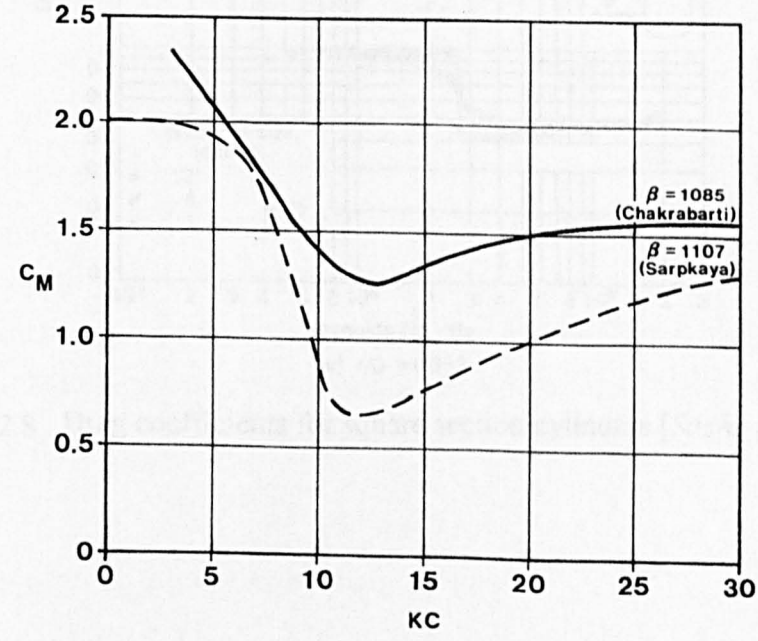

Fig. 2.7 Comparison of drag and inertia coefficients between free surface waves and oscillating flow tests [Chakrabarti (1990)].

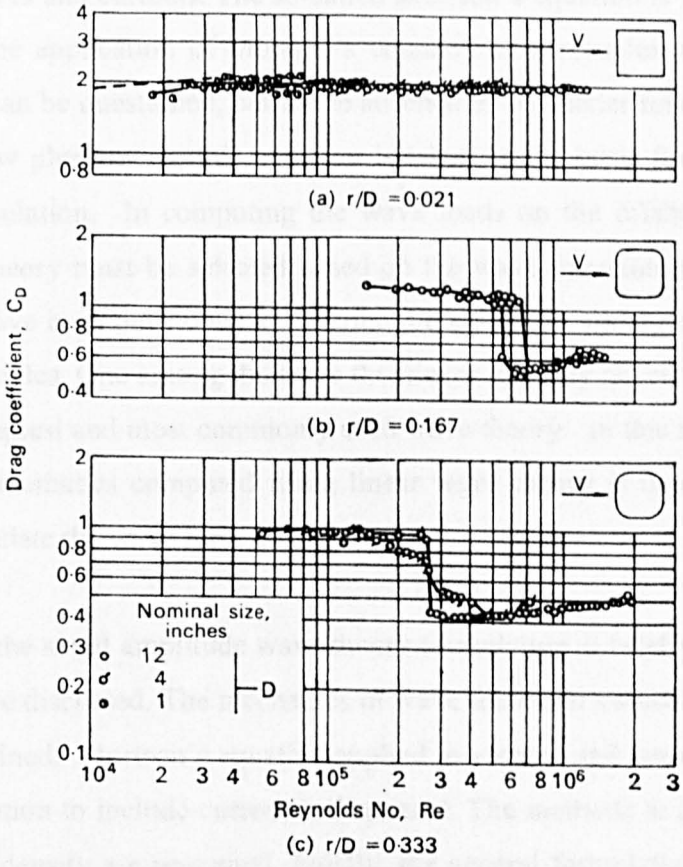

Fig. 2.8 Drag coefficients for square section cylinders [*Sachs (1978)*]

CHAPTER 3
THEORETICAL CONSIDERATIONS

3.1 General

A major factor in the design of offshore structures is to determine the hydrodynamics loads due to waves and currents. The so-called Morison's equation is widely used for this purpose. The application of Morison's equation to a complex time dependent separated flow can be questioned, but in the absence of any better formula which can describe the flow phenomena, this equation is taken as the basis for all the in-line wave force calculation. In computing the wave loads on the offshore structure, a suitable wave theory must be selected based on the wave parameters. A number of wave theories have been developed to describe the kinematic and dynamic properties of the water particles. One among the wave theories is the Airy or linear wave theory, which is the simplest and most commonly used wave theory. In this thesis work, the wave particle kinematics computed using linear wave theory is used in Morison's equation to calculate the wave forces.

In this chapter, the small amplitude wave theory formulation is briefly explained and its limitations are discussed. The mechanics of wave forces on vertical and horizontal cylinders is outlined. Morison's equation applied to vertical and horizontal cylinders and its modification to include current is discussed. The methods to determine wave energy spectral density are presented. Finally, the general formulations and solution procedure for diffraction force calculations are also described.

3.2 Small Amplitude Wave Theory (Airy Theory)

In the laboratory studies the water particle velocity beside the structure can be measured using some instrumentation. These measurements can be differentiated with respect to time to calculate the corresponding water particle acceleration.

However, if such measurements are not available and if only estimates of wave height and corresponding period are available, then the particle kinematics must be estimated using some wave theory. For the formulation of wave theories the potential function $\phi(x,z,t)$ of a two dimensional fluid flow must satisfy the linear governing differential equation or Laplace equation and three boundary conditions [Dean & Dalrymple, 1991]. Finding an exact solution to Laplace equation is difficult due to:

- The free surface boundary conditions are non-linear
- The free surface boundary conditions must be satisfied at the free surface z = η which is constantly changing

There are two general types of approximate theory, which is used to solve the above problem

- One is developed around the wave steepness as a perturbation parameter
- Second is developed as a function of water depth

In the first case the perturbation parameters are limited to a given order of the wave theory. The linear wave theory or Airy theory and the stokes third-order and fifth-order non-linear wave theory are placed in this category and are commonly used in the design of deep-water offshore structures. In this case there is a closed form solution to the problem and the water particle kinematics and dynamic pressures can be calculated through known formulae. In the second case the order of the wave theory remains general and a numerical solution is used to satisfy the boundary condition. The stream function theory is the example that falls in this category [Dean& Dalrymple, 1991].

The most useful and simplest of all wave theories is the small amplitude wave theory, which is also called Airy wave theory or sinusoidal wave theory. It was given by G.B.Airy in 1842. Because of the linearity of the Airy theory with wave height, the computation of the structural response using this theory is often quite straightforward,

though the response is not necessarily linear [Chakrabarti, 1990]. This theory has often been used in design for analysing both linear and non-linear behaviour of offshore structures in their extreme value response analyses. In order to form a tractable solution the following simplifying assumptions are made:

- The water is of constant depth
- The wave motion is two-dimensional, which leads to long crested waves with constant height along the crests
- The waves are of constant form, i.e., they do not change with time
- The fluid (water) is incompressible
- Effects of viscosity, turbulence and surface tension are neglected
- The wave height, H is small compared to the wave length, L and the water depth, d (i.e. $H/L << 1$ and $H/d << 1$)

The governing equations to be solved represent the equations for conservation of mass and momentum. Conservation of mass can be written in terms of Laplace Equation

$$\frac{\partial^2 \phi}{\partial x^2} + \frac{\partial^2 \phi}{\partial z^2} = 0 \tag{3.1}$$

where x and z are the horizontal and vertical coordinates respectively, of the two-dimensional solution domain. The horizontal and vertical components of velocity, u and w are given as

$$u(x,z,t) = \frac{\partial \phi}{\partial x} \tag{3.2}$$

$$w(x,z,t) = \frac{\partial \phi}{\partial z} \tag{3.3}$$

and t is the time.

The conservation of momentum is represented by the unsteady Bernoulli equation

$$\frac{\partial \phi}{\partial t}+\frac{1}{2}(u^2+w^2)+\frac{p}{\rho}+gz=0 \qquad (3.4)$$

Where p is the pressure, ρ the density of the water and g is the gravitational acceleration. In small waves, $u^2+w^2 \to 0$. The boundary conditions are shown in Fig. 3.1.

(i) Dynamic boundary condition at the free surface:

At the free surface, $z = \eta$, the pressure is atmospheric, $p = 0$. Therefore (3.4) becomes

$$\frac{\partial \phi}{\partial t}+g\eta = 0 \text{ at } z=0 \qquad (3.5)$$

This boundary condition is applied at $z = 0$ rather than $z=\eta$ due to the assumption that the waves are of small amplitude (i.e. $\eta \to 0$).

(ii) Kinematic boundary condition at the free surface:

At the free surface, there can be no transport of fluid through the free surface and therefore the vertical velocity of the free surface is equal to the vertical velocity of the fluid (i.e $w = D/Dt[\eta(x,t)]$).

$$w=\frac{\partial \eta}{\partial t}+u\frac{\partial \eta}{\partial x} \quad \text{at } z=\eta \qquad (3.6)$$

substituting (3.3) for w into (3.6) with the assumption that the slope of water surface $\frac{\partial \eta}{\partial x}$ is small ,

$$\frac{\partial \phi}{\partial z} = \frac{\partial \eta}{\partial t} \quad \text{at } z = 0 \tag{3.7}$$

(iii) Kinematic boundary conditions at the bed:

There can be no flow through the soil bed and therefore the kinematic boundary condition at the bottom

$$w = \frac{\partial \phi}{\partial z} = 0 \quad \text{at } z = -d \tag{3.8}$$

Now, (3.1) can be solved using the boundary conditions (3.5), (3.7) and (3.8). The solution can be found by using method of separation of variables as

$$\phi(x,z,t) = \frac{ag}{\omega} \frac{\cosh\left[k(d+z)\right]}{\cosh\left[kd\right]} \sin(kx - \omega t) \tag{3.9}$$

where $a = H/2$ is the wave amplitude , $\omega = 2\pi/T$ is the wave angular frequency, $k = 2\pi/L$ is the wave number, T is the wave period and x & t are variables of space and time. From (3.9) the basic wave properties of linear waves can be developed [see, Chakrabarti (1987), Barltrop & Adams, 1991] and are summarised as:

The wave elevation:

$$\eta(x,t) = \frac{H}{2} cos(kx - \omega t) \tag{3.10}$$

The horizontal particle velocity:

$$u(x,z,t) = \frac{\pi H}{T}\frac{\cosh\left[k(d+z)\right]}{\sinh(kd)}\cos(kx-\omega t) \tag{3.11}$$

The vertical particle velocity:

$$w(x,z,t) = \frac{\pi H}{T}\frac{\sinh\left[k(d+z)\right]}{\sinh(kd)}\sin(kx-\omega t) \tag{3.12}$$

The horizontal particle acceleration:

$$\dot{u}(x,z,t) = \frac{2\pi^2 H}{T^2}\frac{\cosh\left[k(d+z)\right]}{\sinh(kd)}\sin(kx-\omega t) \tag{3.13}$$

The vertical particle acceleration:

$$\dot{w}(x,z,t) = -\frac{2\pi^2 H}{T^2}\frac{\sinh\left[k(d+z)\right]}{\sinh(kd)}\cos(kx-\omega t) \tag{3.14}$$

and the dynamic pressure:

$$p = \rho g\frac{H}{2}\frac{\cosh\left[k(d+z)\right]}{\cosh(kd)}\cos(kx-\omega t) \tag{3.15}$$

The dispersion equation describing the relationship between the wave frequency and wave number is given as

$$\omega^2 = gk\tanh(kd) \tag{3.16}$$

The diagrammatic representation of the motion of a fluid particle beneath a wave is shown in Fig. 3.2 [Chakrabarti, 1987].

3.3 Limitations of Linear wave theory

The linear wave theory assumed that the wave height is so small that the dynamic and kinematic boundary conditions at the free surface could be applied at the still water level, $z = 0$ rather than at the wave surface $z = \eta$. In nature the wave steepness, H/L seldom exceeds 0.05 to 0.08 (Svendsen and Jonsson, 1976) and hence the small amplitude assumption is valid. However, there are some applications, where the simplifying assumptions of linear wave theory become significant. In such cases it is necessary to use a non-linear or finite amplitude wave theory. Basically the difference between linear and finite amplitude theories is that finite amplitude theories consider the influence of the wave itself on its properties. Therefore, in contrast to linear wave theory, the phase speed, wavelength and water surface profile are functions of the actual wave height. Linear wave theory predicts that the crest and trough heights of the wave are equal. The finite amplitude theories predict wave with peaked crest and flat troughs. Hence in applications such as deck elevation calculation of an offshore structure, the use of finite amplitude wave theory would be important. Linear wave theory predicts that water particles move in closed orbits and hence there is no net transport of fluid. In contrast finite amplitude theory predicts a small net fluid transport in the direction of wave propagation. Fig. 3.3 adopted from Barltrop et al., (1991) illustrates the region of application of linear wave theory along with other wave theories.

3.4 Hydrodynamic Forces

The wave forces on an offshore structure are dependent on the size and shape of the structure and also on the wave characteristics. If the characteristic dimension, say, the diameter 'D' of a circular cylinder, is small relative to the wave length 'L' to the limit that $D/L < 0.2$, there is a little alteration of the incident wave when it passes the structure and therefore the diffraction and reflection phenomena are negligible. Force

effects on structures arise from pressure fields, which are approximately superposed as scalar quantities (Clauss et al.(1992)):

- Froude-Krylov force due to the pressure field of the undisturbed incident waves
- Hydrodynamic added mass force due to the pressure field derived from relative acceleration between structural element and fluid
- Drag force due to the pressure field resulting from the relative velocity between structural element and fluid in a viscous flow, which causes a wake region on the downstream side of the structure.

The Morison's equation is applicable when the drag force is significant. When the drag force is small and inertia force predominates, the Froude-Krylov and added mass forces are dominant.

Morison's equation has been used extensively, in predictions of loads on structures, in field experiments and in controlled laboratory experiments, resulting in an abundance of available drag and inertia coefficients for circular cylinders. However, in spite of the wide experience gained from the use of Morison's equation, considerable disagreement and uncertainties still exist about its applicability as a tool for prediction, and on the reliability of the coefficients to be used with it. One of the problems arises from the fact that the coefficients for full-scale use cannot be obtained from laboratory tests, as these are usually at a lower Reynolds number. In addition, the incident flow during laboratory tests is not usually representative of real sea conditions as these tests are commonly done in regular waves or in planar oscillatory flow. Planar oscillatory flow represents a simpler case where the orbit is flat as opposed to elliptical, in waves.

Numerous studies have been reported which attempt to relate the coefficients to dimensionless numbers such as Reynolds number (Re) and Keulegan - Carpenter number (KC) and the results have often shown considerable scatter. This scatter is

attributed to many reasons such as experimental errors, the variation of turbulence in the flow, cylinder roughness, and interference from other structures and the effect of the vortices sweeping back against the cylinder. Scatter in field data and laboratory experiments is also discussed by Dean (1976). In addition to the effects mentioned above, other factors such as irregularity of the incident wave, three dimensionality of the flow and different span wise correlation contribute to the scatter in the field. The methods used in data analysis, both, in field tests and laboratory studies can also induce scatter in the available data. This is particularly relevant to experiments where water particle velocities and accelerations are calculated from measurements of surface elevations coupled with some wave theory. The accuracy of the data thus obtained will depend on the choice of the wave theory and even if the best available theory is used, there is no guarantee that the wave characteristics will be the same from cycle to cycle, especially in field tests.

3.5 Mechanics of Wave Forces

3.5.1 Vertical Cylinder in Waves

The fluid loading on a vertical cylinder is different from that on a horizontal cylinder, fully submerged with its axis parallel to the wave crests. The orientation of a member affects the values of inertia and drag coefficients (Pearcey, 1979). For a vertical cylinder in regular, deep water waves and piercing the free surface, the water-particle circular orbits are co-planar with the axis of the cylinder and the velocity vector which is constant in magnitude has components normal and parallel to the axis of the cylinder. The position of flow separation and the vortex shedding is dependent only on the normal component and the parallel component is not expected to influence the flow phenomena external to the cylinder. The periodic motion is similar to the planar oscillatory motion with the stagnation point on the cylinder switching from fore to aft of the cylinder and then back once in each cycle. Therefore, the whole flow field in the plane normal to the cylinder's axis, generated by the cylinder, accelerates from rest and decelerates again in each half cycle before reversing in the next. The

vortices shed by the cylinder in one half cycle and the velocity deficit of its wake are periodically swept back past the cylinder strongly influencing the flow induced loading. A diagrammatic representation of a vertical cylinder (Pearcey, 1979) in regular, deep-water waves with particle motions in circular orbits is shown in Fig.3.4. The orbits are co-planar with the axis of the cylinder and the velocity vector, constant in magnitude, has components *X, Z* normal and parallel to the axis. The position of separation and vortex shedding will be dependent only on the component normal to the axis. With regard to transverse forces, they can only be associated with vortex effects. Large transverse forces as observed for vertical cylinders are therefore clear evidence that the vortices have significance coherence along the length of the cylinder in spite of the decay of orbital motions with depth. The difference between the vertical cylinder in waves and the cylinder in planar oscillatory incident flow may arise from the component of orbital velocity resolved parallel to the axis of the cylinder or from a smaller wake interaction effect in waves.

3.5.2 Horizontal Cylinder in Waves

For a horizontal cylinder fully submerged in regular, deep water waves with its axis parallel to the wave crests, the plane of the water particles circular orbits is normal to the axis of the cylinder with no axial component of velocity, and also no variation in phase along the length of the cylinder (Fig. 3.5). The forces associated with vortex shedding are co-planar with the orbits and hence there is no force transverse to the plane of the orbits. The velocity vector, constant in magnitude, has vertical and horizontal components both normal to the axis of the cylinder and with associated forces having vertical and horizontal periodic components (Pearcey, 1979).

The forces will have the following principal elements:

- A 'tangential' drag element associated with the tangential velocity, influenced by the separated flow and vortex shedding.
- A vortex induced element normal to this and therefore radial.

- A radial inertia element associated with the Froude-Krylov force and virtual added mass, the later being influenced by viscous flow.
- Each of these elements will have horizontal and vertical components. The resulting total horizontal and vertical components, X and Z do not differ from one another in principle, but, are orthogonal in phase. Each component has a resolved part of each of the three principal elements described above. The resolved parts of the tangential drag and radial inertia will be periodic with the wave motion. The magnitude of the resolved part of the radial vortex element will also vary cyclically.

3.6 Morison Equation for Regular Waves

3.6.1 Vertical Cylinder

3.6.1.1 In-line Force

The semi-empirical force model developed by Morison et al., (1950) has been the most widely used method since its introduction. This approach depends upon a knowledge of water particle kinematics and empirically determined coefficients. The wave force F_H, per unit length on a vertical surface piercing cylindrical pile structure is composed of two parts, one due to drag, and the other due to acceleration of the fluid. This concept necessitates the introduction of a drag coefficient, C_D and an inertia coefficient, C_M in the expression for the force. It should be noted that drag and inertia coefficients cannot be obtained from equations of motion and that the validity of the equation and the limits of its application will have to be determined experimentally. The inertia forces may be interpreted as that due to the pressure gradient associated with the relative acceleration of the ambient fluid. The drag forces are, in general, due to the flow separation induced by the relative velocity of the fluid and structure.

The drag and inertia coefficients are usually functions of Keulegan–Carpenter (KC) number, Reynolds (Re) number, cylinder surface roughness parameters and

interaction parameters. For large values of Keulegan-Carpenter number, when acceleration is small for substantial parts of each cycle, the inertia force term in Morison's equation is negligible and the force approaches the drag force for a cylinder in a steady flow. Conversely, for small values of KC, the drag term is negligible in comparison to the inertia term and the force becomes the pure inertia force associated with the Froude-Krylov and virtual added mass terms calculable from potential flow theory. For values of KC between these extremes, the studies have shown that the drag as well as inertia terms can be strongly influenced by viscous flows. It is well known that over the middle range of KC numbers neither the Morison's equation nor one equivalent to it, can provide an adequate basis for describing the forces transverse to the wave direction and these forces are linked with the vortex velocity fields and motions. At high KC number a lift coefficient can provide an estimate of the transverse fluctuating force on a circular cylinder. The value is however dependent on the motion of the cylinder (see section 3.6.1.2).

In the Morison's equation, drag is proportional to the square of the fluid velocity u and inertia is proportional to the fluid acceleration $\dot{u}$ and the equation for a rectangular cylinder is given by,

$$F_H = \frac{1}{2}\rho\, C_D\, D u|u| + \rho\, C_M\, A\dot{u} \tag{3.17}$$

where,

ρ = Mass density of water

u = In-line water particle velocity

$\dot{u}$ = In-line water particle acceleration

D = Dimension of the cylinder, taken as the side normal to wave direction

A = Cross sectional area of the cylinder

If the forces are calculated using linear wave theory, then the wave surface profile, particle velocity and acceleration are computed using equations (3.10) to (3.14). For the non-linear waves, the wave surface elevation and particle kinematics would be

computed using an appropriate non-linear wave theory such as Stokes wave theories or Stream function wave theory. In the experiments linear theory is expected to be a good predictor of particle kinematics (see section 5.2).

The general form of Morison's equation is used to determine wave force under the restriction that the convective acceleration terms $\partial u/\partial x$ and $\partial u/\partial z$ [Sarpkaya and Isaacson (1981)] are normally ignored (i.e., it is assumed that $du/dt \approx \partial u/\partial t$), furthermore, it is assumed that in the region near the cylinder the kinematics of the undisturbed flow does not change in the incident wave direction. Regarding the ignored convective acceleration terms, it can be shown that the local horizontal acceleration $\partial u/\partial t$ is more than total horizontal acceleration ($\partial u/\partial t + u\partial u/\partial x + w\partial u/\partial z$, where, u and w represent the velocity components in x and z directions respectively) over a wave cycle on the basis of the stream function theory for two design waves of the same depth and period [Refer Fig. 4.24 from Sarpkaya and Isaacson (1981)]. This difference is more significant if steep waves are considered. It can be shown that the use of local acceleration instead of total acceleration to determine the inertia force will generally lead to overestimates. This inaccuracy does not affect the practical application of the Morison's equation which in any case depends on experimental coefficients [Sarpkaya and Issacson (1981)].

3.6.1.2 Transverse Force

The transverse or lift forces acting on a vertical cylinder in waves may be represented in terms, which are related to the case of a cylinder in harmonic flows. However, there are important differences between flow in waves and in harmonic flow. In the case of harmonic flow the incident fluid motion is uniform along the cylinder, but for a vertical cylinder in waves the incident fluid motion varies along its axis of the cylinder and possesses a vertical velocity component. Due to the formation of wake behind the cylinder during the passage of the wave, lift forces occur at right angles to the flow as eddies form and shed from the cylinder surface. A formula used in calculating the lift forces per unit length of the cylinder is given by,

$$F_L(t) = \frac{1}{2} C_L \rho D u^2(t) \tag{3.18}$$

where, C_L is the lift coefficient.

The lift force, in general, has multiple lift frequencies due to a single wave oscillation frequency and therefore, the lift force per unit length can be expressed as,

$$F_L(t) = \frac{1}{2} \rho D U_m^2 \sum_{n=1}^{N} C_L(n) \cos[2\pi n f_O t + \psi(n)] \tag{3.19}$$

where, U_m is the maximum horizontal velocity, $C_L(n)$ is the lift coefficient for the nth harmonic and is assumed to be a function of KC number, f_o is the cyclic wave frequency, N is the number of harmonics and $\psi(n)$ is the phase angle for the nth harmonic force. Simplifying the above equation for $C_L(n)$, we get,

$$C_L(n)\cos\psi(n) = \frac{2}{T}\int_0^T \frac{2\ F_L(t)}{\rho\ D\ U_m^2} \cos[2\pi n f_O t]\, dt \tag{3.20}$$

$$C_L(n)\sin\psi(n) = \frac{2}{T}\int_0^T \frac{2\ F_L(t)}{\rho\ D\ U_m^2} \sin[2\pi n f_O t]\, dt \tag{3.21}$$

From equations (3.20) and (3.21) the values of $C_L(n)$ and $\psi(n)$ can be calculated.

3.6.2 Horizontal Cylinder

The Morison's equation was originally applied to vertical cylinders using only the horizontal water particle velocity. However, for a horizontal cylinder in waves, the vertical component of the water particle velocity is also significant. Chaplin (1988b) discussed the effects of the free surface and bed boundaries, effects of circulation and

the form of Morison's equation to be used for a horizontal cylinder in waves. Chaplin (1988b) reported that a good agreement between measured and simulated forces could be obtained by assigning separate force coefficients for the vertical and horizontal directions. In the present study, the Morison's equation is modified and the forces per unit length of the horizontally submerged rectangular cylinder is expressed as

$$F_X = \frac{1}{2}\rho C_{DX} D u\sqrt{(u^2 + w^2)} + \rho C_{MX} A \dot{u} \tag{3.22}$$

$$F_Y = \frac{1}{2}\rho C_{DY} B w\sqrt{(u^2 + w^2)} + \rho C_{MY} A \dot{w} \tag{3.23}$$

Where, F_X = Wave force in horizontal direction

F_Y = Wave force in vertical direction

C_{DX} = Drag coefficient in horizontal direction

C_{DY} = Drag coefficient in vertical direction

C_{MX} = Inertia coefficient in horizontal direction

C_{MY} = Inertia coefficient in vertical direction

D = Cylinder section depth in vertical direction

B = Cylinder section width in horizontal direction

A = Cross sectional area of the cylinder

u = Horizontal particle velocity

$\dot{u}$ = Horizontal particle acceleration

w = Vertical particle velocity

$\dot{w}$ = Vertical particle acceleration

In addition to the drag and inertia forces, a lift force is also associated with the loading on a horizontal cylinder. This lift force is perpendicular to the velocity vector and rotates around the axis of the cylinder because of the orbital motion of the water particles. However, the magnitude, direction and period of the lift force are unknown, they cannot be added to the Morison's equation and the effect of the vortex shedding

will therefore be shown up as noise in the measurements of the drag and inertia components [Teng and Nath (1985)].

3.7 Morison Equation for Regular Waves and Currents

3.7.1 Vertical Cylinder

Currents commonly occur in the ocean and offshore platforms operate in areas where waves propagate on currents. The interaction of waves and currents and resulting effect on the response of the structure must be considered for the design of an offshore structure. The existence of currents will change the wave parameters and the wave kinematics. The wave and current loading on offshore structures is of a highly non-linear nature due to the non-linear drag force and free surface effects. These non-linearities in the load process may introduce non-linear structural response even if the structure acts as a linear system. Furthermore, non-linear behaviour also implies that the hydrodynamic drag damping caused by the relative velocity between the structure and the surrounding fluid is very important for these concepts and there are significant uncertainties related to the calculation of environmental loads on these structures.

Sarpkaya and Storm (1985) discuss how the coexisting flow fields in a laboratory can be produced by: (i) translating a cylinder in a flume, (ii) oscillating a cylinder in a uniform stream, (iii) moving a cylinder with constant velocity while oscillating it in the desired direction, (iv) by subjecting a fixed cylinder to an oscillating flow with a mean velocity or (v) by translating a cylinder in an oscillating flow and suggested that the method (v) will be more suitable in isolating the effect of current on fluid loading. Teng and Nath (1985) mentioned that towing a cylinder with uniform speed in a wave field takes into account the orbital motion of the water particles and it simulates the linear superposition principle for considering waves and current together. This method is found to be easier and realistic in situations where the simultaneous

generation of waves and current is not possible and hence this method was followed in the present study.

When the cylinder is towed in waves with a speed, U_C, the time period experienced by the cylinder is different from the actual wave period (T) and this can be called as apparent period, T_a, is given by (Teng and Nath (1985)),

$$T_a = \frac{T}{1 - \frac{U_C}{C_W}} \tag{3.24}$$

Where, U_C = current velocity or towing speed and C_W = wave celerity. The current velocity is taken as positive when the cylinder is towed in the direction of wave propagation and negative when the cylinder moves opposite to the direction of wave propagation. Similarly, the time scale during one wave cycle and phase angle can be expressed by equations (3.25) & (3.26) respectively,

$$t_a = \frac{t}{1 - \frac{U_C}{C_W}} \tag{3.25}$$

$$\theta_a = \frac{2\pi t}{T} = \frac{2\pi t_a}{T_a} \tag{3.26}$$

In this thesis, wave period T_a has been used for the calculations of dimensionless parameters, such as KC and Re numbers.

In wave and current coexisting fields Morison's equation for a circular cylinder can be written as follows [Iwagaki et al., (1984), Li &Ye (1990) and Li & Kang (1992)];

$$F = \frac{1}{2}\rho\, C_D\, D(u+U_C)\left|(u+U_C)\right| + \rho\, C_M \frac{\pi D^2}{4}\dot{u} \tag{3.27}$$

where U_C is the current velocity and other parameters are already defined. The above equation in terms of total horizontal acceleration can be written by [Bearman et al., (1994)]

$$F = \frac{1}{2}\rho\, C_D\, D(u+U_C)\left|(u+U_C)\right| + \rho\, C_M \frac{\pi D^2}{4}\frac{d(u+U_C)}{dt} \qquad (3.28)$$

where

$$\frac{d(u+U_C)}{dt} = \frac{\partial(u+U_C)}{\partial t} + (u+U_C)\frac{\partial(u+U_C)}{\partial x} + w\frac{\partial(u+U_C)}{\partial y} \qquad (3.29)$$

For a large uniform value of current and for linear wave theory the above equation may be simplified as

$$\frac{d(u+U_C)}{dt} = \frac{\partial u}{\partial t} + U_C\frac{\partial u}{\partial x} = (1-\frac{U_C k}{\omega})\dot{u} \qquad (3.30)$$

Substituting equation (3.30) in equation (3.28) an extension of Morison's equation can be formed as

$$F = \frac{1}{2}\rho C_D D(u+U_C)\left|(u+U_C)\right| + \rho C_M \frac{\pi D^2}{4}(1-\frac{U_C k}{\omega})\dot{u} \qquad (3.31)$$

This modification of Morison's equation when compared with equation (3.27) implies that currents following to the wave direction increase the inertia force and opposite to the wave direction decrease it.

An alternative form for equation (3.27) may be written so that the effect of current is separated from the wave motion. Then Morison's equation in three terms is given by

$$F = \frac{1}{2}\rho C_D D (C_{D1} u|u| + C_{D2} U_C^2) + \rho C_{M1} \frac{\pi D^2}{4} \dot{u} \qquad (3.32)$$

Sarpkaya et al., (1984) by using the above equation in a test with wave and uniform current co-existing field found that the coefficients C_{MI} and C_{DI} are much different from those in wave only situation. They concluded that the separation of two terms Morison's equation into three terms is not meaningful.

3.7.2 Horizontal Cylinder

When a current is superposed on the waves, first, the current will generate a mean drag in the horizontal direction, which can be expressed in terms of drag coefficient in the usual way and second, the current, combined with viscosity-induced circulation around the cylinder will produce a steady vertical lift, proportional to the product of the current speed and the square of the wave amplitude. When the current flows in the direction of wave propagation, the steady lift will act upwards and for opposite current and waves the lift will act downwards. However, in the case of horizontal cylinders, Morison's equation can be modified for the coexisting case of waves and currents by replacing 'u' by '$u+U_C$ '. Where, u is the horizontal water particle velocity and U_C is the current velocity. The horizontal and vertical forces are calculated from the following expressions,

$$F_X = \frac{1}{2}\rho C_{DX} D (u \pm U_C)\sqrt{((u \pm U_C)^2 + w^2)} + \rho C_{MX} A \dot{u} \qquad (3.33)$$

$$F_Y = \frac{1}{2}\rho C_{DY} B w\sqrt{((u \pm U_C)^2 + w^2)} + \rho C_{MY} A \dot{w} \qquad (3.34)$$

The inertia forces are related to local accelerations that do not include the convective contributions $u\partial u/\partial x$, $u\partial w/\partial x$.

3.8 Morison Equation and Random Waves

3.8.1 Random Wave Model

In general, the sea surface elevation, $\eta(t)$, may be described as an evolutionary stochastic process. However, for short term intervals of the order of a few hours, the sea surface is assumed to be a zero mean, stationary Gaussian process. This means that the statistical properties of the waves are completely described by the mean square spectrum. It is assumed that the waves are uni-directional and long crested and that linear wave theory can be used to relate the water particle kinematics to the surface elevation. Since the governing equation (Laplace equation) and boundary conditions are linear in small amplitude wave theory, it is known from mathematics that small amplitude waves are superposable. This means that the superposition of a number of linear waves with different wave height and wave period results in a random wave. Then the profile of a random wave can be expressed as

$$\eta(x,t) = \sum_{n=1}^{N} \frac{1}{2} H_n \cos(k_n x - \omega_n t + \varepsilon_n) \tag{3.35}$$

where, H_n = wave height, $k_n = 2\pi / L_n$, L_n = wave length at the frequency ω_n, ε_n = the phase associated with the nth component and N is the number of waves.

The random wave water particle velocities and accelerations are given by

$$u = \sum_{n=1}^{N} \frac{1}{2} \omega_n H_n \frac{\cosh\left[k_n (d+z)\right]}{\sinh(k_n d)} \cos(k_n x - \omega_n t + \varepsilon_n) \tag{3.36}$$

$$w = \sum_{n=1}^{N} \frac{1}{2} \omega_n H_n \frac{\sinh\left[k_n (d+z)\right]}{\sinh(k_n d)} \sin(k_n x - \omega_n t + \varepsilon_n) \tag{3.37}$$

$$\dot{u} = \sum_{n=1}^{N} \frac{1}{2} \omega_n^2 H_n \frac{\cosh\left[k_n (d+z)\right]}{\sinh(k_n d)} \sin(k_n x - \omega_n t + \varepsilon_n) \tag{3.38}$$

$$\dot{w} = -\sum_{n=1}^{N} \frac{1}{2} \omega_n^2 H_n \frac{\sinh\left[k_n (d+z)\right]}{\sinh(k_n d)} \cos(k_n x - \omega_n t + \varepsilon_n) \tag{3.39}$$

where, z is the depth at which the kinematics are to be computed, and is measured positive upwards from SWL and k_n is the wave number corresponding to the nth component and is related to the angular frequency through the linear dispersion relationship:

$$\omega_n^2 = k_n g \tanh(k_n d) \tag{3.40}$$

in which g = gravitational acceleration.

Morison's equation itself was only assumed for periodic waves, and its use under conditions of random waves has been questioned (Vugts, 1979). Vugts & Bouquet (1985) in a non-linear frequency domain procedure investigated on the wave force mechanism on an element of a vertical cylinder in long crested random waves without current. They concluded that there remains a degree of uncertainty associated with the use of Morison's equation to calculate extreme local loads on offshore structures. In spite of that they suggested with more confidence in a practical sense that Morison's equation can be extended to the condition of random waves from regular waves.

An expression for the spectral density of the in-line wave force based on linearization of the drag force component in the Morison's equation is given by (Borgman, (1972)),

$$S_{FF}(\omega) = \frac{8}{\pi} K_D^2 \sigma_u^2 S_{uu}(\omega) + K_I^2 S_{\dot{u}\dot{u}}(\omega) \tag{3.41}$$

where,

$S_{FF}(\omega)$ = spectral density of wave force

$S_{uu}(\omega)$ = spectral density of in-line velocity

$S_{\dot{u}\dot{u}}(\omega)$ = spectral density of in-line acceleration

σ_u^2 = variance of the in-line velocity

$K_d = 0.5 C_D \rho D$ and

$K_i = C_M \rho A$

Linearisation of the drag force allows the approximation that the velocity component at one frequency effects only the drag component at that frequency. The steps involved in the estimation of a wave force spectrum (Sarpkaya and Isaacson, 1981) are shown in Fig.3.6. Alternatively, a force spectrum can be obtained through Fast Fourier Transform (FFT) method analysis of the calculated or measured force. Adopting Fourier model, the wave surface elevation can also be represented as

$$\eta(t) = \int_{-\infty}^{\infty} X(f) e^{i\omega t} dt \tag{3.42}$$

where $i = \sqrt{-1}$ and $X(f)$ is the Fourier transform of η. Noting that $e^{i\theta} = \cos\theta + i \sin\theta$, equation (3.42) becomes

$$\eta(t) = \int_{-\infty}^{\infty} X(f) [\cos \omega t + i \sin \omega t] dt \tag{3.43}$$

Since $\eta(t)$ is a real quantity, the integral in equation (3.43) must also be real. The Fourier transform, $X(f)$, in general, be a complex quantity. It can be shown that

$$X(f) = \int_{-\infty}^{\infty} \eta(t) e^{-i\omega t} dt \tag{3.44}$$

or

$$X(f) = \int_{-\infty}^{\infty} \eta(t)[\cos \omega t - i \sin \omega t]dt \qquad (3.45)$$

As $\eta(t)$ is recorded as a discrete series, equation (3.45) can be further shown as

$$X(n/T_r) = \frac{T_r}{N} \sum_{j=0}^{N-1} \eta(jT_r/N)[\cos(2\pi jn/N) - i \sin(2\pi jn/N)] \qquad (3.46)$$

where $(n/T_r) = f$ and $(T_r/N) = dt$ = sampling interval, N is the number of points in the time series, T_r is the length of the time series and n is ranges from 0 to N-1 .

Now, with $X(f)$ the spectrum is given as

$$S_\eta(f) = \frac{2}{T_r}|X(f)|^2 \qquad (3.47)$$

where, $|X(f)|$ is the modulus of the complex Fourier transform. As the Fourier transform is complex, it defines both amplitude and phase.

3.9 Diffraction Forces

3.9.1 General Formulations

The inertia and drag forces on an offshore structure with slender structural members can be calculated using Morison's equation as mentioned in the above sections with the assumption that the water particle velocity and acceleration in the region of the structure do not differ significantly from the values at the cylinder axis. For larger structural diameters the incident wave is significantly disturbed by the presence of the structure. The interference of the incident wave and the body can be derived from the superposition of the potentials of the undisturbed incident wave and an induced wave field of the same frequency, generated by and radiating from the body. Here the

viscous forces are of less significance, since the ratio of wave height to structural diameter remains sufficiently small. According to potential theory, the pressure distribution and the corresponding forces can be calculated from the velocity potential.

In this work, apart from the experimental investigation, a theoretical analysis has been carried out on the cylinders in the diffraction regime using a computer program available in the Department of Naval Architecture and Ocean Engineering, Glasgow University. The details of the program are available in Chan (1990) and a brief description only is given below. The formulation of three-dimensional flow for the computation of the boundary value problem for a rigid body, is based on the assumption that the fluid is ideal and the flow is irrotational. The body is assumed to be rigid. It is also assumed that no flow of energy occur through the bottom surface or the free surface. Energy is gained or lost by the system only through waves arriving or departing at infinity. To represent a possible case of potential flow, it is assumed that a velocity potential exists with assumptions that the fluid is homogeneous, incompressible, inviscid and the surface tension is neglected. Based on these assumptions, the velocity potential of the flow field must satisfy the Laplace's equation, body boundary, bottom boundary and linearised free surface boundary conditions as stated below.

Laplace's equation;

$$\nabla^2\Phi(\bar{x}_0,t) = 0 \tag{3.48}$$

Free surface condition;

$$\left(\frac{\partial^2\Phi}{\partial t^2}\right) + g\frac{\partial\Phi}{\partial z} = 0 \qquad \text{at } z = 0 \tag{3.49}$$

Body Boundary Condition;

$$\nabla\Phi \cdot \vec{n} = 0 \qquad \text{on } S_o \tag{3.50}$$

where, S_o is mean wetted surface area

Sea bed boundary condition;

$$\frac{\partial\Phi}{\partial n} = \frac{\partial\Phi}{\partial z} = 0 \qquad \text{on z = -h} \tag{3.51}$$

where h is the depth of the sea.

Far field radiation condition;

$$\lim_{r \to \infty} \sqrt{r}\Phi = 0 \tag{3.52}$$

The total velocity potential $\Phi(x,y,z,t)$ is decomposed linearly into two distinct components namely the incident potential, ϕ_0 and diffraction potential ϕ_7 as follows:

$$\Phi(x,y,z,t) = \left[\zeta_0(\phi_0 + \phi_7)\right]e^{-iwt} \tag{3.53}$$

where ζ_o is the incident wave amplitude.

The linear boundary value problem posed by equations (3.48) to (3.53) is solved by a three dimensional source-sink Green function method. The two integral equations required for the solution is given as below, which can be derived by applying Greens second identity and the body boundary condition:

$$2\pi\sigma(p) + \int_{S_0}\int \sigma(q)\frac{\partial G(p;q)}{\partial n} ds(q) = 4\pi\frac{\partial\phi(p)}{\partial n} \tag{3.54}$$

$$\iint_{S_0} \sigma(q) G(p;q)\, ds(q) = 4\pi\phi(p) \tag{3.55}$$

where σ represents unknown strength at the source point q and $G(p;q)$ represents the Green function and is given by (Chan 1990) for the finite water depth.

3.9.2 Solution Procedure

The three-dimensional Green function method is an integral equation used in solving a linear boundary value problem which utilises Green function based on Green's second identity to define the velocity potential of the flow field. The Green function itself must satisfy the Laplace equation and the surrounding boundary conditions except the cylinder boundary condition. This Green function in finite water-depth condition is given by (Chan, 1990).

$$G(x,\xi,h,f) = -\frac{1}{r} - \frac{1}{r_h} + H(x,\xi,h,f,\varepsilon) \tag{3.56}$$

The term 1/r is the source singularity and H^* is the regular harmonic function defined by:

$$r_h = \sqrt{(x-\xi)^2 + (y-\eta)^2 + (z+2h+\varsigma)^2}$$

$$H(x,\xi,h,f,\varepsilon) = -\frac{1}{\pi}\int_{-\infty}^{\infty} d\beta \int_{-\infty}^{\infty} d\alpha \left\{ \frac{\left(k+(f+i\varepsilon)^2\right)e^{-kh}\cosh\left(k(z+h)\right)}{k\left(k\tanh(kh)-(f+i\epsilon)^2\right)} \frac{\cosh\left(k(\zeta+h)\right)}{\cosh(kh)}\, e^{i(\alpha x'+\beta y')} \right\} \tag{3.57}$$

where, ε is the Rayleigh artificial viscosity (Lighthill, 1967), f is the non-dimensional wave frequency, h is the water depth and x and ξ are the non-dimensional field and source point locations respectively. With the known Green function, the velocity potential of the flow field on the cylinder boundary surface can be determined by substituting the Green function into the following set of discretized integral equations derived using the cylinder boundary condition and Green theorems.

$$\phi_s(p_i) = \frac{1}{4\pi}\sum_{k=1}^{N}\sigma(q_k)\left\{\iint_{\Delta s_k} G(p_i,q_k)\,ds_q + \frac{U^2}{g}\oint_{\Delta L_k} n_l G(p_i,q_k)\,dy_q\right\} \tag{3.58}$$

$$\frac{1}{2}\sigma(p_i) + \frac{1}{4\pi}\sum_{k=1}^{N}\sigma(q_k)\left\{\iint_{\Delta s_k}\frac{\partial G(p_i,q_k)}{\partial n}\,ds_q + \frac{U^2}{g}\oint_{\Delta L_k} n_l\frac{\partial G(p_i,q_k)}{\partial n}\,dy_q\right\} = -\frac{\partial \phi_0(p_i)}{\partial n} \tag{3.59}$$

for i = 1,2, ... N

where the Green function $G(p,q)$ represents the potential at the field point p due to the unknown strength σ at the source location q and L_0 is the undisturbed waterline contour on the cylinder surface. The variable N is the total number of flat quadrilateral panels used to model the cylinder surface.

To solve the diffraction problem, the rectangular cylinder surface is first discretisized into N number of quadrilateral panels or facets. For example, in Figs 3.7(a) and (b), the typical body surface panels for the vertical rectangular cylinder with aspect ratio = ½ and the same for horizontal rectangular cylinder are shown. The number of panels used is also shown. It has been found that for both the configurations a maximum of about 150 panels are more than enough to produce the maximum accuracy in the results. The water depth used for both vertical and horizontal cylinders is 2.2m

The source strength on each facet is assumed as constant and the centroid is taken as the control point and the variation of the source strength over each panel is assumed constant. Equation (3.59) can now be solved to obtain the unknown source strength after which the surface scattered potential can be determined from equation (3.58).

With the known surface scattered velocity potential, the hydrodynamic pressure loading on the cylinder can now be derived as:

$$\mathbf{F} = -\rho \iint_{S_0} i\omega \mathbf{n}(\phi_0 + \phi_s) ds = -\rho \sum_{j=1}^{N} i\omega \mathbf{n}_j (\phi_0(p_j) + \phi_s(p_j)) \Delta s_j \qquad (3.60)$$

where $\mathbf{n}_j$ is the normal surface vector of the j^{th} panel.

From the above equation, the wave exciting forces and corresponding phase angles can be evaluated. This work allowed an assessment to be made of the importance of diffraction effects for these experiments. The results are reported in section 6.6.

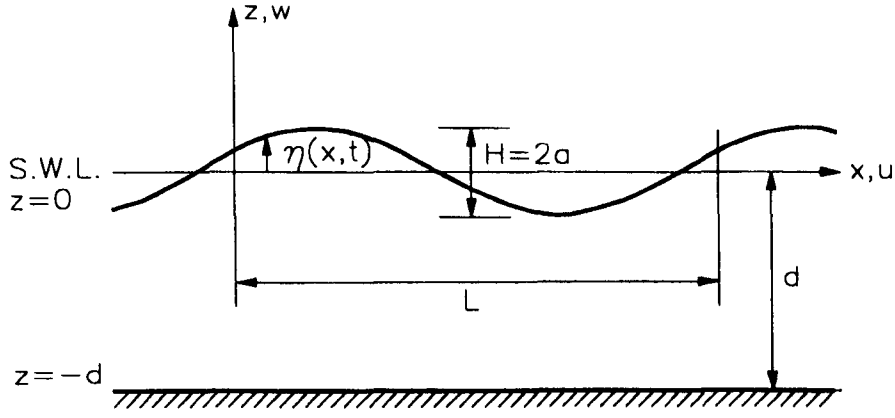

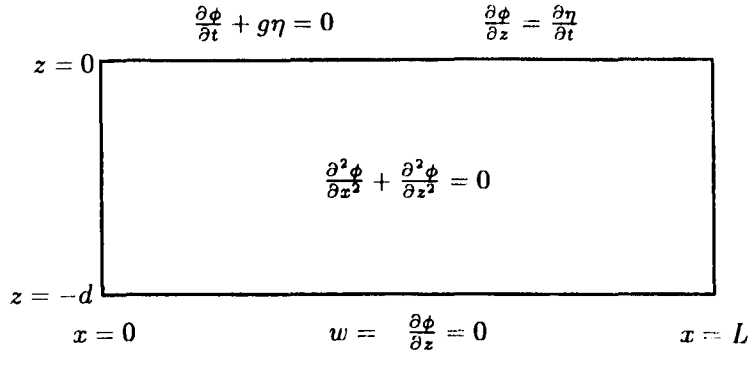

Fig. 3.1 (a) Definition sketch showing the solution domain for linear wave theory. (b) The governing equation, boundary conditions and the solution domain for linear wave theory.

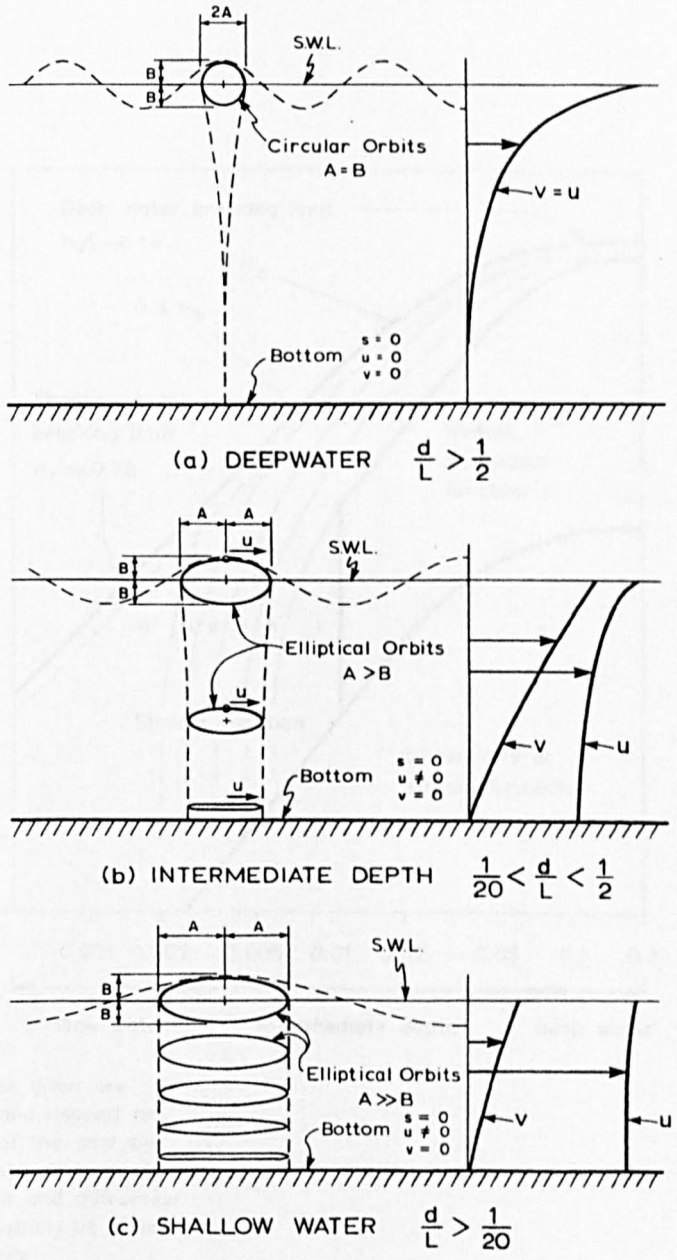

Fig. 3.2 Diagrammatic representation of water particle orbits and kinematics by linear wave theory [Chakrabarti (1987)].

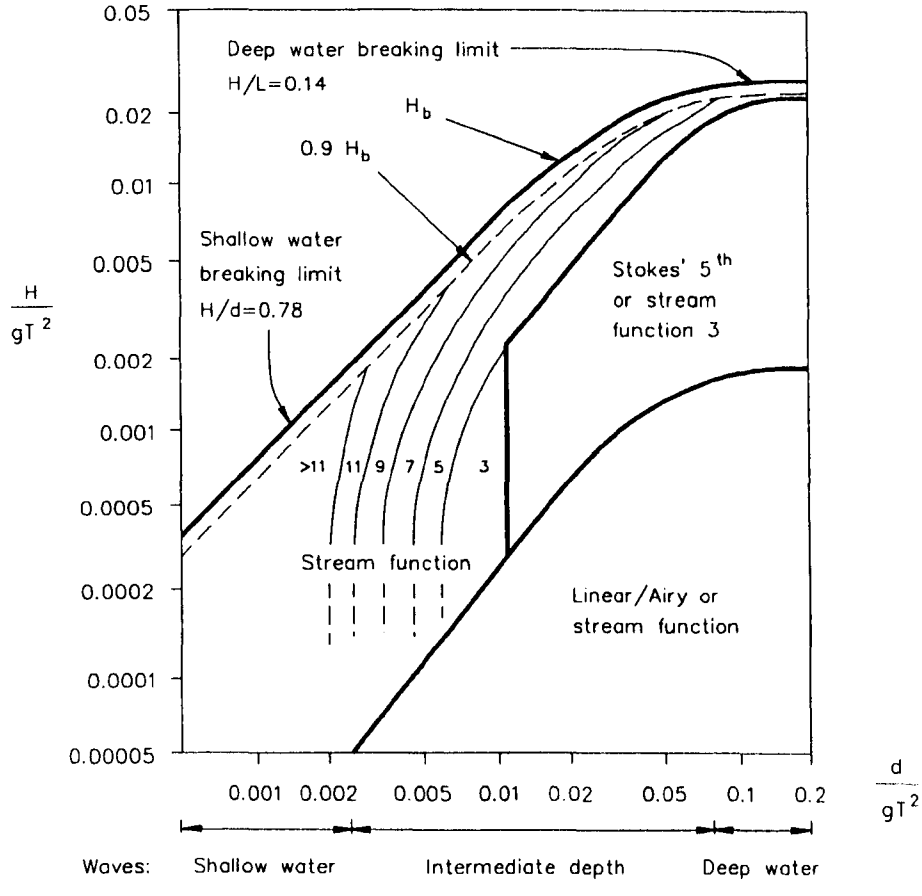

The boundaries given are approximate and depend on the purpose of the analysis being performed. It is accepted that refraction and diffraction analysis will usually be based on linear theory

Fig. 3.3 Regular wave theory selection diagram [Barltrop et al., (1990)].

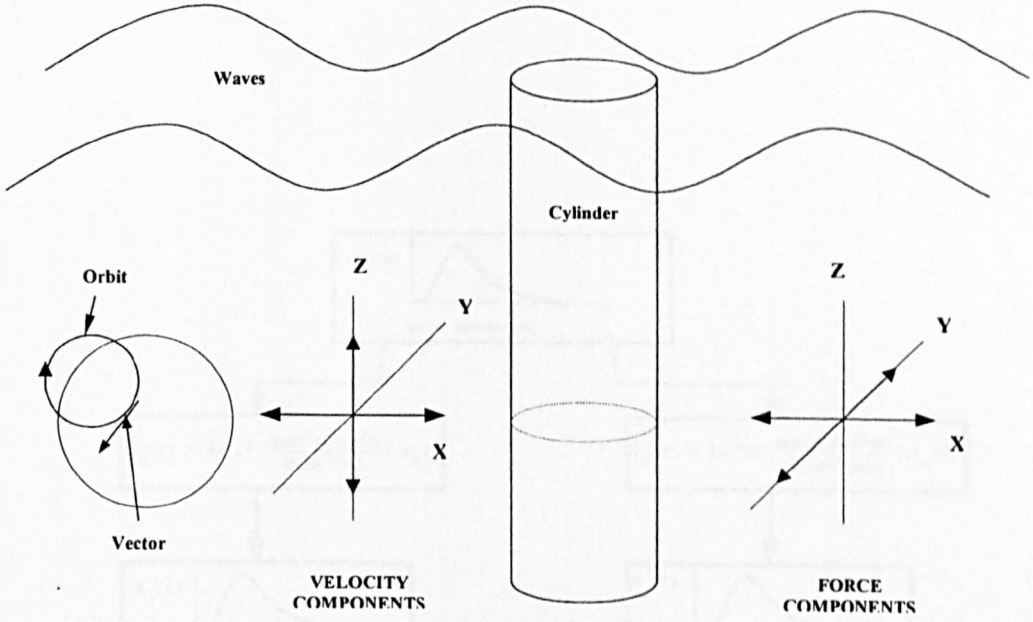

Fig. 3.4 Vertical cylinder in waves [Pearcey, (1979)]

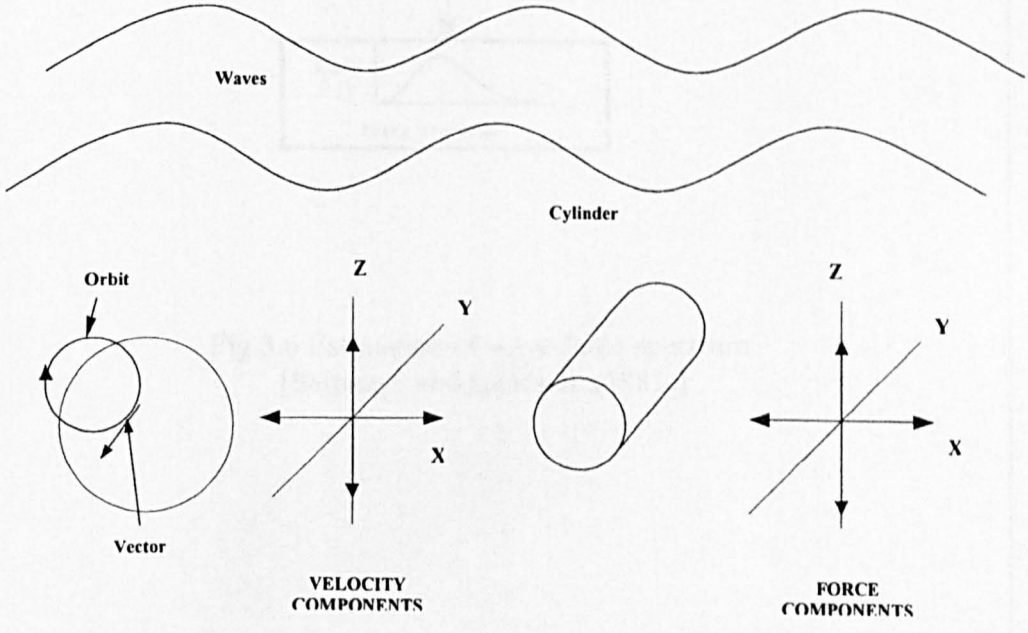

Fig. 3.5 Horizontal cylinder in waves [Pearcey, (1979)]

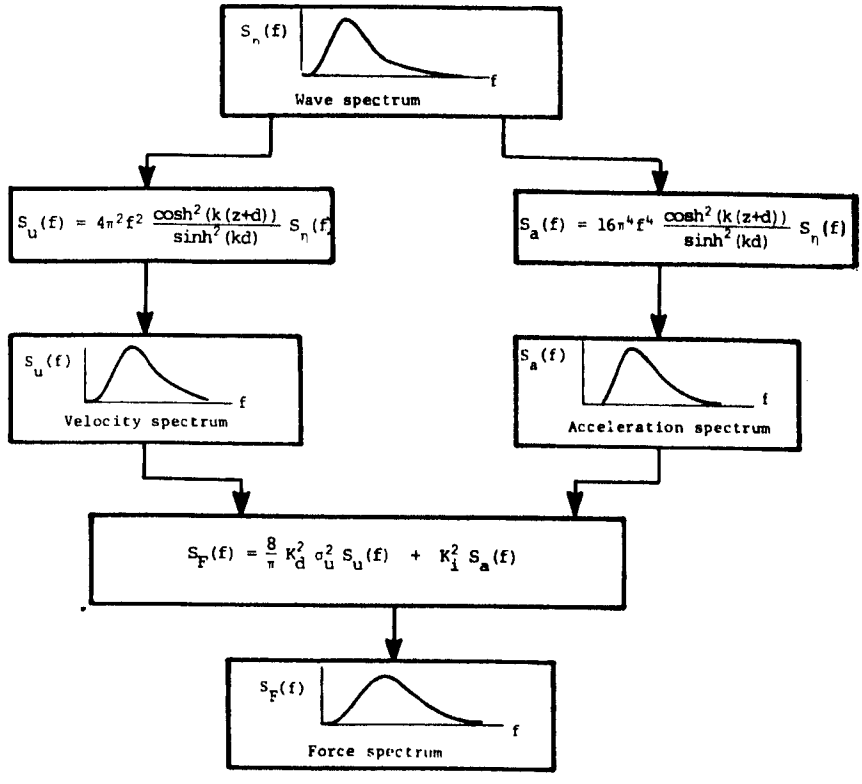

Fig.3.6 Estimation of wave force spectrum
[Sarpkaya and Isaacson, (1981)]

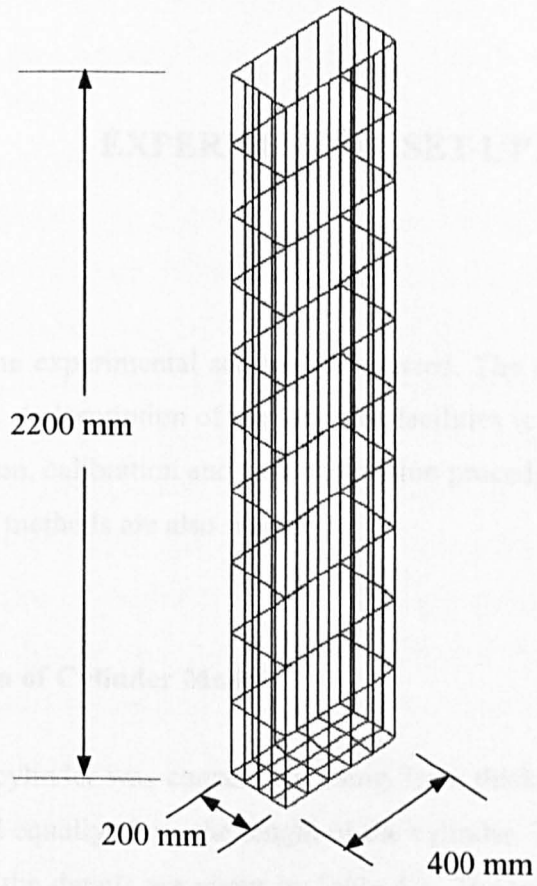

Fig. 3.7(a) Body surface panels for vertical rectangular cylinder with aspect ratio = 1/2 and 2/1; number of panels = 200

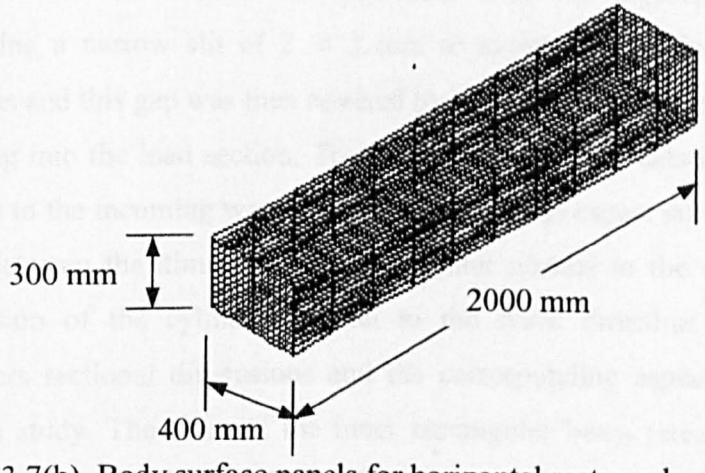

Fig. 3.7(b) Body surface panels for horizontal rectangular cylinder with aspect ratio = ¾; number of panels = 520

CHAPTER 4

EXPERIMENTAL SET-UP AND TECHNIQUES

4.1 General

In this chapter the experimental set up is discussed. The cylinder models built and used are detailed. A description of the tank test facilities is also explained. Details of the instrumentation, calibration and data acquisition procedure adopted are described. Wave generation methods are also included.

4.2 Description of Cylinder Models

The rectangular cylinder was constructed using 7mm thick PVC plates with internal bulkheads spaced equally along the length of the cylinder. Three cylinders were used for the tests and the details are given in Table 4.1. The cylinder was made of three hollow sections connected by an inner rectangular beam (mild steel box sections) at the centre. The centrepiece, being the test section, was situated at the mid-length of the cylinder and is 100 mm long. When all the three sections are joined together they form a cylinder of total length of 2.0 m (Photos 4.1 to 4.3) with a smooth painted surface. The test section was separated from the adjacent dummy sections by providing a narrow slit of 2 to 3 mm to avoid the interference from the dummy sections and this gap was then covered by a flexible thin rubber sheet to prevent water entering into the load section. To study the effect of orientation of the cylinder with respect to the incoming waves, a term is defined as aspect ratio, which is taken as the ratio between the dimension of the cylinder normal to the wave direction and the dimension of the cylinder parallel to the wave direction. Table 4.1 shows the cylinders sectional dimensions and the corresponding aspect ratios chosen for the present study. The sizes of the inner rectangular beam (steel box sections) chosen were 6"x 4", 6"x 3" and 2.5"x 2.5" for cylinders 400x300mm, 400x200mm and

150x150mm respectively. In order to conduct experiments at high Reynolds numbers and at low Keulegan-Carpenter numbers, large sizes of the cylinders were chosen.

The test section was instrumented with four waterproof strain gauge type load cells; one load cell is fixed on each side of the cylinder to measure the forces on the test section. The load cells are NOVATECH model of type F255, manufactured by Novatech Measurements Ltd, UK and made of stainless steel body with a diameter of 30mm and a height of 16mm and is submersible in water. The load cells have two welded stainless steel diaphragms on the top and bottom sides of the active element to protect the load cell. Four strain gauges are in each load cell, making a full bridge connection. Each load cell has a working temperature range of -30^0C to $+80^0$C and is capable of measuring tension and compression loads up to 25 kgf. The load cells have a threaded stud on the base, which was threaded into the cylinder's inner beam flange at the height of the test section and an active threaded stud, which was threaded to one plate of the test section covering it and forming one face of the test section. In a similar way, the other faces of the test section were assembled (Refer Fig. 4.1). Note that this drawing was made for a square cylinder of size 400x400mm and was used only as a reference to other cylinders. The dimensions of the material used for constructing the loading sections for other cylinders are suitably scaled down. The average of the forces measured by the two load cells, fixed on opposite sides of the inner rectangular beam is taken as the force acting from the corresponding direction. The load cells were connected to an amplifier, one load cell per channel, with their cables running inside the test cylinder through a small PVC tube that runs from the test section to one end of the test cylinder, leaving the exterior of the cylinder surface perfectly smooth.

In addition to the load cells, pressure transducers were fixed on a section, which is located at 250 mm from the centre of the load cell test section, to measure the dynamic pressures. Holes were drilled on the surface of the cylinder to the size of the pressure transducers and after fitting the pressure transducers into the model, the gaps were sealed with water proofing material. The pressure transducers are

MEDIAMATE type and manufactured by Control Transducers, UK. The dimensional detail of the pressure transducers is shown in Fig. 4.2. The pressure transducers are capable of measuring pressure up to 15psi. The instantaneous change in the displacement of the diaphragm due to the action of external pressure is proportional to the instantaneous change in applied pressure. The maximum sensitivity of each of the pressure transducer is 50mV at about 20^0C. The location of pressure transducers around the cylinders is conceptually shown in Fig. 4.2. There were 12 pressure transducers used for case C, 10 pressure transducers for case B, but for case A pressure transducers were not used, as the size of the pressure transducers are large and cannot be properly fitted in to the model. The reason for fitting only 10 transducers for the case B is again due to the large size of the transducers and less width of the cylinder. In order to measure the run up on the surfaces, two resistance type wave probes were fixed on the cylinder surface, one at the centre line of the side normal to wave and the other at the centre of the face parallel to the wave.

The cylinders were submerged in water for about 48 hours to make sure that they were watertight.

4.2.1 Effect of End plates

In the present experiments, the end effects on the force measurements were assumed to be negligible as the force measurements were made only on the mid 100 mm instrumented section of a two-meter cylinder, which is located between two dummy sections. It is to be noted that the cylinders in fact had end plates of rectangular shape at their ends; however, they were primarily used as a joining plate to the supporting frames rather than acting as end plates. Even though they were not designed to the proper end plates design requirements, still they can be considered as end plates. From chapter-6, the good comparison of the present results to the exiting results [Bearman et al. (1984), Ikeda et al. (1988b), Arai (1993,1995)], reveals that these plates might have been acted as a proper end plate to some extent to give a two dimensional flow around the cylinder. However, it cannot be denied that the

experiments are completely free from end effects and the results may have been affected by the three-dimensional flow around the cylinder end, but not to a great extend. If the force measurements were made on the total length of the cylinder, then it would not be so easy to make the above statement, as the end effects will certainly have influences on the coefficients. The following literature discusses some detailing on the end plates and their influence on force measurements.

In an investigation with a circular cylinder in wind tunnel Stansby (1974) provided the end plate design and claimed that by using the end plates, the effects of the tunnel wall boundary layer will be removed by causing a two-dimensional flow. The results showed that using rectangular end plates with an upstream dimension (distance of the leading edge from cylinder axis) sufficiently large to isolate horseshoe vortex generated at the wall-model intersection. He has used rectangular end plates with a width of $7D$ normal to the axis (where D is the diameter of the circular cylinder). The distance from the axis of the cylinder to the trailing edge of the plate was $4.5D$ and the distance from the axis of the cylinder to the leading edge of the end plate was varied from $1.5D$ to $3.5D$. The cylinder's length to diameter ratios (l/D) used are about 29 and 14. Stansby reported much low base pressure coefficient for cylinder without end plate compared to the one with end plate for a Reynolds number = $1.6\text{x}10^4$. However, for a higher Reynolds number = $4.0\text{x}10^4$, the base pressure for cylinder without end plate at the centre of the span approaches the value of the base pressure with end plate.

Fox and West (1990) concluded from the tests on circular cylinders in wind tunnel ($Re = 3.3\text{x}10^4$ to $13.2\text{x}10^4$) that if the end plates of the proportions recommended by Stansby(1974) are used, then (i) the length to diameter ratio(l/D) of the cylinder between the end plates must be greater than a critical minimum of 7.0 to ensure the presence of 'two dimensional' flow conditions over the central portions of the cylinder, (ii) the interference effect associated with each plate extend over a constant distance of 3.5 D from the plate and (iii) if the l/D ratio between tunnel walls is

greater than 30, it is not necessary to use end plates to achieve ' two dimensional' flow.

Okamoto and Yagita (1984) studied the flow past a circular cylinder in a shear flow. One end of the cylinder was fixed to a flat plate and was resting on the bottom of the wind tunnel and another end was free. The velocity profile of the uniform shear stream used is of the form $U = U_C + \lambda(z - h/2)$, where U is the local velocity of the free stream, U_C is the velocity of the free stream at $z = h/2$, h is the height of working section of wind tunnel, z is the vertical coordinate with origin at the bottom of the cylinder and λ is the velocity gradient. The length to diameter ratios (l/D) of the cylinders used were 1,3,5,7,9,12,15 and ∞. The drag coefficients were computed from the surface pressure measurements. The experiment was carried out at a Reynolds number = 1.3×10^4. It was concluded that the range of end effect is limited to the region within 3 times diameter from the top of cylinder in such a uniform shear stream.

Nakamura et al. (1991) experimentally investigated the three dimensional effects of hydrodynamic forces acting on finite length vertical circular cylinders each of 32 mm diameter, in an oscillating flow. Four cylinders of different cylinder's length to diameter ratios (l/D = 1, 3, 10, 20) are used without end plates and one cylinder with l/D = 3 was fitted with end plates of diameter of 160 (equal to 5 times cylinder's diameter). The cylinder with l/D = 20 was called as quasi-2D cylinder. The hydrodynamic coefficients were computed from simple harmonic forced surging tests on the cylinders for KC = 4- 40. Their analyses showed, as a general trend, that the C_D for quasi-2D cylinder is slightly smaller than C_D for the cylinder with end plates; and for finite length cylinders C_D decreased with decrease of l/D. The inertia coefficients decreased with increasing l/D and the lift coefficients increased with increase in l/D. However, the important point to be noted here is that the author claims that at the region of $KC \leq 8$, there were no differences in the inertia coefficients between the quasi-2D cylinder and the finite length cylinders. A similar trend was also seen for lift coefficients where the coefficients for all the cylinders

appear to be showing similar values at this range of KC numbers. However, C_D showed a slightly higher values for cylinders with $l/D = 20$ and for quasi-2D cylinder.

Hashino et al.(1993) studied the hydrodynamic forces acting on finite-length vertical circular cylinder oscillating in an uniform flow with l/D ratio between 2 to 15. They have also varied the depth of force measurement with z/D ratio between 0 to 5, where, z is the length of portion the cylinder from the bottom of the cylinder to the measuring section and D is the diameter. The Reynolds number used varied from $3.0x10^3$ to $4.3x10^4$. In oscillating flow tests, the authors claimed that the tendency of drag and inertia coefficients of their study agreed quite well with the results reported by Nakamura et al. (1991). At KC less than about 6, varying l/D ratio did not show any significant change in the inertia and lift coefficients and the values are virtually same as those obtained for a cylinder with $l/D = \infty$.

From the above-mentioned works one would realise the importance of the presence of end plates. It is to be noted that the above literature are related to the circular cylinders and such information for rectangular cylinders are not available in order to establish a relationship to the cylinder l/D ratios and the corresponding flow measurements. However, these research works confirms that the length to diameter ratio of a cylinder will influence the hydrodynamic coefficients only for higher KC values and therefore it gives a satisfactory reason to accept that under the conditions such as used in the present study, the end effects may considered to be ignored at low values of KC. Based on the l/D ratios obtained (Table.4.1) in the present work, it may be possible to argue that within the range of Reynolds number and KC numbers tested in the present experiments, the end effect on the reported force coefficients may be ignored, and even if it did, it will be of negligible amount as the force coefficients compares quite well with the coefficients reported in the literature for both steady and wavy flow.

4.2.2 Natural Frequency Calculations

The natural frequency of the cylinders used for the tests are approximately calculated as follows:

The horizontal cylinders are assumed to be rigidly fixed at both ends. Using classical beam theory the linear spring constants for a beam clamped at both ends and centrally loaded is given by [Barltrop and Adams (1991)]

$$k = \frac{192EI}{l^3} \tag{4.1}$$

where, EI is the flexural stiffness and l is the length of the beam(cylinder). The spring constant for a cantilever beam with one end fixed and other end is free (represents a vertical cylinder) with a load acting at a distance l_o from the fixed end is given as

$$k = \frac{6EI}{l_o^2(3l - l_o)} \tag{4.2}$$

The natural frequency of the cylinder can be calculated as

$$\omega_n = \sqrt{\frac{k}{m}} \quad \text{(rad/sec) or} \tag{4.3}$$

$$f_n = \frac{1}{2\pi}\sqrt{\frac{k}{m}} \quad \text{(Hz)} \tag{4.4}$$

where,

$m = (m_o + C_A \rho A)l$ = total mass

m_o = actual mass per unit length

C_A = added mass coefficient

A = area of the cylinder

The natural frequencies calculated for both vertical and horizontal cylinders are tabulated in Tables 4.2 and 4.3 respectively. The wave frequency used for the experiments ranged from 0.425 – 1.0 Hz and from the tables it is evident that the test cylinder's natural frequencies are nowhere close to the wave frequency.

4.3 The Towing Tank

The experiments were carried out in the towing tank of the Hydrodynamic Laboratory of the Department of Naval Architecture and Ocean Engineering at the University of Glasgow. The dimensions of the tank are 4.6 m wide, 2.7 m deep and 77m long with a working water depth of 2.4m. The experiments for the present study were conducted in a water depth of 2.2. The tank is equipped with an electro-hydraulic paddle/flap type wave maker fitted across the width of the tank at one end. The wave maker can generate regular and random waves in the frequency range of 0.3 - 1.4 *Hz*.

At the other end of the tank, an inclined mesh beach of 6m length is fitted to absorb the energy of the oncoming waves and the beach effectively dissipated most of the wave energy. Further, a time interval of about 15 to 30 minutes were allowed between the experiments to make sure that the water was still at the beginning of each test. The tank is also equipped with an electronically controlled towing carriage with an observation platform, whose dimensions are approximately of 5m x 6m in plan, and running on rails with a maximum carriage speed of 6.4 m/sec. The carriage is driven by four on board servo-controlled electric motors.

The cylinder was rigidly fixed on to the carriage and positioned at the centre of the tank width as shown conceptually in Figs. 4.3 and 4.4, for the vertical and horizontal modes respectively, using a specially designed frame that avoids any vibrations and movements during the wave impact. The centre of the test section was at 0.46 m from the still water level (SWL) for the vertical cylinder. For the horizontal cylinder, two depths of submergence were chosen. For the first depth of submergence, the centre of

the test section was located at 0.47 m from the SWL and for the second depth of submergence, the centre of the test section was at 0.82 m from SWL. Considering, the geometry and strength of the fixing frame, the maximum depth to which the cylinder can be lowered was only 0.82m and hence this depth has been chosen. The carriage with cylinder was positioned at 25m away from the wave maker when the measurements were made for wave alone. When the cylinder was tested horizontally, no end plates were fitted to the cylinder and it was assumed that the effect of flow around the end of the cylinder would not affect the force measurements on the test section as it is located far from the end connections.

The deflections for the cylinder models, at the location of the test section, both in vertical and horizontal fixing modes are found to very small, in the order of a few millimetres. In the above configurations, the frontal area of the biggest cylinder used for tests is 6.63% of the water filled cross section of the flume for the vertical case and 6.82% of for the horizontal case. However, no blockage corrections were applied to the force measurements as there is no reliable technique available to apply the blockage corrections for unsteady separated flows with a free surface [Chaplin (1997)].

4.4 Instrumentation Set-Up and Data Acquisition

The block diagram of the instrumentation set-up used for the present experimental investigation is shown in Fig. 4.5. A resistance type wave probe was placed in transverse line with the axis of the cylinder to measure the wave profile and phase angles. Further, three additional wave probes, connected to a chart recorder, were employed to monitor the linearity of the wave across the tank width, one is fixed at the centre of the tank and others were fixed at quarter width of the flume. The wave probes were connected to the wave amplifier and then the signals were taken to a filter and finally they were stored in the computer. The amplifiers used are of instrumentation type, from a range of RDP DATASPAN modules of version DS2028A and are suitable for dynamic measurements up to 200 Hertz. It consists

essentially of a stable oscillator, a high gain carrier amplifier and a phase-sensitive detector. The signals from the load cells were fed to the input of the amplifier. The amplifier sensitivity was set at 10 milli-volts to achieve a highly accurate representation of the loads on the load cells. The amplifier is of high impedance differential stage with high common mode rejection ratio (CMRR) of 100 dB. This allowed the amplifier to amplify only the signals from the load cells, ignoring any common mode signals.

The output signals from the amplifier were then fed to a low pass filter of type Sallen Key 2 poles Butterworth and had attenuation of 40 dB at 50 Hertz, designed for a cut off frequency of 5 Hertz, to reject any noise and high frequency components in the signals. Subsequently, the signals were stored on a personal computer in data form.

The host computer is an IBM PC 386, connected to the wave making system, which controls the wave maker. Software has been developed by the Department of Naval Architecture and Ocean Engineering for the generation of waves. Regular or random waves are specified by their wave heights (in terms of voltages in the case of regular waves) and wave frequencies and are entered in to this computer. The software generates text files containing time series of the required wave maker flap position and the program sends these data to a digital - analogue card, which converts the data into voltages and this voltage signal is finally fed to the wave maker.

The data were collected using data acquisition software LabVIEW 4.1, by National Instruments Corporation. It has the capability of collecting data with 32 number of channels simultaneously. The computer used for data acquisition and storage is a Pentium-II 266 mHz with 120 MB memory. The physical quantities viz., water surface elevations, pressures and loads on the cylinder were acquired as electric signals (voltages) from the corresponding gauges, transducers and load cells via the amplifier and filter. The data collected in the form of voltages are then fed to an analogue to digital converter and these digital values are then converted to the

required physical variables using corresponding calibration coefficients and the data is stored as text files for further analysis.

4.5 Calibration of Load Cells, Pressure Transducers and Wave Probes

(i) Load Cells:

A special frame consisting of channels and bracing with frictionless pulleys and string was fabricated for the calibration of load cells. The individual load cells were first calibrated in air, before they were fixed inside the cylinder model, by applying known loads and this was done to check their loading performance. The calibration in water was carried out after mounting the cylinder rigidly to the desired orientation. The calibration frame was fixed in such a way that the string connecting the loading pan at the other end of the pulley-string system is perfectly inline with the axis of the load cell, thus ensuring that the load is applied without any eccentricity. The calibration was carried out by adding weights in steps of 100g up to a maximum load of 5kg and then removing the weights in steps of 100g to check the linear behaviour of the load cells. The load cells performed very well in the loading range tested. The calibration procedure was repeated for the same load cell for another time to check for repeatability of the calibration constant and they were found to be the same at all times. The same procedure was repeated for all the load cells and calibration constants were determined for individual load cells. Sample records are shown in Fig. 4.6, for a load of 1 kg and 4 kg applied at a load cell-No.1 as a static run. It is to be noted that when a load cell (say No.1, fitted at face -1) is loaded, the contribution from the load cells (say No. 3 and 4) placed at faces right angles to this load cell-No.1, are very small loads. This ensures that a particular load cell is picking up only the forces acting on it and the coupled loads from other load cells were not much significant. However, the contributions of this small load from the load cells 3&4 were accounted properly while arriving at the calibration constants for load cell-1. A similar procedure was followed for load cell-2. All the four loads have been checked

in this way. The measurements with the calibration constant has reproduced the original loads within ± 3%.

(ii) Wave probes:

The wave probe is fixed in water and the still water reading was recorded as zero reading. Then, the wave probe was lowered into the water in steps of 5cm up to 30cm and the readings were noted. Again the wave probe was raised in steps of 5cm up to 30 cm above the still water level and the values were recorded and this was done to check the linearity for wave crest and trough. From the recorded value the calibration constant was calculated. The same procedure is repeated for all the wave probes. The accuracy of the measurements was within ± 2.0mm.

(iii) Pressure transducers:

The pressure transducers were calibrated by using a hand held pressure pump. The pressure from the pressure pump was applied in steps of 2psi and calibration charts were prepared. The accuracy of the measurements was within ± 0.001psi.

4.6 Wave Characteristics

4.6.1 Regular Waves

For the generation of regular waves a software 'WAVE', developed by the Hydrodynamic Laboratory has been used. WAVE is a simple program that reads a time series file of voltage values and sends them via a D/A card in the computer to the wave maker control hardware. There are other programs called 'GENERATE', which generates the regular wave time series, and 'RANDOM' which creates the random sea time series file. WAVE and GENERATE are written in Turbo PASCAL and runs on the wave maker control computer. RANDOM is written in FORTRAN and runs on the ALPHA system.

For the tests with regular waves, the wave heights selected ranged from 0.05m to 0.38m and the wave periods selected ranged from 1.0 to 2.35 sec. The tests with above wave heights and periods indicate that most of the experiments pertain to deeper water region and some are in the intermediate water depth. For each aspect ratio of the cylinder, experiments were carried out for about 50 waves with different combinations of wave heights and wave periods. A list of wave heights and wave periods measured for aspect ratio = 1/2 is shown in Table 4.4. The wave profile and forces were recorded for 60 seconds with a sampling interval of 0.025 sec. Sample records of the measured wave profile are shown in Fig. 4.7, for a sampling time up to 40 seconds and these plots illustrate that the wave profiles are not affected by the reflected waves. However, long period waves were disturbed by the reflected waves after a time period of about 40 to 50 seconds, and the data with reflection were excluded from the analysis. Note that the wave elevations in Fig. 4.7 are recorded with the presence of cylinder.

For regular waves and currents, the cylinder is towed in regular waves for following (positive current) sea and head sea (negative current) to produce co-existing wave-current effect. The cylinder was towed with speeds of 0.1m/s, 0.2m/s, 0.3m/s and 0.4 m/s in both directions.

4.6.2 Random Waves

The program RANDOM, simulates random wave field by random phase method. The sea surface elevation can be represented as:

$$\eta(t) = \sum_{n=1}^{N} A_n \cos(2\pi f_n t + \varepsilon_n) \qquad \text{for } t = 0 \text{ to } T_L$$

where, A_n is the wave amplitude of the nth component and f_n is the frequency of the nth component, both chosen from the energy spectrum, in our case it is a Jonswap and a Pierson-Moskowitz spectrum. The spectrum is divided into N equal frequency

components, each of width Δf, over the range of frequencies 0 and f_m, where f_m is the maximum generated frequency. The random phase angle ε_n is uniformly distributed in the interval 0 to 2π. The amplitudes, A_n, associated with wave frequencies in the small interval Δf is

$$A_n = \sqrt{2S_\eta(n\Delta f)\Delta f} \qquad n=1,2,....N \tag{4.1}$$

The value of Δf is chosen such that

$$\Delta f = \frac{1}{T_R} \tag{4.2}$$

where T_R is the length of simulation time and is given by $T_R = (M\text{-}1)\Delta t$, M is the number of data points in a record.

The minimum and maximum cut of frequencies set are 0.35 Hz and 1.4 Hz respectively. For the random wave force studies, the wave field is assumed to follow a two parameter Pierson-Moscowitz (P-M) and JONSWAP spectra and these spectra are given by expressions (4.3) and (4.4) respectively,

$$S_\eta(\omega) = \frac{5H_S^2}{16\omega_o}\left(\frac{\omega_o}{\omega}\right)^5 exp\left[-\frac{5}{4}\left(\frac{\omega_o}{\omega}\right)^4\right] \tag{4.3}$$

$$S_\eta(\omega) = \frac{\alpha g^2}{(2\pi)^4\omega^5} exp\left[-\frac{5}{4}\left(\frac{\omega_o}{\omega}\right)^4\right]\gamma^\beta \tag{4.4}$$

Where, $S_\eta(\omega)$ = Wave spectral density,

H_S = Significant wave height,

ω_o = Peak frequency

ω = $2\pi/T$.

γ = Peak enhancement factor = 3.0

σ = 0.07 for $\omega < \omega_O$

σ = 0.09 for $\omega \geq \omega_O$ and

$$a = exp\left[\frac{-(\omega/\omega_O - 1)^2}{2\sigma^2}\right]$$

The present tests were carried out with the assumption that the linear wave theory is valid to predict the water particle kinematics under random waves at the axis of the cylinder. It was further assumed that the reflection from the beach and side walls of the tank has negligible effects on the measured water surface profile and forces on the cylinder.

The significant wave height and peak period used for the tests are shown in Tables.4.5 & 4.6 respectively for PM and JONSWAP spectra. At each frequency three different significant wave heights were applied. Each random wave profile and forces were recorded for 120 seconds with a sampling interval of 0.05 sec.

The combination of random waves and currents has not been reported in this study. Some trials showed that towing the cylinder in random waves affected the wave surface profiles.

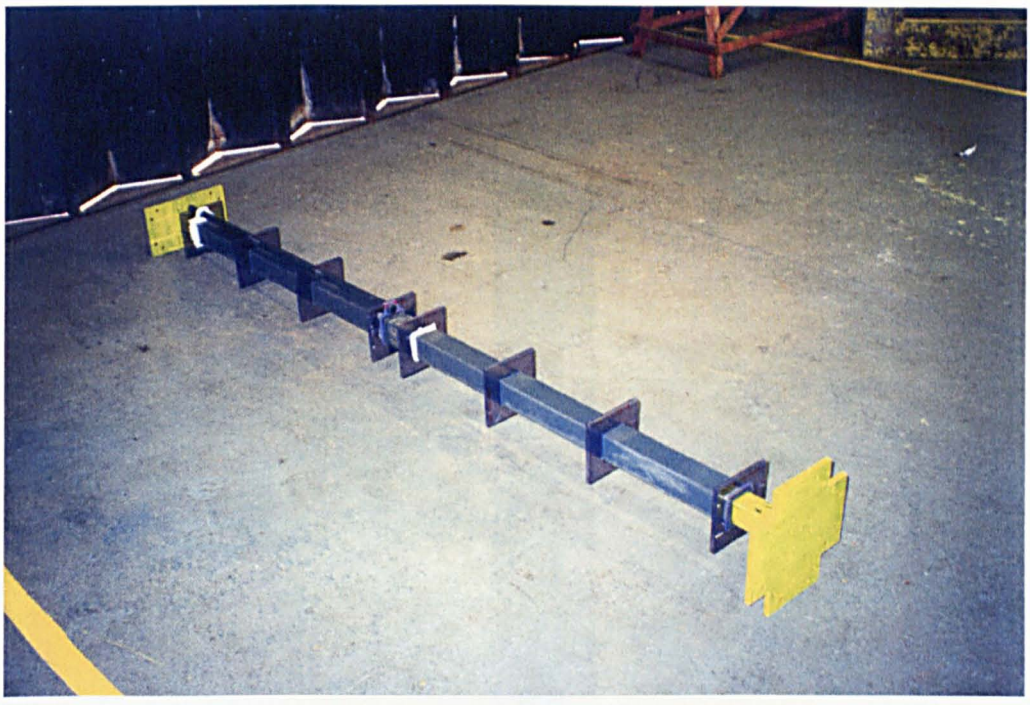

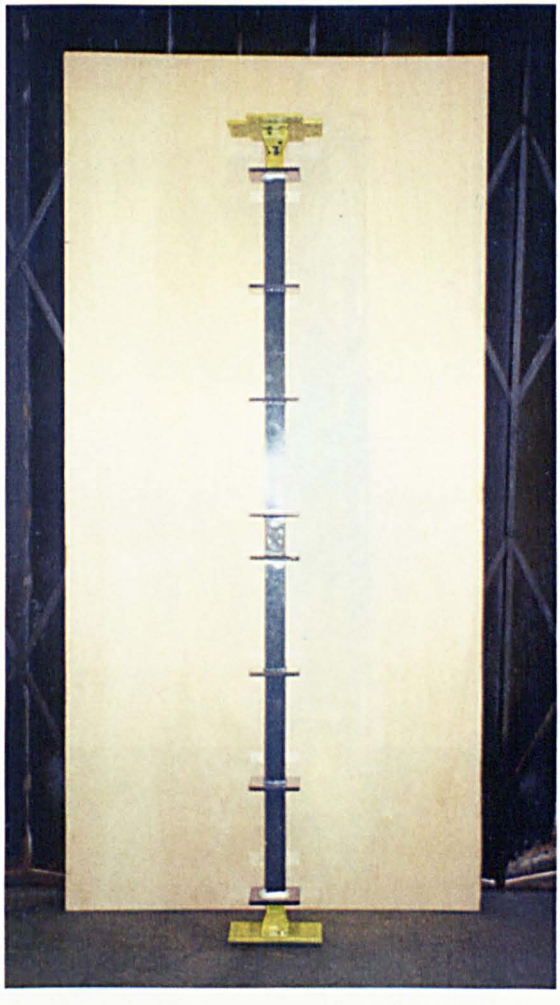

Photo 4.1 Square cylinder under construction

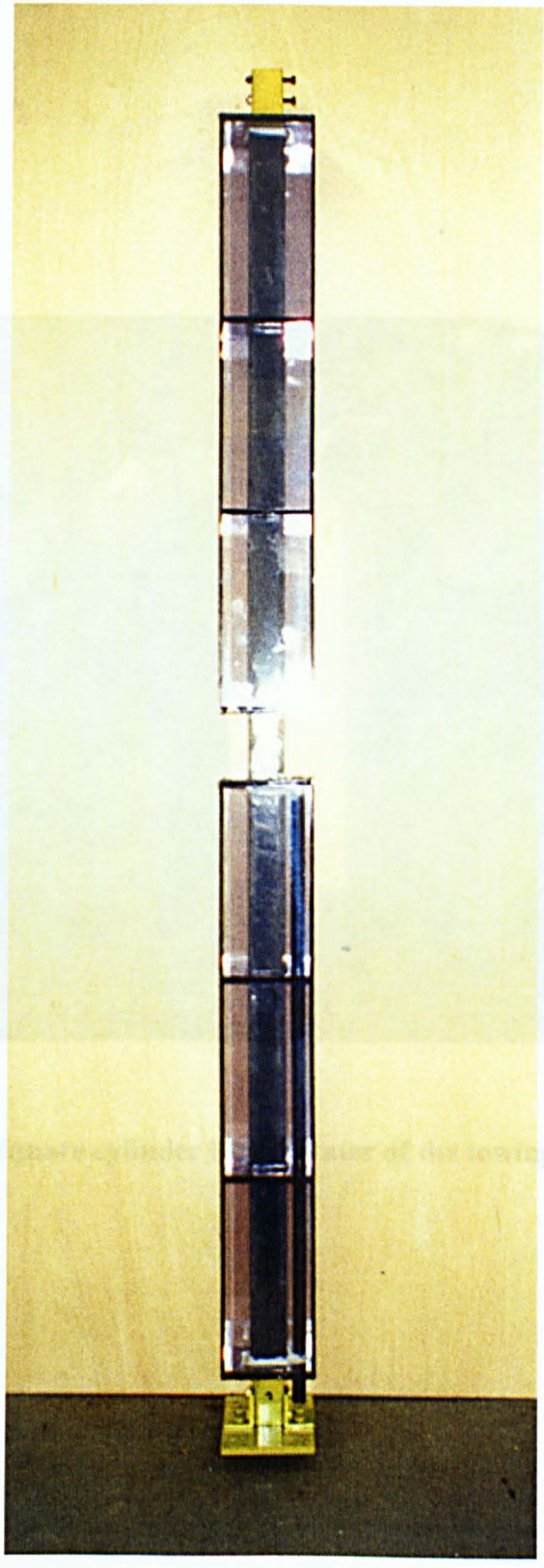

Photo 4.2 Square cylinder with bulkheads covered with smooth PVC plates

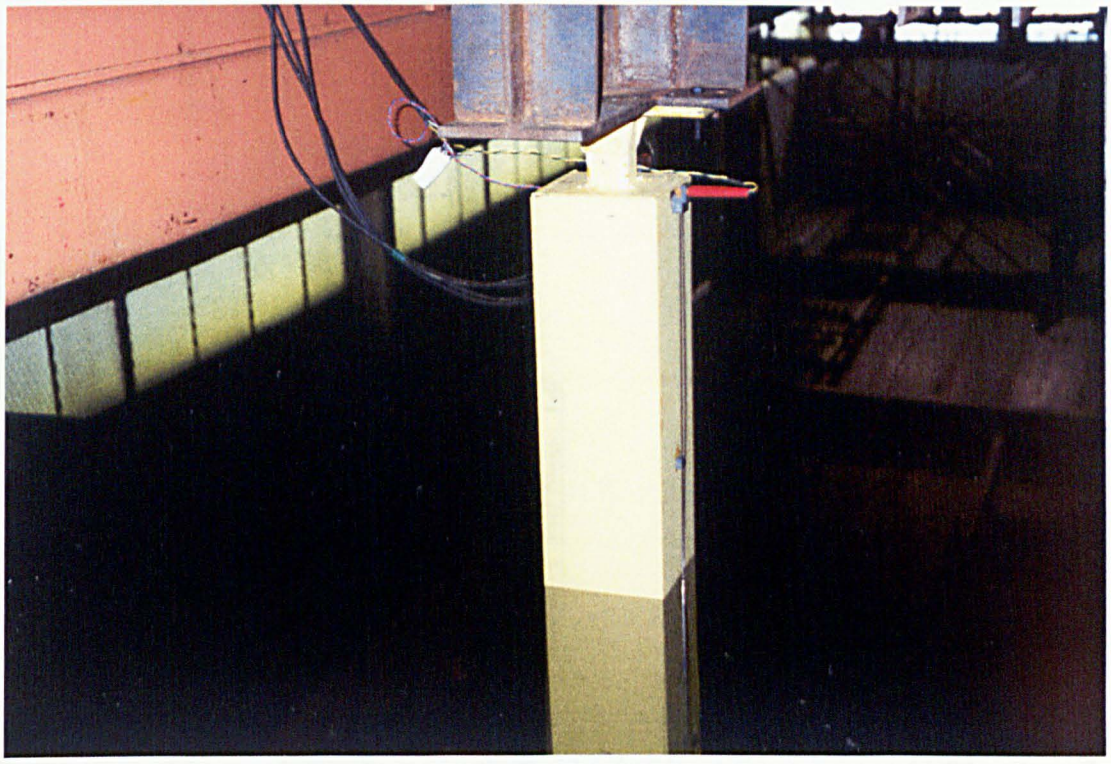

Photo 4.3 Square cylinder in still water of the towing tank

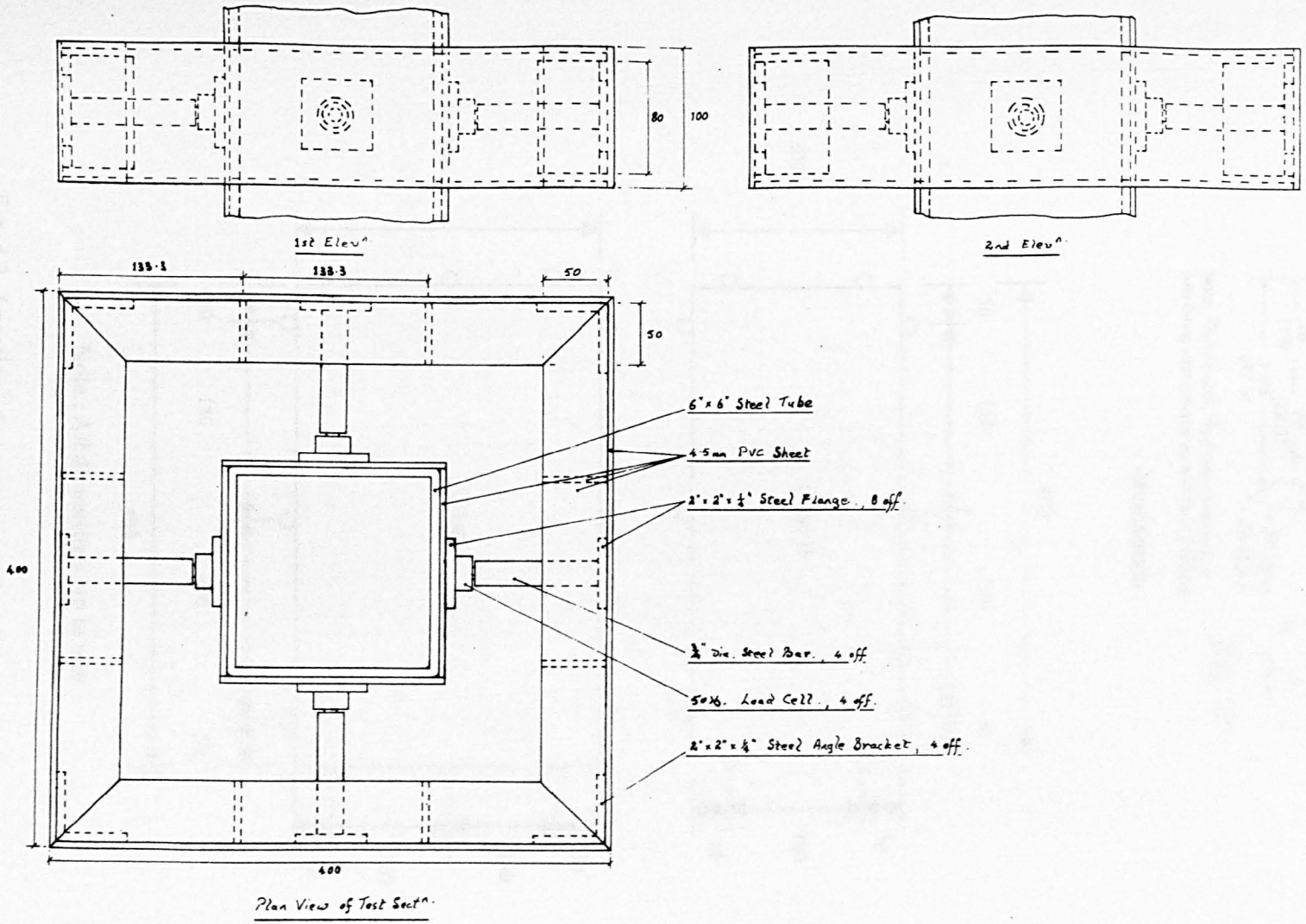

Fig. 4.1 Details of loading section with load cells

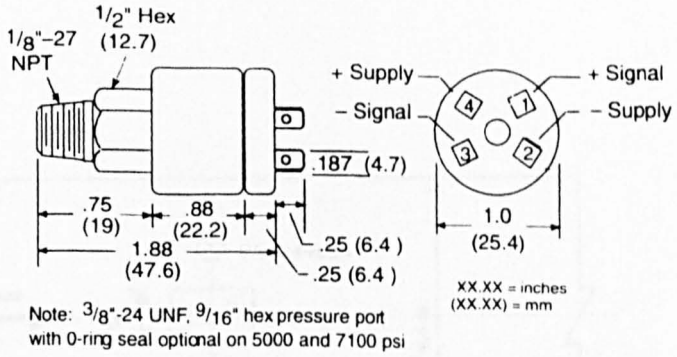

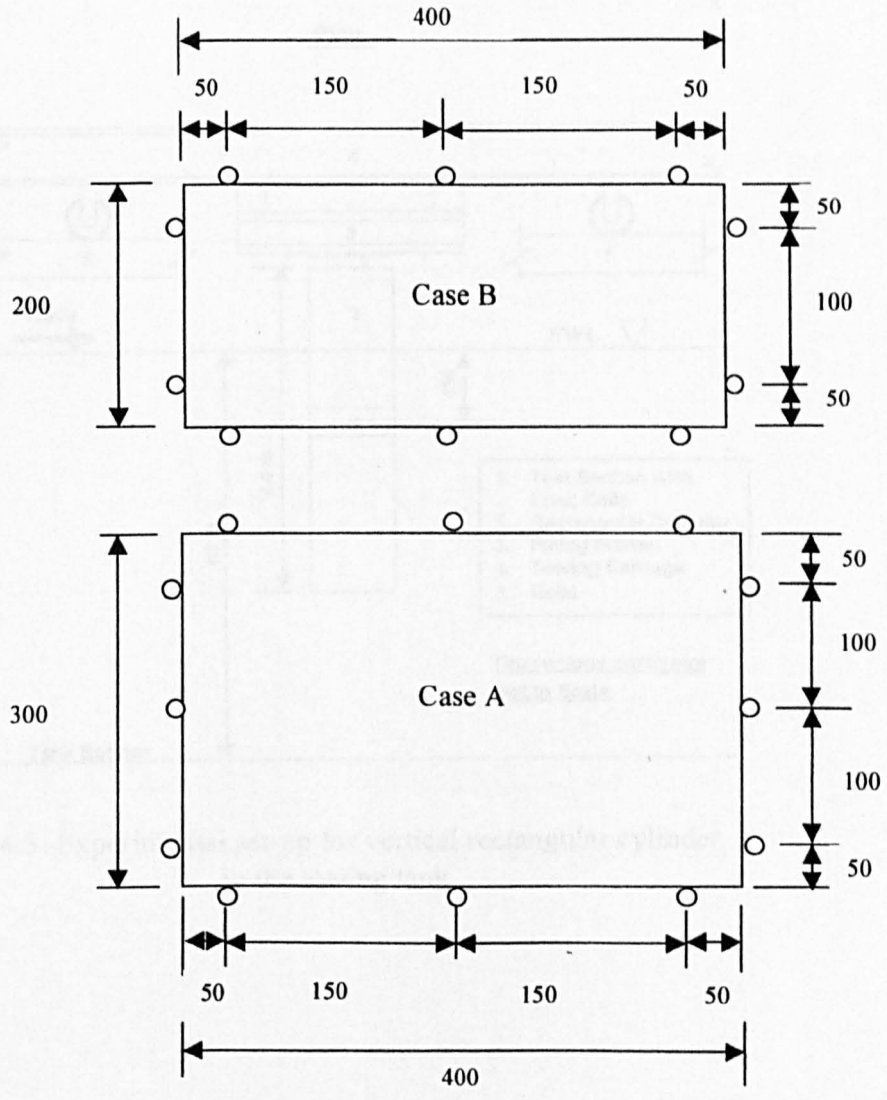

Note : All dimensions are in mm

Fig. 4.2 Location of pressure transducers around the cylinder

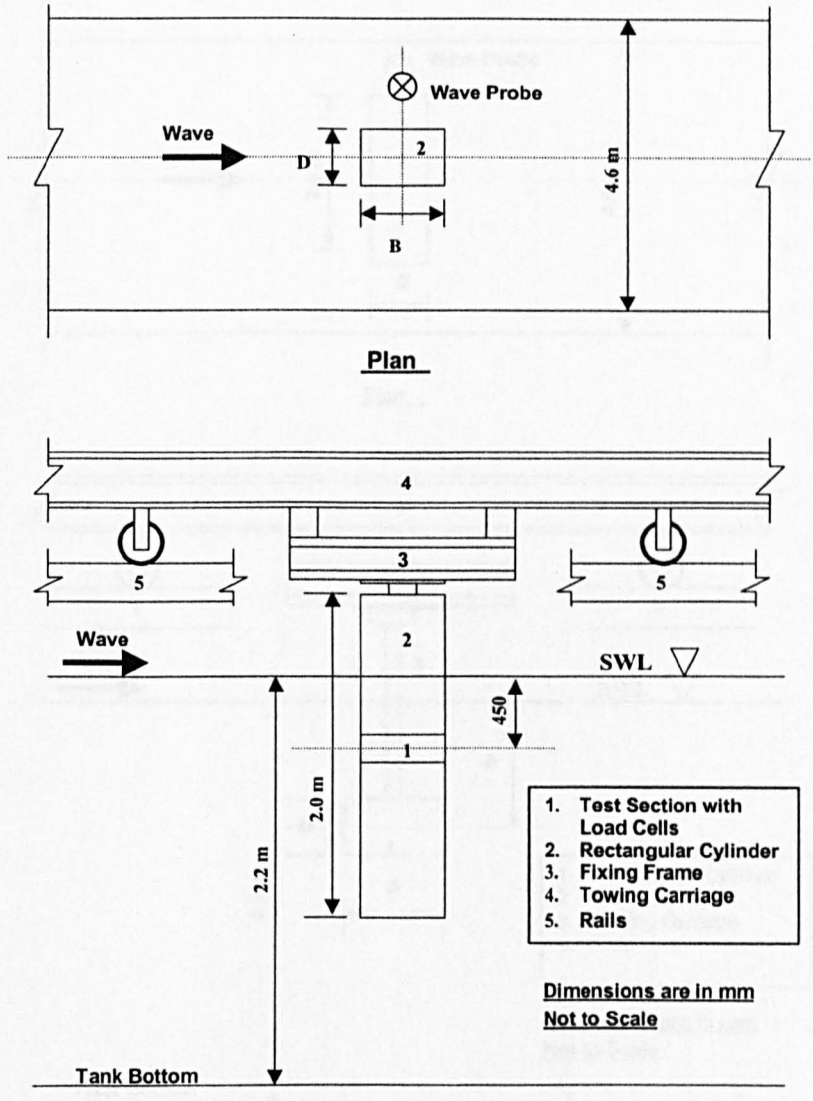

Fig.4.3 Experimental set-up for vertical rectangular cylinder in the towing tank

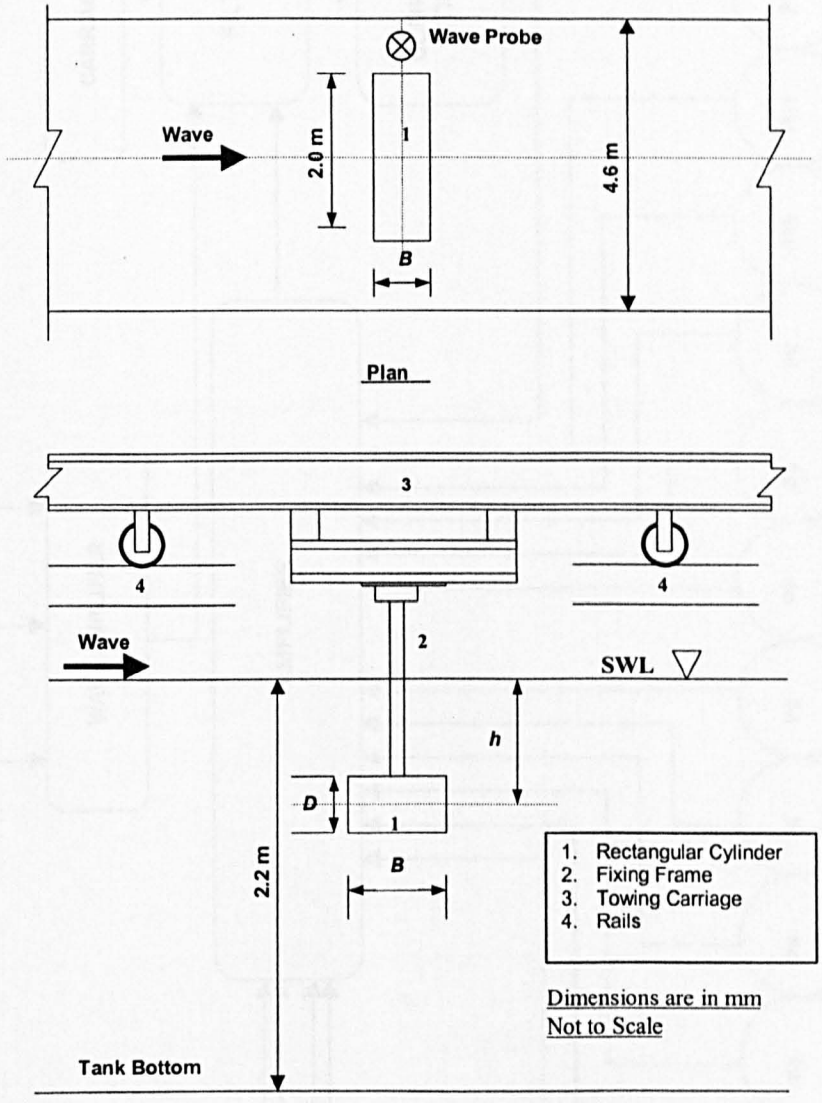

Fig.4.4 Experimental set-up for horizontal rectangular cylinder in the towing tank

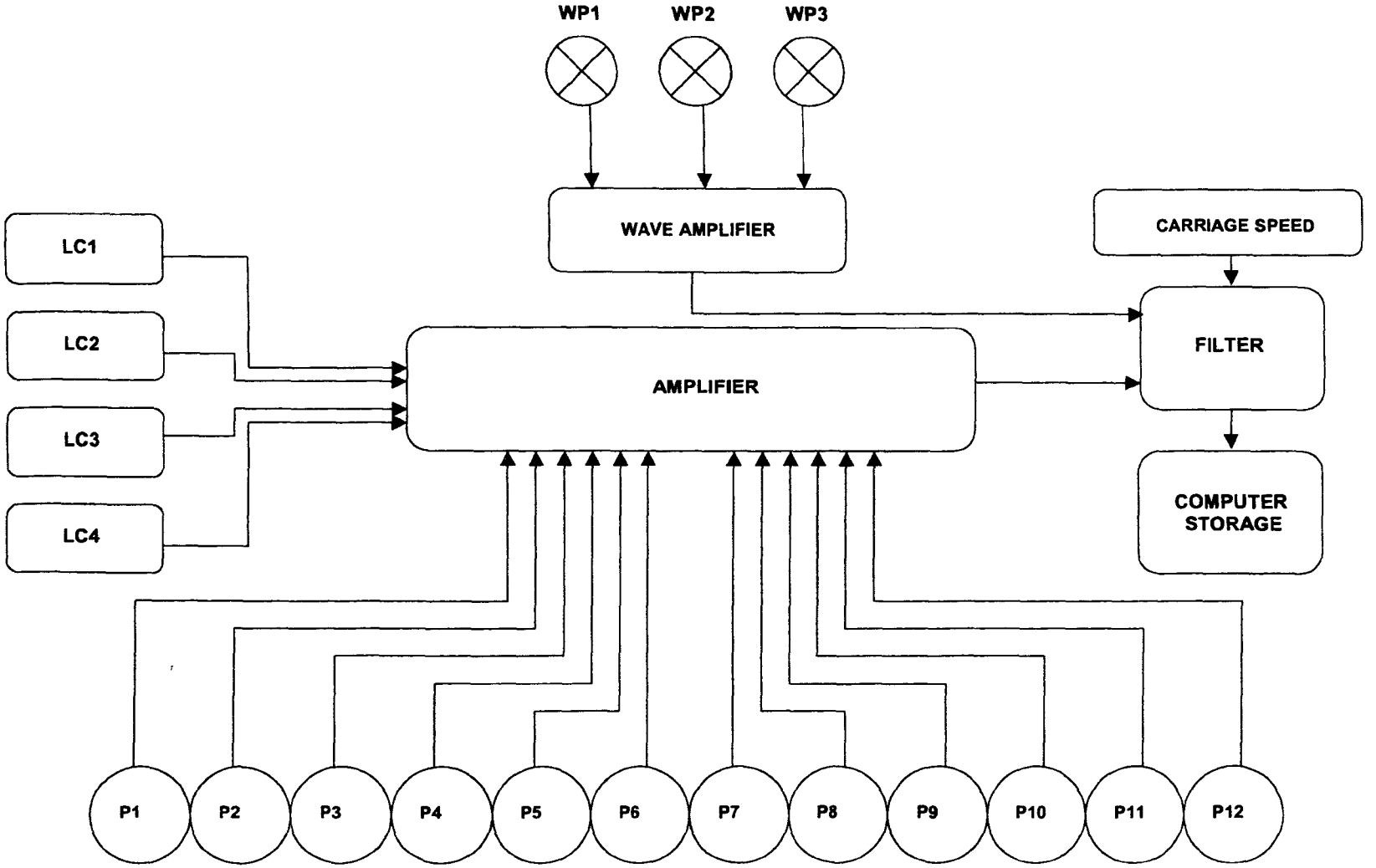

LC1,LC2,LC3 & LC4 – Load Cells
P1,P2,P3,P4,P5, P6, P7, P8, P9, P10, P11& P12 – Pressure Transducers
WP1,WP2 & WP3 – Wave Probes

Fig. 4.5 General instrumentation set-up

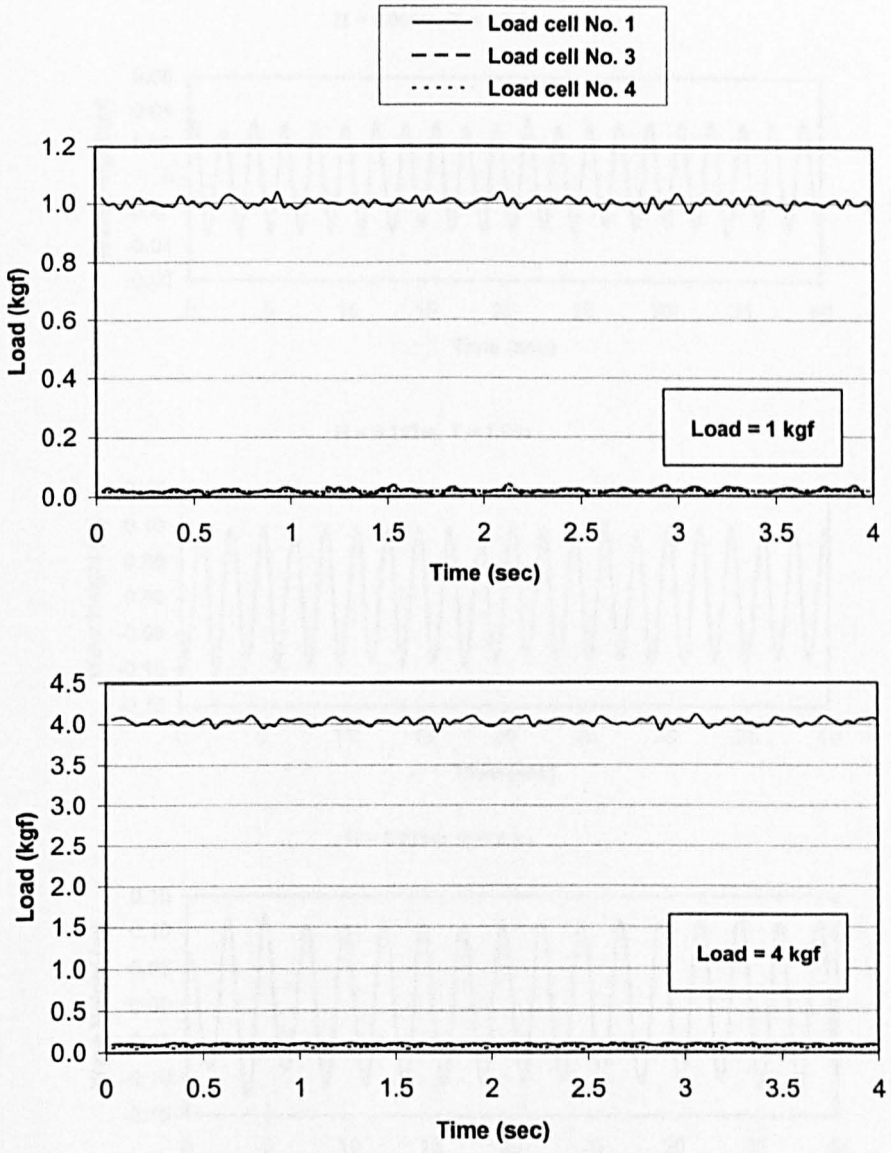

Fig. 4.6 Calibration of load cells for a load of 1 Kgf and 4 Kgf

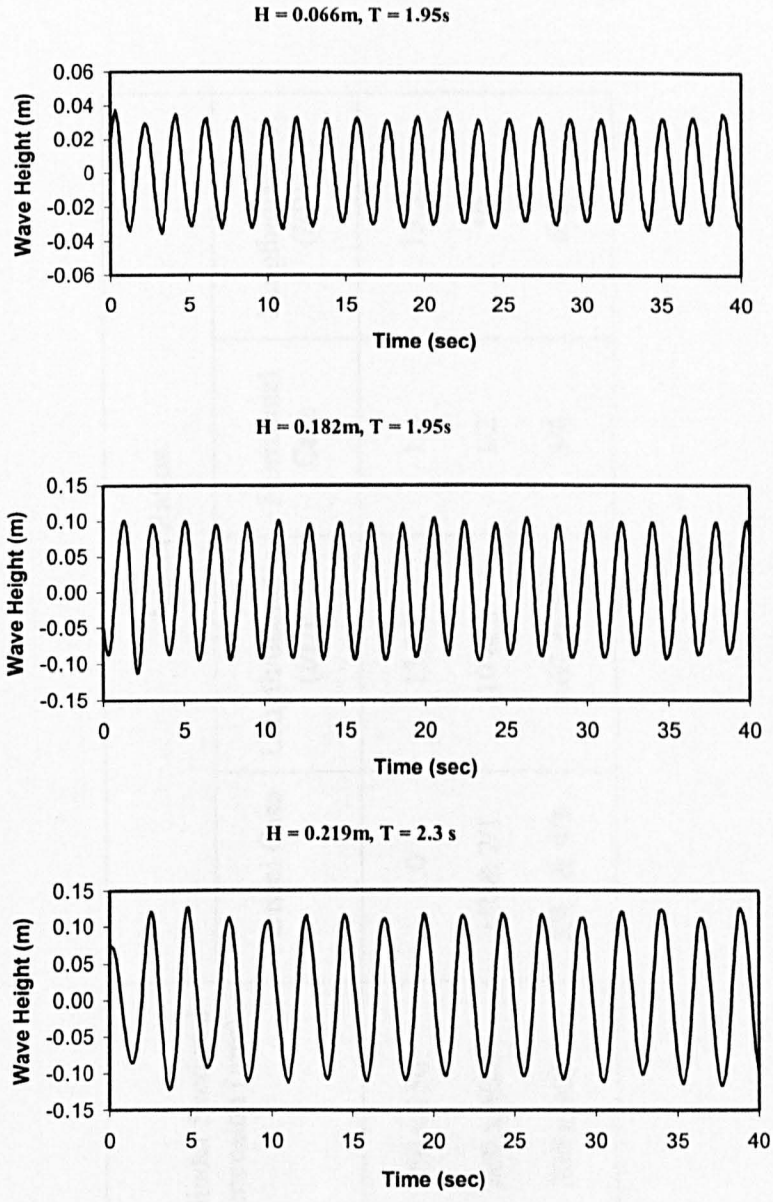

Fig. 4.7 Sample records of wave elevation

Table 4.1. Cylinder model details

Case	Cylinder Sectional Dimension (mm)	Aspect Ratios			
		Vertical Case	Length/diameter (*l/D*)	Horizontal Case	Length/diameter (*l/D*)
A	150 x 150	1.0	13.33	1.0	13.33
B	200 x 400	1/2 & 2/1	10 & 5	1/2	10
C	300 x 400	3/4 & 4/3	6.67 & 5	3/4	6.67

Table 4.2. Natural frequency calculations for vertical cylinders

$E_P = 3.4$ GN/m^2, $E_S = 195$ GN/m^2, $\rho_P = 1200$ kg/m^3 and $\rho_S = 7800$ kg/m^3, (s for Steel and p for Perspex)

Aspect ratio	A_P (m^2)	A_S (m^2)	C_A	m (kg)	EI x10^4 (kg-m^2)	k x10^5 (kg/m)	f_n (Hz)
1.0	0.0040	0.0015	1.2	74.9	4.076	0.238	2.84
1/2	0.0082	0.0027	0.67	146.9	80.02	4.674	8.96
2/1	0.0082	0.0027	2.14	318.6	20.02	1.168	3.05
3/4	0.0096	0.0031	0.90	235.6	112.8	6.584	8.41
4/3	0.0096	0.0031	1.50	340.7	56.57	3.301	4.95

Table 4.3. Natural frequency calculations for horizontal cylinders

Aspect ratio	A_P (m^2)	A_S (m^2)	C_A	m (kg)	EI x10^4 (kg-m^2)	k x10^5 (kg/m)	f_n (Hz)
1.0	0.0040	0.0015	1.2	89.48	4.076	9.784	16.64
1/2	0.0082	0.0027	0.67	175.91	20.02	48.05	26.3
3/4	0.0096	0.0031	0.90	293.9	56.57	135.77	34.2

Table. 4.4 List of wave heights and wave periods for regular waves for aspect ratio = ½ (measured)

Sl. No	Wave Ht (m)	Wave Period (sec)	Sl.No	Wave Ht (m)	Wave Period (sec)
1	0.0811	2.3453	27	0.2936	1.7173
2	0.0955	2.3373	28	0.3313	1.713
3	0.1075	2.3333	29	0.3589	1.7062
4	0.1358	2.3397	33	0.1604	1.5679
5	0.1819	2.33	34	0.2291	1.5652
6	0.2214	2.3421	35	0.3029	1.5615
7	0.3164	2.3287	36	0.0528	1.359
8	0.0598	2.1391	37	0.1022	1.3642
9	0.1211	2.1384	38	0.1193	1.3567
10	0.1681	2.1308	39	0.1663	1.3574
11	0.2211	2.1391	40	0.2093	1.3529
12	0.235	2.1473	41	0.2154	1.3605
13	0.2887	2.1534	42	0.2486	1.3547
14	0.3329	2.1325	43	0.2843	1.3613
15	0.0604	1.9458	44	0.0614	1.1721
16	0.1252	1.951	45	0.1305	1.1763
17	0.1542	1.9388	46	0.1808	1.1773
18	0.1773	1.9494	47	0.2359	1.1745
19	0.2239	1.9469	48	0.2226	1.1743
20	0.2898	1.9461	49	0.2645	1.1737
21	0.3848	1.9464	50	0.2887	1.1743
22	0.0606	1.72			
23	0.1154	1.7111			
24	0.1411	1.7196			
25	0.1624	1.7193			
26	0.2409	1.7163			

Table. 4.5 List of wave heights and wave periods for random waves PM spectrum (measured)

Wave. No	Significant Wave Ht. H_s (m)	Peak Period T_p (sec)
PM_S15_1	0.069	1.39
PM_S15_2	0.135	1.40
PM_S15_3	0.171	1.41
PM_S15_4	0.086	1.60
PM_S15_5	0.155	1.59
PM_S15_6	0.176	1.60
PM_S15_7	0.101	1.95
PM_S15_8	0.155	1.95
PM_S15_9	0.186	1.96

Table. 4.6 List of wave heights and wave periods for random waves JONSWAP spectrum (measured)

Wave. No	Significant Wave Ht. H_s (m)	Peak Period T_p (sec)
JS_S15_1	0.075	1.46
JS_S15_2	0.098	1.46
JS_S15_3	0.151	1.46
JS_S15_4	0.107	1.67
JS_S15_5	0.139	1.66
JS_S15_6	0.161	1.67
JS_S15_7	0.098	1.89
JS_S15_8	0.118	1.88
JS_S15_9	0.158	1.90

CHAPTER 5
DATA ANALYSIS

5.1 General

The purpose of measuring forces in waves is to compute the hydrodynamic coefficients, C_D and C_M for different wave conditions. It should be noted that drag and inertia coefficients may not be obtained reliably using numerical methods and that the validity of the coefficients, the equation and the limits of its application have to be determined experimentally. It is assumed that these coefficients are constant throughout a given cycle of wave force. There are many methods available for estimating force coefficients from the data produced from experiments in waves, wave and current and other oscillatory flows. In the present work mainly the wave-by-wave method is employed for analysing the data and the procedure is described in this chapter.

5.2 Calculation of Particle Kinematics using Linear wave theory

As mentioned earlier, in this, water particle velocity has not been directly measured in the tank. Instead, velocity and accelerations are computed using linear wave theory for the evaluation of drag and inertia coefficients. This was done using Fourier transforms and the general method is outlined here.

Each physical process can be described either in time domain (signal Vs time) or in frequency domain. The aim of the Fourier Transform is to convert some arbitrary time signal to its representation in frequency domain. In other words, a time series is represented by linear set of periodic functions. Each periodic function can be represented by three properties: amplitude, frequency and phase. Inverse Fourier

Transform does exactly the opposite: receiving a group of periodic functions it combines them into the corresponding time dependent signal.

The above paragraph refers to a general Fourier analysis. But in numerical methods we often need to find an algorithm that works much faster. Such algorithm is called a Fast Fourier Transform (FFT), and it has one limitation - the length of the data should be to the power of 2. If the length of the data is not exactly the power of two, then only first N points that satisfy this condition will be taken. In the present work, a FORTRAN code (Numerical Recipes-Fortran 77) has been used to perform FFT and IFFT on the data. The calculation of wave particle velocities and accelerations from the measured wave profile is conceptually given in the flow chart-1. Based on linear wave theory, the frequency response function for horizontal, $R_u(\omega)$ and vertical, $R_w(\omega)$ components are respectively given by:

$$R_u(\omega_n) = \frac{\omega_n \cosh k_n(d+z)}{\sinh k_n d} \tag{5.1}$$

$$R_w(\omega_n) = \frac{\omega_n \sinh k_n(d+z)}{\sinh k_n d} \tag{5.2}$$

Using the above response functions the time histories of wave kinematics can be generated.

Even though, most of the experiments are conducted at deep water limit, validation of the use of linear wave theory is necessary. To do that, the values of measured wave height are presented in the form of dimensionless wave steepness, H/gT^2 with dimensionless relative depth, d/gT^2. These values are superposed on the wave theory selection diagram (Fig. 5.1) of Barltrop et al. (1991), where, H is the wave height, T is the wave period, d is the water depth and g is acceleration due to gravity. This plot indicate that about 40% of data points lies in the Airy/linear wave region and about

60% of the data points are falling in the stream function theory of 3rd order region. The error involved in applying linear wave theory outside its theoretical range of applicability is given by Barltrop et al (1991) and the error curves are also plotted in Fig.5.1. The curves in Fig.5.1 are plotted for horizontal particle velocity under wave crest at MWL with reference to Airy theory as % of wave theory shown. It is evident from this plot that using linear wave theory for the calculation of wave velocity, the data points in the region out of linear wave theory are between the 100% and 105% curves and therefore it can be concluded that linear wave theory can be used for all the waves generated in the present experiments. A similar assurance can be obtained from Fig.5.2 plotted for vertical particle acceleration under the wave crest at MWL.

5.3 Estimation of Hydrodynamics Coefficients

The Morison's equation is commonly used for predicting wave forces in regular and irregular waves, however the values of drag and inertia coefficients obtained for irregular wave forces are not necessarily the same as those determined from regular waves. On the other hand, it is also expected that these force coefficients will depend on the shape of the spectrum. Hence, for these reasons it will be most appropriate to estimate force coefficients directly from random wave force measurements. The different methods used to estimate C_D and C_M from measured random data are given by Borgman (1972), Sarpkaya and Isaacson (1981), Chakrabarti (1987) and Isaacson et al. (1991). These methods can be classified into two groups, depending on whether or not the drag and inertia coefficients are assumed constant for a particular wave record.

(i) Time Domain Analysis:

Time domain analysis gives direct information related to average or typical wave characteristics such as asymmetry in shape of crests and troughs, wave height, zero up-crossing and zero down-crossing period. The effects of non-linearity of sea

surface can be included in time domain analysis techniques. From the methods of time domain analysis for evaluation of Morison force coefficients, the comparison between measured and predicted force can be easily done.

(ii) Frequency Domain Analysis:

In frequency domain analysis the power spectral density from a record is estimated by Fourier transform operation. The time series are usually divided into segments of equal length and the power spectral density at each frequency is obtained by averaging the estimates from the segments. Sometimes the time series may be treated as a single long record instead of dividing to some equal segments. In this method the peak frequency is considered where the energy is most concentrated, the wave height parameter H_S, is an estimate of significant wave height, can be derived from zeroth moment of power spectral density curve. Some of the other useful parameters of waves, which can be easily derived from time domain analysis, are not available in the frequency domain.

All of these methods involve some kind of fit between the measured and predicted wave forces and usually involves a least squares fit or method of moments. These may be applied to (i) the time series, (ii) the spectral density or covariance function, (iii) the probability density of the force, or (iv) the cross-spectrum between the free surface elevation and the wave force. The most common methods used are:

- Least-squares fit of the force time series
- Least-squares fit of the force spectrum
- Least squares fit on a wave by wave basis.
- Method of moments applied to the force probability distribution
- Cross-spectra fitting between surface elevation and force

One of the most straightforward methods for estimating the force coefficients, which are used in both time domain and frequency domain analysis, is the least square method. The method of least squares approach has the most general application as it can also be applied in cases where the water particle kinematics are not sinusoidal as in to irregular waves or non-linear waves. Generally, the least square method is found to provide reliable force coefficients, when the wave kinematics are directly measured or computed using a suitable wave theory and hence this method is followed in the present study for the analysis of data. Using the numerical simulation of wave forces, Isaacson et al (1991) reported that the method of least squares is reliable and accurate.

5.3.1 Least Squares time series method (LS-TS)

This method consists of the minimization of the error between the measured and calculated force time histories and results in constant values of drag and inertia coefficients. By this method the coefficients can be estimated by minimizing the square of the difference between the time series of the measured and predicted forces. This method can be used for every individual wave cycle defined between successive zero up or down crossings, or for whole wave records and it is assumed that C_D and C_M are constant in each cycles or for the whole sets of the wave data respectively. The formulation of this method is given below. Considering e_f is the error of force expressed as

$$e_f = f - f_e = f - \left(0.5\rho D C_D u|u| + A\rho C_M \dot{u}\right) \tag{5.3}$$

where, f is the measured force and f_e is the estimated force. The mean square error, $\bar{E}$ is given by

$$\bar{E} = \frac{1}{N}\sum_{i=1}^{N} e_f^2 \tag{5.4}$$

where, N is the number of data. The mean square error is minimised here,

$$\frac{\partial \overline{E}}{\partial C_D} = 0.5\rho D C_D \sum u^4 + A\rho C_M \sum u|u|\dot{u} - \sum u|u|f = 0 \tag{5.5}$$

$$\frac{\partial \overline{E}}{\partial C_M} = 0.5\rho D C_D \sum u|u|\dot{u} + A\rho C_M \sum \dot{u}^2 - \sum \dot{u} f = 0 \tag{5.6}$$

where the summations are made for N number of data. Now simultaneous solution of equations (5.5) and (5.6) leads to the coefficients C_D and C_M,

$$C_D = \frac{\sum f u|u| \sum \dot{u}^2 - \sum f\dot{u} \sum u|u|\dot{u}}{0.5\rho D\left(\sum u^4 \sum \dot{u}^2 - \left(\sum u|u|\dot{u}\right)^2\right)} \tag{5.7}$$

$$C_M = \frac{\sum f\dot{u} \sum u^4 - \sum f u|u| \sum u|u|\dot{u}}{A\rho\left(\sum \dot{u}^2 \sum u^4 - \left(\sum u|u|\dot{u}\right)^2\right)} \tag{5.8}$$

If we consider the waves to be linear and use of data over the full wave cycle, then

$$\sum u|u|\dot{u} = 0 \tag{5.9}$$

and equations (5.7) and (5.8) are simplified as

$$C_D = \frac{\sum f u|u|}{0.5\rho D\left(\sum u^4\right)} \tag{5.10}$$

$$C_M = \frac{\sum f\dot{u}}{A\rho\left(\sum \dot{u}^2\right)} \tag{5.11}$$

Once C_D and C_M are determined, the mean square error from equation (5.4) can be written as

$$\begin{aligned}\bar{E} &= (A\rho C_M)^2\overline{\dot{u}^2} + \overline{f^2} + 2(0.5\rho DC_D)(A\rho C_M)\overline{u|u|\dot{u}} \\ &\quad - 2(0.5\rho DC_D)\overline{fu|u|} - 2(A\rho C_M)\overline{f\ddot{u}} + (0.5\rho DC_D)^2\overline{u^4}\end{aligned} \tag{5.12}$$

where the over bar indicate averaging over N values of data. This equation defines a quadratic error surface where the minimum value is obtained with the value of C_D and C_M as defined by equations (5.10) and (5.11). Using equation (5.9), the equation (5.12) is a form of an equation of an ellipse in rectangular co-ordinates with C_D and C_M as axes and can be written as:

$$\alpha\left(C_D^2 - 2C_D(\beta/\alpha) + (\beta/\alpha)^2\right) + \gamma\left(C_M^2 - 2C_M(\delta/\gamma) + (\delta/\gamma)^2\right)$$

$$= \bar{E} + (\beta^2/\alpha) + (\delta^2/\gamma) - f^2 \tag{5.13}$$

or in standard ellipse form it is given by:

$$\frac{(C_D - \beta/\alpha)^2}{\zeta/\alpha} + \frac{(C_M - \delta/\gamma)^2}{\zeta/\gamma} = 1 \tag{5.14}$$

Where $\alpha = (0.5\rho D)\overline{u^4}$, $\beta = \overline{fu|u|}$, $\gamma = (A\rho)\overline{\dot{u}^2}$, $\delta = \overline{f\ddot{u}}$ and ζ is a constant equal to the right hand side of equation (5.13). The eccentricity of the ellipse is $e = \sqrt{1-(\alpha/\gamma)}$ if $\alpha < \gamma$ or $e = \sqrt{1-(\gamma/\alpha)}$ if $\alpha > \gamma$. When e is equal to zero then the ellipse is a circle and when $e \to 1$ then the ellipse will be flattened. If the ellipse is as shown in Fig. 5.3, then C_D could take a range of values without changing the mean square error, so the data are well conditioned for C_M and are not suitable for determination of C_D. When e is equal to zero then the data are well conditioned for determination of both C_D and C_M.

The above method was developed by Dean (1976). He showed that depending on the wave and cylinder characteristics, data could be well or poorly conditioned for resolving C_M and C_D. Dean (1976) suggested that much of the scatter in the reported coefficients could be due to poorly conditioned data. In practice when the data is in the low range of Reynolds number, *Re*, then the drag force is a small part of total force, so the data would not be well conditioned for finding the drag coefficient while for high Re numbers it is true for evaluation of inertia coefficient. The range of reliable data for evaluation of hydrodynamic coefficients can be determined by the method as used by Dean. If we consider that the minimum value of error, $\overline{E}_{\min}$ is associated with C_D and C_M as determined from equations (5.10) and (5.11) then using a truncated Taylor series for a two variable function, the error surface function can be written as:

$$\overline{E} = \overline{E}_{\min} + \frac{\partial \overline{E}}{\partial C_D}\Delta C_D + \frac{\partial \overline{E}}{\partial C_M}\Delta C_M$$

$$+ \frac{1}{2!}\left(\frac{\partial^2 \overline{E}}{\partial C_D^2}(\Delta C_D)^2 + 2\frac{\partial^2 \overline{E}}{\partial C_D \partial C_M}\Delta C_D \Delta C_M + \frac{\partial^2 \overline{E}}{\partial C_M^2}(\Delta C_M)^2 \right) \quad (5.15)$$

Using equation. (5.5) and (5.6) the above equation can be reduced to

$$\overline{E} = \overline{E}_{\min} + \frac{\partial^2 \overline{E}}{\partial C_D^2}\frac{(\Delta C_D)^2}{2} + \frac{\partial^2 \overline{E}}{\partial C_M^2}\frac{(\Delta C_M)^2}{2} + \frac{\partial^2 \overline{E}}{\partial C_D \partial C_M}\Delta C_D \Delta C_M \quad (5.16)$$

and finally using equations (5.5), (5.6) and (5.9) the above equation is given by:

$$\overline{E} = \overline{E}_{min} + 2(0.5\rho D)^2 \overline{u^4}\frac{(\Delta C_D)^2}{2} + 2(A\rho)^2 \overline{\dot{u}^2}\frac{(\Delta C_M)^2}{2} \quad (5.17)$$

Now by keeping C_M constant the change in C_D associated with a change in error surface is given by:

$$\Delta C_D = \frac{2}{\rho D}\sqrt{\frac{\overline{E} - \overline{E}_{\min}}{\overline{u^4}}} \tag{5.18}$$

and the same approach for C_M

$$\Delta C_M = \frac{1}{\rho A}\sqrt{\frac{\overline{E} - \overline{E}_{min}}{\overline{\dot{u}^2}}} \tag{5.19}$$

where if ΔC_M is small, the data are well conditioned for determining C_M and when ΔC_D is small the data are suitable for determining C_D. Dean introduced a reliability ratio for determining drag or inertia coefficients by the ratio of the axes of the error ellipse as:

$$R = \frac{\Delta C_M}{\Delta C_D} = \frac{2}{\pi D}\sqrt{\frac{\overline{u^4}}{\overline{\dot{u}^2}}} \tag{5.20}$$

Dean showed with a special example that if the mean square error is of the order of 10 %, then the error of calculated value of C_M and C_D can be of the order of 85% and 50% respectively. Dean suggested that data can be well conditioned for evaluating C_M and C_D when $0.25<R<4$ and for C_M when $0<R<0.25$ and for C_D when $R>4$. It can be shown that equation (5.20) is true even when, from the data, equation (5.9) is not satisfied. In this case equation (5.17) changes but equations (5.18),(5.19) & (5.20) remain unchanged.

Applying the above procedure, in the case of a rectangular cylinder, the horizontal and vertical force coefficients are given by,

$$C_{D_{X,Y}} = \frac{2}{\rho D}\left[\frac{f_1 f_2 - f_3 f_4}{f_2 f_5 - f_4^{\,2}}\right] \tag{5.21}$$

$$C_{M_{X,Y}} = \frac{1}{\rho A}\left[\frac{f_3 f_5 - f_1 f_4}{f_2 f_5 - f_4^{\,2}}\right] \tag{5.22}$$

Where, $F_{M_{X,Y}}$ represent the instantaneous measured forces in horizontal and vertical directions denoted by suffix 'X' and 'Y' respectively and,

$$f_1 = \sum_i^N F_{M_{X,Y}}(i) V_{X,Y}(i) \left| V_{X,Y}(i) \right|$$

$$f_2 = \sum_i^N \dot{V}_{X,Y}(i)^2$$

$$f_3 = \sum_i^N F_{M_{X,Y}}(i) \dot{V}_{X,Y}(i)$$

$$f_4 = \sum_i^N V_{X,Y}(i) \left| V_{X,Y}(i) \right| \dot{V}_{X,Y}(i)$$

$$f_5 = \sum_i^N V_{X,Y}(i)^4$$

$V_{n_{X,Y}}$ = Water particle velocity

$\dot{V}_{n_{X,Y}}$ = Water particle acceleration

Note that, for a vertical cylinder, the drag and inertia coefficients are obtained corresponding to the force in the X - direction (in-line force) and for a horizontal cylinder, drag and inertia coefficients are derived for both horizontal (X) and vertical (Y) forces.

According to Dean (1976) if the inertia force components tend to dominate, reasonable resolution in the inertia coefficients can be expected and the data are better

conditioned for determining inertia coefficients, along with contamination of the calculated drag coefficients. Here, the values of Dean's index, R, have been evaluated based on the results reported in Chapter-6. The values of R obtained through the present experiments are put together in Fig. 5.4 for horizontal cylinders, corresponding to the vertical and horizontal force components. The maximum value of R obtained is about 0.35 for horizontal cylinders and around the same value is obtained for vertical cylinders as well. This indicates that the data is well conditioned for determining the inertia coefficients and also to some extend to the drag coefficients as some of the data falls into second category. However, a majority of the data are within the limit $R<0.25$, therefore suitability of data for determining the drag coefficients is questionable. It has to be remembered that direct measurement of drag coefficients at very low KC numbers is extremely difficult because the fluid loading is dominated by the inertia component. Bearman & Russell (1997) gave a calculation that at $KC = 1$ and $\beta = 3\text{x}10^4$, the maximum drag load in a cycle is only about 2% of the maximum inertia load and at $KC = 0.1$ it drops to about 1%. Thus, at low KC numbers the total force is mainly determined by inertial component and since the conditioning of the data is more suitable for evaluating the inertia coefficients, the force calculation using the inertia coefficients as reported in this study can be safely carried out, even if one thinks that an error is involved in the drag coefficients.

5.3.2 Least squares by wave by wave (WW-TS)

Another approach which incorporates the variability of the force coefficients within a given wave record may be developed by assuming that C_D and C_M are constant for individual waves, and that their variability can be examined by separately analysing individual waves within a given wave record. A simple deterministic version of this approach is to approximate the waves as sinusoidal on a wave by wave or half-wave by half-wave basis. In this method, each wave force cycle from the whole force time history is identified and the least square method is then applied to the measured and predicted forces. The drag and inertia coefficients for each individual wave cycle are

estimated and from this result, the average values of the force coefficients (generally, for regular waves) can be calculated. In random flow conditions, individual cycles will have a distribution of KC and β values and this method requires statistical reduction of the resultant data. Results of analysis from individual cycles are grouped in intervals of KC values and from the grouped results, mean or median values are computed to yield the values of C_D, C_M versus KC. After obtaining drag and inertia coefficients it is fairly straightforward to calculate a wave by wave predicted force. The procedure is essentially the reverse of the fitting process by which C_D and C_M are determined. The coefficients for a particular wave are substituted back into Morison's equation together with the original velocity and acceleration signals to obtain the force signal. The residual force can then be calculated by subtracting the predicted force from the measured force signal.

5.3.3 Root mean square force coefficients

In addition to drag and inertia coefficients, a few other coefficients are also in use to represent the force. The maximum and root mean square coefficients for the in-line force are expressed as,

$$C_{Fmax} = \frac{F_{X\,max}}{0.5\rho D U_{rms}^2} \tag{5.23}$$

$$C_{Frms} = \frac{F_{Xrms}}{0.5\rho D U_{rms}^2} \tag{5.24}$$

$$C_{Trms} = \frac{\sqrt{(F_{Xrms}^{\ 2} + F_{Lrms}^{\ 2})}}{0.5\rho D U_{rms}^2} \tag{5.25}$$

Where, F_{Xmax} is the maximum in-line force, F_{Xrms} and F_{Lrms} are the rms forces for in-line and transverse forces respectively and U_{rms} is the root mean square horizontal velocity.

The maximum transverse force coefficient (C_{Lmax}) and the root mean square lift coefficient (C_{Lrms}) can be calculated by equations (5.26) and (5.27) respectively,

$$C_{Lmax} = \frac{F_{Lmax}}{0.5\rho DU_{rms}^2} \tag{5.26}$$

$$C_{Lrms} = \frac{F_{Lrms}}{0.5\rho DU_{rms}^2} \tag{5.27}$$

Where, F_{Lmax} is the maximum transverse force and F_{Lrms} is the rms transverse force.

5.4 Wave-Force Spectral Density

The force spectral density has been calculated by using the FFT technique as explained in Chapter 3. The number of data points used for spectral density estimate for most of the time series are 1024. A Hanning window is used for smoothing the spectral density. The spectral densities in the frequency domain are smoothened by the nine points moving average method. For the above, standard Fortran routines from Numerical Recipes in FORTRAN 77 are used. In addition a double check has been made with standard MATLAB routines.

5.5 Definitions of Flow Parameters

In regular waves, the following expressions are used for defining Keulegan-Carpenter number and Reynolds numbers:

$$KC = \frac{U_m T}{B} \tag{5.28}$$

$$Re = \frac{U_m B}{\nu} \tag{5.29}$$

where, U_m is the maximum horizontal particle velocity at the elevation of the centre of the test section, B is the dimension of the cylinder normal to wave crests (Ref. Fig. 4.4), ν is the kinematic viscosity and T is the wave period.

The frequency parameter (β) can be expressed as *Re/KC*, which is equal to $D^2/\gamma T$. The *KC* number is a measure of the water particle orbital amplitude with respect to the cylinder diameter and has been defined in terms of the amplitude of the water particle velocity. This gives the relationship of the circumference of the wave particle path to the structural diameter. The Reynolds number arises from the ratio of inertia force to viscous force.

A simple dimensional analysis which links the hydrodynamic force coefficients with *Re* and *KC* number gives [(Sarpkaya, (1977)],

$$[C_D, C_M, C_L, ...] = f(KC, Re, k/D) \tag{5.30}$$

where, *k/D* is the relative roughness of the cylinder surface. For periodically oscillating flow, Reynolds number is not the most suitable parameter involving viscosity [Sarpakaya (1977)] as the primary reasons are being that the effect of viscosity is relatively small and maximum particle velocity appears in both *KC* and *Re*. Hence replacing, *Re* in the above equation by *Re/KC*, which is the frequency parameter, equation (5.30) is rewritten as

$$[C_D, C_M, C_L, ...] = f(KC, \beta, k/D) \tag{5.31}$$

From laminar boundary layer theory, β represents the ratio of the rate of diffusion through a distance δ (i.e., υ/δ^2, where υ is the kinematic viscosity and δ is the boundary layer thickness) to the rate of diffusion through a distance D (i.e., υ/D^2, D is cylinder's diameter) [Sarpkaya and Issacson (1981)]. The frequency parameter could be constant for a set of experiments conducted at a constant water temperature

on a cylinder of a particular diameter and for a constant value of wave period, but for different values of wave heights. This allows obtaining different values of KC numbers and the results may be plotted for a constant β. One would easily recover the Reynolds number from the relationship $Re = \beta KC$.

While KC number is related to the ratio of the distance particles convect during a flow cycle to the cylinder diameter, β can be explained as being related to the ratio of the time it takes for viscosity to diffuse particles a distance equal to the cylinder diameter to the flow time period. In waves, for a vertical cylinder, the KC is maximum at the surface and decreases with depth of the cylinder, whereas β remains constant over the depth of the cylinder.

Sarpkaya and Storm (1985) have listed the various possible Keulegan-Carpenters and Reynolds number to relate the data in a better way and also to reduce the number of governing parameters for the coexisting wave and current conditions and are given by:

Kuelegan-Carpenter number:

$$KC\left(1+\left|\left(\frac{U_C}{U_m}\right)\right|\right) \tag{5.32}$$

Reynolds number:

$$Re\left(1+\left|\left(\frac{U_C}{U_m}\right)\right|\right) \tag{5.33}$$

In the above expressions, KC and Re are calculated as per equations (5.28) and (5.29) respectively.

In sinusoidal flow conditions, the definition of the Keulegan-Carpenter number is based on U_m, the peak or maximum velocity in a cycle and T, the period of oscillation which is constant from cycle to cycle. In random oscillatory flow, the

velocity scale in the Keulegan-Carpenter number, changes from cycle to cycle as does the zero up-crossing period. Consequently, as is common in analysis of ocean wave height data, an average zero up-crossing period in stationary random conditions, is defined in the analysis of flow velocity data as T_Z. In the present study, in random waves, for the methods of least-squares fit of the force time series, the KC number is defined in terms of the characteristic velocity, $U_C = \sqrt{2}\sigma_u$, and the characteristic wave period, $T_C = 2\pi\sigma_u / \sigma_a$, and the resulting expression is given as,

$$KC = \frac{2\pi}{B}\sqrt{2}\frac{\sigma_u^2}{\sigma_a} \tag{5.34}$$

$$Re = \frac{\sqrt{2}\,\sigma_u\, B}{\nu} \tag{5.35}$$

where, σ_u and σ_a are the standard deviations of velocity and accelerations respectively. For wave by wave method, KC number for each wave is defined as $KC_w = u_w T/B$, where u_w is the amplitude of the fundamental frequency component of the horizontal velocity.

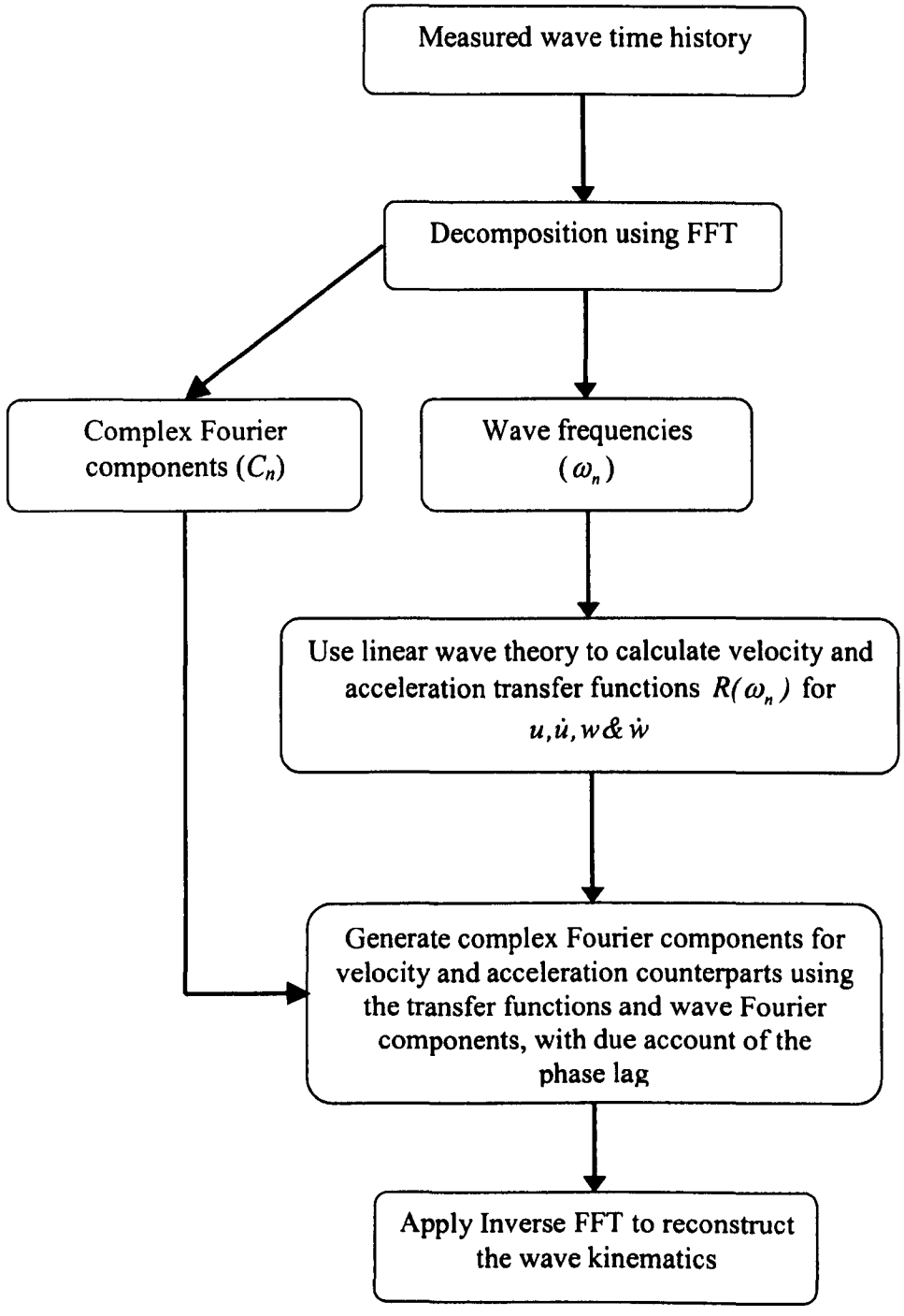

Flow chart. 1. Wave particle kinematics calculation using FFT and IFFT

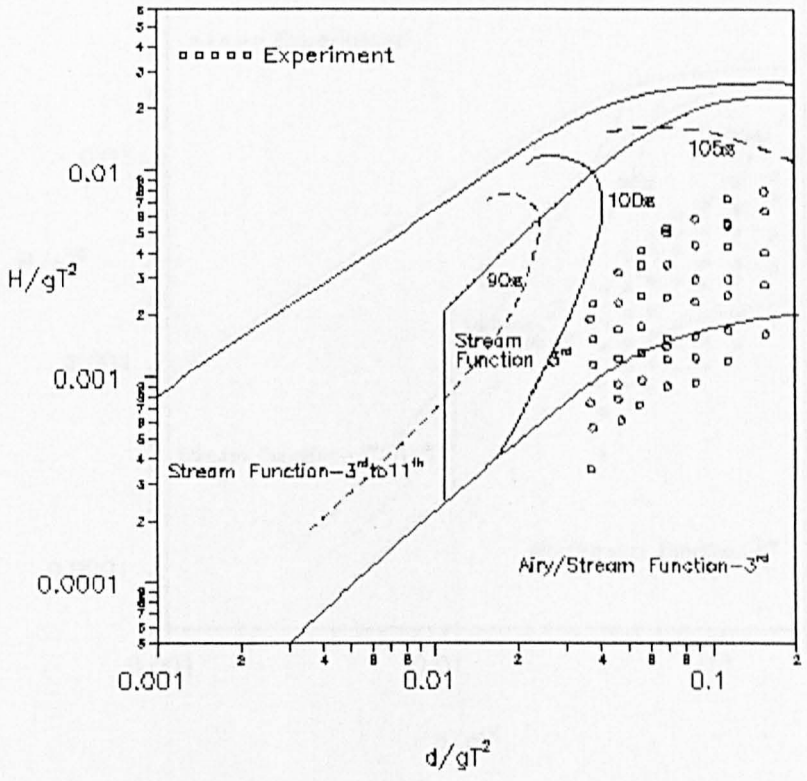

Fig. 5.1 Horizontal particle velocity under the wave crest at MWL: Airy theory as % of theory shown in Fig. 3.3 (Barltrop et al, 1990)

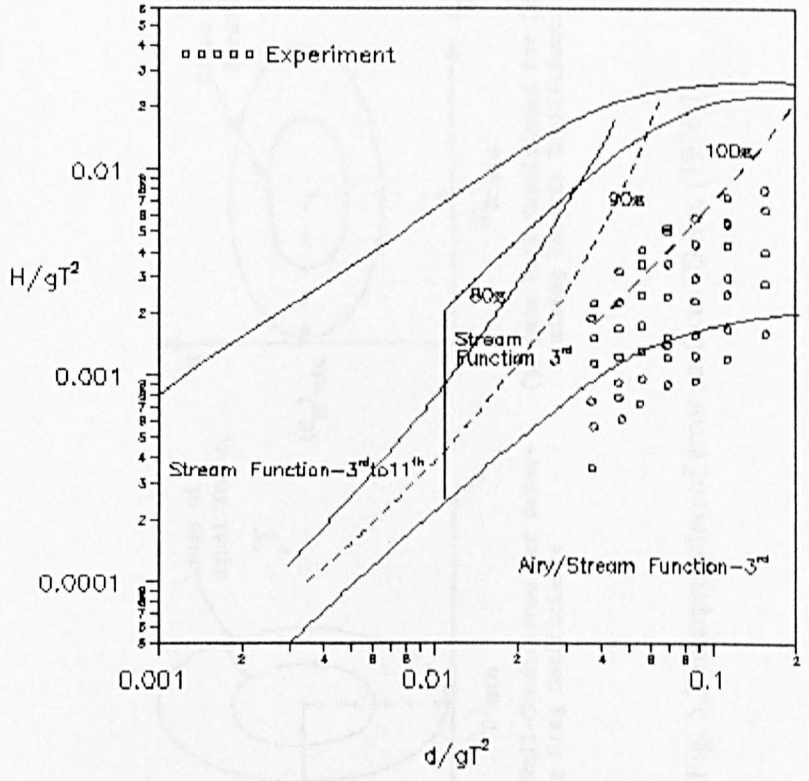

Fig. 5.2 Vertical particle acceleration under the wave crest at MWL: Airy theory as % of theory shown in Fig. 3.3 (Barltrop et al, 1990)

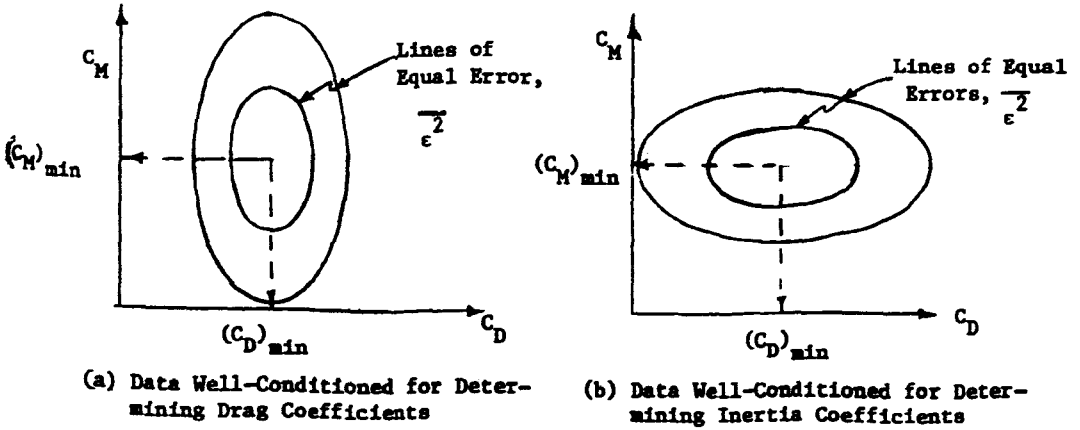

Fig. 5.3 Interpretation of error surfaces [Dean, (1976)]

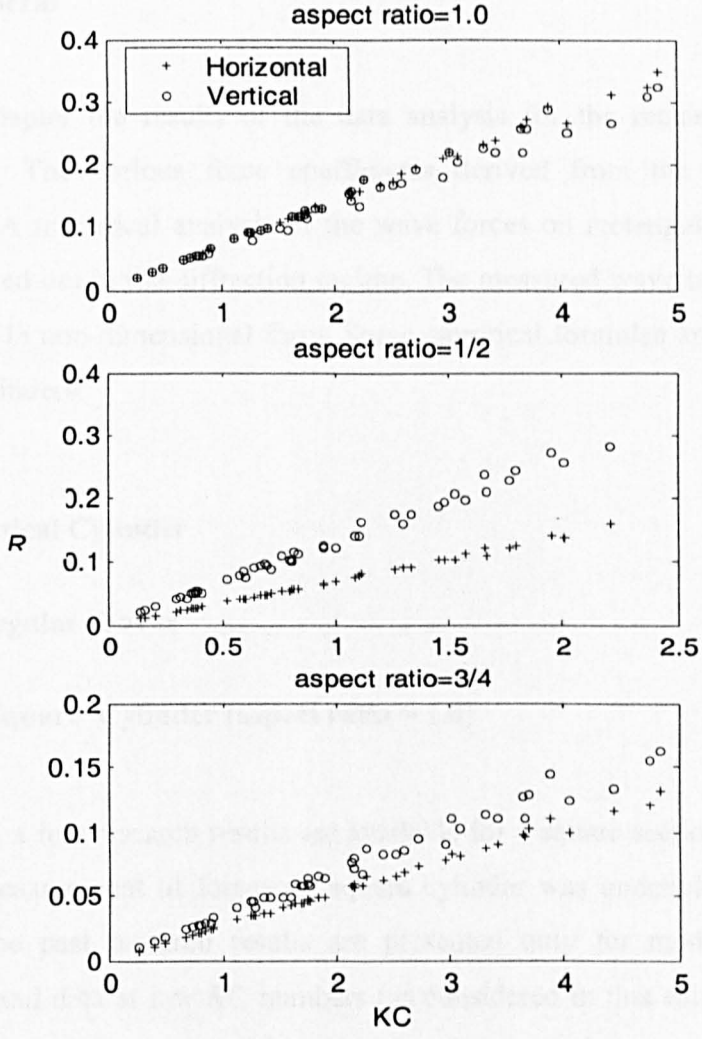

Fig. 5.4 Dean's index (R) with KC number

CHAPTER 6

RESULTS AND DISCUSSIONS

6.1 General

In this chapter the results of the data analysis for the rectangular cylinders are presented. The various force coefficients derived from the measured data are reported. A numerical analysis of the wave forces on rectangular cylinder has also been carried out in the diffraction regime. The measured wave induced pressures are presented in non-dimensional form. Some empirical formulae are derived for run-up on the cylinders.

6.2 Vertical Cylinder

6.2.1 Regular Waves

6.2.1.1 Square Cylinder (aspect ratio = 1.0)

Although, a few research results are available for a square section cylinder in waves, further measurement of forces on square cylinder was undertaken for two reasons. Firstly, the past research results are presented only for moderate or higher KC numbers and data at low KC numbers (as considered in this study) are not available for vertical square cylinder and hence the present experiments were performed at low KC numbers and for higher Reynolds numbers. Secondly, results of the force measurement on a square cylinder were needed to compare with the existing results in order to build up confidence on the measurements of forces on other rectangular sections. Also, comparison of present results with the results obtained by other researchers serves as an ideal method of testing not only the apparatus and equipment used, but also as a check on the experimental technique and method of data analysis.

The dimensions of the square cylinder are 150x150 mm. The in-line and transverse forces on the cylinder are measured and the results are discussed as below. The results for the square cylinder are presented in Figs.6.1 to 6.9 to show the variation of force coefficients with Keulegan-Carpenter (KC) number. For the analysis of force coefficients, both least squares wave by wave method and least squares time series method have been used.

The maximum value of KC number obtained for square cylinder, from the experiments is about 4.5, the Reynolds number obtained varies from 6.397×10^3 to 3.96×10^4 and β varies from 7407 to 12675. In order to show the effect of frequency parameter on the force coefficients, Fig. 6.1 is plotted for six representative values of β. It is observed from this plot that C_M shows little variation within the range of β tested, whereas the drag coefficients are found to increase with increase in β values.

It is to be noted that sharp edged cylindrical bodies, such as square sections, rectangular sections and flat plates, develop wider wake and shed vortices in oscillatory flow even at very low KC numbers and as a result, they experience larger drag coefficients than circular cylinders. Generally, the drag coefficients show large scatter at these low KC numbers. This is due to the fact that the wave and measured forces are in the inertia dominated range of KC numbers, and hence the drag component of the force is small. Therefore, it is difficult to isolate the drag force and corresponding drag coefficients accurately. Further, the waves at low KC number are generally smaller and hence the forces exerted on the cylinder during the passage of these waves are also relatively smaller and one would expect that the measured forces will be susceptible to the influence of any strong vortices from the preceding waves that may be carried back across the cylinder. Hence the calculated values of drag coefficients at low KC numbers are scattered.

The drag and inertia coefficients with KC are replotted in Fig. 6.2 along with the results obtained by Bearman et al.(1984) in planar oscillatory flow for a frequency parameter, $\beta = 213$. For KC less than about 5, where incidentally the inertia force is

likely to be most important, the variation of C_M with KC, as shown in Fig.6.2, are in fairly good agreement with the results by Bearman et al.(1984). The drag coefficients in the present study are generally found to be much higher than those reported by Bearman et al.(1984), especially, for $KC < 3$, the drag coefficients from the present results are found to be significantly larger. This could be attributed to the difference of flow patterns between wavy and planar oscillatory flow or due to the higher frequency parameter. Higher values of drag coefficients at low KC numbers in regular waves were also reported by Li and He (1995) for a vertical square cylinder. A drag coefficient of about 7.0 is reported by Li and He, at a KC number of about 10.

The resulting coefficients from least squares wave by wave method and least squares time series method are compared in Fig. 6.3. In this plot, only a slight difference is observed between the drag and inertia coefficients from both the methods. A difference in KC number between the two methods of analysis is noticed and this is because, in the wave by wave method, for each wave, a KC number is calculated and then an average value of KC numbers is taken as the KC number for the force record, whereas, in the least squares time series method, a single KC number is calculated for the whole time series. In Fig.6.3, the KC number calculated from wave by wave method is used for plotting coefficients for both methods. These plots reveal that drag and inertia coefficients from both the methods are almost the same and it can be concluded that at the range of KC reported, the force coefficients can be used from either of the above two methods.

The other force coefficients such as root mean square force coefficients and maximum force coefficients for in-line and lift forces, reported below, are calculated only from the wave by wave method, for all aspect ratios of the cylinder tested, as this method accounts for the variability of the force coefficients for individual waves.

The variation of maximum in-line force coefficients, C_{Fmax} and root mean square in-line force coefficients, C_{Frms} with KC number are plotted in Fig.6.4. Both these coefficients show the trend that at low KC numbers, the values of C_{Fmax} and C_{Frms}

exhibit higher values and they gradually decrease with increase in KC. The root mean square coefficient is found to correlate the data without large scatter. Best fit curve through the data is also drawn with equations displayed. C_{Fmax} is found to be about 32% higher than C_{Frms} at the highest KC number tested.

The maximum lift force coefficient (C_{Lmax}) and rms lift force coefficient (C_{Lrms}) are shown in Fig. 6.5 with KC number. Surprisingly, these two force coefficients show less scatter in their values. C_{Lmax} is found to be about 43% higher than C_{Lrms} at highest KC number obtained. Best-fit value curve is also plotted in these graphs. The relationship between the lift coefficients for the first five harmonics ($C_{Lrms(n)}$, n =1,2,3,4,5) with KC number is shown in Figs. 6.6 to 6.8. The fundamental frequency component of the lift coefficient $C_{Lrms(1)}$ shows a good trend with KC number without much scatter. Higher values of this coefficient are observed at lower KC and its value decreases gradually with increase in KC and this trend is similar to the trend observed for inline force coefficients. A value of about 1.52 corresponding to KC = 0.654 (lowest KC) and 0.285 at KC = 4.54 (highest KC) is observed. The second frequency component, $C_{Lrms(2)}$, third frequency component, $C_{Lrms(3)}$, fourth frequency component, $C_{Lrms(4)}$ and fifth frequency component, $C_{Lrms(5)}$ are all found to exhibit large scatter for all the KC numbers and their values are found to be less than 0.25 for all frequency components. From the above plots it is seen that $C_{Lrms(2)}$, $C_{Lrms(3)}$, $C_{Lrms(4)}$ & $C_{Lrms(5)}$ are less than the first harmonic component, and their values decreases with increasing 'n' with KC number.

The root mean square total force coefficient, C_{Trms} with KC number is plotted in Fig. 6.9. Comparing this plot with C_{Frms} (Fig. 6.4) and C_{Lrms} (Fig. 6.5), it is observed that C_{Frms} is found to be about 98% of C_{Trms} and C_{Lrms} is found to be about 20% of C_{Trms} at higher KC tested.

The measured and computed forces using Morison's formula are shown in Fig, 6.10 and 6.11 for four sample cases. The comparison is found to be good and in some

cases the crests are under predicted. The measured and computed peak forces are plotted in Fig. 6.12. Each point represents the average over a complete time series.

In order to compute an overall measure of the measured and computed forces, a ratio is defined as:

$$R_{x^*} = \frac{F_{xp}}{F_{xc}} \tag{6.1}$$

where, F_{xp} and F_{xc} are the measured and computed in-line peak forces, calculated from the average peaks over a complete time series. The '*' symbol is used as 'p' for positive peaks and 'n' for negative peaks. The means ($\overline{R_{x^*}}$) and standard deviations (σ_{x^*}) of this ratio in regular waves are given in Table. 6.1.

It is evident from Fig. 6.12 and Table. 6.1, the measured and computed peak forces are different. The positive peaks are underestimated to a maximum extent of up to 11% (for steep waves) and to a mean value of about 3.5%. The negative forces differ by about 7%. The above error occurs in the range of $d/gT^2 > 0.14$ and $H/gT^2 > 0.0093$. This error may be attributed to the use linear wave theory for the particle kinematics computation. The range of $d/gT^2$and H/gT^2, where the under prediction of peak forces occur, indicate a region of higher order wave theories and if the particle kinematics are directly measured then this error could have been avoided.

6.2.1.2 Rectangular Cylinder with Aspect ratios = 1/2 and 2/1

The results obtained for rectangular cylinder with aspect ratio = 1/2 are shown in Figs. 6.13 to 6.23. For the aspect ratio of ½, the narrow cylinder dimension (200mm) is facing the wave. Fig. 6.13 shows C_D and C_M versus KC for six representative values of β obtained. The maximum value of KC number obtained is about 1.8 and the value of β ranges from 25671 to 45460. The Reynolds number ranges from

6.71×10^3 to 5.12×10^4. The variation of these coefficients show different trends with KC numbers, in general, C_D decreases with increase in KC, whereas, C_M increases with increase in KC as the case of square cylinder. It must be remembered that the increase in Keulegan-Carpenter number is an indication of larger in-line water particle displacement, resulting in a higher in-line force. The effect of frequency parameter, β does not seem to have significant influence on drag and inertia coefficients. The force coefficients obtained by both least squares wave by wave method and least squares time series method have shown almost similar values as compared in Fig. 6.14 and therefore further comparison of these two methods will not be made for other cylinders.

The variation of maximum in-line force coefficients, C_{Fmax} and root mean square in-line force coefficients, C_{Frms} with KC number are plotted in Fig.6.15. The trend of these coefficients is similar to the trend obtained for square cylinder. Less scatter is observed for both these coefficients. C_{Fmax} is found to be about 39% higher than C_{Frms} at the highest KC number tested.

The maximum lift force coefficient (C_{Lmax}) and rms lift force coefficient (C_{Lrms}) are shown in Fig. 6.16 with KC number. C_{Lmax} is found to be about 45% higher than C_{Lrms} at highest KC. Best fit curve with equation is also plotted in these graphs. The lift coefficient for the first five harmonics with KC number is shown in Figs. 6.17 to 6.19. $C_{Lrms(1)}$ shows a trend similar to C_{Lrms} with KC number with a little scatter at low KC. The first frequency component, $C_{Lrms(1)}$ is found to be higher than other components. In general, for KC less than 1.0, $C_{Lrms(2)}$, $C_{Lrms(3)}$, $C_{Lrms(4)}$ and $C_{Lrms(5)}$ are found to exhibit large scatter and the values of $C_{Lrms(3)}$, $C_{Lrms(4)}$ and $C_{Lrms(5)}$ are found to be about less than 0.5.

The root mean square total force coefficient, C_{Trms} with KC number is plotted in Fig. 6.20. The measured and computed force using Morison's formula is shown in Fig, 6.21 and 6.22 for four cases with different β. In general, the comparison is found to be good. The measured and computed peak forces are plotted in Fig. 6.23. Table 6.1

indicate a ratio of 0.988 between the measured and computed positive peak forces. Here again, a mean value of 6% error is observed for negative forces.

A similar trend in the variation of C_D and C_M is observed for another aspect ratio = 2/1 as well, and the results are shown in Figs. 6.24 to 6.33. In this case, cylinder dimension, 400mm is facing the wave. For this aspect ratio, the maximum value of KC obtained is about 4.25. Also note that β values obtained for aspect ratio = 2/1, are different from those observed for aspect ratio = 1/2 and the frequency parameter ranges from 14048 to 29864. The Reynolds number ranges from 7.88×10^3 to 1.18×10^5.

Maximum in-line force coefficients, C_{Fmax} and root mean square in-line force coefficients, C_{Frms} with KC number are plotted in Fig.6.25 and the maximum lift force coefficient (C_{Lmax}) and rms lift force coefficient (C_{Lrms}) are shown in Fig. 6.26. Best fit curve with equation is also plotted in these graphs. The lift coefficient for the first five harmonics with KC number is shown in Figs. 6.27 to 6.29. The trend in these coefficients is similar to aspect ratio =1/2.

The root mean square total force coefficient, C_{Trms} with KC number is plotted in Fig. 6.30. The measured and computed forces using Morison's formula are shown in Fig. 6.31 and 6.32 for four cases with different β. The comparison is found to be good only for lower KC numbers. The measured and computed peak forces are plotted in Fig. 6.33. The positive peak forces are larger than the calculated forces up to a maximum of 30% with a mean value of about 19%.

The drag and inertia coefficients are replotted for aspect ratios = 1/2 and 2/1 and are shown in Fig. 6.34. It is observed from these plots that the aspect ratio clearly has a large influence on the hydrodynamic coefficients. For a given value of KC number, inertia coefficients corresponding to aspect ratio = 2/1 are higher those obtained for aspect ratio = 1/2. The inertia coefficients for aspect ratio = 2/1 are found to be nearly twice the inertia coefficients observed for aspect ratio = 1/2. Further, it is

noted that the inertia coefficients for both aspect ratios are approaching its potential flow values at low KC numbers. Note that the potential flow values of inertia coefficients [Barltrop and Adams, (1991)] for aspect ratio = 1/2, is C_M = 1.67 and for aspect ratio = 2/1, is C_M = 3.14. A large difference is also seen for drag coefficients with the respect to aspect ratio. The C_D values corresponding to aspect ratio = 2/1 are larger than the drag coefficients for aspect ratio = 1/2. The steady flow drag coefficients [Barltrop and Adams, (1991)] are 2.5 and 1.5 respectively for aspect ratios 2/1 and 1/2.

6.2.1.3 Rectangular Cylinder with Aspect ratio = 3/4 and 4/3

The results for the rectangular cylinder with aspect ratio 3/4 are plotted in Figs. 6.35 to 6.41 to show the variation of the force coefficients with KC numbers. The variations of drag and inertia coefficients with KC are plotted in Fig. 6.35. It is inferred from these plots that both drag and inertia coefficients shows a similar trend as those obtained for the aspect ratios 1, 1/2 and 2/1. The maximum value of KC number obtained is about 2.2 and values of β ranges from 39660 to 69235. The C_D values corresponding to higher β are found to be larger. The inertia coefficients approaches its potential flow value (C_M = 1.97, refer Fig. 6.271) at low KC number and its value increases with increase in KC number up to the range of KC tested.

The maximum in-line force coefficient and root mean square in-line coefficients are plotted with KC number in Fig. 6.36. These plots show that C_{Fmax} is about 18% higher than C_{Frms} at highest KC number.

The maximum lift force coefficient, C_{Lmax} and rms lift force coefficients C_{Lrms} are shown in Fig. 6.37. The scatter of data points in C_{Lmax} is more than C_{Lrms}. The lift coefficient for the first five harmonics with KC number is shown in Figs. 6.38 to 6.40. The root mean square total force coefficient, C_{Trms} with KC number is plotted in Fig. 6.41. The measured and computed force using Morison's formula is shown in

Fig, 6.42 and 6.43 for four cases with different β. The comparison is found to be good for almost all KC values. The measured and computed peak forces are plotted in Fig. 6.44, which shows a good comparison. Note that for this aspect ratio, waves with larger heights were avoided due to a problem with the beach.

Drag and inertia coefficients for aspect ratio 4/3 are shown in Fig. 6.45 for β in the range of 29006 to 50583. The maximum KC number obtained is about 2.75. The other force coefficients with KC numbers are shown in Figs. 6.46 to 6.51 and all these coefficients show a similar trend as with other aspect ratios discussed above. The lift coefficient for the first five harmonics with KC number shows a good trend without much scatter. The measured and computed forces using Morison's formula are shown in Figs. 6.52 and 6.53. The measured and computed peak forces are plotted in Fig. 6.54. A mean error of 8% is observed between measured and calculated positive peak forces.

The drag and inertia coefficients are replotted for aspect ratios = 3/4 and 4/3 as shown in Fig. 6.55 and this plot demonstrates the effect of aspect ratio on drag and inertia coefficients for this cylinder. Inertia coefficients corresponding to aspect ratio = 4/3 are higher than those observed for aspect ratio = 3/4 and at low KC numbers, the inertia coefficient values are similar to potential flow values (C_M = 1.97 for aspect ratio = 3/4 and 2.53 for aspect ratio = 4/3, refer Figs. 6.271 and 6.273). The drag coefficient for aspect ratio = 3/4 is larger than those for aspect ratio = 4/3.

The mean values of this force ratio for all the cylinders are close to unity and the standard deviations are less than 0.09. This indicates that the linear wave theory can provide reasonable force predictions.

Some of the transverse force time series recorded for vertical cylinders in regular waves are shown in Appendix-C. Most of records show a regular trend. For square cylinder, irrespective of KC and β parameters, the transverse force time series are more regular. For aspect ratio =1/2 and 2/1, the shape of the force-time series are not

that regular compared to square cylinder and with increase in KC transverse forces become more irregular. Same trend is found for aspect ratio 3/4 and 4/3.

Table 6.1. Means and standard deviations of measured and computed peak force ratios for vertical cylinder in waves

Aspect ratio	$\overline{R}_{xp}$	$\overline{R}_{xn}$	σ_{xp}	σ_{xn}
1.0	1.035	1.073	0.0419	0.0470
1/2	0.988	1.065	0.0345	0.0473
2/1	1.193	1.052	0.0919	0.0841
3/4	0.995	0.987	0.0444	0.0324
4/3	1.086	1.014	0.0600	0.0338

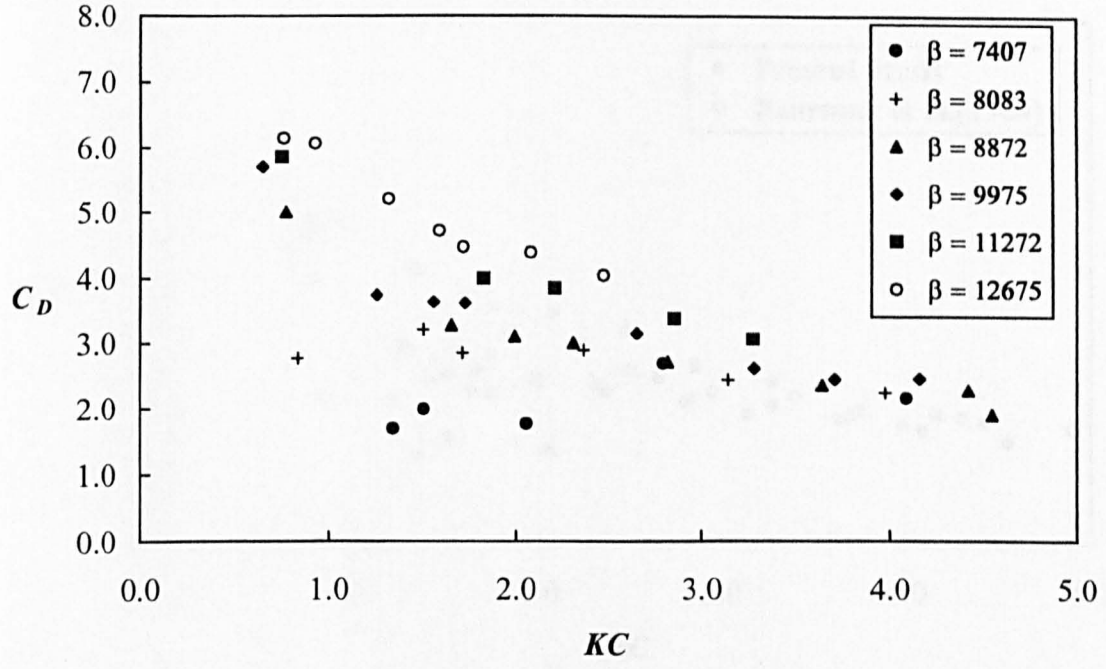

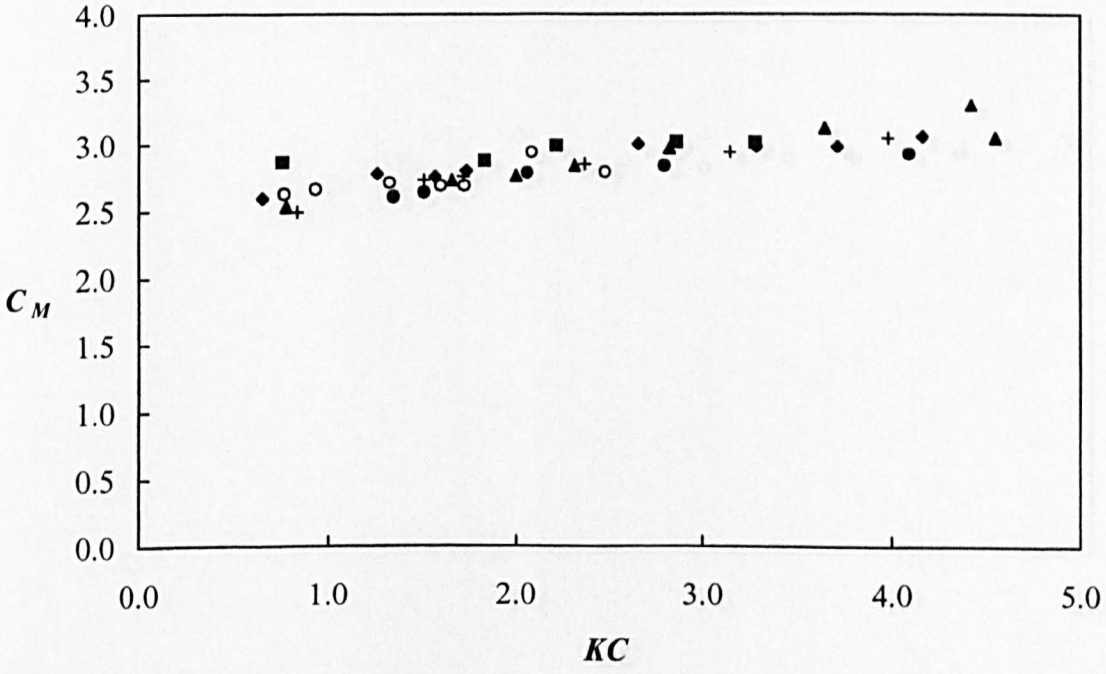

Fig. 6.1 Drag and inertia coefficients for vertical square cylinder with Keulegan-Carpenter number for different Frequency parameter

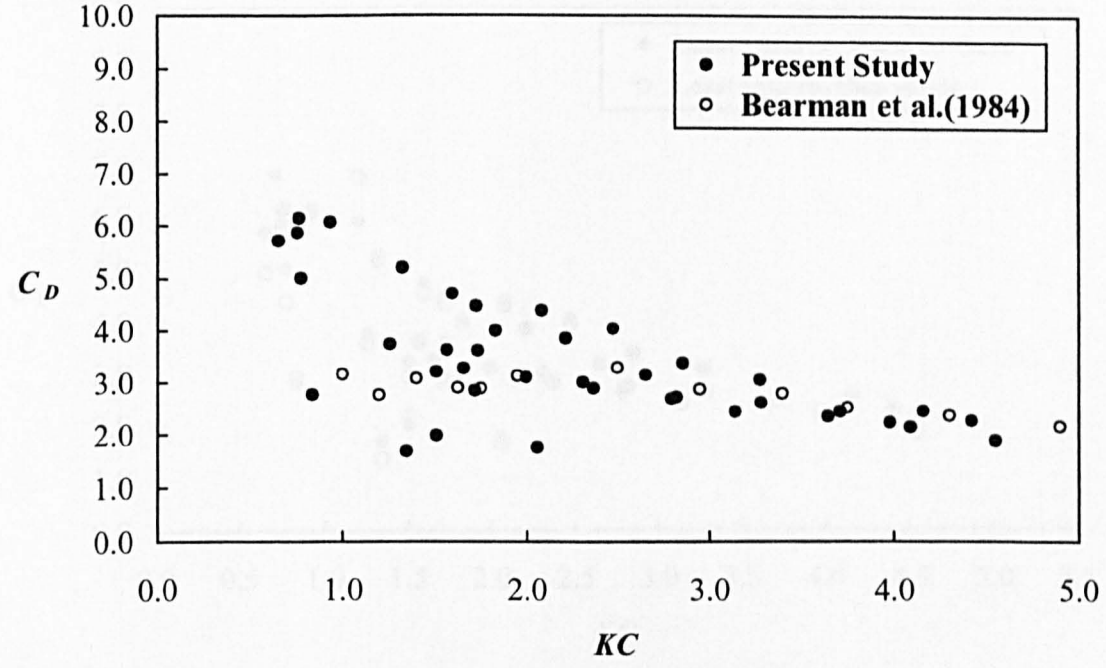

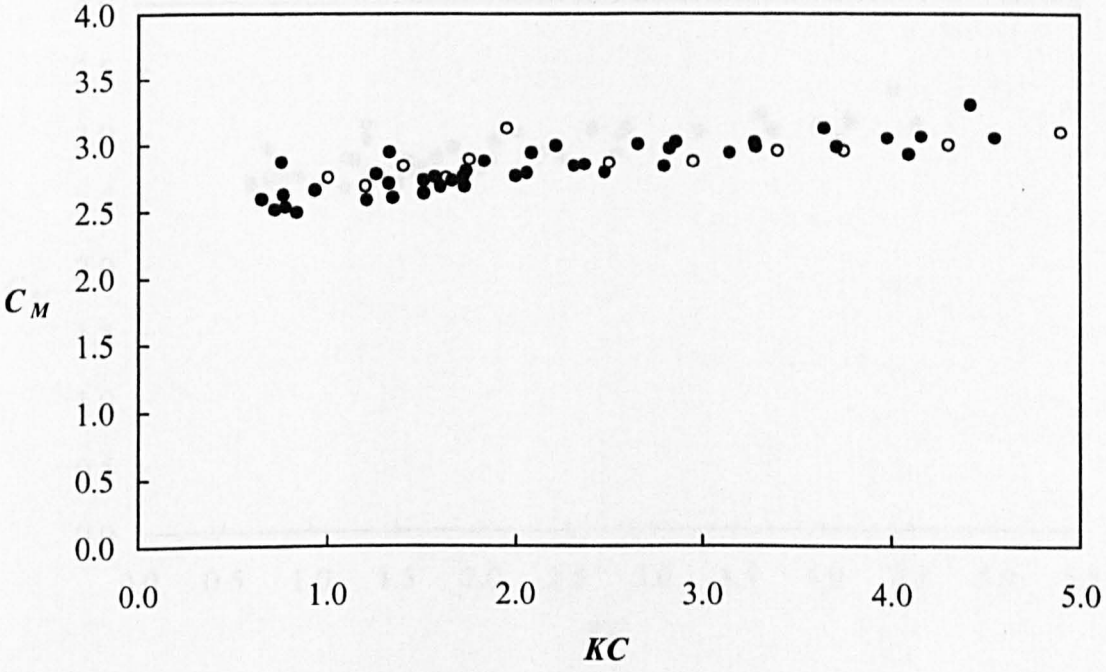

Fig. 6.2 Comparison of drag and inertia coefficients for vertical square cylinder with existing results

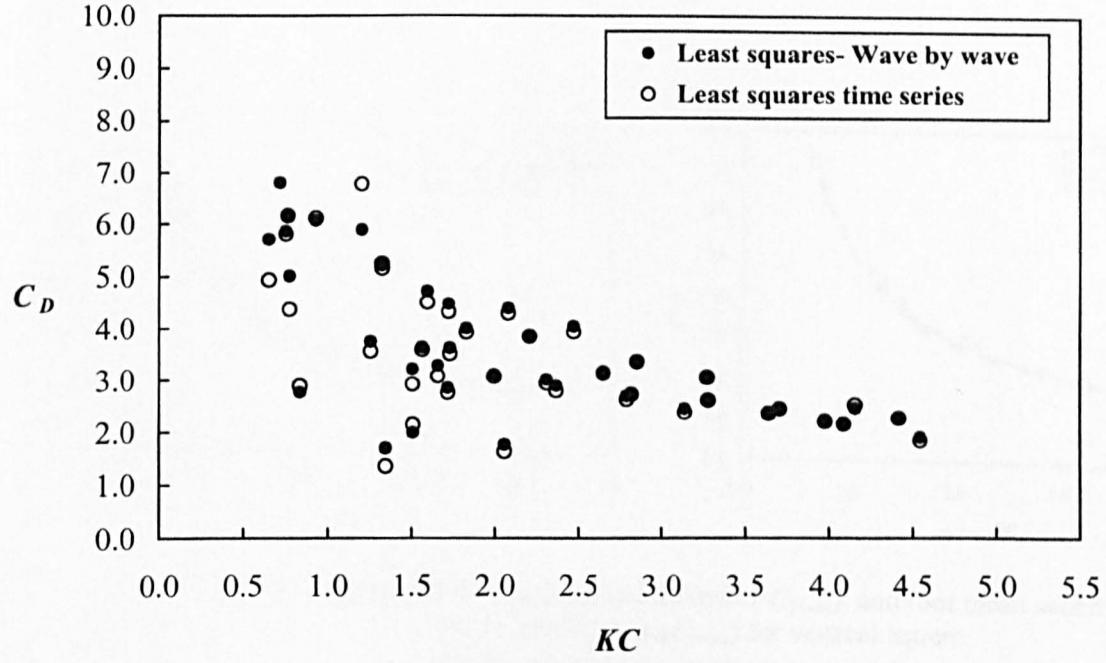

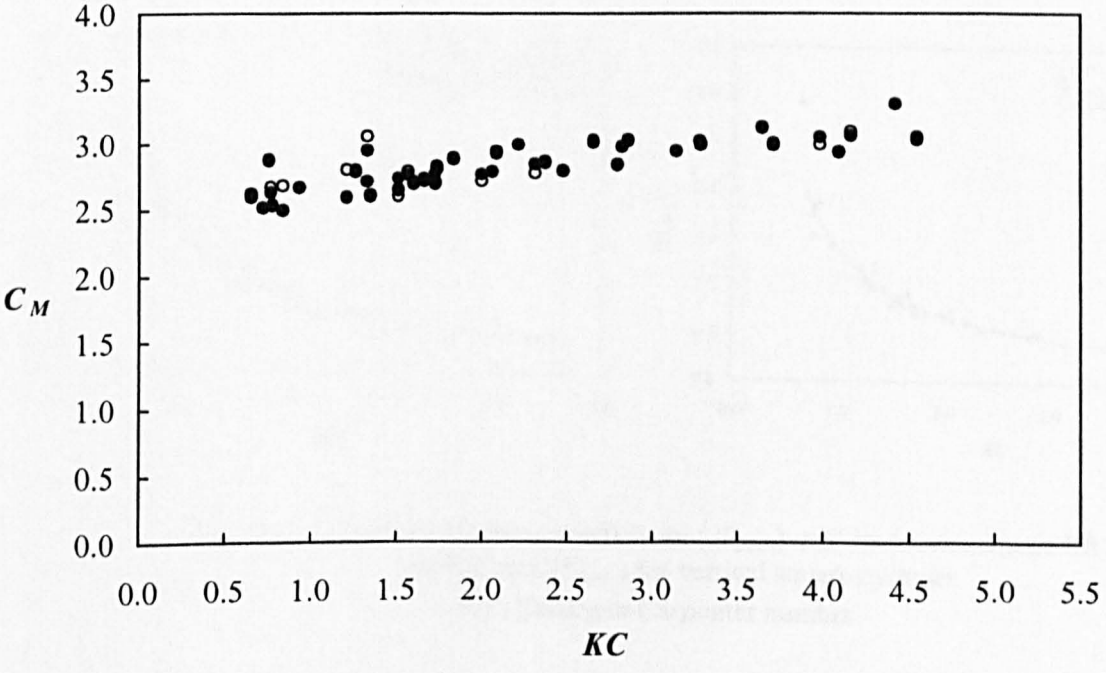

Fig. 6.3 Comparison of least squares wave by wave method and least squares time series method for vertical square cylinder

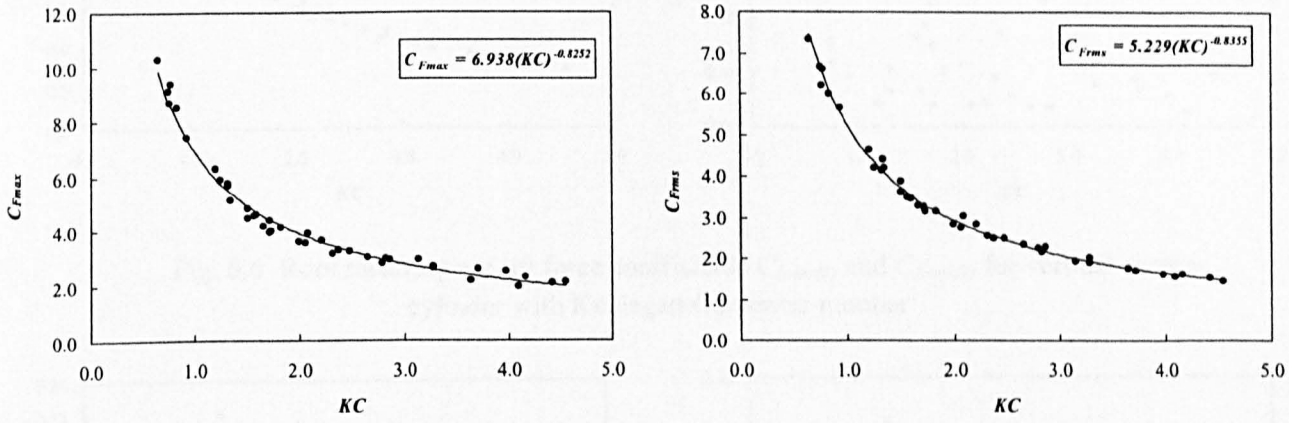

Fig. 6.4 Maximum in-line force coefficients (C_{Fmax}) and root mean square in-line force coefficients (C_{Frms}) for vertical square cylinder with Keulegan-Carpenter number

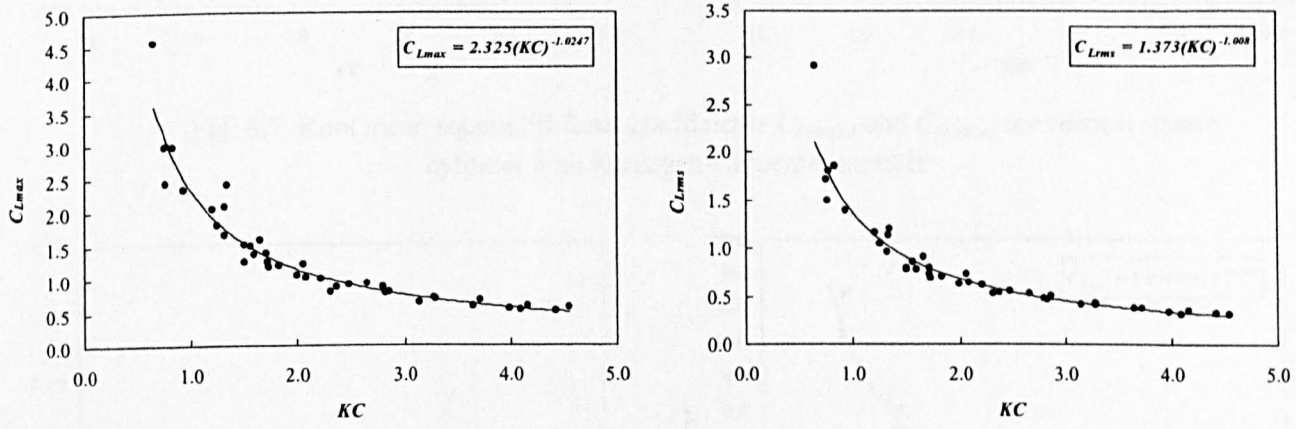

Fig. 6.5 Maximum lift force coefficients (C_{Lmax}) and root mean square lift force coefficients (C_{Lrms}) for vertical square cylinder with Keulegan-Carpenter number

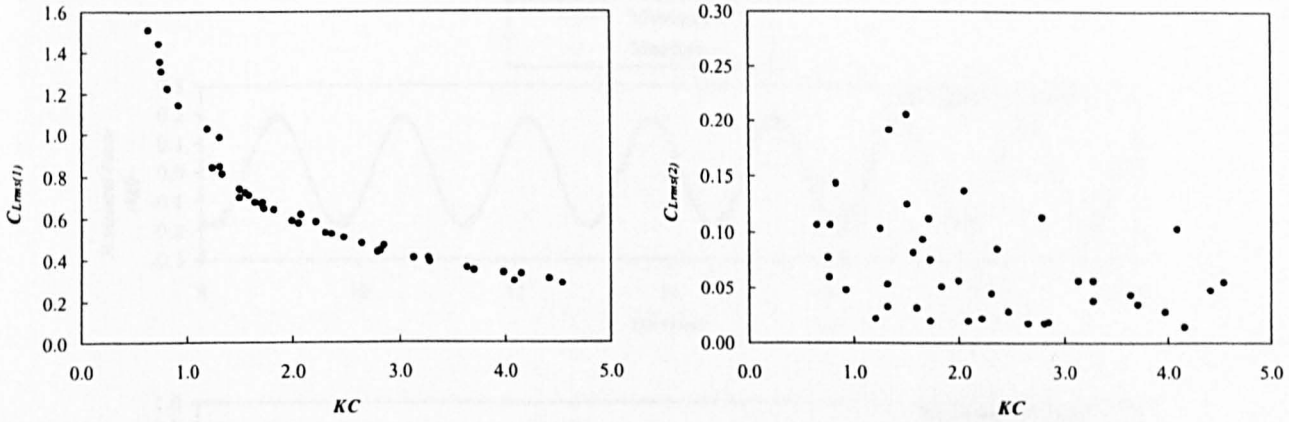

Fig. 6.6 Root mean square lift force coefficients $C_{Lrms(1)}$ and $C_{Lrms(2)}$ for vertical square cylinder with Keulegan-Carpenter number

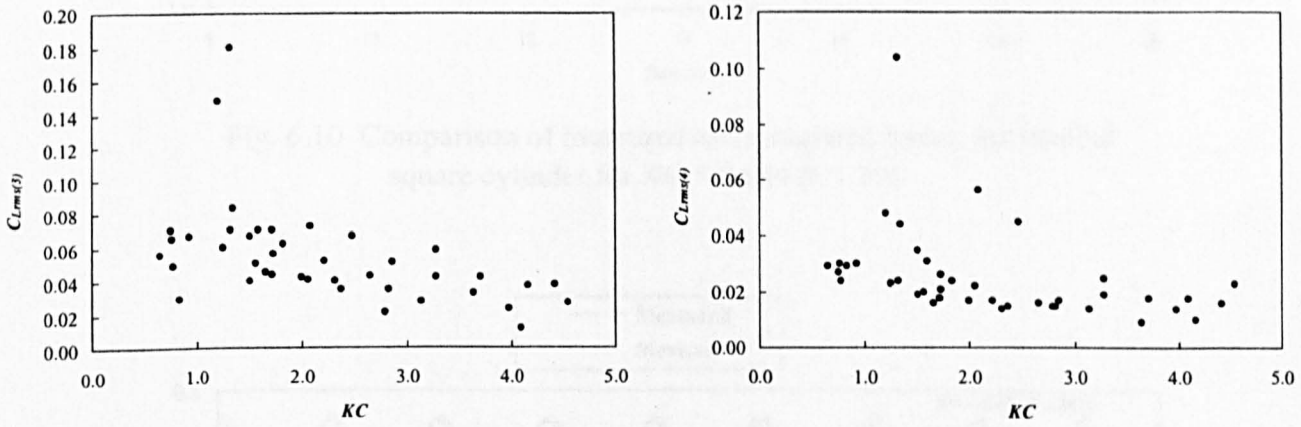

Fig. 6.7 Root mean square lift force coefficients $C_{Lrms(3)}$ and $C_{Lrms(4)}$ for vertical square cylinder with Keulegan-Carpenter number

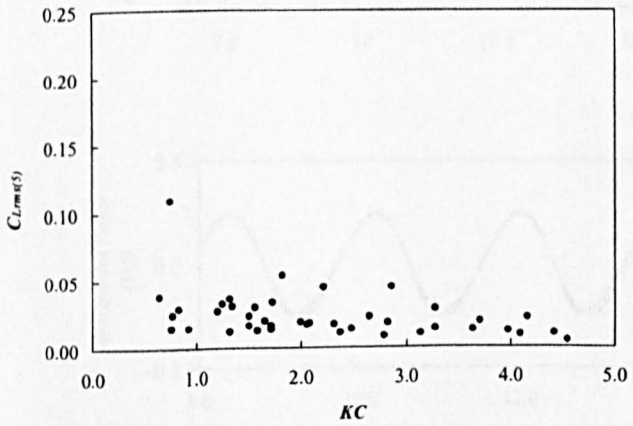

Fig. 6.8 Root mean square lift force coefficients, $C_{Lrms(5)}$ for vertical square cylinder with Keulegan-Carpenter number

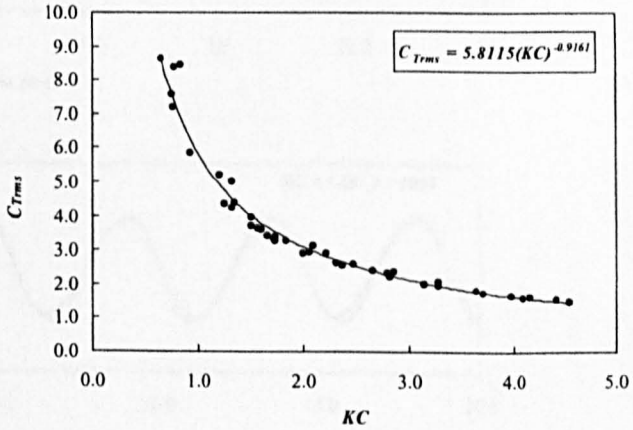

Fig. 6.9 Root mean square total force coefficients, C_{Trms} for vertical square cylinder with Keulegan-Carpenter number

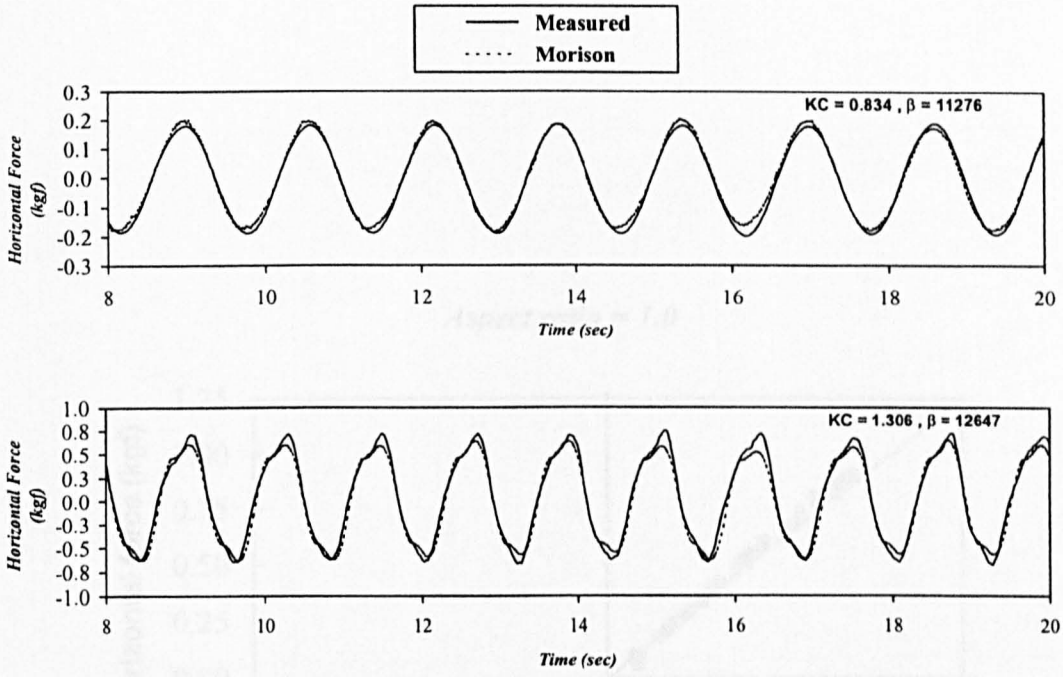

Fig. 6.10 Comparison of measured and computed forces for vertical square cylinder for $KC = 0.834$ & 1.306

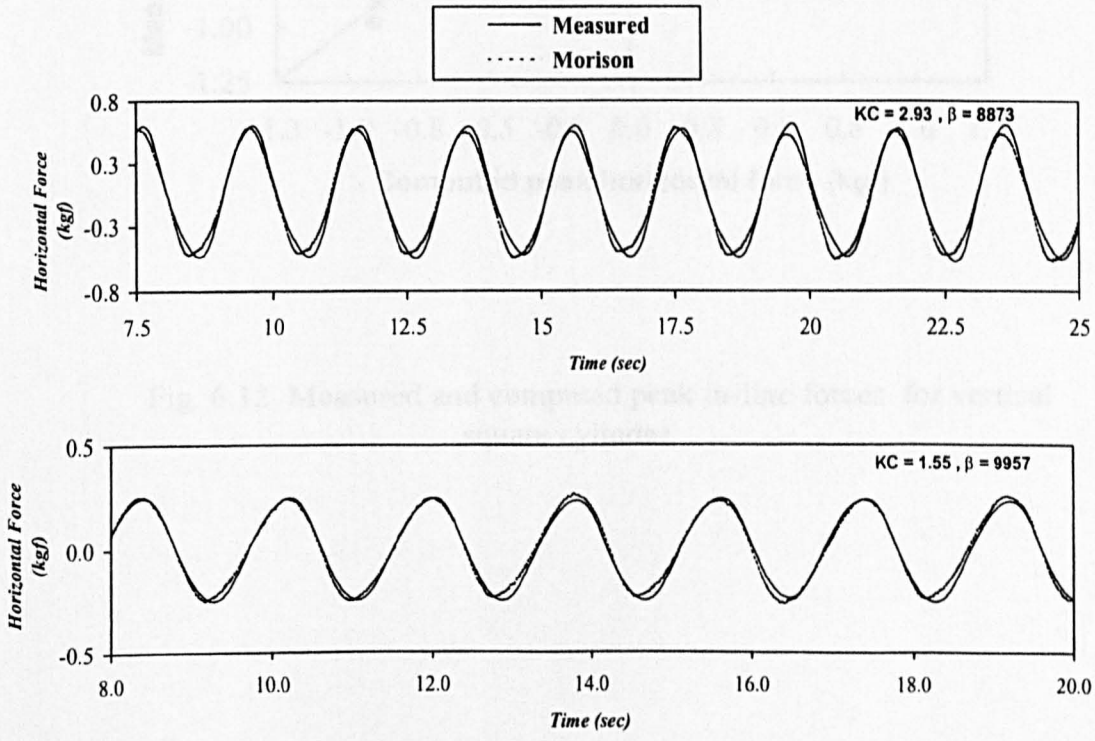

Fig. 6.11 Comparison of measured and computed forces for vertical square cylinder for $KC = 2.93$ & 1.55

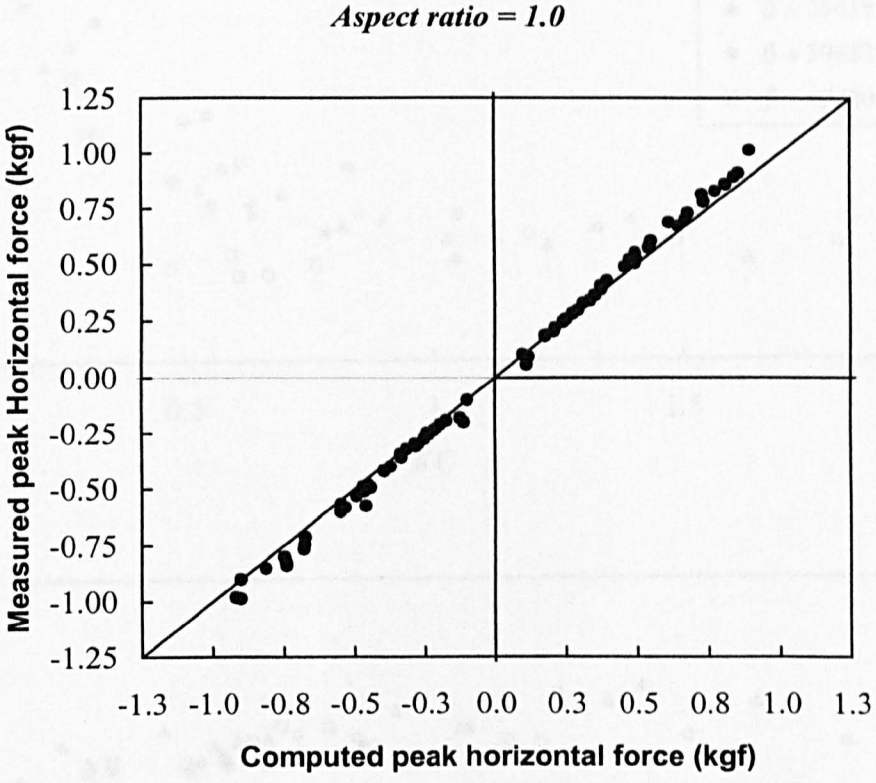

Fig. 6.12 Measured and computed peak in-line forces for vertical square cylinder

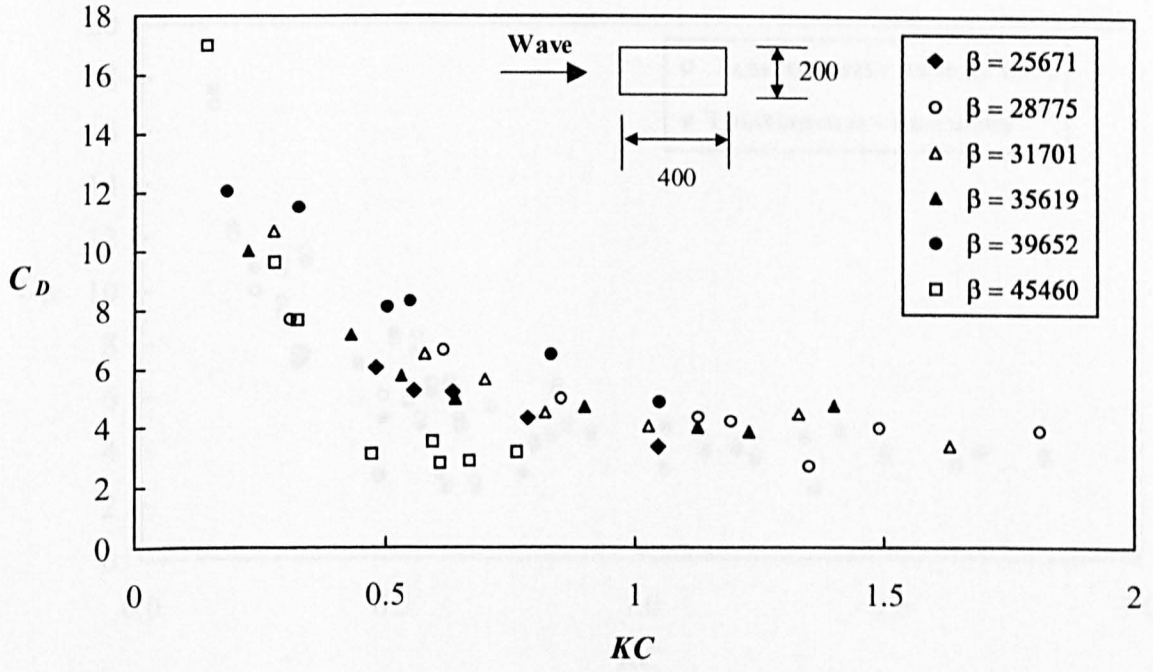

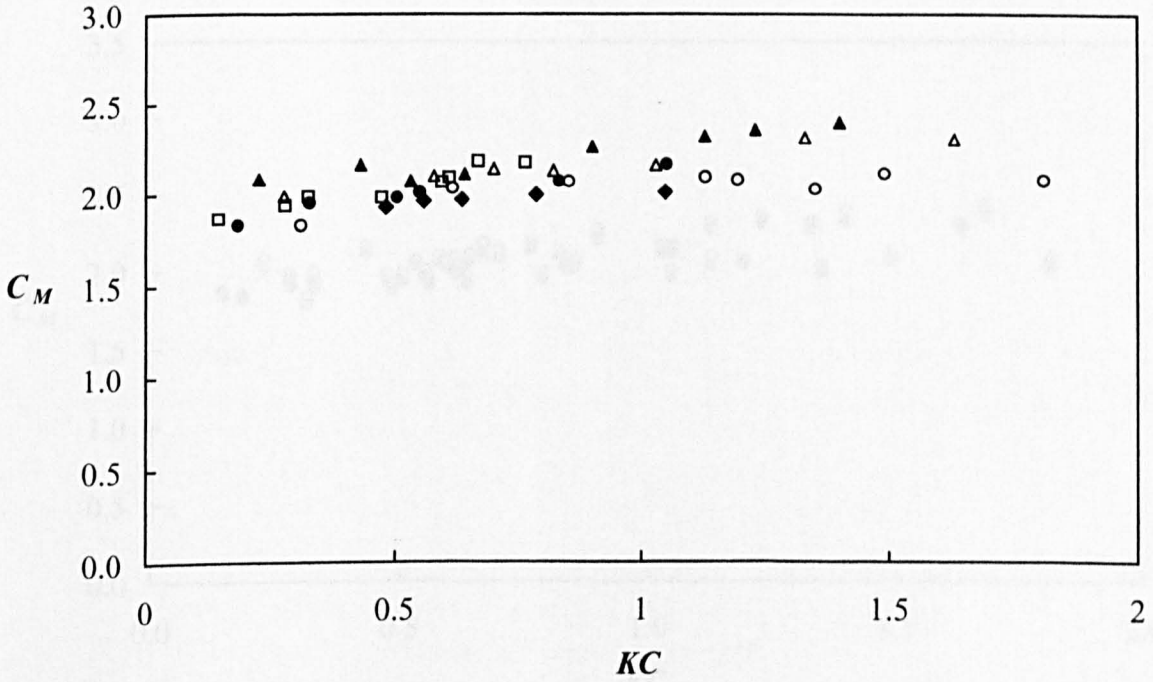

Fig. 6.13 Drag and inertia coefficients for vertical rectangular cylinder with aspect ratio = 1/2

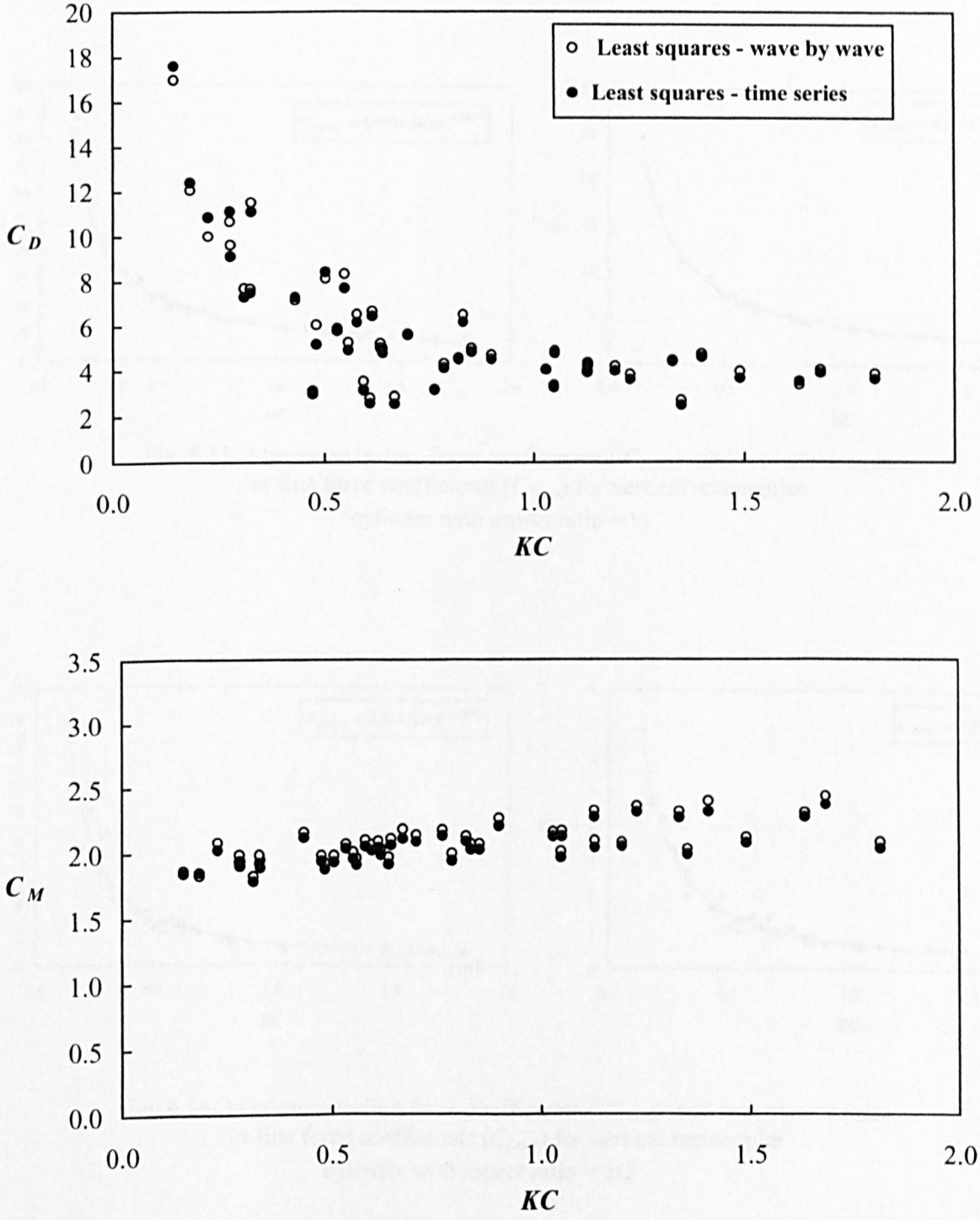

Fig. 6.14 Comparison of least squares wave by wave and least squares time series methods for vertical rectangular cylinder with aspect ratio = 1/2

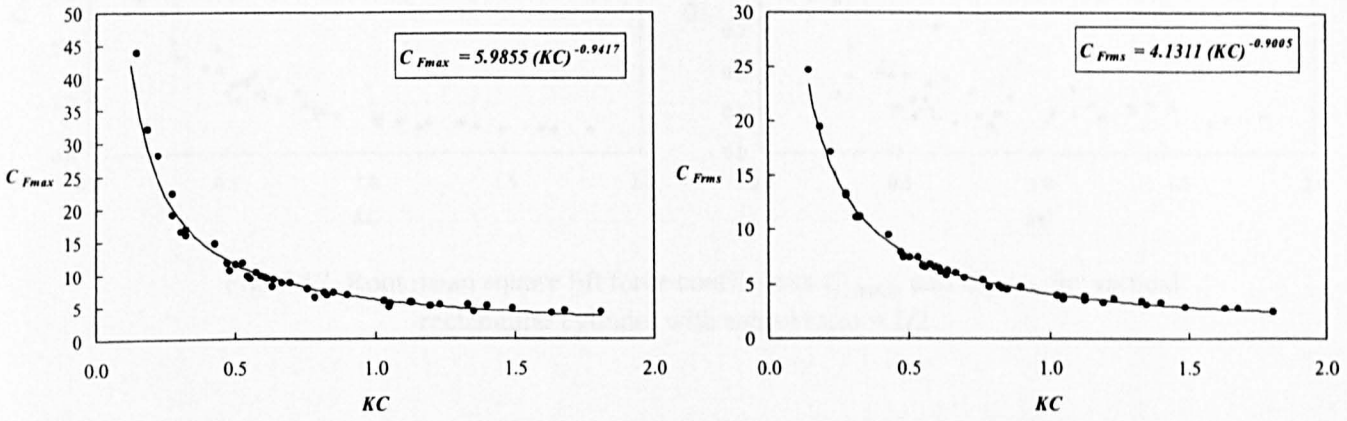

Fig. 6.15 Maximum in-line force coefficients (C_{Fmax}) and root mean square in-line force coefficients (C_{Frms}) for vertical rectangular cylinder with aspect ratio = ½

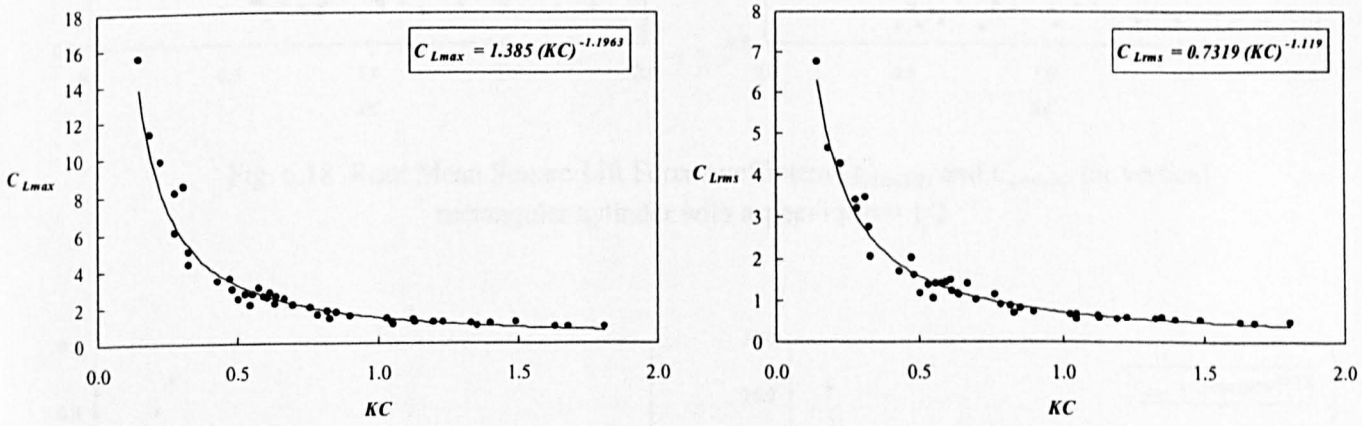

Fig. 6.16 Maximum in-line force coefficients (C_{Lmax}) and root mean square in-line force coefficients (C_{Lrms}) for vertical rectangular cylinder with aspect ratio = 1/2

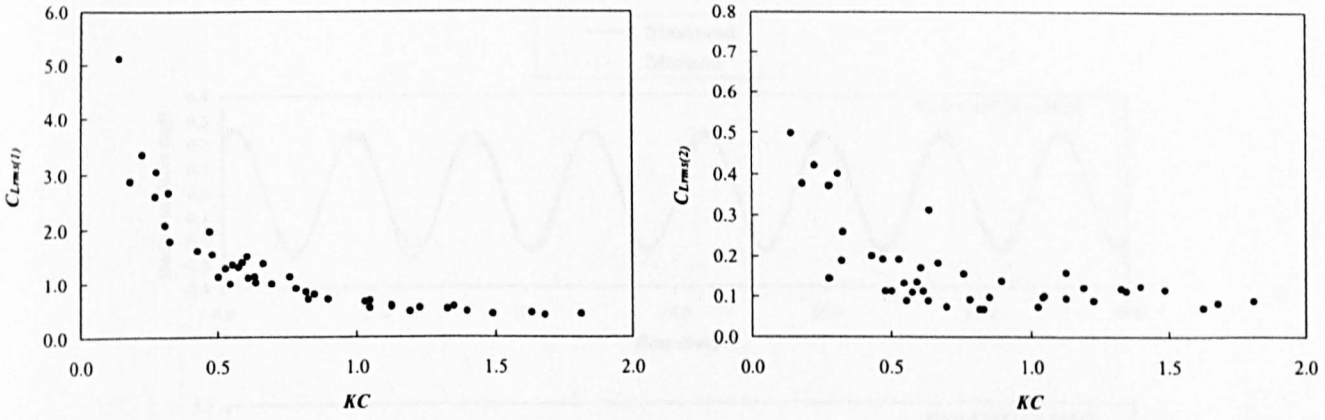

Fig. 6.17 Root mean square lift force coefficients $C_{Lrms(1)}$ and $C_{Lrms(2)}$ for vertical rectangular cylinder with aspect ratio = 1/2

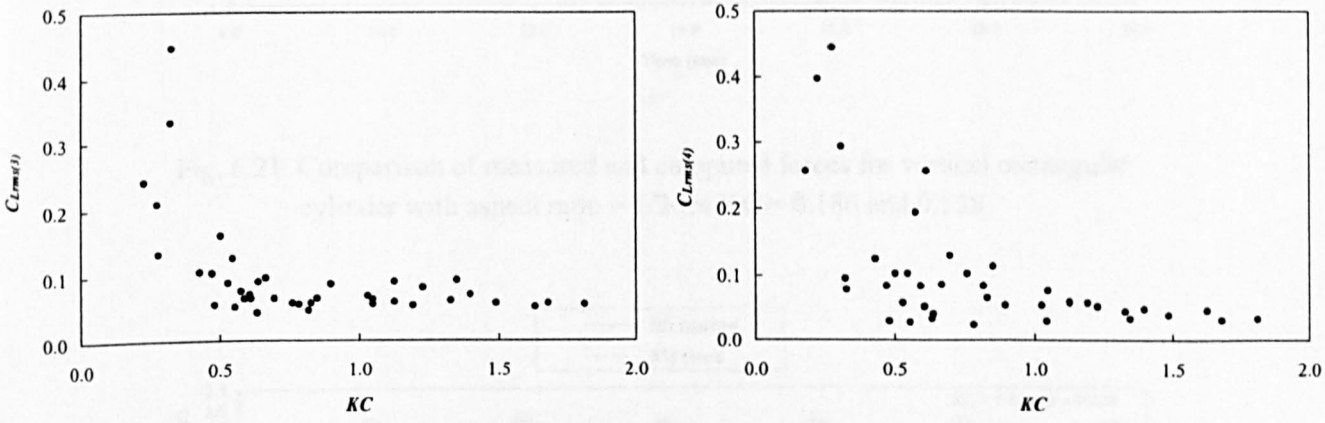

Fig. 6.18 Root Mean Square Lift Force coefficients $C_{Lrms(3)}$ and $C_{Lrms(4)}$ for vertical rectangular cylinder with aspect ratio = 1/2

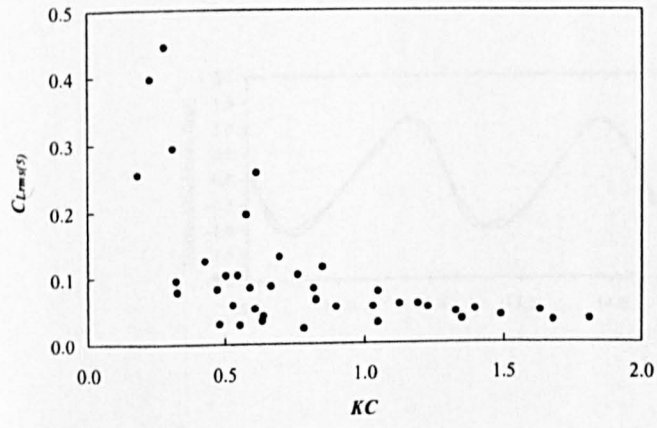

Fig. 6.19 Root Mean Square Lift Force coefficients $C_{Lrms(5)}$ for vertical rectangular cylinder with aspect ratio = 1/2

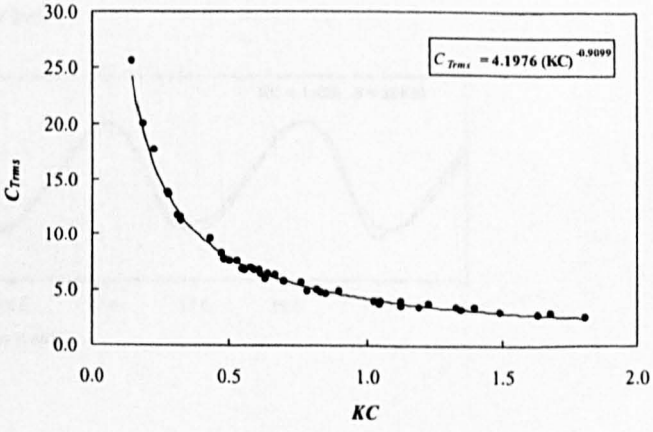

Fig. 6.20 Root Mean Square Total Force coefficients C_{Trms} for vertical rectangular cylinder with aspect ratio = 1/2

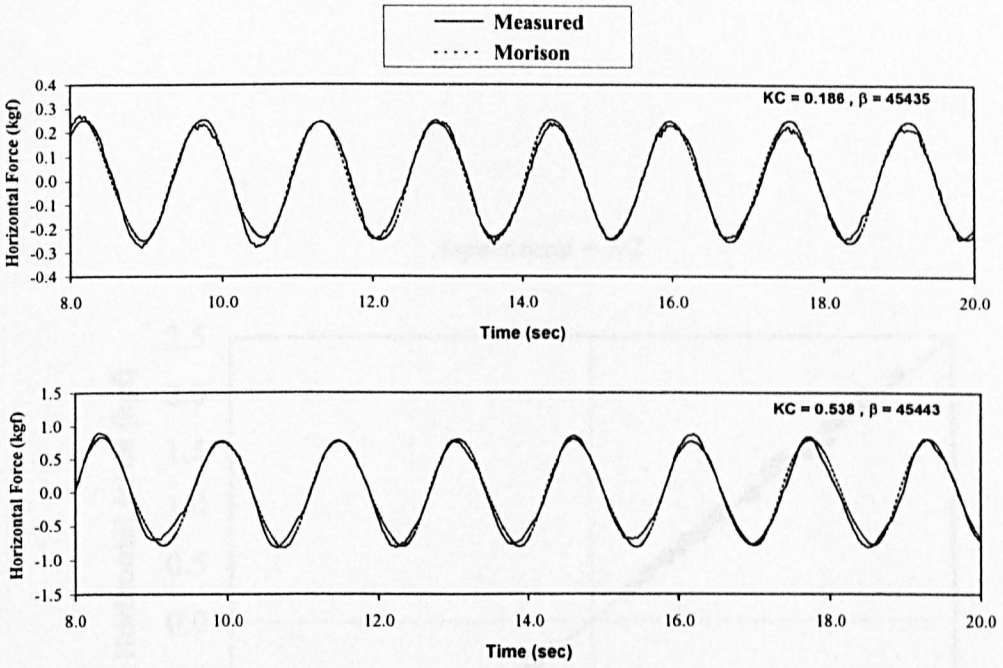

Fig. 6.21 Comparison of measured and computed forces for vertical rectangular cylinder with aspect ratio = 1/2 for KC = 0.186 and 0.538

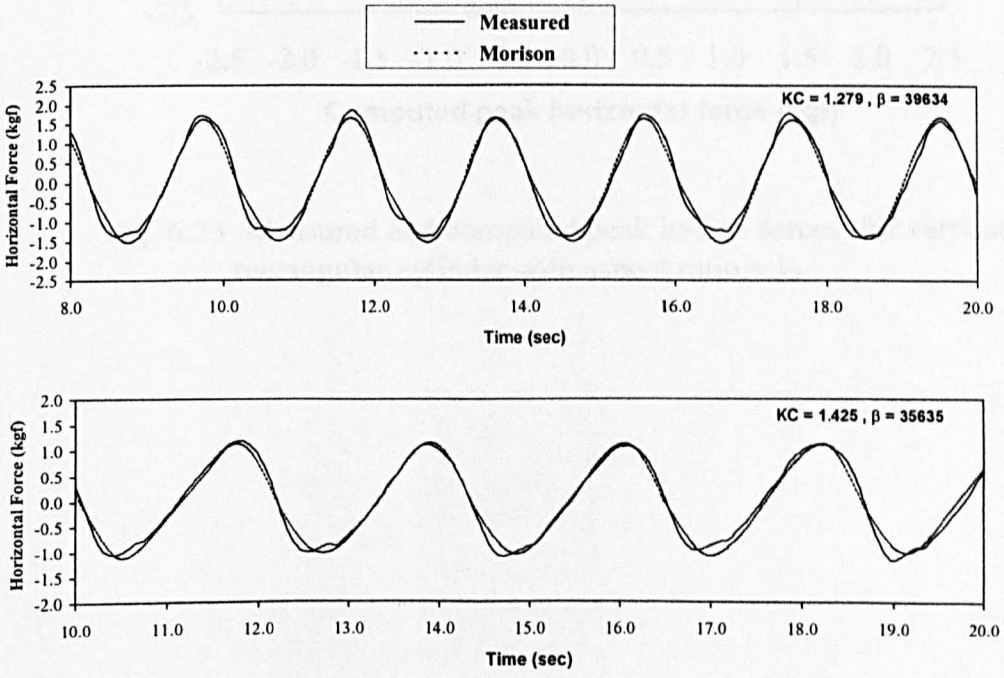

Fig. 6.22 Comparison of measured and computed forces for vertical rectangular cylinder with aspect ratio = 1/2 for KC = 1.279 and 1.425

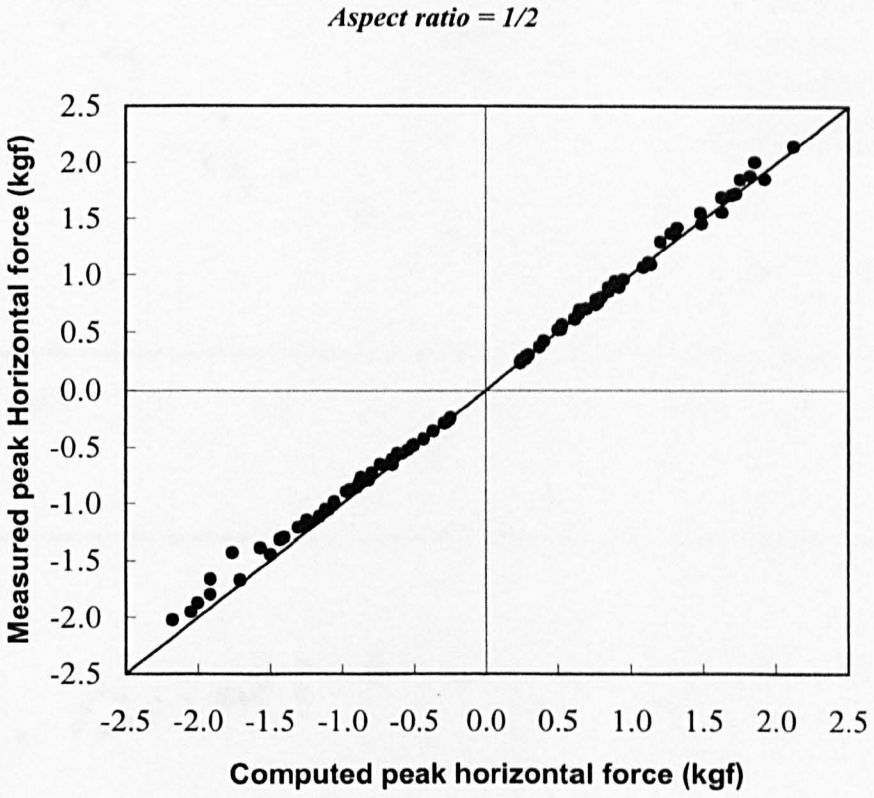

Fig. 6.23 Measured and computed peak in-line forces for vertical rectangular cylinder with aspect ratio = ½.

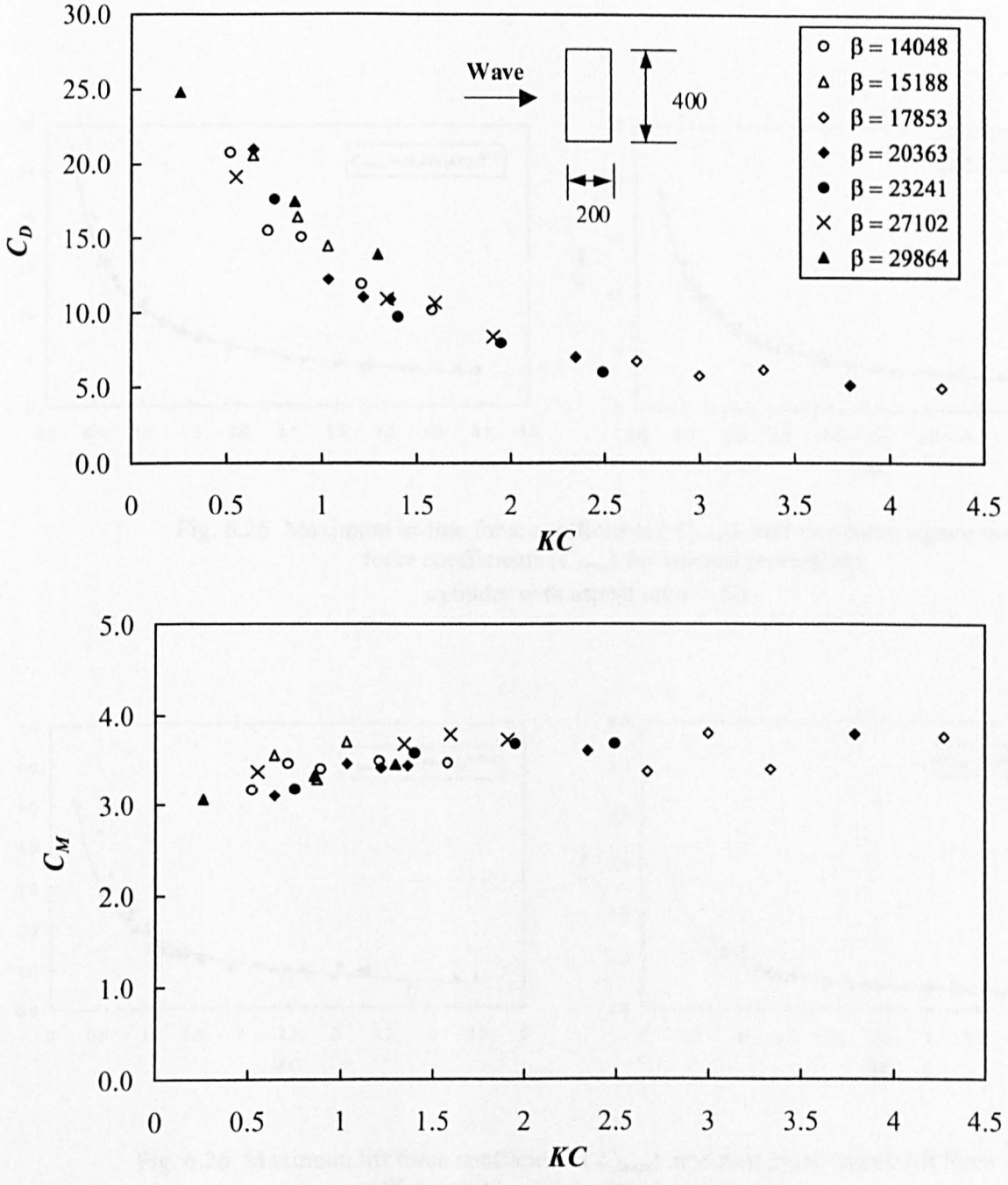

Fig. 6.24 Drag and inertia coefficients for vertical rectangular cylinder with aspect ratio = 2/1 with Keulegan-Carpenter number

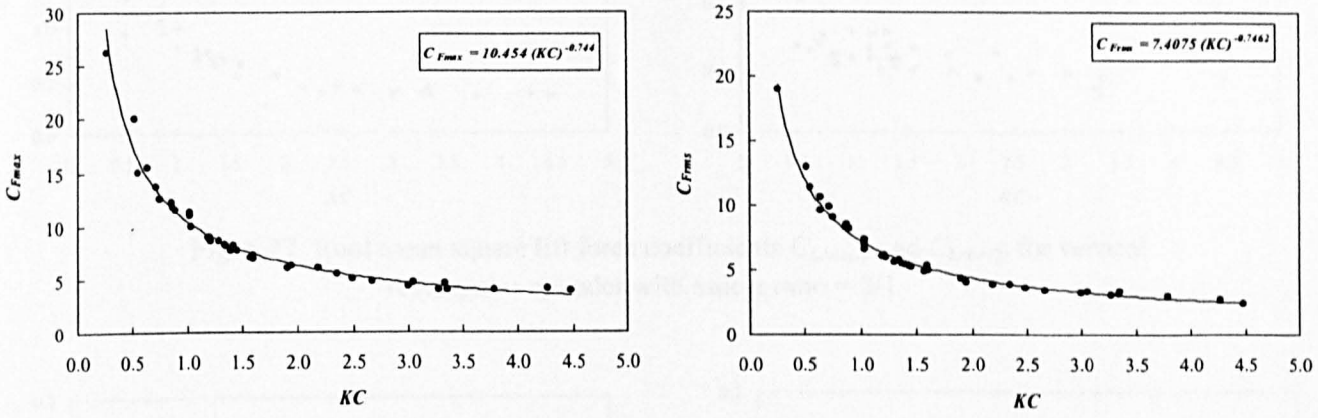

Fig. 6.25 Maximum in-line force coefficients (C_{Fmax}) and root mean square in-line force coefficients (C_{Frms}) for vertical rectangular cylinder with aspect ratio = 2/1

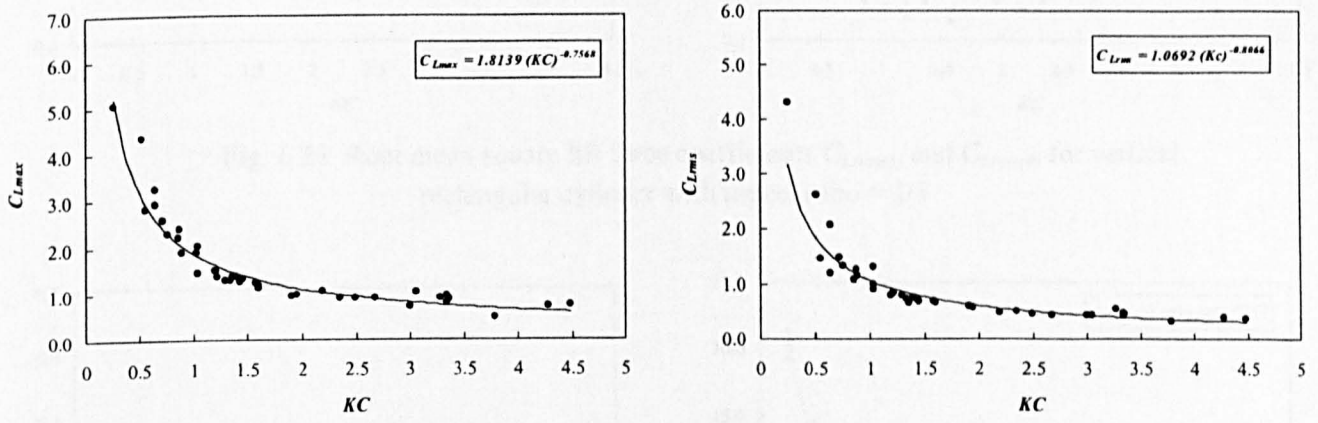

Fig. 6.26 Maximum lift force coefficients (C_{Lmax}) and root mean square lift force coefficients (C_{Lrms}) for vertical rectangular cylinder with aspect ratio = 2/1

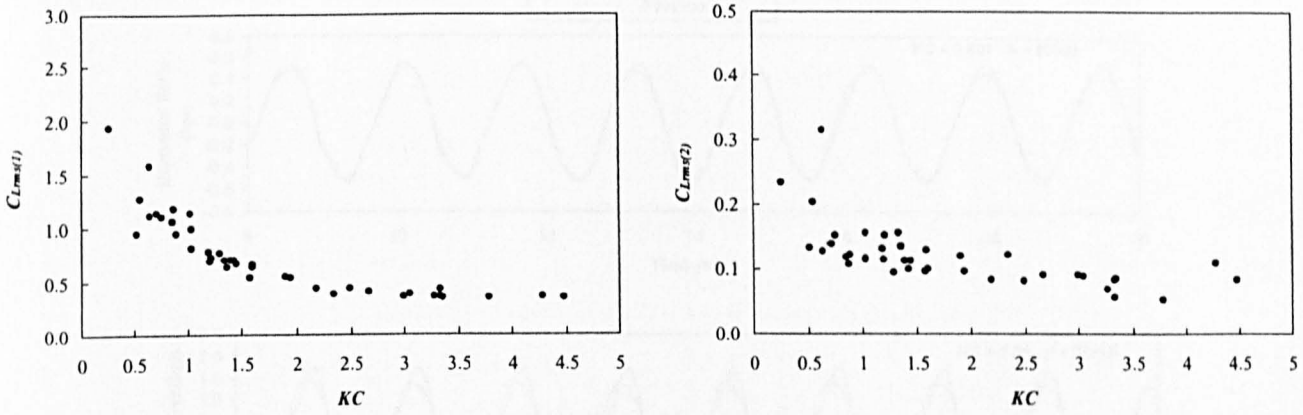

Fig. 6.27 Root mean square lift force coefficients $C_{Lrms(1)}$ and $C_{Lrms(2)}$ for vertical rectangular cylinder with aspect ratio = 2/1

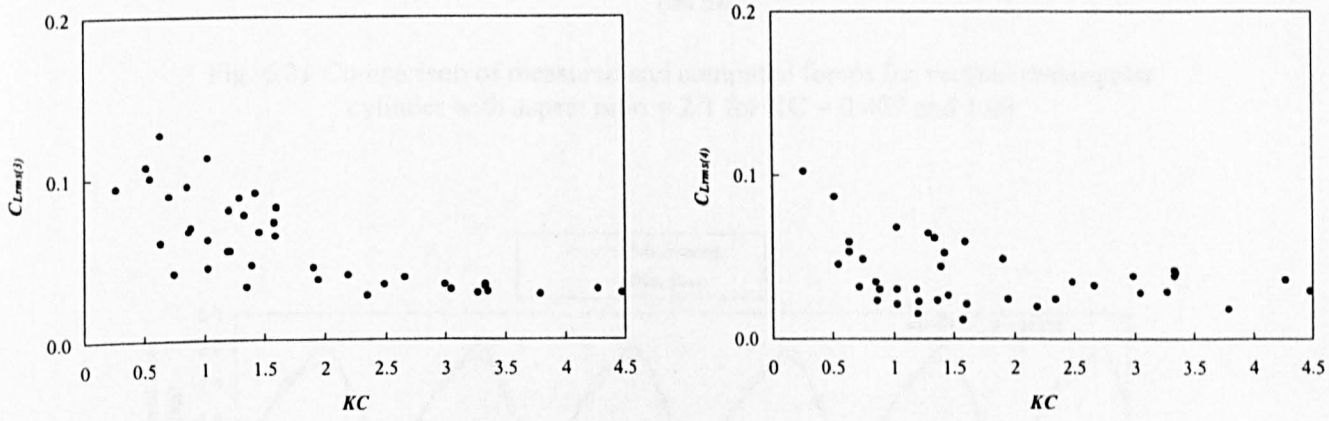

Fig. 6.28 Root mean square lift force coefficients $C_{Lrms(3)}$ and $C_{Lrms(4)}$ for vertical rectangular cylinder with aspect ratio = 2/1

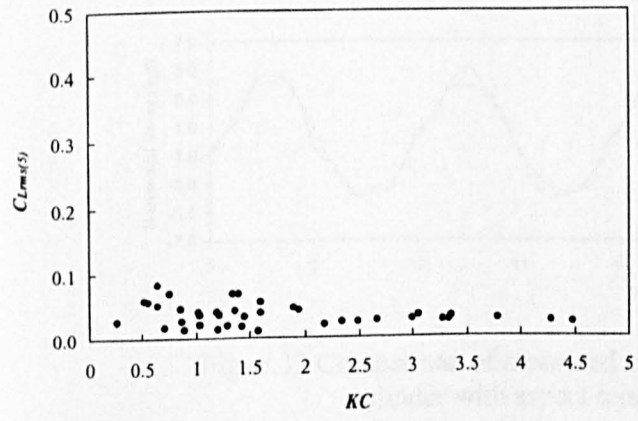

Fig. 6.29 Root mean square lift force coefficients $C_{Lrms(5)}$ for vertical rectangular cylinder with aspect ratio = 2/1

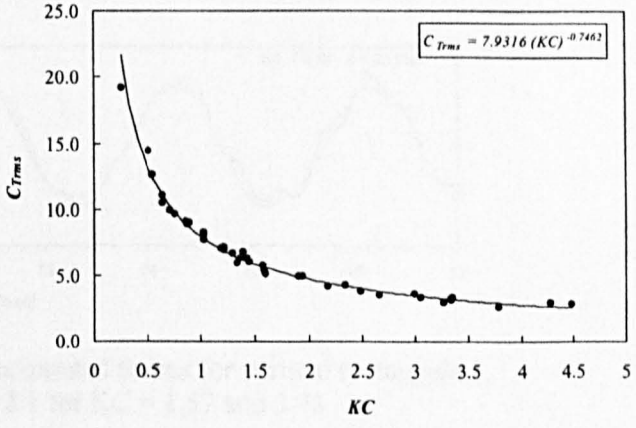

Fig. 6.30 Root mean square total force coefficients C_{Trms} for vertical rectangular cylinder with aspect ratio = 2/1

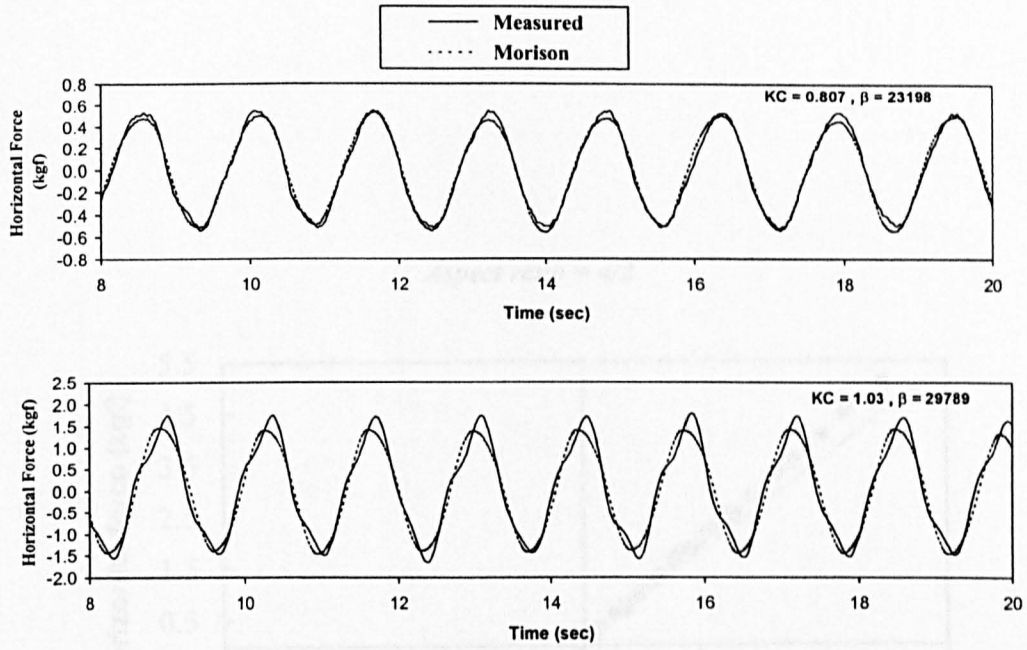

Fig. 6.31 Comparison of measured and computed forces for vertical rectangular cylinder with aspect ratio = 2/1 for KC = 0.807 and 1.03

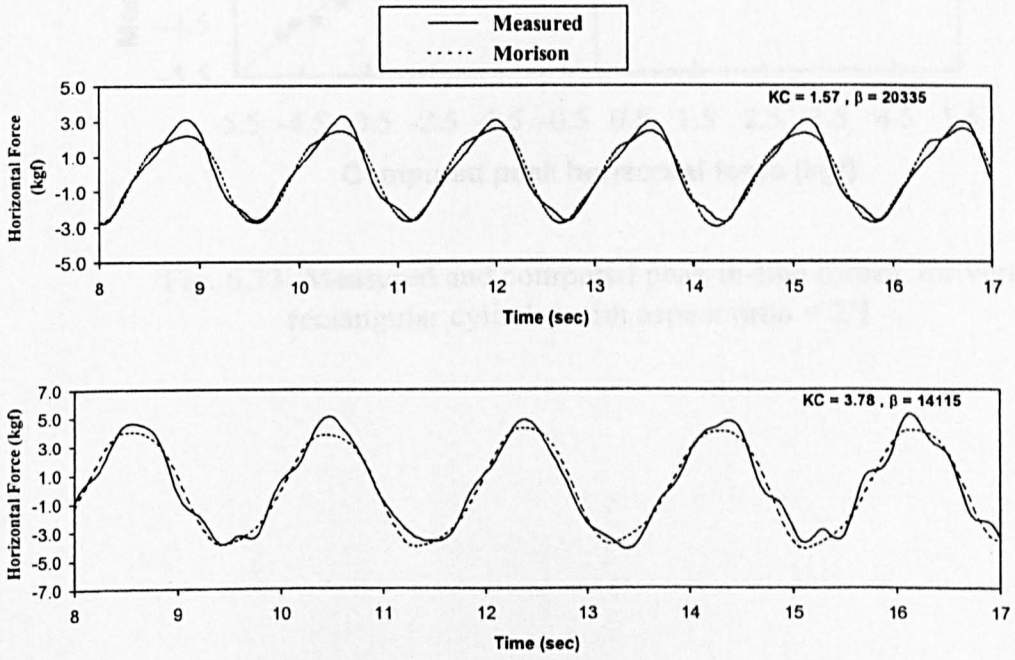

Fig. 6.32 Comparison of measured and computed forces for vertical rectangular cylinder with aspect ratio = 2/1 for KC = 1.57 and 3.78

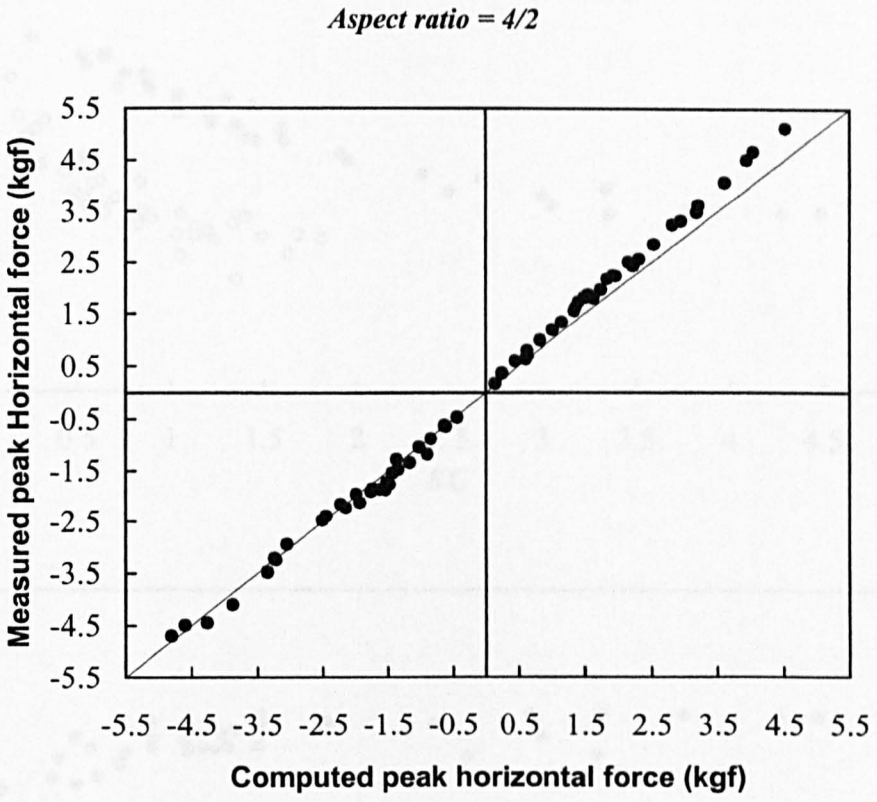

Fig. 6.33 Measured and computed peak in-line forces for vertical rectangular cylinder with aspect ratio = 2/1

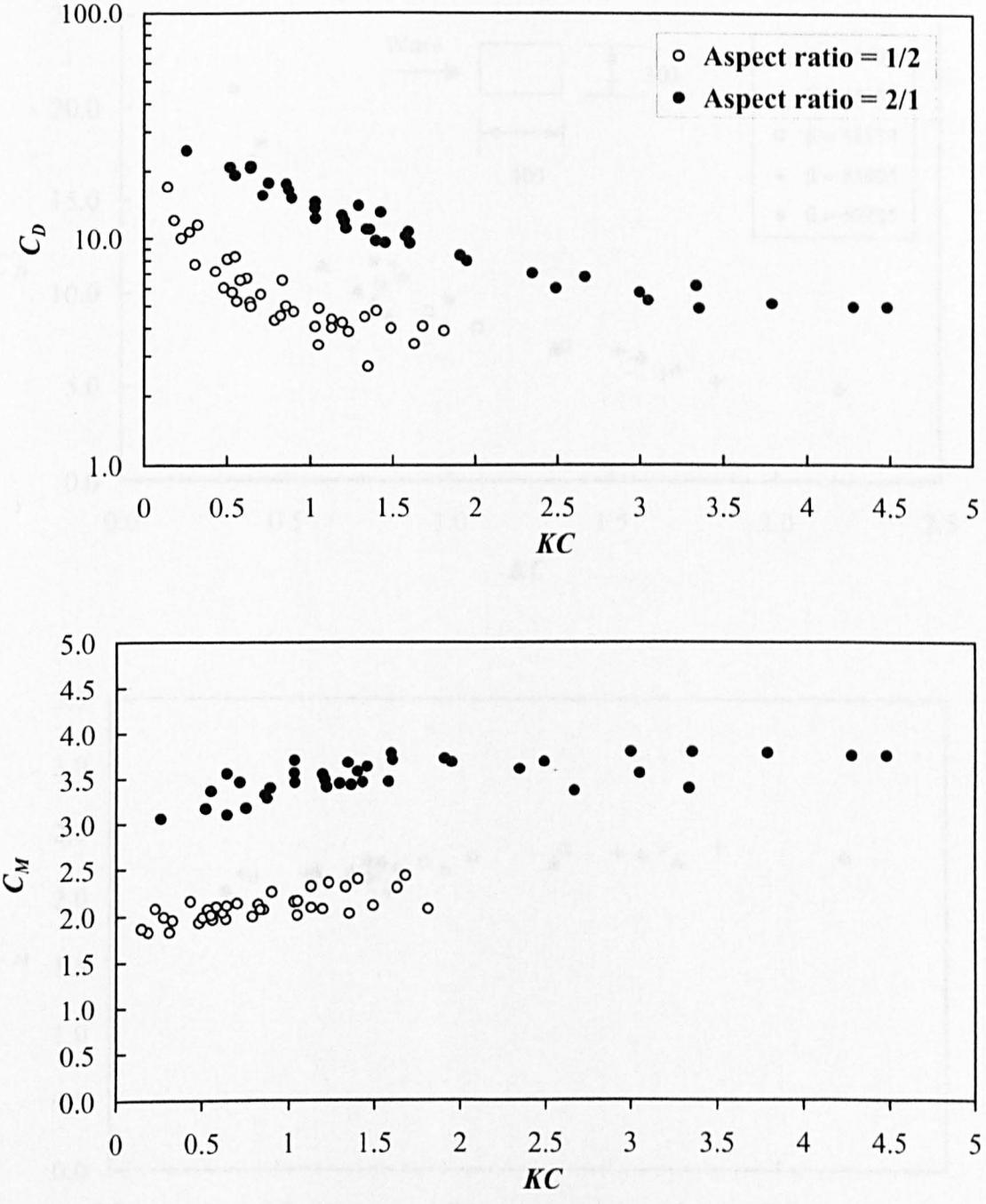

Fig. 6.34 Comparison of drag and inertia coefficients for vertical rectangular cylinder with aspect ratios = ½ & 2/1

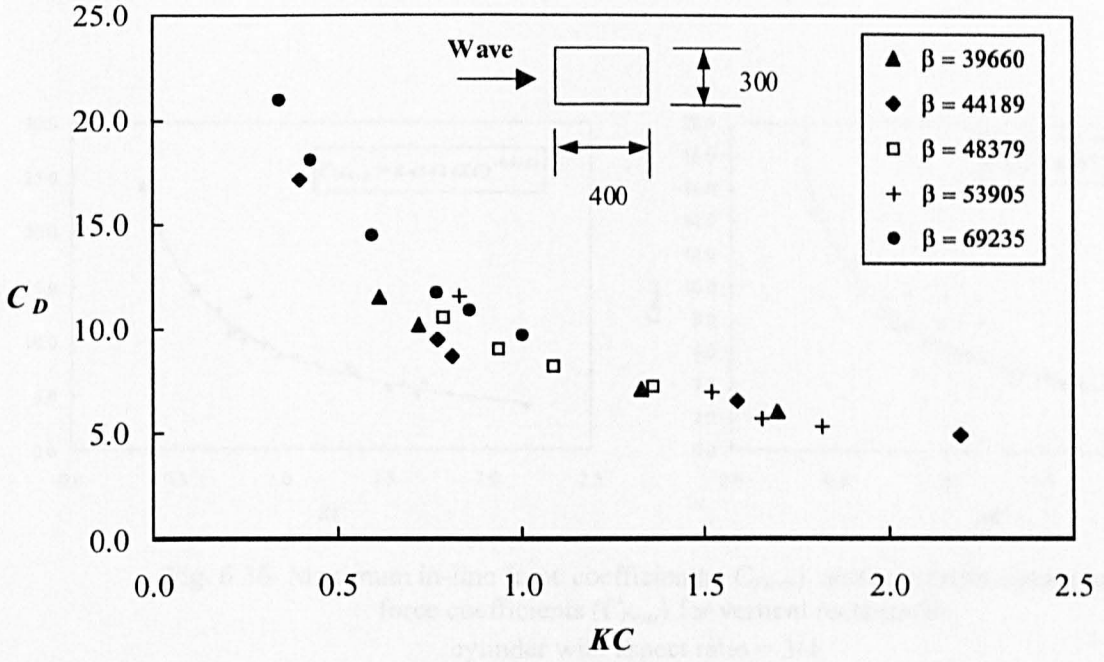

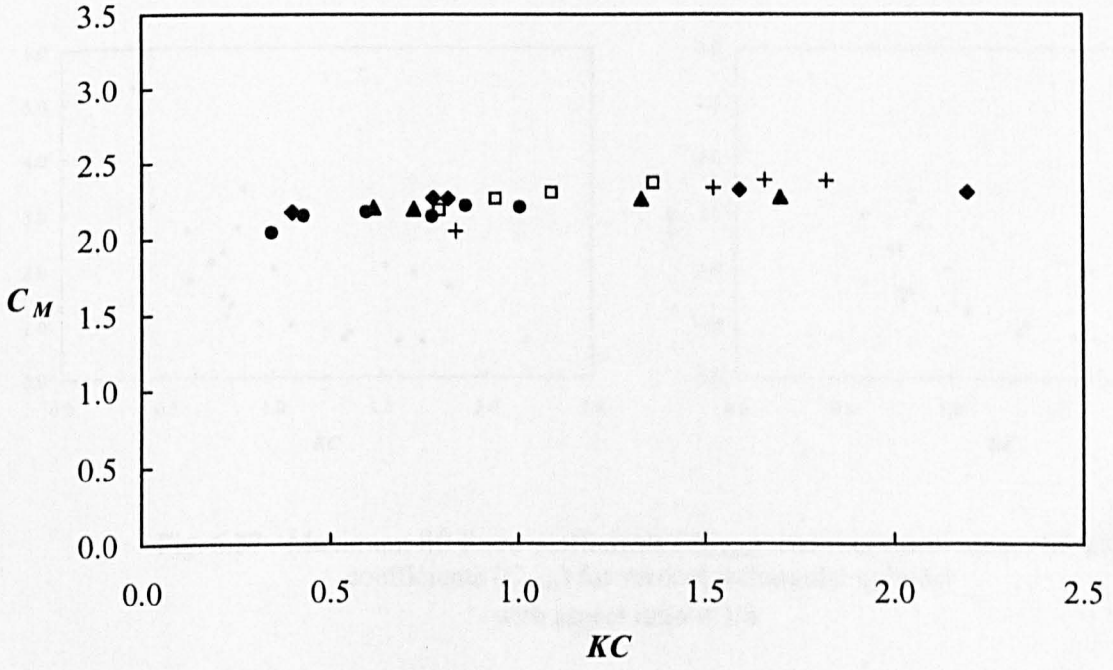

Fig. 6.35 Drag and inertia coefficients for vertical rectangular cylinder with aspect ratio = 3/4 for different frequency parameter

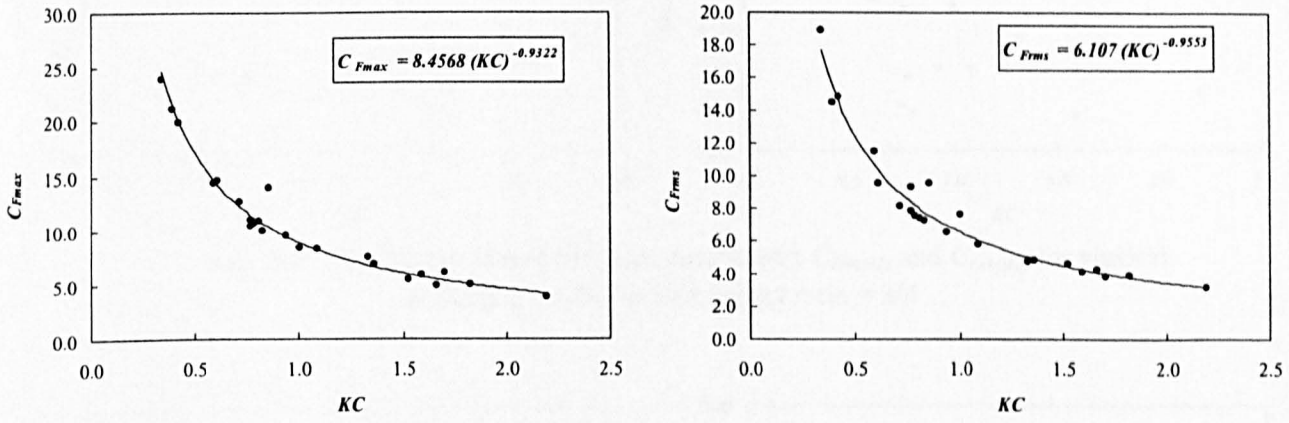

Fig. 6.36 Maximum in-line force coefficients (C_{Fmax}) and root mean square in-line force coefficients (C_{Frms}) for vertical rectangular cylinder with aspect ratio = 3/4

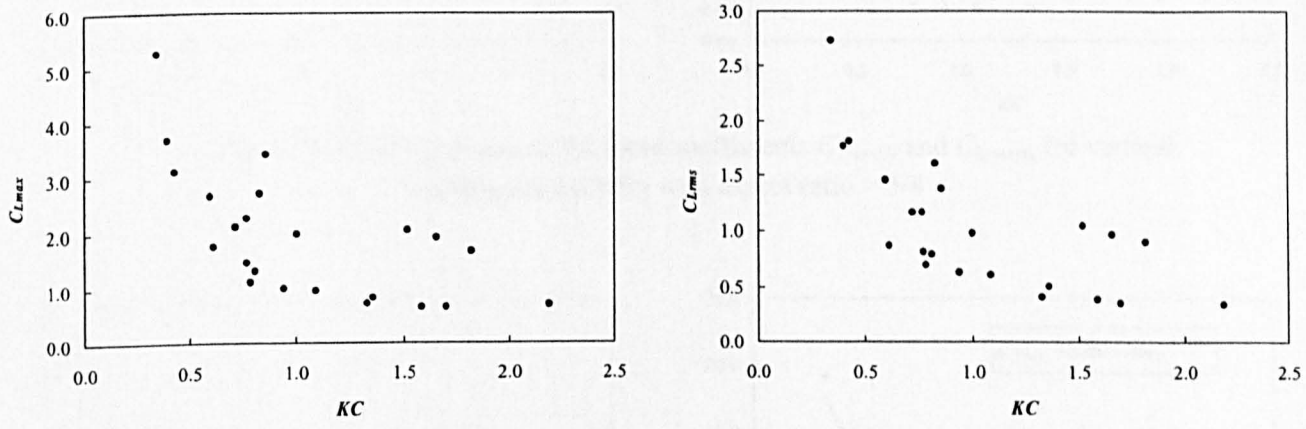

Fig. 6.37 Maximum lift force coefficients (C_{Lmax}) and root mean square lift force coefficients (C_{Lrms}) for vertical rectangular cylinder with aspect ratio = 3/4

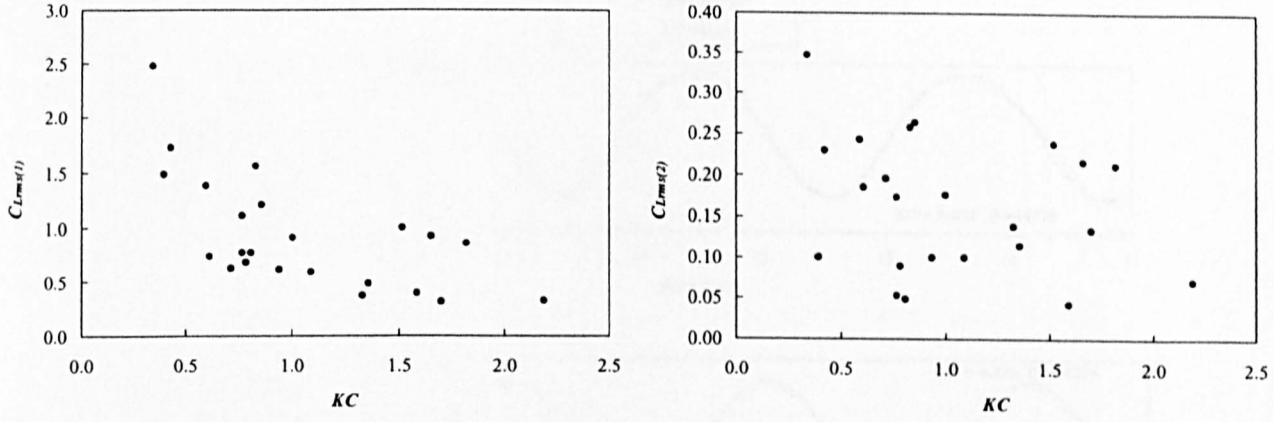

Fig. 6.38 Root mean square lift force coefficients $C_{Lrms(1)}$ and $C_{Lrms(2)}$ for vertical rectangular cylinder with aspect ratio = 3/4

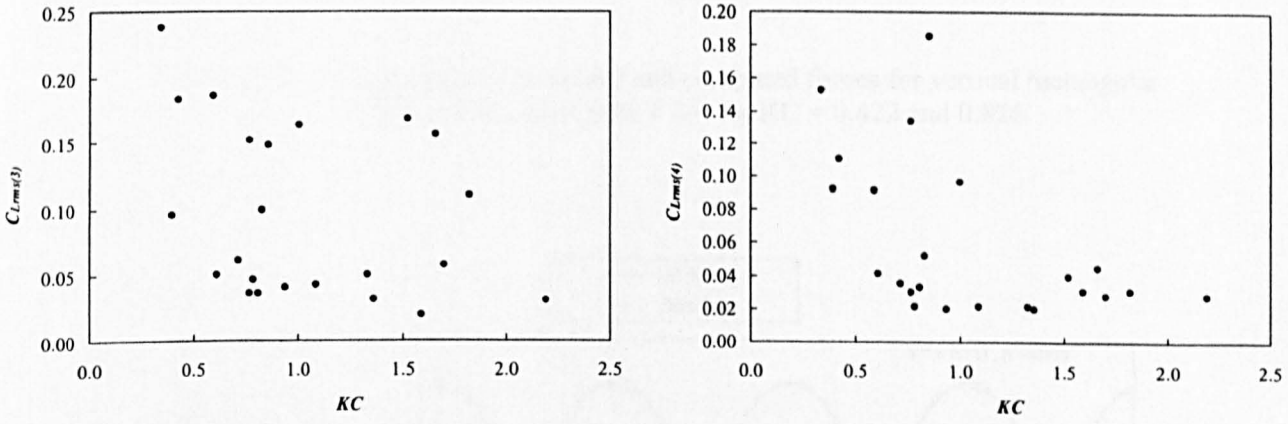

Fig. 6.39 Root mean square lift force coefficients $C_{Lrms(3)}$ and $C_{Lrms(4)}$ for vertical rectangular cylinder with aspect ratio = 3/4

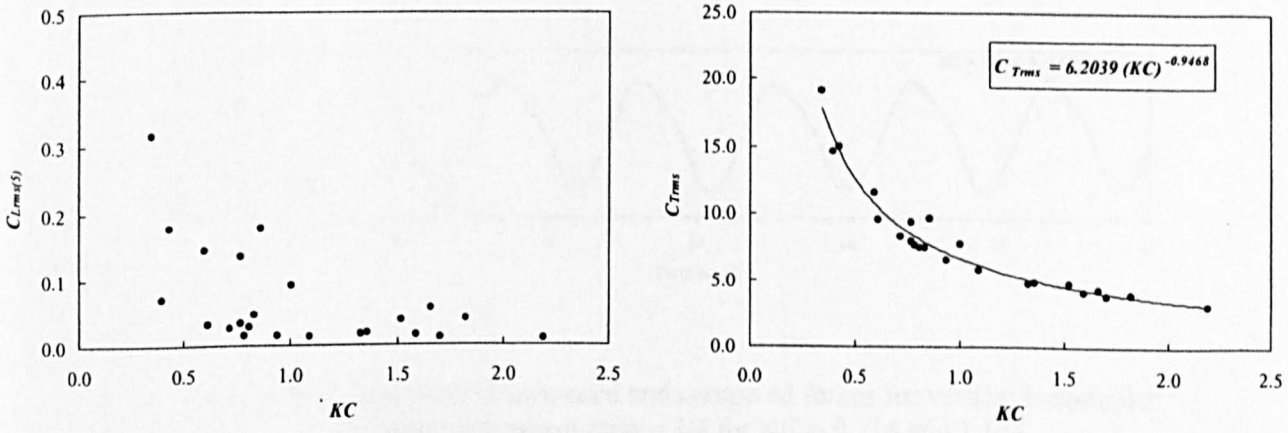

Fig. 6.40 Root mean square lift force coefficients, $C_{Lrms(5)}$ for vertical rectangular cylinder with aspect ratio = 3/4

Fig. 6.41 Root mean square total force coefficients, C_{Trms} for vertical rectangular cylinder with aspect ratio = 3/4

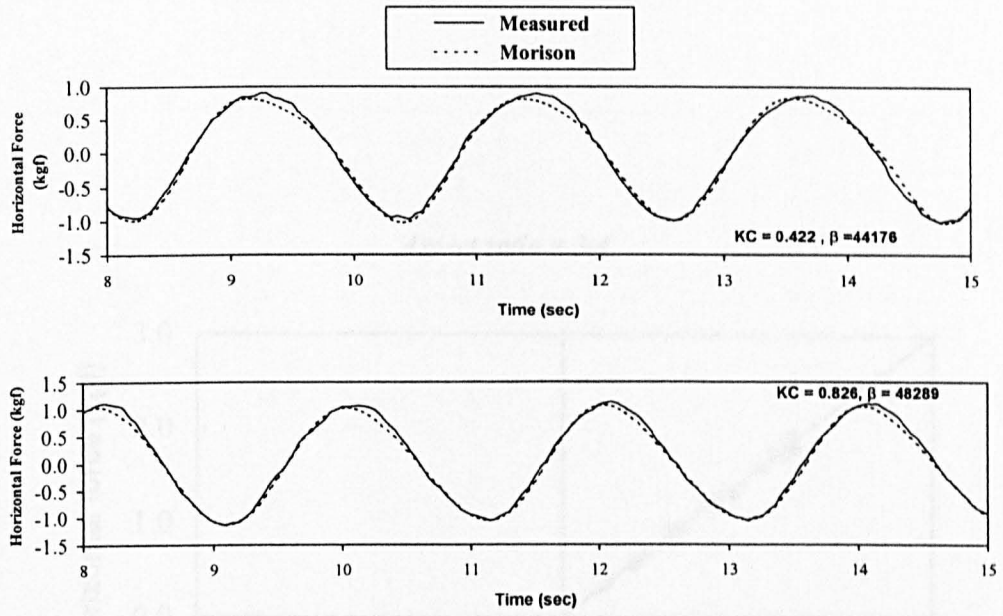

Fig. 6.42 Comparison of measured and computed forces for vertical rectangular cylinder with aspect ratio = 3/4 for KC = 0.422 and 0.826

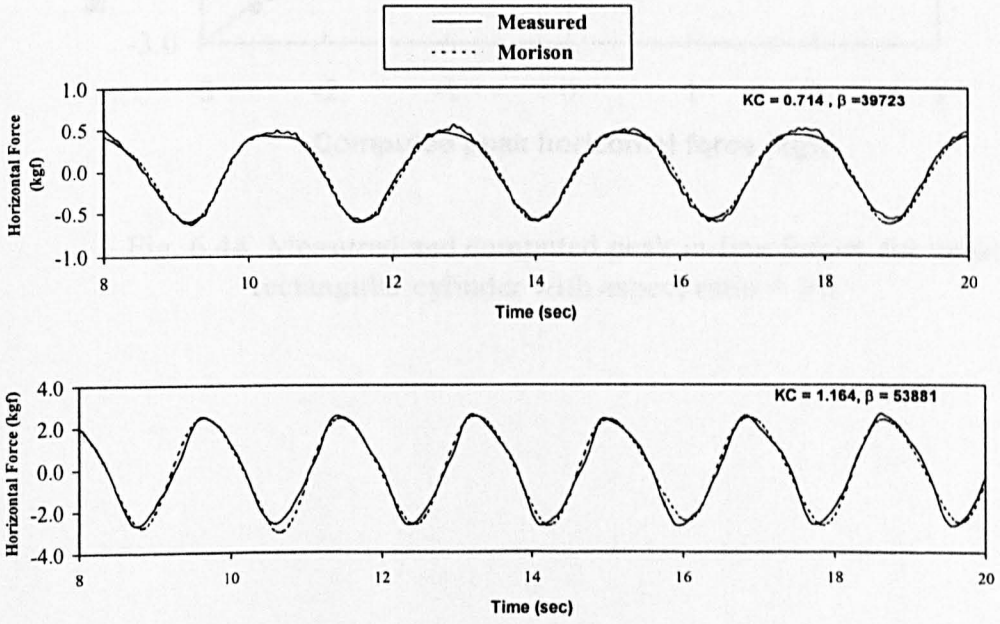

Fig. 6.43 Comparison of measured and computed forces for vertical rectangular cylinder with aspect ratio = 3/4 for KC = 0.714 and 1.164

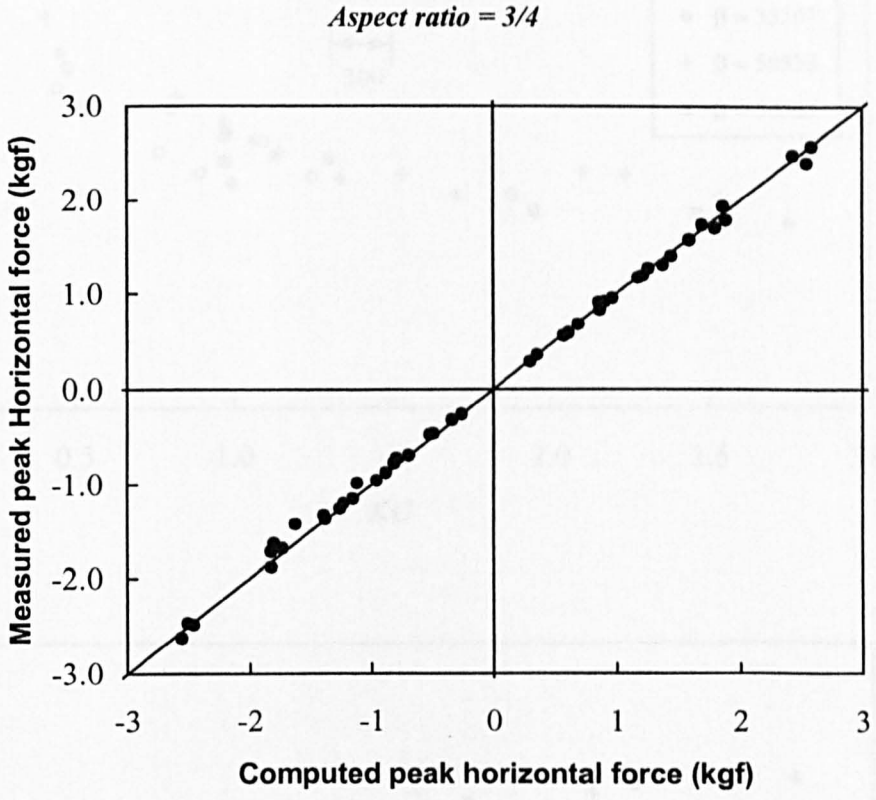

Fig. 6.44 Measured and computed peak in-line forces for vertical rectangular cylinder with aspect ratio = 3/4

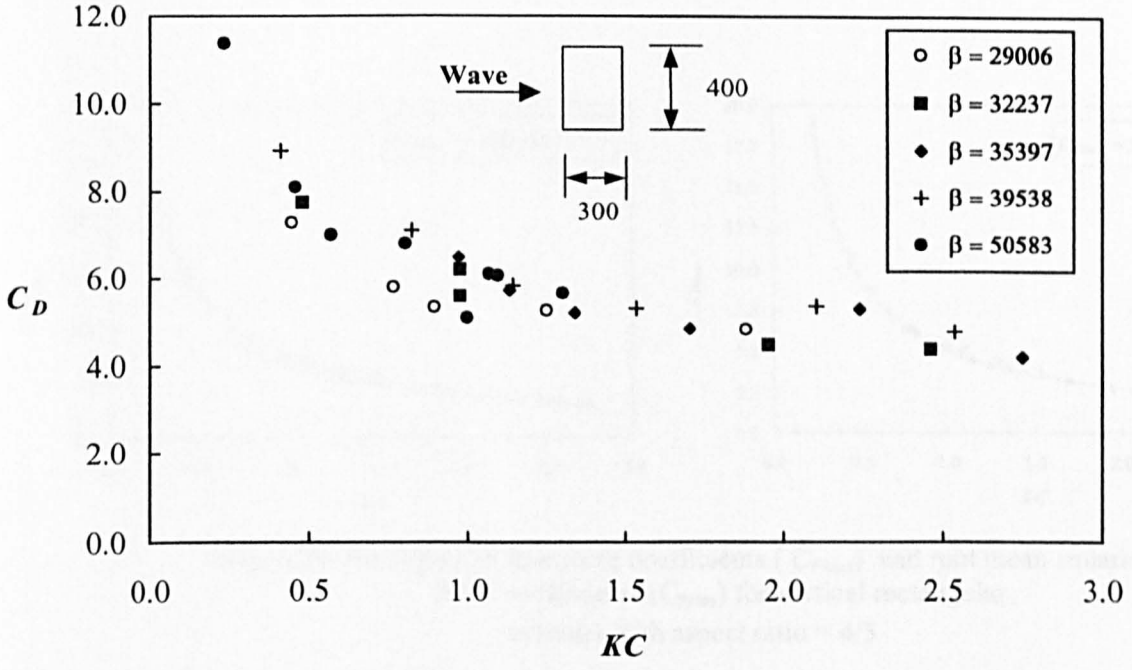

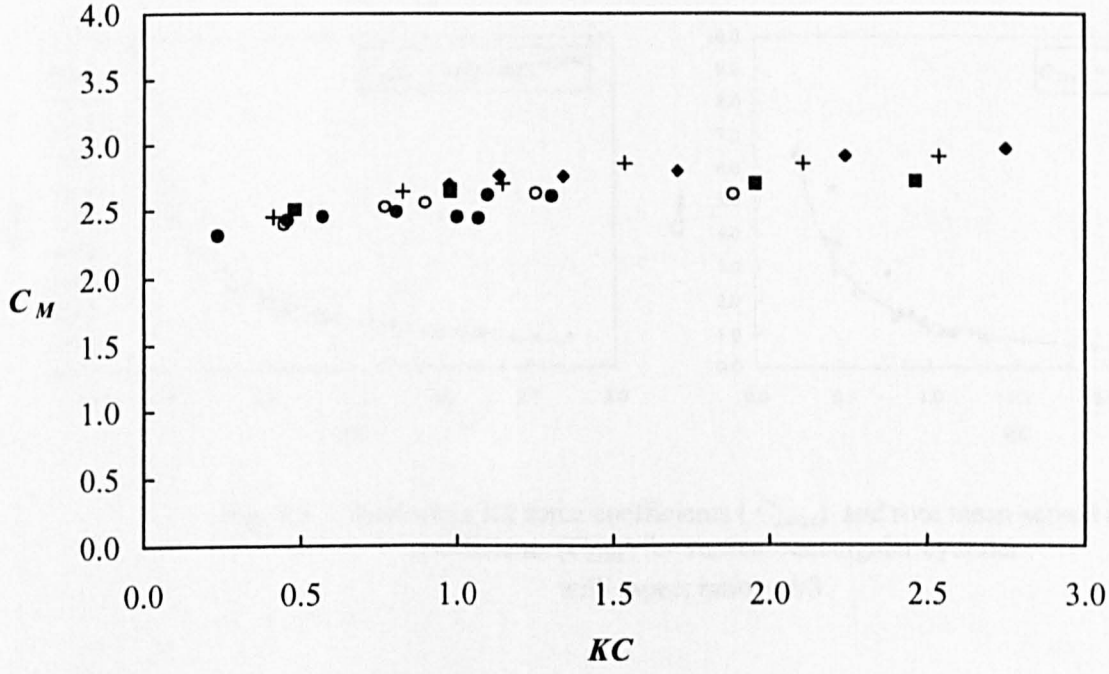

Fig. 6.45 Drag and inertia coefficients for vertical rectangular cylinder with aspect ratio = 4/3 for different frequency parameter

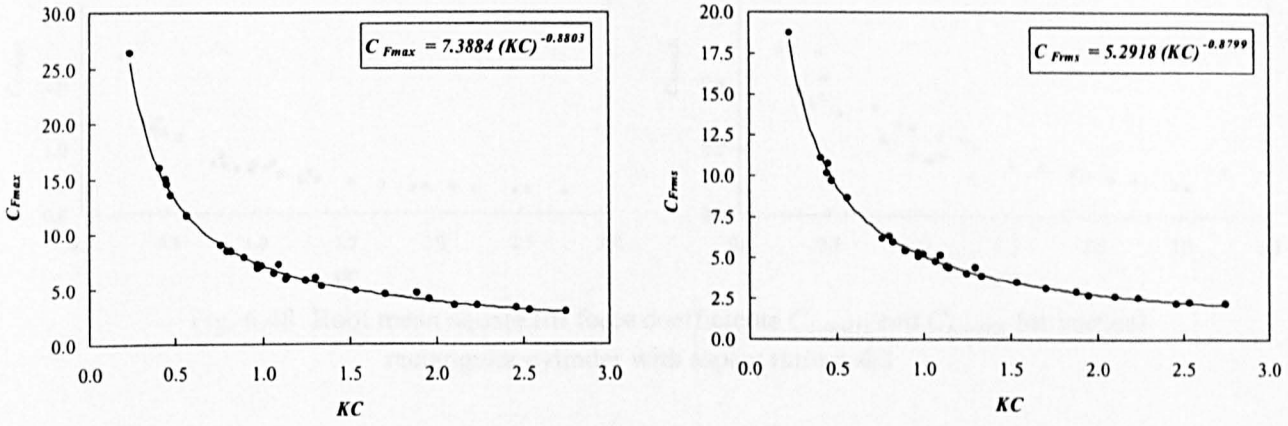

Fig. 6.46 Maximum in-line force coefficients (C_{Fmax}) and root mean square in-line force coefficients (C_{Frms}) for vertical rectangular cylinder with aspect ratio = 4/3

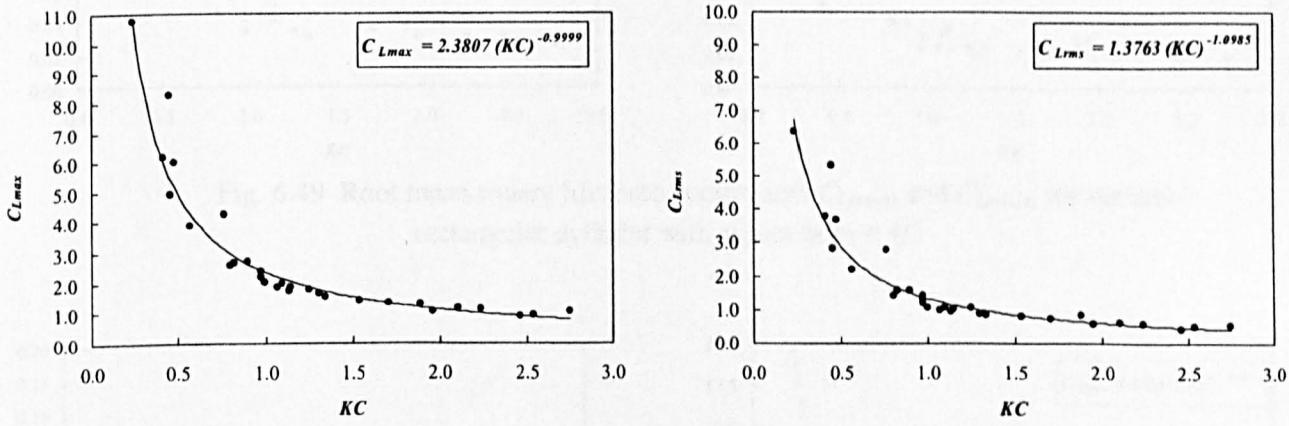

Fig. 6.47 Maximum lift force coefficients (C_{Lmax}) and root mean square lift force coefficients (C_{Lrms}) for vertical rectangular cylinder with aspect ratio = 4/3

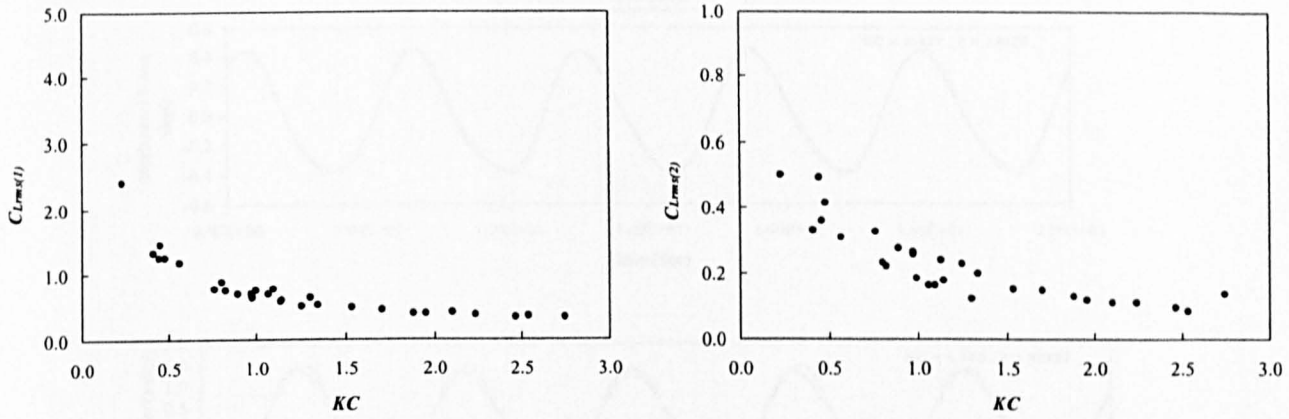

Fig. 6.48 Root mean square lift force coefficients $C_{Lrms(1)}$ and $C_{Lrms(2)}$ for vertical rectangular cylinder with aspect ratio = 4/3

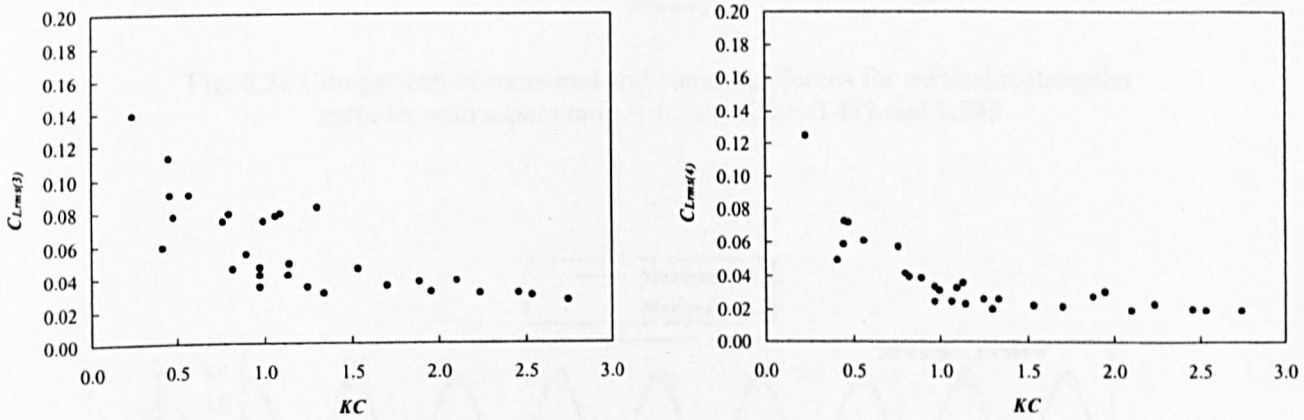

Fig. 6.49 Root mean square lift force coefficients $C_{Lrms(3)}$ and $C_{Lrms(4)}$ for vertical rectangular cylinder with aspect ratio = 4/3

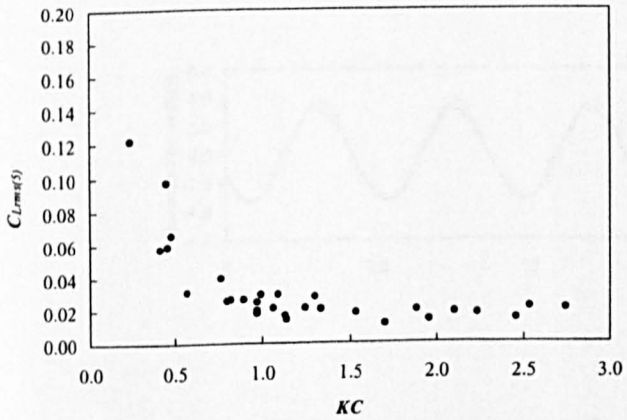

Fig. 6.50 Root mean square lift force coefficients, $C_{Lrms(5)}$ for vertical rectangular cylinder with aspect ratio = 4/3

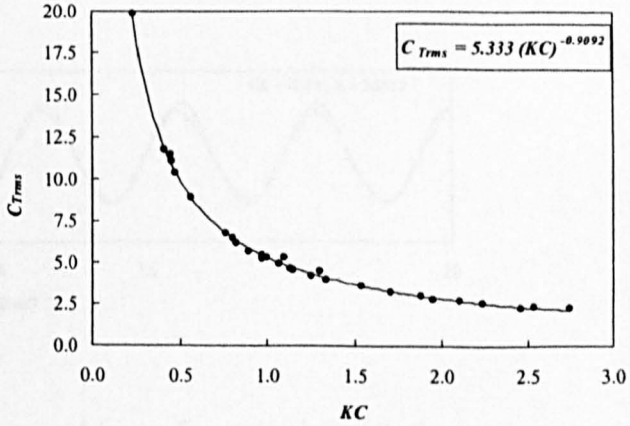

Fig. 6.51 Root mean square total force coefficients, C_{Trms} for vertical rectangular cylinder with aspect ratio = 4/3

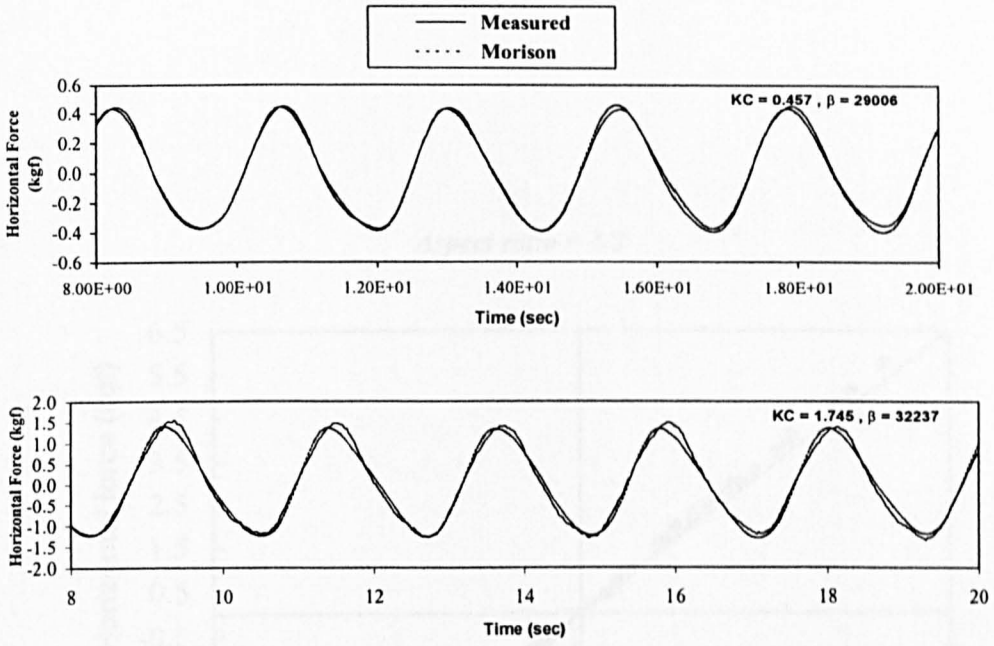

Fig. 6.52 Comparison of measured and computed forces for vertical rectangular cylinder with aspect ratio = 4/3 for KC = 0.457 and 1.745

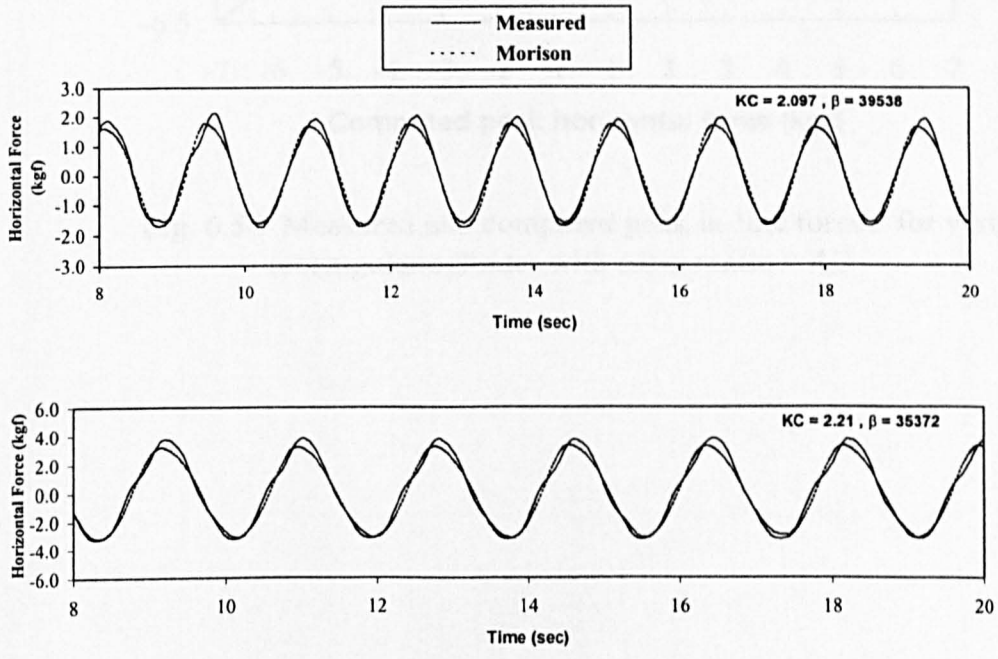

Fig. 6.53 Comparison of measured and computed forces for vertical rectangular cylinder with aspect ratio = 4/3 for KC = 2.097 and 2.21

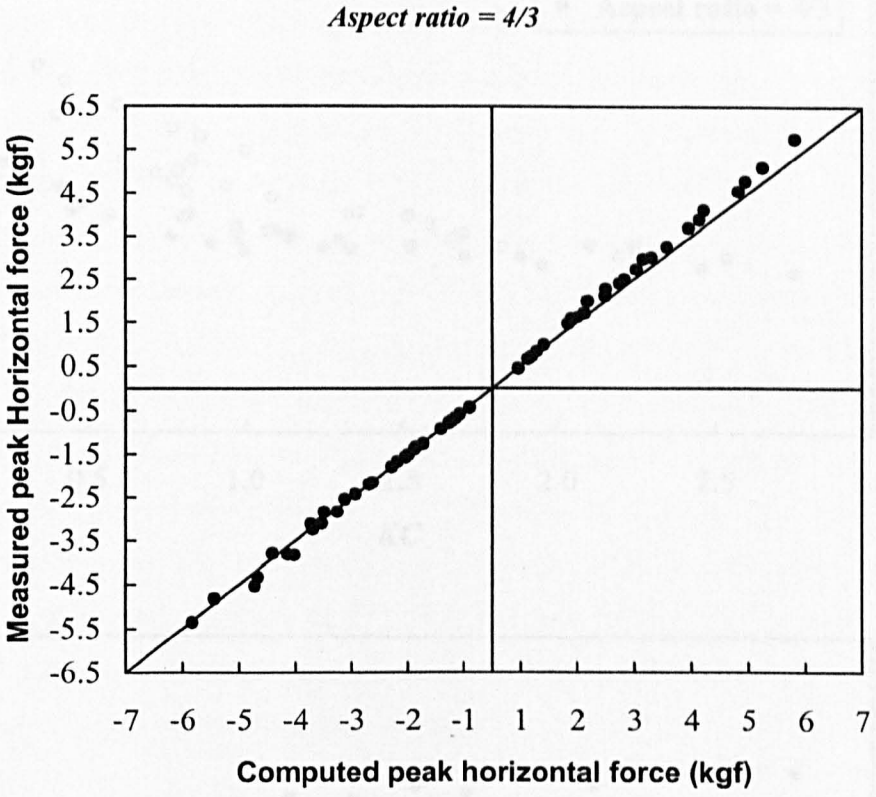

Fig. 6.54 Measured and computed peak in-line forces for vertical rectangular cylinder with aspect ratio = 4/3

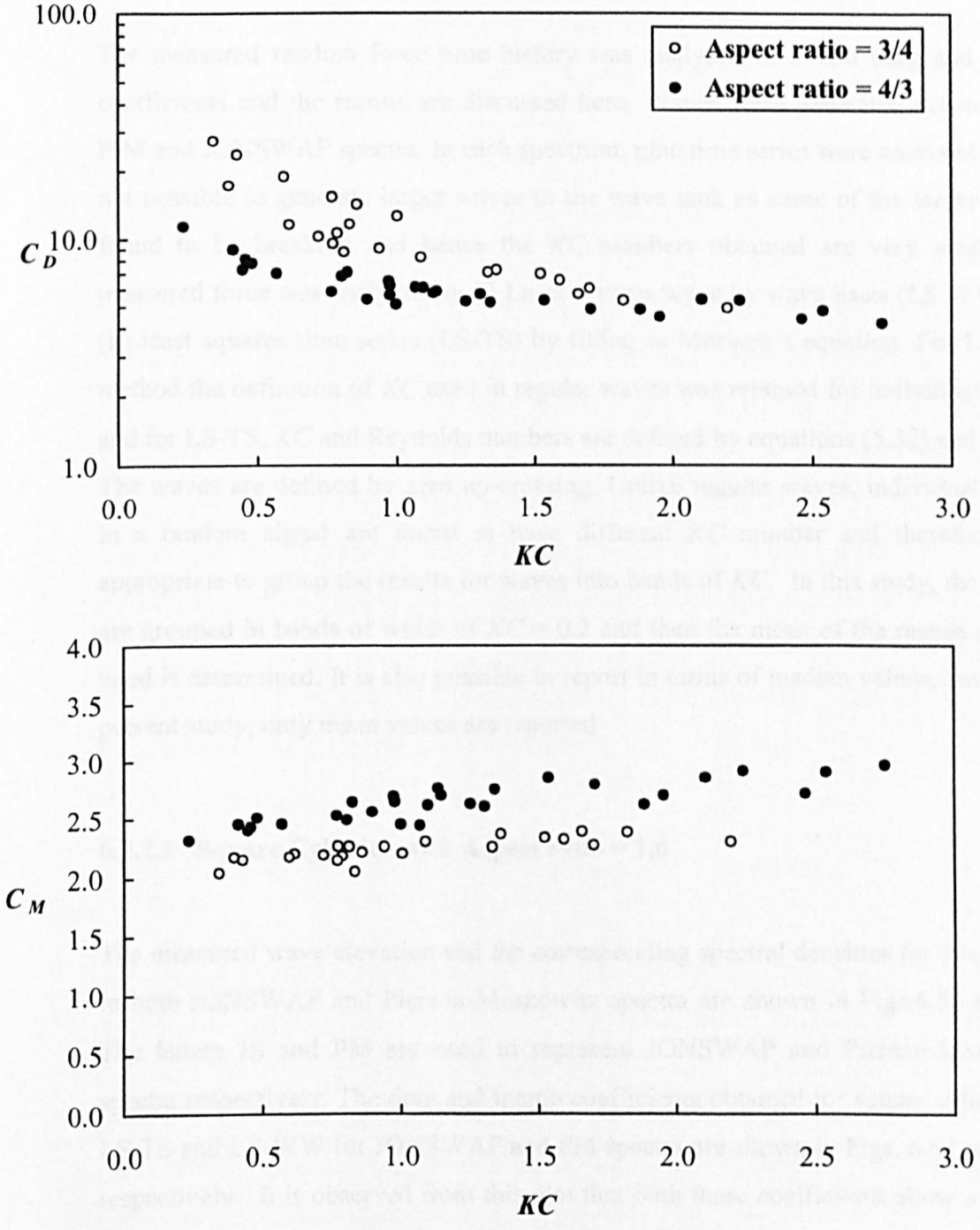

Fig. 6.55 Comparison of drag and inertia coefficients for vertical rectangular cylinder with aspect ratios = 3/4& 4/3

6.2.2 Random Waves

The measured random force time history was analysed to obtain drag and inertia coefficients and the results are discussed here. Waves were generated according to P-M and JONSWAP spectra. In each spectrum, nine time series were analysed. It was not possible to generate larger waves in the wave tank as some of the larger waves found to be breaking and hence the *KC* numbers obtained are very small. The measured force was analysed by (i) Least squares wave by wave basis (LS-WW) and (ii) least squares time series (LS-TS) by fitting to Morison's equation. For LS-WW method the definition of *KC* used in regular waves was retained for individual waves and for LS-TS, *KC* and Reynolds numbers are defined by equations (5.32) and (5.33). The waves are defined by zero up-crossing. Unlike regular waves, individual waves in a random signal are found to have different *KC* number and therefore it is appropriate to group the results for waves into bands of *KC*. In this study, the results are grouped in bands of width of $KC = 0.2$ and then the mean of the results in each band is determined. It is also possible to report in terms of median values, but, in the present study, only mean values are reported.

6.2.2.1 Square Cylinder with Aspect ratio = 1.0

The measured wave elevation and the corresponding spectral densities for three cases in both JONSWAP and Pierson-Moskowitz spectra are shown in Figs.6.56 to 6.61. The letters JS and PM are used to represent JONSWAP and Pierson-Moskowitz spectra respectively. The drag and inertia coefficients obtained for square cylinder by LS-TS and LS-WW for JONSWAP and PM spectra are shown in Figs. 6.62 and 6.63 respectively. It is observed from this plot that both these coefficients show a similar trend to those from regular waves, i.e., drag coefficients shows larger values at low *KC* numbers and decrease sharply with increase in *KC* number and the inertia coefficients approaches its potential flow value at low *KC* number and is found to increase with further increase in *KC* numbers. The band-width *KC* number based

coefficients from LS-WW method show a good trend without much scatter, whereas LS-TS method shows scatter for both drag and inertia coefficients. Note that the KC number calculated for LS-TS method is different from the KC number reported for LS-WW. The inertia coefficients for JS spectra are found to be slightly higher than C_M calculated for PM spectra.

The force coefficients computed from the random wave analysis are used in Morison's formula to obtain the theoretical force. The values of C_D and C_M obtained from LS-TS method is used for calculating the Morison's force. The force-time histories are then subjected to a frequency-domain analysis to obtain respective spectral densities, and the first 2048 samples are used for the FFT analysis with a sampling frequency of 20 Hz. The measured and computed force-time histories and the corresponding spectral densities for three cases are shown in Figs. 6.64 to 6.69 for JONSWAP & PM spectra, the comparison is found to be reasonable. The measured in-line peak forces in each wave are plotted against the calculated peak force and are shown in Fig. 6.70 for JS and PM spectra respectively. The results are shown for all nine random waves analysed. Each point represents one wave. The scatter is found to be greater than in the regular wave tests.

6.2.2.2 Rectangular Cylinder with Aspect ratio = 1/2 and 2/1

The drag and inertia coefficients for JS and PM spectra for aspect ratio = 1/2 is shown in Figs.6.71 and 6.72 respectively. The inertia coefficients approach its potential flow value at low KC number. The measured and computed spectral densities for the in-line forces for three cases are shown in Figs. 6.73 and 6.74 for JS & PM spectra and the comparison is good. The measured in-line peak force in each wave is plotted against the predicted peak force and is shown in Figs. 6.75 for both spectra.

The results for rectangular cylinder with aspect ratio = 2/1 are shown in Figs. 6.76 to 6.80. In Fig.6.79, only 1024 points are used for the calculation of spectrum. Measured and computed force spectra for the in-line force is found to be well correlated.

6.2.2.3 Rectangular Cylinder with Aspect ratio = 3/4 and 4/3

The results for aspect ratio = 3/4 is shown in Figs. 6.81 to 6.85 and for aspect ratio = 4/3 is presented in Figs.6.86 to 6.90. At low KC numbers, inertia coefficients approach potential flow theoretical value. Correlation between measured and computed force spectra for the in-line force corresponding to PM and JS spectra are observed to be good.

6.2.3 Effect of aspect ratio – Periodic Flow

In the present work, flow visualisation studies have not been made, however, as demonstrated by Arai (1993,1995) the flow and the nature of force around rectangular cylinder have behaved the same way as it has occurred for a square cylinder. In the following paragraphs, the flow patterns around the vertical and horizontal square cylinder are illustrated and an explanation is given for why and how the force coefficients takes different values when the cylinders aspect ratio is changed.

Singh (1979) carried out a flow visualisation on circular, square, diamond cylinders and flat plates in planar oscillatory flow. On a square cross sectional cylinder, he observed three regions of flow patterns, a symmetric region for $KC<5$, an asymmetric region $5<KC<25$ and a pseudo-Karman street for $KC>25$. In the symmetric region the flow was observed to separate from the leading edges resulting in re-circulating fluid on the upper and lower surfaces. As the flow reversed the re-circulating fluid on the upper and the lower surfaces moved back along these faces, creating new vorticity of opposite sign. This resulted in weak local disturbances as the flow between the re-circulating region and the growing vortex along the upper and lower surfaces

departed rapidly away from the cylinder. As the flow developed further, separation occurred at the trailing edges. No re-attachment of the separated shear layers took place and the flow developed as in the previous half cycle. In the asymmetric region, at $5<KC<12$, the flow was observed to separate at the leading edges.

From the force measurements and flow visualization study carried out by Singh (1979), the variation of inertia coefficients for circular and square cylinder showed different trends with KC number, particularly for KC between 10 to 20 a minimum value of C_M is observed for circular cylinder, whereas, the results for the square cylinder are almost constant for $KC<25$, and then gradually decreases as KC increases beyond this value. This difference between these results is associated with differences in flow pattern. For circular cylinder throughout the entire range of KC, the wake is composed of rather large distinct vortices and in particular in the region of $KC = 15$, these vortices are very strong and set up clearly defined motions around the body. These variations in wake characteristics for values of KC in the region of 15 results in minimum inertia coefficients. On the other hand, the square section does not produce any distinct vortex structure for $KC<25$. Vortices do form, but they are weak (that their influence on the inline force is not very important) and do not go into any clearly defined motions about the body, instead they interact with each other with the body and soon decay. Therefore, dramatic changes in the wake do not take place. The upper and lower surfaces cause some delay in interaction between separated shear layers, often with some partial reattachment and produces only weak vortices. This results in an inertia coefficient, which is almost constant at its potential flow value for $KC<25$.

In the case of horizontally submerged circular cylinder beneath the waves, Chaplin (1984a,b) reported that the inertia coefficients for horizontal cylinders decrease rapidly with increase KC number to a value as low as one-half of the potential flow inertia coefficients. It was suggested that this is caused by the non-linear effect of oscillatory boundary layer due to viscosity. Later, Chaplin (1988a) investigating the non linear forces on circular cylinders horizontally submerged in waves at low KC

numbers and under circular orbital flow conditions, argued that the reduction of inertia coefficients are associated with a lift force caused by the circulation of the flow relative to the cylinder, acting in opposite direction to the inertia force. Chaplin and Retzler (1992) explain further that beneath a wave, at a point, the velocity and acceleration vectors rotate with the acceleration vector leading the velocity vector by 90°. The boundary layer present on the surface of the cylinder, even though the ambient flow is oscillatory, generates a steady flow parallel to the boundary which is known as 'steady streaming'. For a horizontally submerged cylinder under waves, this steady streaming circulates around the cylinder. A force is generated by the combination of circulation and the ambient flow, which is referred by the authors as 'lift' and it acts at right angles to the incident flow. There is continuous change in the orientation of the incoming flow and the lift. The consequence is the result of a non-linear reduction in loading. The reduction of forces is also observed in the case of a square pontoon section [Chaplin and Retzler (1993)].

Otsuka et al. (1998) studied the flow around a square cylinder at low KC numbers experimentally and also by Navier-stokes simulations. The vortex shedding patterns are briefly summarised below with reference to Fig. 6.91 reproduced from their work. This figure shows vorticity distributions obtained by numerical work for KC = 2.0, 3.0 and 4.0. The incident flow directions are indicated by arrow and the solid and dotted contours represent the clockwise and anticlockwise vorticity respectively. The elapsed time is 't' from the start of the motion. The four corners of the cylinder section are named as A,B,C and D. For all the KC numbers, the first two clockwise vortices created at corners A and B does not grow large and remain at around the corners. The anticlockwise vortices separated from corners C, D and A one after the other grow largely and shed from the cylinder. Now, the third and fourth clockwise vortices separated from corners C and D grow larger due to the induced velocities of the anticlockwise vortices. These clockwise vortices form bubbly vortices in the left side in relation to the incident flow. The flow velocities at the immediate outer side of the bubbly vortices are much higher than those at the right side relating to the incident flow. This means that the lift force occurs in the opposite direction to the flow

acceleration (inertia force direction). The scale of the vortices increases with increasing KC and the anticlockwise vortices shed further from the cylinder for large KC number.

It is clear from the literature and above descriptions that in oscillatory flow, for circular and square cylinders vortices do form at very low KC numbers. For circular cylinders at subcritical Reynolds number, vortices are found for all KC numbers above about 3 and for bodies with sharp edges they may be present at much lower KC values [Bearman et al (1984)]. Okajima et al.(1998) filmed clear vortices on a square cylinder at KC = 2.2. In this small KC range, both the leading and trailing vortex shedding are symmetrical and with increase in KC, symmetrical feature of the trailing vortex shedding collapses, while the leading vortex shedding maintains the symmetry. Moreover, at low KC numbers (less than about 7), the C_D values of a square cylinder are comparatively larger than circular a cylinder, which is corresponding to a wide wake width due to the development of the leading vortex. The leading vortex shedding on the square cylinder makes the wake width spread, accompanied by growth in size of the separated vortices, which results in large C_D values in comparison to those for a circular cylinder. Also in a KC number range where C_D reaches a constant value, the wake width shows no marked change and even if KC is increased further, the wake width is nearly kept constant [Okajima et al. (1998] with almost a constant value of drag coefficients, as the flow patterns are less variable. Similar to square cylinder, for rectangular cylinders, at low KC numbers, it is anticipated that the wake width increases with the growth of the size of separated vortices and hence C_D values are large. On the other hand for higher values of KC numbers, the wake width is expected to shrink and C_D values become small. Further, it is obvious that the C_D values are strongly related to the cylinders width/height ratio and therefore the growth of the separated vortices are accompanied by the dimensions of the rectangular cylinder which alters the wake width, resulting a larger drag coefficient for wider wake (for larger aspect ratio) and smaller drag for smaller wake (for smaller aspect ratio).

With regard to inertia coefficients, at very low KC numbers close to zero, there is a tendency towards an attached and undisturbed flow with vortex strength tending to zero and therefore the inertia coefficients approaches its potential flow value. At low KC numbers, the C_M value is considered to be closely related to the flow volume (i.e., the area of the near wake field in which fluid moves) around the cylinder. A larger C_M corresponds to a large amount of flow volume or vice versa and this is clearly reflected in the values of the inertia coefficients. The C_M values for all the cylinders approached its potential flow values at KC close to zero and then starts to increase with increase in KC which indicates an increase in amount of flow volume (as demonstrated by Okajima et al.(1998) for a circular cylinder) and the amount of flow volume is considered to corresponds to the added mass. This is indeed true as one can see from Table. 6.5. A cylinder with larger side exposed to the wave experiences large inertia coefficient and smaller side facing the flow results in smaller inertia coefficients. The inertia coefficients obtained for other cylinders whose aspect ratio are in between these two limits of aspect ratios will have inertia coefficients in relation to the added mass coefficients.

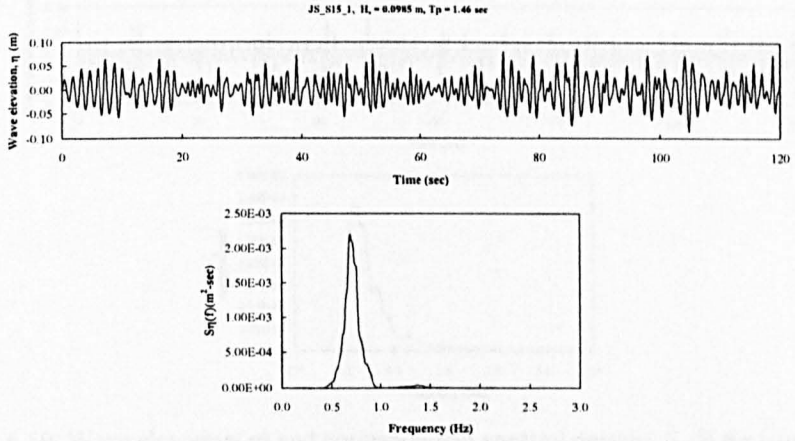

Fig. 6.56 Wave elevation(η) and corresponding spectral density, $S_\eta(f)$ for vertical square cylinder for run number JS_S15_1

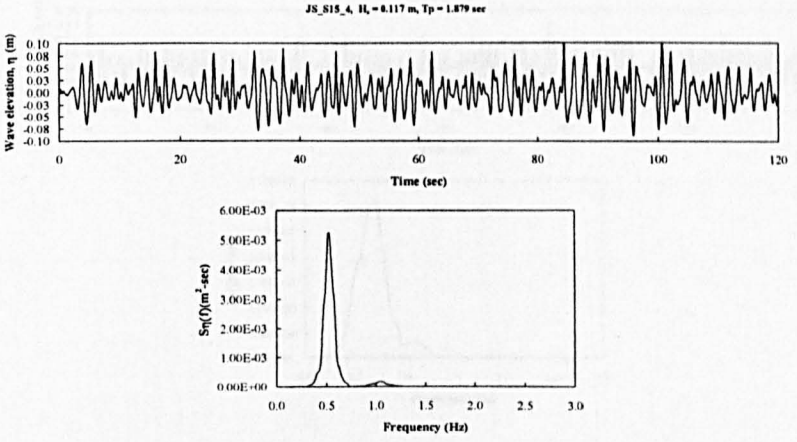

Fig. 6.57 Wave elevation(η) and corresponding spectral density, $S_\eta(f)$ for vertical square cylinder for run number JS_S15_4

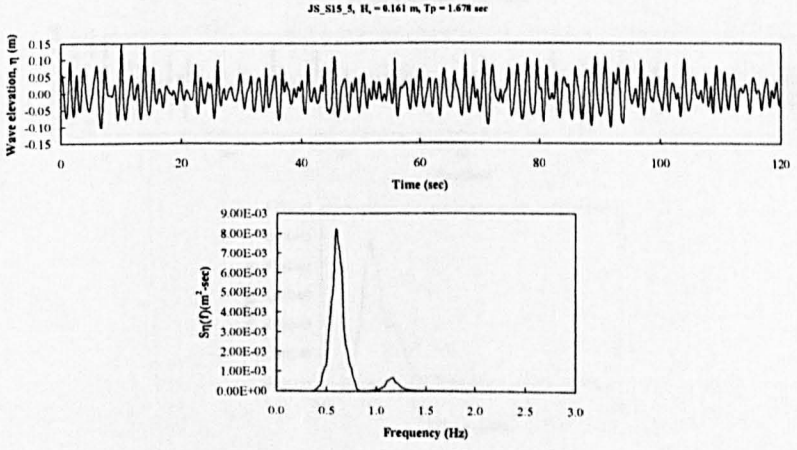

Fig. 6.58 Wave elevation(η) and corresponding spectral density, $S_\eta(f)$ for vertical square cylinder for run number JS_S15_5

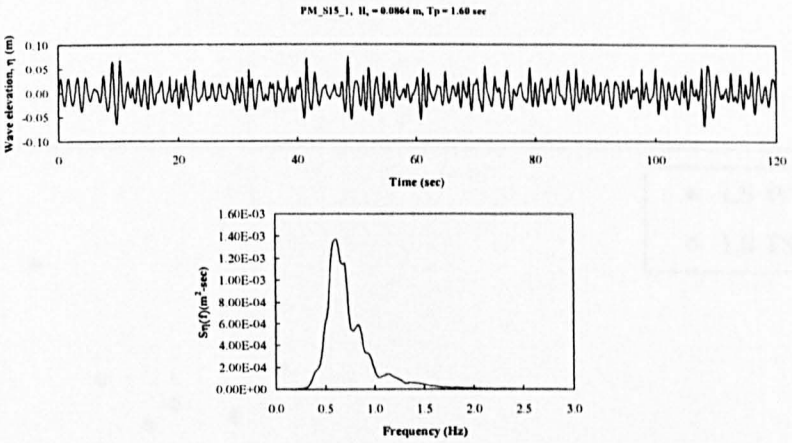

Fig. 6.59 Wave elevation(η) and corresponding spectral density, $S_\eta(f)$ for vertical square cylinder for run number PM_S15_1

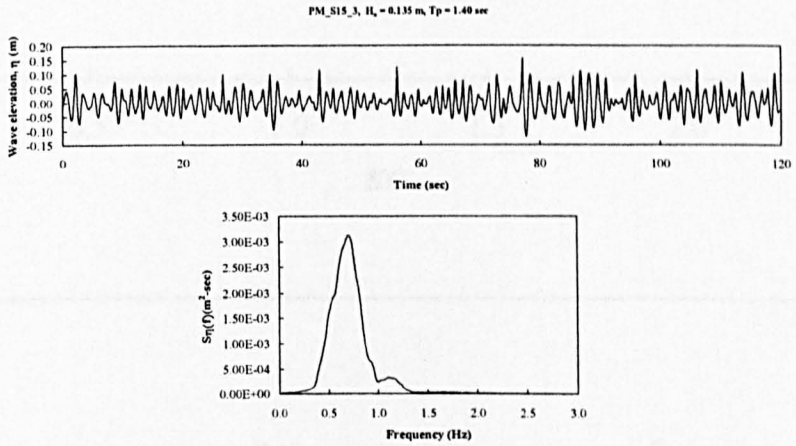

Fig. 6.60 Wave elevation(η) and corresponding spectral density, $S_\eta(f)$ for vertical square cylinder for run number PM_S15_3

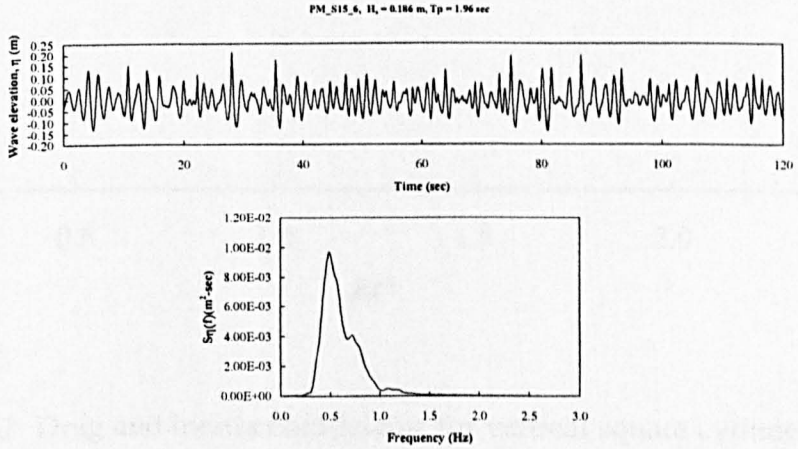

Fig. 6.61 Wave elevation(η) and corresponding spectral density, $S_\eta(f)$ for vertical square cylinder for run number PM_S15_6

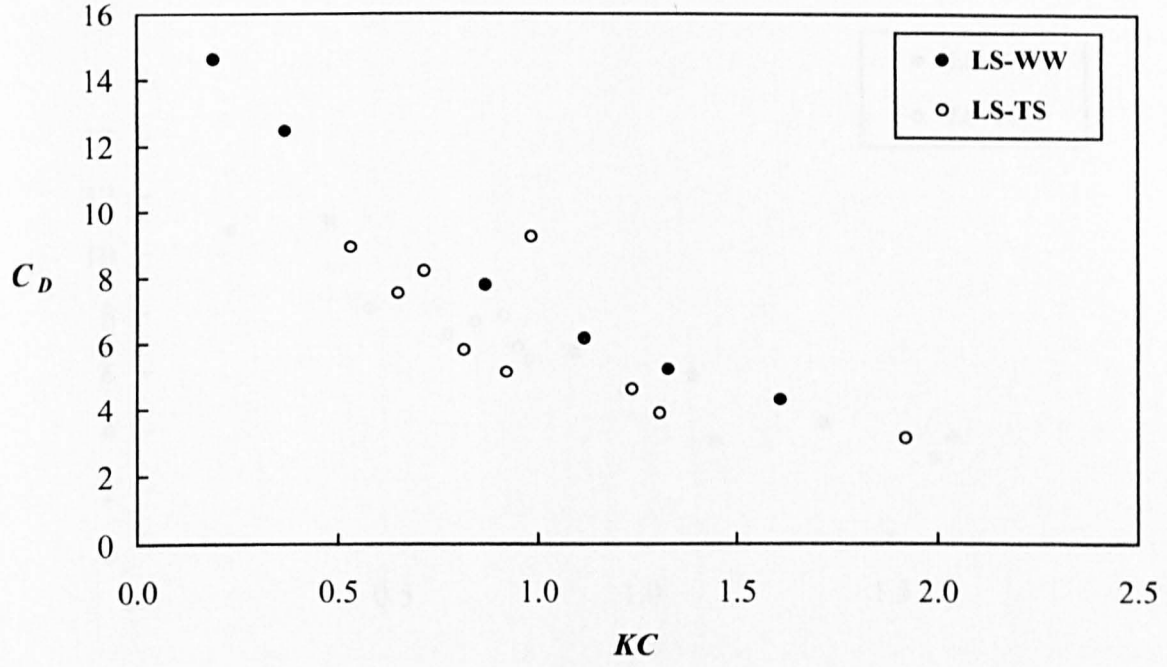

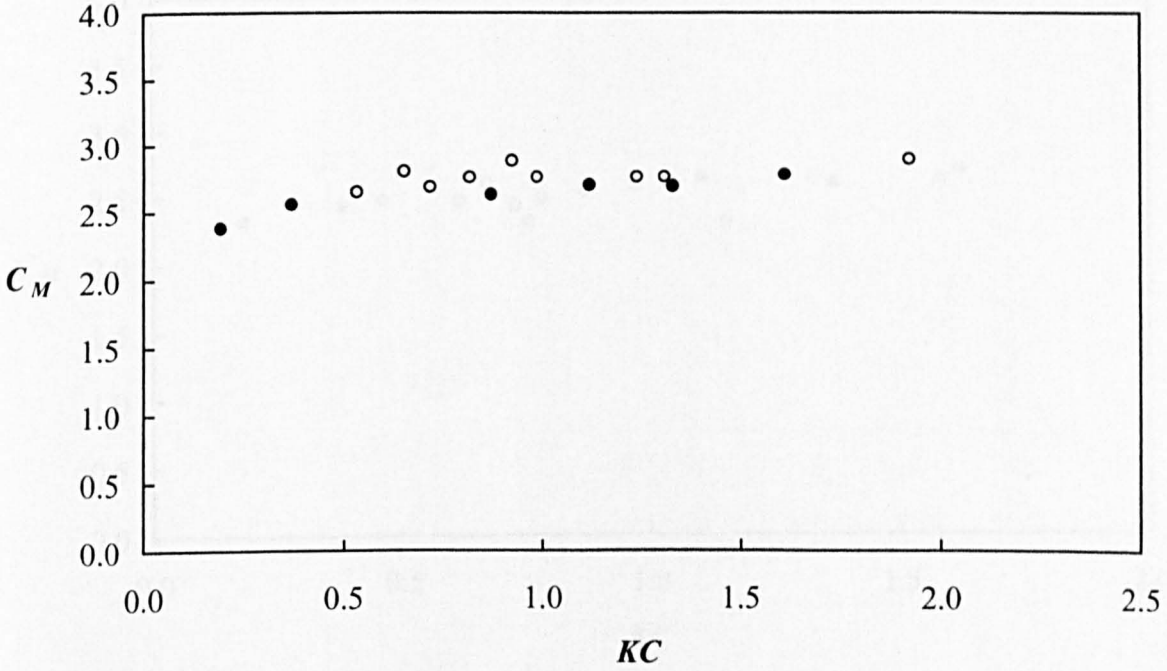

Fig. 6.62 Drag and inertia coefficients for vertical square cylinder for JONSWAP spectrum

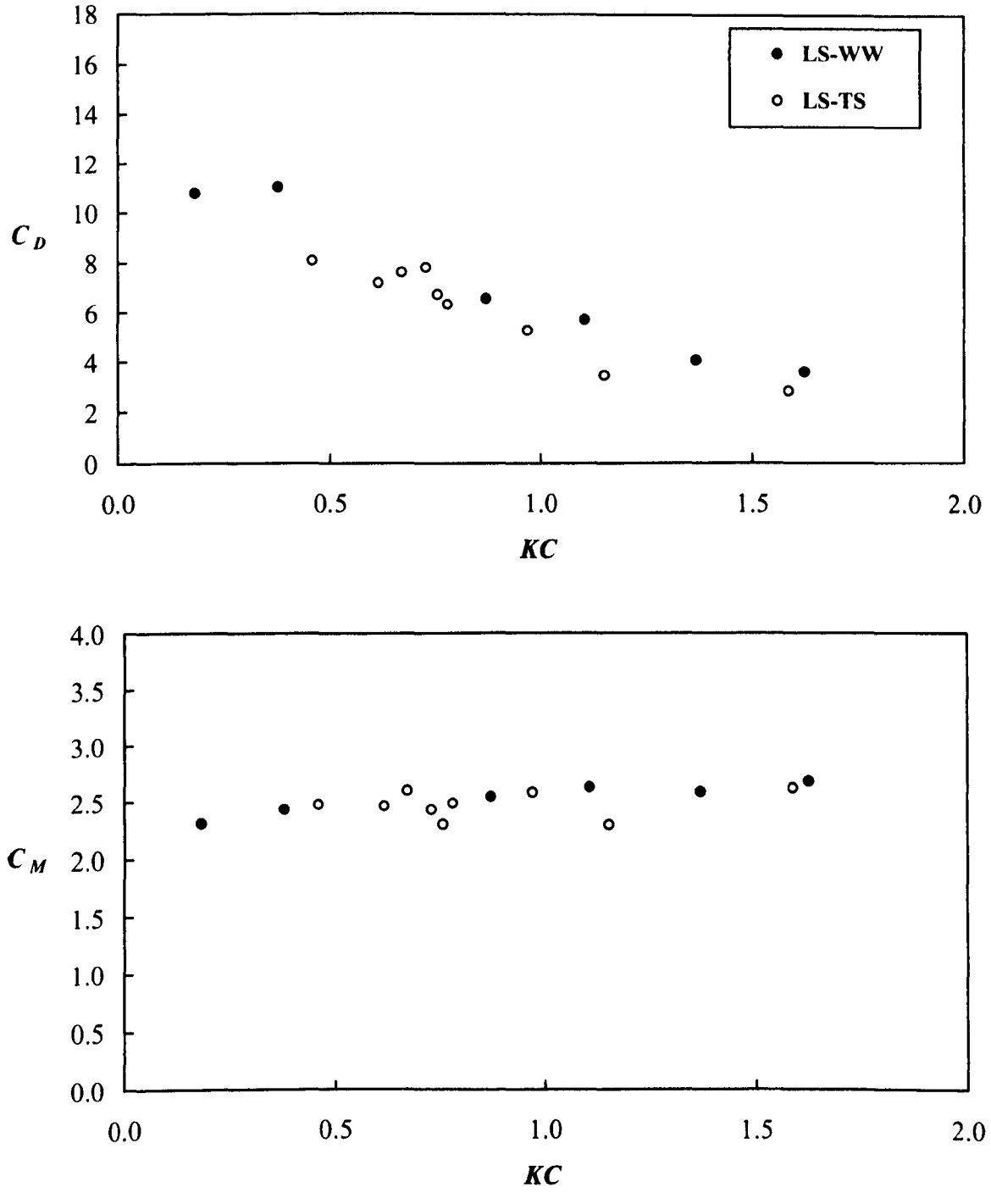

Fig. 6.63 Drag and inertia coefficients for vertical square cylinder for PM spectrum

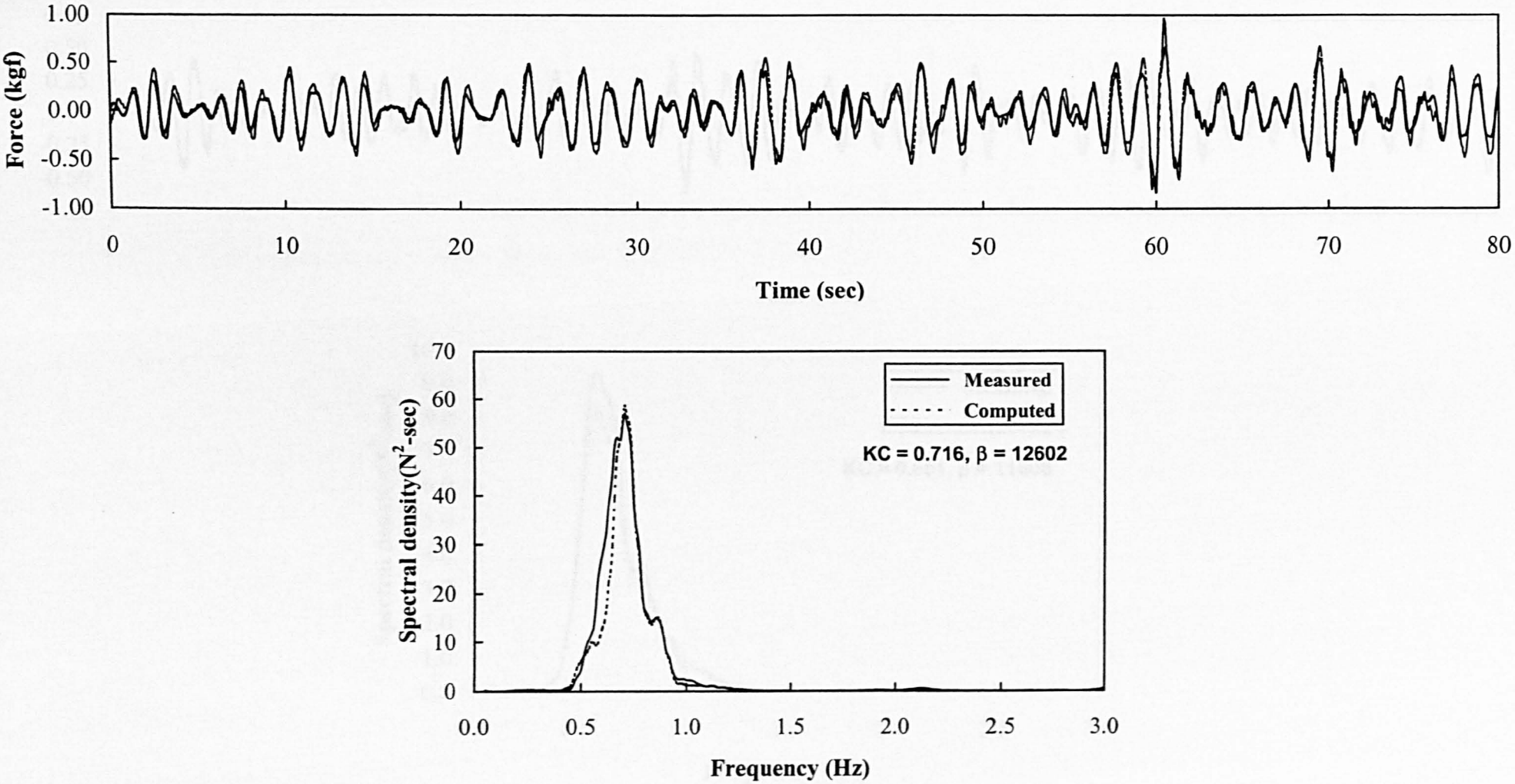

Fig. 6. 64 Measured and computed force time series and corresponding spectral densities for vertical square cylinder for run number JS_S15_1

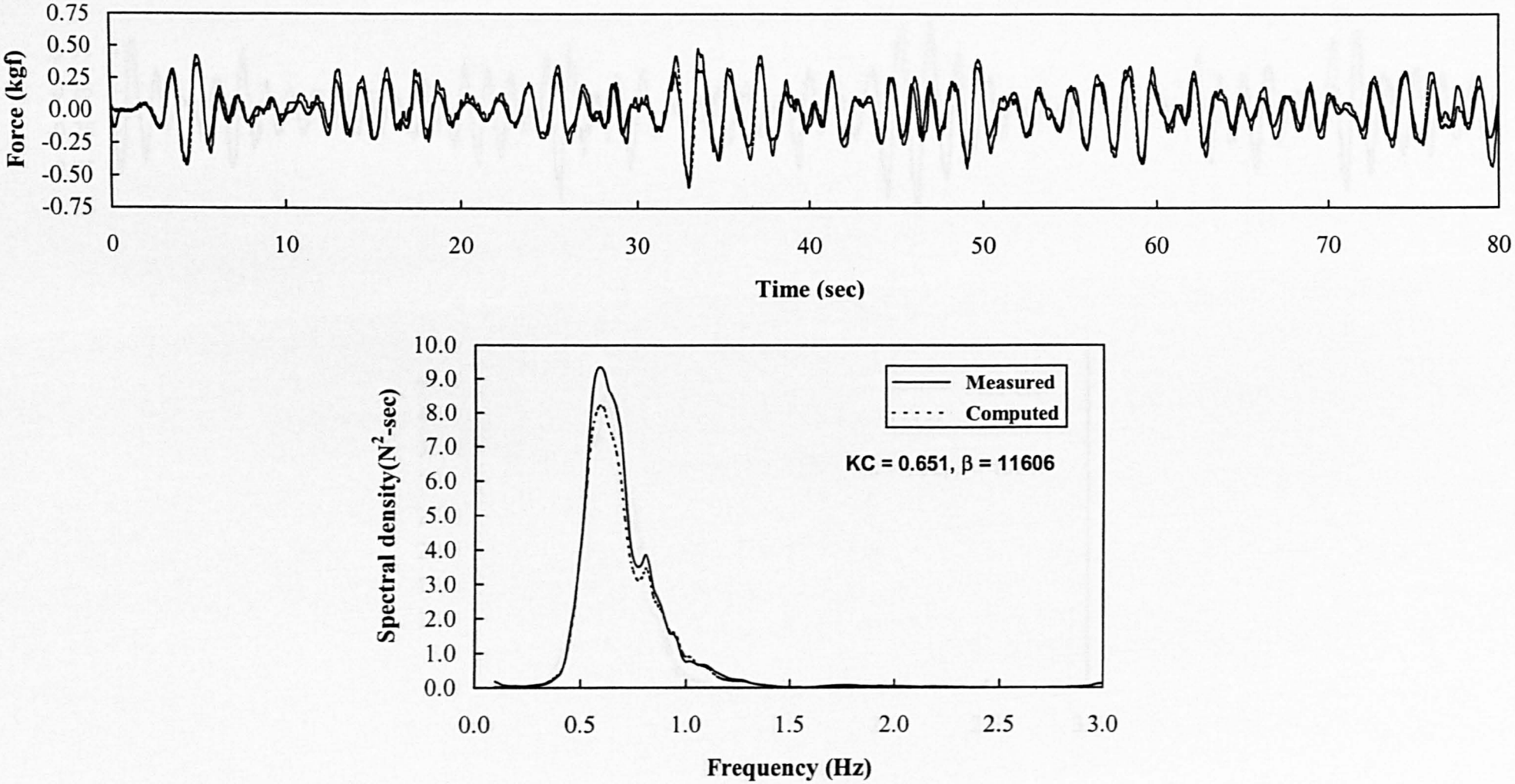

Fig. 6. 65 Measured and computed force time series and corresponding spectral densities for vertical square cylinder for run number JS_S15_4

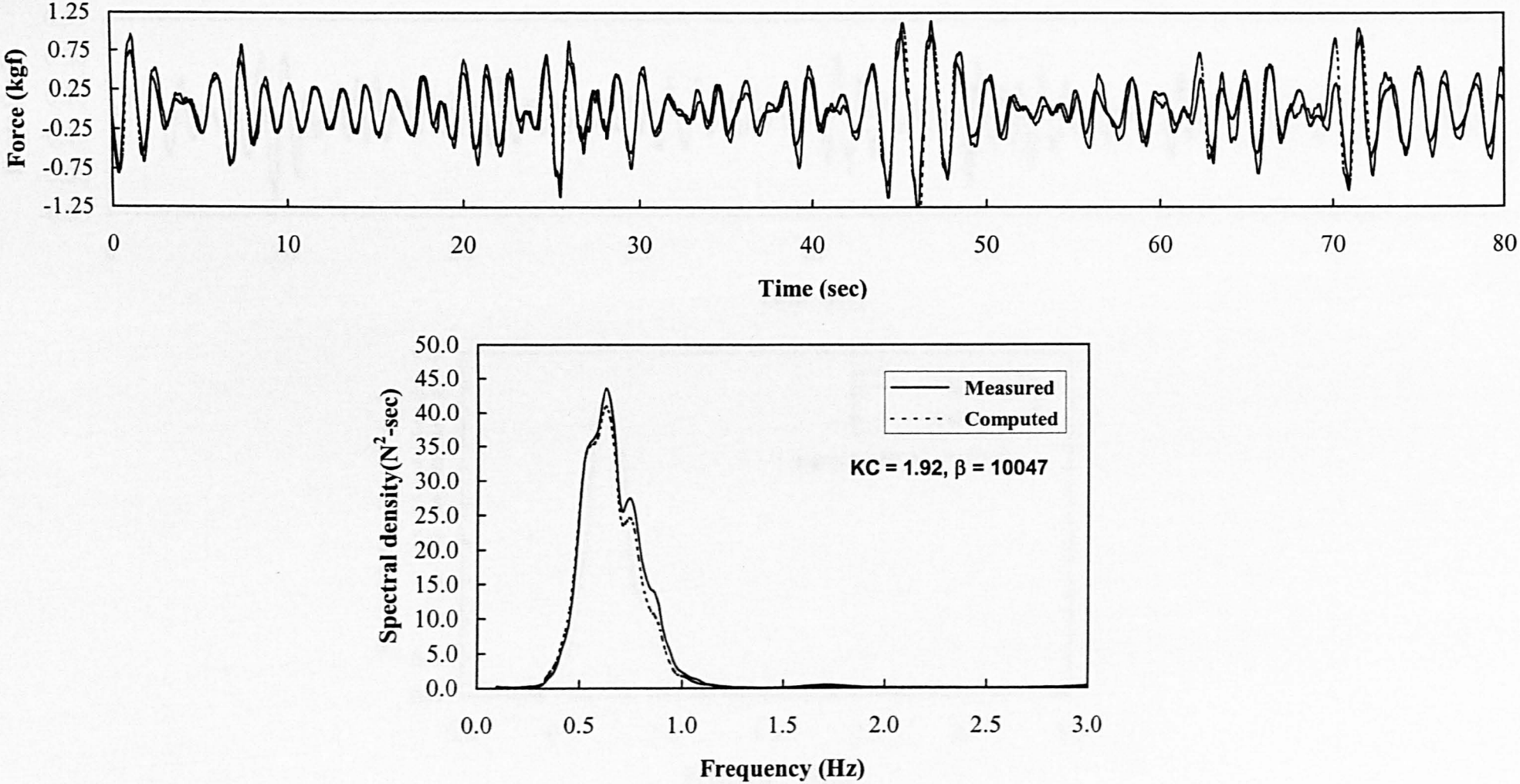

Fig. 6. 66 Measured and computed force time series and corresponding spectral densities for vertical square cylinder for run number JS_S15_6

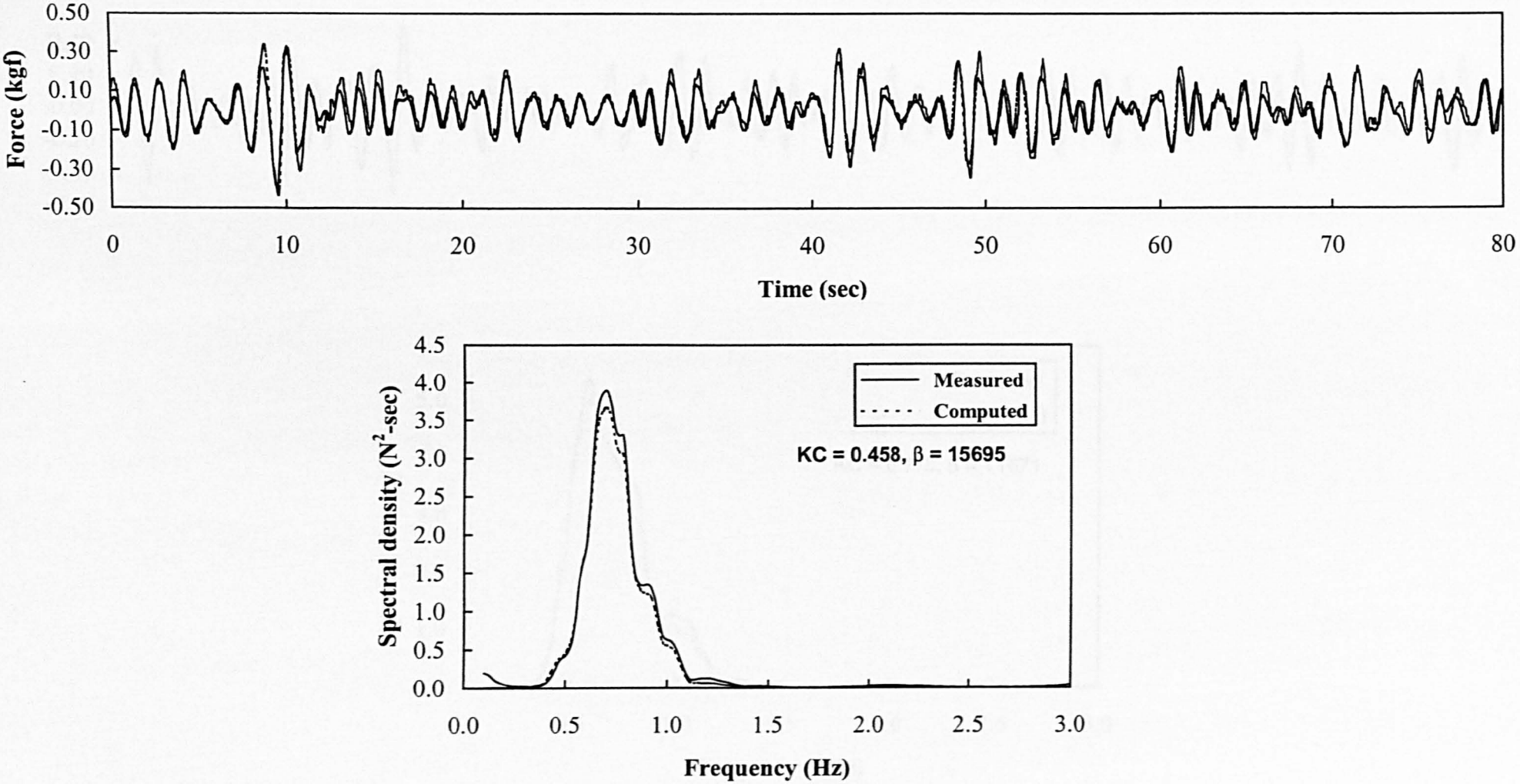

Fig. 6. 67 Measured and computed force time series and corresponding spectral densities for vertical square cylinder for run number PM_S15_1

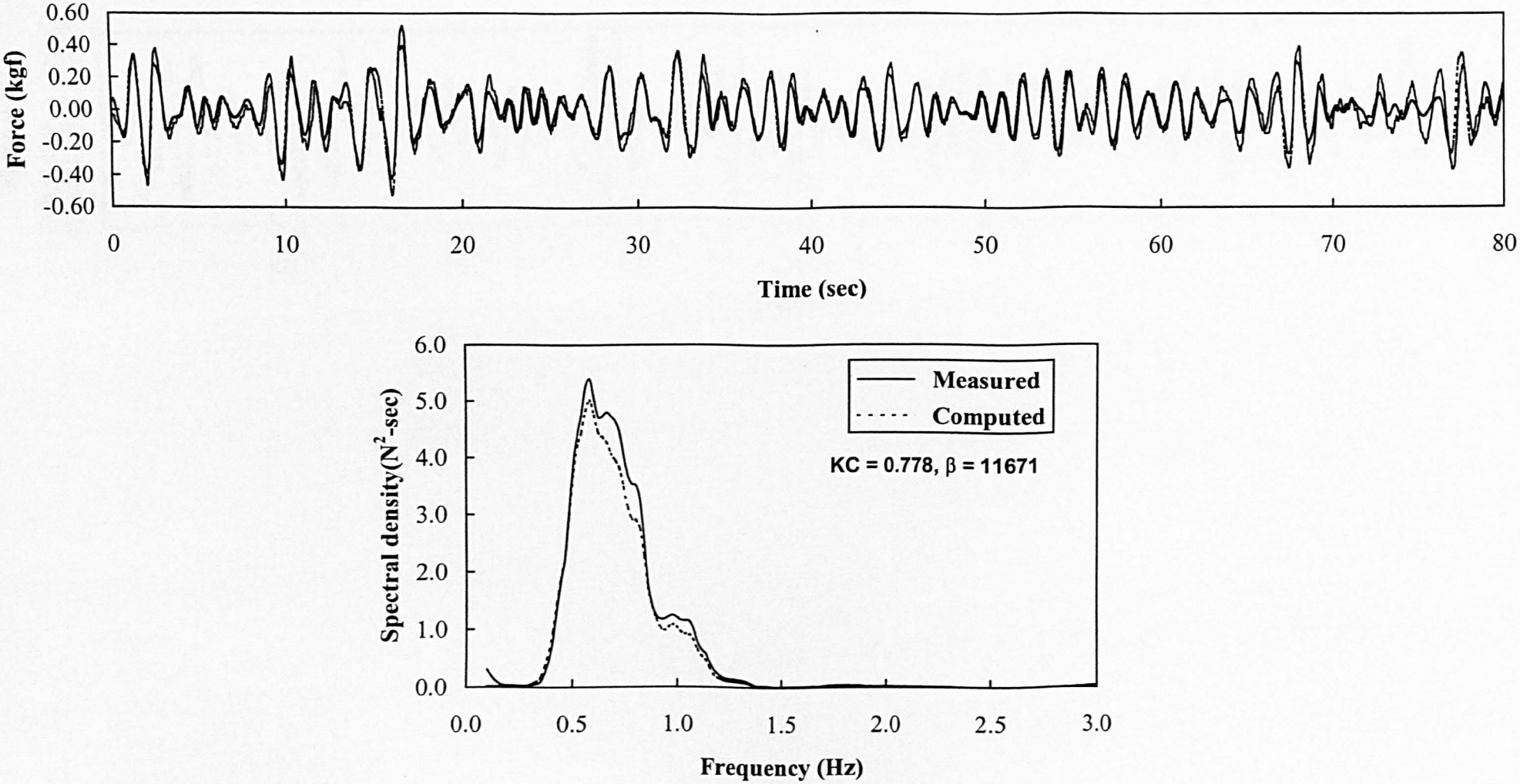

Fig. 6. 68 Measured and computed force time series and corresponding spectral densities for vertical square cylinder for run number PM_S15_4

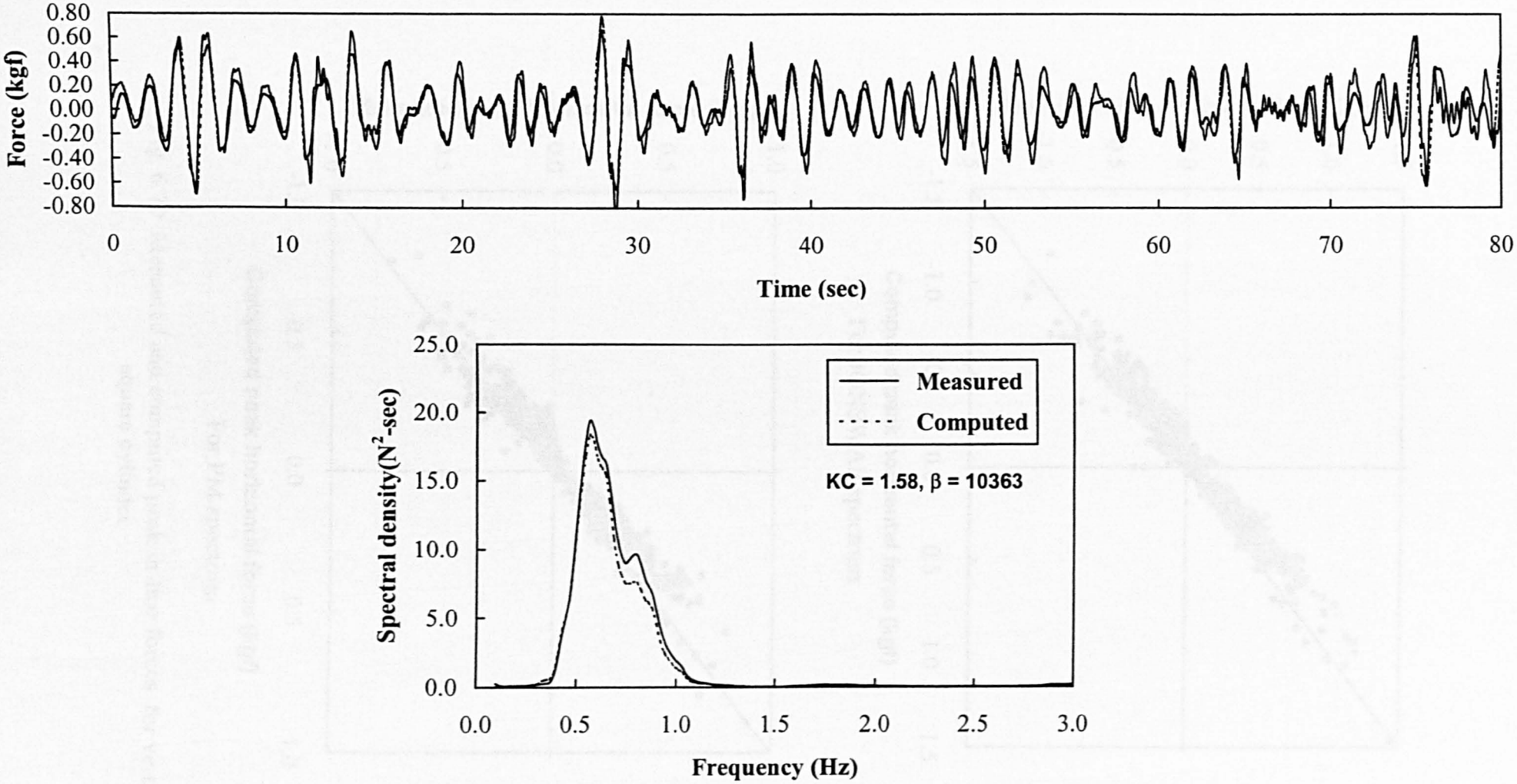

Fig. 6. 69 Measured and computed force time series and corresponding spectral densities for vertical square cylinder for run number PM_S15_6

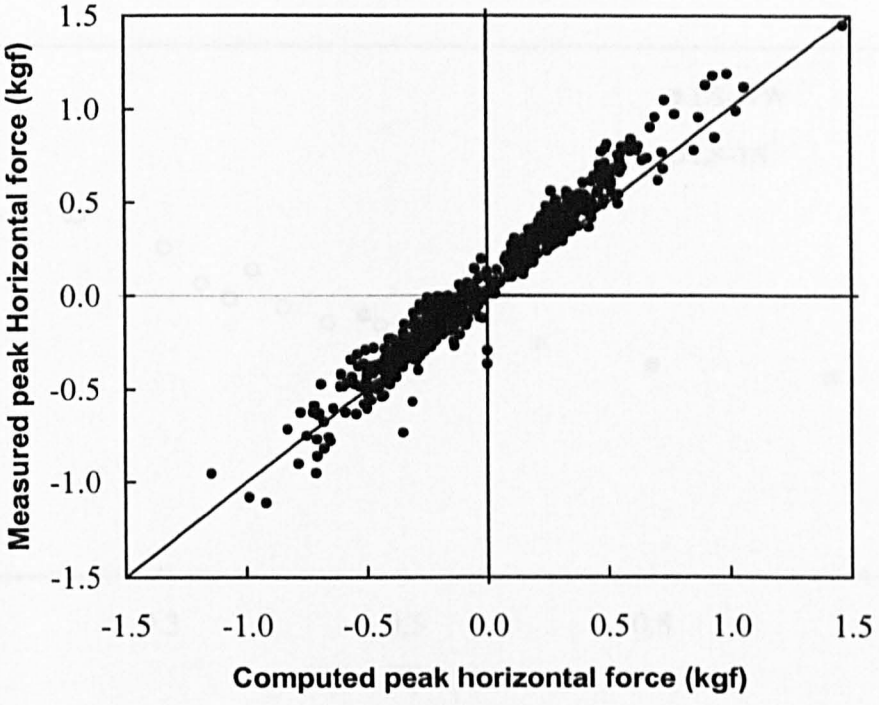

For JONSWAP spectrum

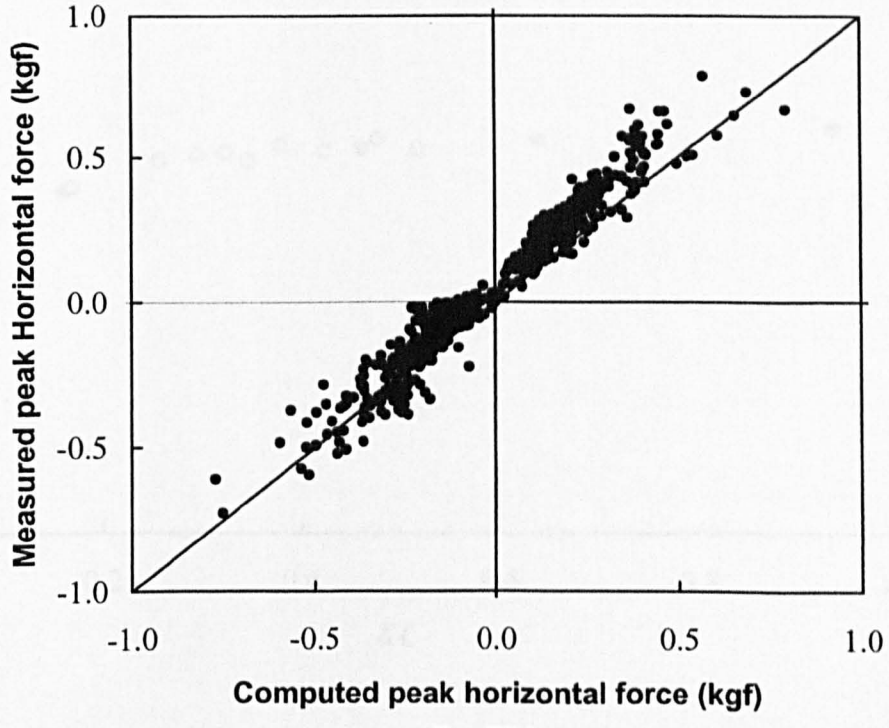

For PM spectrum

Fig. 6.70 Measured and computed peak in-line forces for vertical square cylinder

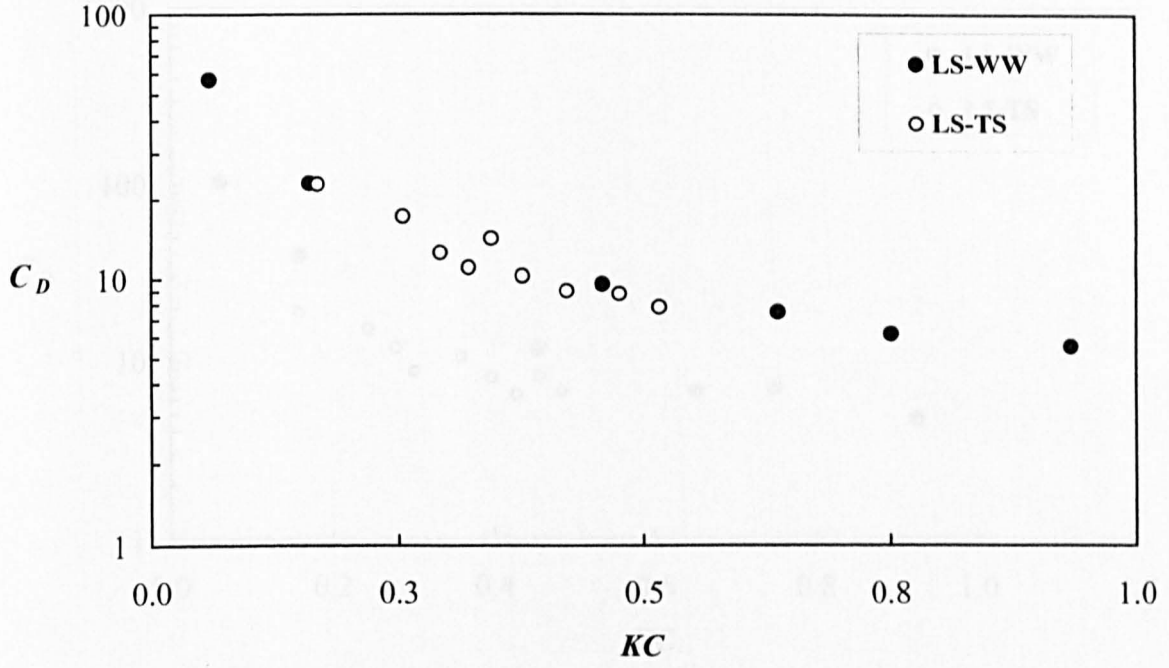

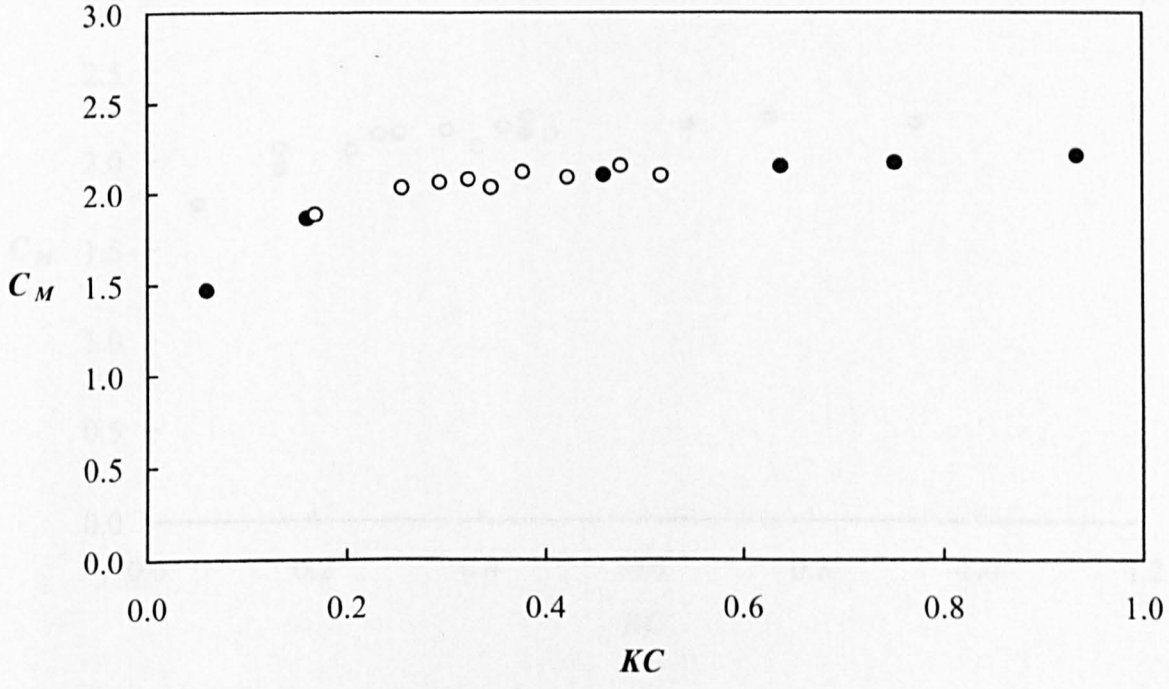

Fig. 6.71 Drag and inertia coefficients for vertical rectangular cylinder with aspect ratio = ½ for JONSWAP spectrum

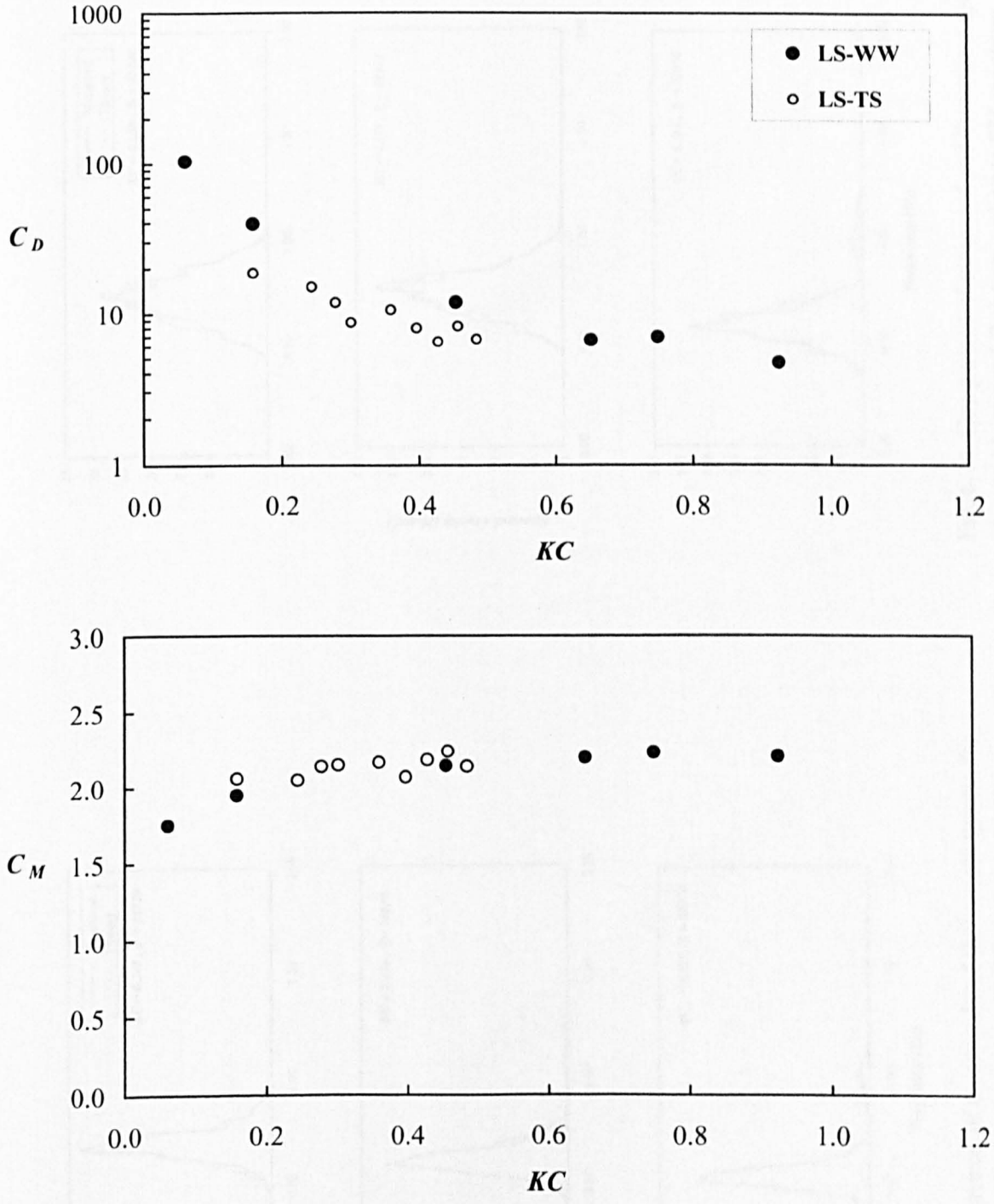

Fig. 6.72 Drag and inertia coefficients for vertical rectangular cylinder with aspect ratio = ½ for PM spectrum

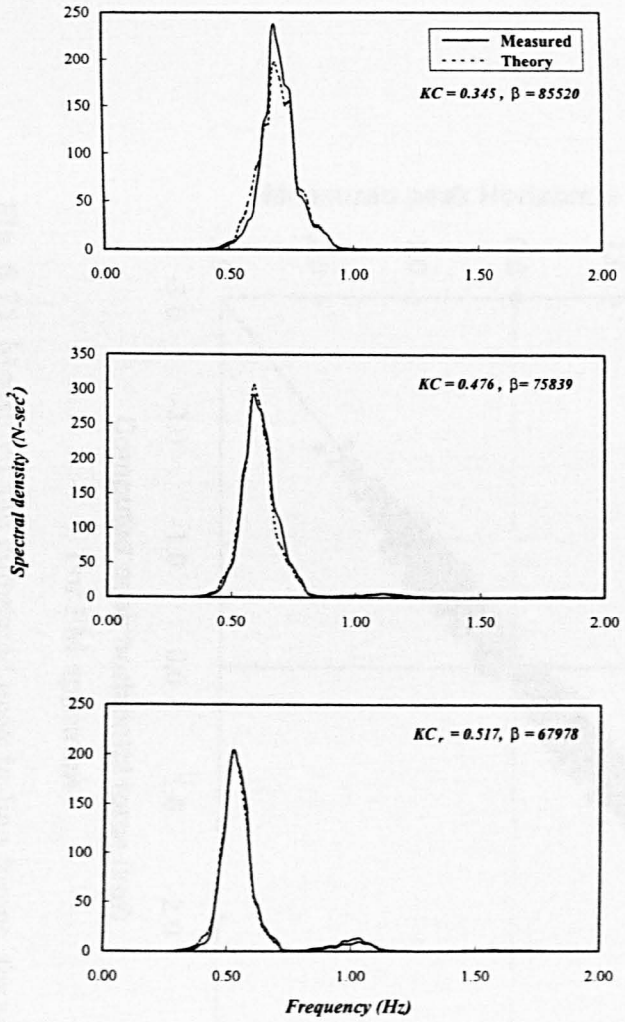

Fig. 6.73 Comparison of measured and theoretical spectra for aspect ratio = 1/2 corresponding to JONSWAP spectrum

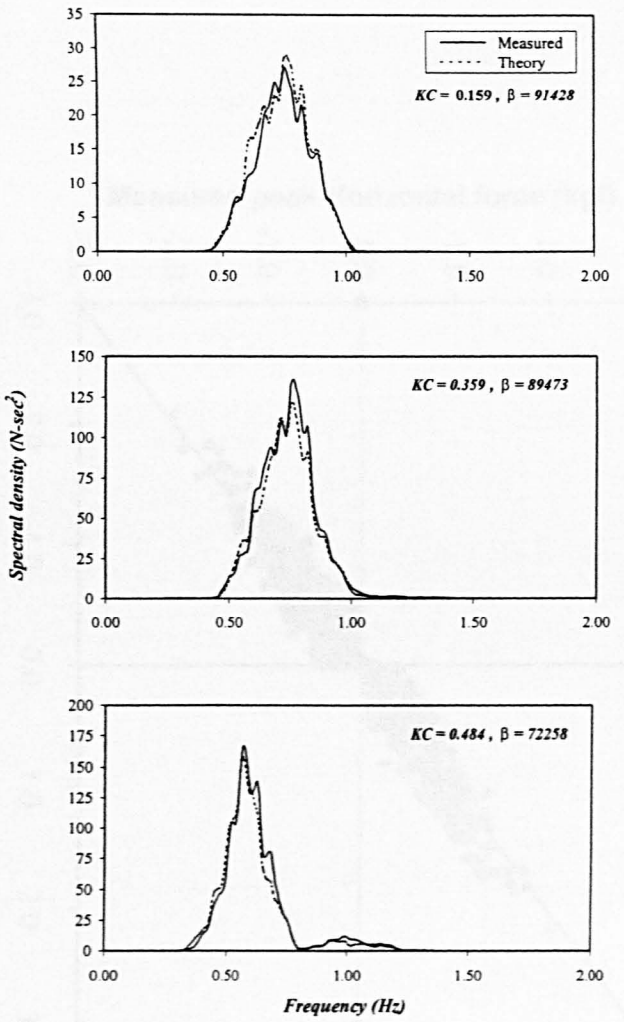

Fig. 6.74 Comparison of measured and theoretical spectra for aspect ratio = 1/2 corresponding to PM spectrum

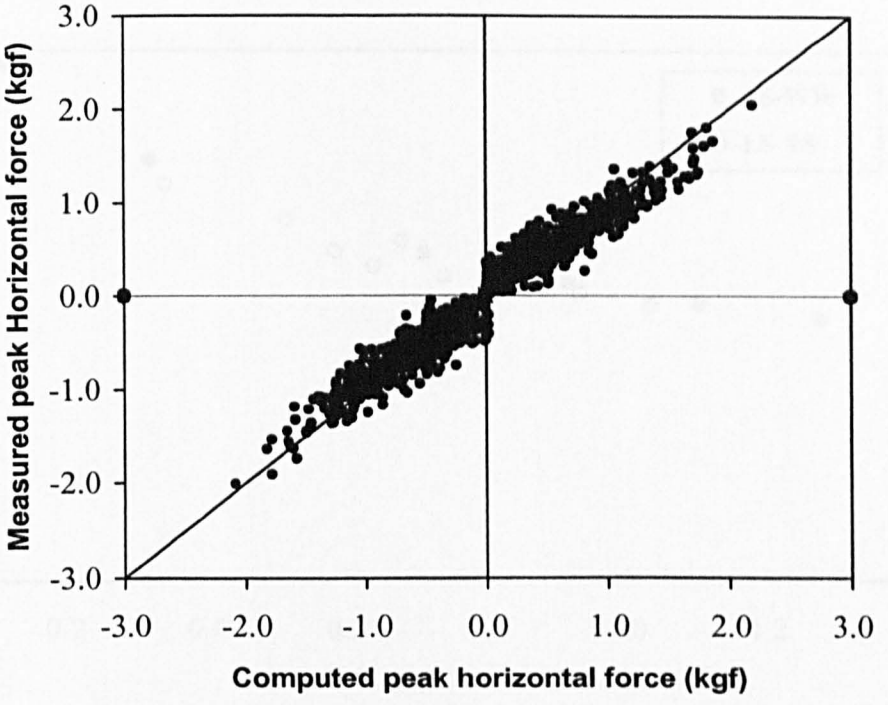

For JONSWAP spectrum

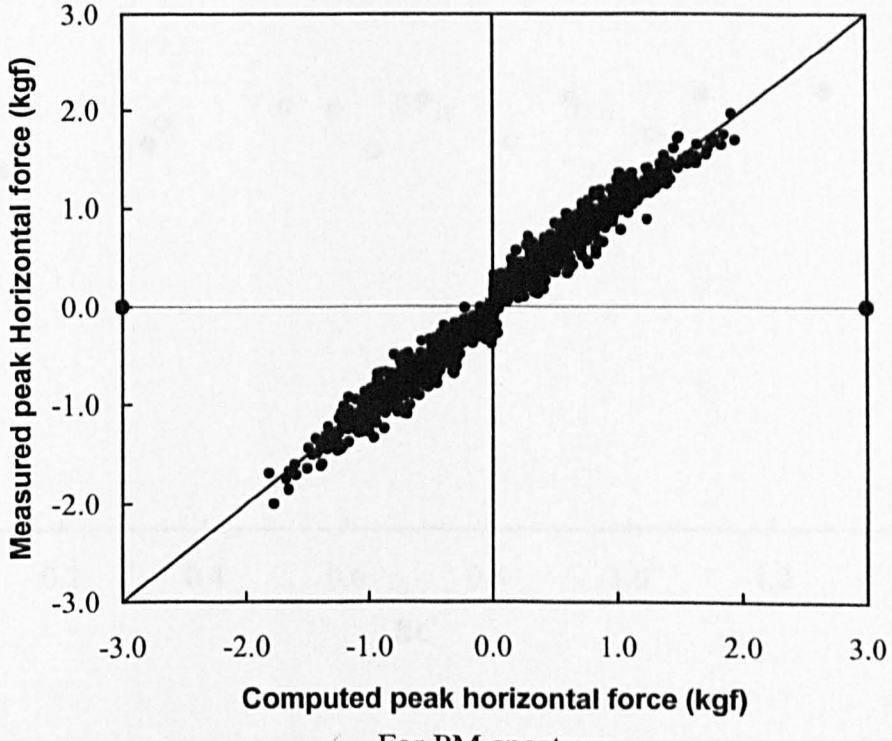

For PM spectrum

Fig. 6.75 Measured and computed peak in-line forces for vertical rectangular cylinder with aspect ratio = 1/2

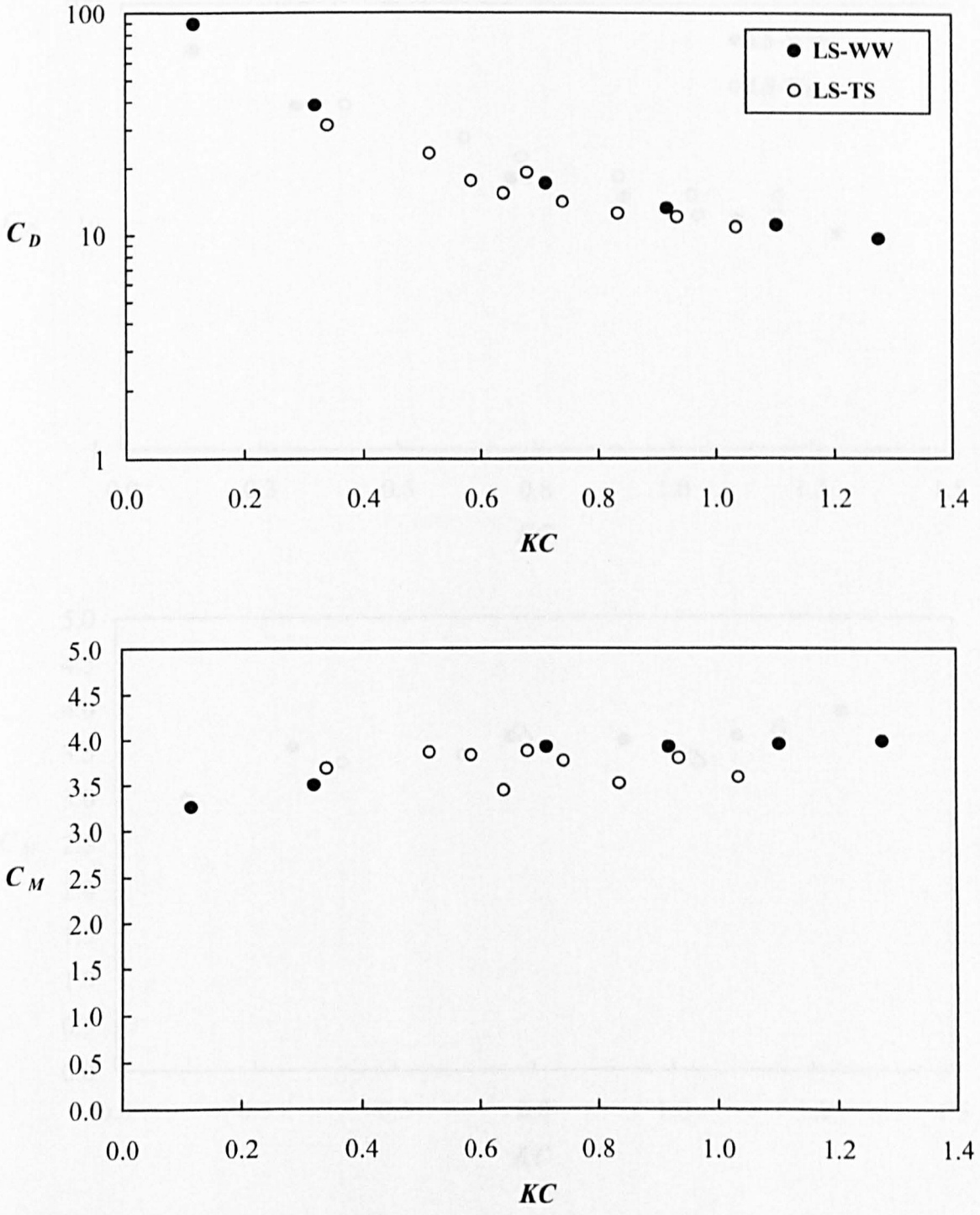

Fig. 6.76 Drag and inertia coefficients for vertical rectangular cylinder with aspect ratio = 2/1 for JONSWAP spectrum

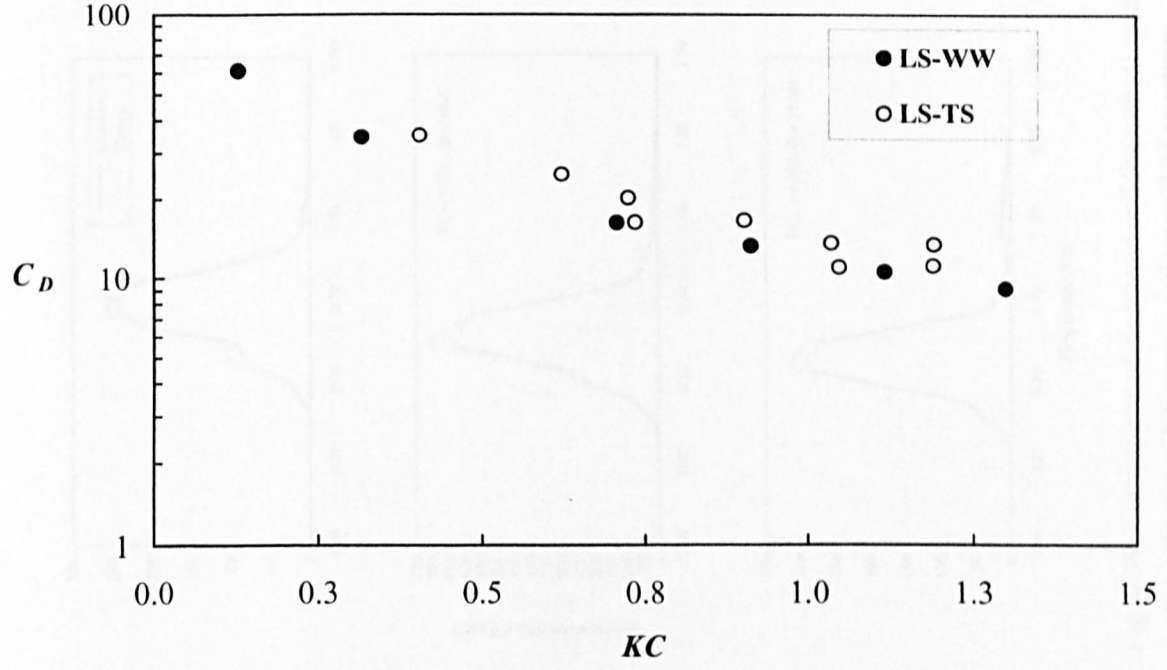

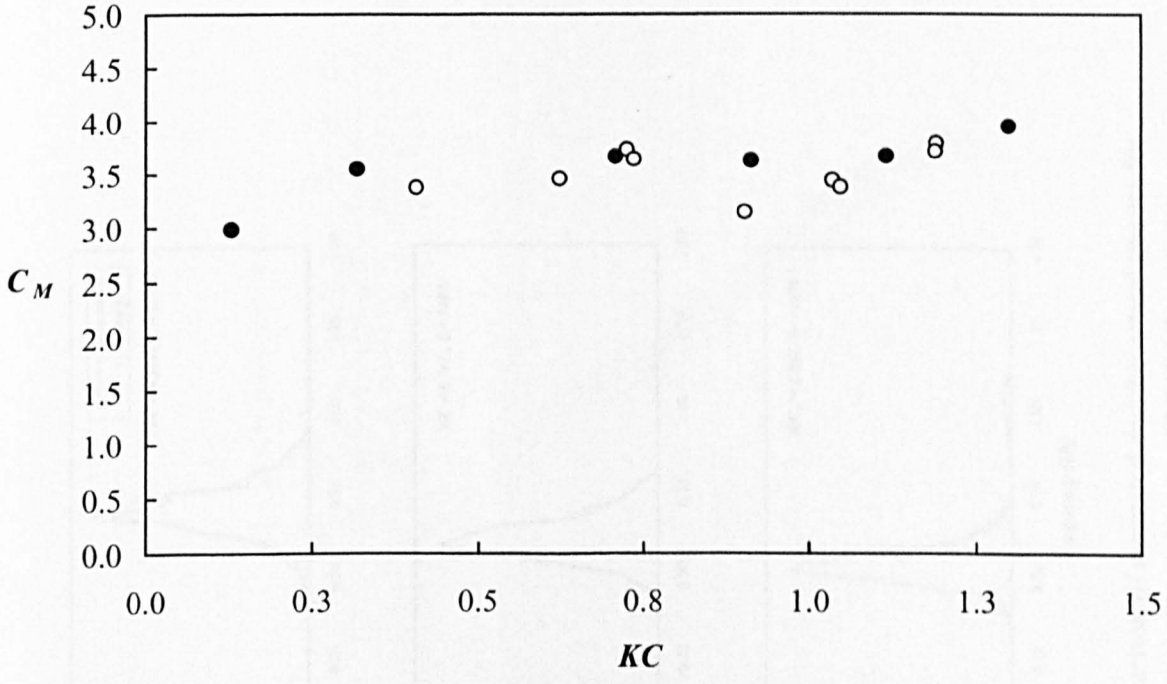

Fig. 6.77 Drag and inertia coefficients for vertical rectangular cylinder with aspect ratio = 2/1 for PM spectrum

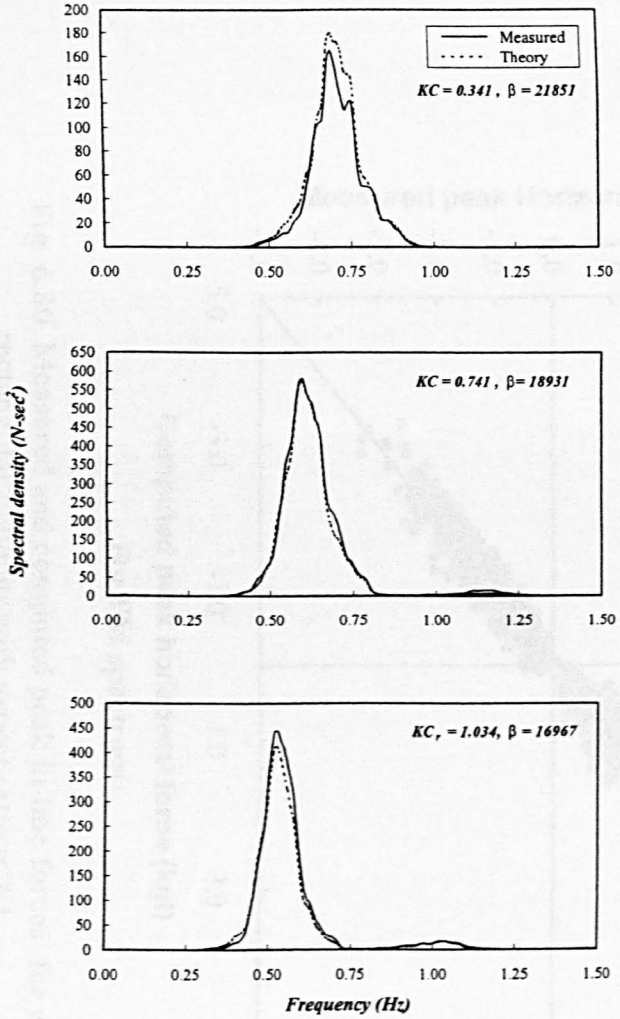

Fig. 6.78 Comparison of measured and theoretical spectra for aspect ratio = 2/1 corresponding to JONSWAP spectrum

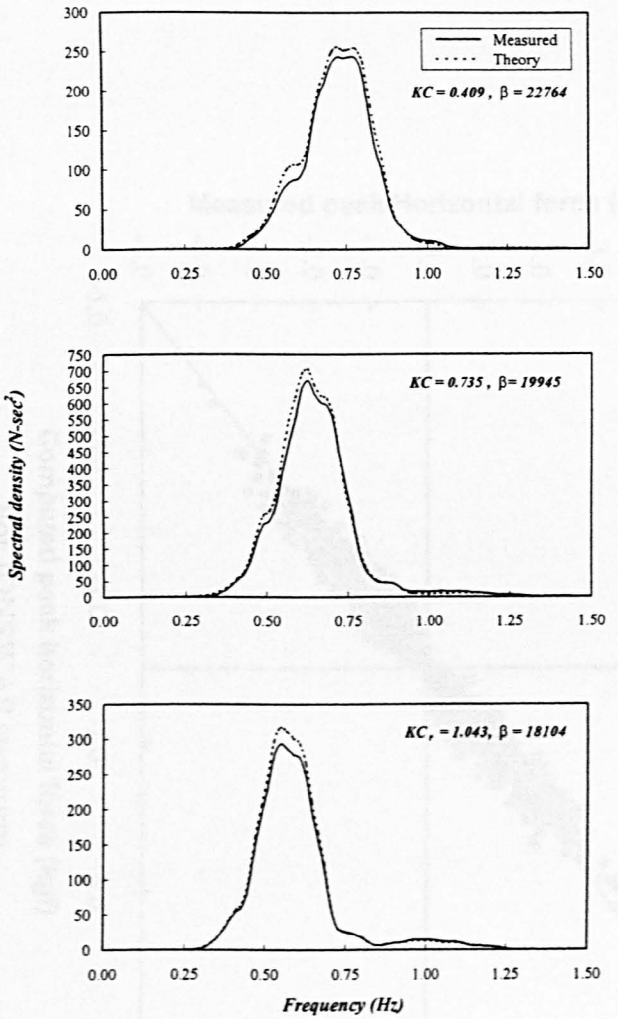

Fig. 6.79 Comparison of measured and theoretical spectra for aspect ratio = 2/1 corresponding to P-M spectrum

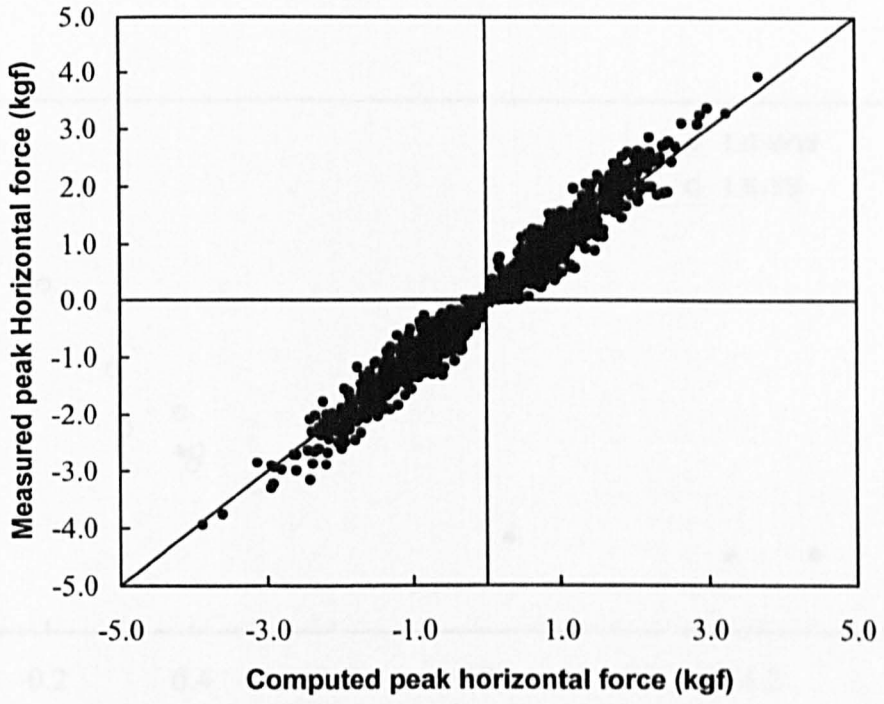

For JONSWAP spectrum

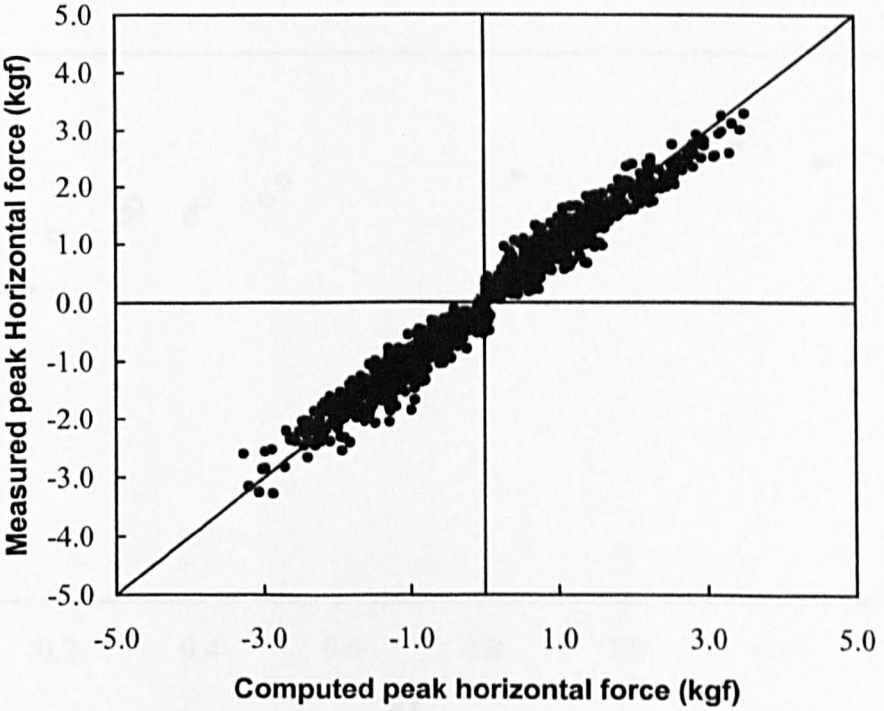

For PM spectrum

Fig. 6.80 Measured and computed peak in-line forces for vertical rectangular cylinder with aspect ratio = 2/1

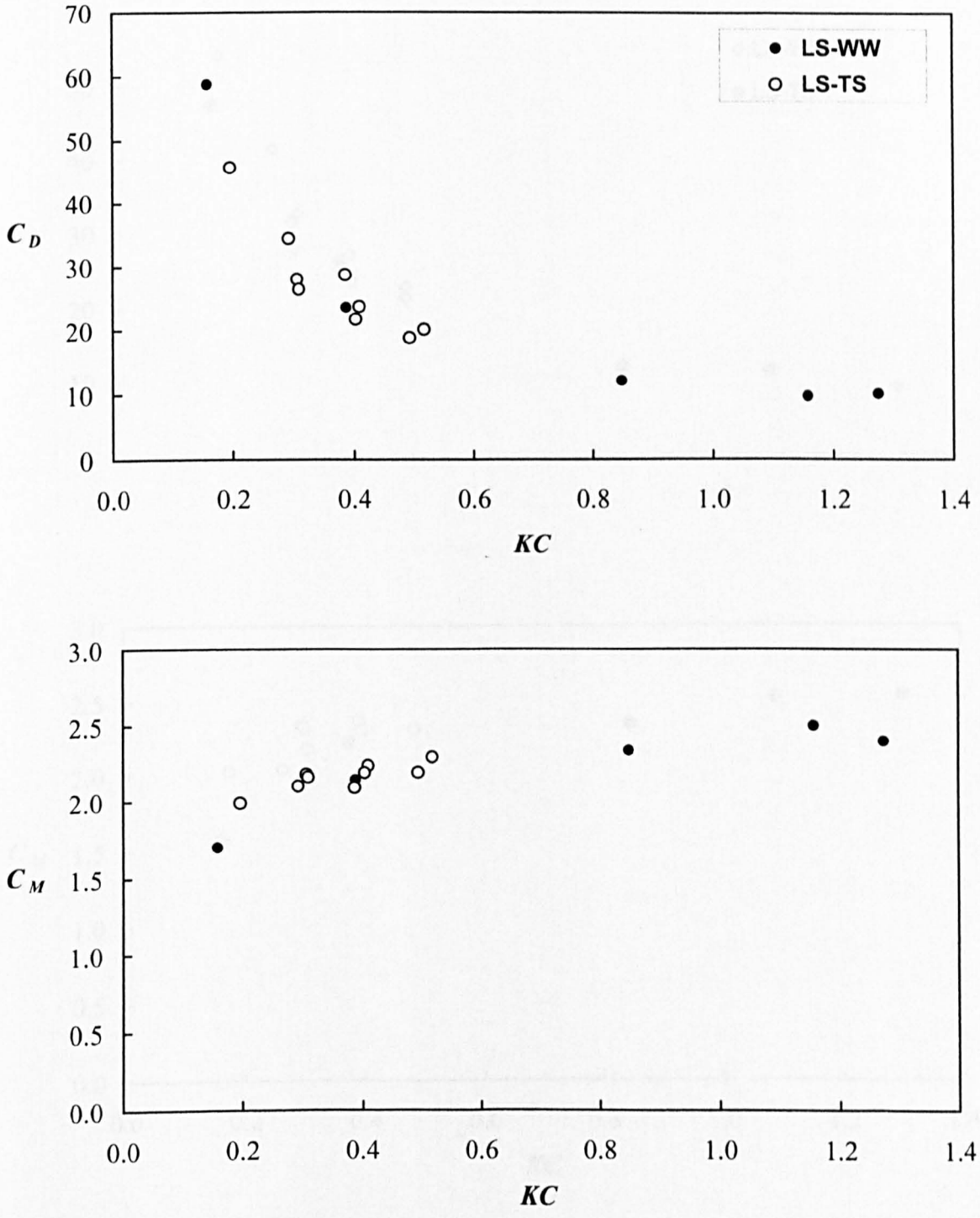

Fig. 6.81 Drag and inertia coefficients for vertical rectangular cylinder with aspect ratio = 3/4 for JONSWAP spectrum

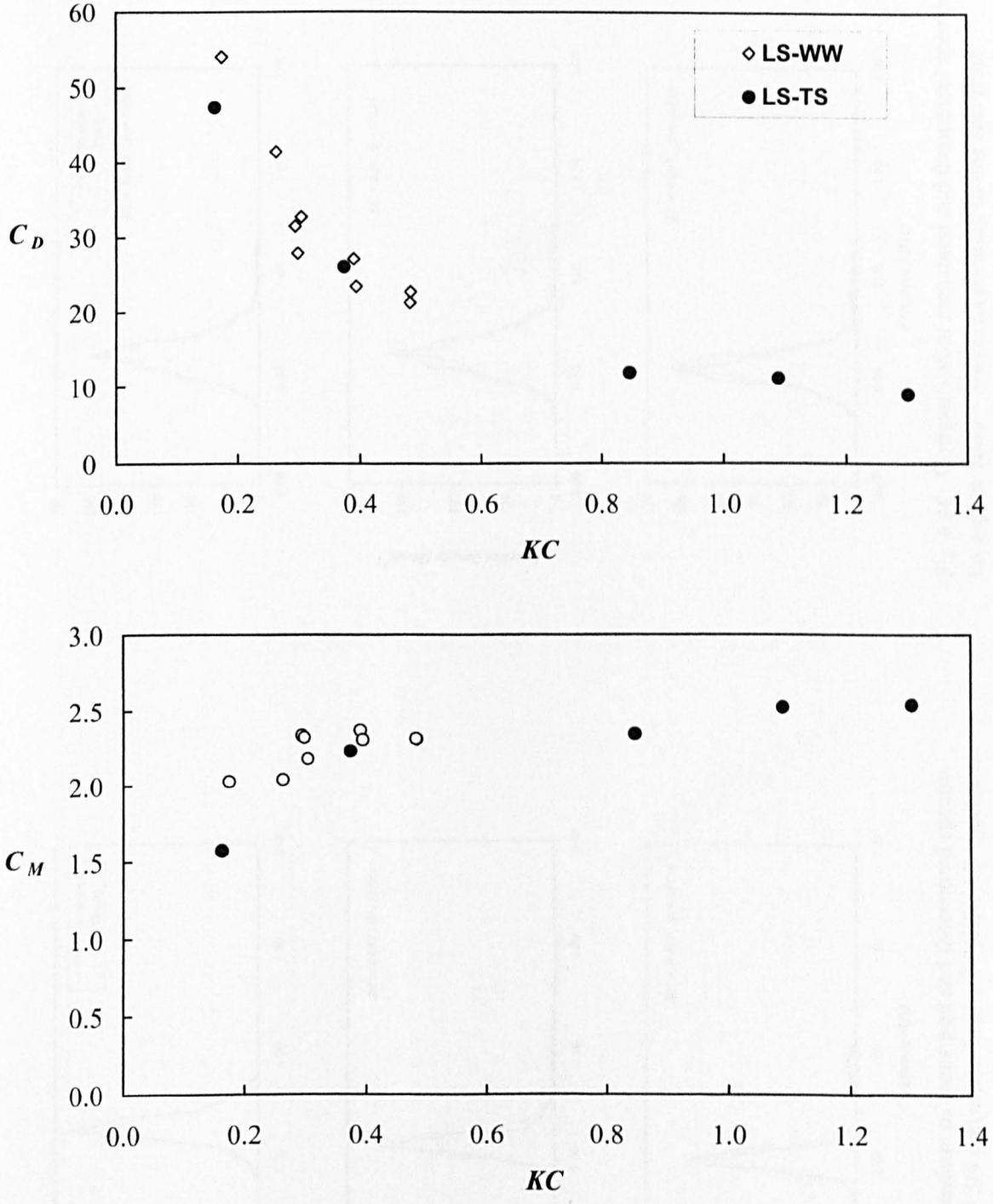

Fig. 6.82 Drag and inertia coefficients for vertical rectangular cylinder with aspect ratio = 3/4 for PM spectrum

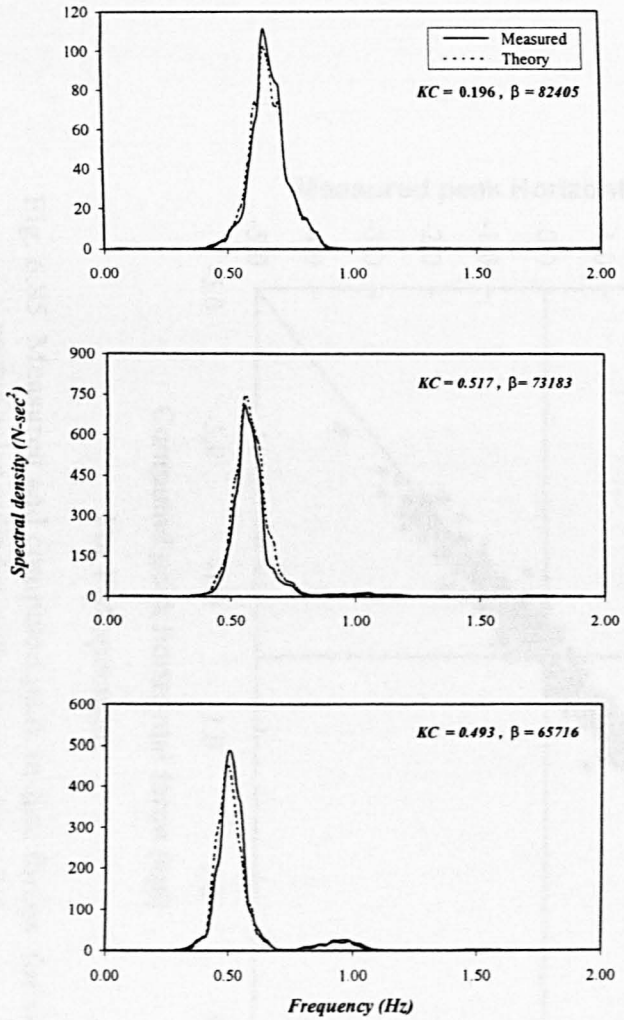

Fig. 6.83 Comparison of measured and theoretical spectra for aspect ratio = 3/4 corresponding to JONSWAP spectrum

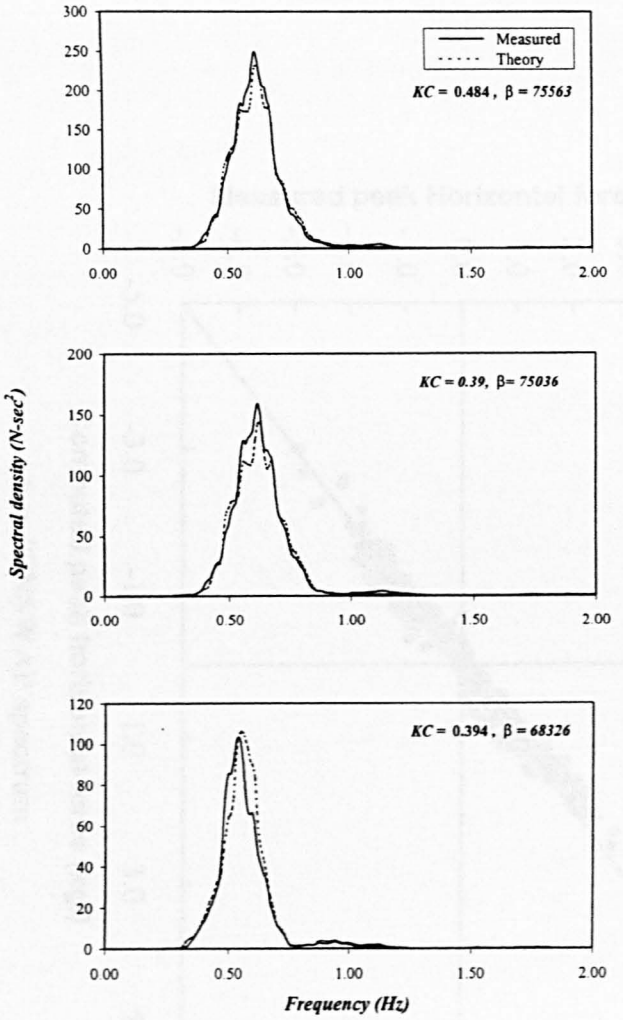

Fig. 6.84 Comparison of measured and theoretical spectra for aspect ratio = 3/4 corresponding to PM spectrum

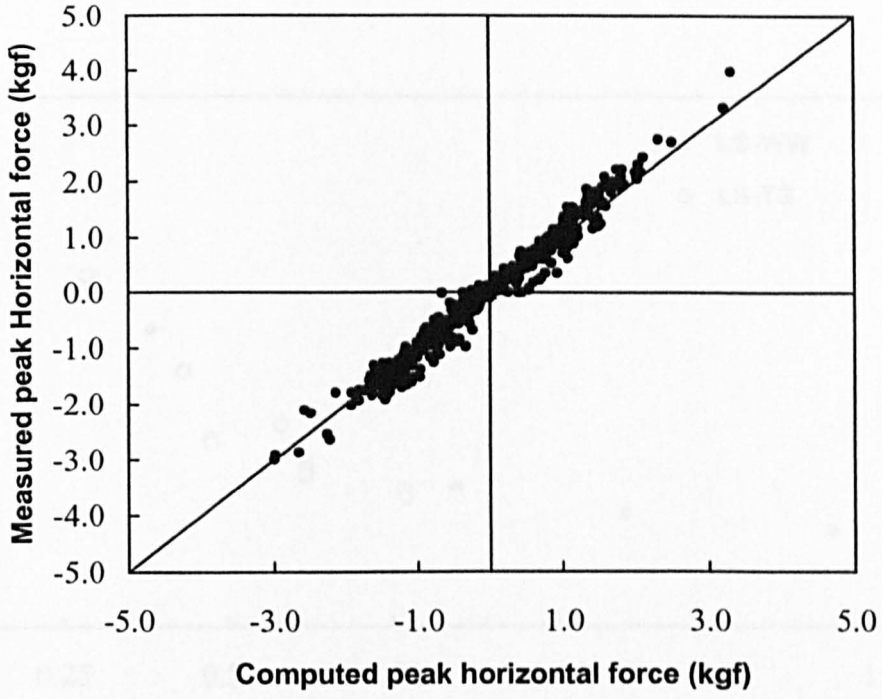

For JONSWAP spectrum

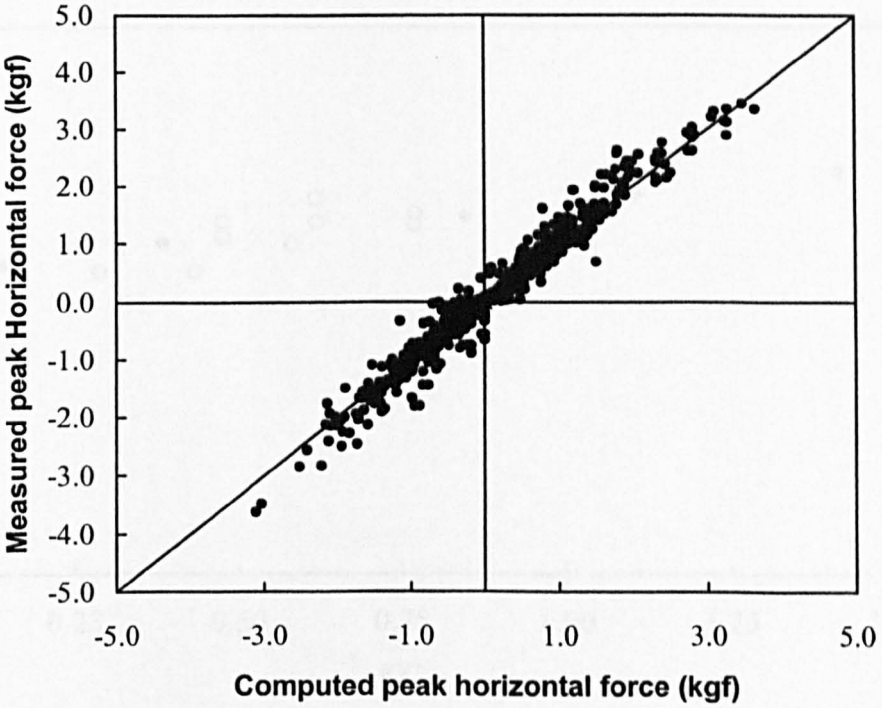

For PM spectrum

Fig. 6.85 Measured and computed peak in-line forces for vertical rectangular cylinder with aspect ratio = 3/4

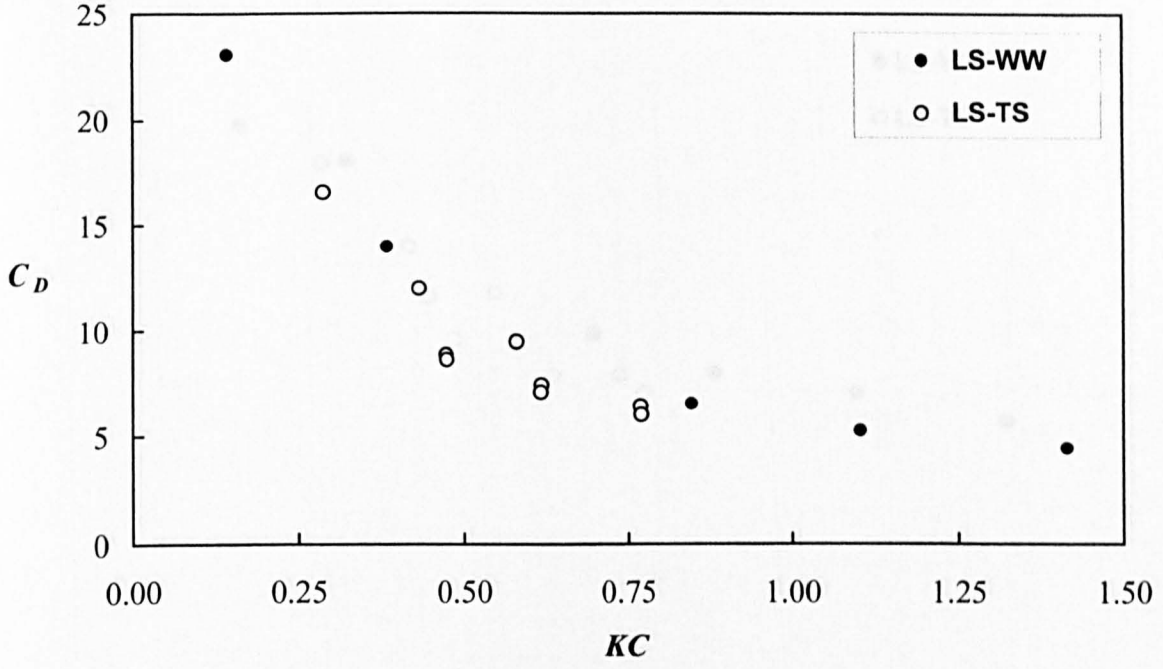

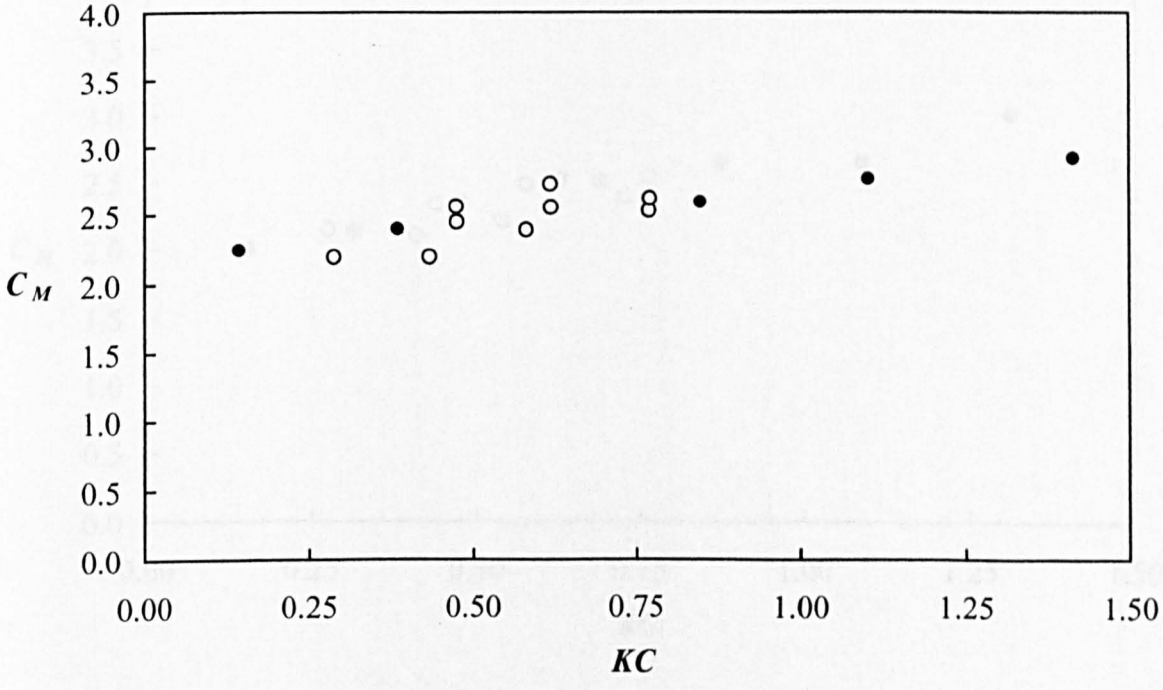

Fig. 6.86 Drag and inertia coefficients for vertical rectangular cylinder with aspect ratio = 4/3 for JONSWAP spectrum

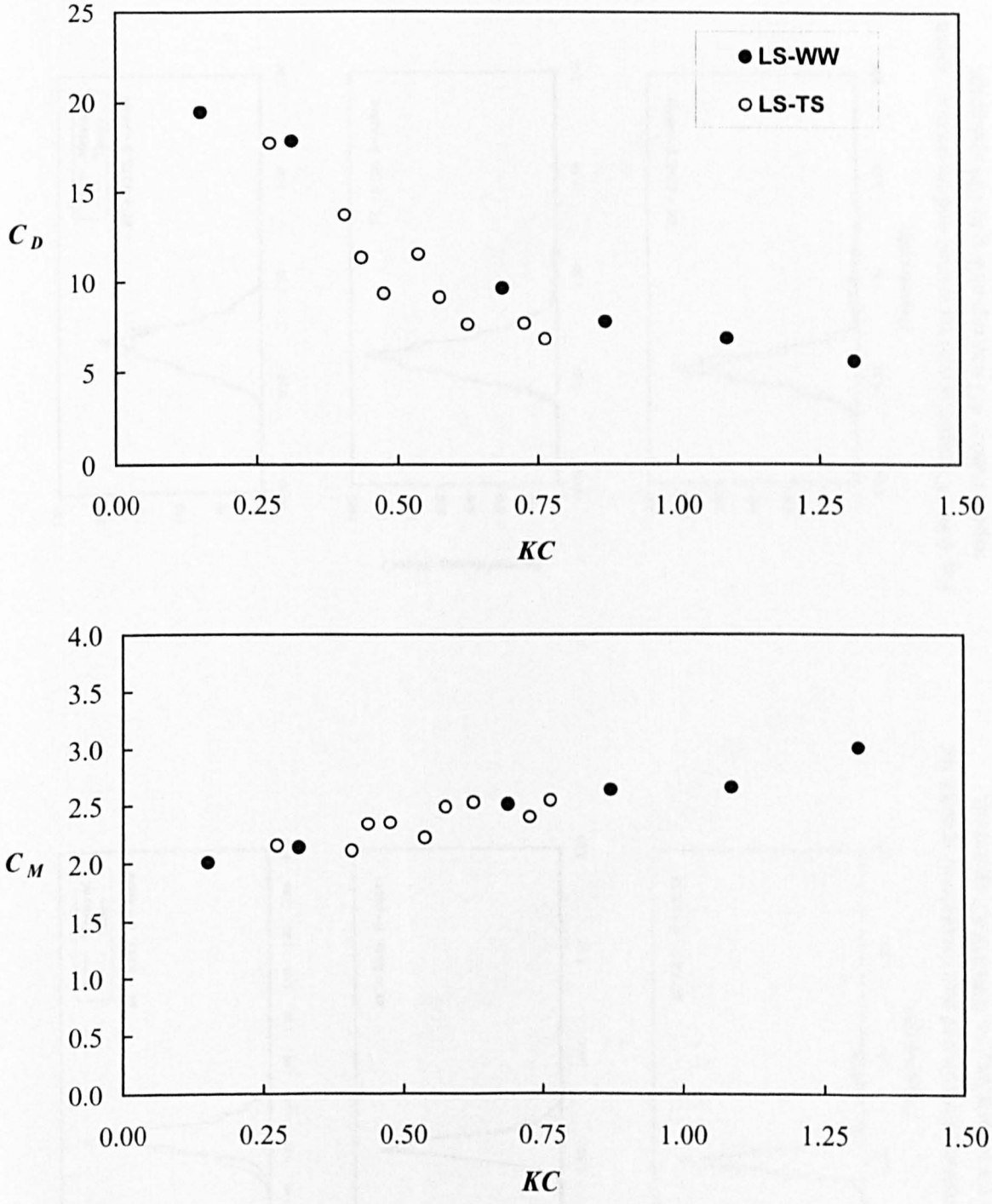

Fig. 6.87 Drag and inertia coefficients for vertical rectangular cylinder with aspect ratio = 4/3 for PM spectrum

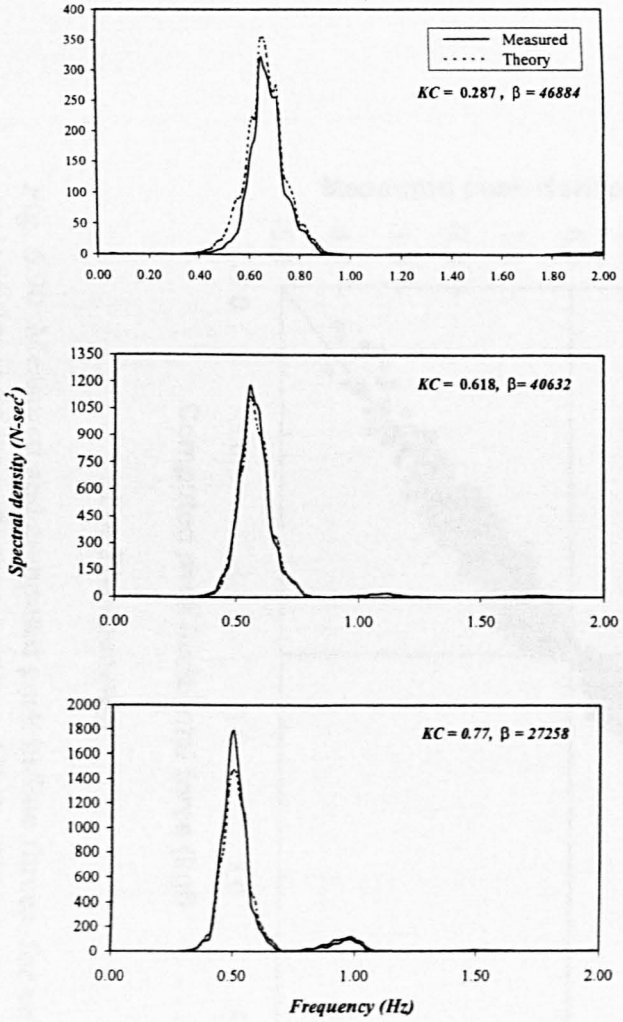

Fig. 6.88 Comparison of measured and theoretical spectra for aspect ratio = 4/3 corresponding to JONSWAP spectrum

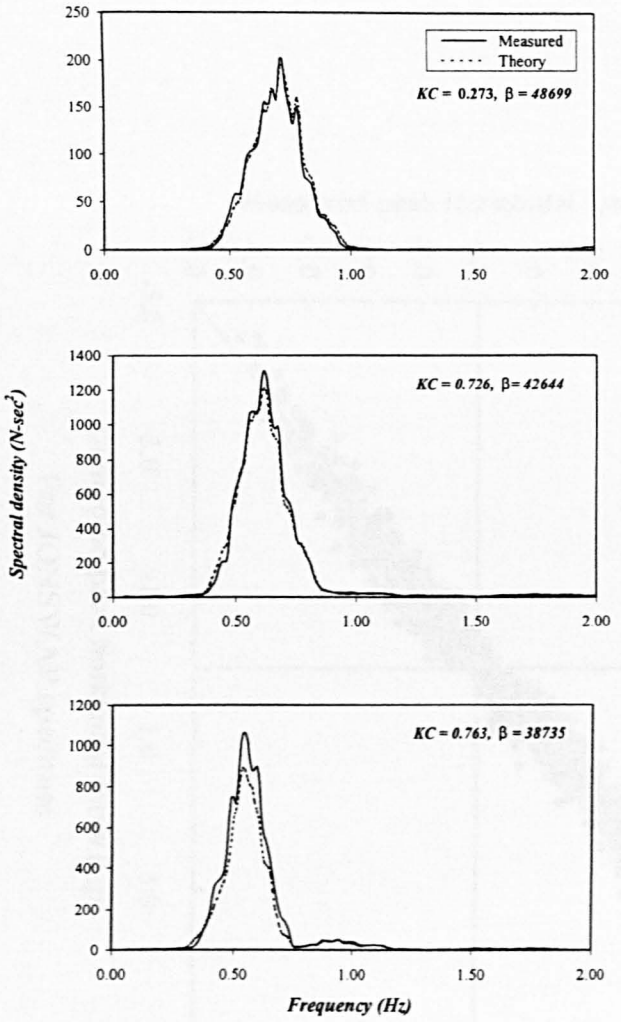

Fig. 6.89 Comparison of measured and theoretical spectra for aspect ratio = 4/3 corresponding to PM spectrum

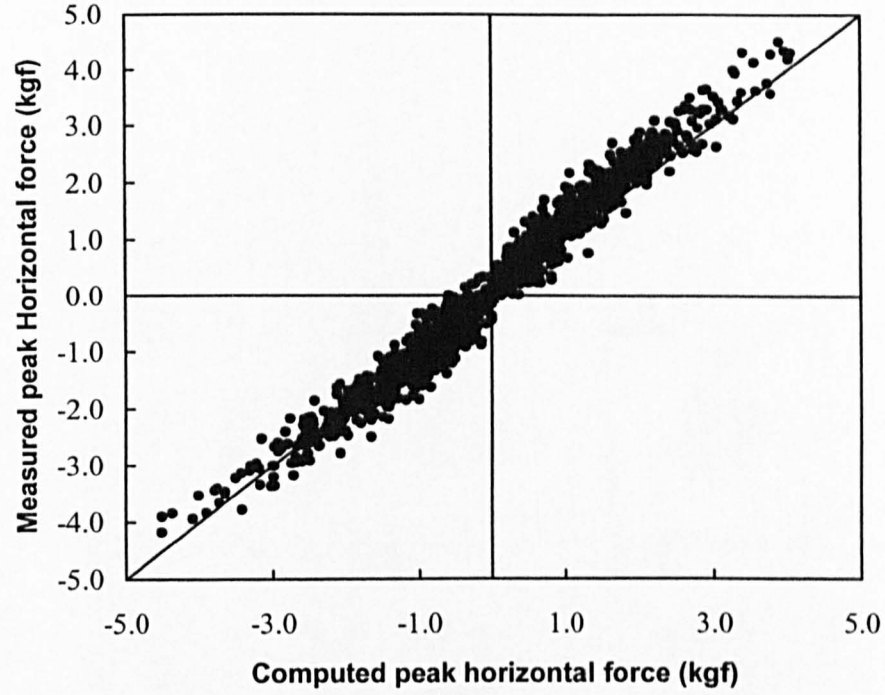

For JONSWAP spectrum

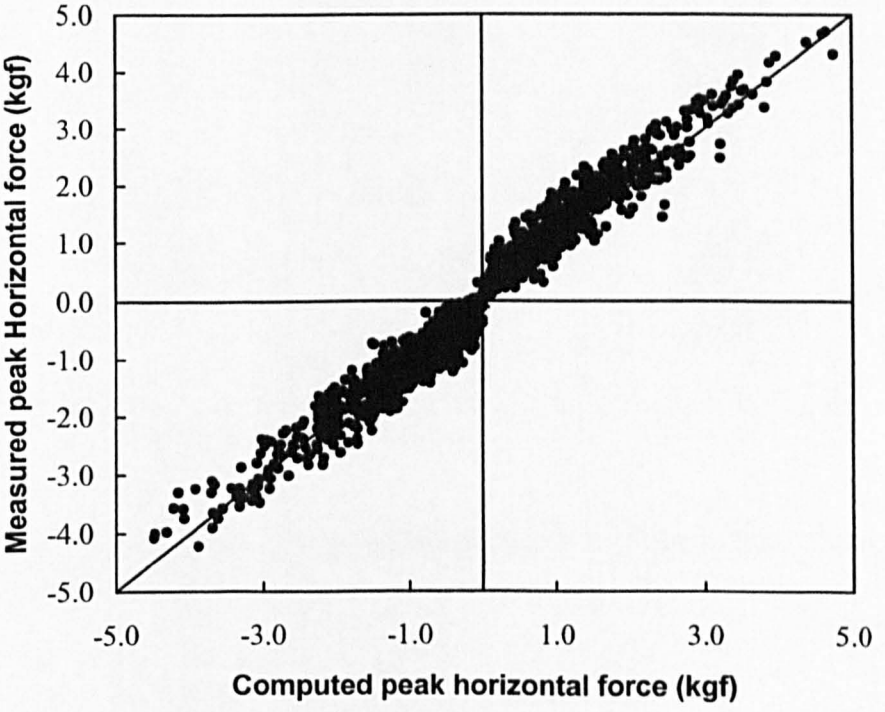

For PM spectrum

Fig. 6.90 Measured and computed peak in-line forces for vertical rectangular cylinder with aspect ratio = 4/3 for PM spectrum

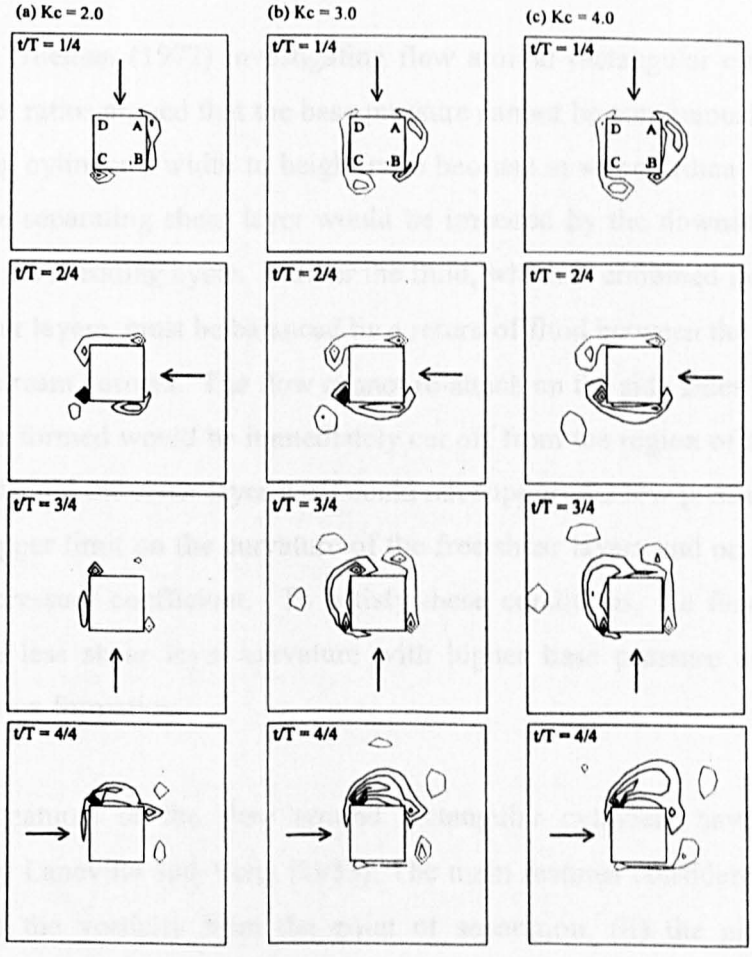

Fig. 6.91 Vorticity distributions for square cylinder at various *KC* numbers [*Otsuka et al. (1998)*]

6.2.4 Steady Flow - effects of change of aspect ratios of cylinders

The changes that take place in force coefficients and flow around rectangular cylinders with variation in sectional ratio of the cylinders are discussed below.

Bearman and Trueman (1972) investigating flow around rectangular cylinders with different aspect ratios argued that the base pressure cannot be continuously decreased with increasing cylinder's width to height ratio because at some critical block depth the path of the separating shear layer would be impeded by the downstream corner during part of the shedding cycle. Further the fluid, which is entrained into the initial part of the shear layers, must be balanced by a return of fluid between the shear layers and the downstream corners. The flow cannot re-attach on the side faces because if it did, the bubble formed would be immediately cut off from the region of low pressure behind the body and the shear layer itself could not support the low pressure required. This sets an upper limit on the curvature of the free shear layers and on the value of the negative pressure coefficient. To satisfy these conditions, the flow has to re-adjust to give less shear layer curvature with higher base pressure and a longer distance to vortex formation.

The general features of the flow around rectangular cylinders have been well summarised by Laneville and Yong (1983). The main features considered are (i) the distribution of the vorticity from the point of separation, (ii) the growth of the separation bubble and (iii) the formation of the wake vortex. With reference to the vortex formation the authors used various normalised parameter to illustrate the flow around rectangular cylinders of various sectional ratios. The wet length, 'L' [refer Fig. 6.92 (a)] is an indication of the minimum size of the separation bubble and 'c' is the distance to the closure point and is an indication of the wake vortex strength. Laneville and Yong obtained good correlation between the above parameters (normalised form as c/D and d/D) with H/D ratios, where H is the cylinder width and D is the cylinder height. They reported that as H/D increases from 0.24 to 3.0, the closure point moves towards the cylinder base area and returns downstream for

cylinders with H/D >1.0. In phase, the position of the forming vortices moves transversely towards the wake centre line and then returns towards the trailing edge corner. The reason for the larger drag coefficient at H/D = 0.6, is the direct result of the wake vortex formation occurring on the centre line. As the wake vortices are forming closer to the base area, they induce lower base pressures and therefore resulting in high drag.

A line sketch [Fig. 6.92(b)] presented by Laneville and Yong (1983) explains the flow around a rectangular cylinder in steady flow. At the point of separation the boundary layer from the upstream face separates and a growing separation bubble near the leading edge absorbs part of its vorticity. In Fig. 6.91(b), '*a*' represents the initial vorticity and '*b*' as the vorticity absorbed by the bubble. The unabsorbed part of vorticity '*c*' continues in the shear layer in a proportion controlled by the cylinder width (H) to height (D) ratio (also known as after body length, H/D). In here the flow flows in a direction parallel to the width of the cylinder. The vorticity and fluid contained in this shear layer feed, according to the time of the cycle, either the opposite vortex or the adjacent vortex while they are forming. As the adjacent wake vortex forms, the separation bubble takes different sizes and can be considered as a buffer region filling itself with fluid and vorticity and then releasing them at maturity. When the adjacent vortex has just been shed the separation bubble shrinks to its minimum size. At the end of its growth the bubble exhausts its vorticity and the fluid either in the forming wake vortex (H/D < 3) or in patches of vorticity in the case of cylinders experiencing reattachment (H/D > 3).

For cylinders with H/D <3, the side wall is not long enough to trap the bubble, so that the bubble at the end of its growth vents its portion '*d*' of fluid and vorticity directly into the adjacent rolling vortex. Portion '*c*' of the shear layer rolls as well in the forming vortex. In its formation, the adjacent vortex is also supplied with fluids from the wake (portion '*e*') and the opposite shear layer (portion '*f*'). As the vortex reaches the final size with the bubble venting, part of the opposite shear layer is drawn across the wake, the fluid supply from the shear layer (portion '*c*') is cut off,

the wake vortex is then released and the separation bubble has shrunk to its minimum size. As this vortex is shed, the opposite vortex starts to form.

The effect of after body length, *H/D* on the process is critical in the sense of the distribution of the initial vorticity and the interaction between the separation bubble and the forming vortex. For cylinders with $H/D > 3$, the separation bubble is trapped and cannot exhaust directly the wake vortex. As previously, the separation bubble grows during the periodic cycle till it reaches the maximum size and then vents by releasing a patch of fluid and vorticity on the side wall. These released patches of fluid marching downstream ($H/D = 5$), form a secondary region. As they are entrained by the mean external flow, the released patches of fluid diffuse.

The effect of variation of *H/D* and the corresponding flow change around the rectangular cylinder falls into different regimes [Laneville and Yong (1983)] and are briefly given below.

Regime-1: when the model dimensions are in the range $0< H/D <0.5$, this regime occurs. The model width or side wall is too short in this regime. A small bubble is present from the point of separation and it extracts a minimal amount of vorticity from the shear layer. As *H/D* increases, the cylinder's sides are progressively wet by the bubble. Because of the relative strength of the wake vortex, the point of closure of the near wake is far away down stream of the rear wall at a distance from 2D to 3D.

Regime-2: ($0.5 < H/D < 1.0$): In this regime, the minimum size of the separation bubble from the leading edge has elongated and when they fully expanded, the bubble projects over the entire side wall. A substantial part of the vorticity in the initial shear layer is absorbed by the bubble. Now the separation bubble interacts with the forming wake vortex and its vorticity forces the wake vortex to roll up closer to the wake centreline. For cylinder with $H/D = 0.625$, the wake vortices form on the centreline and are responsible for the local high suction on the cylinder base area. A similar statement has also been made by Bearman and Trueman (1972). The substantial

vorticity available to the wake vortex causes a low base pressure and high drag coefficients.

Regime-3: ($1.0 < H/D < 3.0$): For this regime, the side walls are longer than the frontal dimension and characterised by a more elongated separation bubble and the wake vortex formation located away from centreline. The separation bubble undergoes a longitudinal stretching and vents directly into the wake vortex. The proportion of fluid and vorticity released into the venting is smaller than in the previous regime because of the relatively larger dimension of the minimum size of the separation bubble. In comparison to the regime-1, here the distribution of vorticity is reversed. The separation bubble absorbs most of the vorticity contained in the initial shear layer. The resulting wake vortex is weaker and the drag coefficients of the cylinder are lower.

With the above understanding, steady towing tests were carried out on the cylinders to check the loading performance as towing the cylinder for simulating current effect need to be justified. This was done by towing the cylinder in both vertical and horizontal positions. A cylinder immersed either vertically or horizontally in steady flow would experience a similar flow pattern and hence would be subjected to an identical drag force. The drag coefficient in steady towing can be calculated as $C_D = F/(0.5\rho U^2 D)$, where, F is mean horizontal force, U is the carriage speed and D is diameter of the cylinder. The results are presented as function of Reynolds number, Re in Figs. 6.93 – 6.95. The average value of the drag coefficients in each aspect ratio is compared with the previous experimental results of Nakaguchi et al. (1968), Bearman & Trueman (1972) and Courchesne and Laneville (1979) who conducted experiments in wind tunnels. The present results show good agreement, except for aspect ratio = 2/1, for which a slightly lower drag coefficient is observed and thus steady towing the cylinder is validated and therefore it can be concluded that the force measuring system works very well within the range of Reynolds numbers tested.

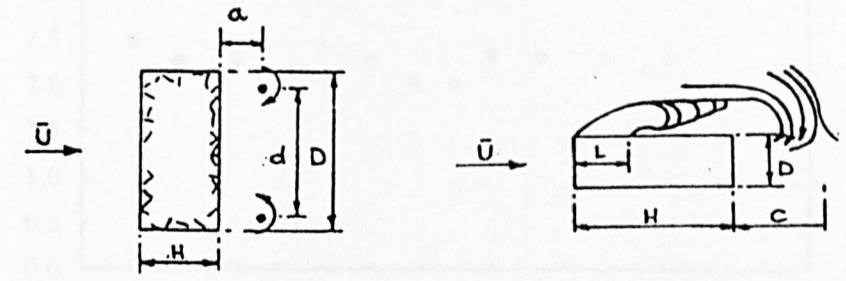

(a)

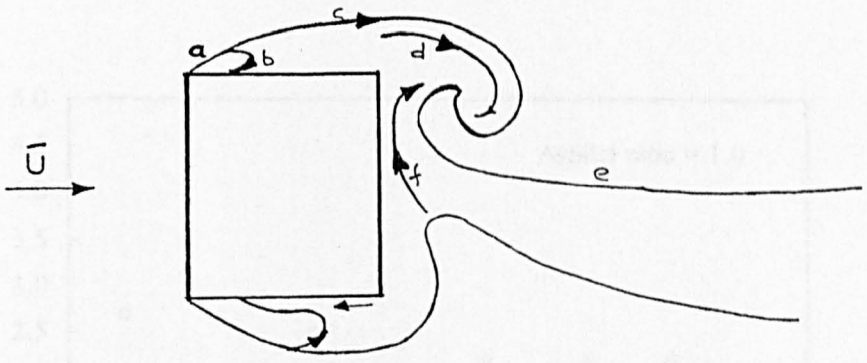

(b)

Fig. 6.92 Line sketch of flow pattern around rectangular cylinder in steady flow [*Laneville and Yong (1983)*]

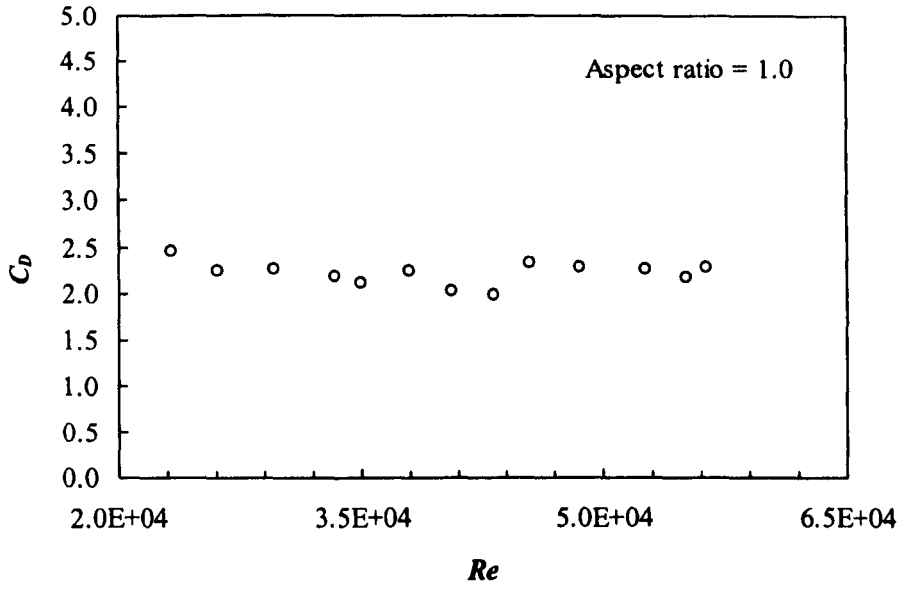

(a) Vertical square cylinder

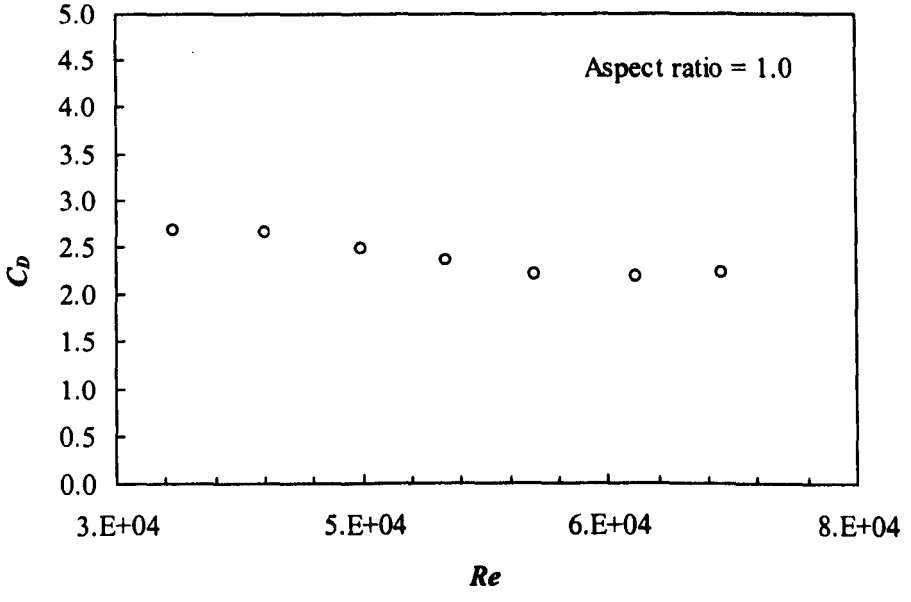

(b) Horizontal square cylinder

Fig. 6.93 Steady flow drag coefficients for square cylinder

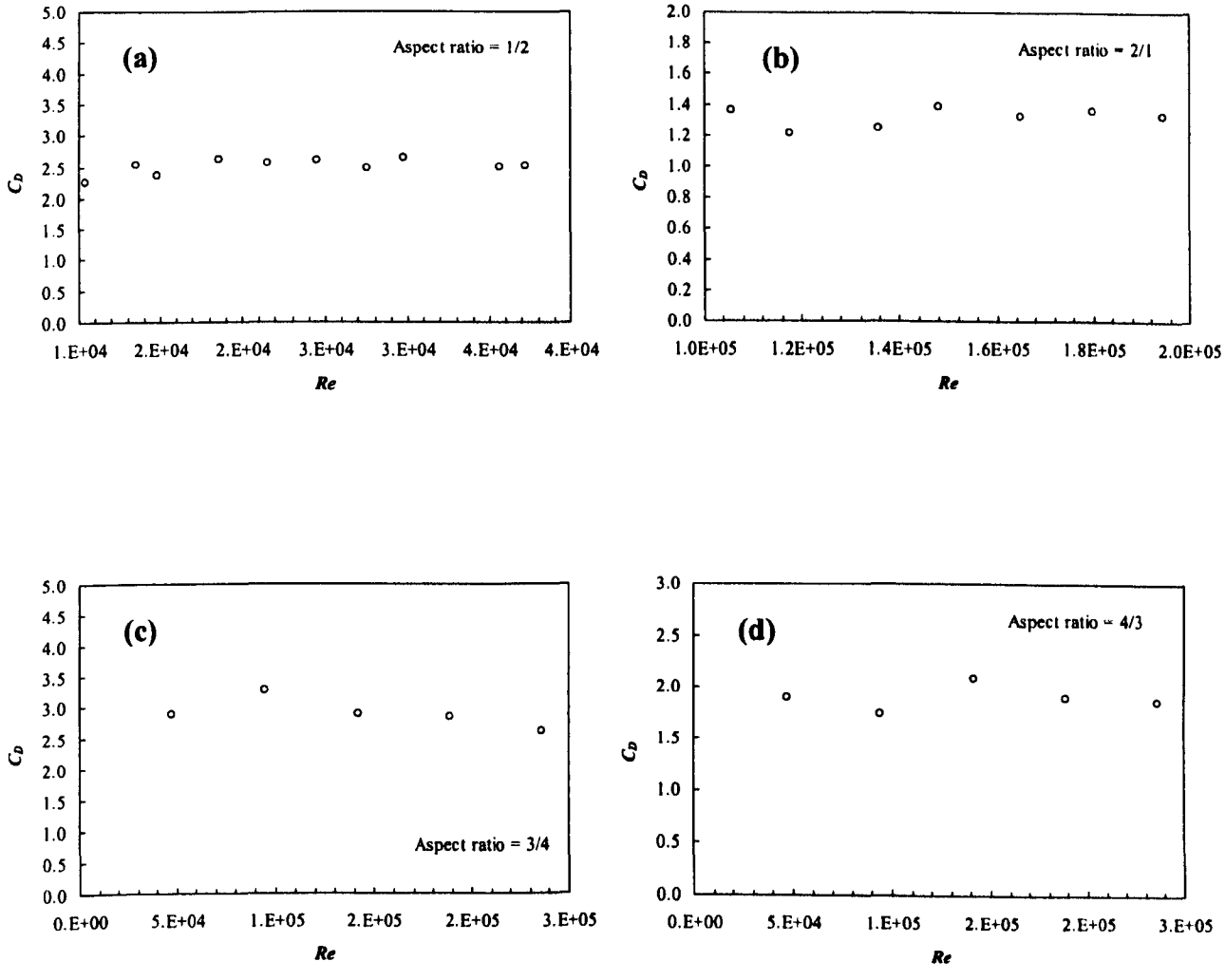

Fig. 6.94 Steady flow drag coefficients for rectangular cylinders: (a) horizontal cylinder for aspect ratio = ½; (b) vertical cylinder for aspect ratio = 2/1; (c) horizontal cylinder for aspect ratio = 3/1 and (d) vertical rectangular cylinder for aspect ratio = 4/3.

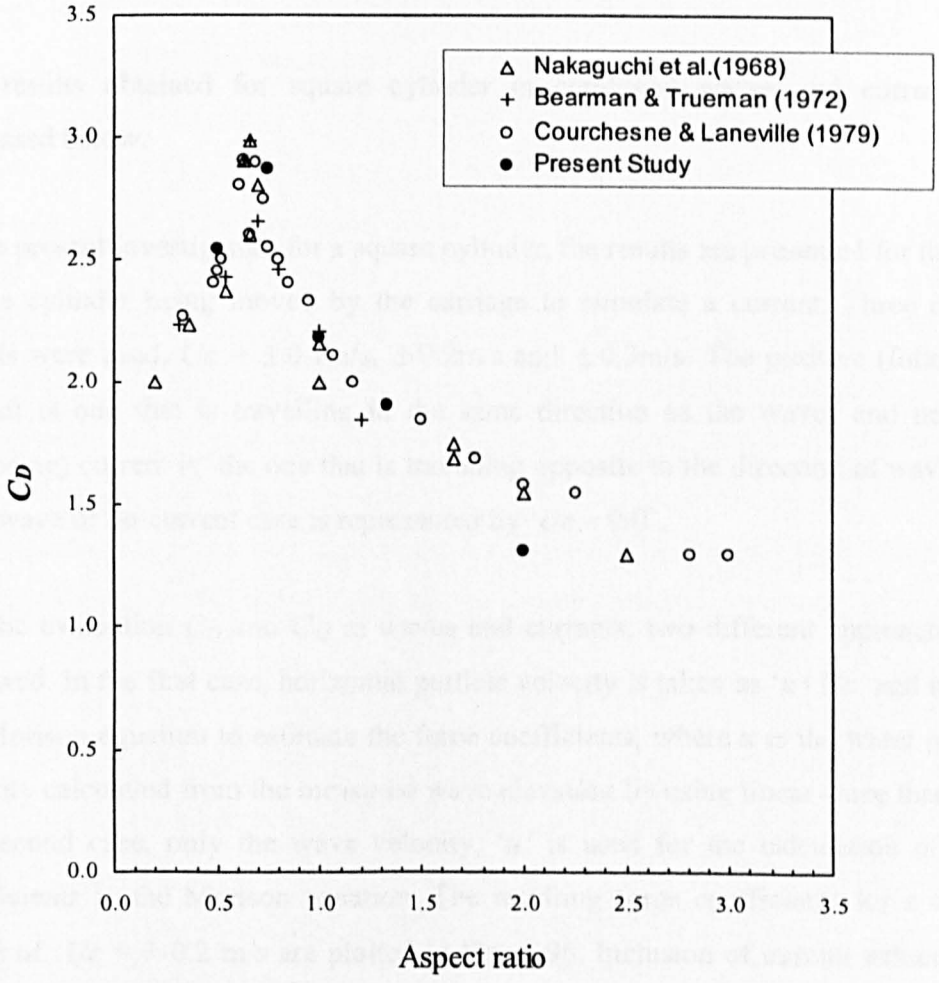

Fig. 6.95 Steady flow drag coefficients for rectangular cylinders

6.2.5 Regular Waves and Coexisting Current

6.2.5.1 Square Cylinder with Aspect ratio = 1.0

The results obtained for square cylinder in combined waves and currents are discussed below.

In the present investigation for a square cylinder, the results are presented for the case of the cylinder being moved by the carriage to simulate a current. Three current speeds were used, $Uc = \pm 0.1$m/s, ± 0.2m/s and ± 0.3m/s. The positive (following) current is one that is travelling in the same direction as the waves and negative (opposing) current is the one that is travelling opposite to the direction of wave. The pure wave or no-current case is represented by '$Uc = 0.0$'.

For the evaluation C_D and C_M in waves and currents, two different approaches are followed. In the first case, horizontal particle velocity is taken as '$u+Uc$' and used in the Morison equation to estimate the force coefficients, where u is the water particle velocity calculated from the measured wave elevation by using linear wave theory. In the second case, only the wave velocity, 'u' is used for the calculation of force coefficients in the Morison equation. The resulting force coefficients for a current speed of $Uc = + 0.2$ m/s are plotted in Fig. 6.96. Inclusion of current velocity, Uc affects the drag coefficients drastically. When wave velocity is alone considered, the drag coefficients exhibit large values at low KC numbers and it decreases sharply as KC number increases.

The inclusion of current velocity, Uc completely changes the value of drag coefficients. At low KC numbers, negative values of drag coefficients are observed and with increase in KC number, C_D is found to increase. On the other hand, inertia coefficients are not affected by the inclusion of current and take identical values for both cases. In Fig. 6.97, force coefficients are plotted for $Uc = - 0.2$ m/s and a similar

trend as discussed above can be seen not only for this current speed, but also for all the current speeds and for all the cylinders.

For practical purposes it is necessary to choose the right drag coefficients for the force calculation. The calculated force coefficients are substituted in Morison equation to obtain the force time histories. In Fig. 6.98(a), a current, $Uc = + 0.2$ m/s is included along with wave velocity, u, for the computation of force coefficients and the corresponding Morison force, for $KC = 1.37$. In Fig. 6.98(b), only the wave velocity, u, is used and drag and inertia coefficients are evaluated and these coefficients are then used to obtain the Morison force. It is evident from these plots that, inclusion of current induces a phase shift between the measured and calculated forces and when the wave velocity is alone used, the phase shift is not observed. The same observation is made for a higher $KC = 3.89$ as well, as seen in Fig. 6.99(a) and (b). Although, it is not shown here, the above-described observation is made for all the force time series, tested in combined waves and currents.

The effect of current can also be seen in Fig. 6.100. In this case, the drag and inertia coefficients are first calculated from the experimental data, measured for zero current. Then the current speed is included as $u+Uc$, while calculating the Morison force. The poor correlation between the forces reveals that the current velocity cannot be simply added to the wave velocity while force coefficients obtained for pure wave is used for the force calculation.

Three different observations are made from the above paragraphs. (i) a phase shift is obvious between measured and computed forces, when current velocity is added to the wave velocity for the estimation of drag coefficients and Morison forces (ii) phase shift can be avoided, if the current velocity is excluded and (iii) force coefficients obtained for pure wave cannot be used for force calculation when the Morison equation used with Uc term. From the foregoing discussion, it can be concluded that for a better comparison of measured and computed forces in waves and currents, the drag coefficients derived by excluding the current Uc can be used when a cylinder is

towed in waves with a wave probe moving as same speed as the cylinder (i.e., by using encountered wave period). All the force coefficients reported hereafter are corresponding to this procedure. Encountered wave period is used for all calculations.

The variation of C_D and C_M with KC number for square section cylinder is shown in Figs. 6.101 to 6.105. The results reported here are computed on a wave by wave basis. The presence of current is found to have significant effect on the force coefficient. The C_D and C_M for current speeds ± 0.1, ± 0.2, and ± 0.3 m/s are shown in Figs. 6.101, 6.102 and 6.103 respectively. In the plots, the scatter in the coefficients is found to be very large, even then few trends are apparent. The drag coefficients show a trend similar to those found for wave alone, they exhibit large values at low KC number and decreases sharply with increase in KC numbers. When the corresponding drag coefficient for an equal and opposite magnitude of current is plotted, the current direction does not appear to have much influence on the drag coefficients, except for ± 0.3 m/s. In this case, the drag coefficients for $U_C = + 0.3$ m/s are found to be significantly lower than those for $U_C = - 0.3$ m/s. Regarding inertia coefficients, some of the data points of inertia coefficient for a current = + 0.3 m/s are found to be lower than those found for the negative current of the same magnitude, otherwise the inertia coefficients for positive and negative currents are found to be of the same order of values.

The C_D and C_M are re-plotted along with the coefficients obtained for wave alone (no current) in Figs. 6.104 and 6.105 for the positive and negative currents respectively. In both these plots it is evident that C_D and C_M for waves and currents are found to be significantly lower than the C_D for waves alone. It is further noticed that inertia coefficients are found to decrease with increase in current speed and this trend is distinctly observed for positive current. One can conclude from the above results that irrespective of the direction of current, the inertia coefficient decreases with increase in current speed and the values of inertia coefficients are much lower than those

found for waves alone (in the absence of current). Note a similar trend is reported in Marine Research Review11(1997) for circular cylinders in waves and currents.

The root mean square in-line and lift force coefficients are plotted in Figs. 6.106 and 6.107. Here again, wave velocity with encountered wave period is alone used in the definition of rms force coefficients. The C_{Lrms} for negative currents are found to be larger than those in waves alone and C_{Lrms} for positive currents are observed to be lower than the coefficients in waves alone. C_{Lrms} in positive currents are found to be larger compared to negative currents. The total mean square coefficients for both negative and positive currents are plotted in Fig. 6.108. For negative currents and waves, C_{Trms} is found to be higher compared to C_{Trms} for positive currents. The measured and computed in-line peak forces for all the current speeds are shown in Fig. 6.109. The means and standard deviations for all current speeds are given in Table 6.2. The computed positive peak forces are lower than the measured peak forces up to a maximum of 38% in positive currents and the maximum standard deviation is 0.372. In negative currents this difference between measured and computed forces are less.

6.2.5.2 Rectangular Cylinder with Aspect ratio = 1/2 and 2/1

The results of wave and current force measurement for rectangular cylinder with aspect ratio = 1/2 are shown in Figs. 6.110 to 6.114. Here again, three current speeds in the following and opposing waves are considered. C_D and C_M for current speeds ± 0.1, ± 0.2, and ± 0.3 m/s are shown in Figs. 6.110, 6.111 and 6.112 respectively. A trend similar to the results reported for square cylinder is seen for this aspect ratio. Drag and inertia coefficients in positive and negative currents display nearly equal values, irrespective of the current direction.

The C_D and C_M are re-plotted along with the coefficients obtained for wave alone in Figs. 6.113 and 6.114 for the positive and negative currents respectively. C_D for waves and currents are found to be lower than C_D in waves alone. The inertia

coefficients are also observed to be significantly lower than the C_M obtained for waves alone for both the current directions. The root mean square in-line and lift force coefficients for positive and negative currents are plotted in Figs. 6.115 and 6.116 respectively. C_{Frms} and C_{Lrms} for waves and currents are found to be lower than C_{Frms} and C_{Lrms} for waves alone. The total mean square coefficients for both negative and positive currents are plotted in Fig. 6.117 and C_{Trms} for waves and currents is found to be about 20 to 35% lower than C_{Trms} for waves alone. The measured and computed in-line peak forces for current speeds ± 0.1m/s, ± 0.2m/s and ± 0.3m/s are shown in Fig. 6.118. The means and standard deviations are given in Table 6.2. The computed positive peak forces are found to be up to 35% lower than the measured peak forces with a maximum standard deviation of 0.107.

A similar trend as discussed above is observed in drag and inertia coefficients for aspect ratio of the cylinder equals to 2/1. The results of wave and current force measurement for rectangular cylinder with aspect ratio = 2/1 is shown in Figs. 6.119 to 6.122. For this aspect ratio, the force measurements are made for only two current speeds ± 0.2, and ± 0.4 m/s. C_D and C_M are re-plotted along with the coefficient obtained for wave alone in Figs. 6.119 and 6.120 for the positive and negative currents respectively. C_D for waves and currents are found to lower than C_D in waves alone. The inertia coefficients are observed to be lower than the C_M obtained for wave alone for both the current directions. The root mean square in-line and lift force coefficients for positive and negative currents are plotted in Fig. 6.123 and 6.124 respectively. The total mean square coefficients for both negative and positive currents are plotted in Fig. 6.125. C_{Trms} for waves and currents is found to be about 20 to 40% lower than C_{Trms} for waves alone. The measured and computed in-line peak forces for the two current speeds are shown in Fig. 6.126. The computed positive peak forces are found to be up to 35% lower than the measured peak forces. The maximum standard deviation value from Table 6.2 is 0.323 for a current of +0.4 m/s.

6.2.5.3 Rectangular Cylinder with Aspect ratio = 3/4 and 4/3

The results of wave and current force measurement for rectangular cylinder with aspect ratio = 3/4 are discussed here for three current speeds in the following and opposing waves. C_D and C_M for current speeds ± 0.1, ± 0.2, and ± 0.3 m/s are shown in Figs. 6.127, 6.128 and 6.129 respectively. Drag coefficients in positive and negative currents display equal values, irrespective of the current direction, whereas, the inertia coefficients show different values. At low KC numbers inertia coefficients for positive currents show much lower values.

The C_D and C_M are re-plotted along with the coefficient obtained for wave alone in Figs. 6.130 and 6.131 for the positive and negative currents respectively. C_D and C_M for waves and currents are found to be lower than those calculated in waves alone. With increase in positive current speed, some of the data points (corresponding to larger frequency parameters) are found to have much lower values of inertia coefficients and the reason for this trend is unclear. The root mean square in-line and lift force coefficients for positive and negative currents are plotted in Figs. 6.132 and 6.133 respectively. The total mean square coefficients for both negative and positive currents are plotted in Fig. 6.134 and here again, C_{Trms} for waves and currents is found to be lower than C_{Trms} for waves alone. The measured and computed in-line peak forces all current speeds are shown in Fig. 6.135. From Table 6.2, the computed positive peak forces are found to be about 33% lower than the measured peak forces for the largest positive current used.

The C_D and C_M for aspect ratio = 4/3 are plotted in Figs. 6.136 to 6.140 for the positive and negative currents. For this aspect ratio, the C_D values in waves and currents are found to be only slightly smaller than C_D in waves alone. The inertia coefficients are observed to be significantly lower than the C_M obtained for waves alone, for both the current directions. A large reduction in inertia coefficients with increase in positive currents is also observed for this aspect ratio. The root mean square in-line and lift force coefficients for positive and negative currents are plotted

in Fig. 6.141 and 6.142 respectively. The total mean square coefficients for both negative and positive currents are plotted in Fig. 6.143. The measured and computed in-line peak forces are shown in Fig. 6.144. The computed positive peak forces are found to be up to 35% lower than the measured peak forces.

In Table 6.2, the means ($\overline{R_{x^*}}$) and standard deviations (σ_{x^*}) of the force ratio are given for all the cylinders. The mean values take a maximum of 1.38 and the maximum value of standard deviations is 0.37. For all the positive currents, the measured forces are higher than the Morison forces.

Table. 6.2. Means and standard deviations of measured and computed peak force ratios for vertical cylinder in waves and currents

Current (m/s)	Aspect ratio = 1.0		Aspect ratio = ½		Aspect ratio = 2/1	
	$\overline{R}_{xp}$	σ_{xp}	$\overline{R}_{xp}$	σ_{xp}	$\overline{R}_{xp}$	σ_{xp}
+0.1	1.381	0.356	1.247	0.074	-	-
+0.2	1.358	0.336	1.298	0.067	1.342	0.092
+0.3	1.317	0.372	1.345	0.107	-	-
+0.4	-	-	-	-	1.354	0.323
-0.1	1.248	0.134	1.201	0.107	-	-
-0.2	1.115	0.149	1.148	0.148	1.066	0.126
-0.3	0.978	0.102	1.092	0.195	-	-
-0.4	-	-	-	-	0.962	0.274

Current (m/s)	Aspect ratio = 3/4		Aspect ratio = 4/3	
	$\overline{R}_{xp}$	σ_{xp}	$\overline{R}_{xp}$	σ_{xp}
+0.1	1.269	0.088	1.187	0.187
+0.2	1.265	0.175	1.358	0.201
+0.3	1.335	0.249	1.324	0.368
+0.4	-	-	-	-
-0.1	1.245	0.141	1.104	0.221
-0.2	1.137	0.152	1.041	0.354
-0.3	1.083	0.199	0.907	0.225
-0.4	-	-	-	-

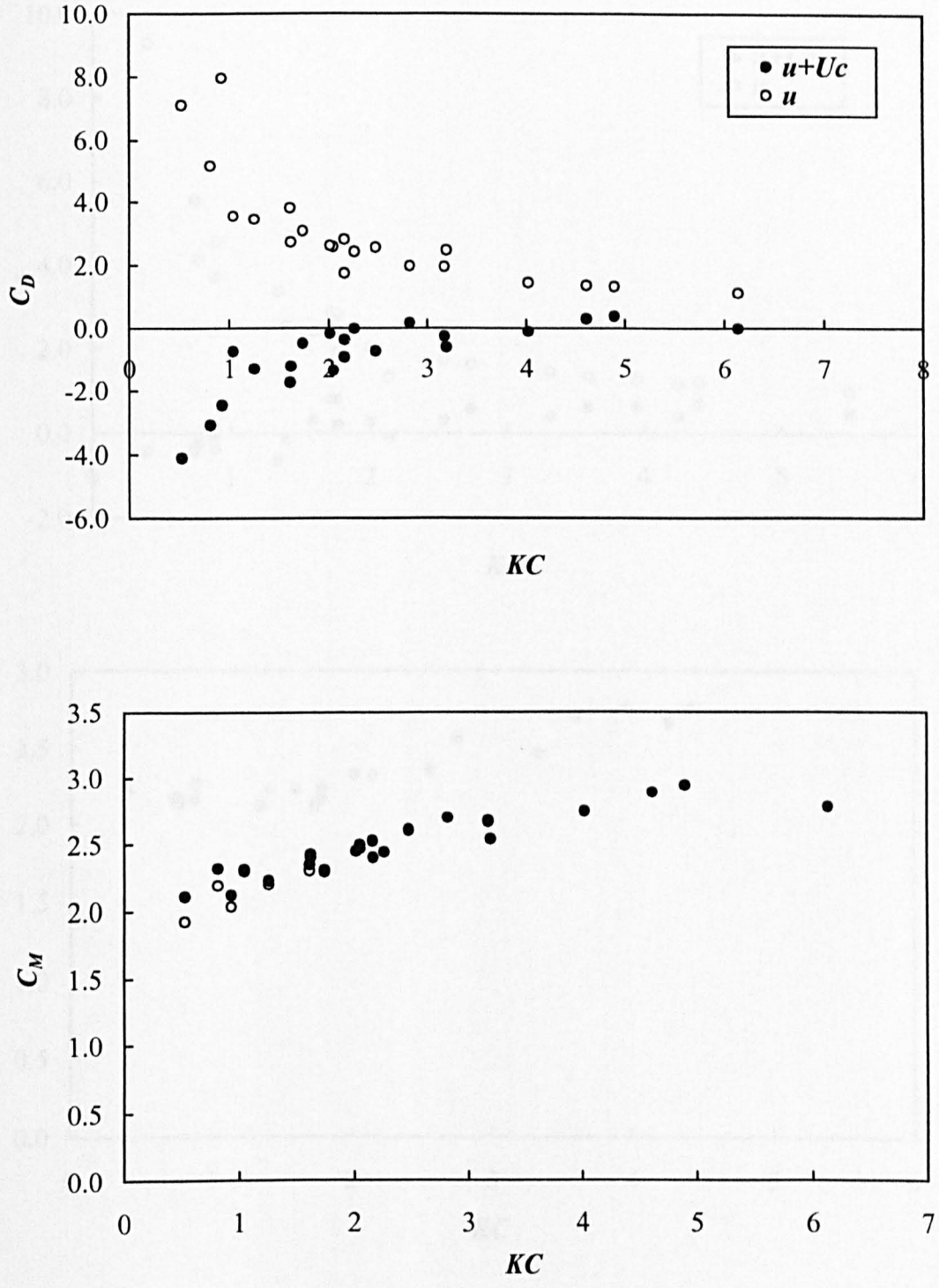

Fig. 6.96 Drag and inertia coefficients for vertical square cylinder in co-existing waves and currents for Uc = 0.2 m/s

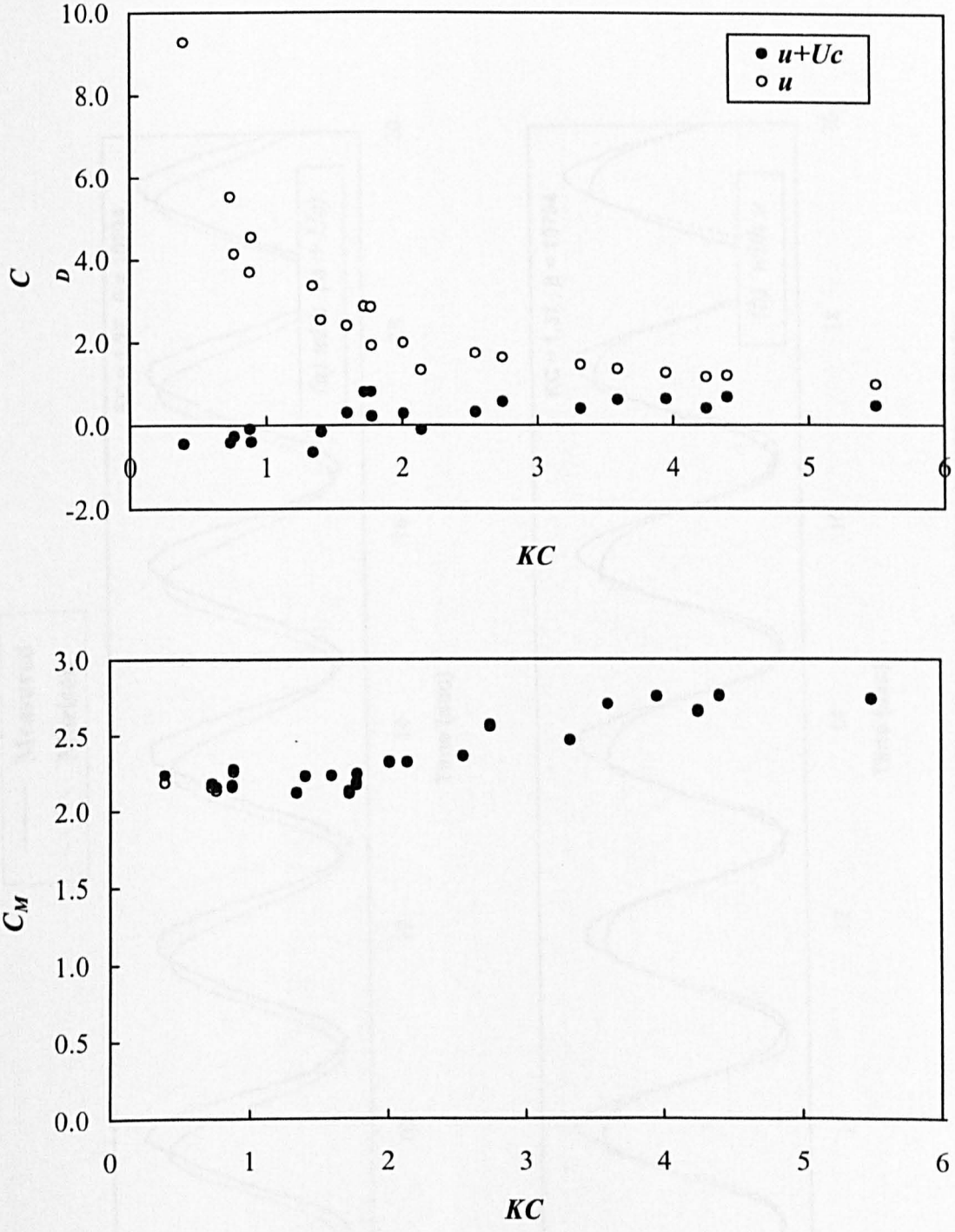

Fig. 6.97 Drag and inertia coefficients for vertical square cylinder in co-existing waves and currents for Uc = - 0.2 m/s

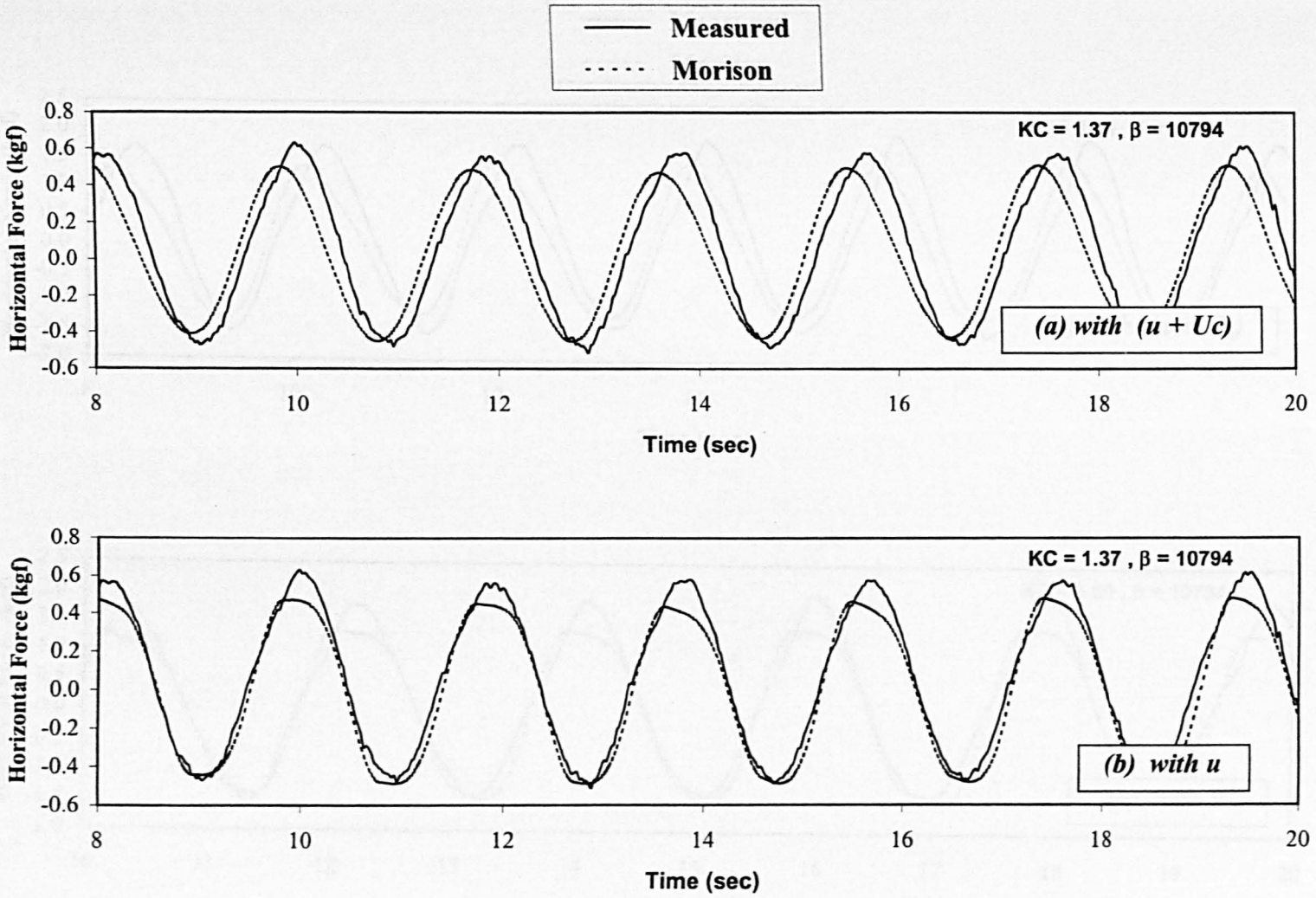

Fig. 6.98 Effect of *Uc* on in-line forces for vertical square cylinder for $Uc = +0.2$ m/s and $KC = 1.37$

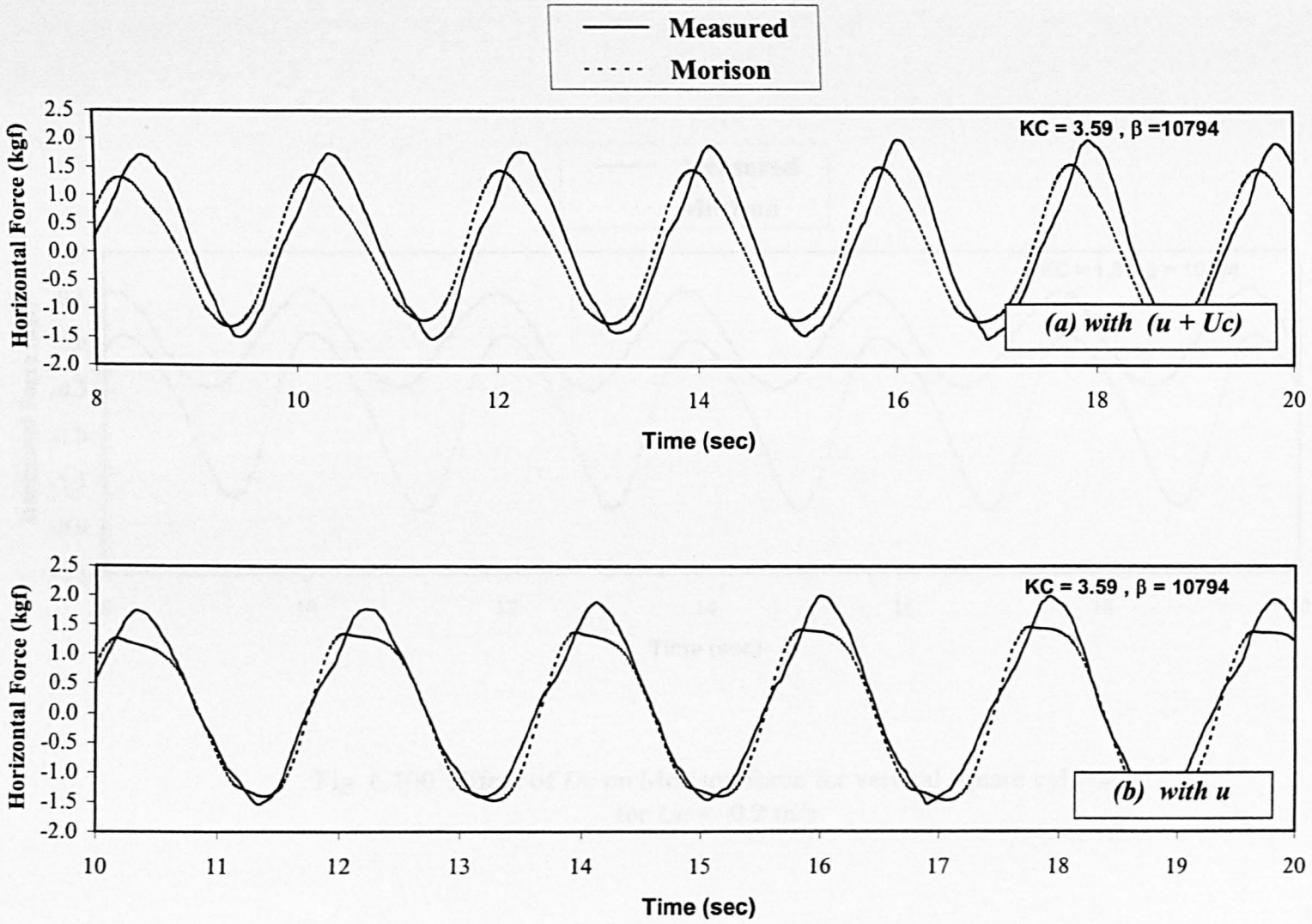

Fig. 6.99 Effect of *Uc* on in-line forces for vertical square cylinder for $Uc = +0.2$ m/s and $KC = 3.59$

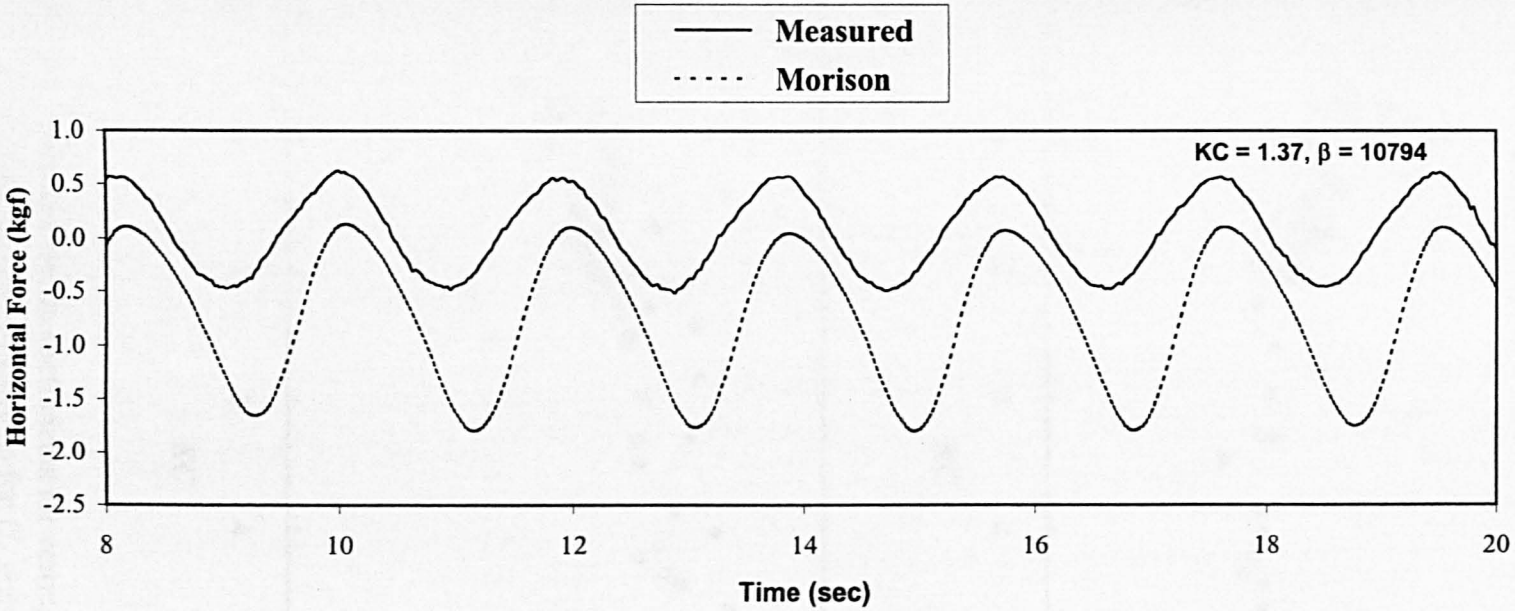

Fig. 6.100 Effect of *Uc* on Morison force for vertical square cylinder for *Uc* = -0.2 m/s

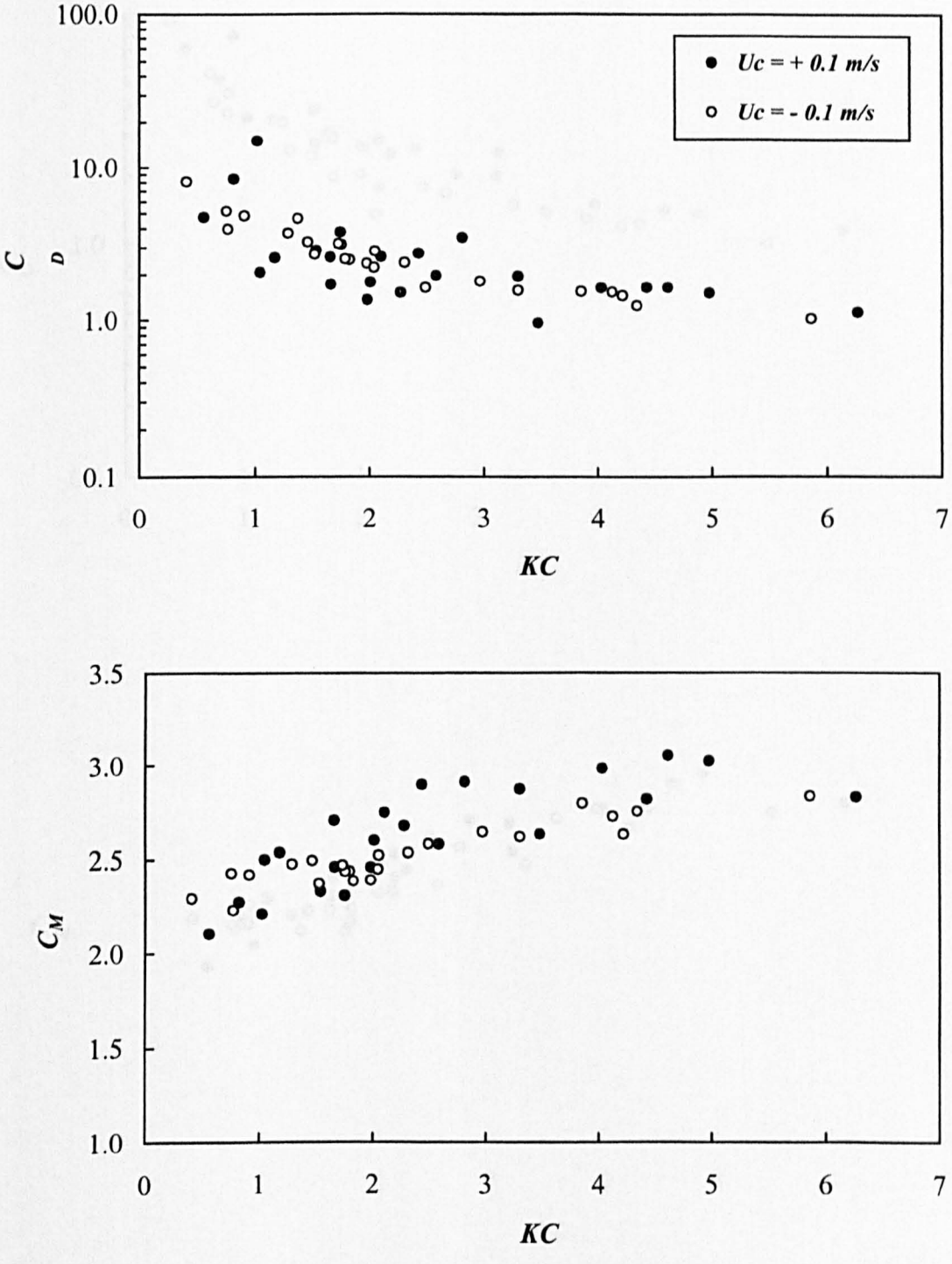

Fig. 6.101 Drag and inertia coefficients for vertical square cylinder in co-existing waves and currents for $U_C = \pm 0.1$ m/s

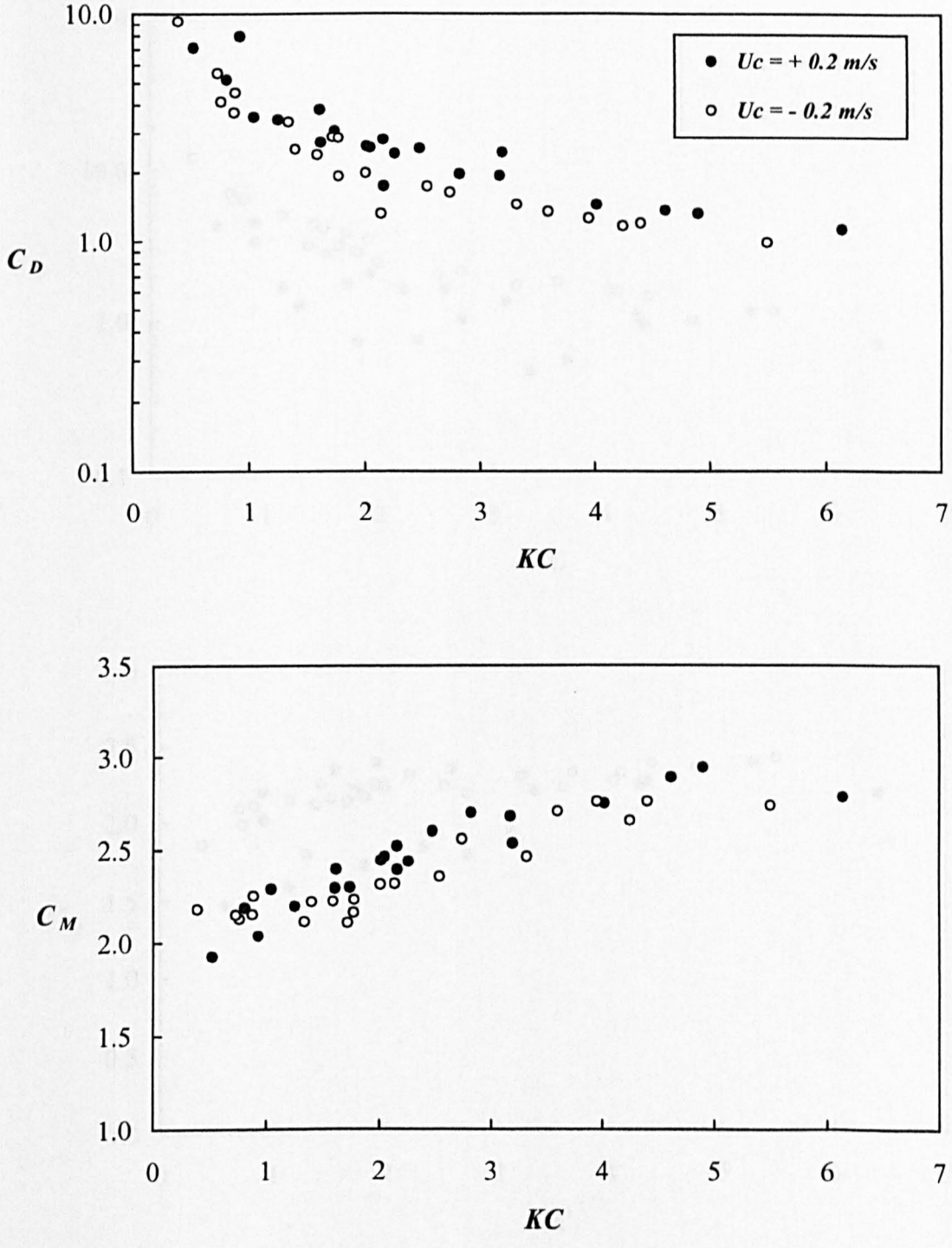

Fig. 6.102 Drag and inertia coefficients for vertical square cylinder in co-existing waves and currents for $U_C = \pm 0.2$ m/s

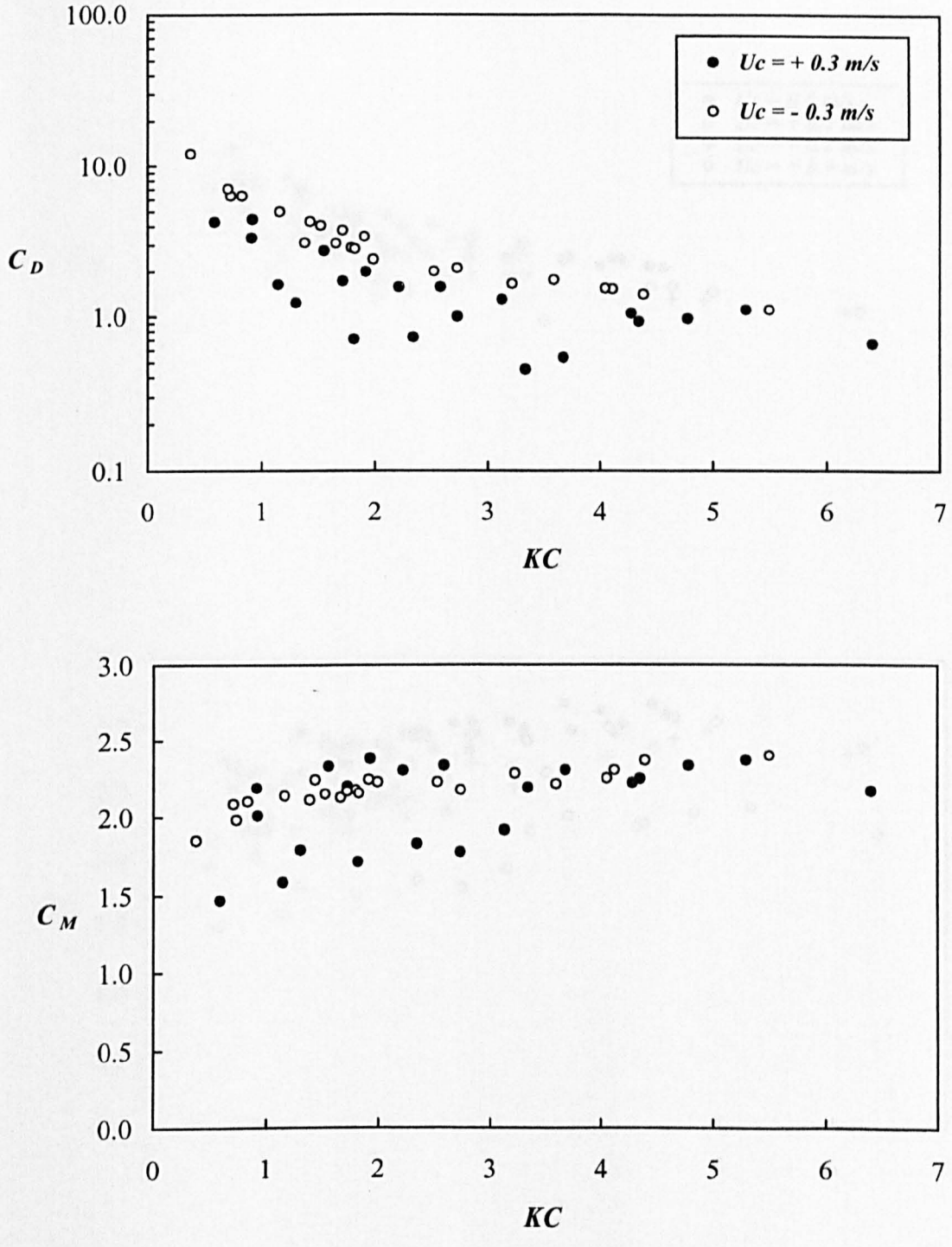

Fig. 6.103 Drag and inertia coefficients for vertical square cylinder in co-existing waves and currents for $U_C = \pm 0.3$ m/s

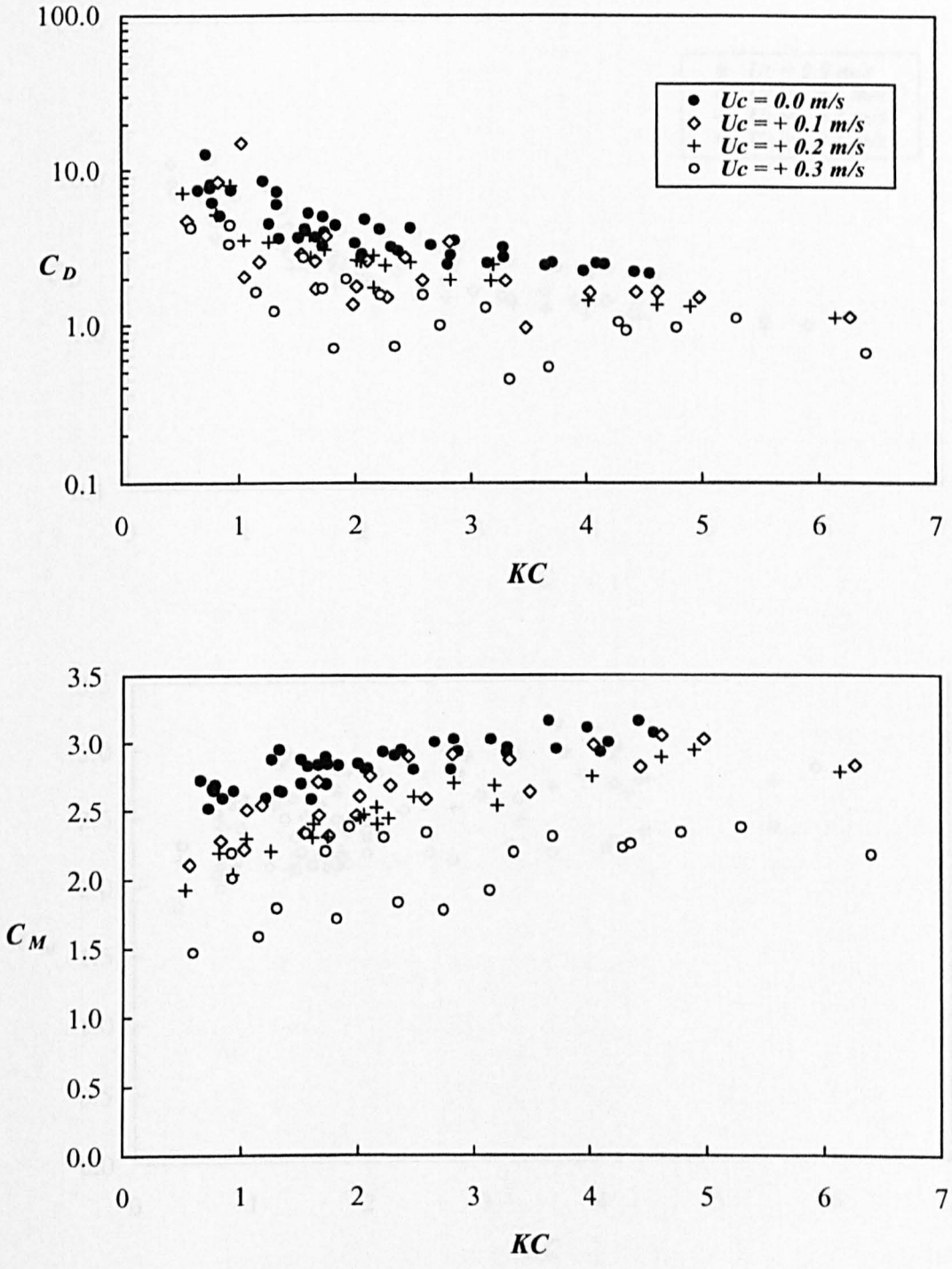

Fig. 6.104 Drag and inertia coefficients for vertical square cylinder in co-existing waves and currents for Positive currents

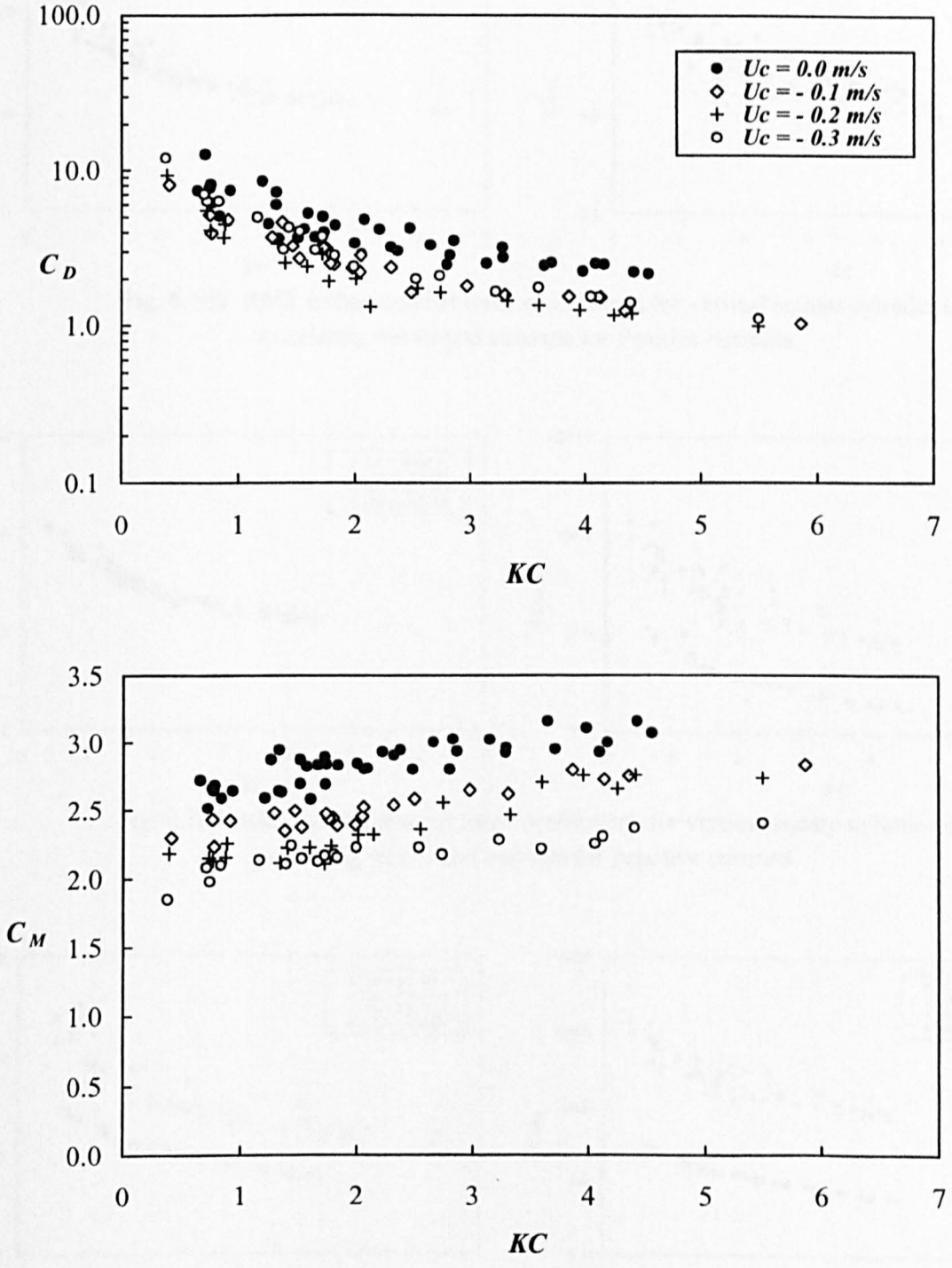

Fig. 6.105 Drag and inertia coefficients for vertical square cylinder in co-existing waves and currents for negative currents

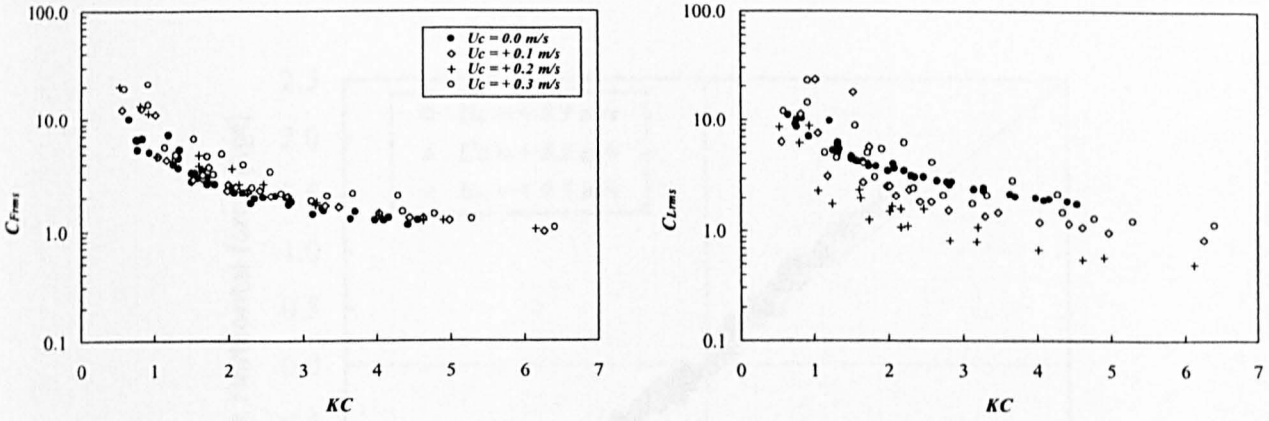

Fig. 6.106 RMS in-line and lift force coefficients for vertical square cylinder in co-existing waves and currents for Positive currents

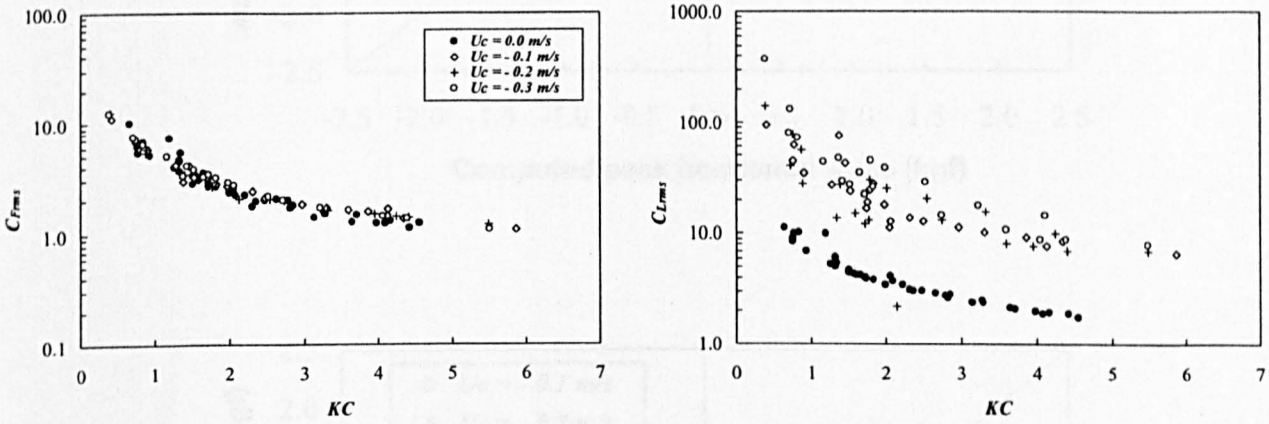

Fig. 6.107 RMS in-line and lift force coefficients for vertical square cylinder in co-existing waves and currents for negative currents

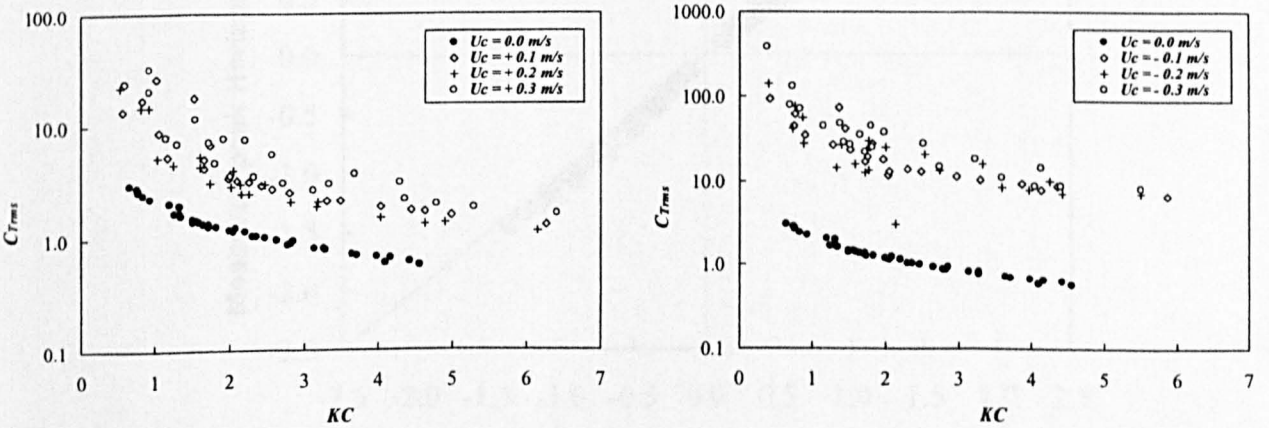

Fig. 6.108 Total rms force coefficients for vertical square cylinder in co-existing waves and currents

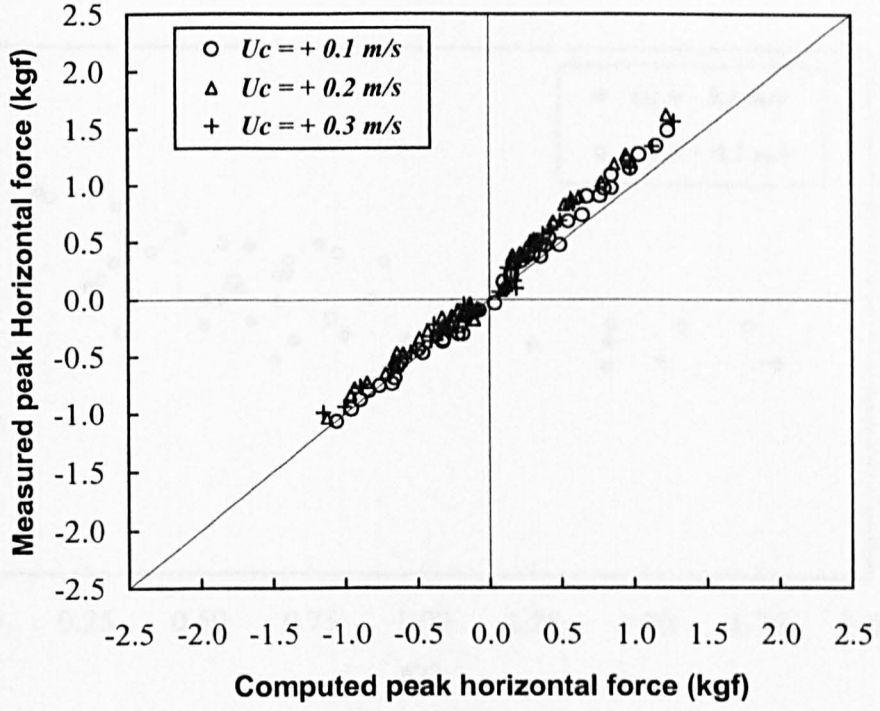

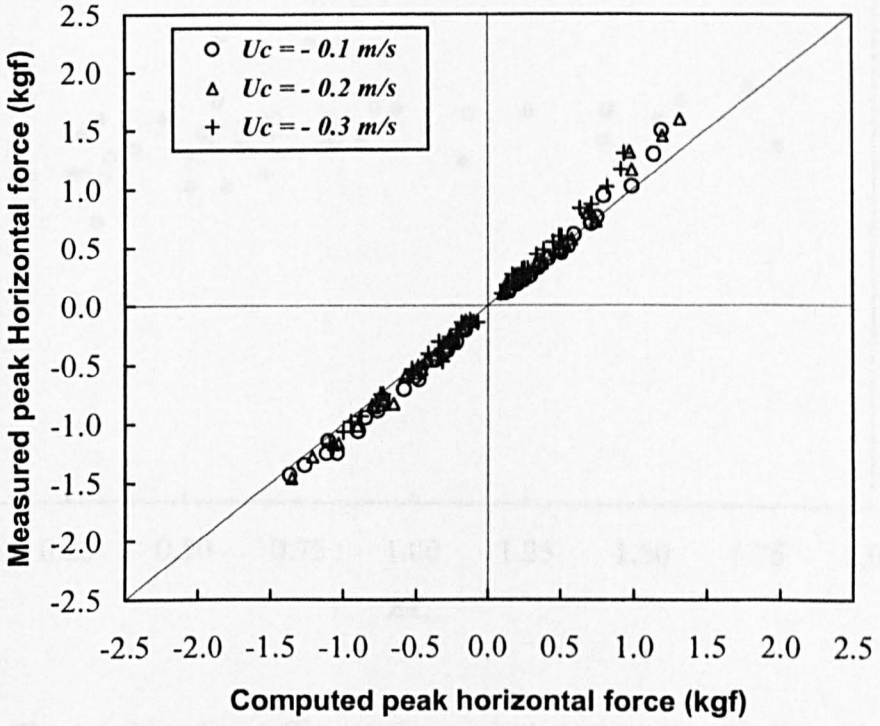

Fig. 6.109 Measured and computed peak forces for vertical square cylinder in co-existing waves and currents

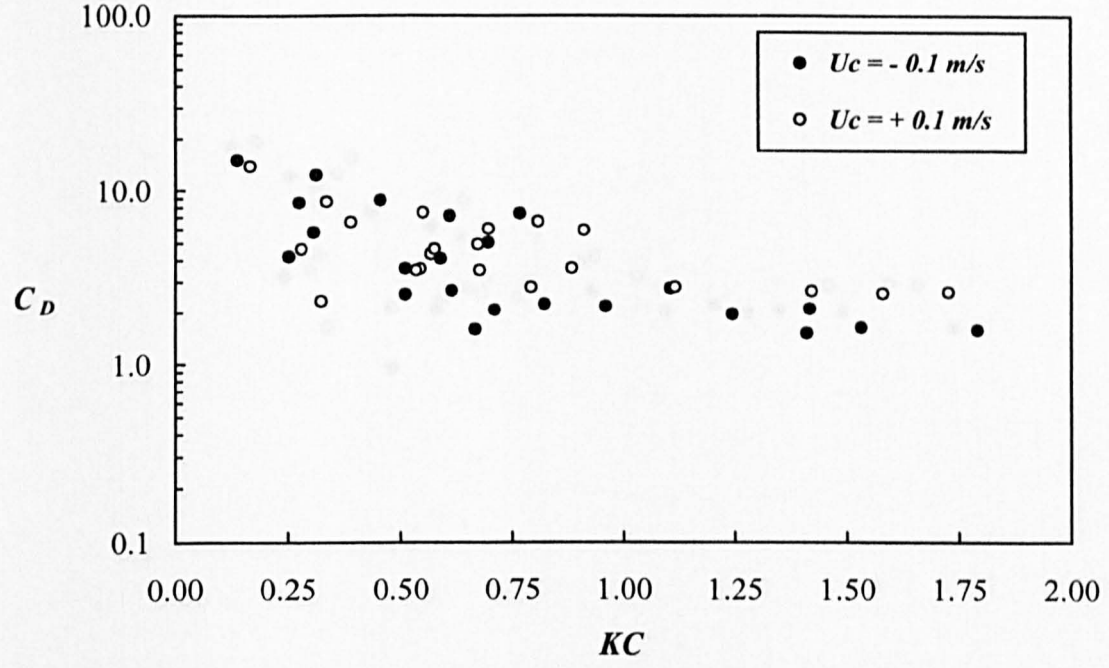

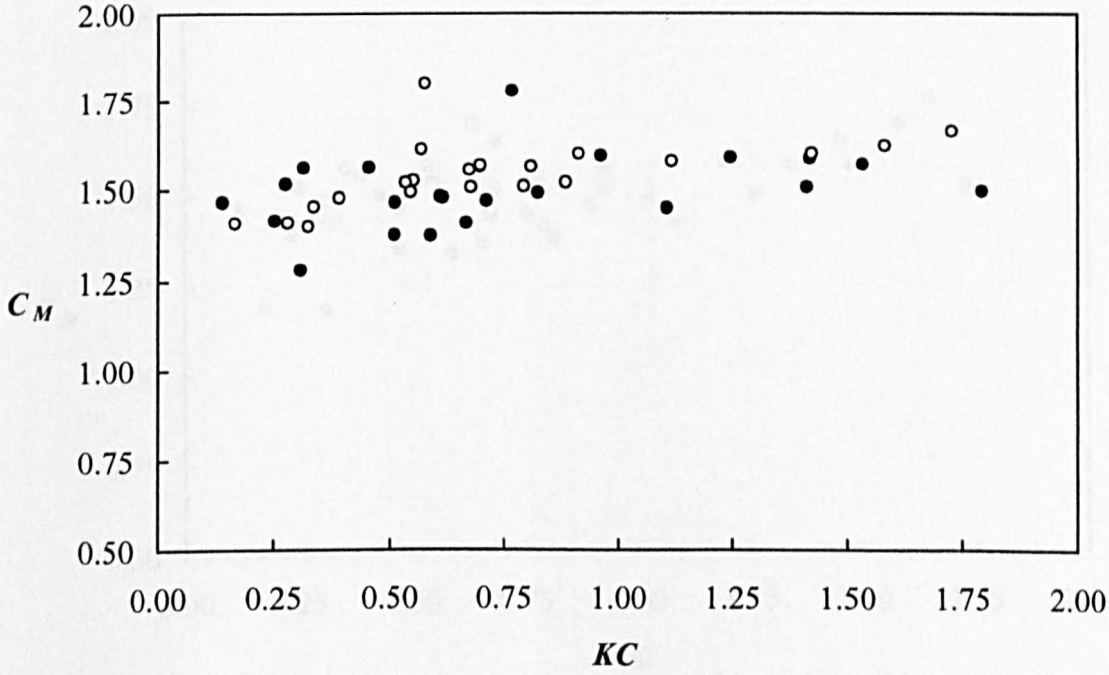

Fig. 6.110 Drag and inertia coefficients for vertical rectangular cylinder for aspect ratio = 1/2 in co-existing waves and currents for Uc = ± 0.1 m/s

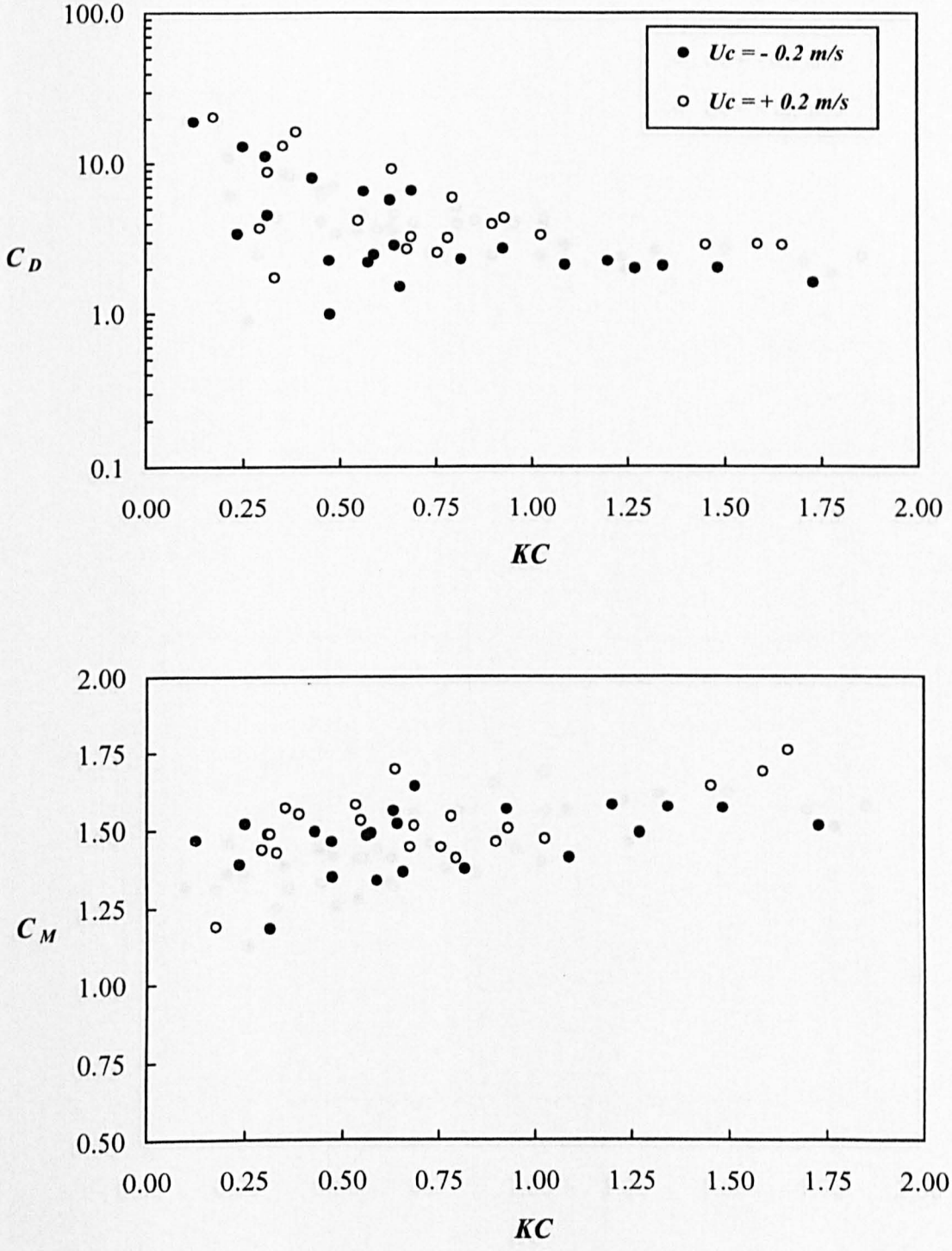

Fig. 6.111 Drag and inertia coefficients for vertical rectangular cylinder for aspect ratio = 1/2 in co-existing waves and currents for Uc = ± 0.2 m/s

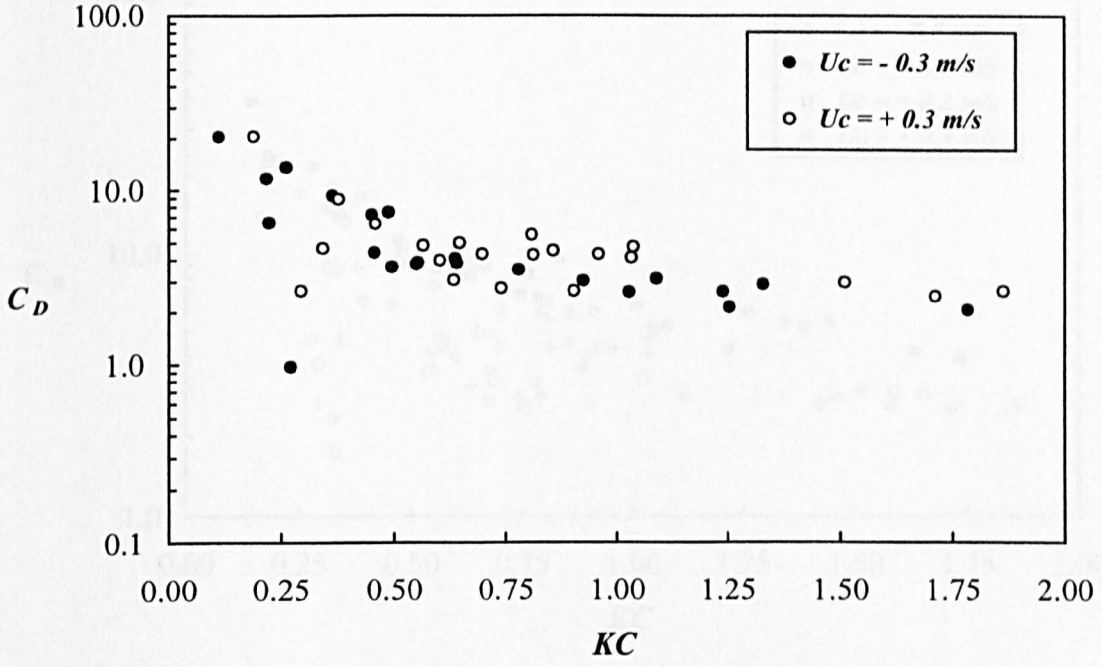

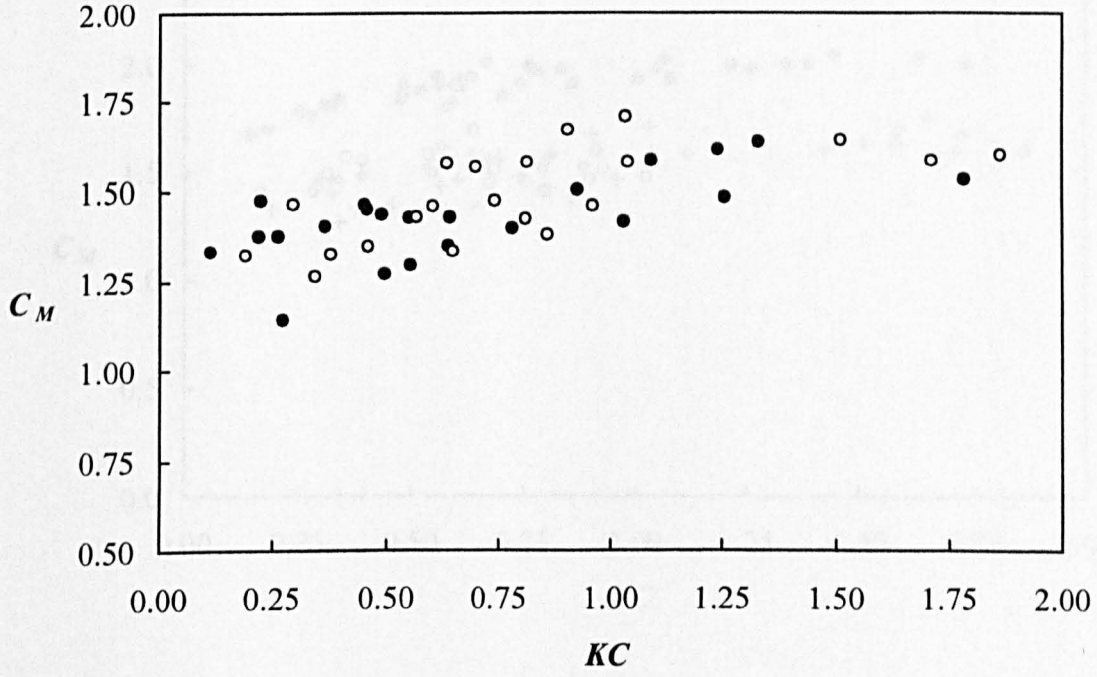

Fig. 6.112 Drag and inertia coefficients for vertical rectangular cylinder for aspect ratio = 1/2 in co-existing waves and currents for Uc = ± 0.3 m/s

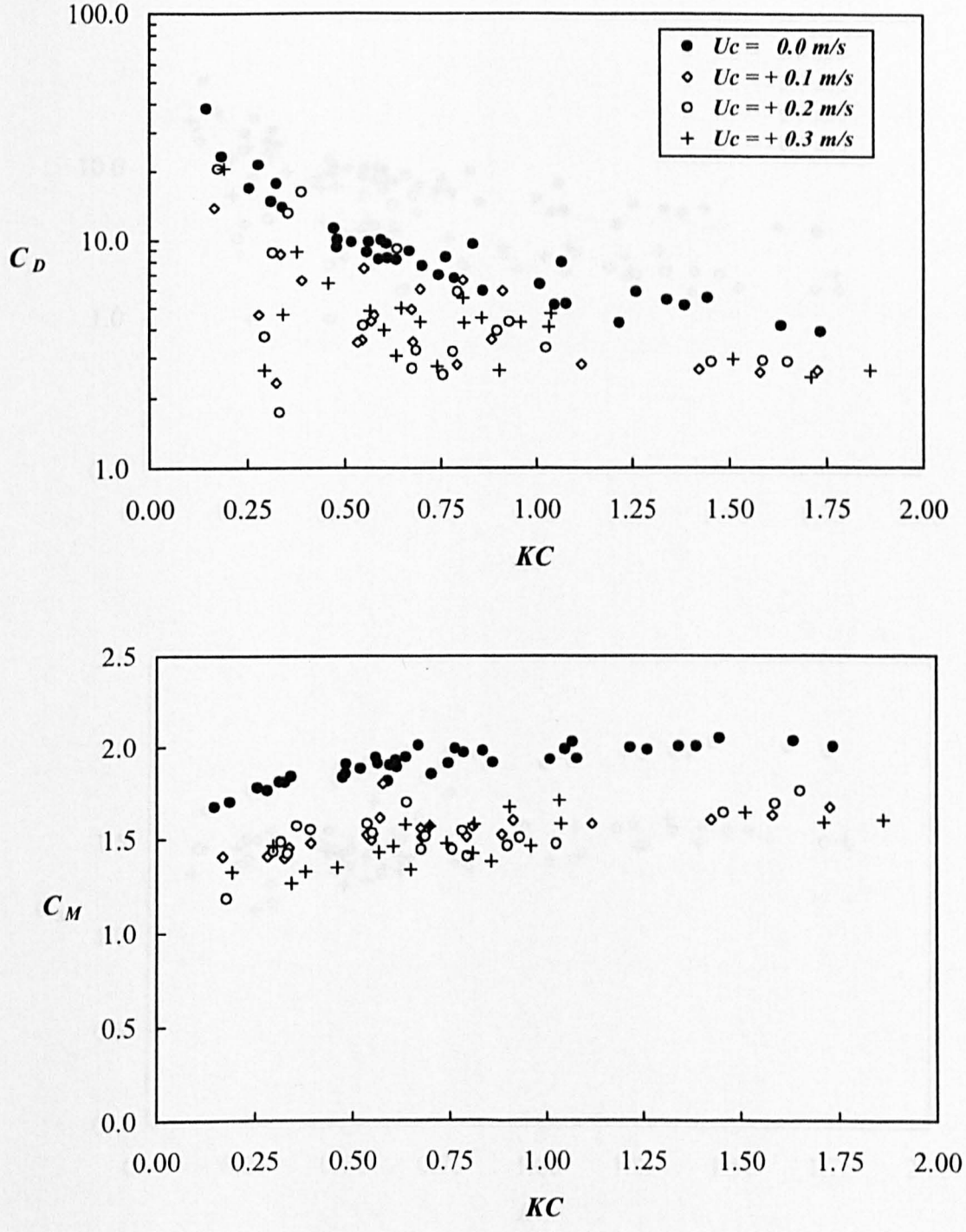

Fig. 6.113 Drag and inertia coefficients for rectangular cylinder in co-existing waves and currents for positive currents

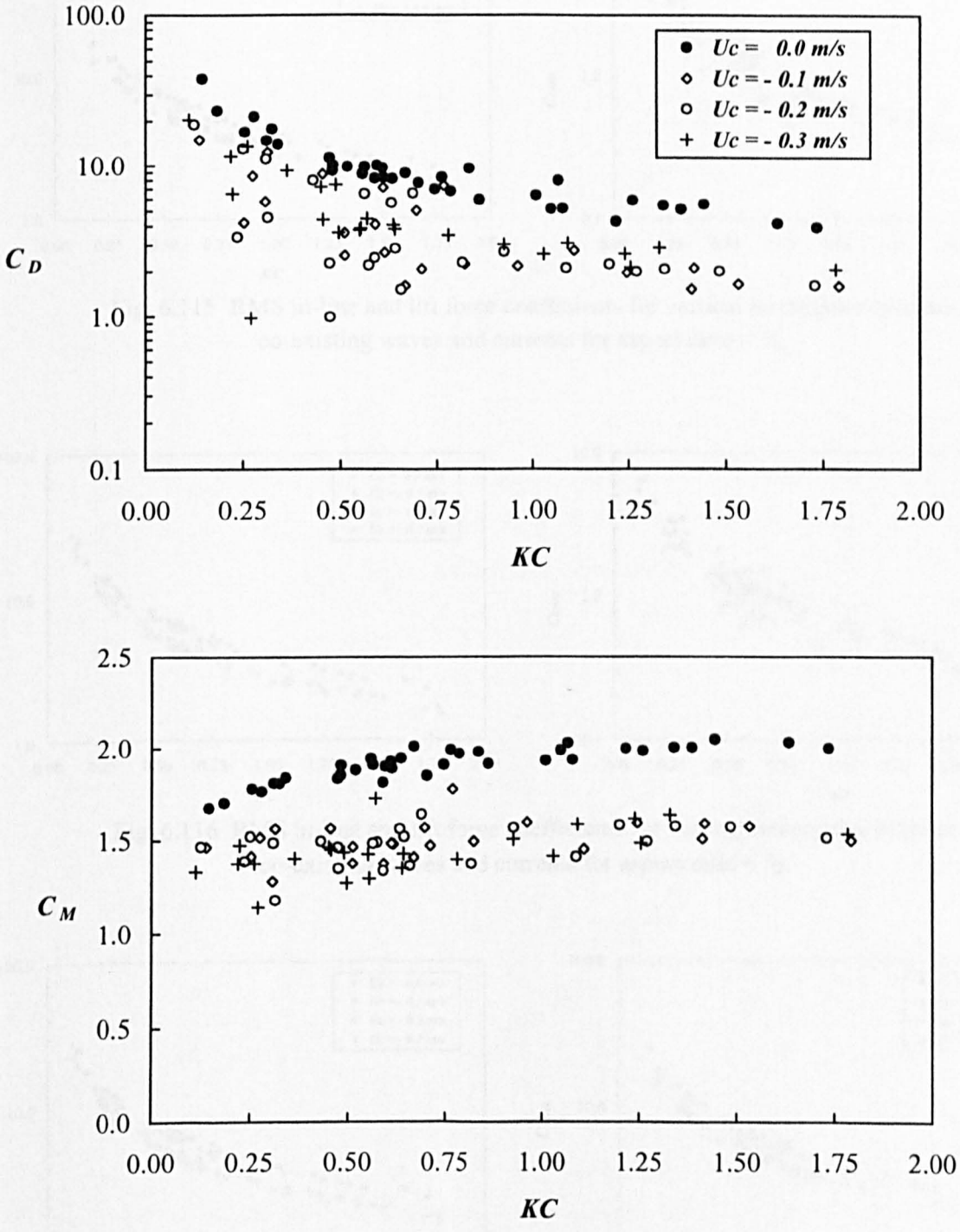

Fig. 6.114 Drag and inertia coefficients for rectangular cylinder in co-existing waves and currents for negative currents

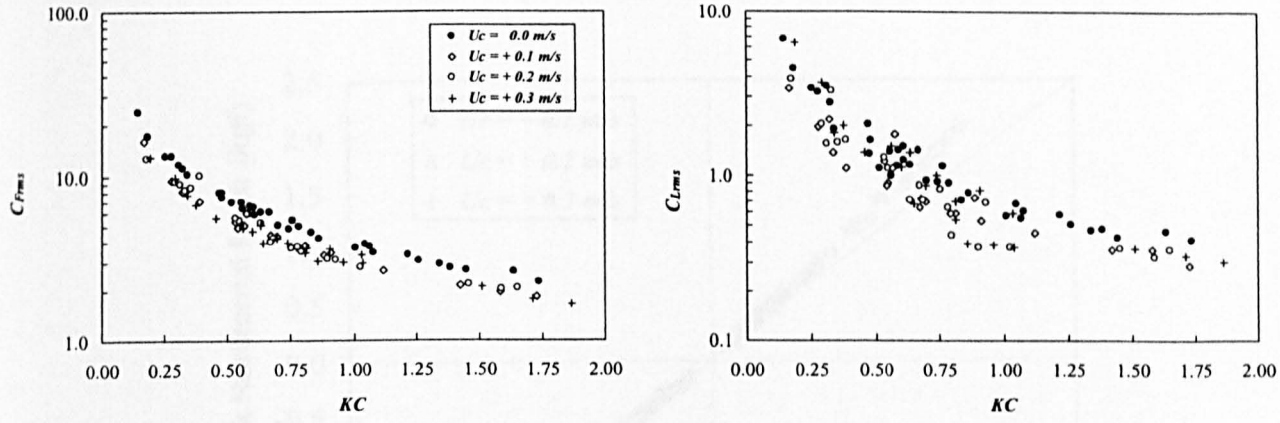

Fig. 6.115 RMS in-line and lift force coefficients for vertical rectangular cylinder in co-existing waves and currents for aspect ratio = ½.

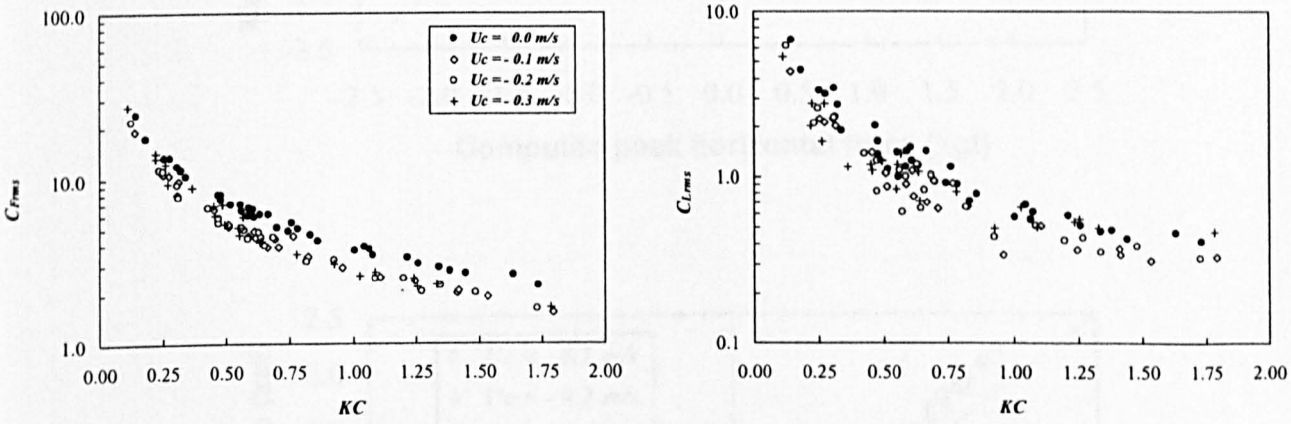

Fig. 6.116 RMS in-line and lift force coefficients for vertical rectangular cylinder in co-existing waves and currents for aspect ratio = ½.

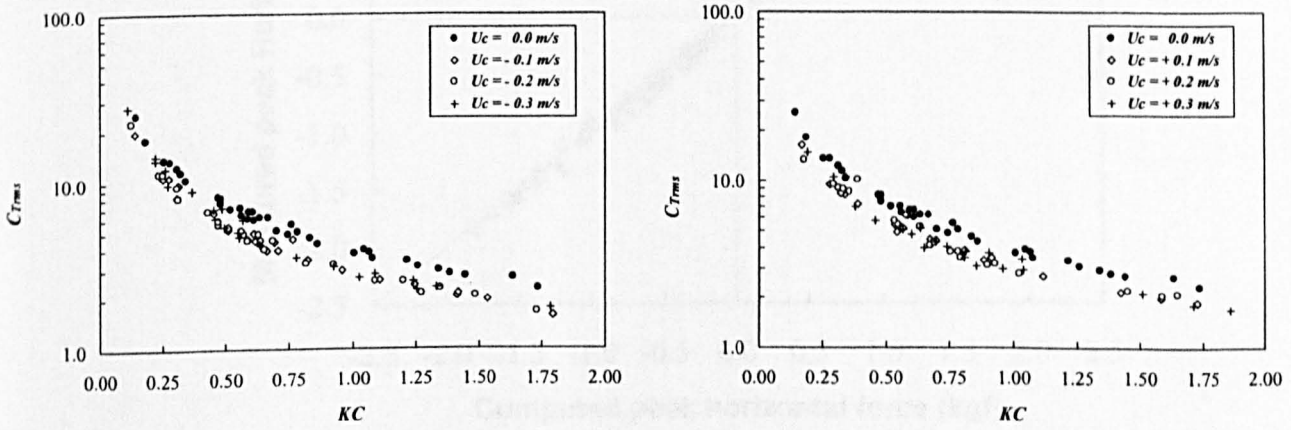

Fig. 6.117 RMS total force coefficients for vertical rectangular cylinder in co-existing waves and currents for aspect ratio = ½.

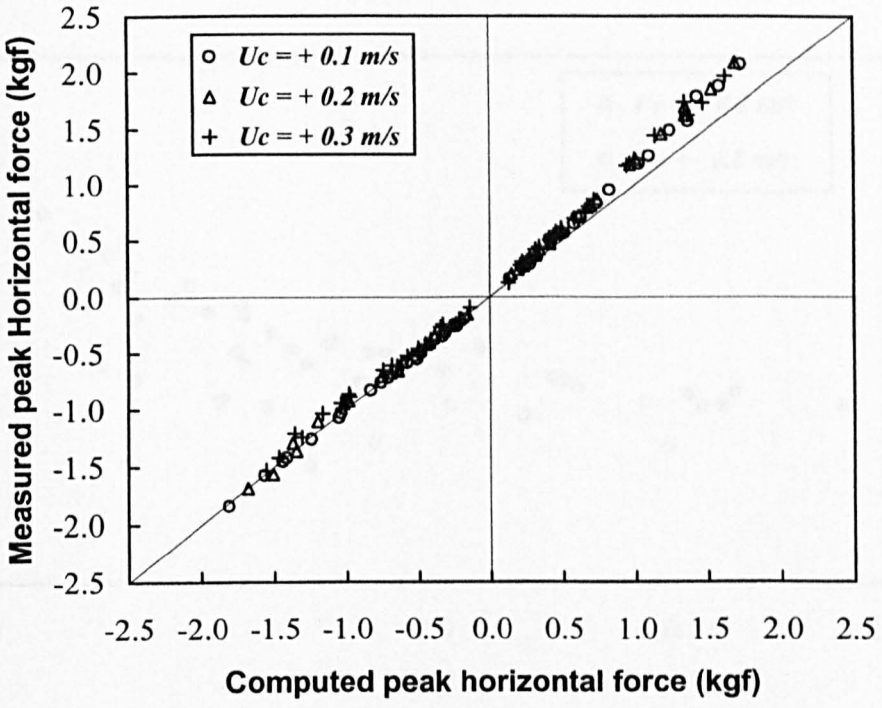

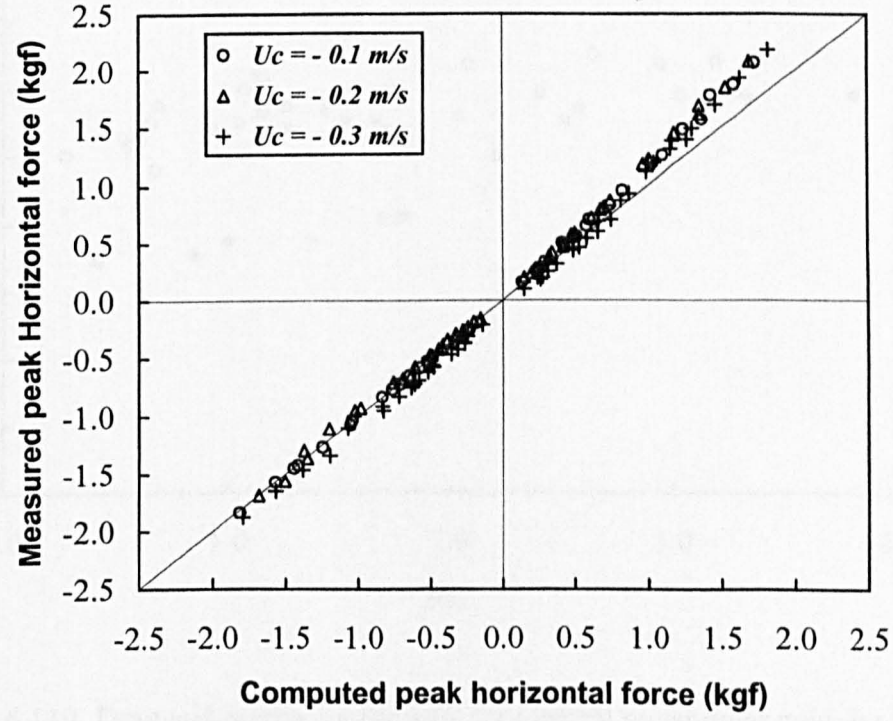

Fig. 6.118 Measured and computed peak forces for vertical rectangular cylinder for aspect ratio = 1/2 in co-existing waves and currents

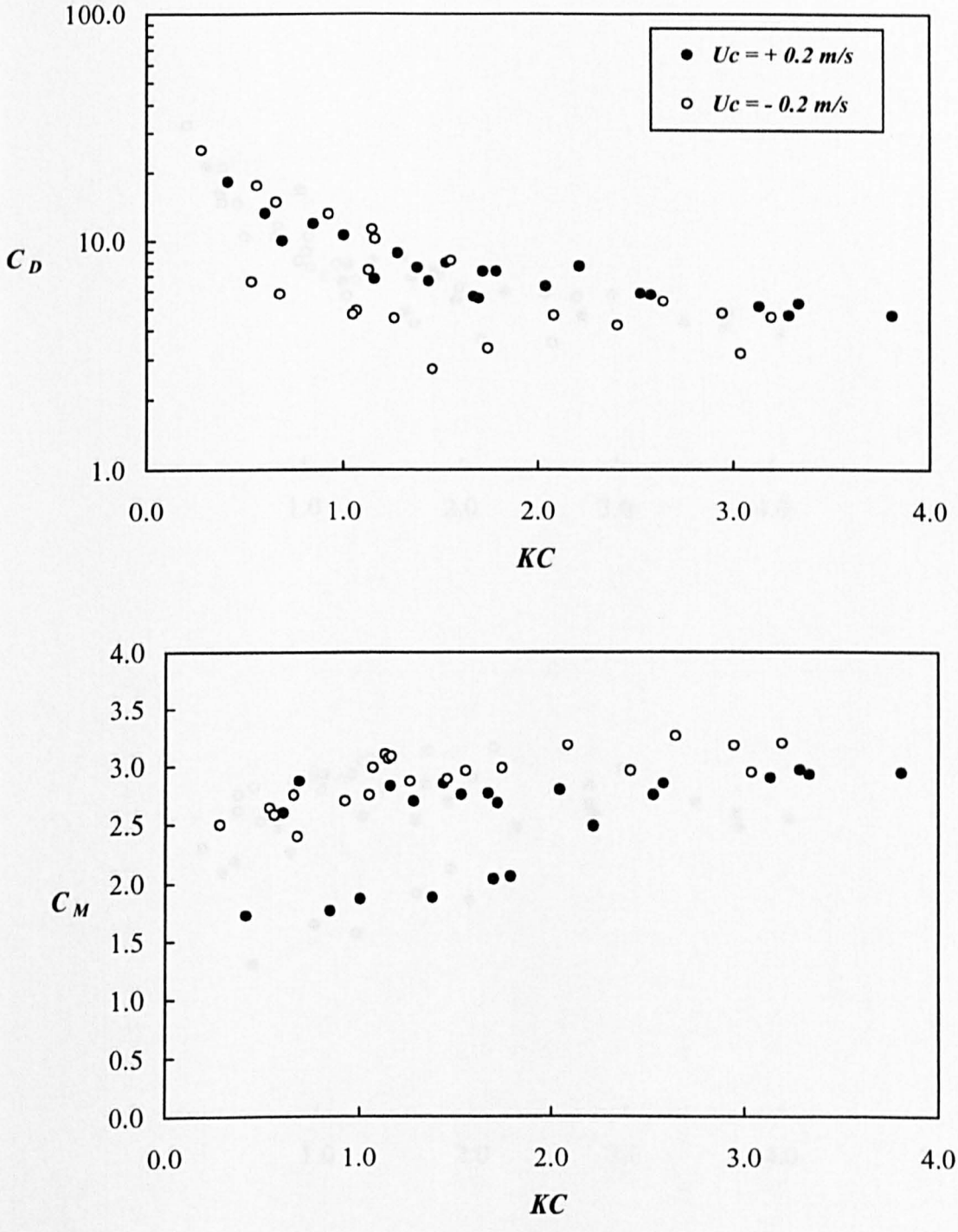

Fig. 6.119 Drag and inertia coefficients for vertical rectangular cylinder for aspect ratio = 2/1 in co-existing waves and currents for $U_C = \pm 0.2$ m/s

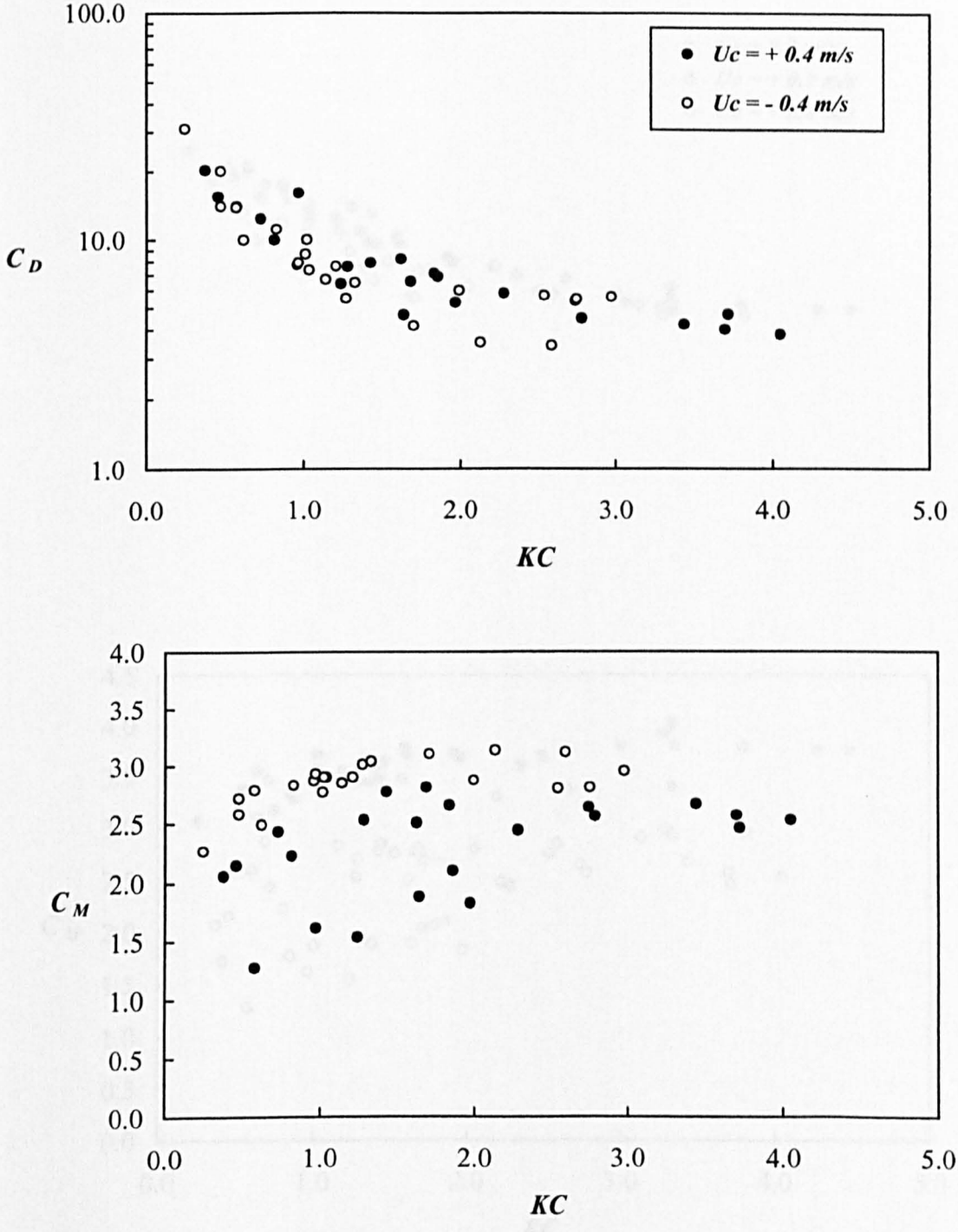

Fig. 6.120 Drag and inertia coefficients for vertical rectangular cylinder for aspect ratio = 2/1 in co-existing waves and currents for $U_C = \pm 0.4$ m/s

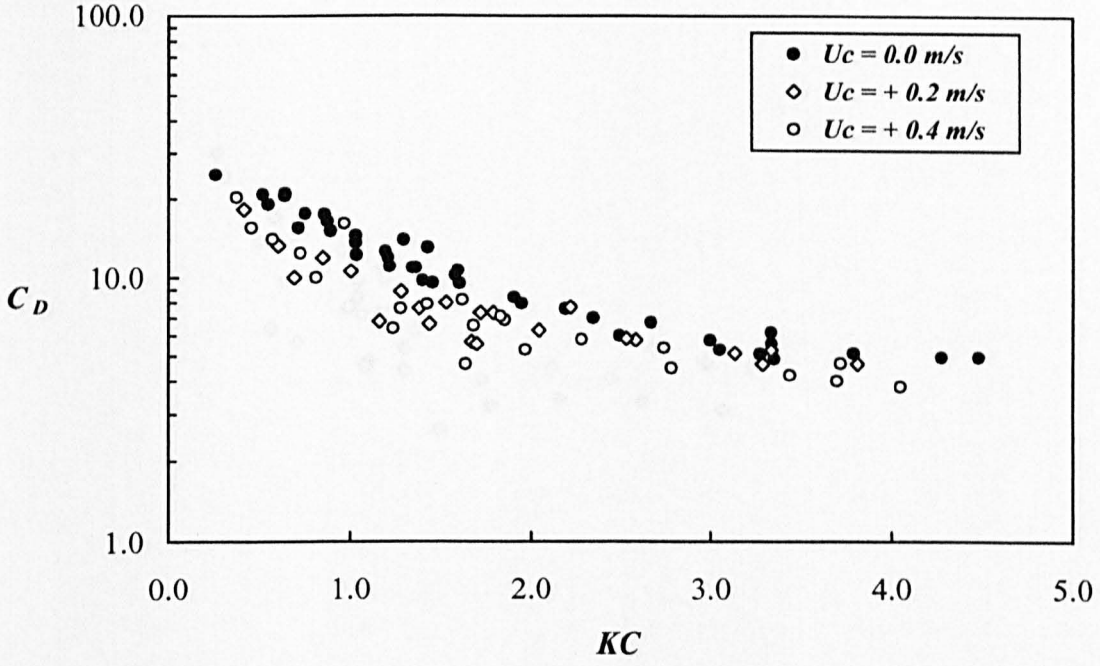

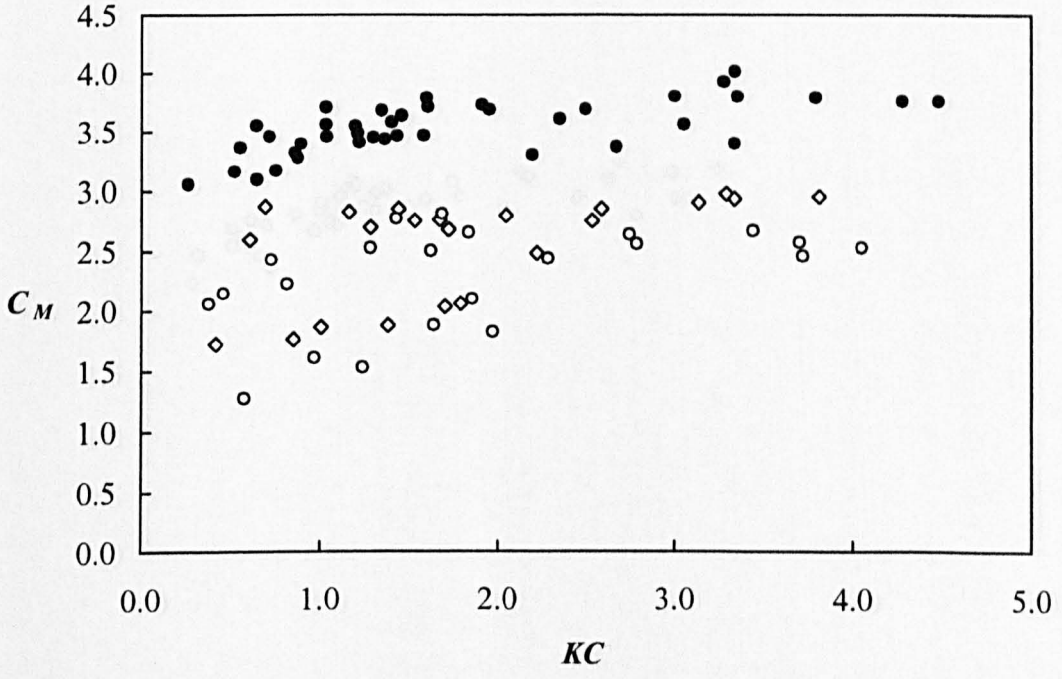

Fig. 6.121 Drag and inertia coefficients for rectangular cylinder with aspect ratio = 2/1 for positive currents

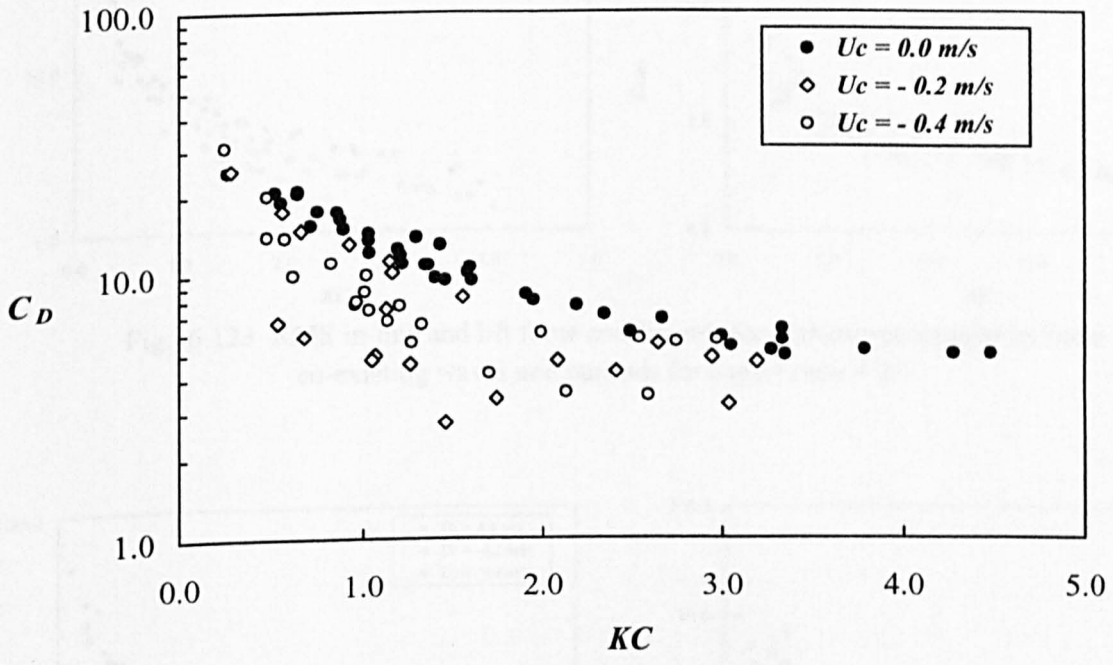

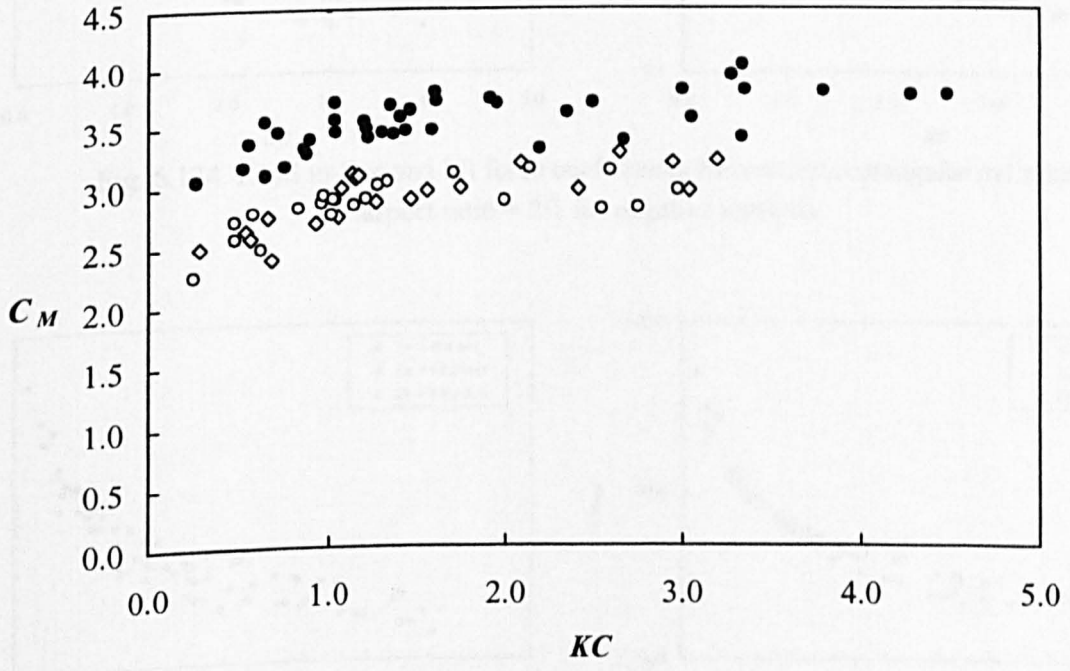

Fig. 6.122 Drag and inertia coefficients for rectangular cylinder with aspect ratio = 2/1 for negative currents

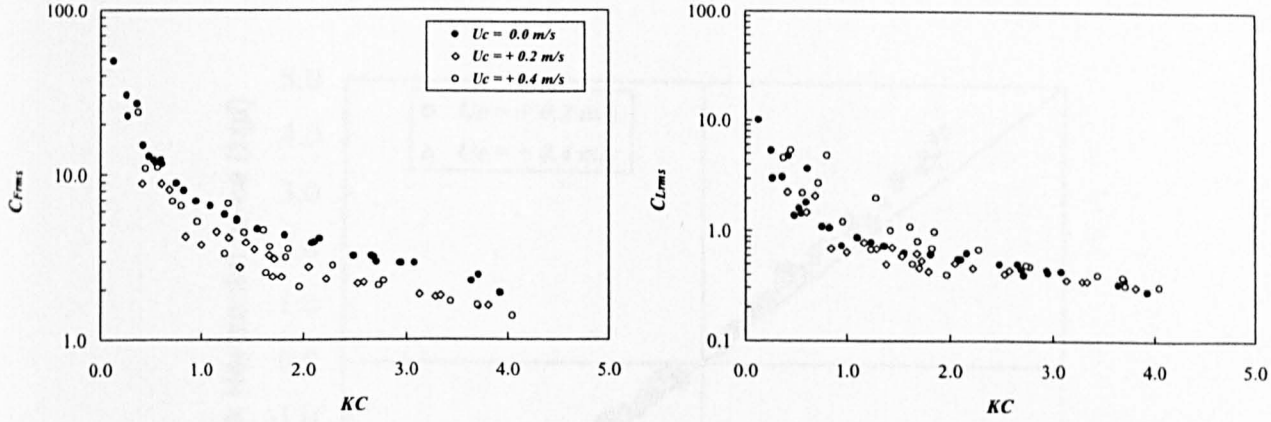

Fig. 6.123 RMS in-line and lift force coefficients for vertical rectangular cylinder in co-existing waves and currents for aspect ratio = 2/1

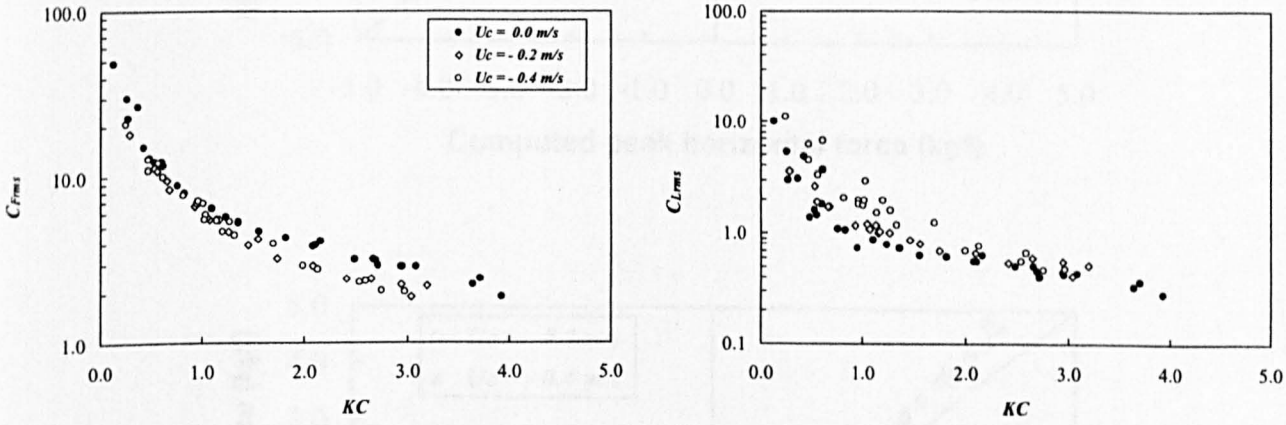

Fig. 6.124 RMS in-line and lift force coefficients for vertical rectangular cylinder with aspect ratio = 2/1 for negative currents

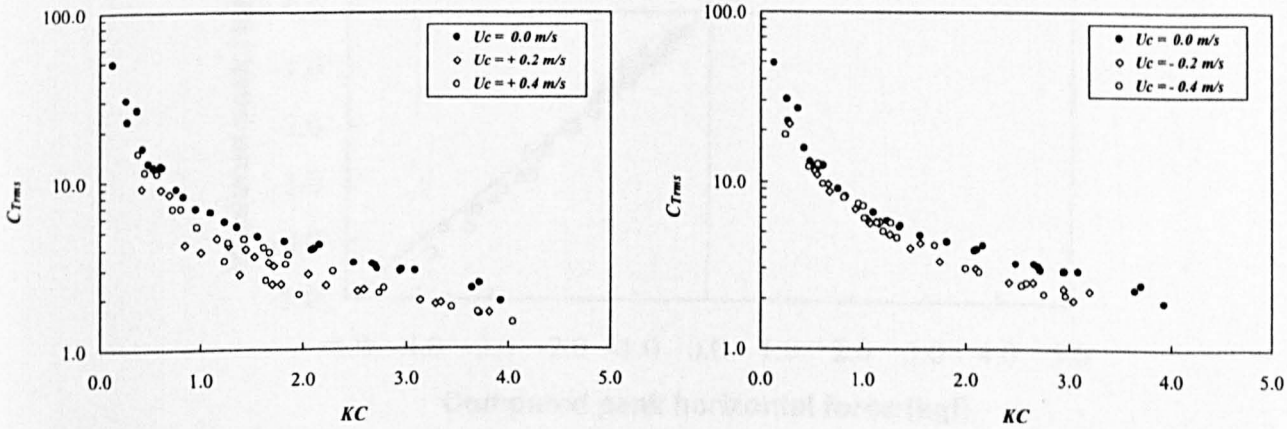

Fig. 6.125 RMS total force coefficients for vertical rectangular cylinder in co-existing waves and currents for aspect ratio = 2/1

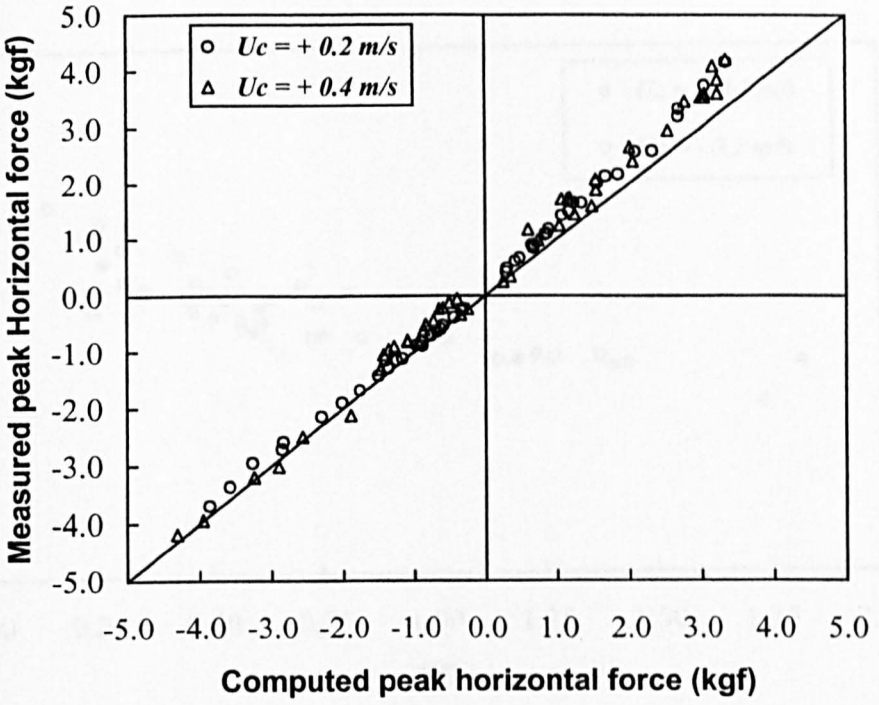

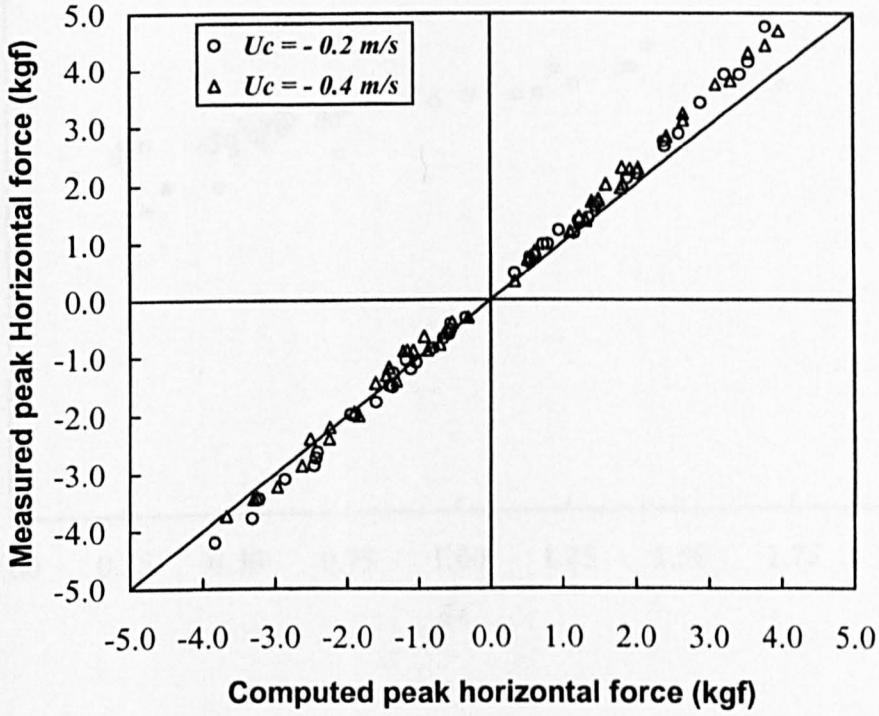

Fig. 6.126 Measured and computed peak forces for vertical rectangular cylinder for aspect ratio = 2/1 in co-existing waves and currents

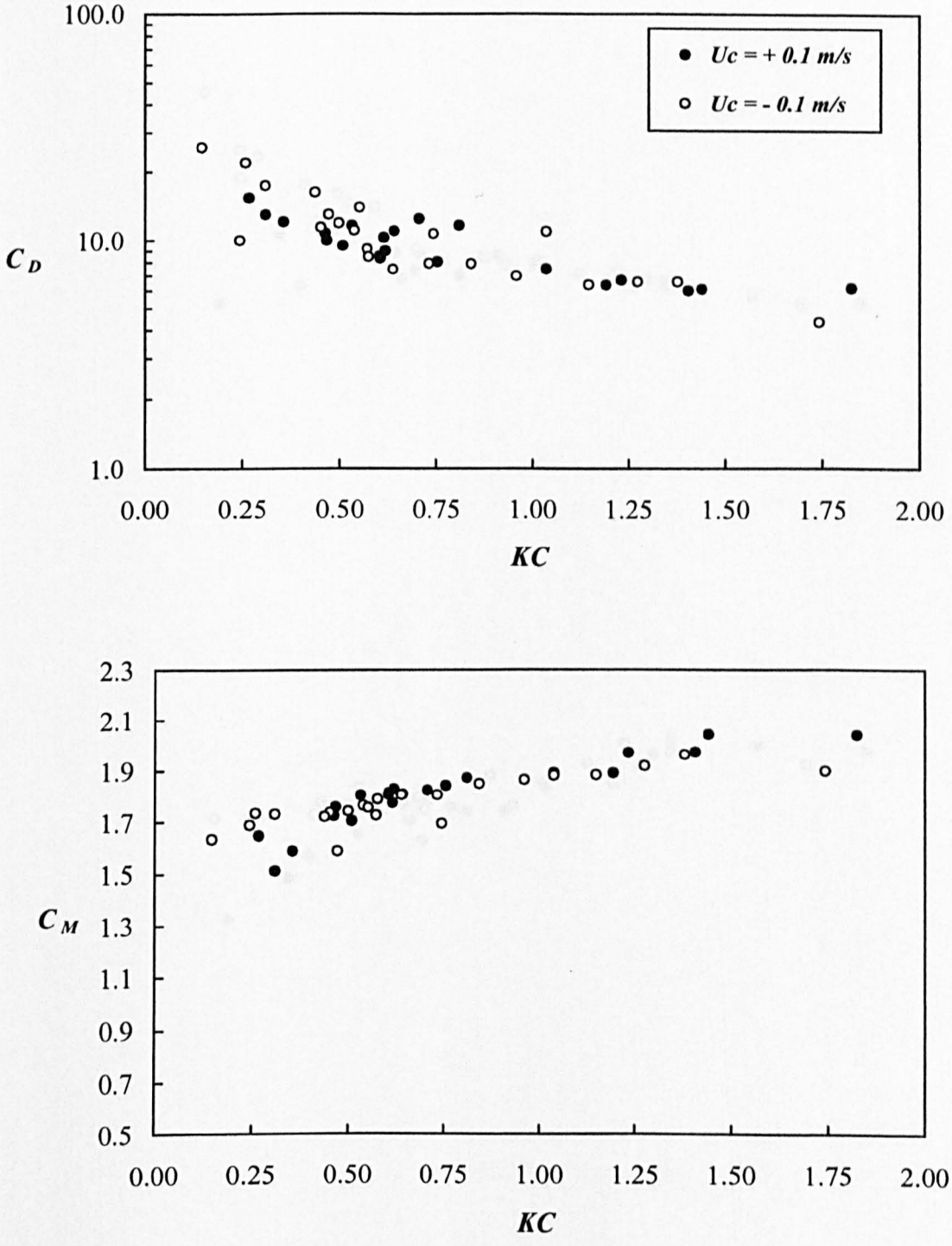

Fig. 6.127 Drag and inertia coefficients for vertical rectangular cylinder for aspect ratio = 3/4 in co-existing waves and currents for $U_C = \pm 0.1$ m/s

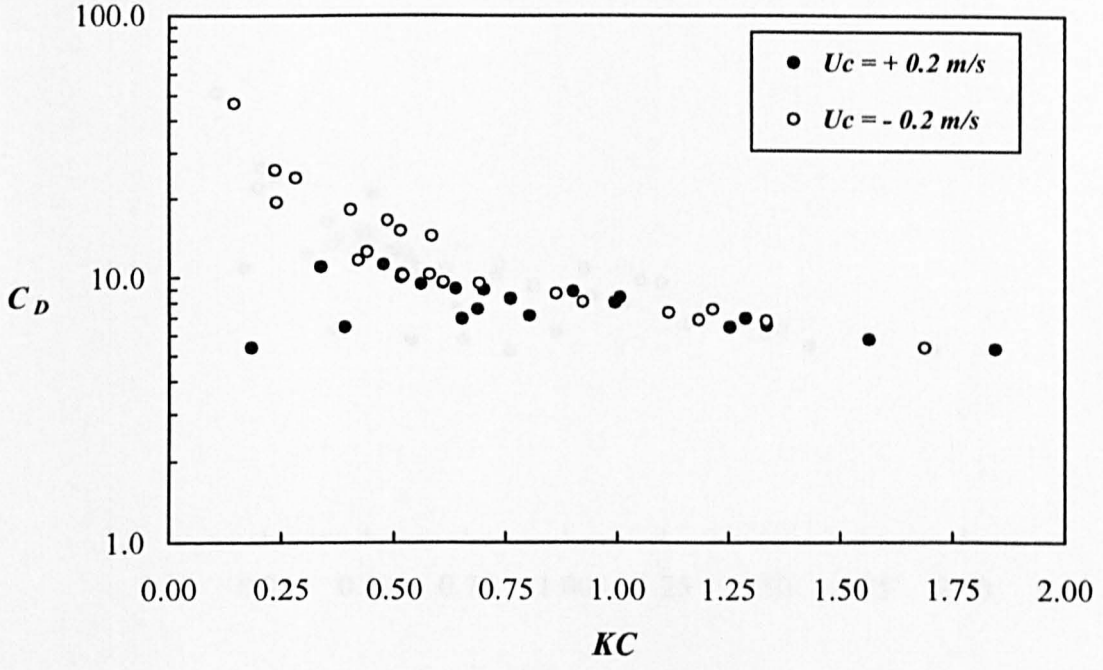

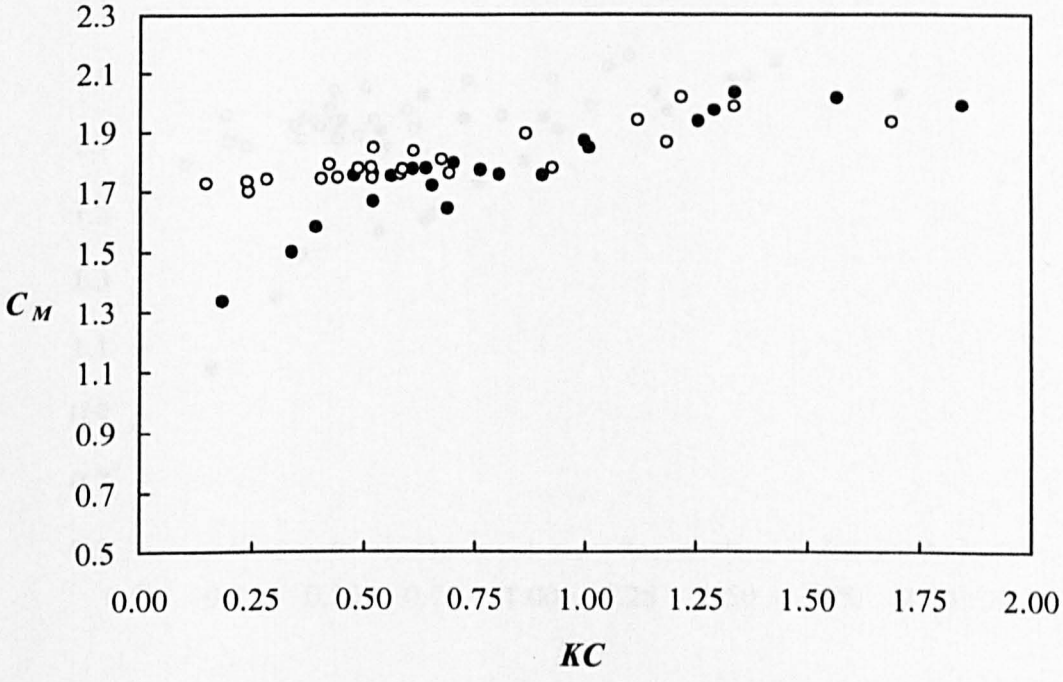

Fig. 6.128 Drag and inertia coefficients for vertical rectangular cylinder for aspect ratio = 3/4 in co-existing waves and currents for $U_C = \pm 0.2$ m/s

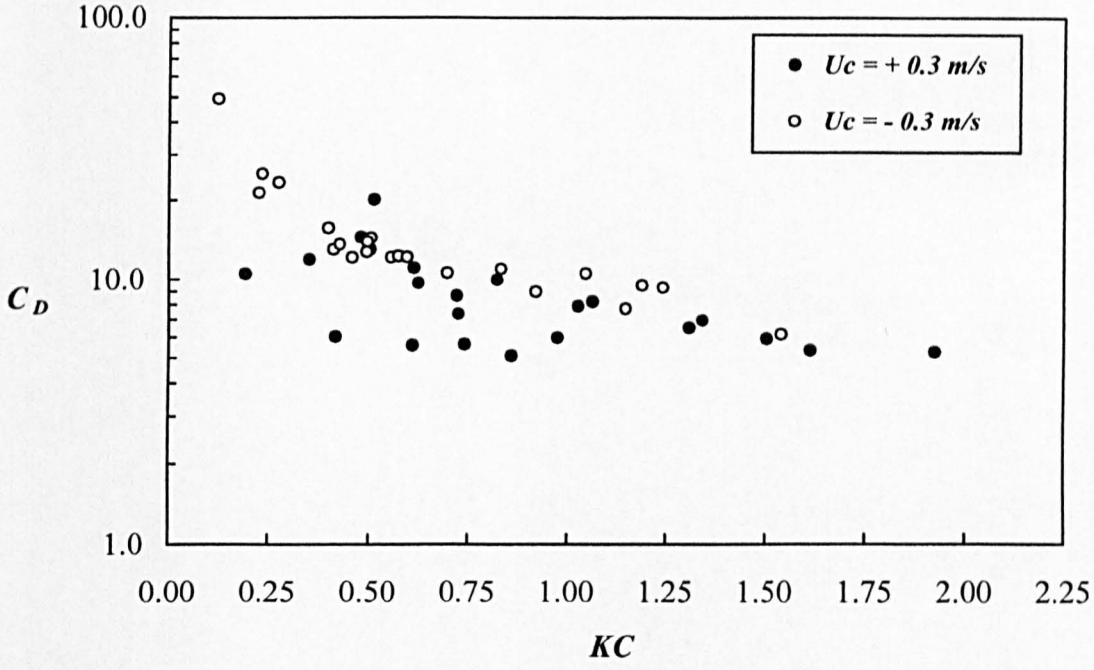

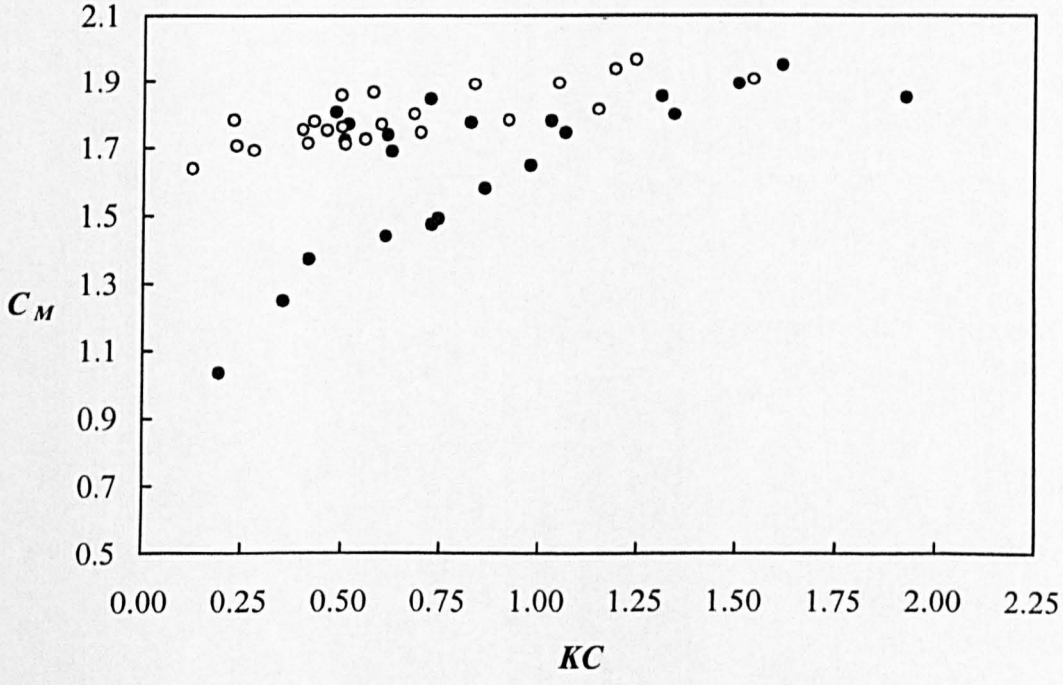

Fig. 6.129 Drag and inertia coefficients for vertical rectangular cylinder for aspect ratio = 3/4 in co-existing waves and currents for $U_C = \pm 0.3$ m/s

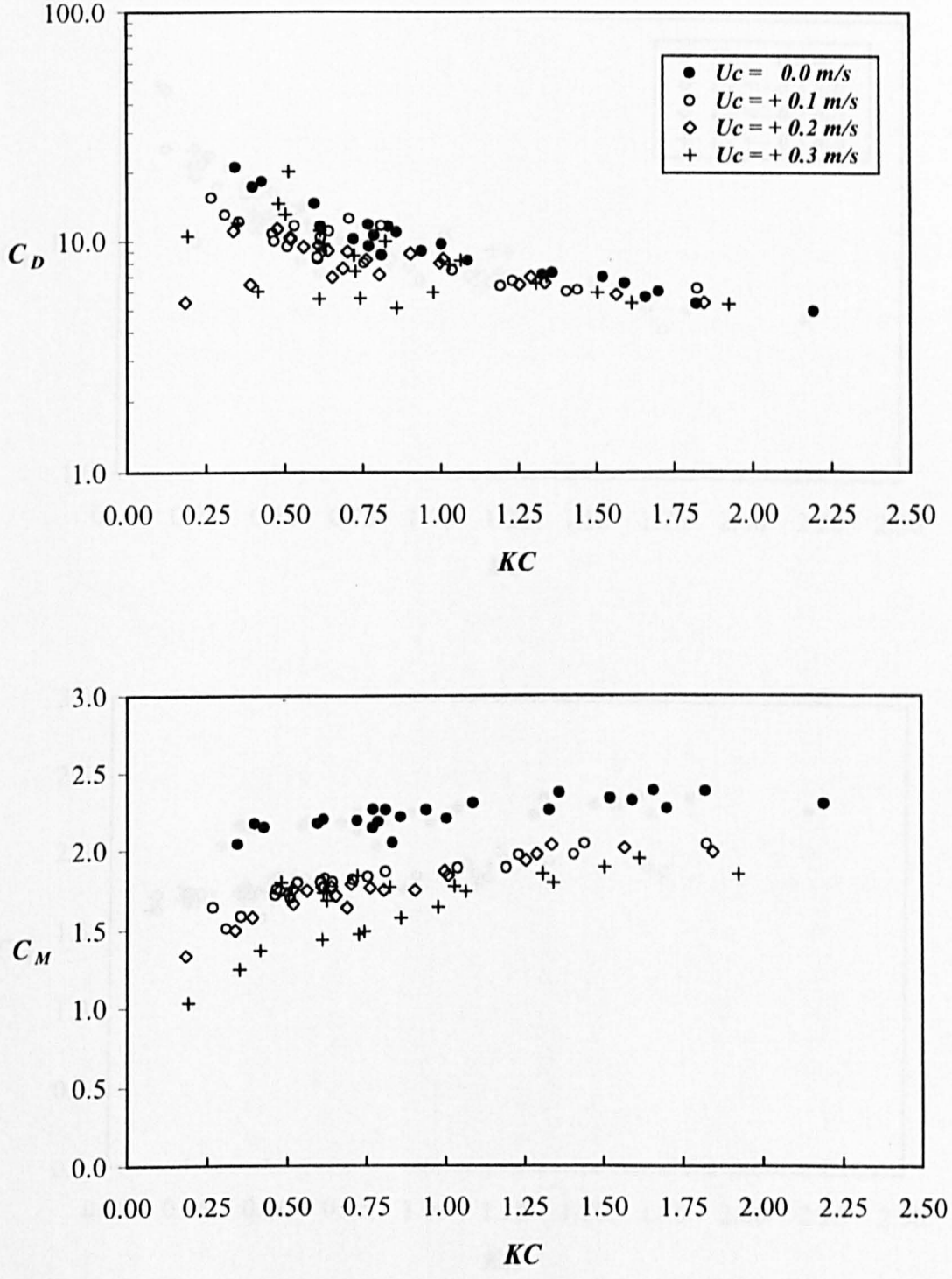

Fig. 6.130 Drag and inertia coefficients for vertical rectangular cylinder with aspect ratio = ¾ in waves and positive currents

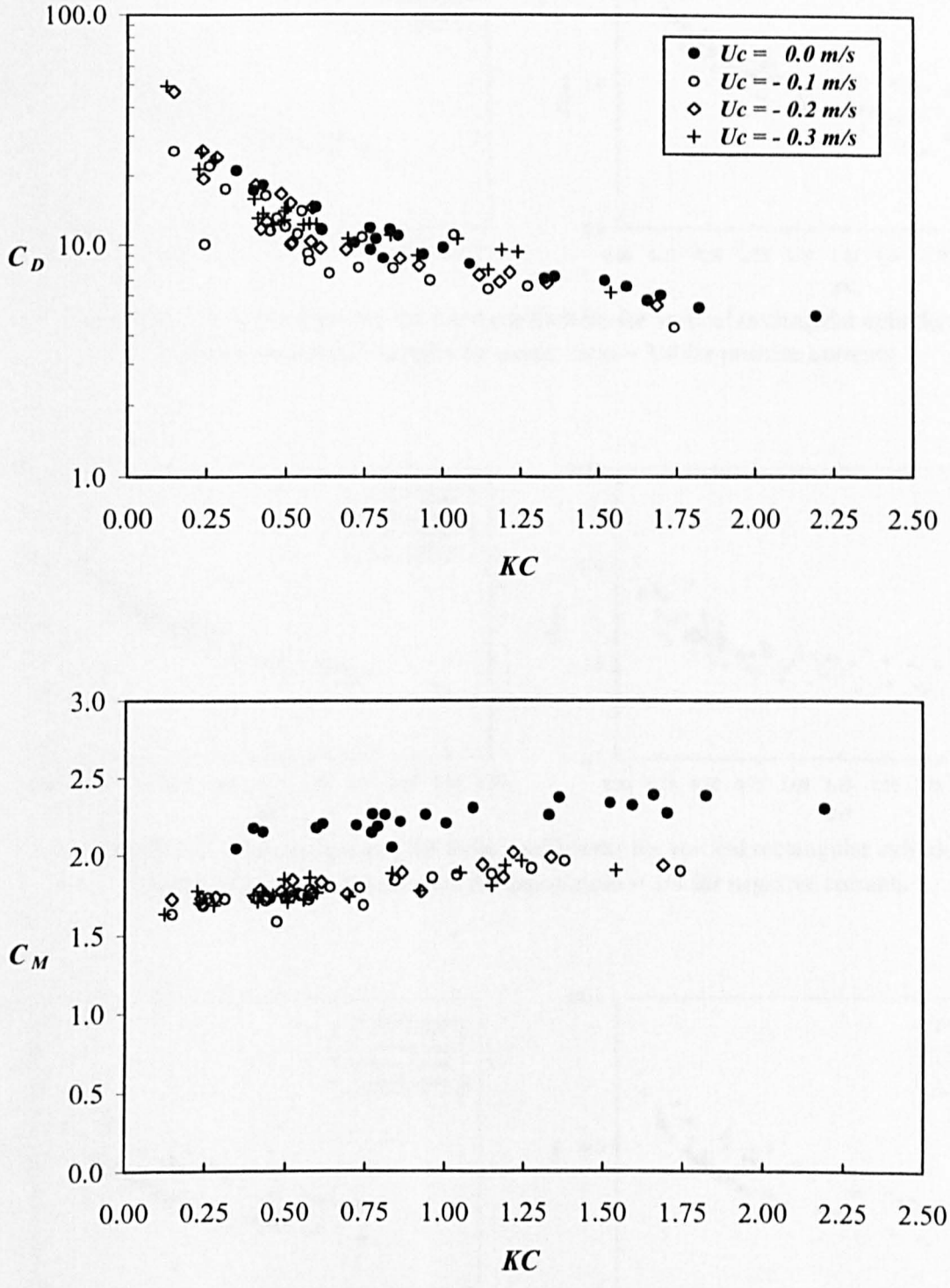

Fig. 6.131 Drag and inertia coefficients for vertical rectangular cylinder with aspect ratio = ¾ in waves and negative currents

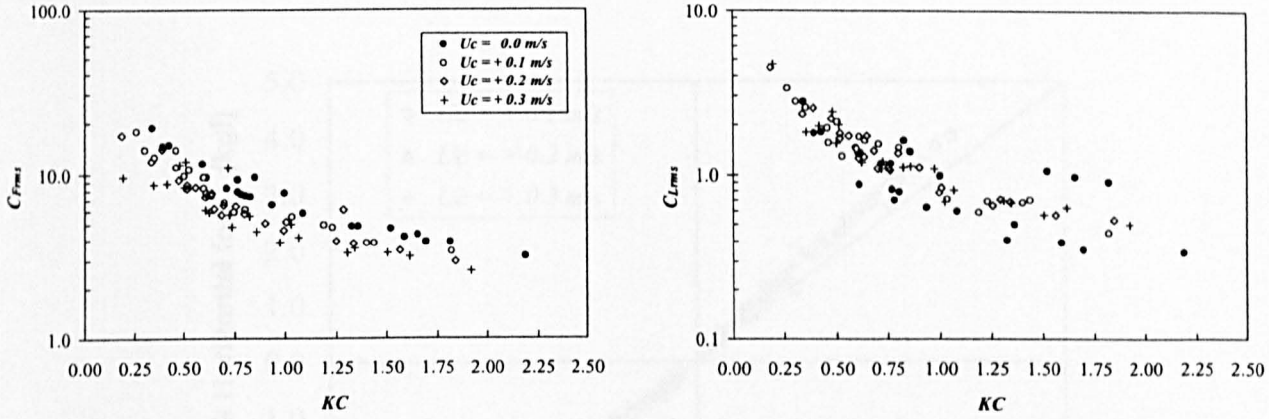

Fig. 6.132 RMS in-line and lift force coefficients for vertical rectangular cylinder in co-existing waves and currents for aspect ratio = 3/4 for positive currents

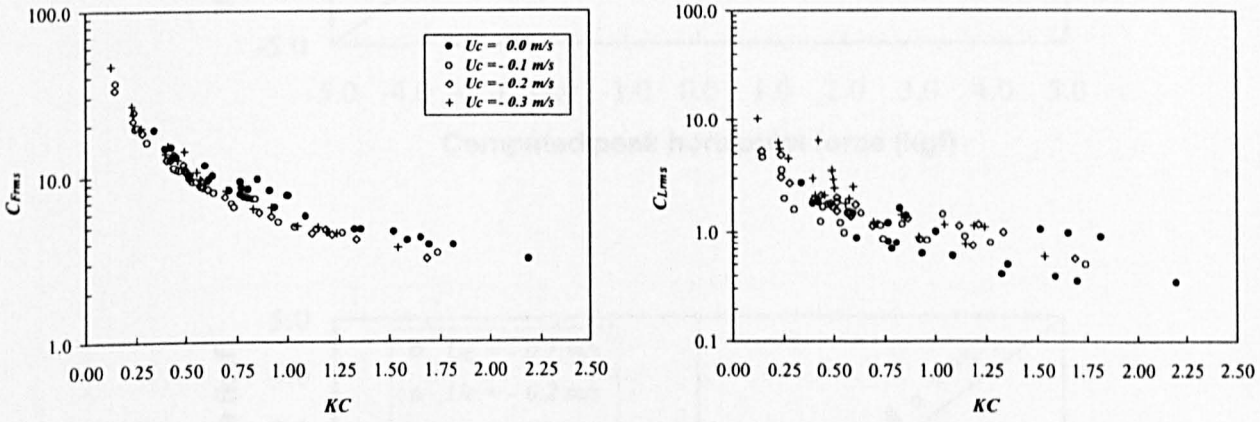

Fig. 6.133 RMS in-line and lift force coefficients for vertical rectangular cylinder in co-existing waves and currents for aspect ratio = 3/4 for negative currents

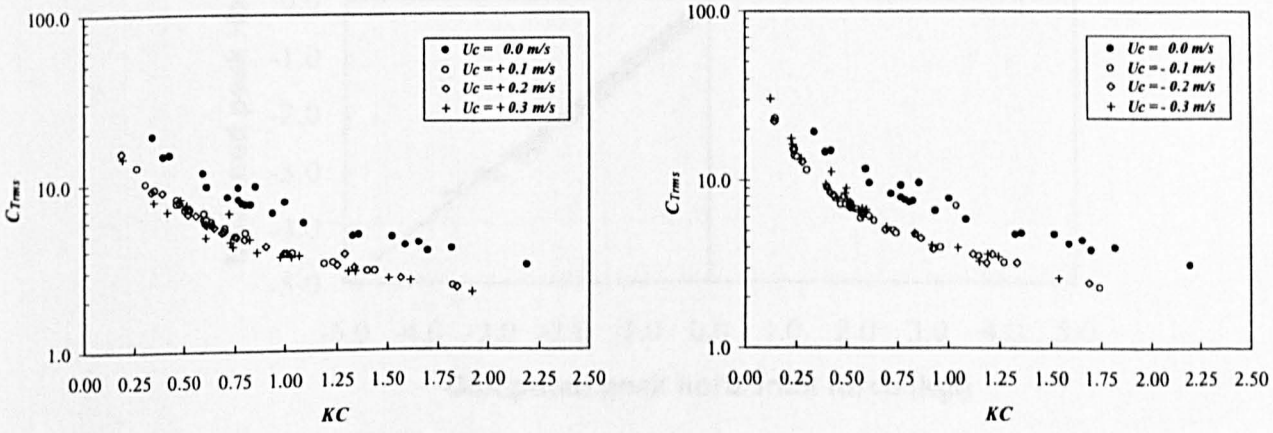

Fig. 6.134 RMS total force coefficients for vertical rectangular cylinder in co-existing waves and currents for aspect ratio = 3/4

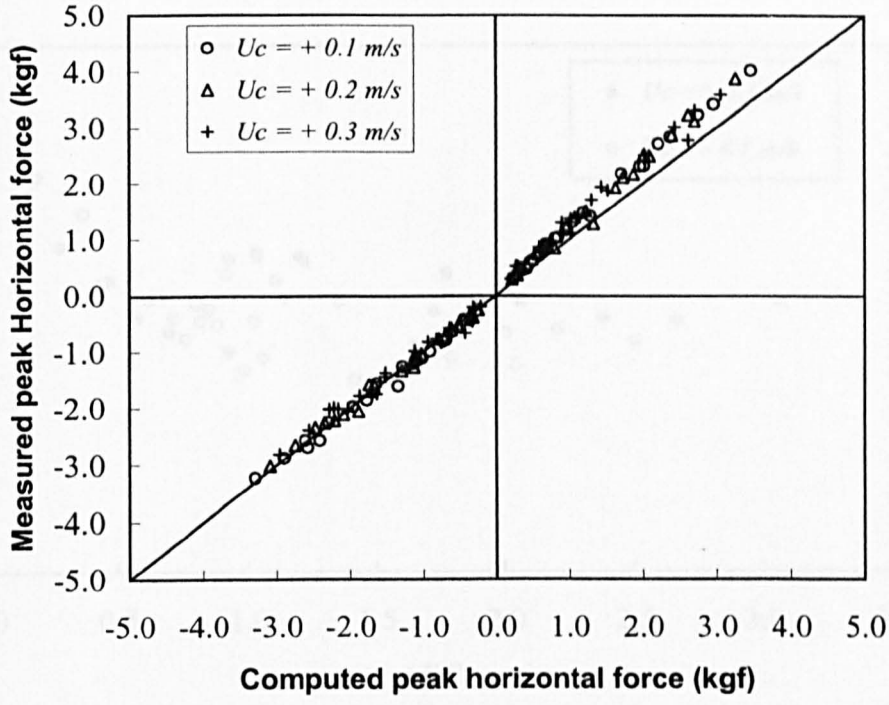

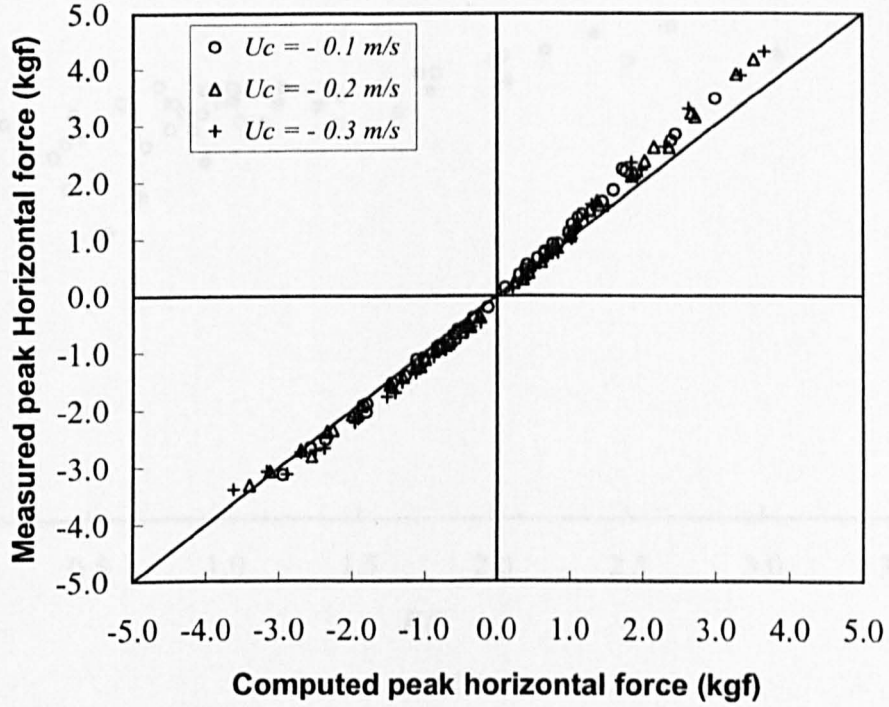

Fig. 6.135 Measured and computed peak forces for vertical rectangular cylinder for aspect ratio = 3/4 in co-existing waves and currents

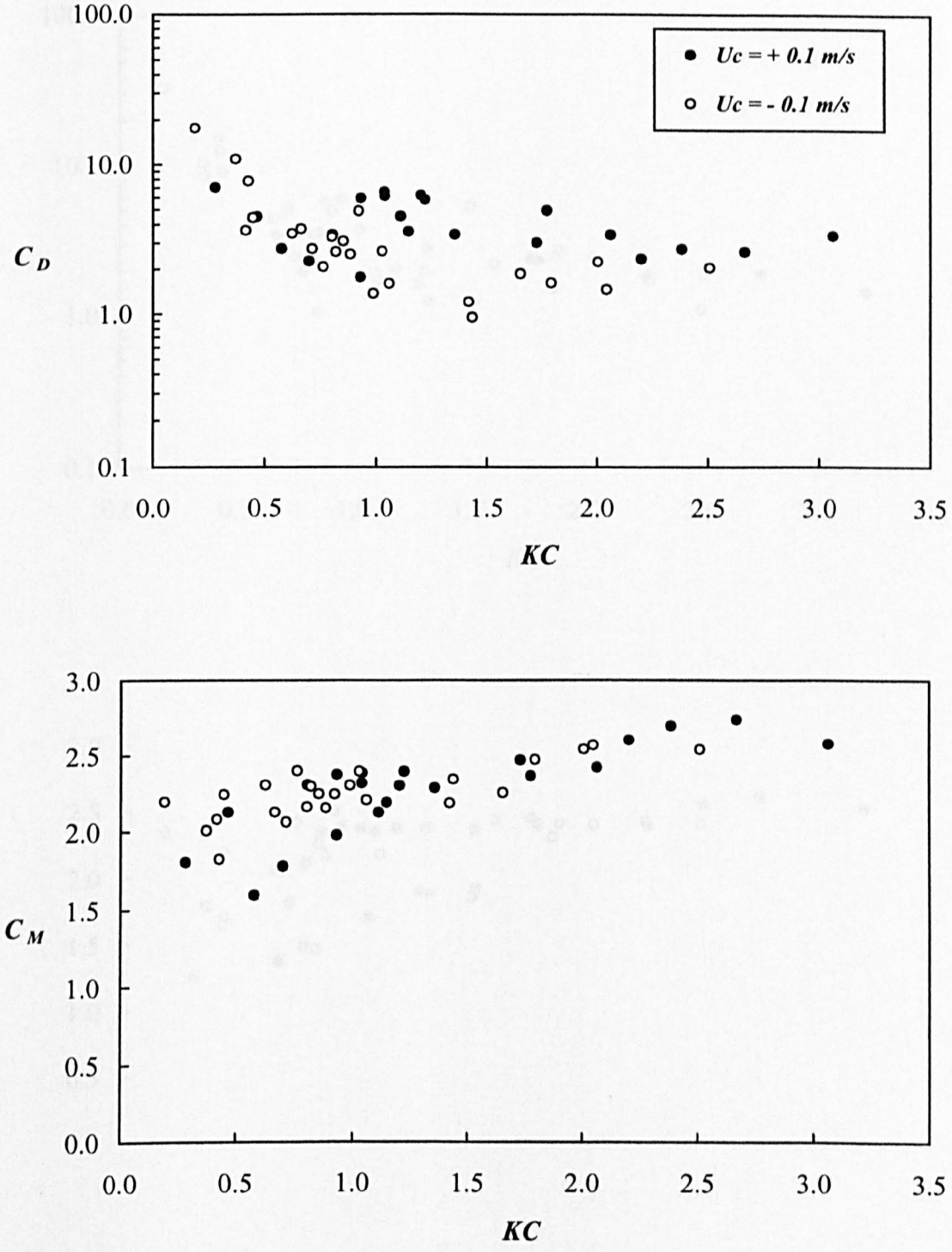

Fig. 6.136 Drag and inertia coefficients for vertical rectangular cylinder for aspect ratio = 4/3 in co-existing waves and currents for $U_C = \pm 0.1$ m/s

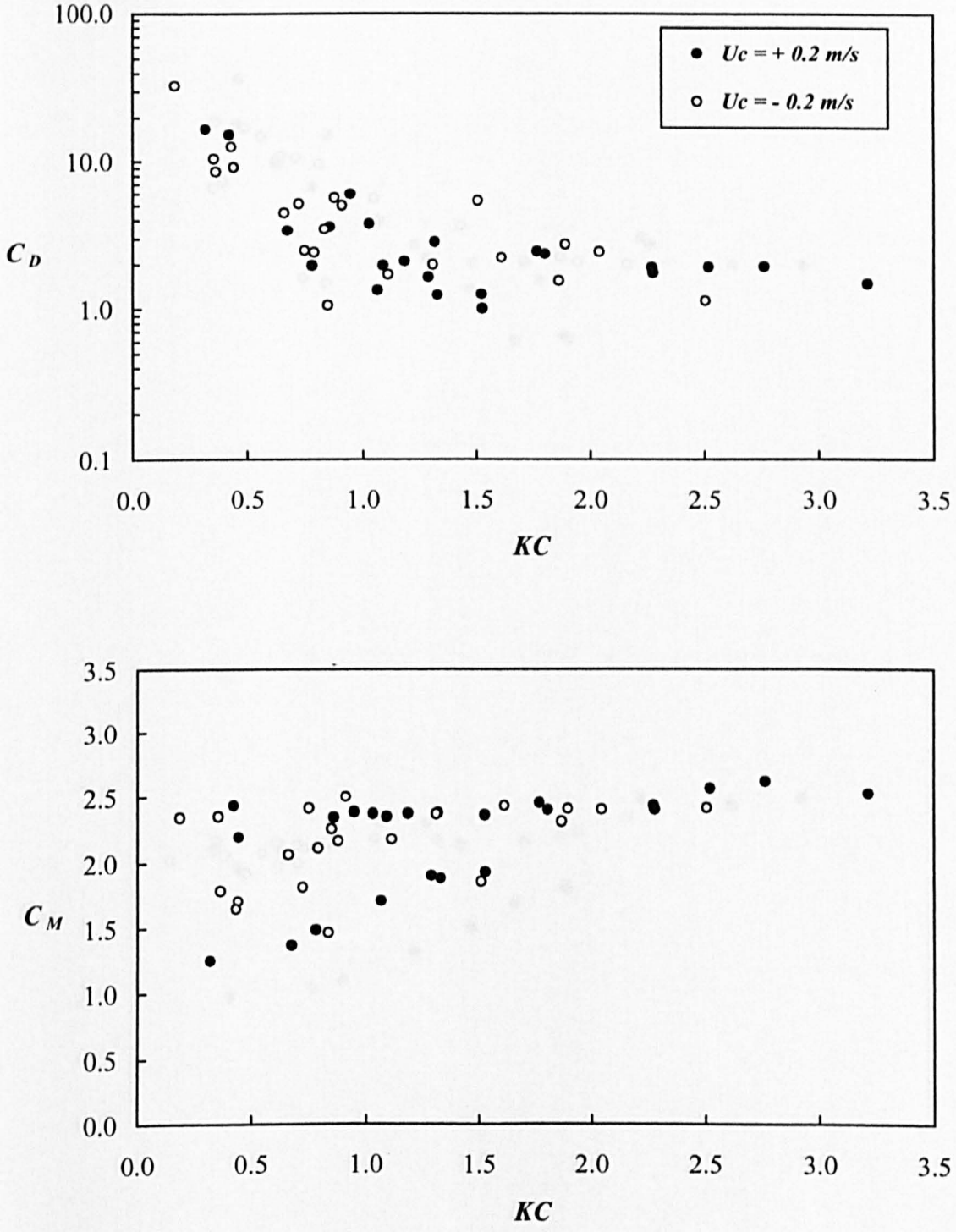

Fig. 6.137 Drag and inertia coefficients for vertical rectangular cylinder for aspect ratio = 4/3 in co-existing waves and currents for $U_C = \pm 0.2$ m/s

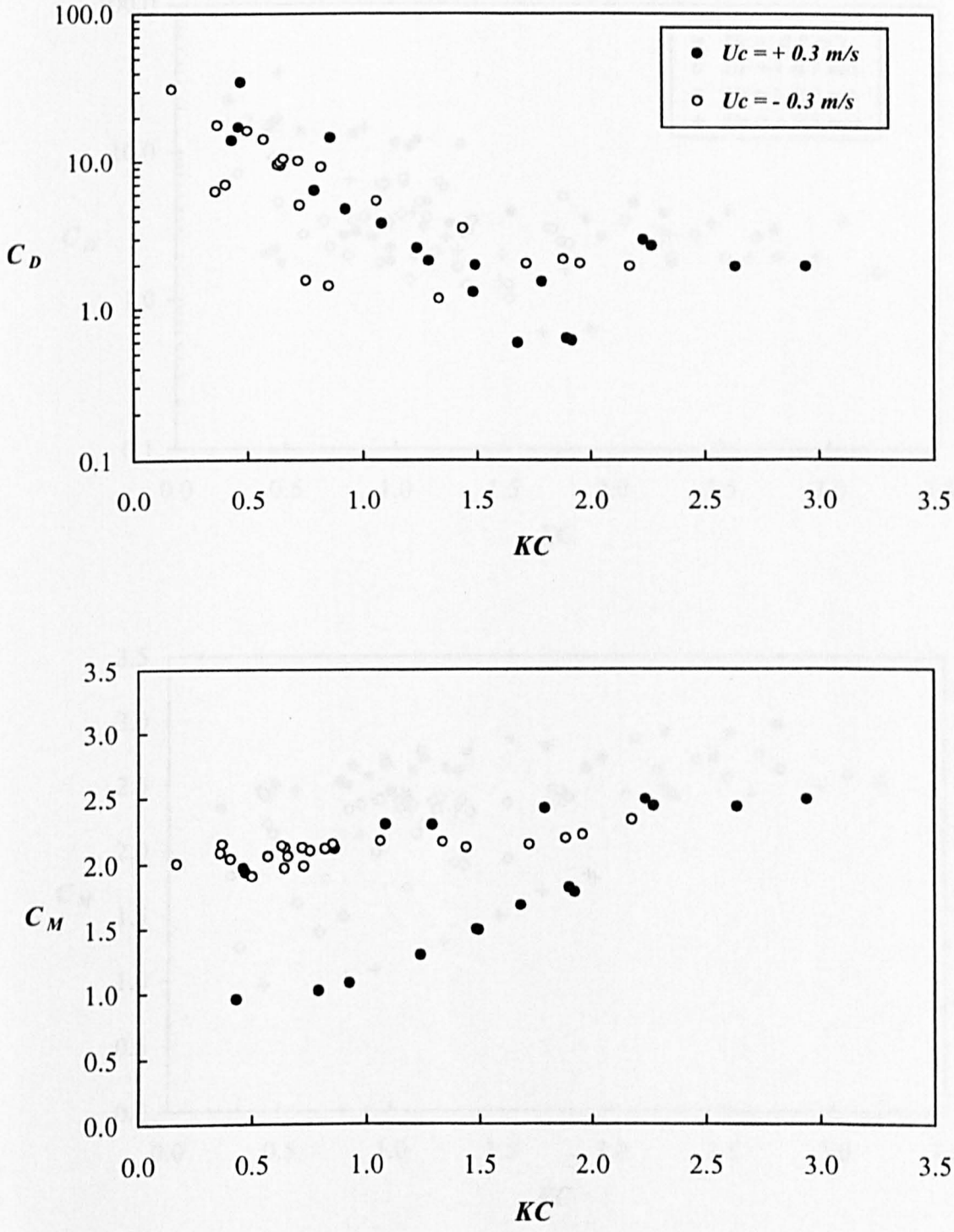

Fig. 6.138 Drag and inertia coefficients for vertical rectangular cylinder for aspect ratio = 4/3 in co-existing waves and currents for $U_C = \pm 0.3$ m/s

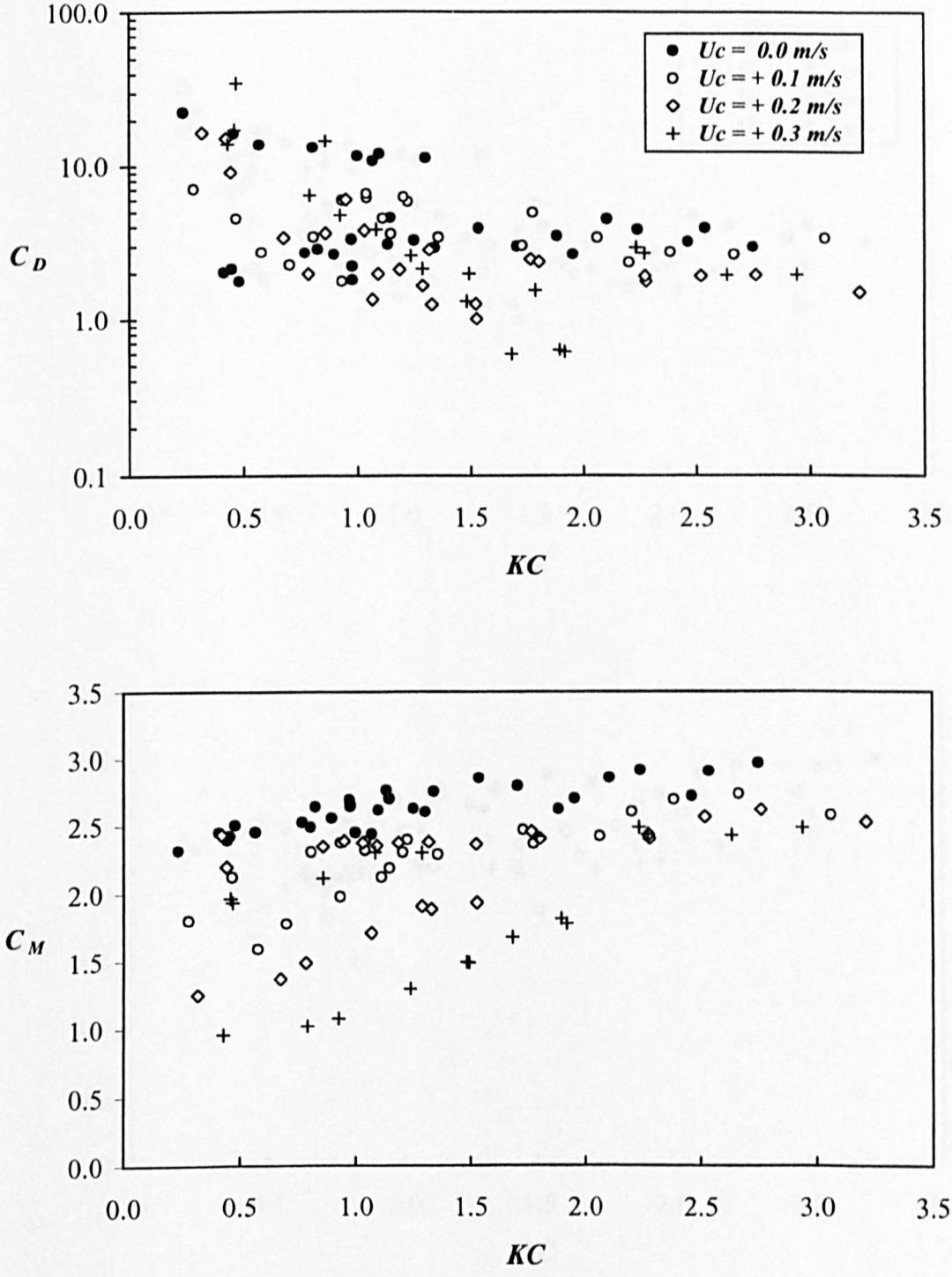

Fig. 6.139 Drag and inertia coefficients for vertical rectangular cylinder with aspect ratio =4/3 in waves and positive currents

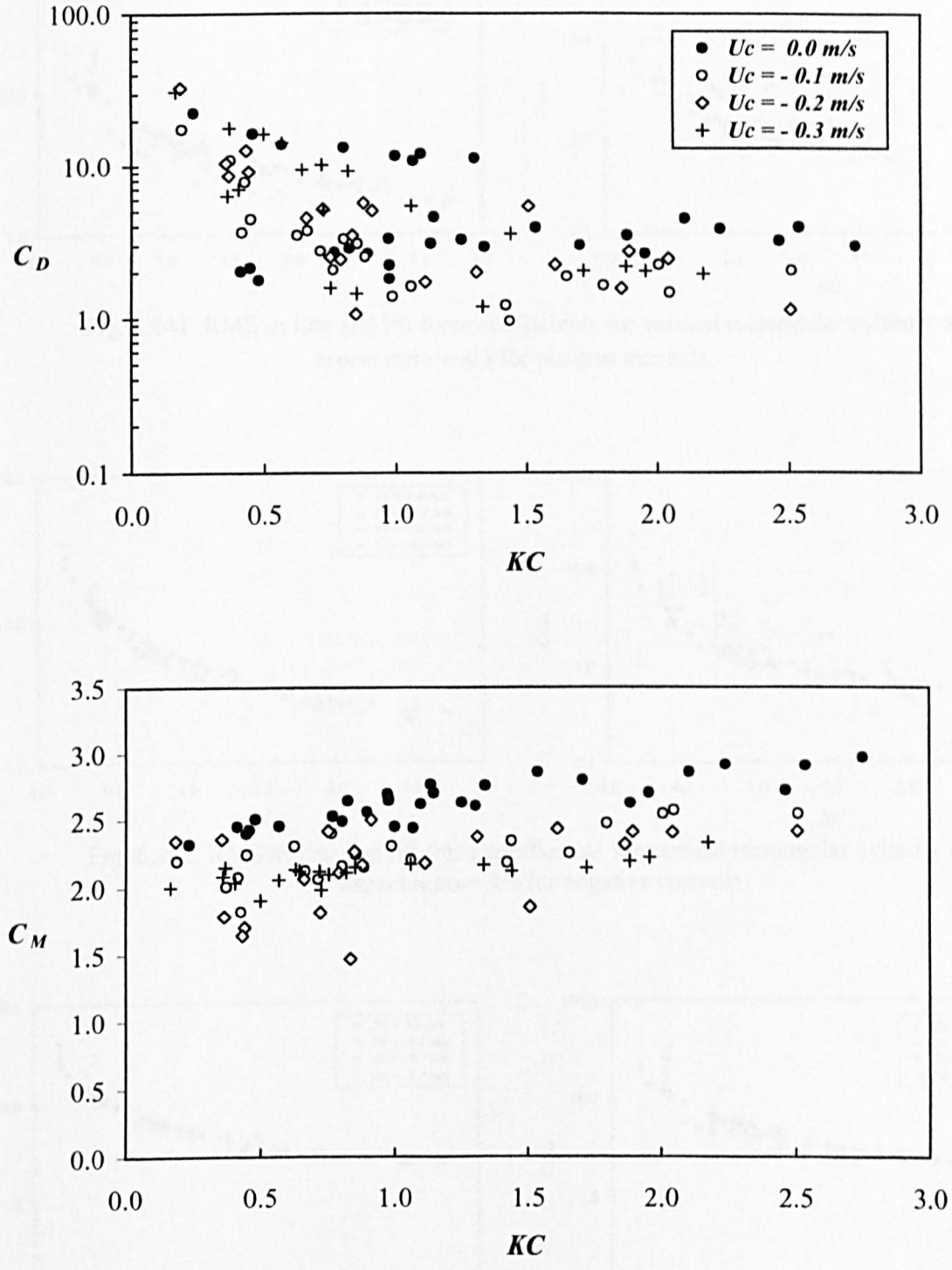

Fig. 6.140 Drag and inertia coefficients for vertical rectangular cylinder with aspect ratio 4/3 in waves and negative currents

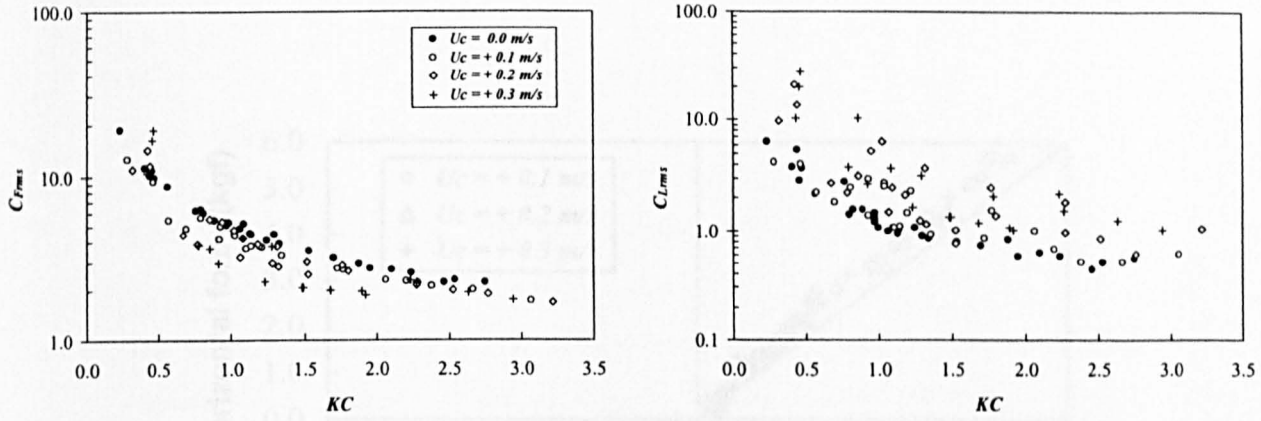

Fig. 6.141 RMS in-line and lift force coefficients for vertical rectangular cylinder with aspect ratio = 4/3 for positive currents

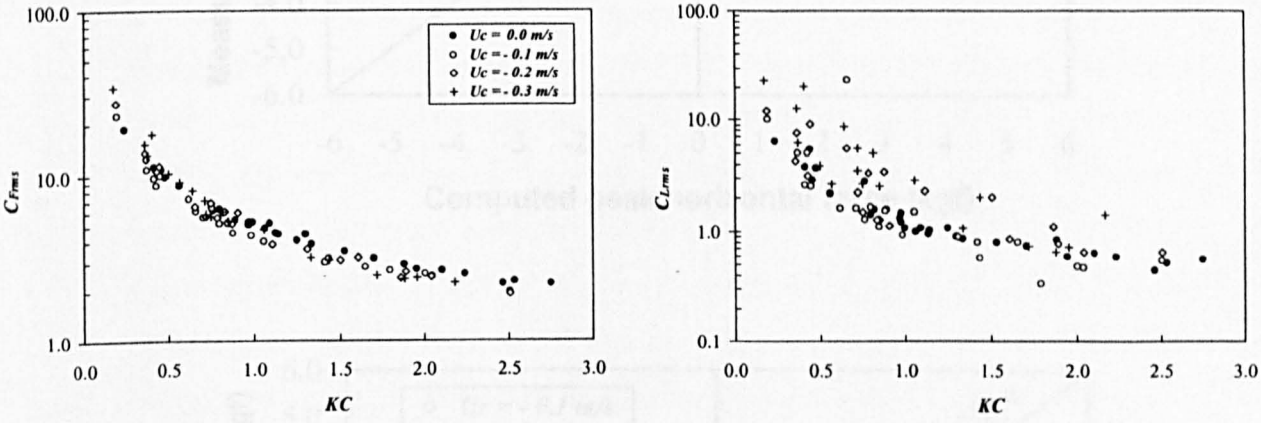

Fig. 6.142 RMS in-line and lift force coefficients for vertical rectangular cylinder with aspect ratio = 4/3 for negative currents

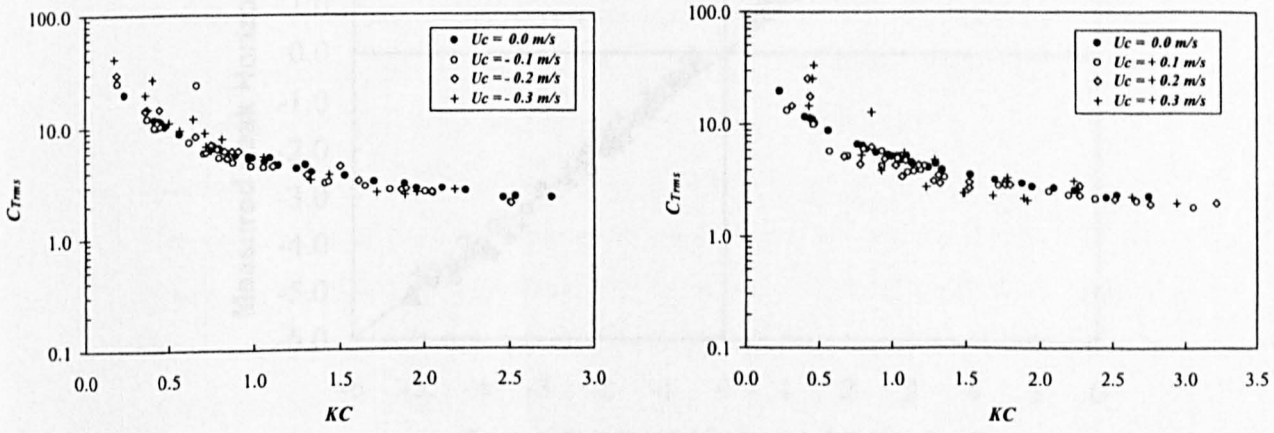

Fig. 6.143 RMS total force coefficients for vertical rectangular cylinder in co-existing waves and currents for aspect ratio = 4/3

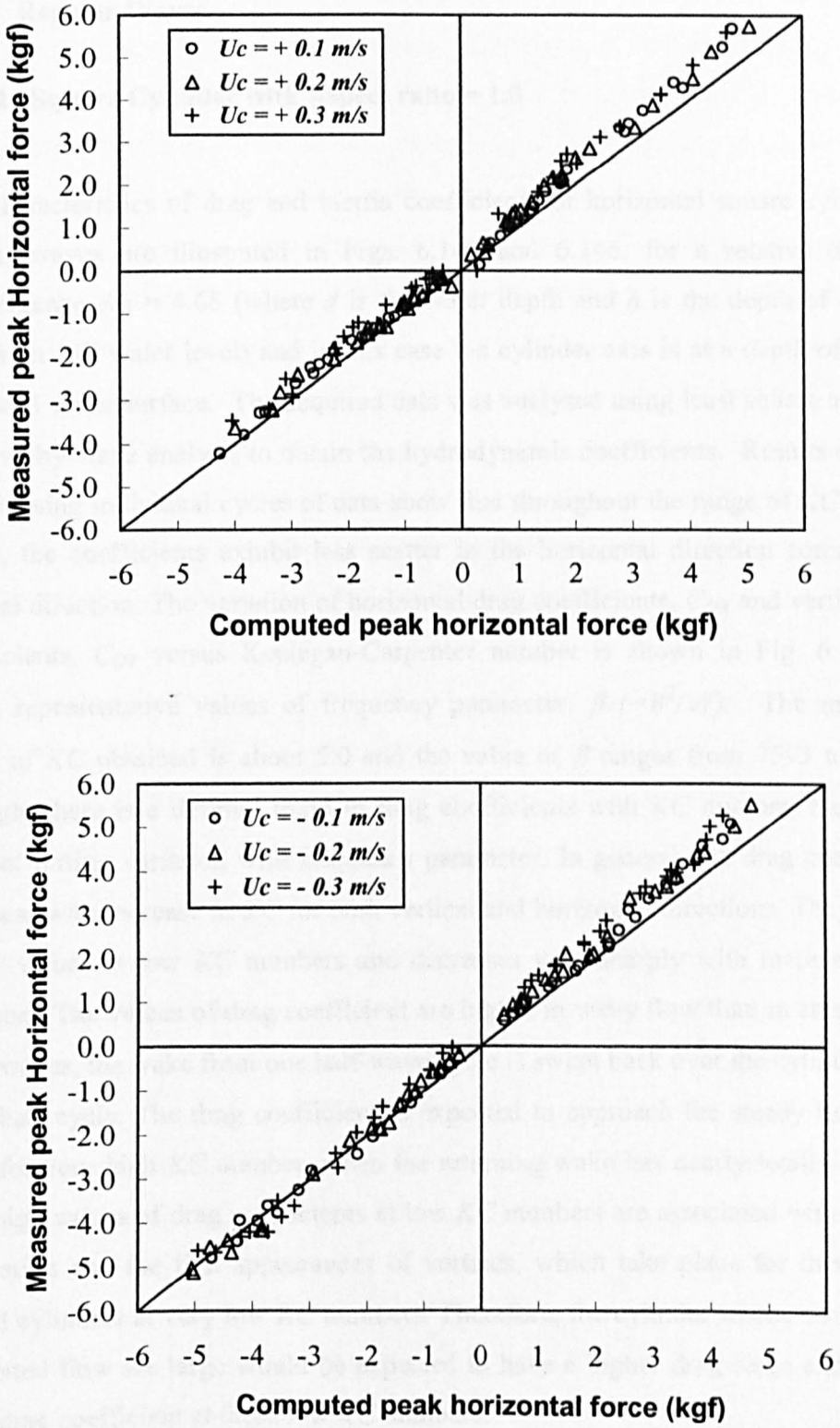

Fig. 6.144 Measured and computed peak forces for vertical rectangular cylinder for aspect ratio = 4/3 in co-existing waves and currents

6.3 Horizontal Cylinder

6.3.1 Regular Waves

6.3.1.1 Square Cylinder with Aspect ratio = 1.0

The characteristics of drag and inertia coefficients of horizontal square cylinder in regular waves are illustrated in Figs. 6.145 and 6.146, for a relative depth of submergence d/h = 4.68 (where d is the water depth and h is the depth of cylinder axis from still water level) and in this case the cylinder axis is at a depth of 0.47 m from still water surface. The acquired data was analysed using least square approach of wave-by-wave analysis to obtain the hydrodynamic coefficients. Results obtained by analysing individual cycles of data show that throughout the range of KC number tested, the coefficients exhibit less scatter in the horizontal direction compared to vertical direction. The variation of horizontal drag coefficients, C_{DX} and vertical drag coefficients, C_{DY} versus Keulegan-Carpenter number is shown in Fig. 6.145, for seven representative values of frequency parameter, β $(=B^2/\nu T)$. The maximum value of KC obtained is about 5.0 and the value of β ranges from 7593 to 15495. Though, there is a definite trend in drag coefficients with KC number, there is no distinct further variation with frequency parameter. In general, the drag coefficients decrease with increase in KC for both vertical and horizontal directions. They exhibit larger values at low KC numbers and decreases very sharply with increase in KC numbers. The values of drag coefficient are higher in wavy flow than in steady flow, as in waves, the wake from one half-wave cycle is swept back over the cylinder in the next half cycle. The drag coefficient is expected to approach the steady flow value only for very high KC number, when the returning wake has nearly totally decayed. The high values of drag coefficients at low KC numbers are associated with the flow separation and the first appearances of vortices, which take place for these sharp-edged cylinders at very low KC numbers. Therefore, the cylinder whose vortices and separated flow are large would be expected to have a higher drag force and hence a high drag coefficient at these low KC numbers.

Fig. 6.146 is plotted for horizontal inertia coefficients, C_{MX} and vertical inertia coefficients, C_{MY} versus Keulegan-Carpenter number. The effect of varying frequency parameter does not show any significant difference in inertia coefficients. It is observed from these plots that at low KC numbers, both C_{MX} and C_{MY} approaches potential flow value, when KC number tends to zero. However, C_{MX} is found to reach a value of about 2.5, which is higher than the potential flow value of 2.2. Further increase in KC numbers results in a sharp reduction in C_{MX} and C_{MY} values. This reduction in C_{MX} is observed up to KC number of around 3.5 to 3.75, where it reaches a minimum value of around 1.2 for C_{MX} and 0.96 for C_{MY} and then these values increases with further increase in KC number. The reason for this reduction in inertia coefficients is attributed to the existence of a circulating flow [Chaplin, (1984a, 1984b)] created by rotating separated vortices around the cylinder at low KC numbers. For higher KC numbers, the weakening of the circulating flow around the cylinder, results in an increase of the inertia forces.

Figs.6.147 and 6.148 are replotted for C_{MX}, C_{MY}, C_{DX} and C_{DY} along with the experimental results obtained by Ikeda et al. (1988a) for two wave periods, T = 1.4sec and 1.6sec. The C_{DX} values in the present study are comparatively higher and the inertia coefficients, in general, show a good comparison with Ikeda et al. (1988a) results. The root mean square force coefficients are plotted in Fig. 6.149 for both horizontal and vertical forces. The forces are normalised with $0.5\,\rho\,B\,U_{rms}^2$. The measured forces are compared with the corresponding Morison forces in Figs. 6.150 and 6.151 for two cases.

For horizontal cylinders, the mean of the force ratio in horizontal (x) and vertical (y) directions are defined as

$$R_{xp} = \frac{F_{xp}}{F_{xc}} \tag{6.2}$$

$$R_{yp} = \frac{F_{yp}}{F_{yc}} \tag{6.3}$$

In Table.6.3 these values are presented. Note only positive peaks are given for both directions.

The measured peak forces are compared with computed peak forces in Fig.6.152. It is observed from these plots that the positive peak forces are underestimated to an amount of up to 17% in horizontal direction and for vertical forces it is about 26% and the scatter in the data points indicate the presence of vortex shedding forces.

In order to show the effect of changing the submergence depth, tests were conducted for another relative depth of submergence, d/h = 2.68, the axis of the cylinder is at an elevation of 0.82 m from still water level. Figs 6.153 & 6.154 are plotted for drag and inertia coefficients respectively for two d/h values. Drag coefficients in the horizontal direction takes almost identical values for both d/h ratios, however, for the vertical direction, drag coefficients corresponding to d/h = 2.68 are found to be comparatively larger than C_{DY} for d/h = 4.68. Inertia coefficients corresponding to d/h = 2.68 are found to be slightly smaller than the inertia coefficients obtained for d/h = 4.68.

6.3.1.2 Rectangular Cylinder with Aspect ratio = 1/2

The variation of horizontal drag coefficients, C_{DX} and vertical drag coefficients, C_{DY} versus Keulegan-Carpenter number is shown in Fig. 6.155 for aspect ratio = 1/2, for relative depth of submergence d/h = 4.68. The maximum value of KC obtained is about 2.25 and the value of β ranges from 26860 to 56537. In general, the drag coefficients decrease with increase in KC for both directions. Fig. 6.156 is a plot of the horizontal inertia coefficients, C_{MX} and vertical inertia coefficients, C_{MY} versus Keulegan-Carpenter number. The effect of varying frequency parameter does not show any significant difference in inertia coefficients. It is observed from these plots

that at low KC numbers, both C_{MX} and C_{MY} approaches potential flow value, when KC number tends to zero. C_{MX} is found to reach a value of about 2.0 at KC about 0.2. The further increase in KC numbers results in a reduction in C_{MX} and C_{MY} values. For example, at $KC = 2.25$, $C_{MX} = 0.846$ and $C_{MY} = 2.259$.

Fig. 6.157 is replotted for C_{DX} and C_{DY} along with the experimental results obtained by Arai (1993). The drag coefficients in the present work are found to be higher than those reported by Arai (1993). In Fig. 6.158, inertia coefficients are compared with the data obtained by Ikeda et al.(1988b) and Arai (1993,1995). A good comparison exists for horizontal force with Ikeda et al.(1988b) and Arai(1995) results. The root mean square force coefficients are plotted in Fig. 6.159 for both horizontal and vertical forces. The vertical rms force coefficient, C_{FYrms} is found to be about 47% to 54% higher than C_{FXrms}. The measured forces are compared with the corresponding Morison forces in Figs. 6.160 and to 6.161 corresponding to the lowest and highest KC numbers tested. Measured peak forces are compared with computed peak forces in Fig. 6.162. The positive peak forces are underestimated to an amount of up to 17% and 7.6% respectively in horizontal and vertical directions.

The effect of submergence depth on drag and inertia coefficients are depicted in Figs. 6.163 and 6.164 for two relative depth of submergence, d/h = 4.68 and 2.68. Drag coefficients in the horizontal and vertical direction for d/h = 2.68 are observed to be comparatively higher. The inertia coefficients corresponding to d/h = 2.68 are found to be slightly smaller than the inertia coefficients obtained for d/h = 4.68.

6.3.1.3 Rectangular Cylinder with Aspect ratio = 3/4

A similar trend in the variation of force coefficients is observed for another aspect ratio = 3/4. The variation of horizontal drag coefficients, C_{DX} and vertical drag coefficients, C_{DY} versus Keulegan-Carpenter number is shown in Fig. 6.165. The maximum value of KC obtained is about 1.7 and the value of β ranges from 39956 to

84941. In general, the drag coefficients decrease with increase in KC for both directions.

Fig. 6.166 is plotted for horizontal inertia coefficients, C_{MX} and vertical inertia coefficients, C_{MY} versus Keulegan-Carpenter number and here again, frequency parameter does not show any large variation in inertia coefficients and both C_{MX} and C_{MY} approaches potential flow value, when KC number tends to zero. Increase in KC numbers results in a reduction in C_{MX} and C_{MY} values as found for other cylinders.

The root mean square force coefficients are plotted in Fig. 6.167 for both horizontal and vertical forces. The horizontal rms force coefficient, C_{FYrms} is found to be about 58% higher than C_{FXrms} at highest KC. The measured forces are compared with the corresponding Morison forces in Figs. 6.168 and 6.169. The measured peak forces are compared with computed peak forces in Fig. 6.170. A difference of 7.9% in horizontal direction and 12.8% in vertical direction between measured and computed positive peak forces are observed.

The effect of submergence depth on drag and inertia coefficients are illustrated in Figs. 6.171 and 6.172 for two relative depth of submergence, d/h = 4.68 and 2.68. Similar to rectangular cylinder with aspect ratio = 1/2, drag coefficients in the horizontal and vertical direction for d/h = 2.68 are observed to be comparatively higher. Inertia coefficients corresponding to d/h = 2.68 are found to be slightly smaller than the inertia coefficients obtained for d/h = 4.68.

The inertia coefficients for horizontal cylinders decrease rapidly with increase KC number. This was first reported by Chaplin (1984a,b) in the case of a horizontally submerged circular cylinder beneath the waves. It was suggested that this is caused by the non-linear effect of oscillatory boundary layer due to viscosity. Later, Chaplin (1988a) investigating the non linear forces on circular cylinders horizontally submerged in waves at low KC numbers and under circular orbital flow conditions, argued that the reduction of inertia coefficients are associated with a lift force caused

by the circulation of the flow relative to the cylinder, acting in the opposite direction to the inertia force. Chaplin and Retzler (1992) explain further that beneath a wave, at a point, the velocity and acceleration vectors rotate with the acceleration vector leading the velocity vector by 90°. The boundary layer present on the surface of the cylinder, even though the ambient flow is oscillatory, generates a steady flow parallel to the boundary which is known as 'steady streaming'. For a horizontally submerged cylinder under waves, this steady streaming circulates around the cylinder. A force is generated by the combination of circulation and the ambient flow, which is referred by the authors as 'lift' and it acts at right angles to the incident flow. There is continuous change in the orientation of the incoming flow and the lift and now the total force is the ideal flow force minus the lift force. The consequence is the result of a non-linear reduction in loading. The authors also indicated that the force associated with the circulation will not be strongly affected by Reynolds number and the loading is non-linear as it is proportional to the product of the incident velocity and the circulation and the force is proportional to the cube of the wave height and oscillates at the wave frequency. They also mentioned that separation and vortex shedding might cause substantial modifications to the loading due to viscosity.

In the present work, it is believed that the above phenomenon takes place and this is the reason, for decrement of the inertia coefficients at low KC numbers, for horizontal cylinders. For the square cylinder, a maximum reduction of inertia force from their potential flow values, in horizontal and vertical directions are found to be 52% and 55% respectively for $KC < 4.0$. Similarly for aspect ratio = 1/2, a maximum reduction of inertia force in horizontal and vertical directions are 52 % and 55% respectively for $KC < 2.5$ and for aspect ratio = 3/4, these value are 26% and 23% respectively for $KC < 2.75$. It is to be noted that the percentage of reduction given for aspect ratio = 1/2 and 3/4 are not necessarily the limiting values for the maximum reduction and if the experiments are performed to higher KC numbers, then there are chances of these values being different.

Table. 6.3. Means and standard deviations of measured and computed peak force ratios for horizontal cylinder in waves

Current (m/s)	$\overline{R}_{xp}$	$\overline{R}_{yp}$	σ_{xp}	σ_{yn}
1.0	1.176	1.262	0.117	0.236
1/2	1.176	1.076	0.140	0.101
3/4	1.079	1.128	0.108	0.103

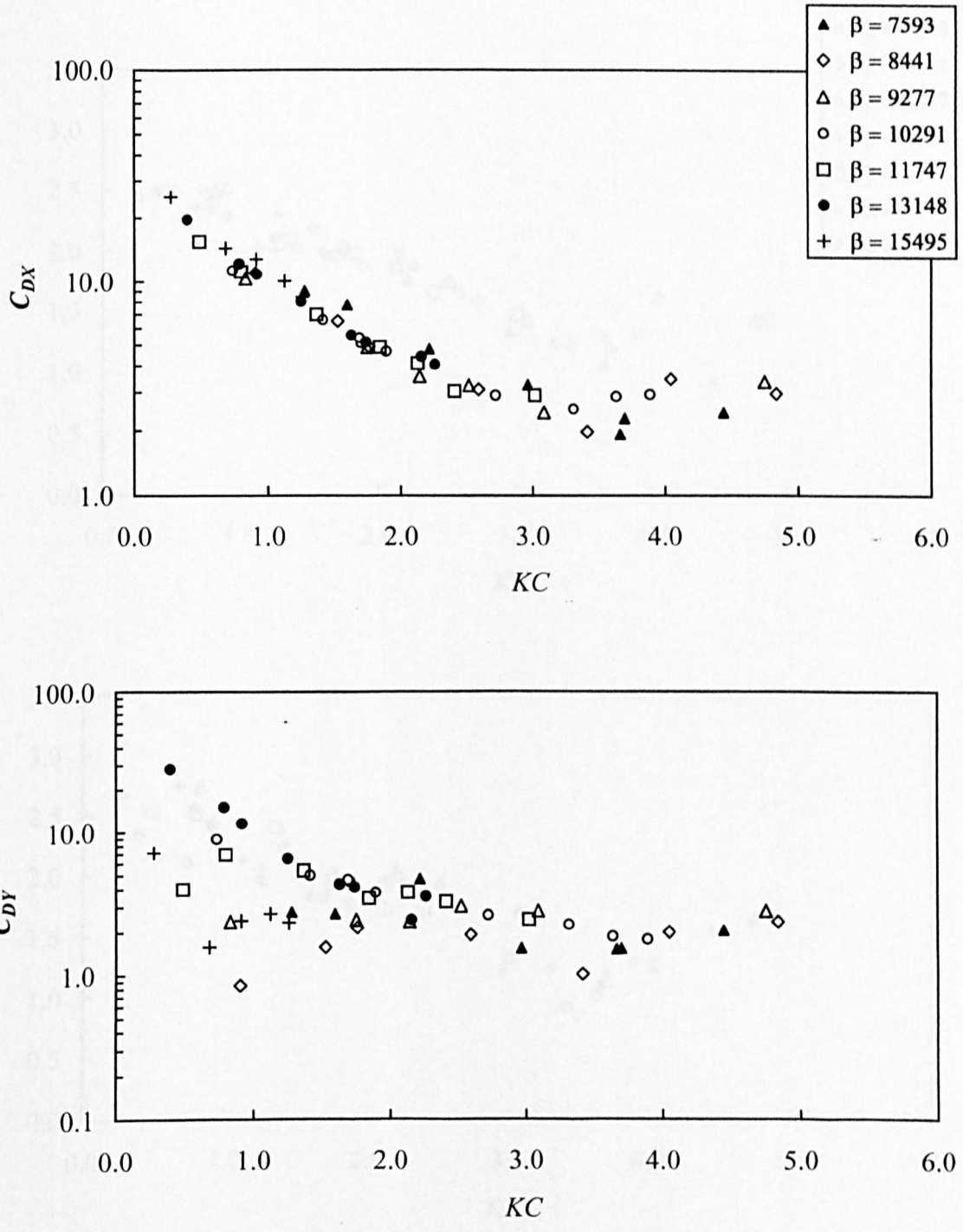

Fig. 6.145 Horizontal and vertical drag coefficients for horizontal square cylinder for different frequency parameter

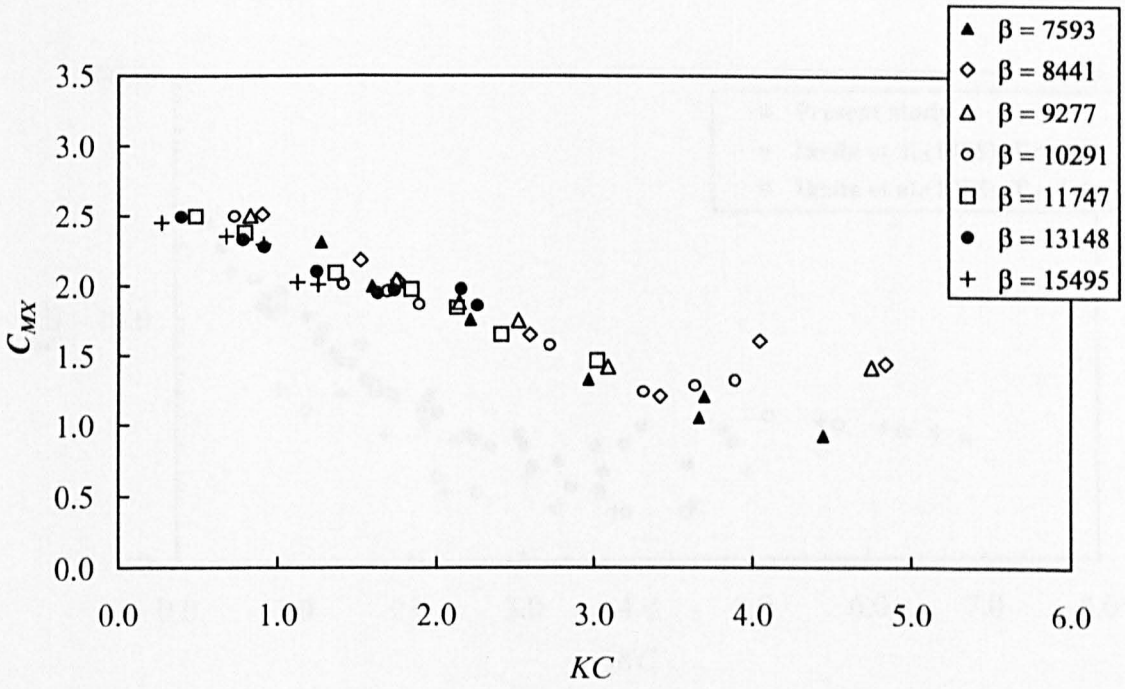

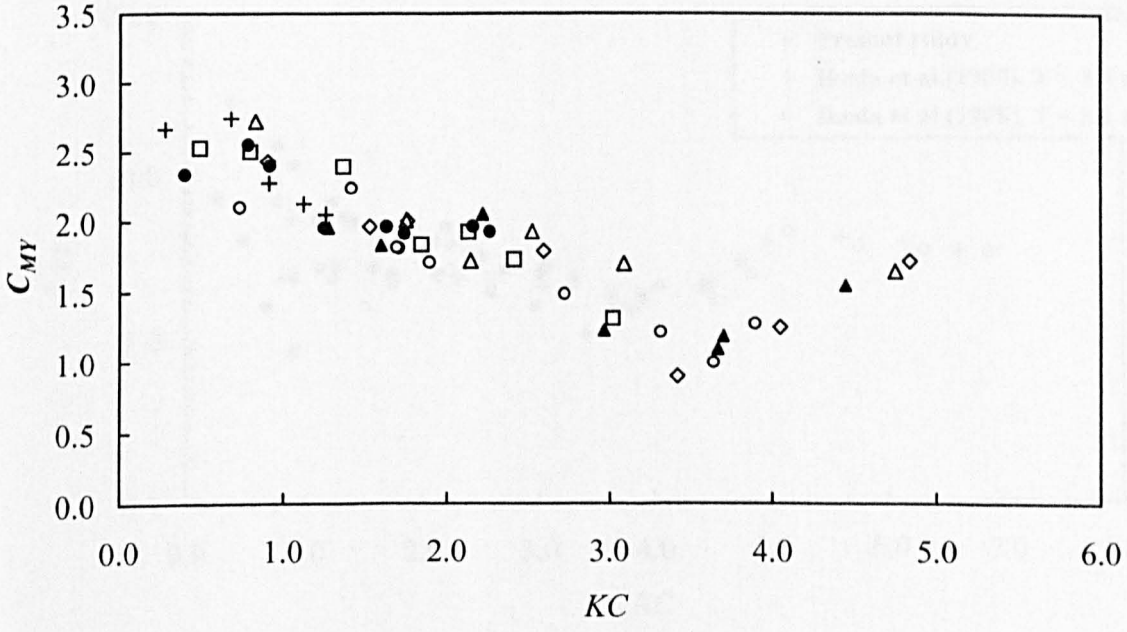

Fig. 6.146 Horizontal and vertical inertia coefficients for horizontal square cylinder for different frequency parameter

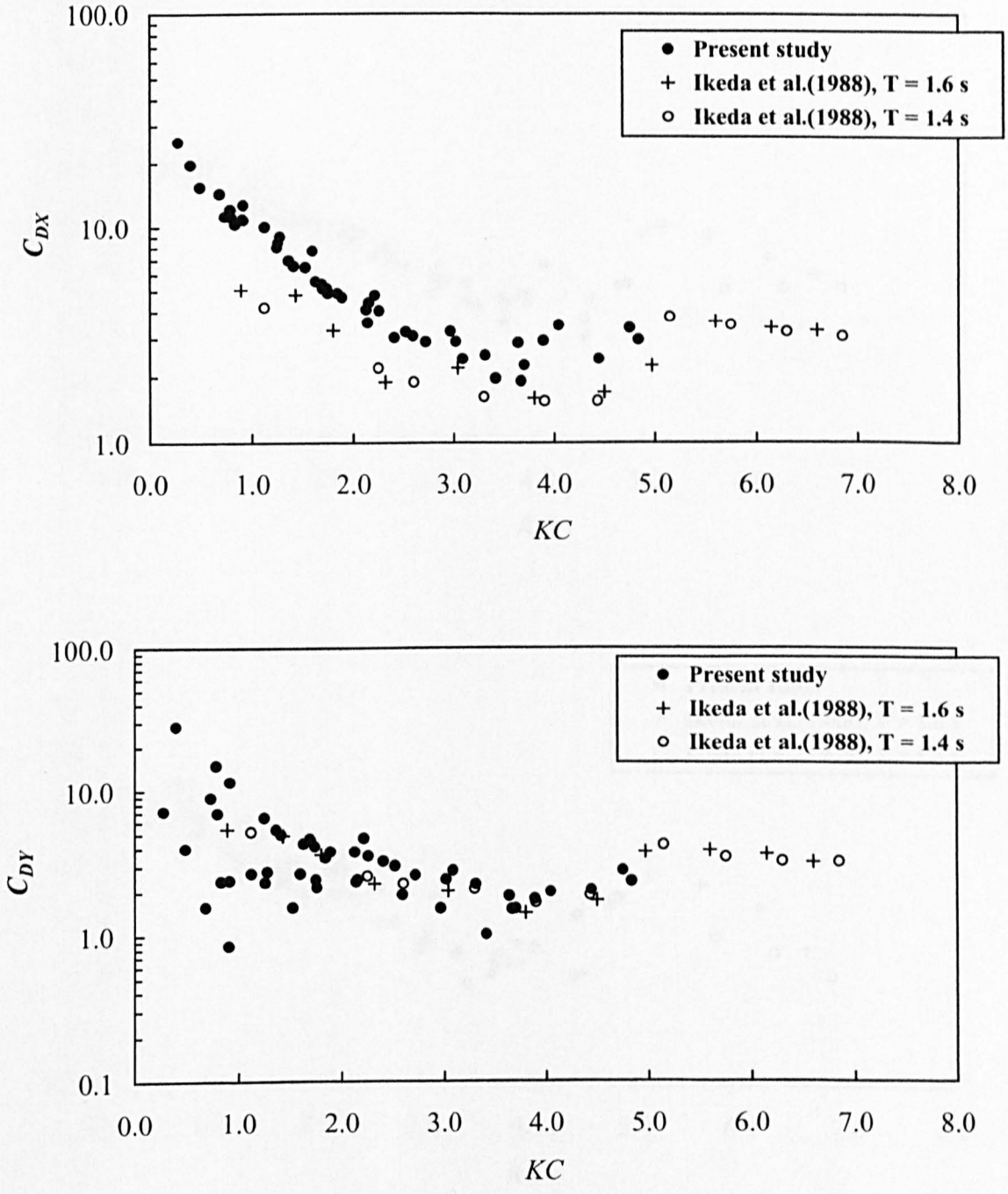

Fig. 6.147 Horizontal and vertical drag coefficients for horizontal square cylinder

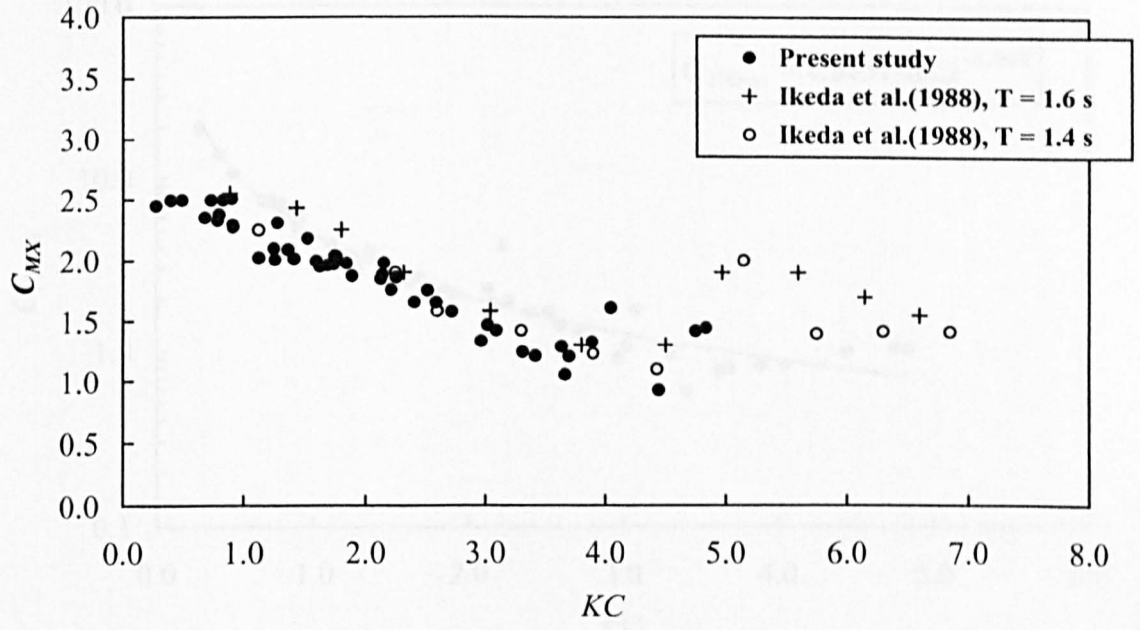

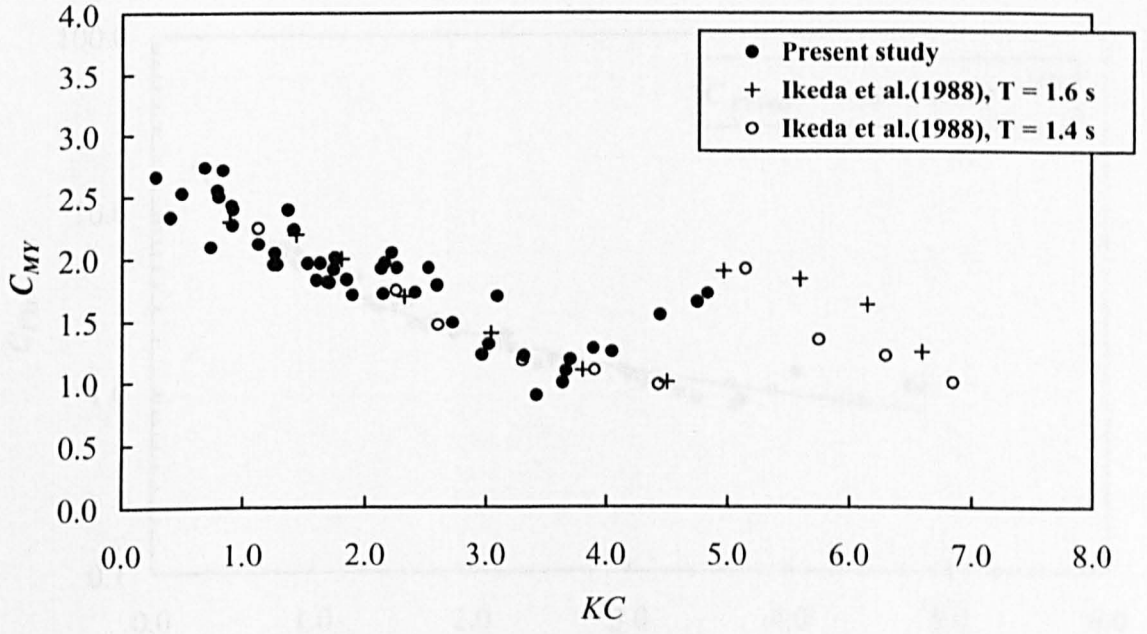

Fig. 6.148 Horizontal and vertical inertia coefficients for horizontal square cylinder

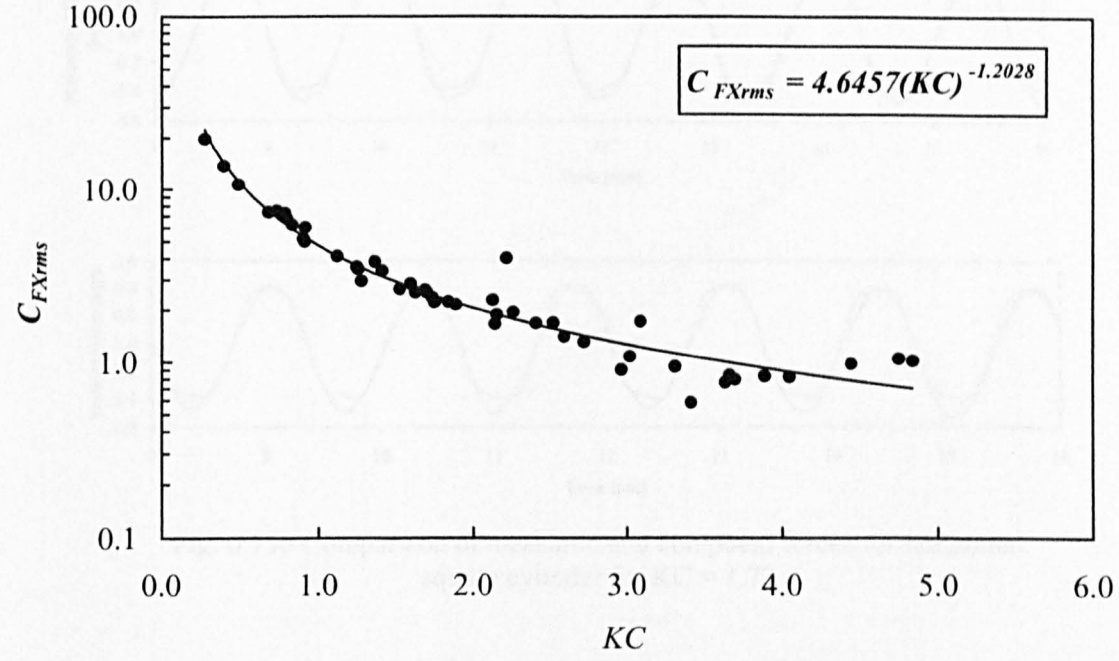

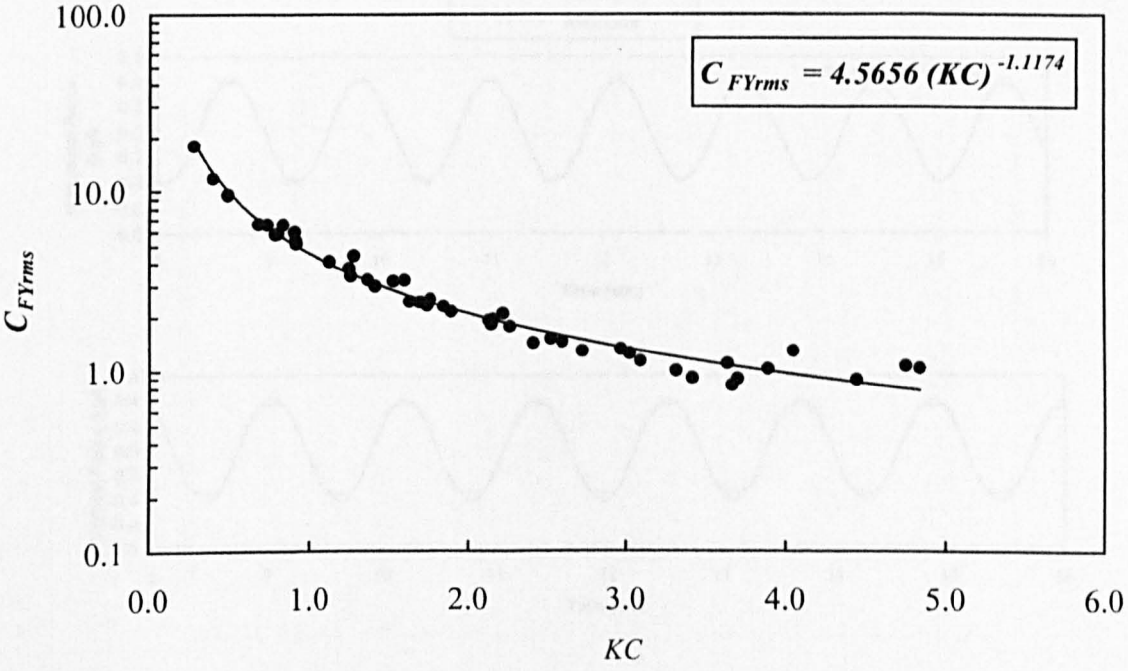

Fig. 6.149 Horizontal and vertical rms force coefficients for horizontal square cylinder

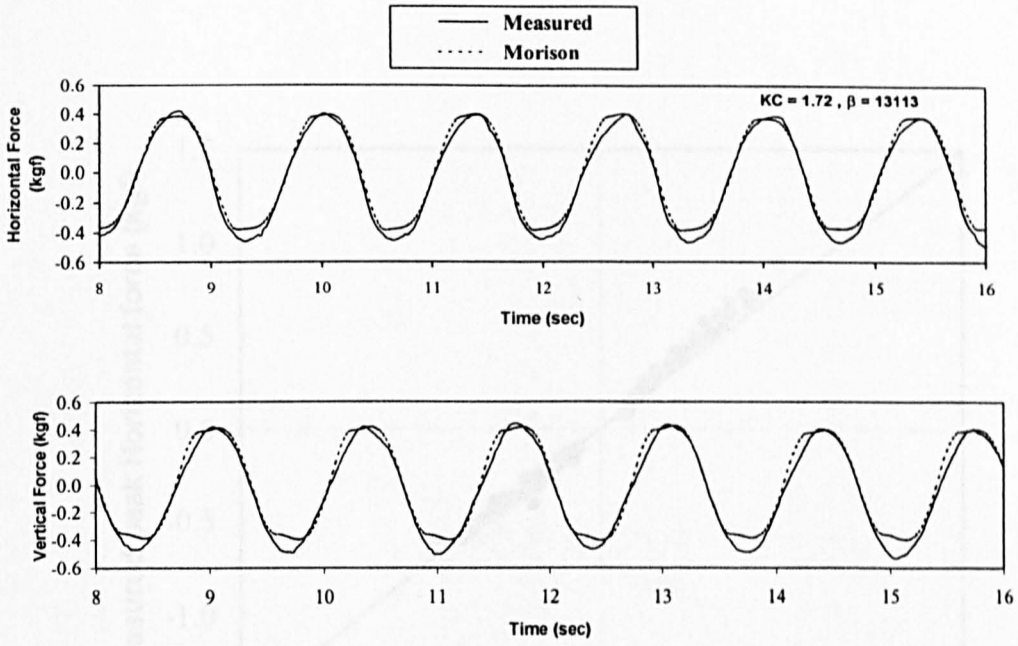

Fig. 6.150 Comparison of measured and computed forces for horizontal square cylinder for KC = 1.72

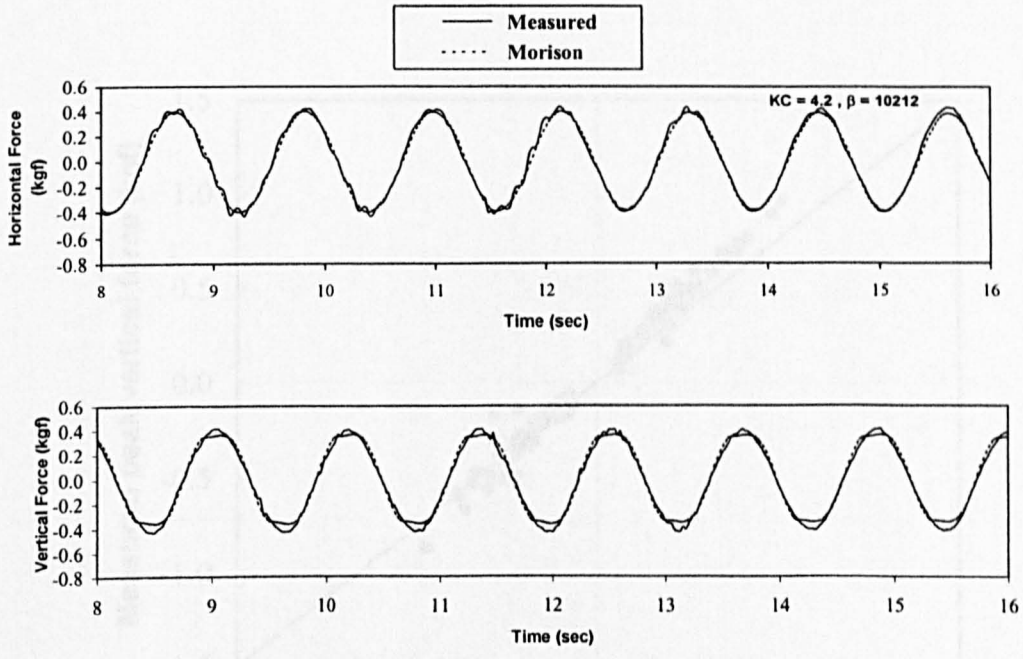

Fig. 6.151 Comparison of measured and computed forces for horizontal square cylinder for KC = 4.2

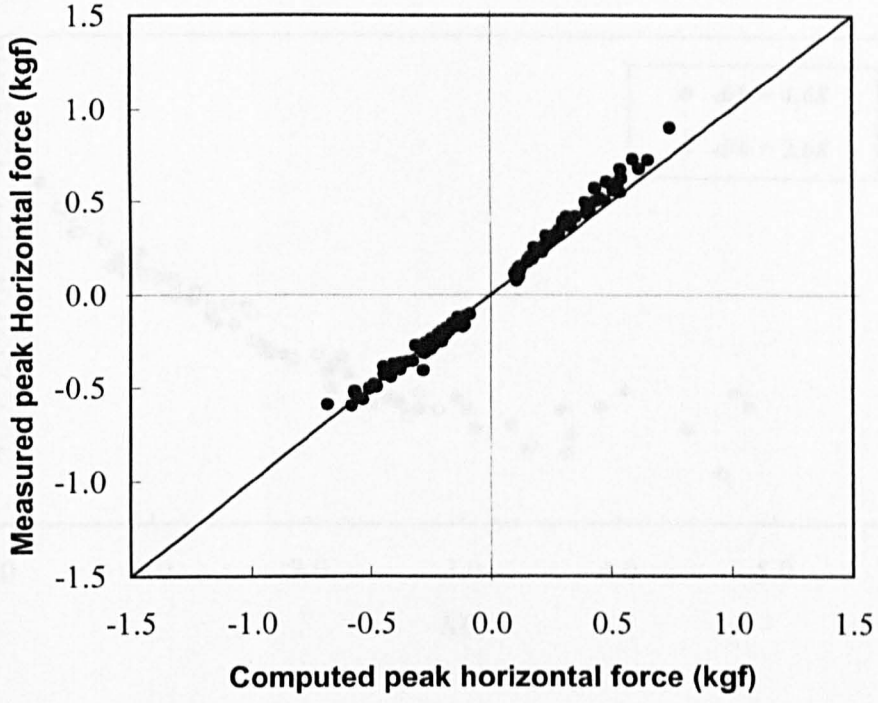

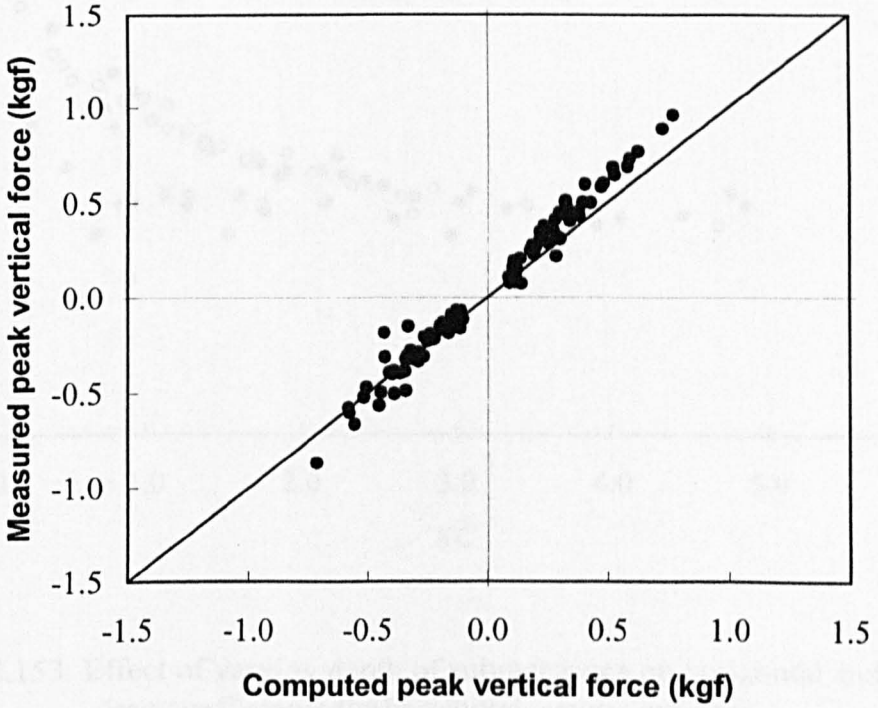

Fig. 6.152 Measured and computed peak forces for horizontal square cylinder

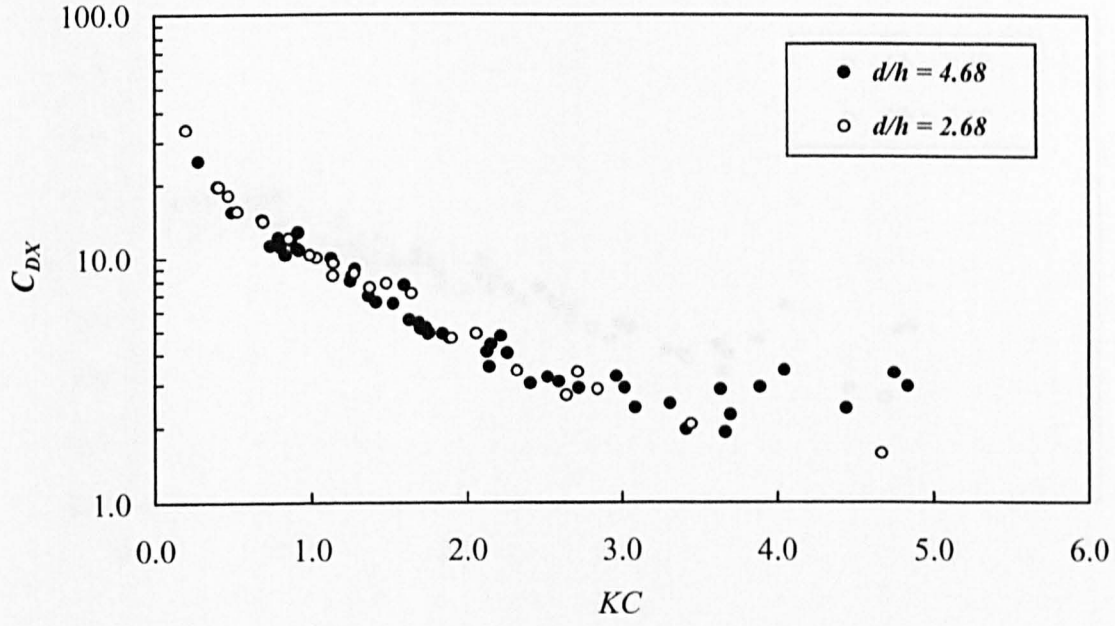

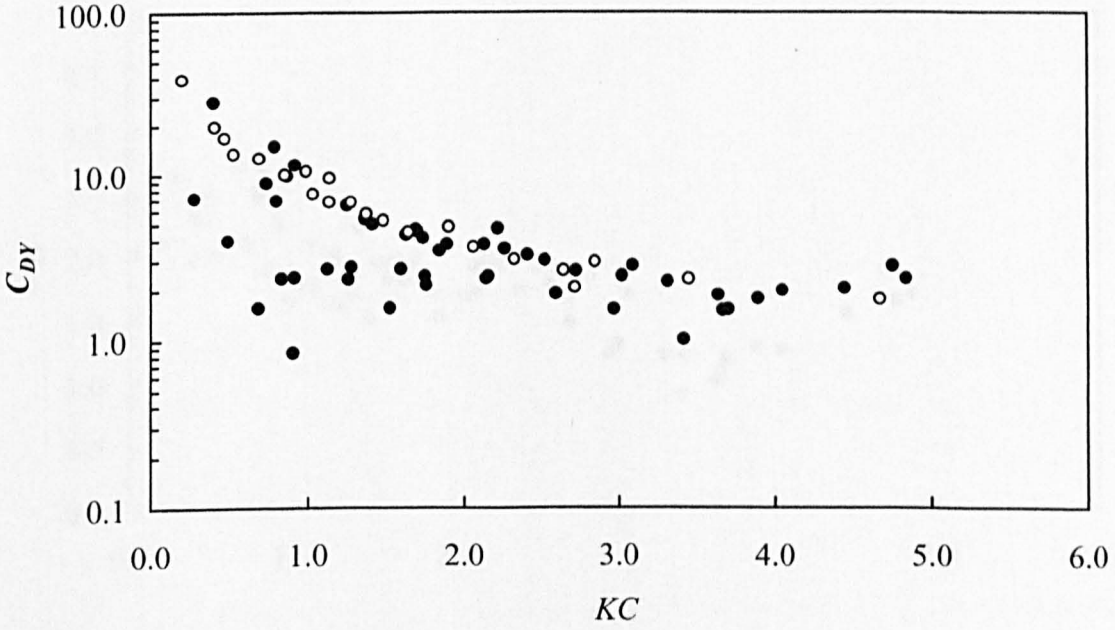

Fig. 6.153 Effect of varying depth of submergence on horizontal and vertical drag coefficients for horizontal square cylinder

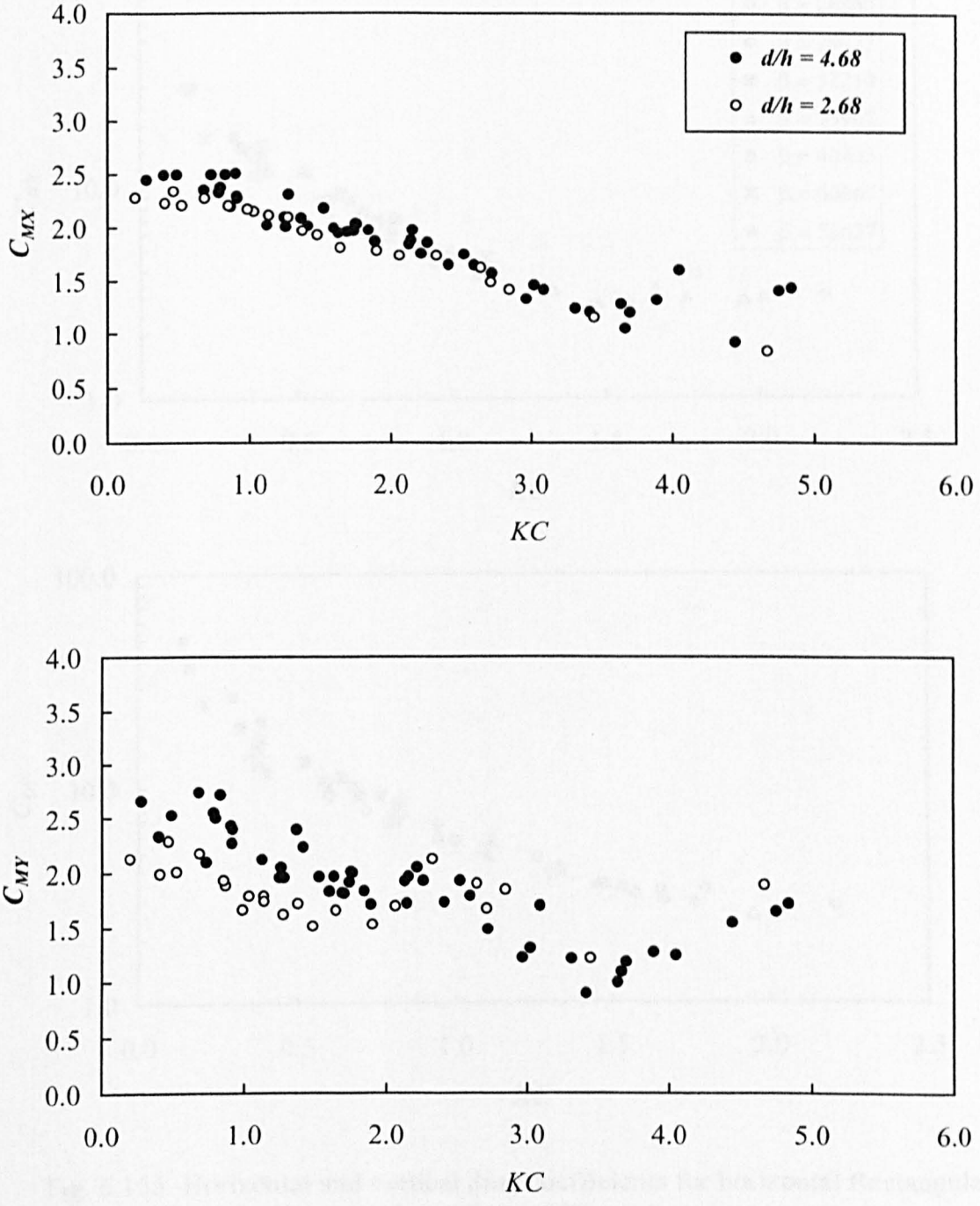

Fig. 6.154 Effect of varying depth of submergence on horizontal and vertical inertia coefficients for horizontal square cylinder

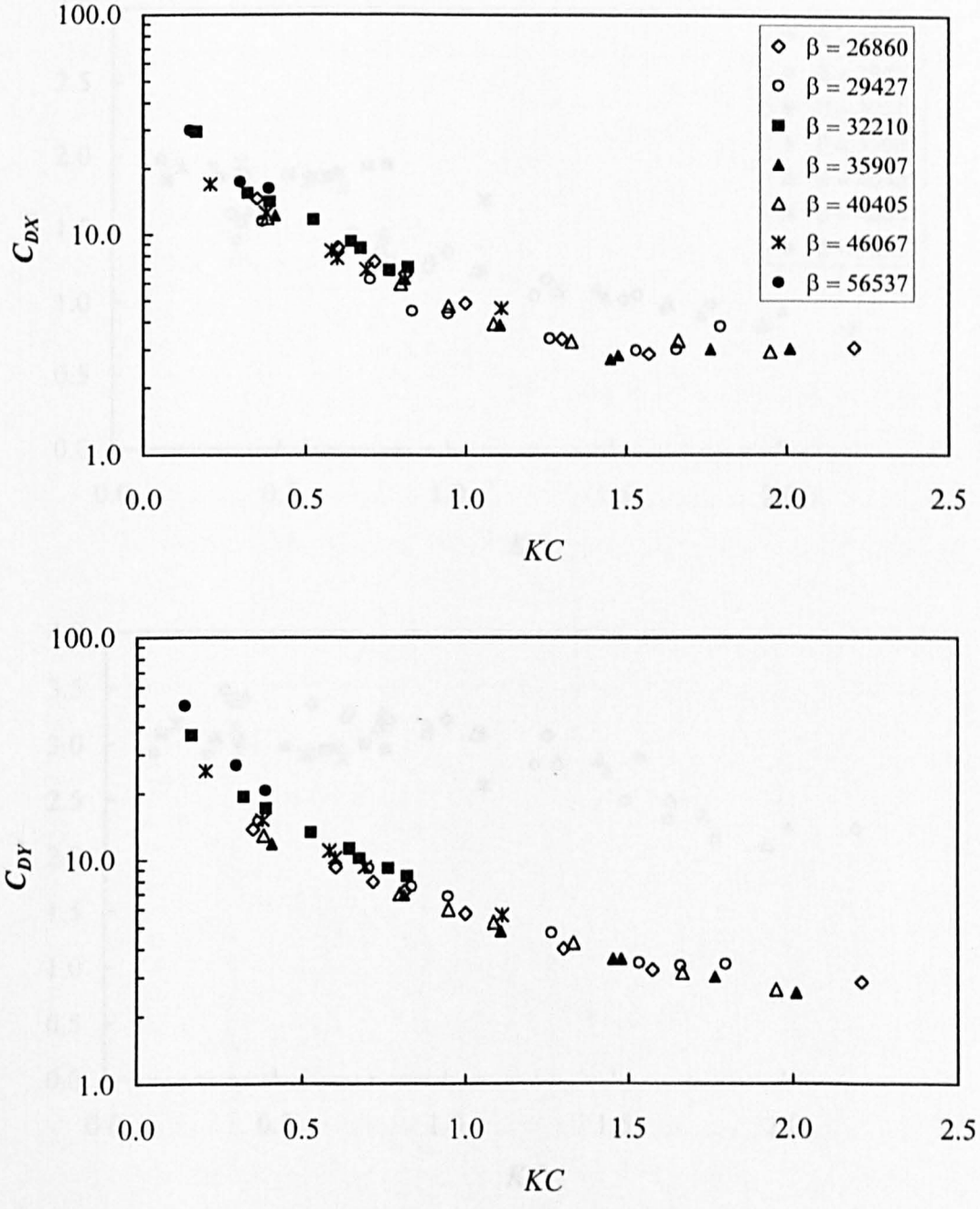

Fig. 6.155 Horizontal and vertical drag coefficients for horizontal Rectangular Cylinder for aspect ratio = 1/2 for different frequency parameter

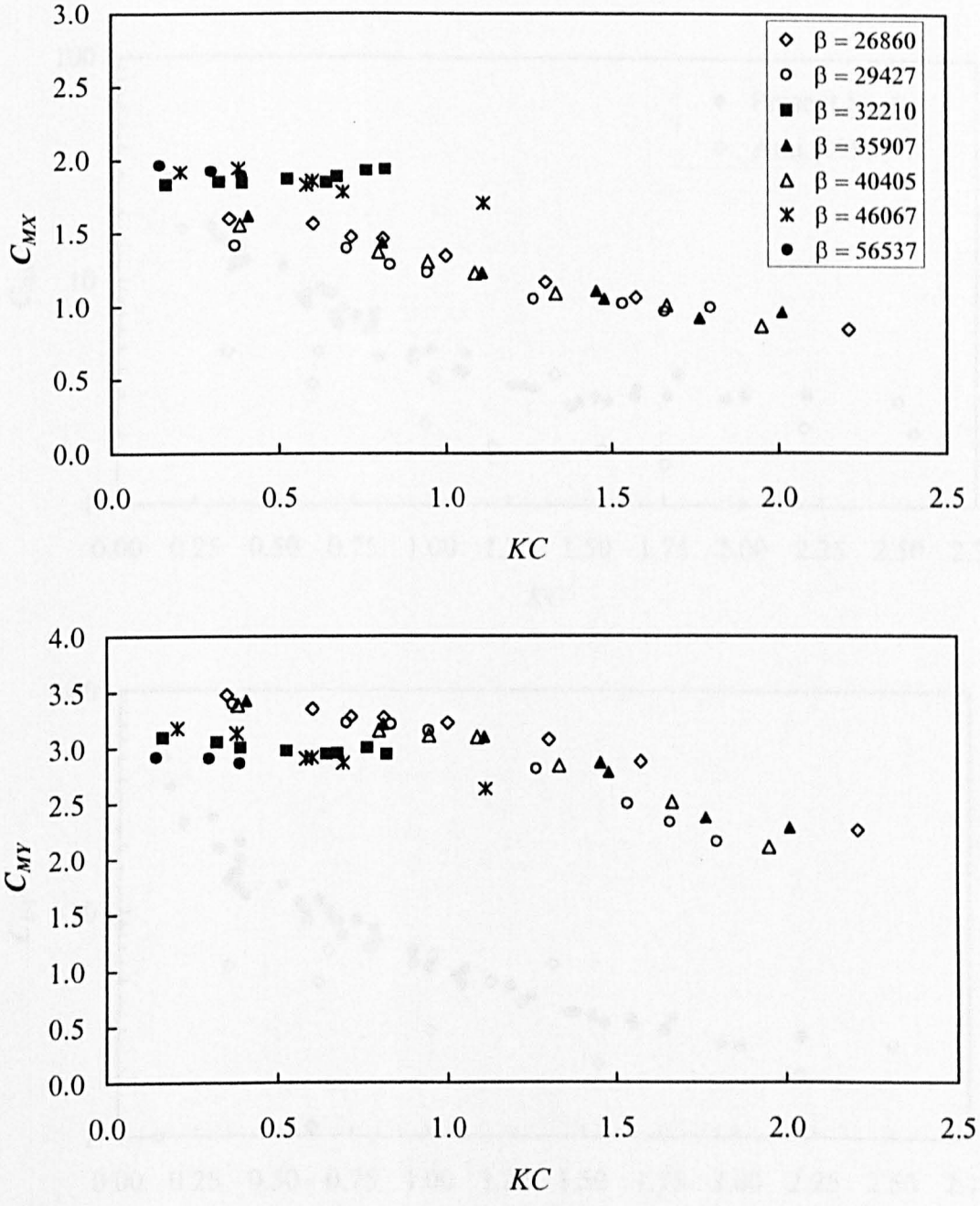

Fig. 6.156 Horizontal and vertical inertia coefficients for horizontal rectangular Cylinder for aspect ratio = 1/2 for different frequency parameter

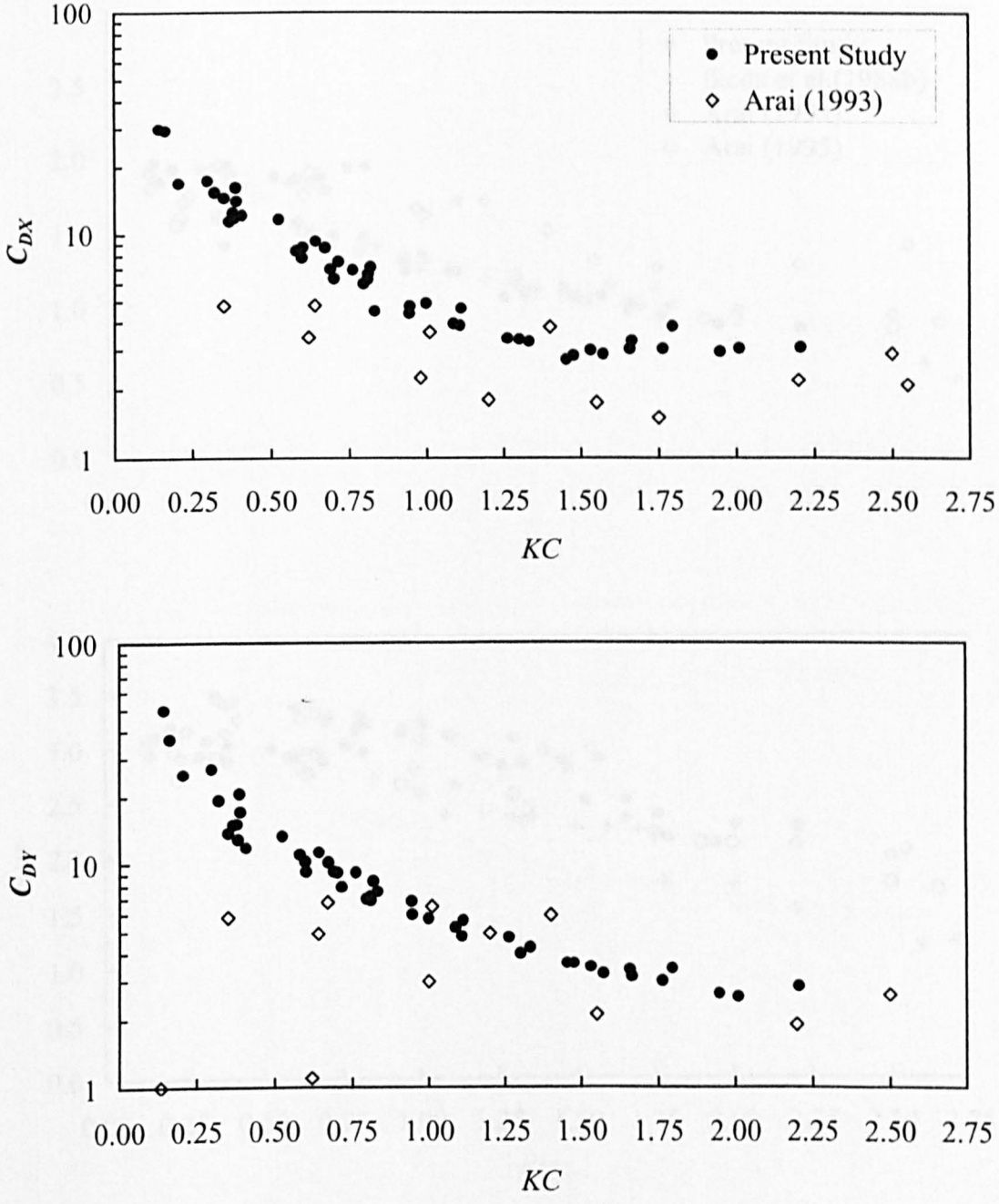

Fig. 6.157 Horizontal and vertical drag coefficients for horizontal rectangular cylinder for aspect ratio = 1/2

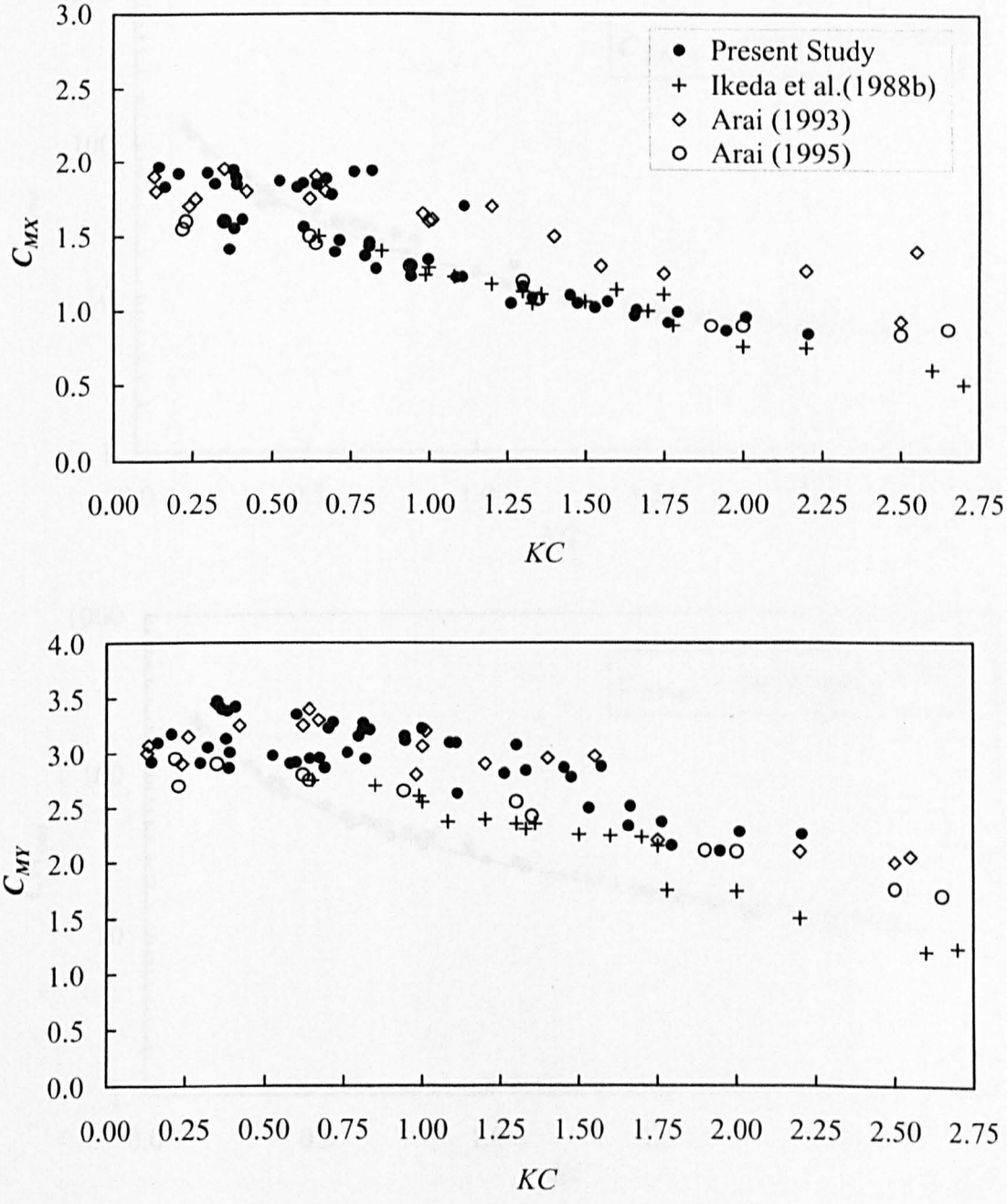

Fig. 6.158 Horizontal and vertical inertia coefficients for horizontal rectangular cylinder for aspect ratio = 1/2

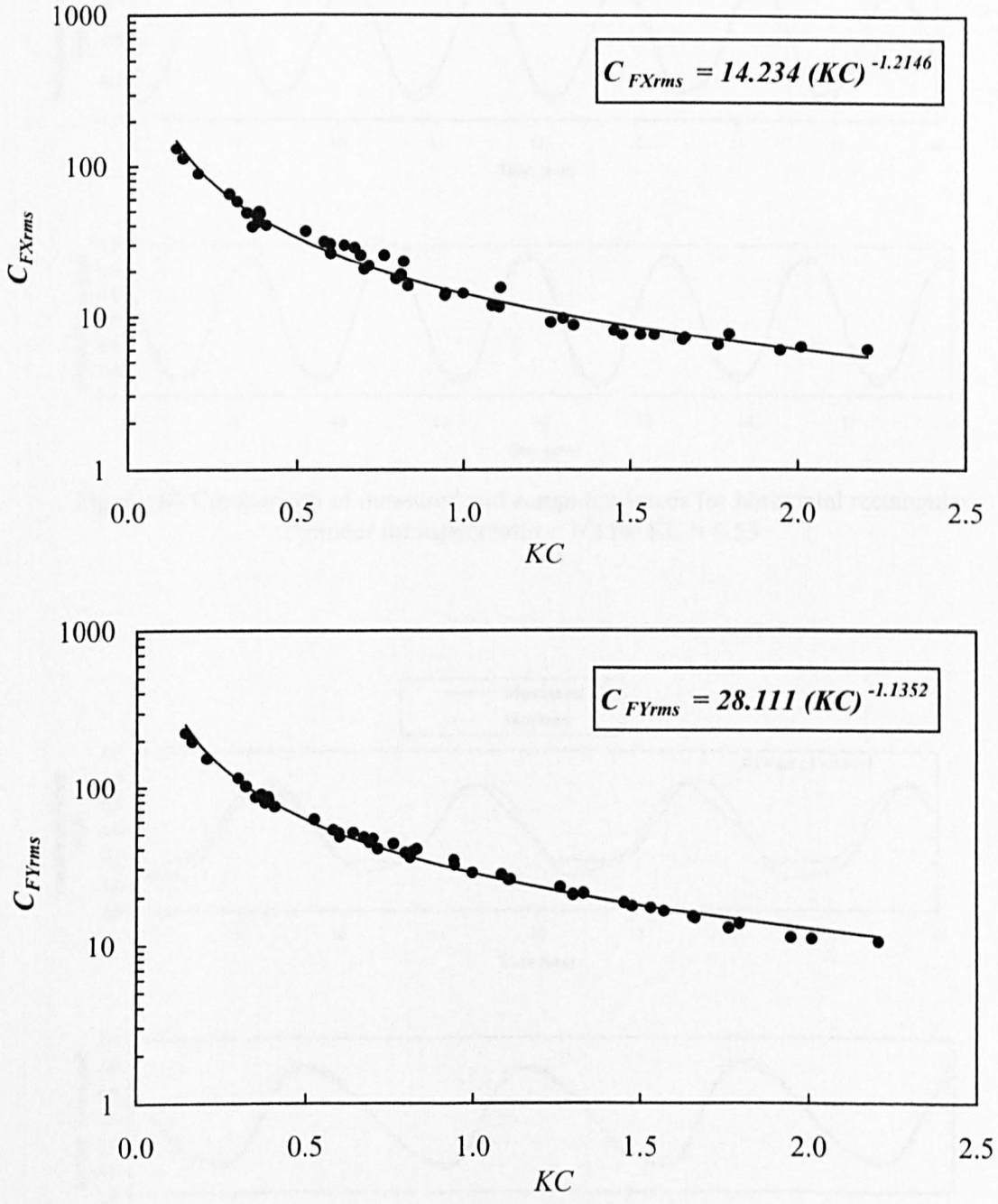

Fig. 6.159 Horizontal and vertical rms force coefficients for horizontal rectangular cylinder for aspect ratio = 1/2

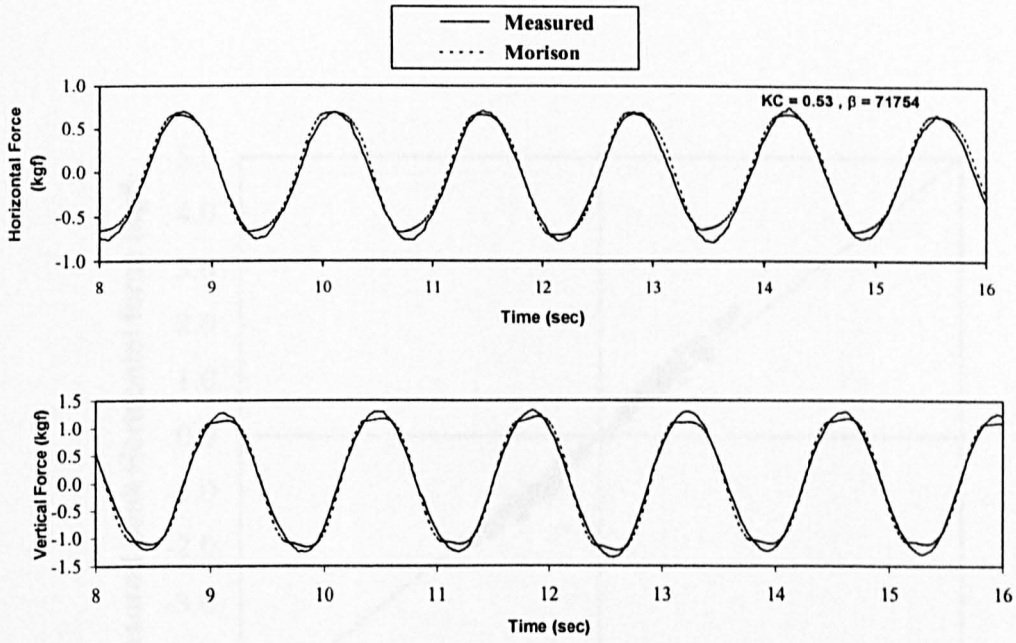

Fig. 6.160 Comparison of measured and computed forces for horizontal rectangular cylinder for aspect ratio = 1/2 for KC = 0.53

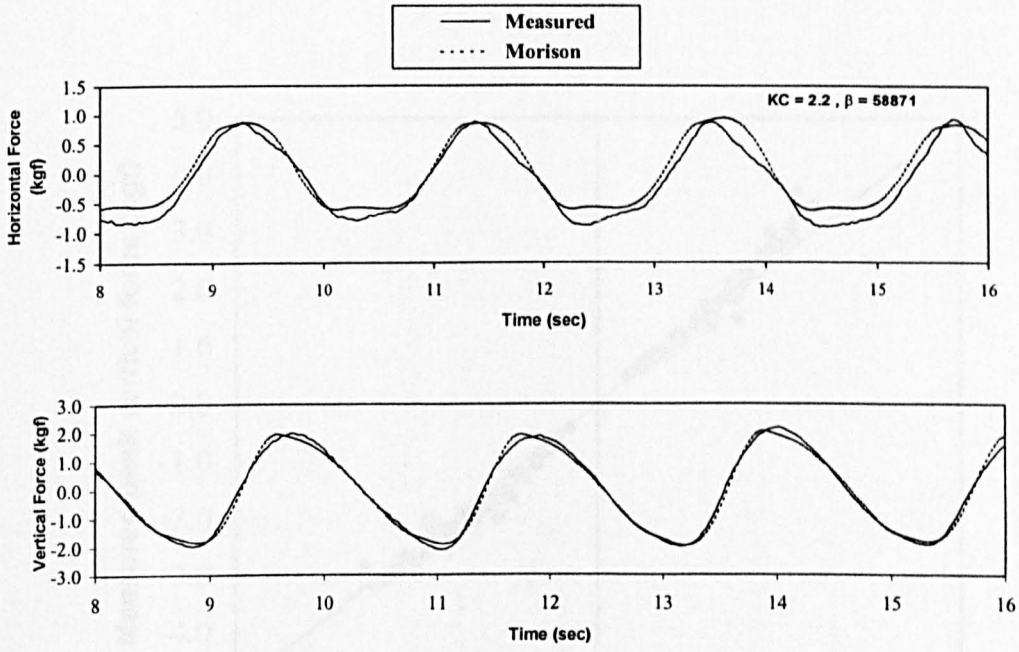

Fig. 6.161 Comparison of measured and computed forces for horizontal rectangular cylinder for aspect ratio = 1/2 for KC = 2.2

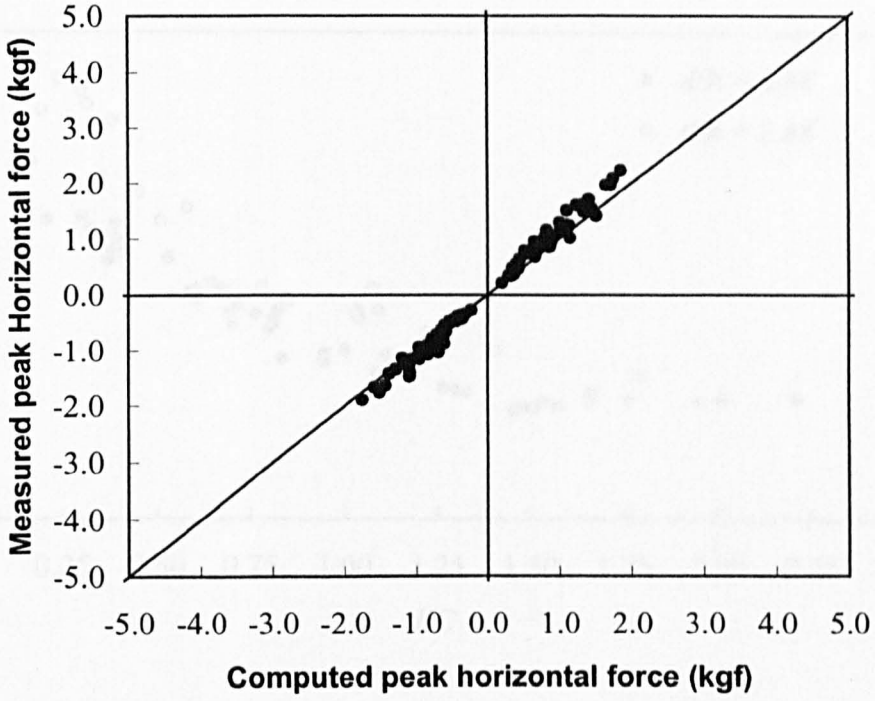

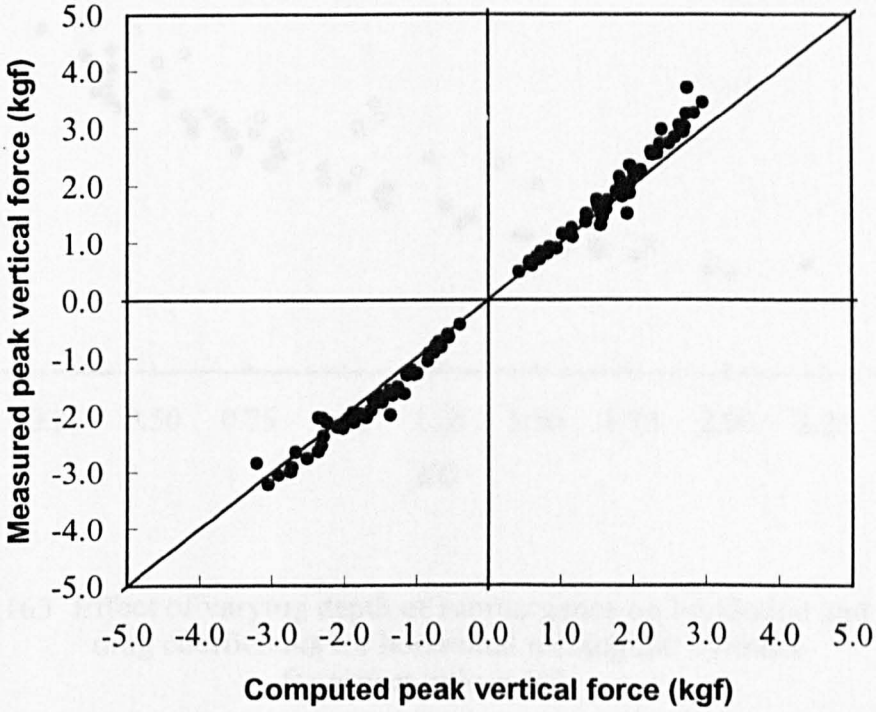

Fig. 6.162 Measured and computed peak forces for horizontal rectangular cylinder for aspect ratio = 1/2

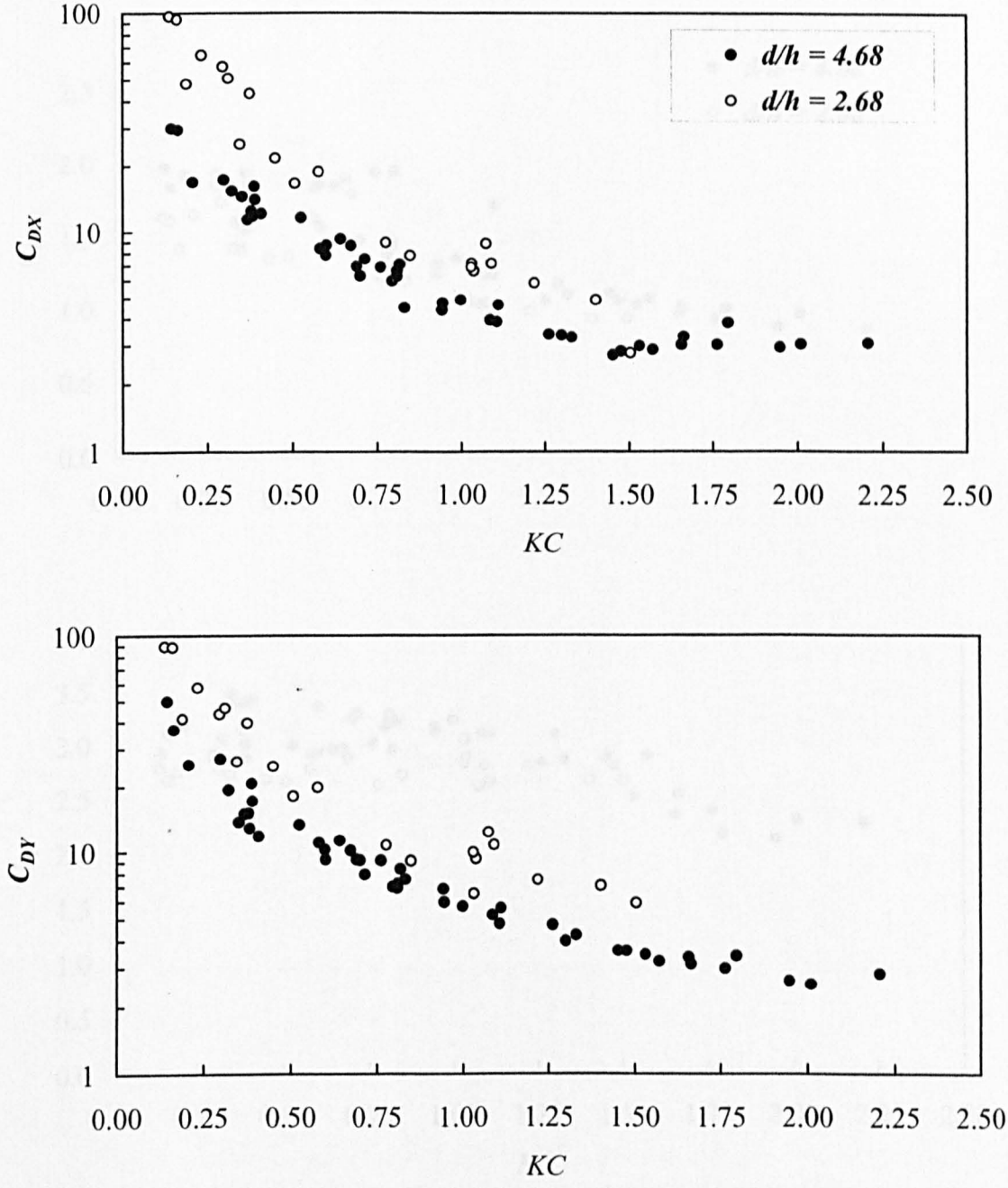

Fig. 6.163 Effect of varying depth of submergence on horizontal and vertical drag coefficients for horizontal rectangular cylinder for aspect ratio = 1/2

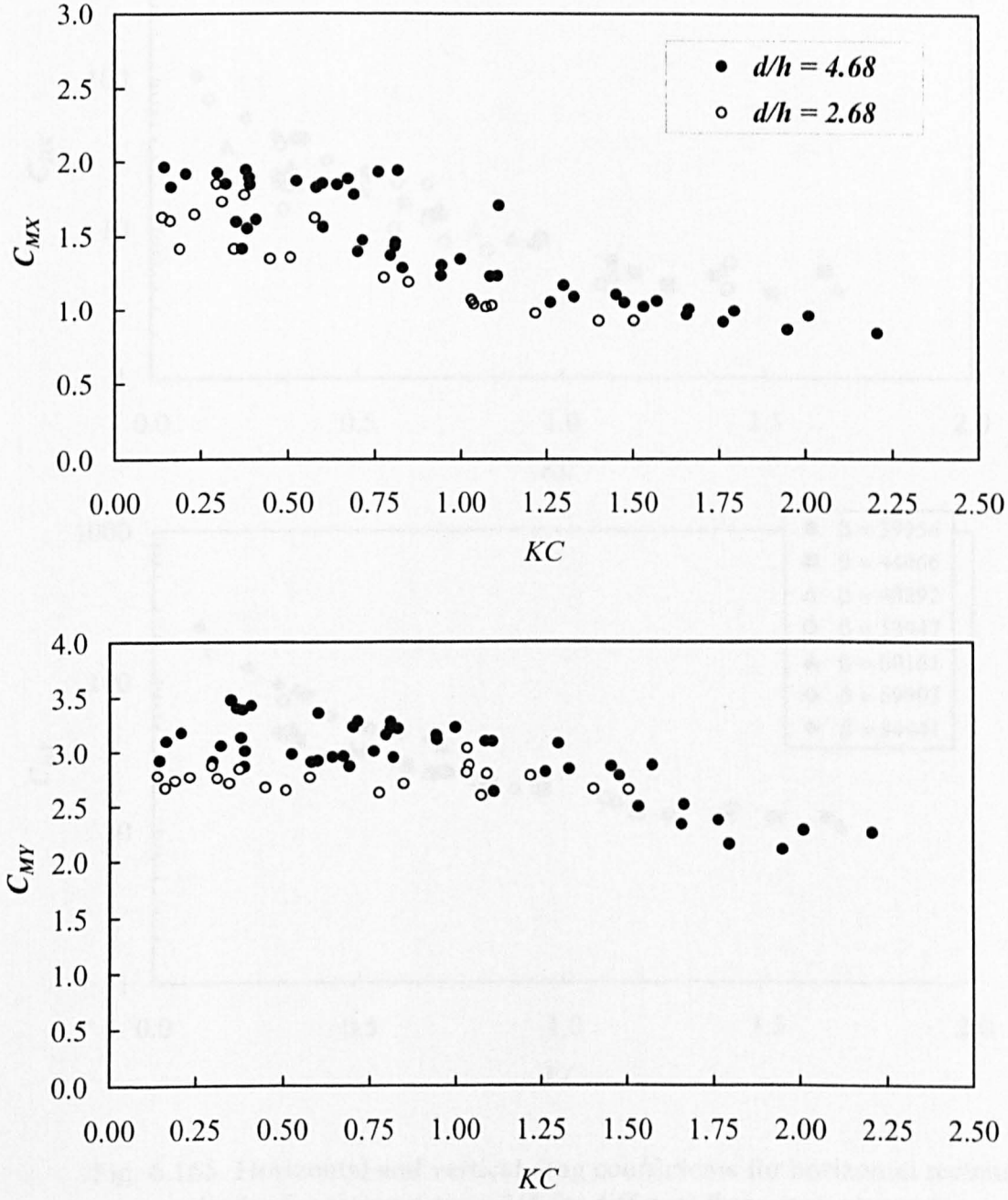

Fig. 6.164 Effect of varying depth of submergence on horizontal and vertical inertia coefficients for horizontal rectangular cylinder for aspect ratio = 1/2

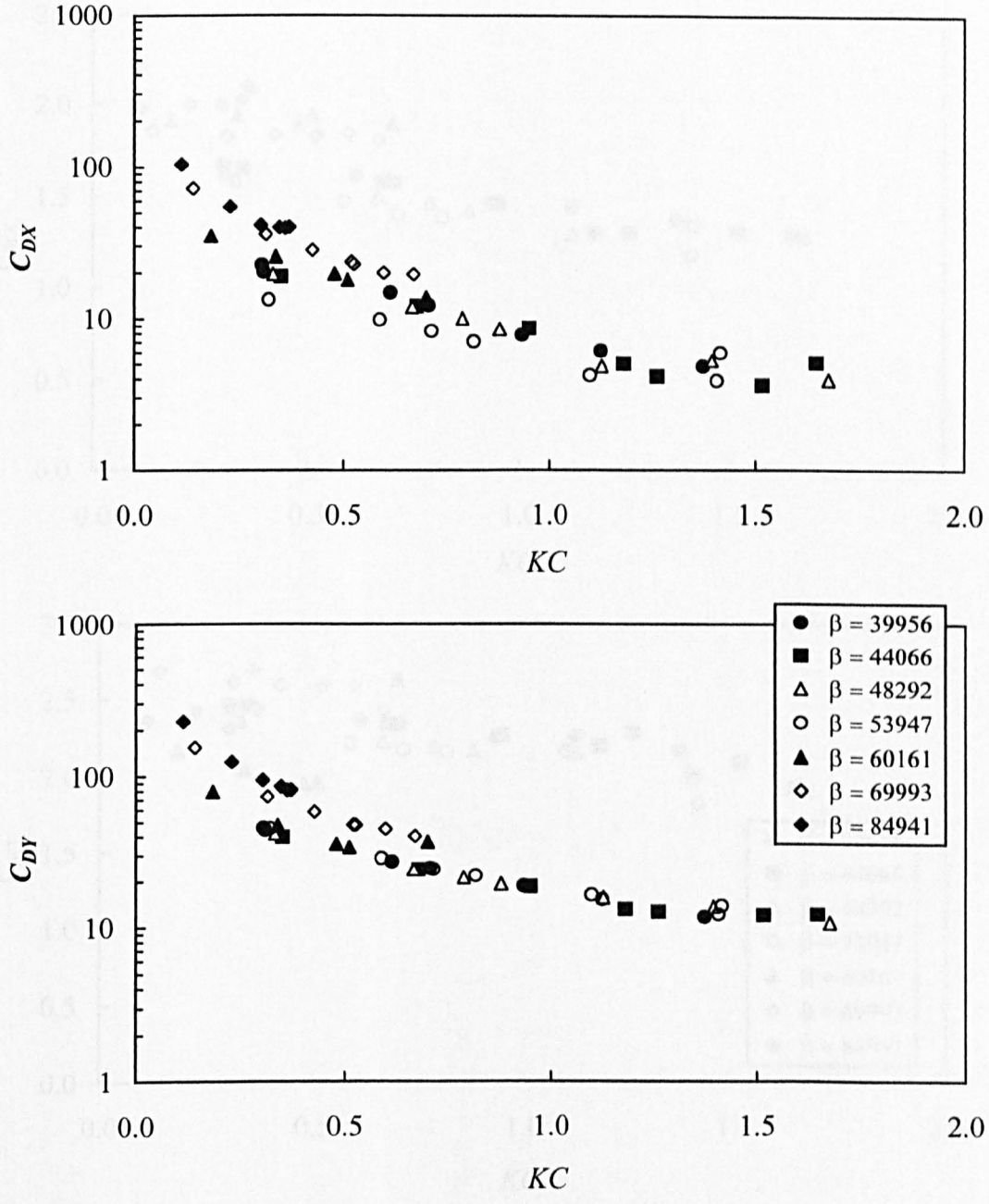

Fig. 6.165 Horizontal and vertical drag coefficients for horizontal rectangular cylinder for aspect ratio = 3/4 for different frequency parameter

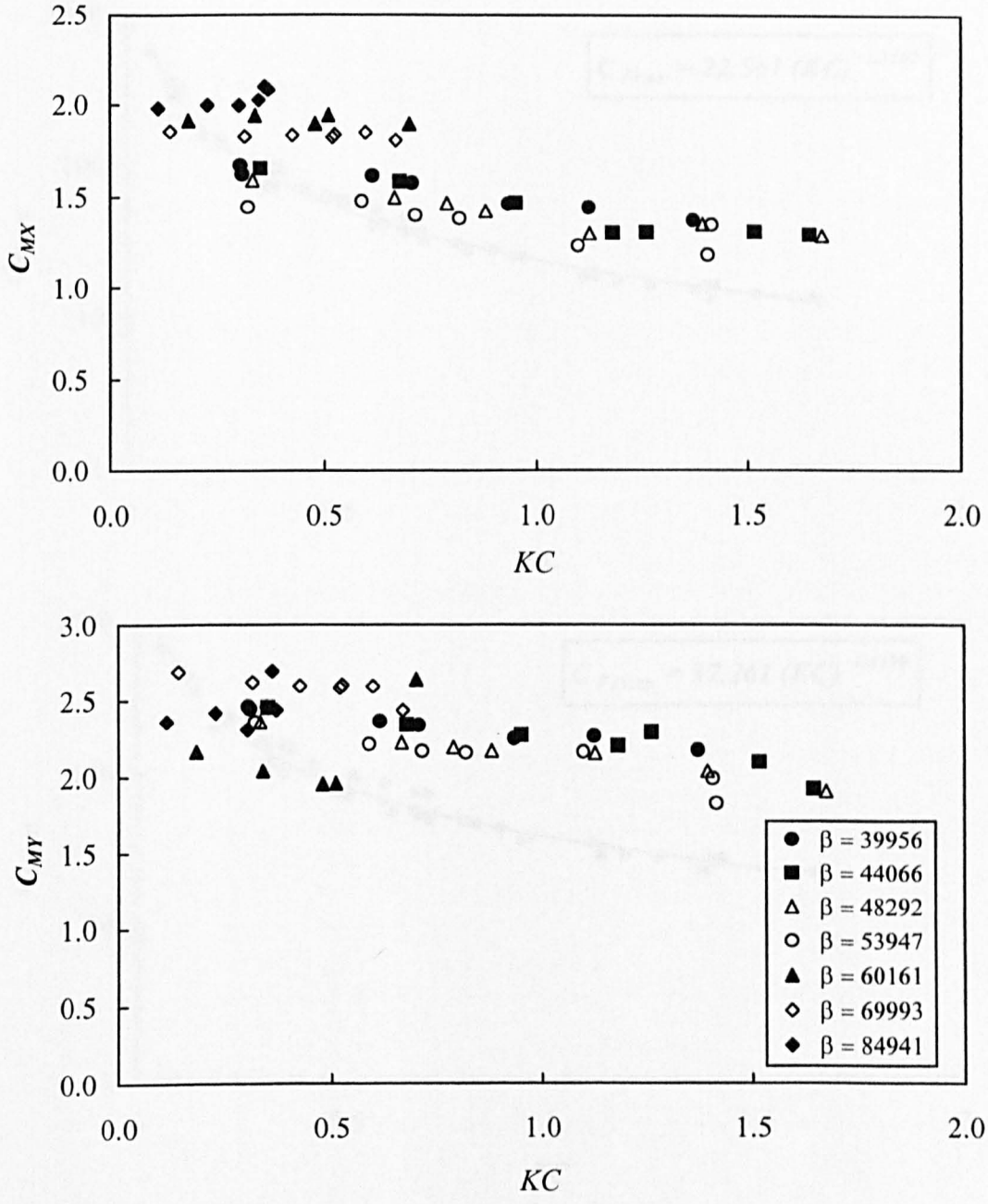

Fig. 6.166 Horizontal and vertical inertia coefficients for horizontal rectangular cylinder for aspect ratio = 3/4 for different frequency parameter

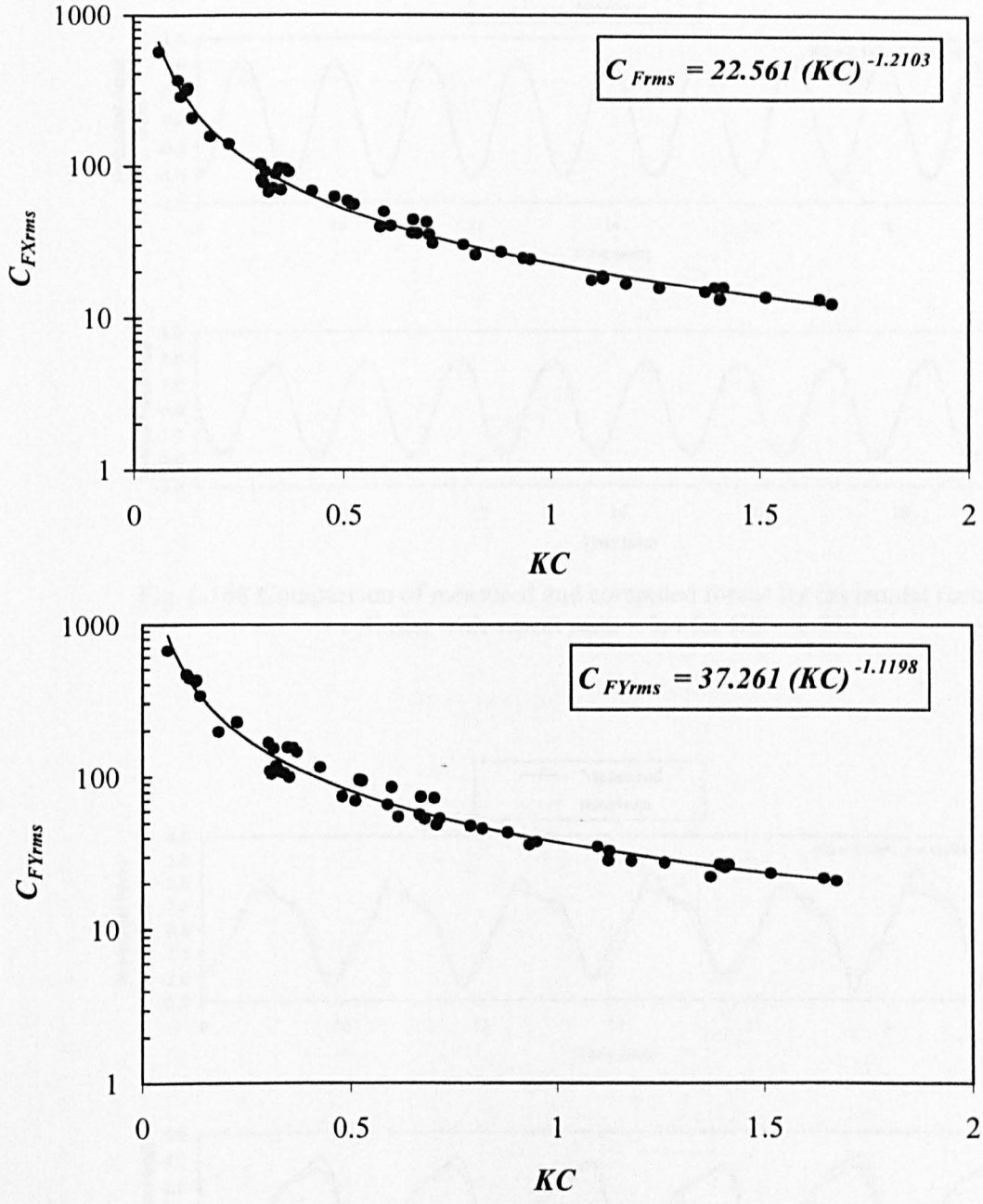

Fig. 6.167 Horizontal and vertical rms force coefficients for horizontal rectangular cylinder for aspect ratio = 3/4

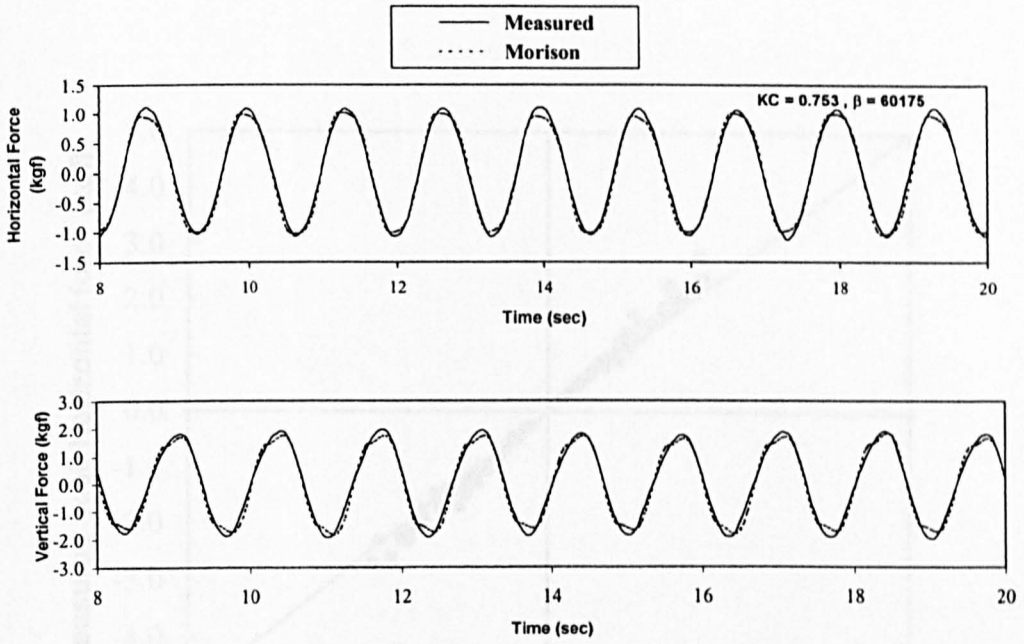

Fig. 6.168 Comparison of measured and computed forces for horizontal rectangular cylinder with aspect ratio = 3/4 for KC = 0.753

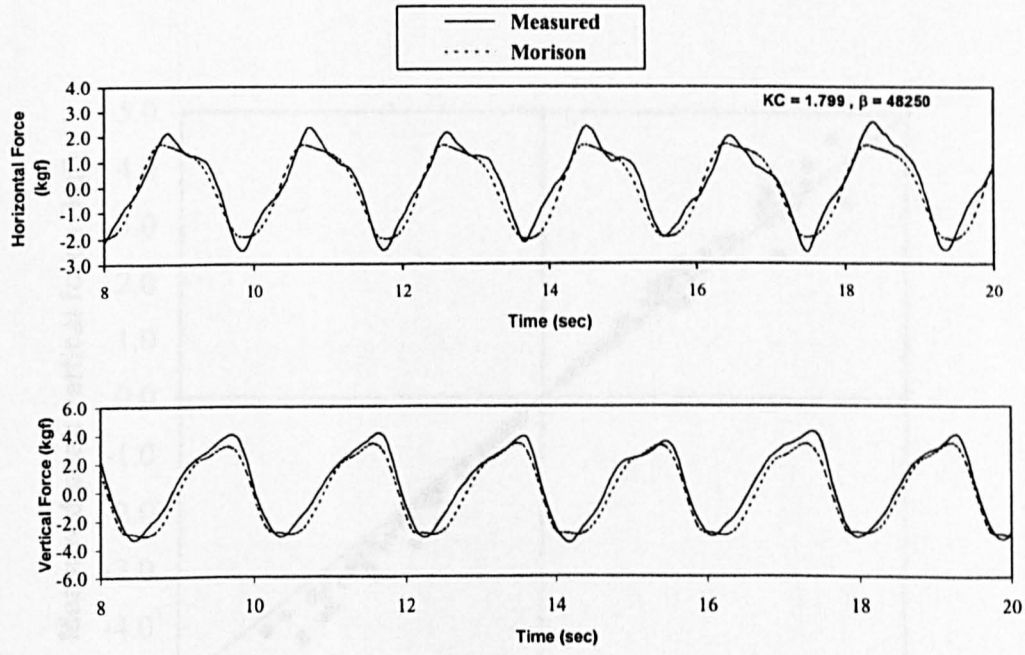

Fig. 6.169 Comparison of measured and computed forces for horizontal rectangular cylinder with aspect ratio = 3/4 for KC = 1.799

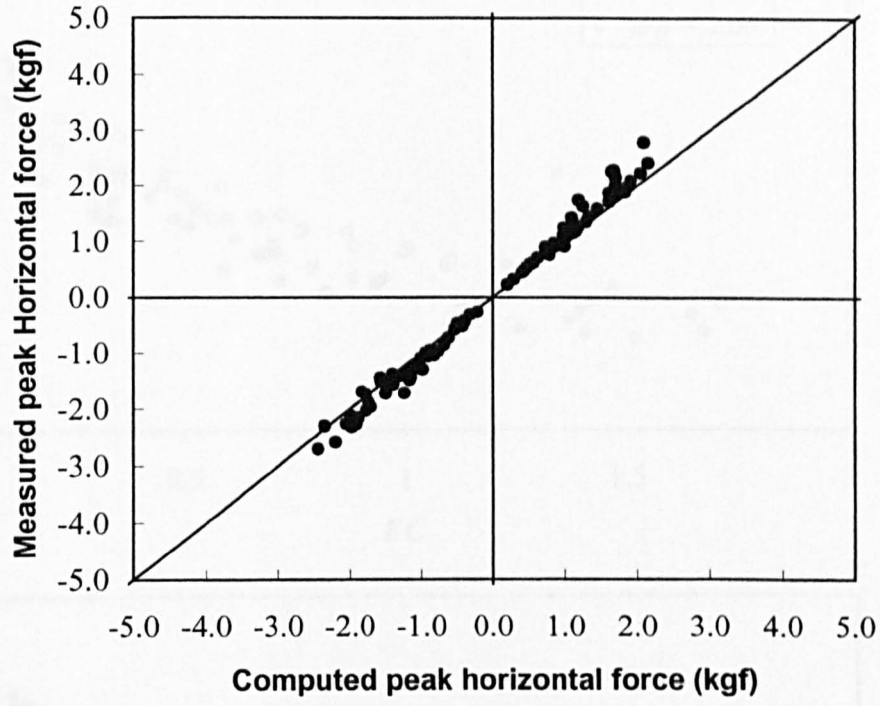

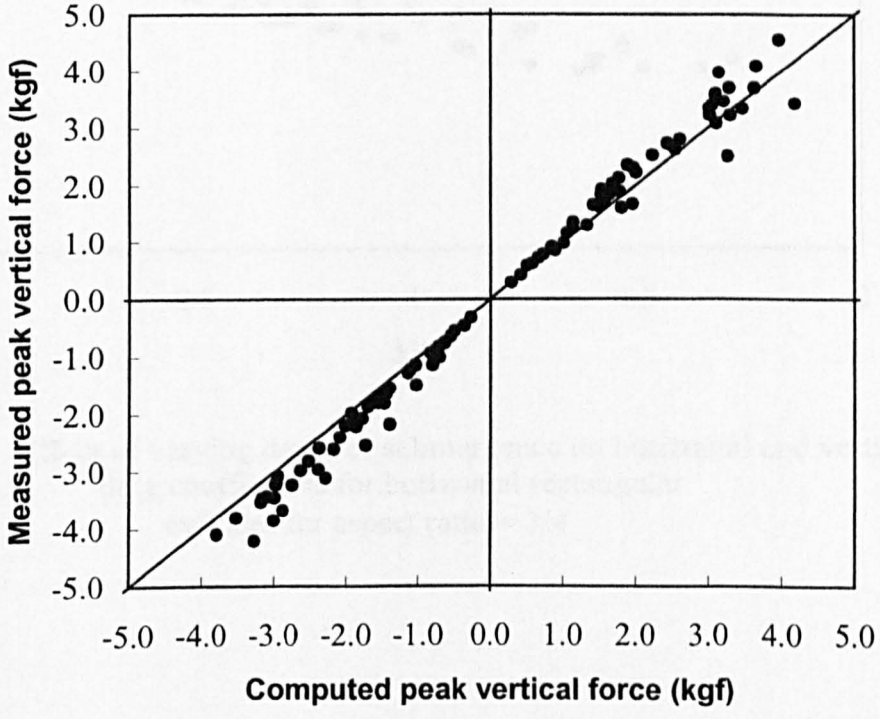

Fig. 6.170 Measured and computed peak forces for horizontal rectangular cylinder for aspect ratio = 3/4

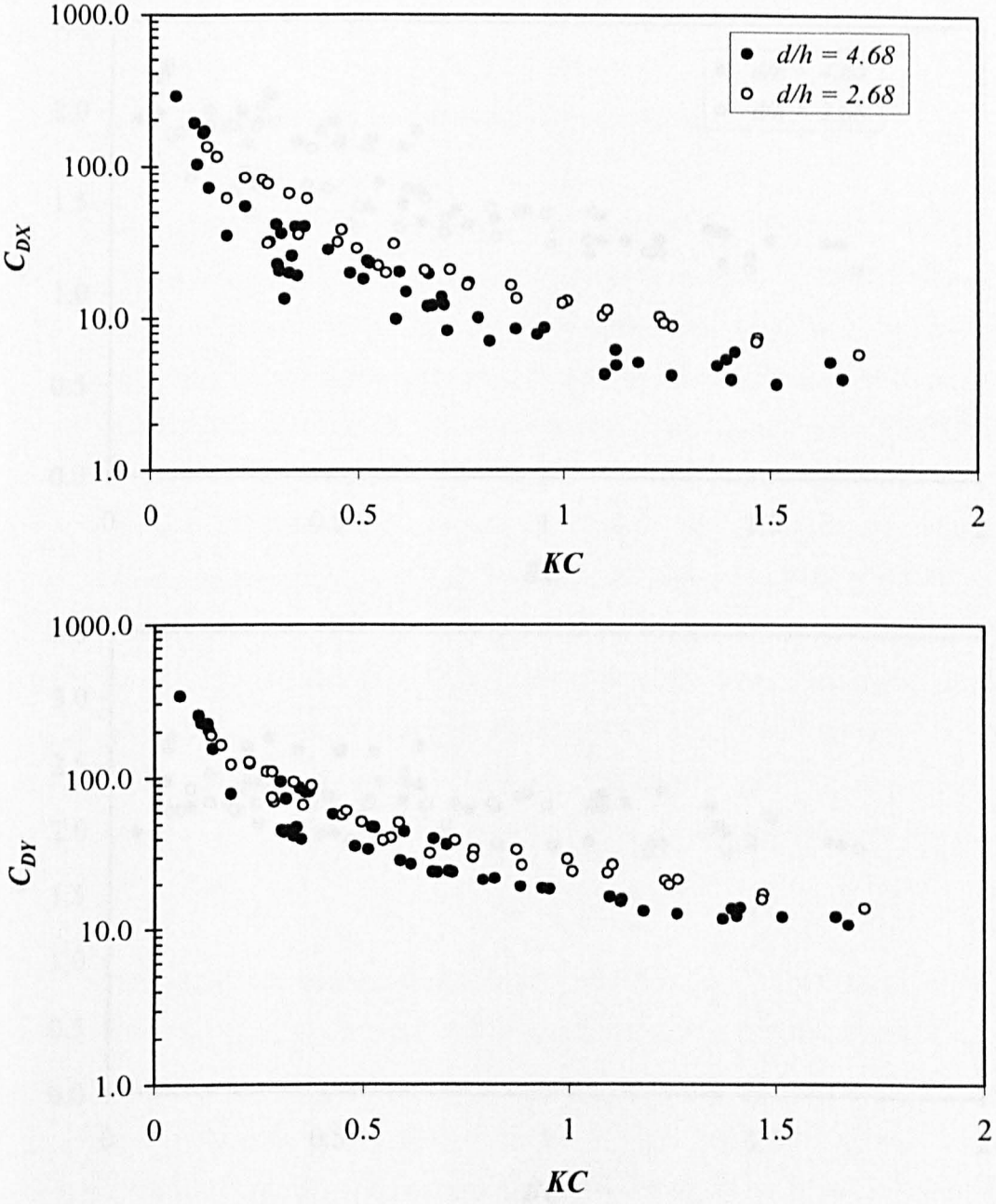

Fig. 6.171 Effect of varying depth of submergence on horizontal and vertical drag coefficients for horizontal rectangular cylinder for aspect ratio = 3/4

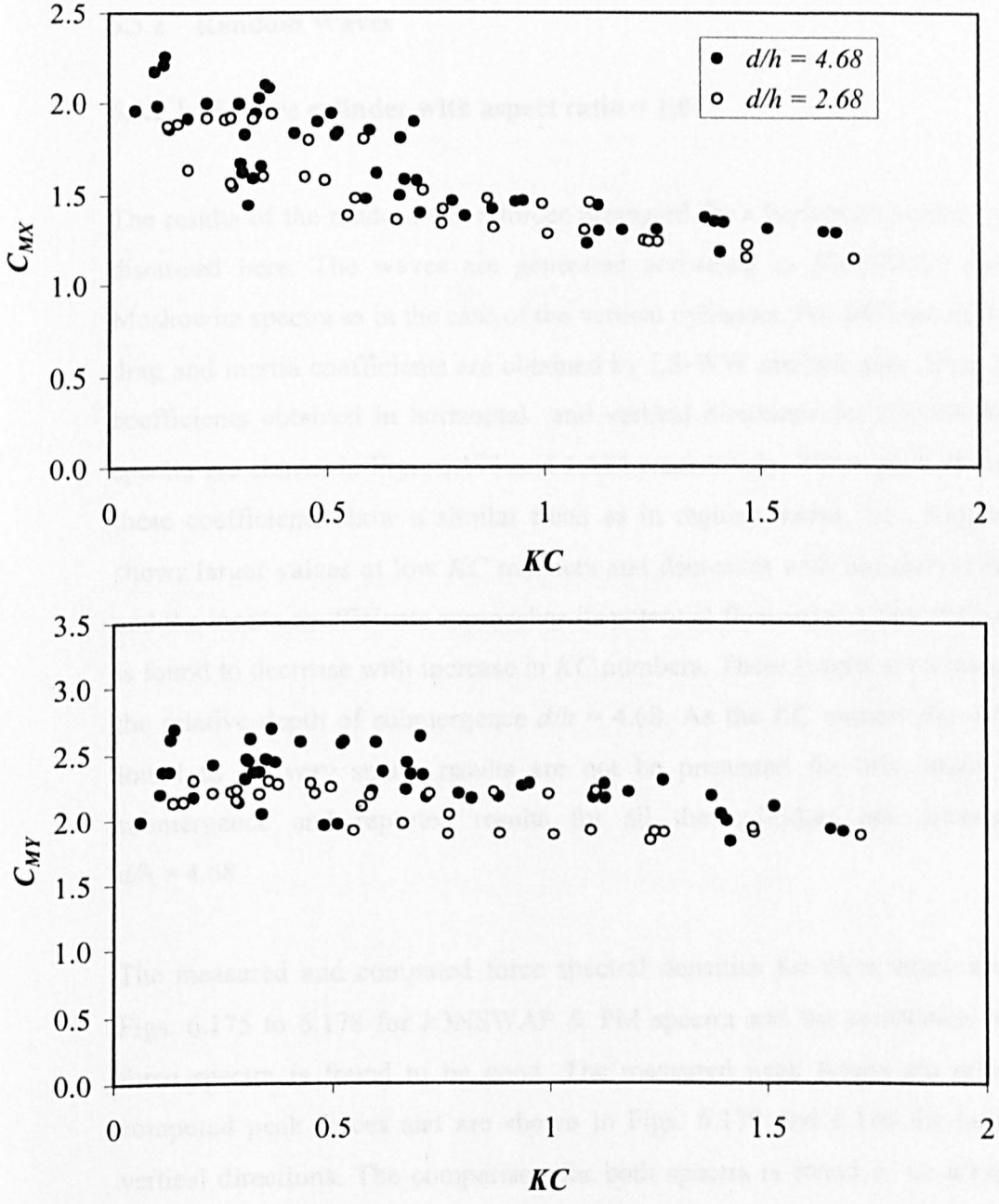

Fig. 6.172 Effect of varying depth of submergence on horizontal and vertical inertia coefficients for horizontal rectangular cylinder for aspect ratio = 3/4

6.3.2 Random Waves

6.3.2.1 Square cylinder with aspect ratio = 1.0

The results of the random wave forces measured for a horizontal square cylinder are discussed here. The waves are generated according to JONSWAP and Pierson-Moskowitz spectra as in the case of the vertical cylinders. For all horizontal cylinders, drag and inertia coefficients are obtained by LS-WW method only. Drag and inertia coefficients obtained in horizontal and vertical directions for JONSWAP and PM spectra are shown in Figs. 6.173 and 6.174 respectively. These plots show that both these coefficients show a similar trend as in regular waves, i.e., drag coefficients shows larger values at low KC numbers and decreases with increase in KC number and the inertia coefficients approaches its potential flow value at low KC number and is found to decrease with increase in KC numbers. These results are corresponding to the relative depth of submergence d/h = 4.68. As the KC number for d/h = 2.68 is found to be very small, results are not be presented for this relative depth of submergence and reported results for all the cylinders are corresponding to d/h = 4.68.

The measured and computed force spectral densities for three cases are shown in Figs. 6.175 to 6.178 for JONSWAP & PM spectra and the correlation between the force spectra is found to be good. The measured peak forces are plotted against computed peak forces and are shown in Figs. 6.179 and 6.180 for horizontal and vertical directions. The comparison for both spectra is found to be good, however, measured positive peak forces in the vertical direction are over predicted.

6.3.2.2 Rectangular Cylinder with Aspect ratio = 1/2

Drag and inertia coefficients for horizontal and vertical forces for rectangular cylinder with aspect ratio = 1/2 is shown in Figs.6.181 and 6.182. Drag coefficients

corresponding to PM spectra are found to be slightly higher compared to the coefficients from JS spectrum.

The measured and computed force spectral densities for three cases are shown in Figs. 6.183 to 6.186 for JONSWAP & PM spectra and the correlation between the force spectra is found to be good. The measured peak forces are plotted against computed peak forces and are shown in Fig. 6.187 and 6.188 for horizontal and vertical directions.

6.3.2.3 Rectangular Cylinder with Aspect ratio = 3/4

Drag and inertia coefficients for horizontal and vertical forces for rectangular cylinder with aspect ratio = 3/4 is shown in Figs.6.189 and 6.190. Both drag and inertia coefficients take identical values for both spectra. The measured and computed force spectral densities for three cases are shown in Figs. 6.191 to 6.194 for JONSWAP & PM spectra and the correlation between the spectra is found to be good. The measured peak forces are plotted against computed peak forces and are shown in Fig.6.195 and 6.196 for horizontal and vertical directions.

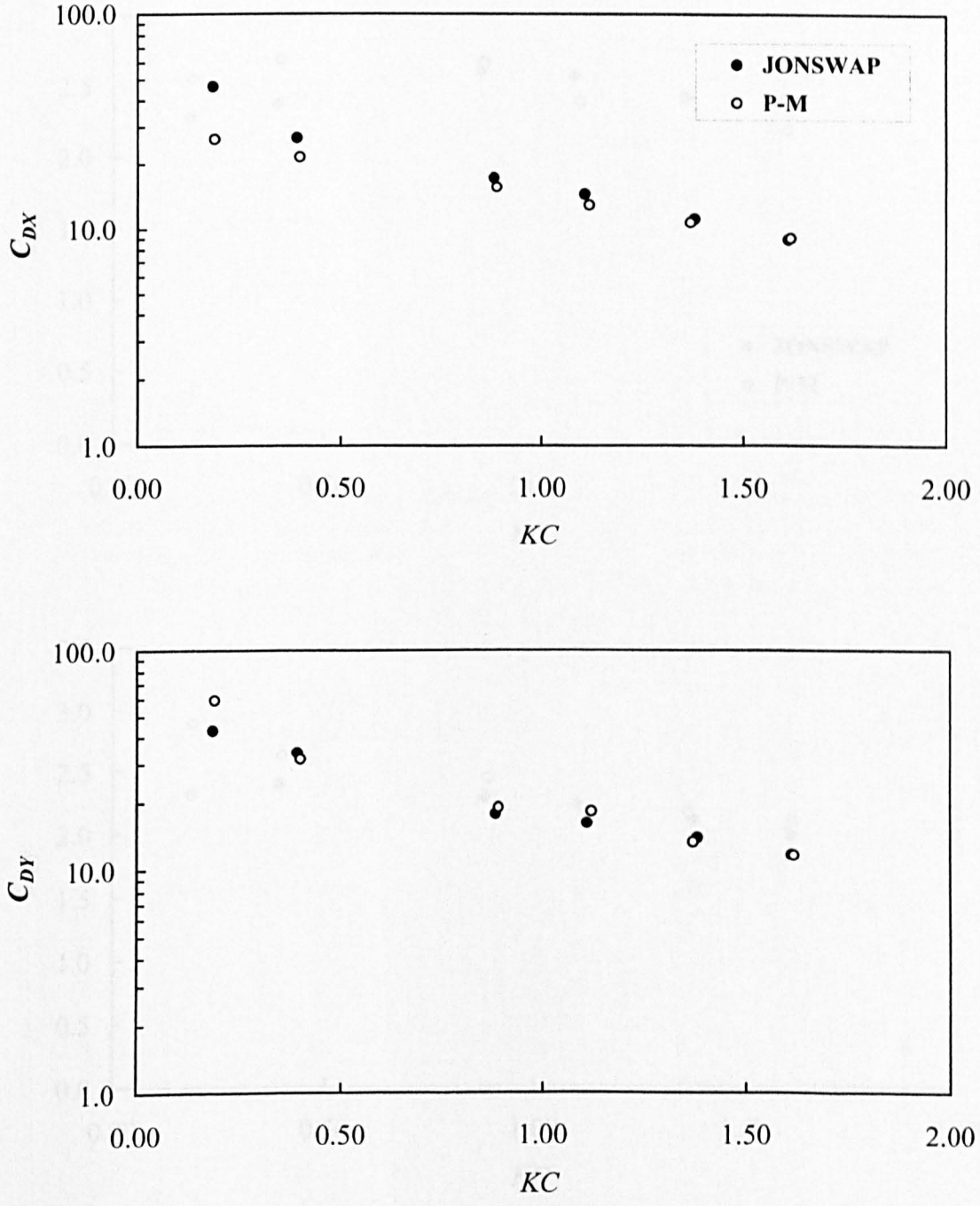

Fig. 6.173 Horizontal and vertical drag coefficients for horizontal square cylinder in random waves

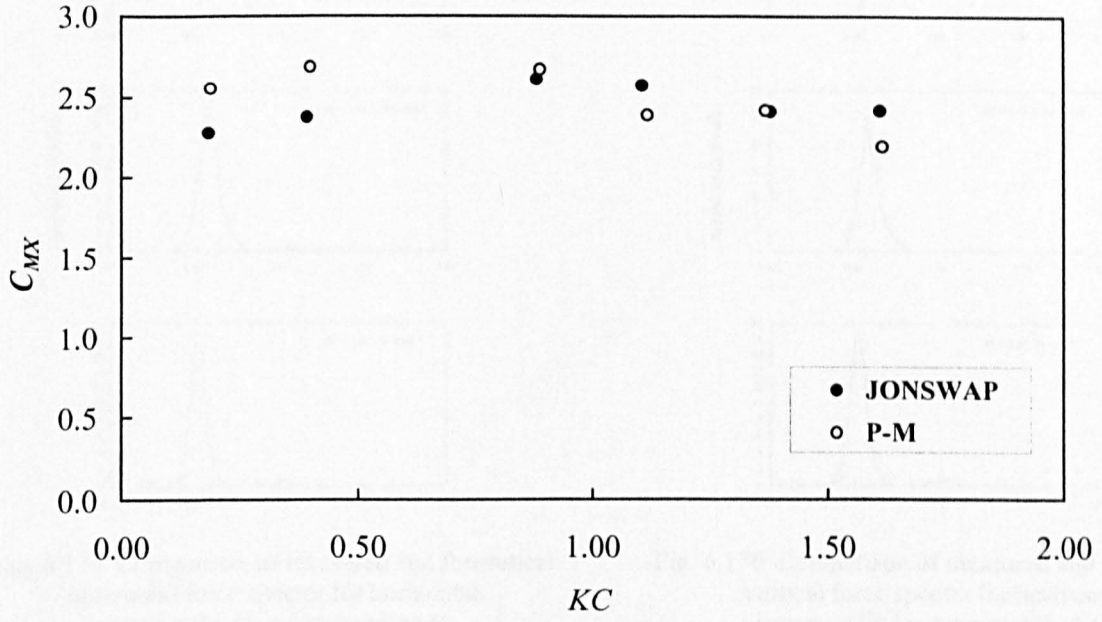

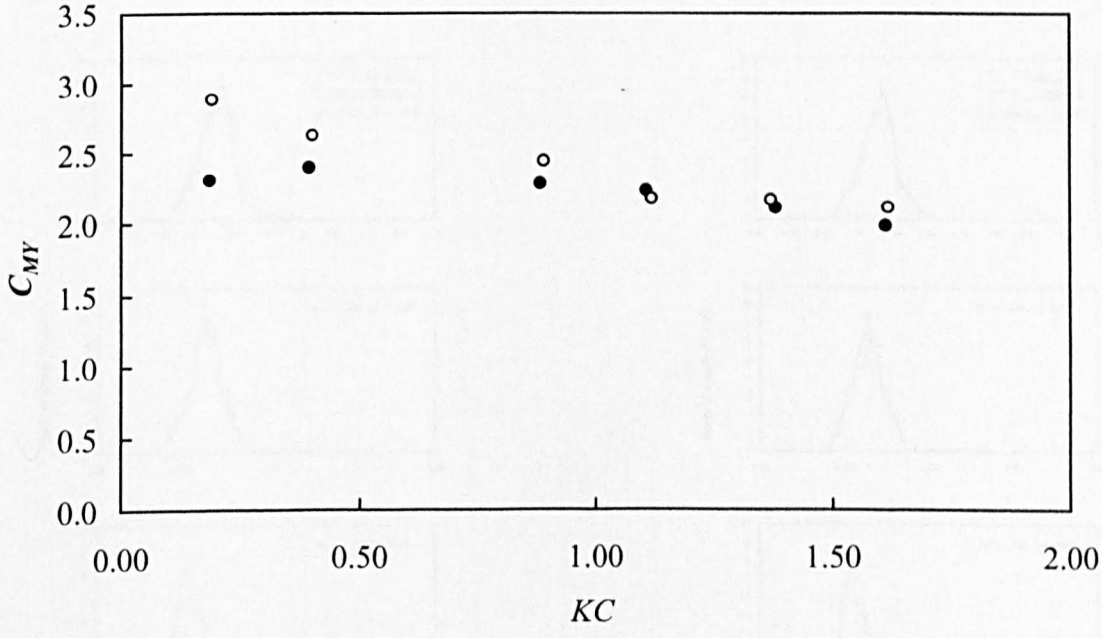

Fig. 6.174 Horizontal and vertical inertia coefficients for horizontal square cylinder for random waves

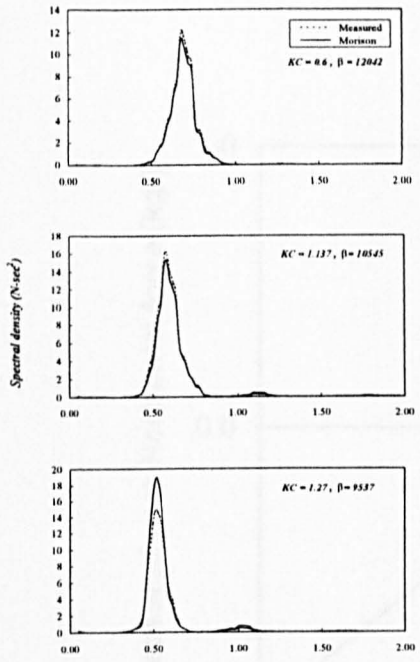

Fig. 6.175 Comparison of measured and theoretical horizontal force spectra for horizontal square cylinder corresponding to JONSWAP spectrum

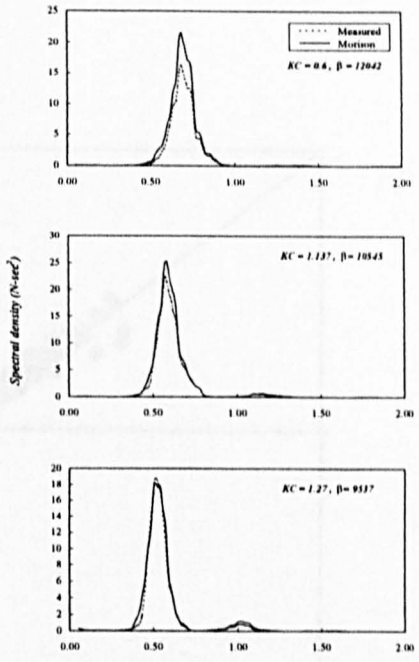

Fig. 6.176 Comparison of measured and theoretical vertical force spectra for horizontal square cylinder corresponding to JONSWAP spectrum

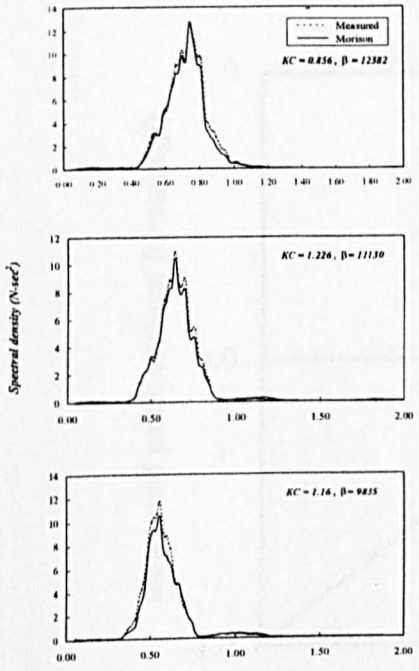

Fig. 6.177 Comparison of measured and theoretical horizontal force spectra for horizontal square cylinder corresponding to P-M spectrum

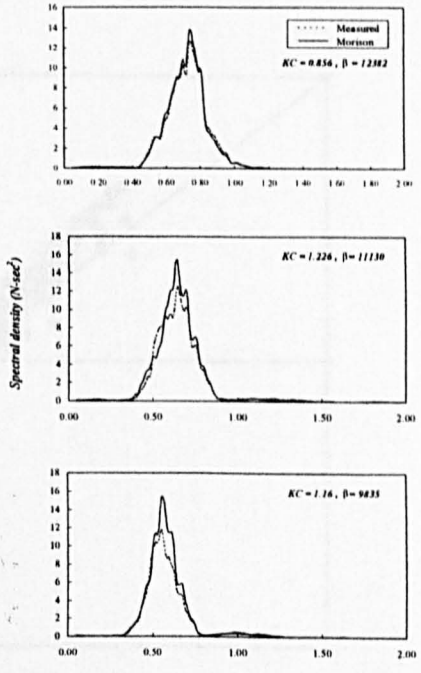

Fig. 6.178 Comparison of measured and theoretical vertical force spectra for horizontal square cylinder corresponding to P-M spectrum

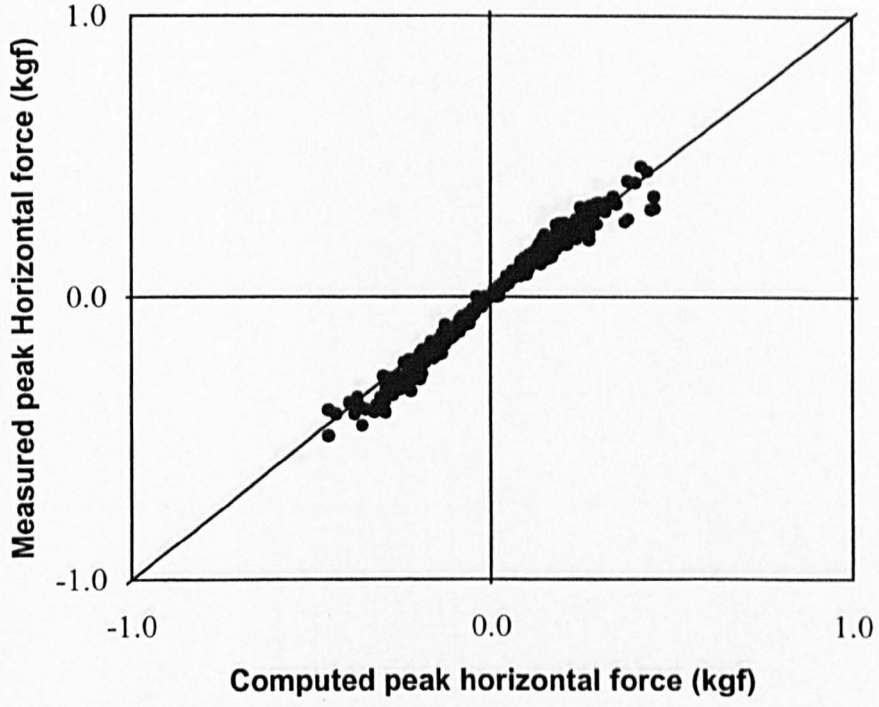

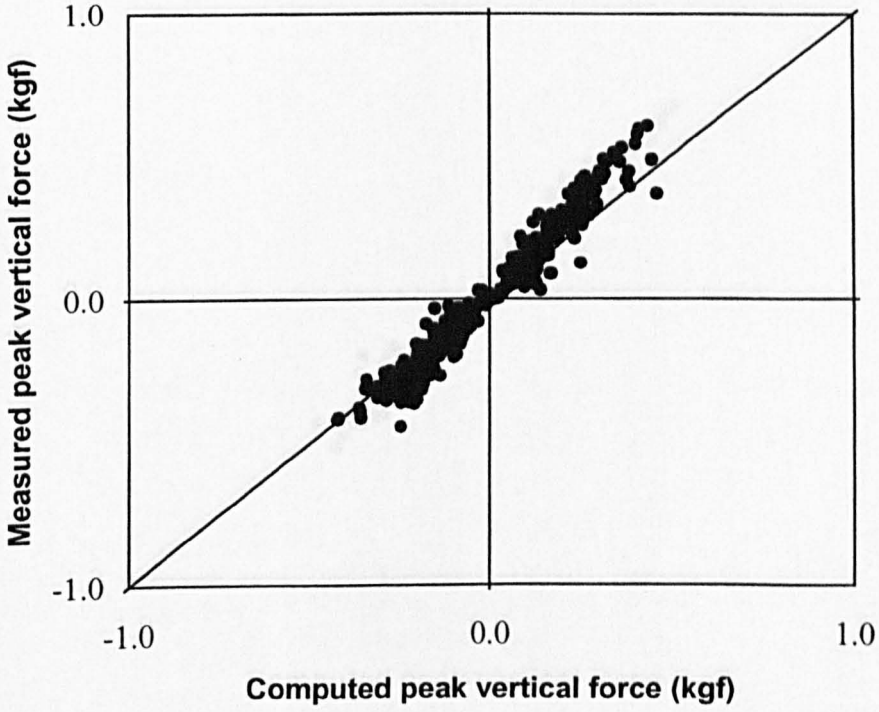

Fig. 6.179 Measured and computed peak forces for horizontal square cylinder for JONSWAP spectrum

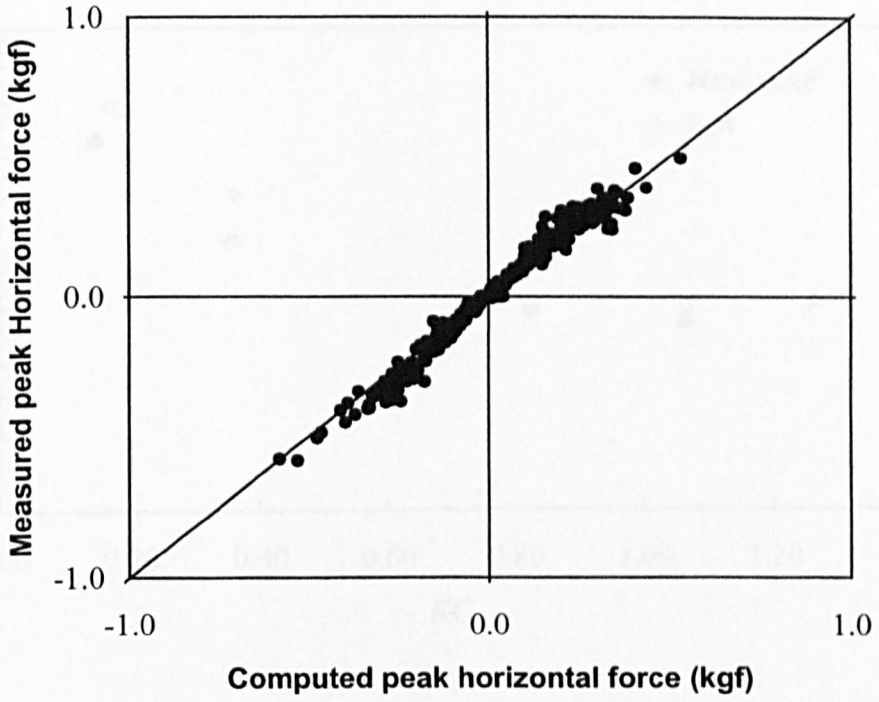

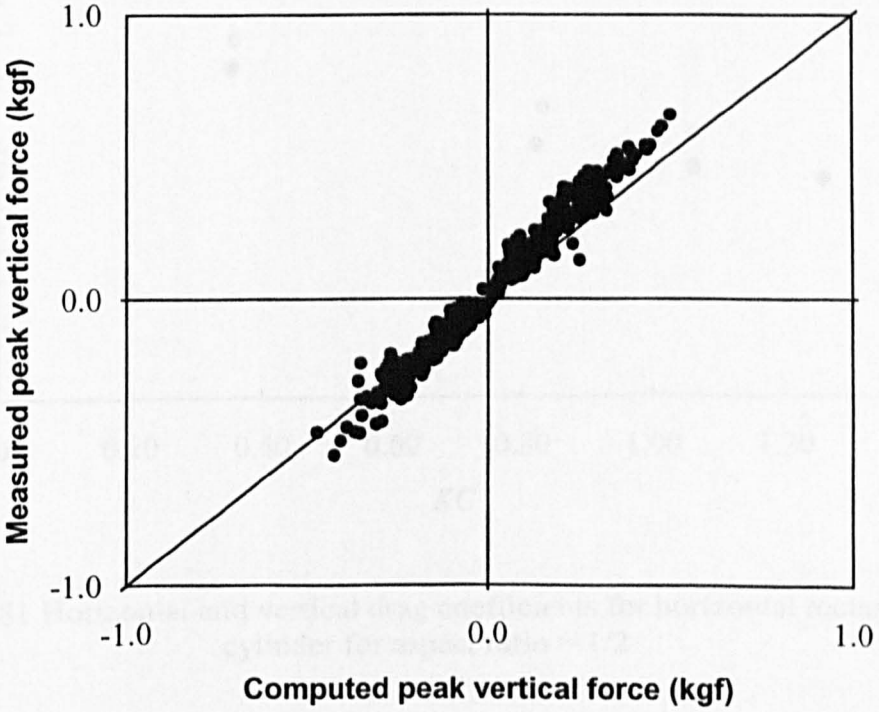

Fig. 6.180 Measured and computed peak forces for horizontal square cylinder for P-M spectrum

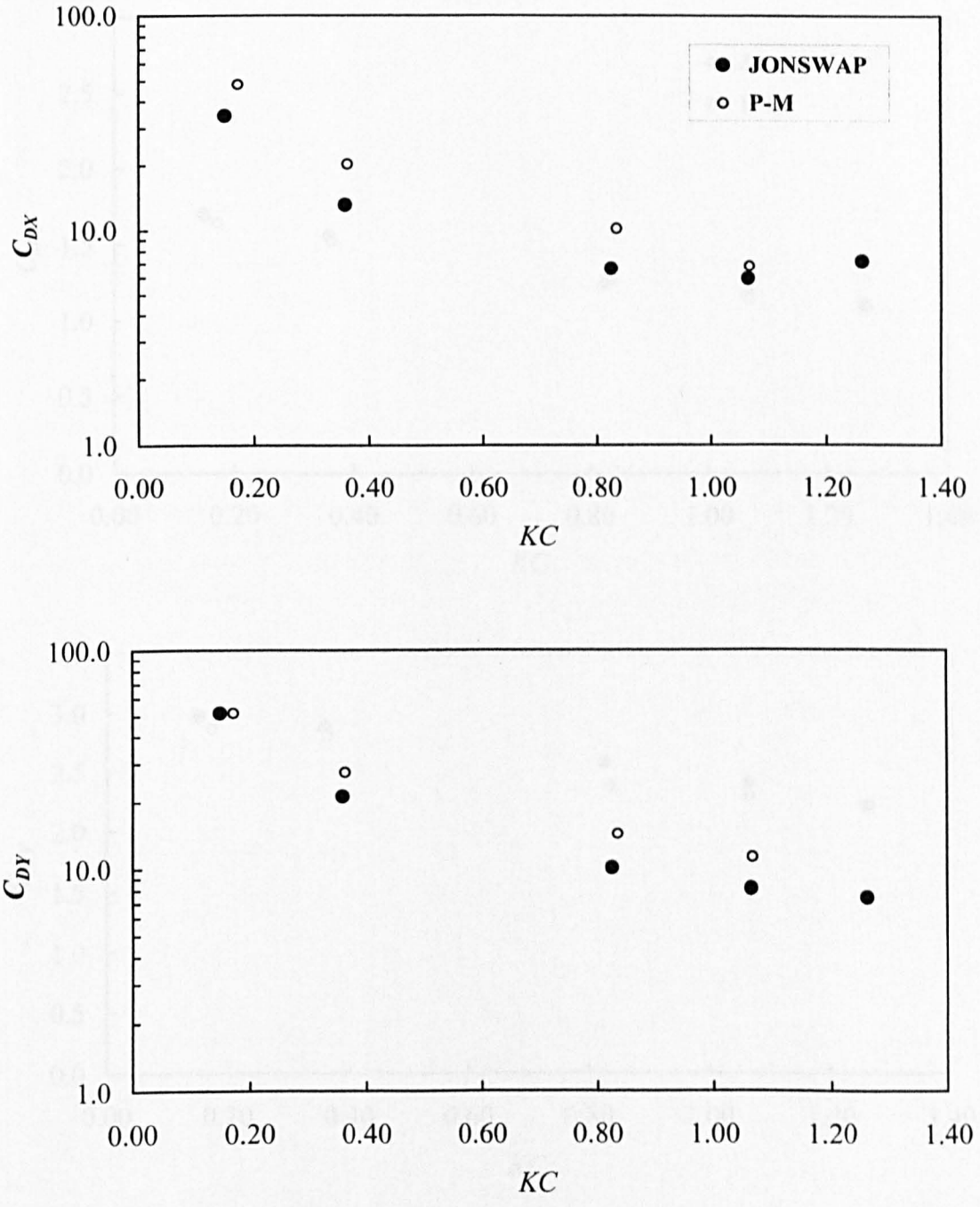

Fig. 6.181 Horizontal and vertical drag coefficients for horizontal rectangular cylinder for aspect ratio = 1/2

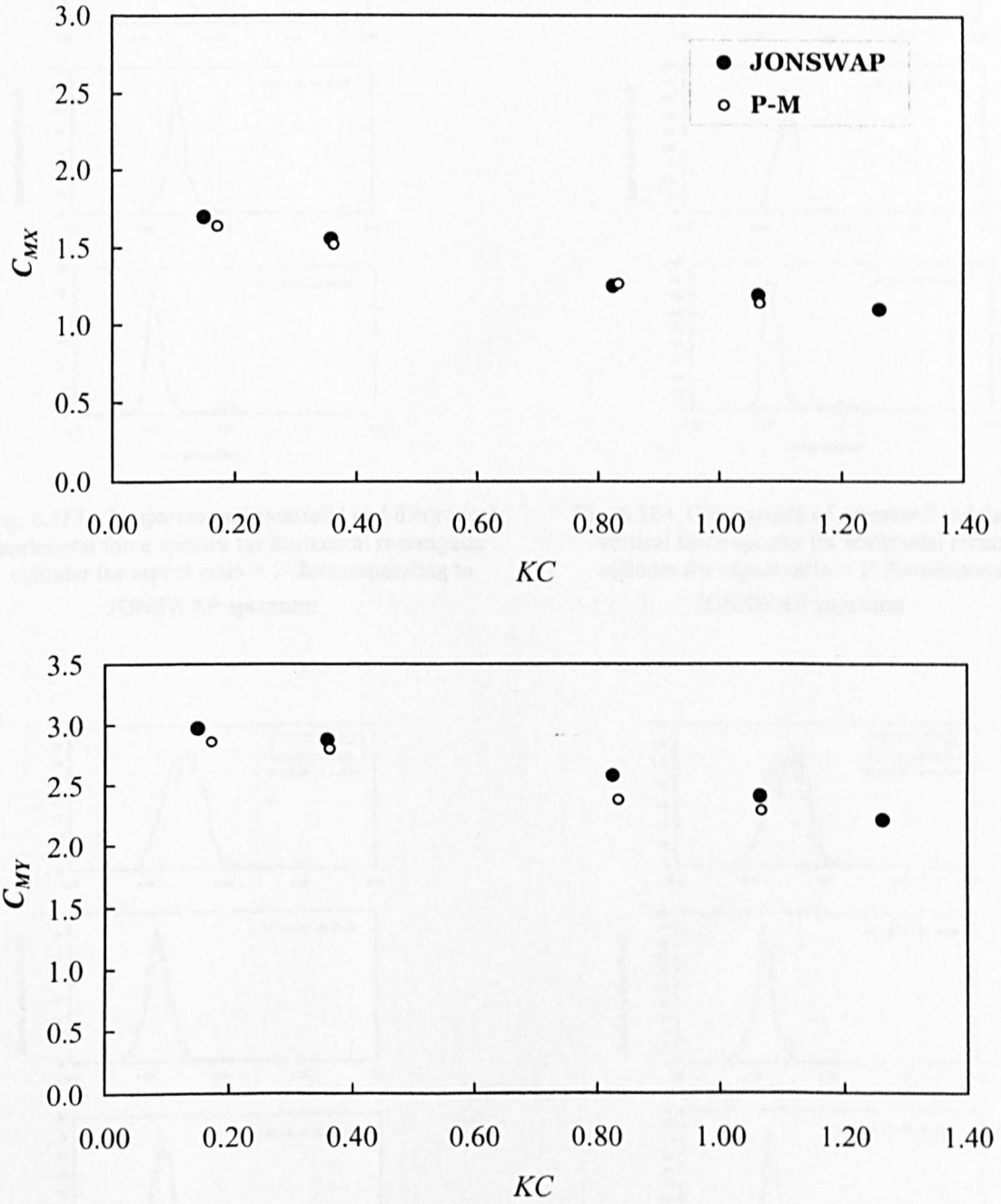

Fig. 6.182 Horizontal and vertical inertia coefficients for horizontal rectangular cylinder for aspect ratio = 1/2

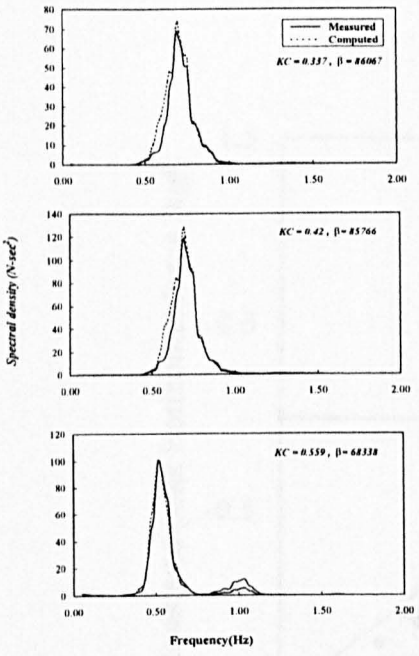

Fig. 6.183 Comparison of measured and theoretical horizontal force spectra for horizontal rectangular cylinder for aspect ratio = 1/ 2corresponding to JONSWAP spectrum

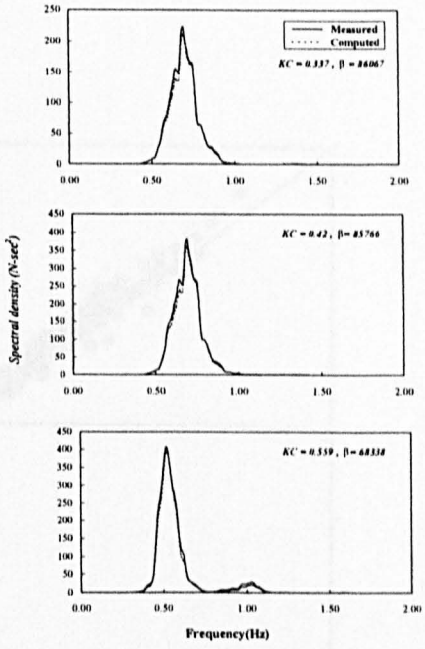

Fig. 6.184 Comparison of measured and theoretical vertical force spectra for horizontal rectangular cylinder for aspect ratio = 1/ 2corresponding to JONSWAP spectrum

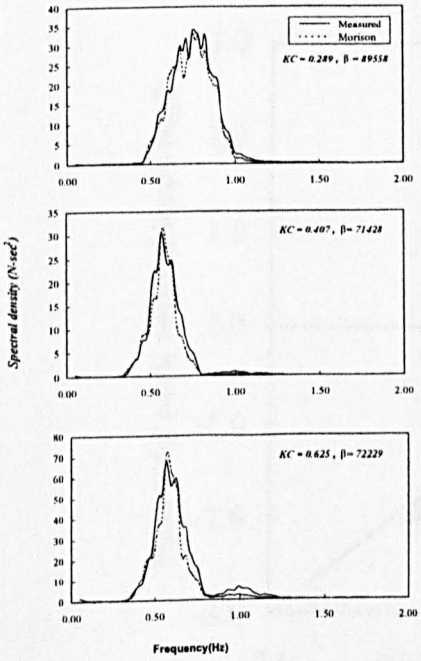

Fig. 6.185 Comparison of measured and theoretical horizontal force spectra for horizontal rectangular cylinder for aspect ratio = 1/ 2 corresponding to P-M spectrum

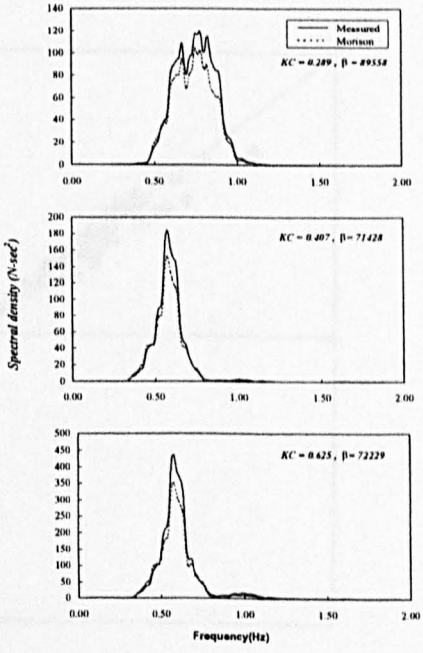

Fig. 6.186 Comparison of measured and theoretical vertical force spectra for horizontal rectangular cylinder for aspect ratio = 1/ 2 corresponding to P-M spectrum

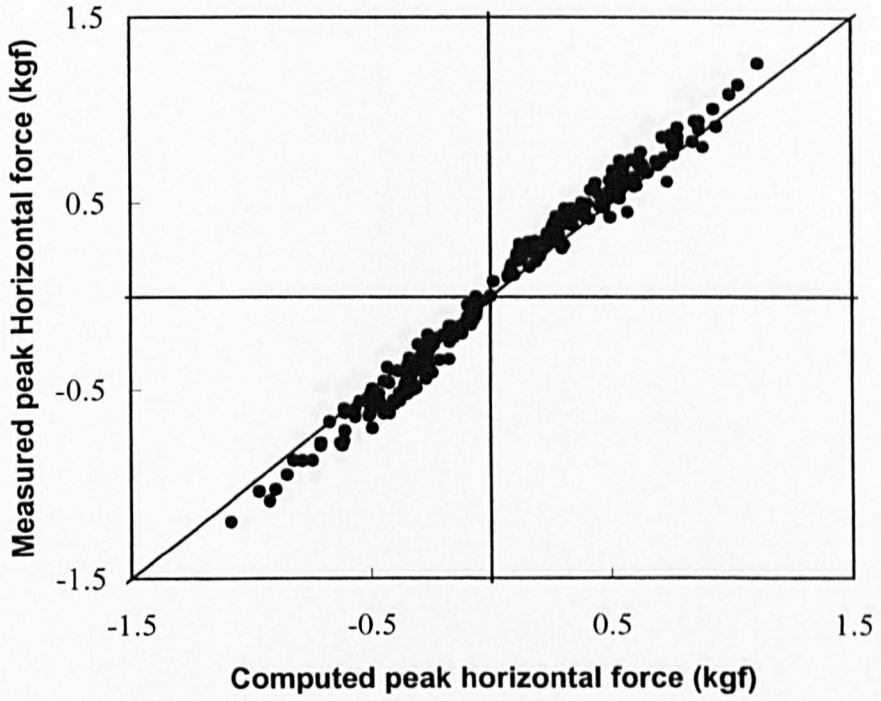

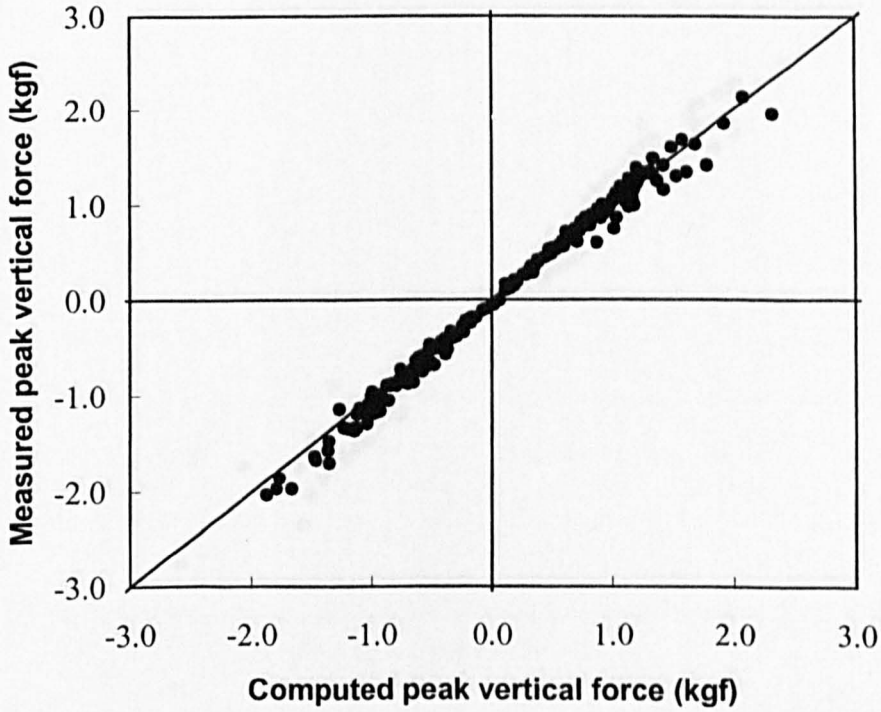

Fig. 6.187 Measured and computed peak forces for horizontal rectangular cylinder for aspect ratio = ½ for JONSWAP spectrum

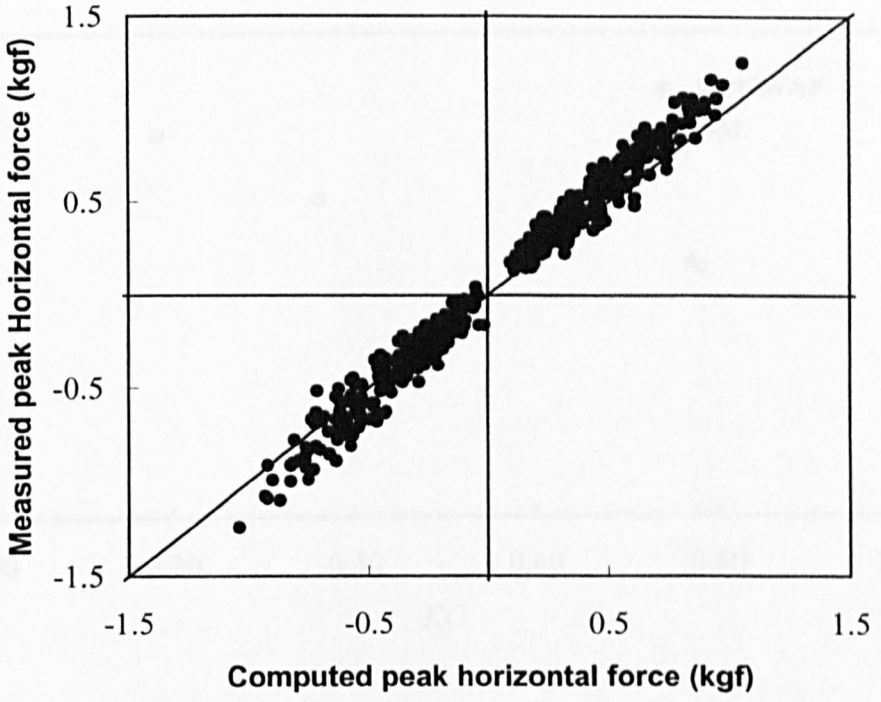

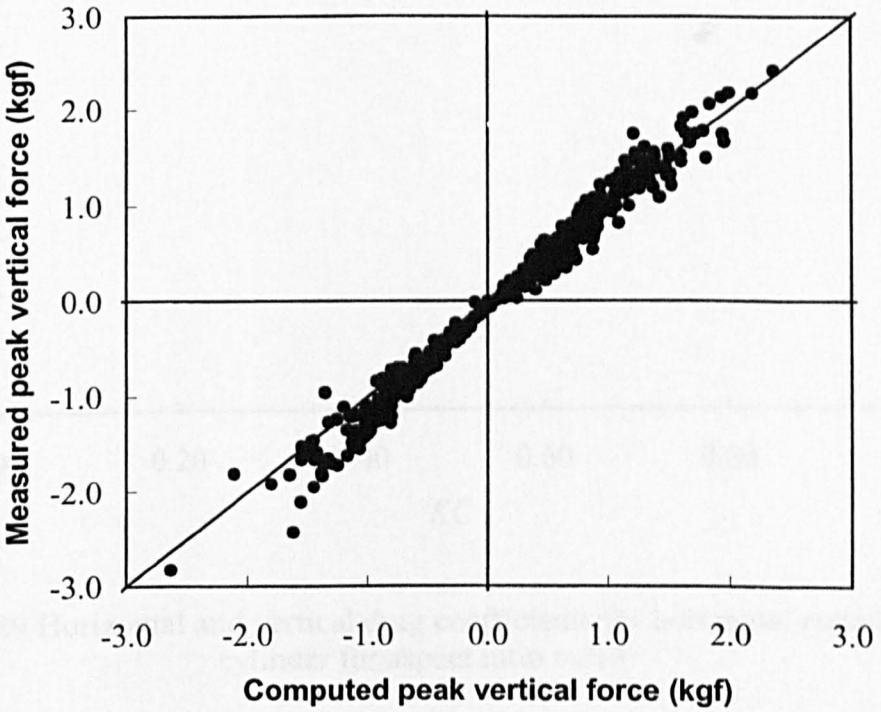

Fig. 6.188 Measured and computed peak forces for horizontal rectangular cylinder for aspect ratio = ½ for P-M spectrum

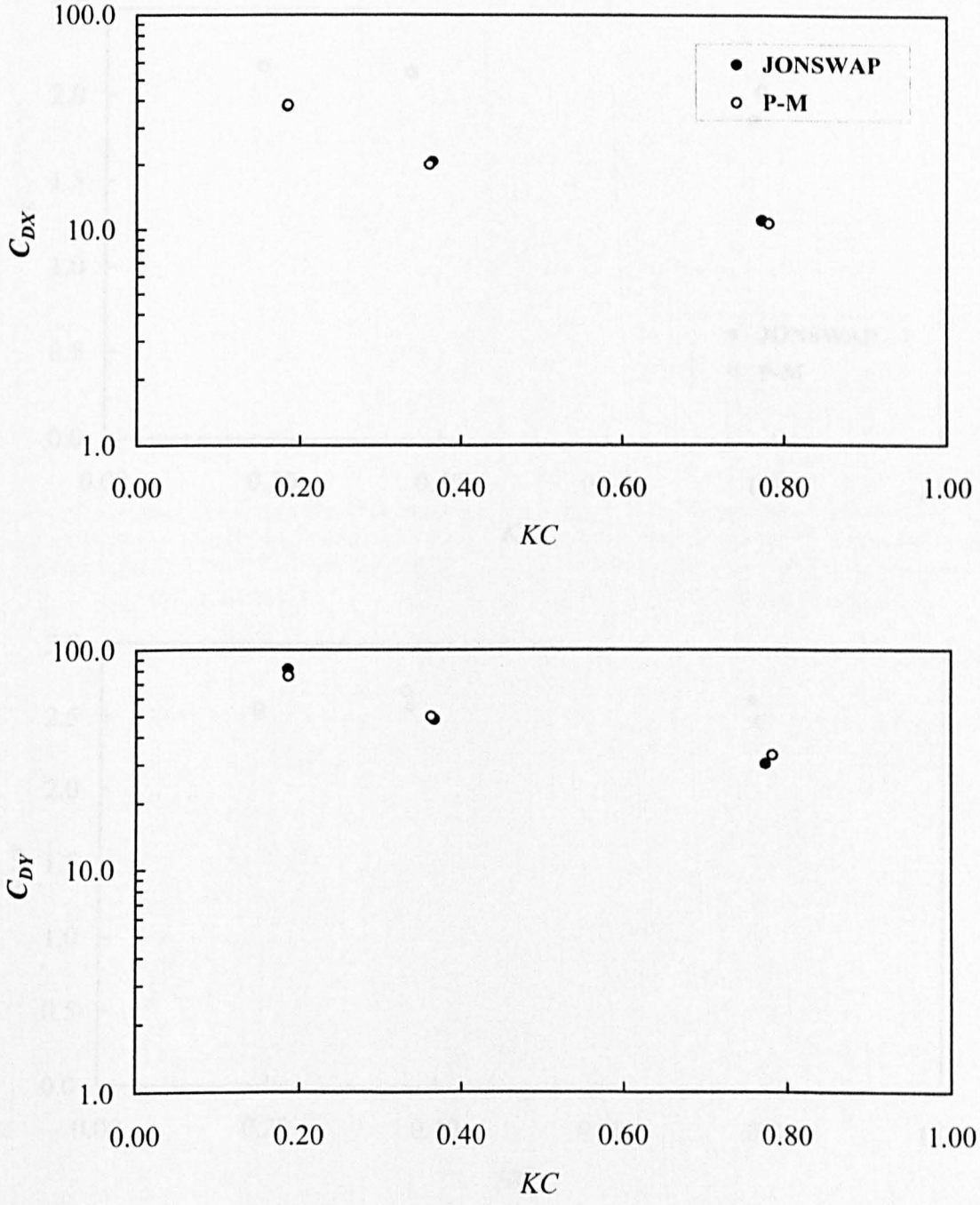

Fig. 6.189 Horizontal and vertical drag coefficients for horizontal rectangular cylinder for aspect ratio = 3/4

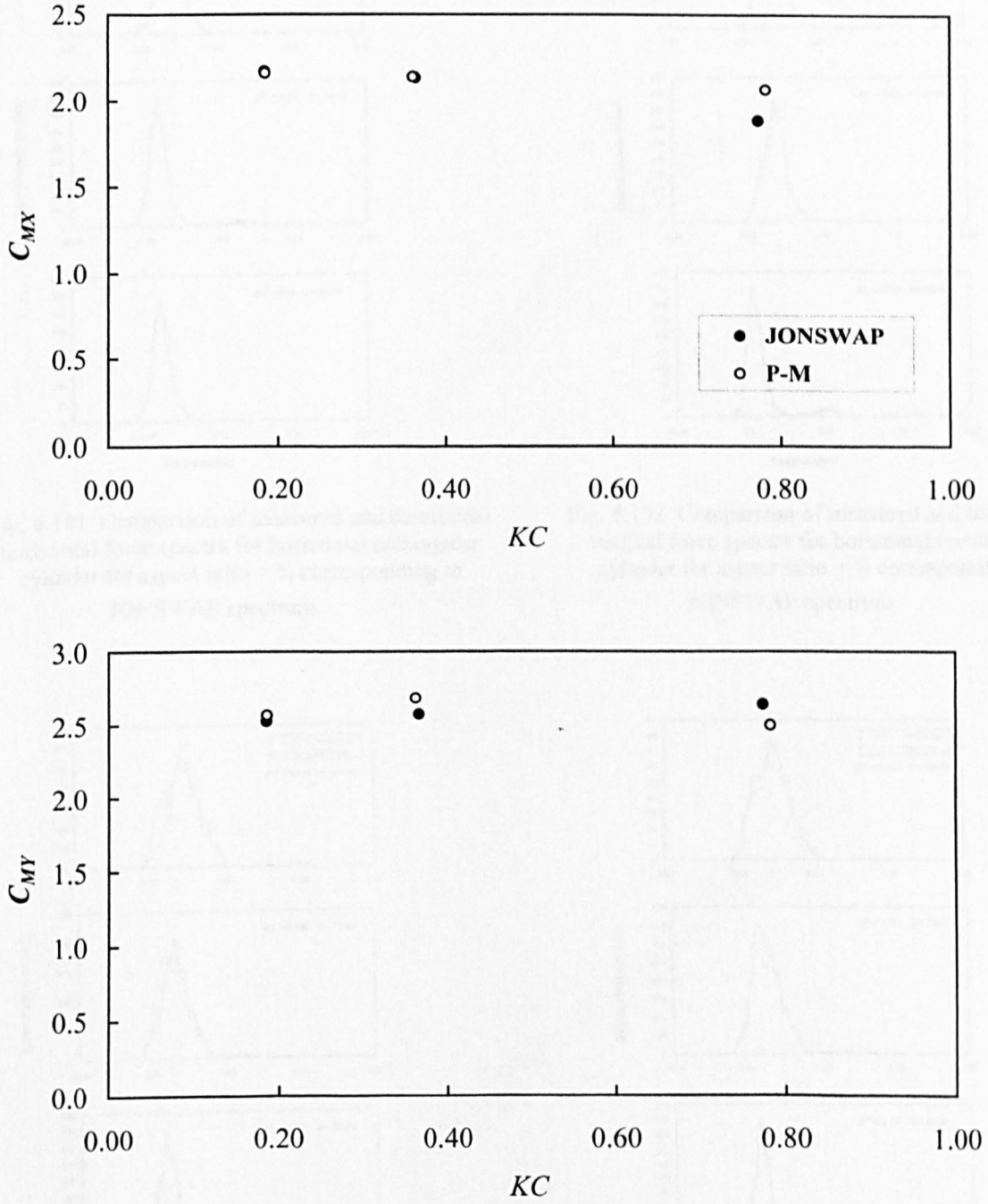

Fig. 6.190 Horizontal and vertical inertia coefficients for horizontal rectangular cylinder for aspect ratio = 3/4

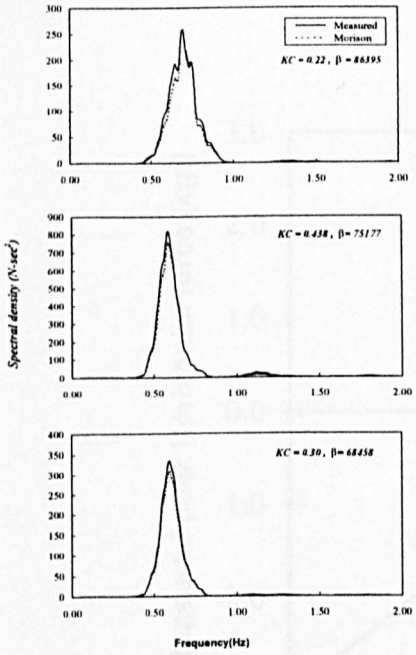

Fig. 6.191 Comparison of measured and theoretical horizontal force spectra for horizontal rectangular cylinder for aspect ratio = ¾ corresponding to JONSWAP spectrum

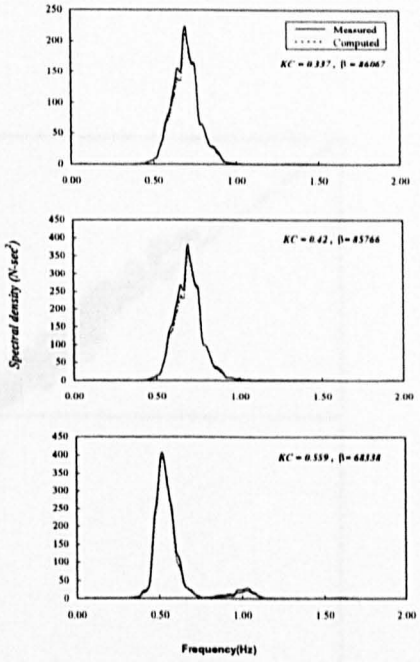

Fig. 6.192 Comparison of measured and theoretical vertical force spectra for horizontal rectangular cylinder for aspect ratio = ¾ corresponding to JONSWAP spectrum

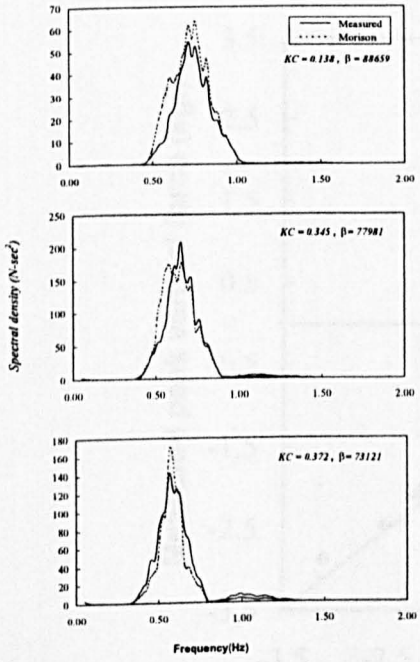

Fig. 6.193 Comparison of measured and theoretical horizontal force spectra for horizontal rectangular cylinder for aspect ratio = 3/4 corresponding to P-M spectrum

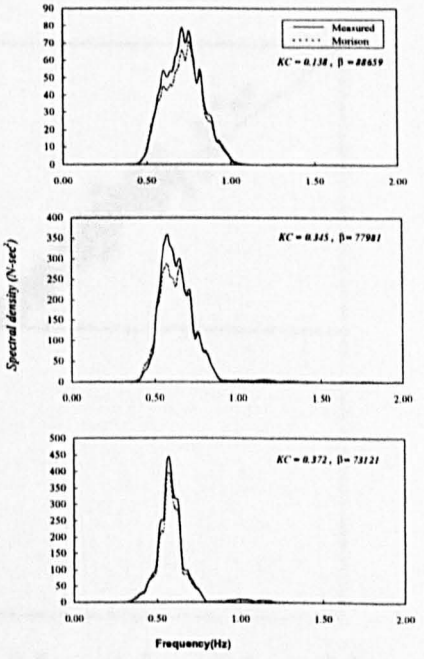

Fig. 6.194 Comparison of measured and theoretical vertical force spectra for horizontal rectangular cylinder for aspect ratio = 3/4 corresponding to P-M spectrum

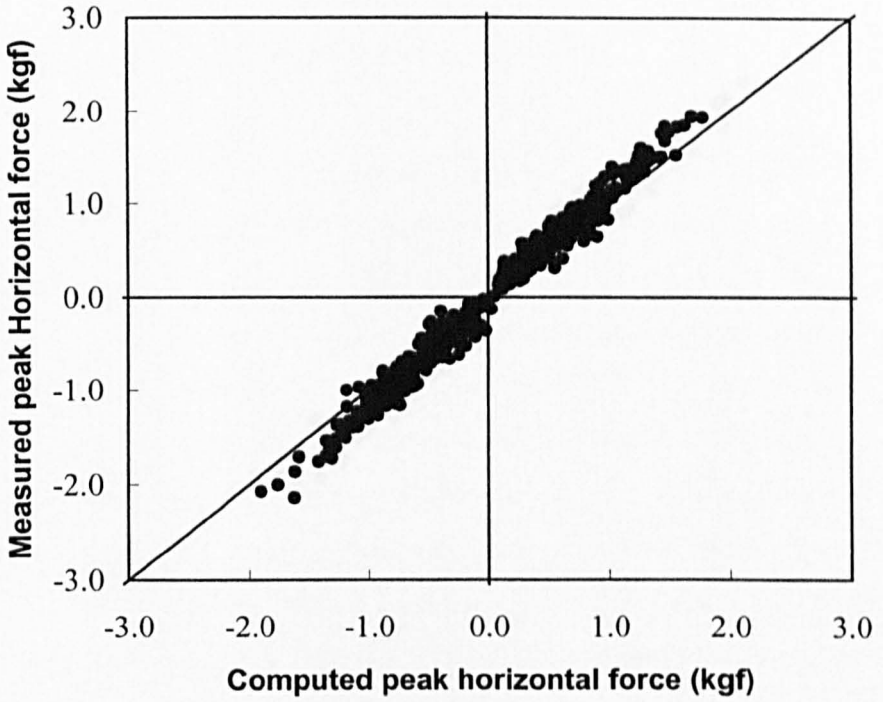

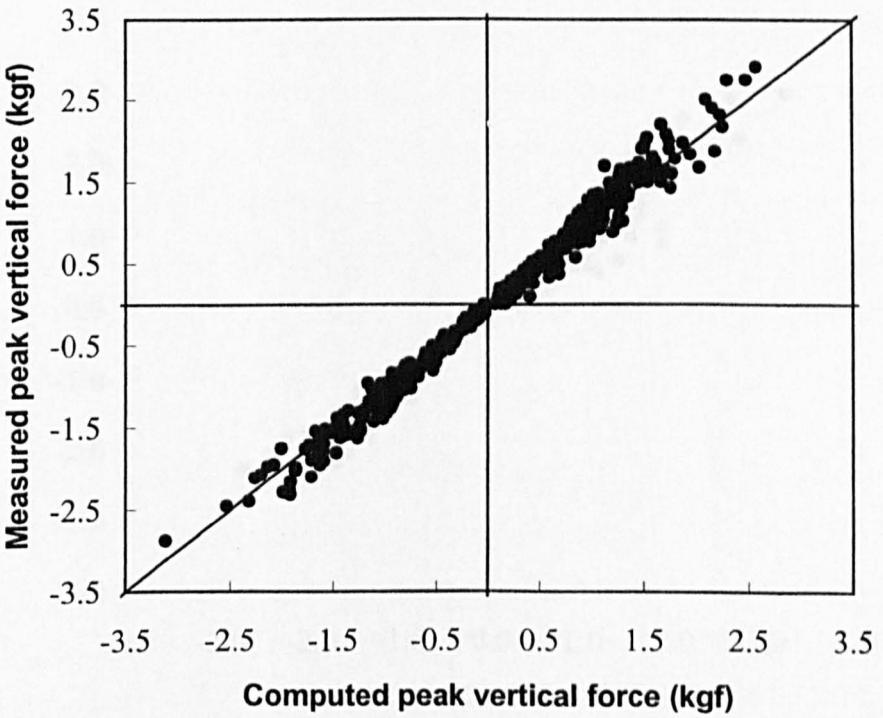

Fig. 6.195 Measured and computed peak forces for horizontal rectangular cylinder for aspect ratio = ¾ for JONSWAP spectrum

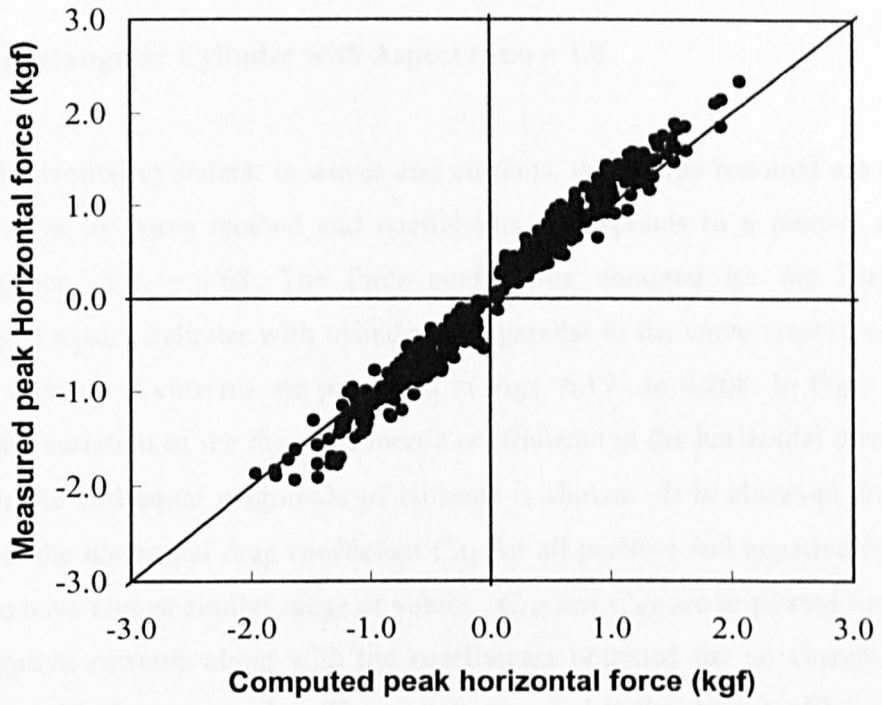

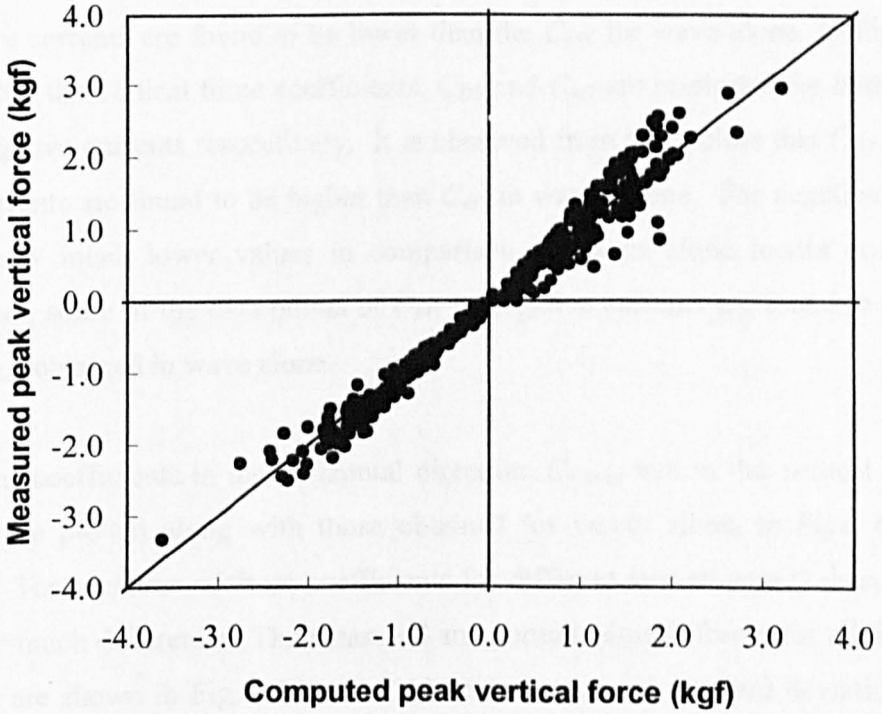

Fig. 6.196 Measured and computed peak forces for horizontal Rectangular cylinder for aspect ratio = ¾ for P-M spectrum

6.3.3 Regular Waves and Current

6.3.3.1 Rectangular Cylinder with Aspect ratio = 1.0

For all horizontal cylinders, in waves and currents, the results reported are obtained by the wave by wave method and coefficients corresponds to a relative depth of submergence, d/h = 4.68. The force coefficients obtained for the horizontally submerged square cylinder with cylinder axis parallel to the wave crest in combined regular waves and currents are presented in Figs. 6.197 to 6.208. In Figs. 6.197 to 6.202, the variation of the drag and inertia coefficients in the horizontal direction for the opposite and equal magnitude of currents is shown. It is observed from these plots that the horizontal drag coefficient C_{DX} for all positive and negative currents is found to have almost similar range of values. C_{DX} and C_{MX} are re-plotted for positive and negative currents along with the coefficients obtained for no current in Figs. 6.203 and 6.204 respectively. These plots reveal that the drag coefficients in the horizontal direction are significantly larger than the drag coefficients for waves alone. A large scatter is observed for C_{MX} values and for $KC < 2.5$, some of the data for negative currents are found to be lower than the C_{MX} for wave alone. In Figs. 6.205 and 6.206 the vertical force coefficients, C_{DY} and C_{MY} are re-plotted for both positive and negative currents respectively. It is observed from these plots that C_{DY} in waves and currents are found to be higher than C_{DY} in waves alone. For negative currents, C_{MY} show much lower values in comparison to waves alone inertia coefficients. However, some of the data points of C_{MY} in negative currents are found to be higher than C_{MY} obtained in wave alone.

The rms coefficients in the horizontal direction, C_{FXrms} and in the vertical direction, C_{FYrms} are plotted along with those obtained for waves alone, in Figs. 6.207 and 6.208. The variation of these coefficients for different current speeds does not seem to have much difference. The measured and computed peak forces for all the current speeds are shown in Fig. 6.209. In Table 6.4, means and standard deviations for all

current speeds are provided. For negative currents, a maximum of 39% difference is observed between the measured and Morison forces in horizontal direction.

6.3.3.2 Rectangular Cylinder with Aspect ratio = 1/2

The variation of the drag and inertia coefficients in the horizontal direction for aspect ratio = 1/2 are shown in Figs. 6.210 to 6.221. For Uc = -0.1 m/s, C_{DX} is found to be considerably lower than C_{DX} for Uc = +0.1 m/s. C_{DX} for Uc = -0.2 m/s is again found to be lower than C_{DX} for Uc = +0.2 m/s. . However, C_{DX} is found to have similar values for Uc = -0.3 m/s and +0.3 m/s. C_{MX} for Uc = -0.2 m/s is found to be significantly higher than C_{MX} for Uc = +0.2 m/s. For example, C_{MX} for Uc = +0.2 m/s is found to vary from about 0.9 to 1.3 whereas, C_{MX} for Uc = -0.2 m/s is found to vary from 1.0 to 2.0. A similar trend in C_{MX} is also found for Uc = -0.3 m/s as can be seen in Fig. 6.212. C_{DY} and C_{MY} are shown in Fig. 6.213 and 6.215. C_{DY} is found to be less influenced by current direction and speed. C_{MY} for Uc = - 0.1 m/s is found to be less than C_{MY} for Uc = + 0.1 m/s.

In Figs. 6.216 and 6.217, C_{DX} and C_{MX} for all the positive and negative currents are plotted along with the coefficients for no current case (Uc = 0.0 m/s). These plots reveal that the drag coefficients in the horizontal direction for positive currents and waves are 3 to 3.5 times larger than the drag coefficients for waves alone and for negative currents and waves it is found to be 2 to 3 times larger than the drag coefficients for waves alone. The inertia coefficients for waves and currents are lower than those for waves alone. Beyond KC = 1.25, inertia coefficients for combined waves and currents and for the wave alone are converging. In Figs. 6.218 and 6.219, C_{DY} and C_{MY} for all the positive and negative currents are plotted along with the coefficients for no current case. It is observed from these plots that the drag coefficients in waves and currents are slightly higher than the drag coefficients in waves alone. C_{MY} is found to be lower than the C_{MY} obtained for waves alone.

The rms coefficients in the horizontal direction, C_{FXrms} and in vertical direction C_{FYrms} are plotted along with those obtained for waves alone, in Figs. 6.220 and 6.221 respectively. These coefficients do not change very much with different current speeds. C_{FXrms} in waves and positive currents are observed to be 4.5 to 8.6 times lower than C_{FXrms} in waves alone and C_{FYrms} is found to be about 12 to 23 times lower than C_{FYrms} in pure wave. C_{FXrms} in waves and negative currents are observed to be 4 to 5 times lower than C_{FXrms} in waves alone and C_{FYrms} is found to be about 11 to 13.5 times higher than C_{FYrms} in pure wave. The measured and computed peak forces for all the current speeds are shown in Fig. 6.222. From Table 6.4, for positive currents, both horizontal and vertical peak forces show less error compared to negative currents.

6.3.3.3 Rectangular Cylinder with Aspect ratio = 3/4

The variation of the drag and inertia coefficients in the horizontal direction for aspect ratio = 3/4 are shown in Figs. 6.223 and 6.224. For this aspect ratio, the results are available only for two current speeds, $Uc = \pm 0.2$ and ± 0.3 m/s. For Uc = -0.2 m/s, C_{DX} is found to be higher than C_{DX} for Uc = +0.2 m/s. In Fig. 6.224, C_{MX} for Uc = - 0.3 m/s concentrates between 0.9 and 1.6, whereas, for Uc = + 0.3 m/s, many data points of C_{MX} are found to have a value between 2.0 and 2.5. C_{DX} is found to have similar values for Uc = -0.3 m/s and +0.3 m/s. The variation of the drag and inertia coefficients in the vertical direction is shown in Figs.6.225 and 6.226. C_{DY} for negative currents are found to be lower than C_{DY} for positive currents. Similarly, C_{MY} for negative currents is found to be lower than C_{MY} for positive current. In Fig. 6.227 and 6.228, C_{DX} and C_{MX} for the two positive and negative currents are respectively plotted along with the coefficients for no current case. C_{MX} is found to have most of its values lower than the wave alone values. In Figs. 6.229 and 6.230, C_{DY} and C_{MY} for positive and negative currents are plotted along with the coefficients for no current case. It is observed from these plots that the drag coefficients for positive currents, do not differ much from the drag coefficients in waves alone and the vertical inertia coefficients in waves and currents are found to be lower than those

measured in waves alone. For $KC > 1.0$, C_{MY} in positive currents tends to take values higher than the wave alone coefficients, whereas, for negative currents, it keeps decreasing for all KC numbers.

The rms coefficients in the horizontal direction, C_{FXrms} and in vertical direction C_{FYrms} are plotted along with those obtained for waves alone, in Figs. 6.231 and 6.232. C_{FXrms} in waves and positive currents are observed to be about 7.5 to 12.5 times lower than C_{FXrms} in waves alone and C_{FYrms} is found to be about 15 to 30 times higher than C_{FYrms} in pure wave. C_{FXrms} in waves and negative currents are observed to be 7 to 20 times lower than C_{FXrms} in waves alone and C_{FYrms} is found to be about 18 to 32 times higher than C_{FYrms} in pure wave. The measured and computed peak forces for all the current speeds are shown in Fig. 6.233. It can be seen from Table 6.4 that the negative currents show a difference up to 66% between measured and Morison forces in horizontal direction, whereas, for the vertical direction, an under prediction by an average value of about 23% is observed. The standard deviations are around 0.12 and 0.094 in horizontal and vertical directions respectively.

Table. 6.4. Means and standard deviations of measured and computed peak force ratios for horizontal cylinder in waves and currents

Current (m/s)	Aspect ratio = 1.0			
	$\overline{R}_{xp}$	σ_{xp}	$\overline{R}_{yp}$	σ_{yp}
+0.1	1.268	0.137	1.152	0.186
+0.2	0.942	0.246	0.947	0.209
+0.3	0.938	0.283	0.966	0.225
-0.1	1.270	0.107	1.172	0.190
-0.2	1.397	0.284	1.214	0.176
-0.3	1.379	0.294	1.225	0.256

Current (m/s)	Aspect ratio = ½			
	$\overline{R}_{xp}$	σ_{xp}	$\overline{R}_{yp}$	σ_{yp}
+0.1	0.988	0.151	1.115	0.082
+0.2	1.116	0.128	1.181	0.037
+0.3	1.047	0.243	1.286	0.127
-0.1	1.498	0.114	1.238	0.081
-0.2	1.173	0.287	1.268	0.124
-0.3	1.307	0.306	1.215	0.093

Current (m/s)	Aspect ratio = 3/4			
	$\overline{R}_{xp}$	σ_{xp}	$\overline{R}_{yp}$	σ_{yp}
+0.1	-	-	-	-
+0.2	1.304	0.107	1.286	0.059
+0.3	1.415	0.141	1.216	0.097
-0.1	-	-	-	-
-0.2	1.503	0.117	1.261	0.119
-0.3	1.663	0.169	1.202	0.110

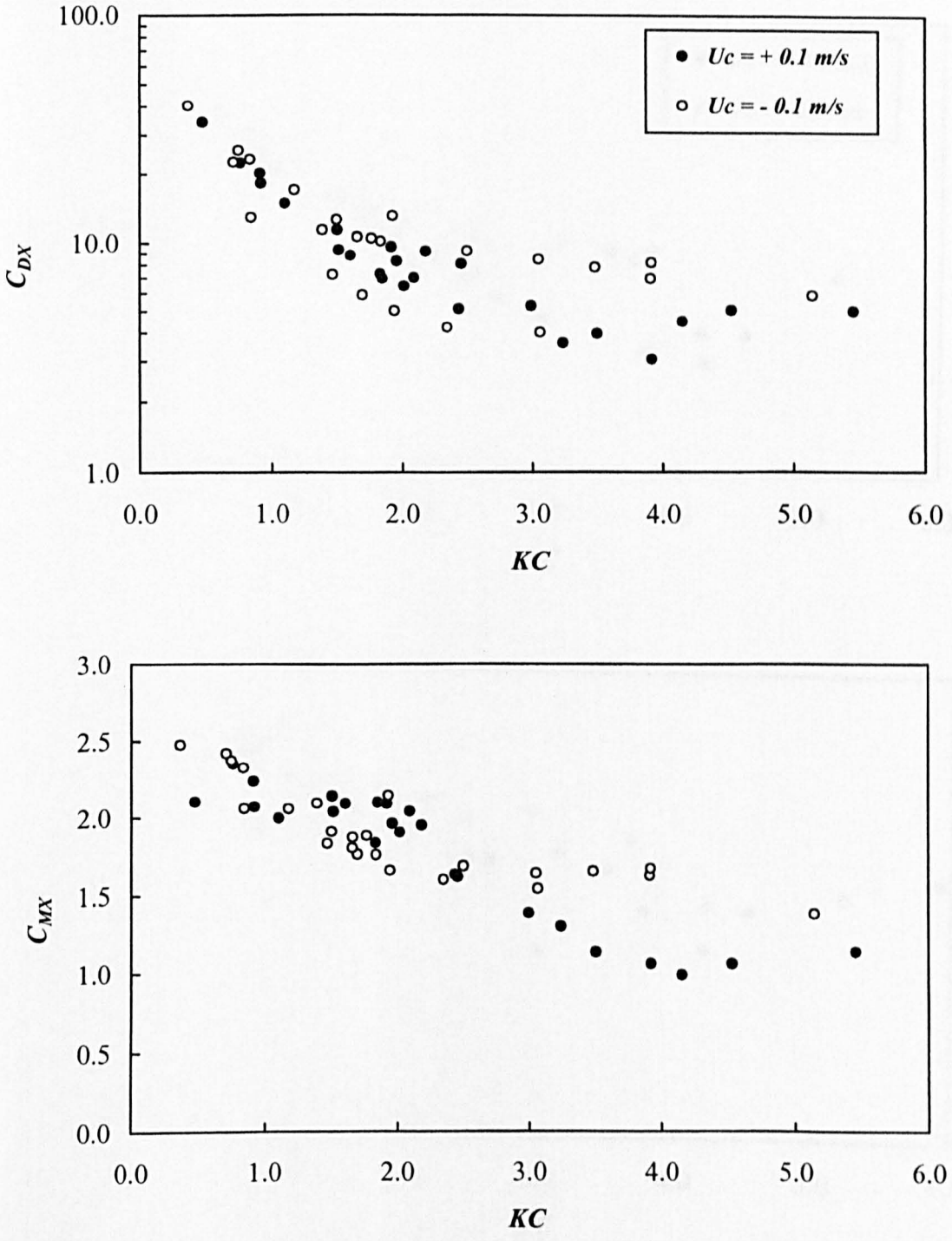

Fig. 6.197 Horizontal drag and inertia coefficients for horizontal square cylinder in co-existing waves and currents for $U_C = \pm 0.1$ m/s

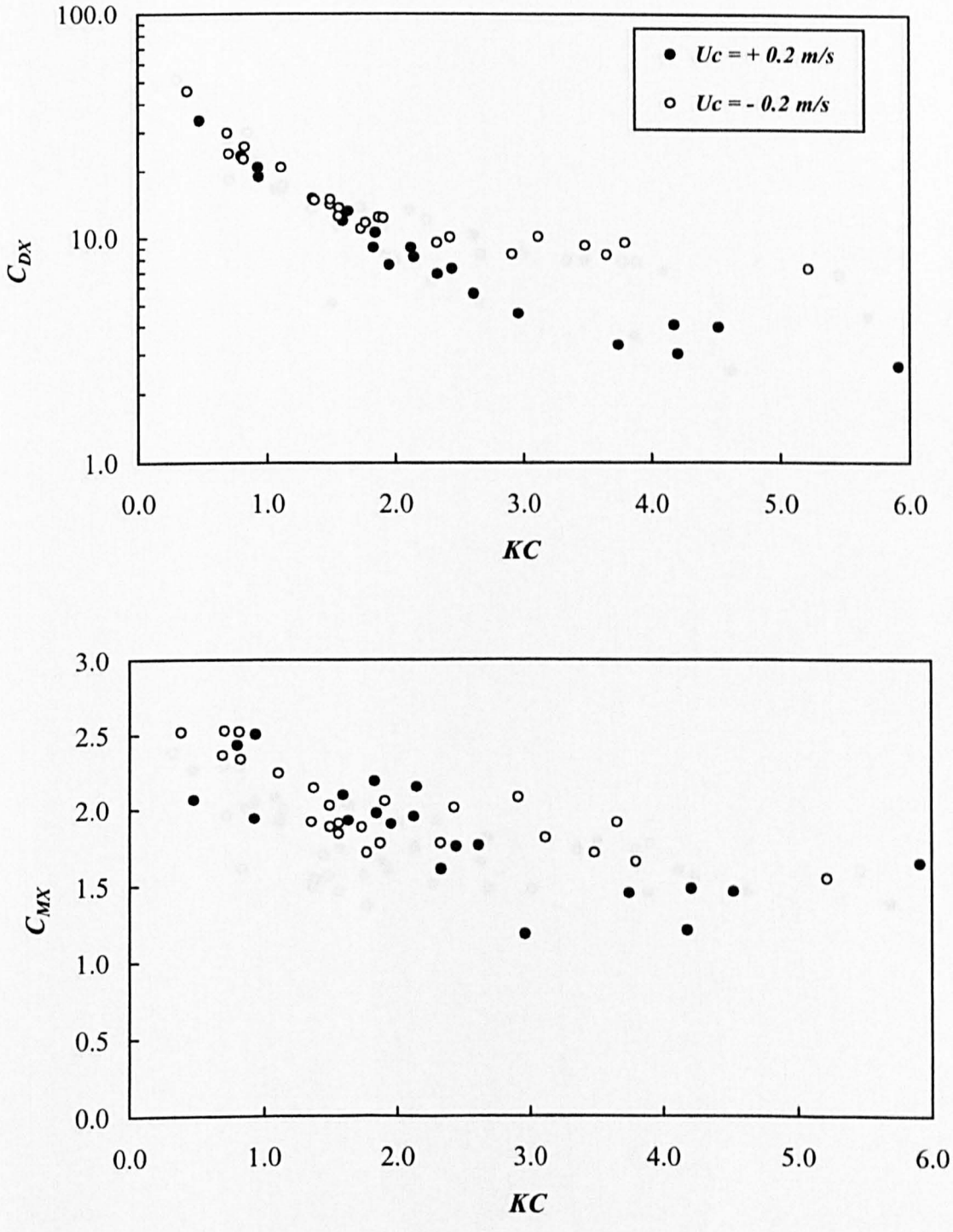

Fig. 6.198 Horizontal drag and inertia coefficients for horizontal Square Cylinder in co-existing waves and currents for $U_C = \pm 0.2$ m/s

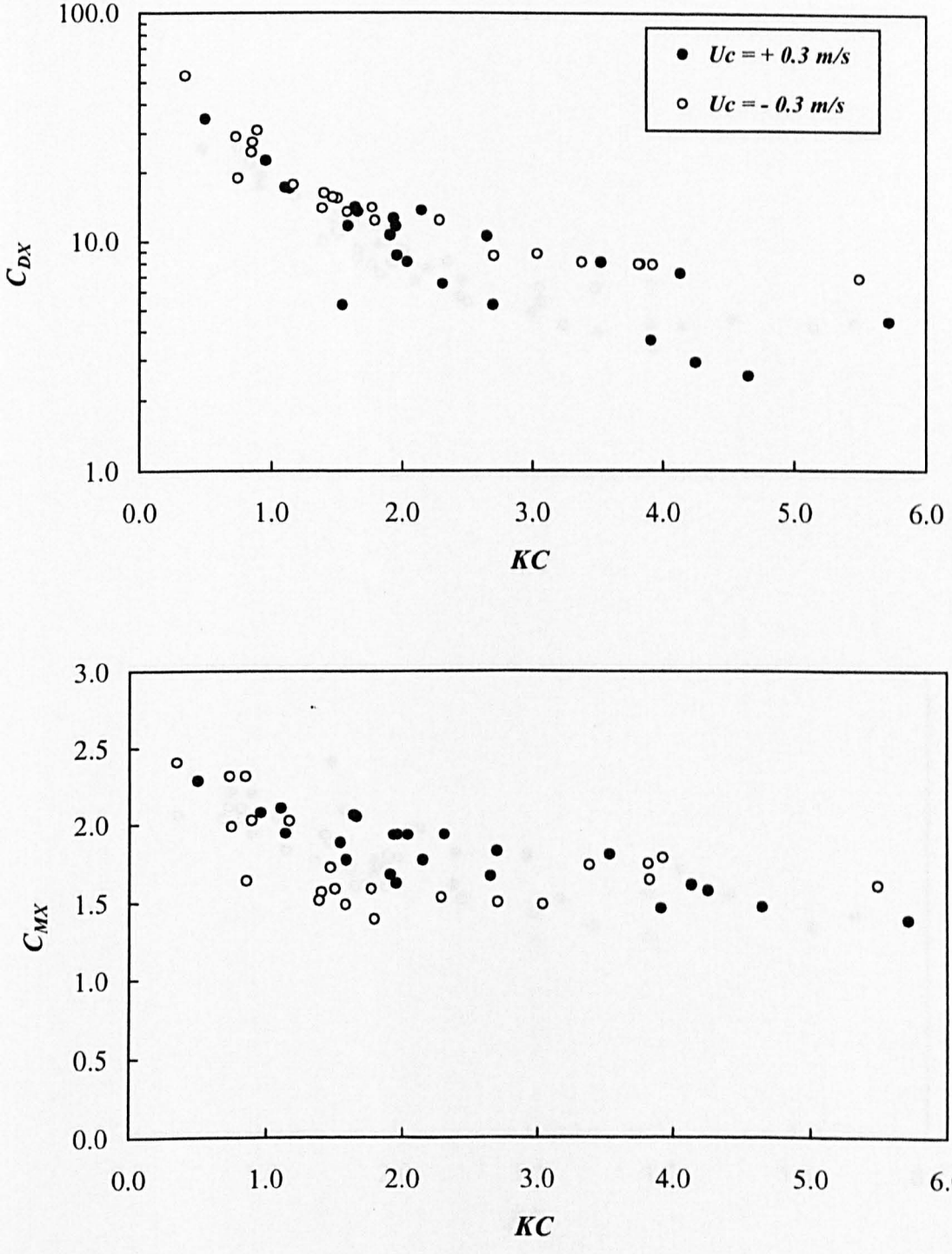

Fig. 6.199 Horizontal drag and inertia coefficients for horizontal Square Cylinder in co-existing waves and currents for $U_C = \pm 0.3$ m/s

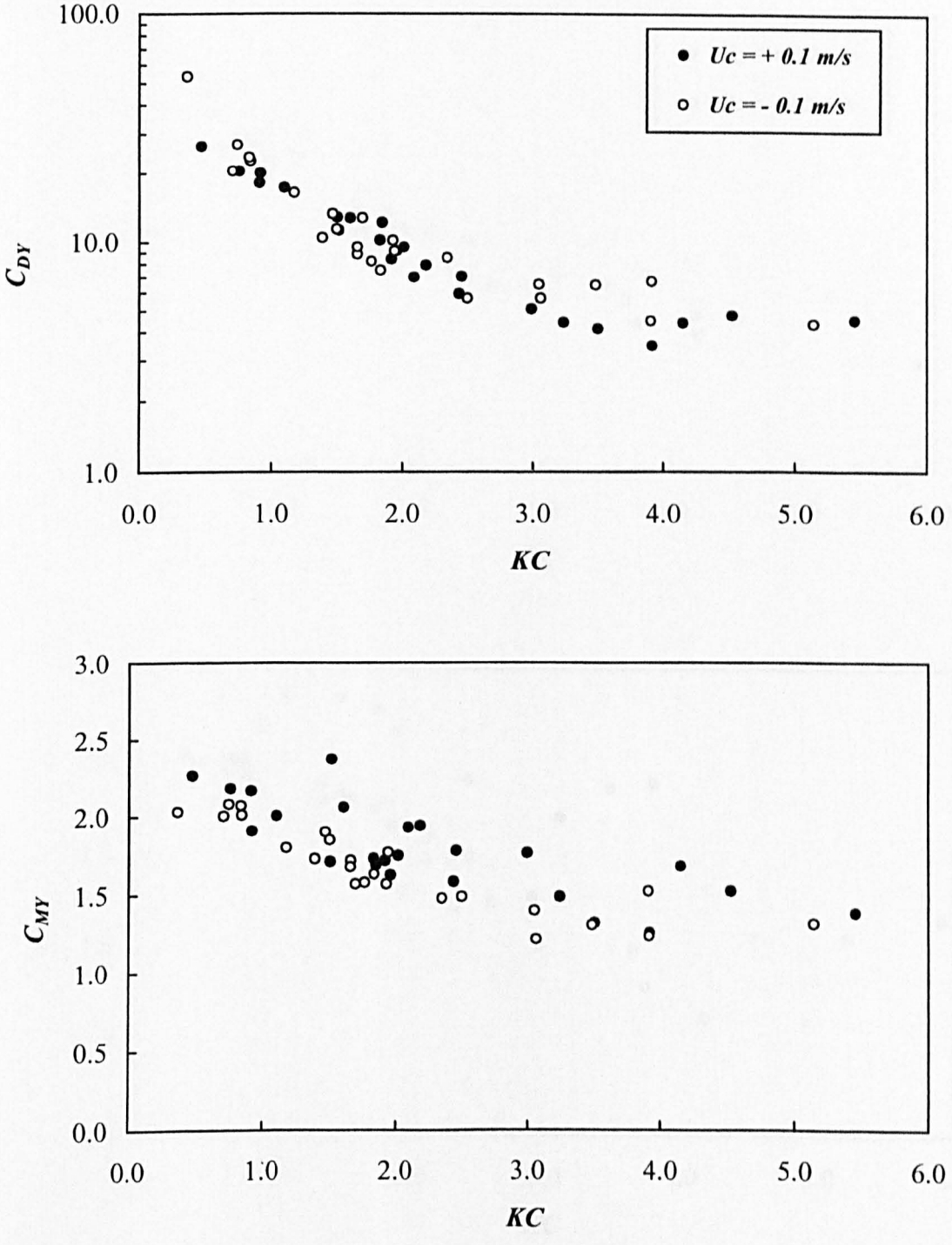

Fig. 6.200 Vertical drag and inertia coefficients for horizontal square cylinder in co-existing waves and currents for $U_C = \pm 0.1$ m/s

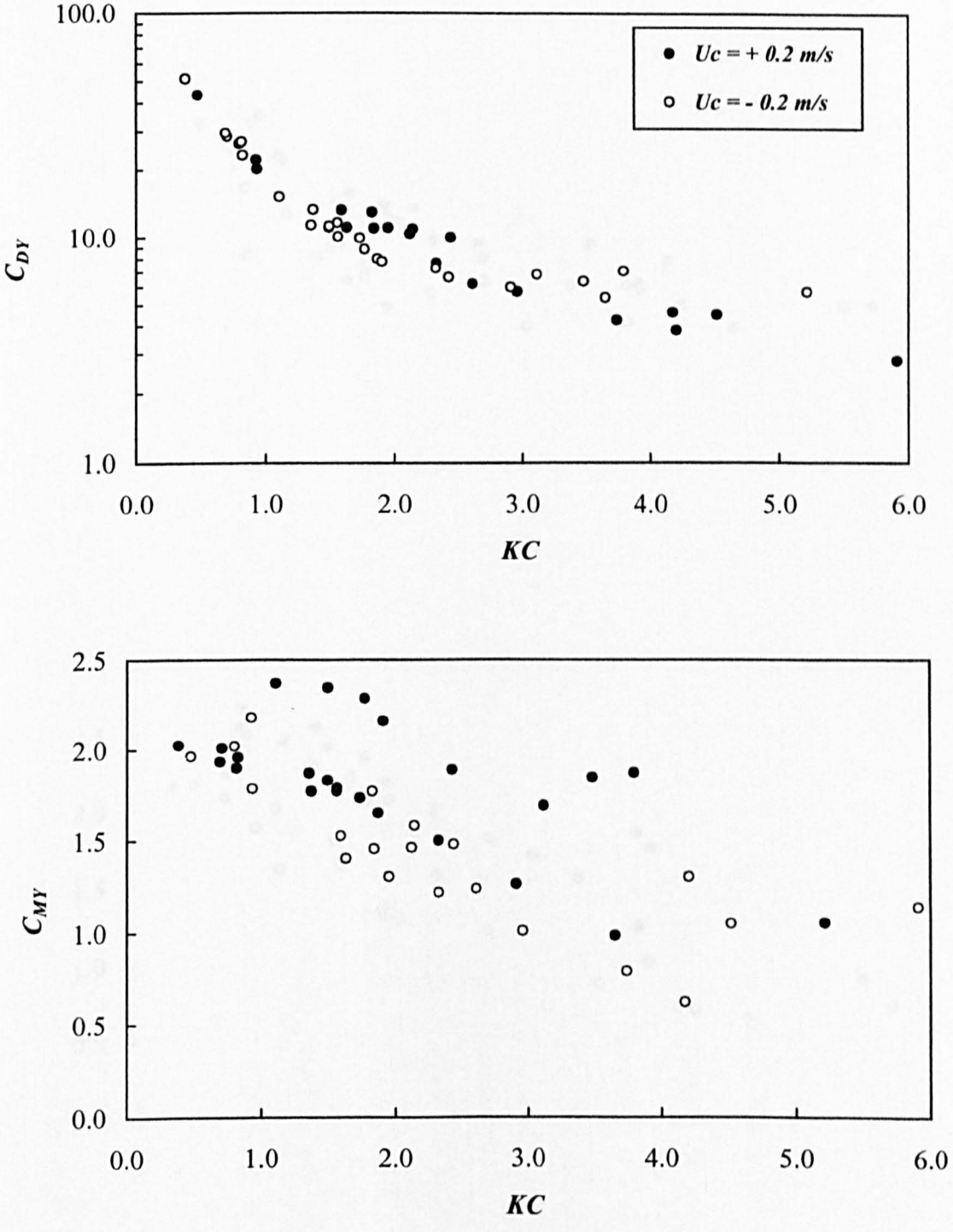

Fig. 6.201 Vertical drag and inertia coefficients for horizontal Square Cylinder in co-existing waves and currents for $U_C = \pm 0.2$ m/s

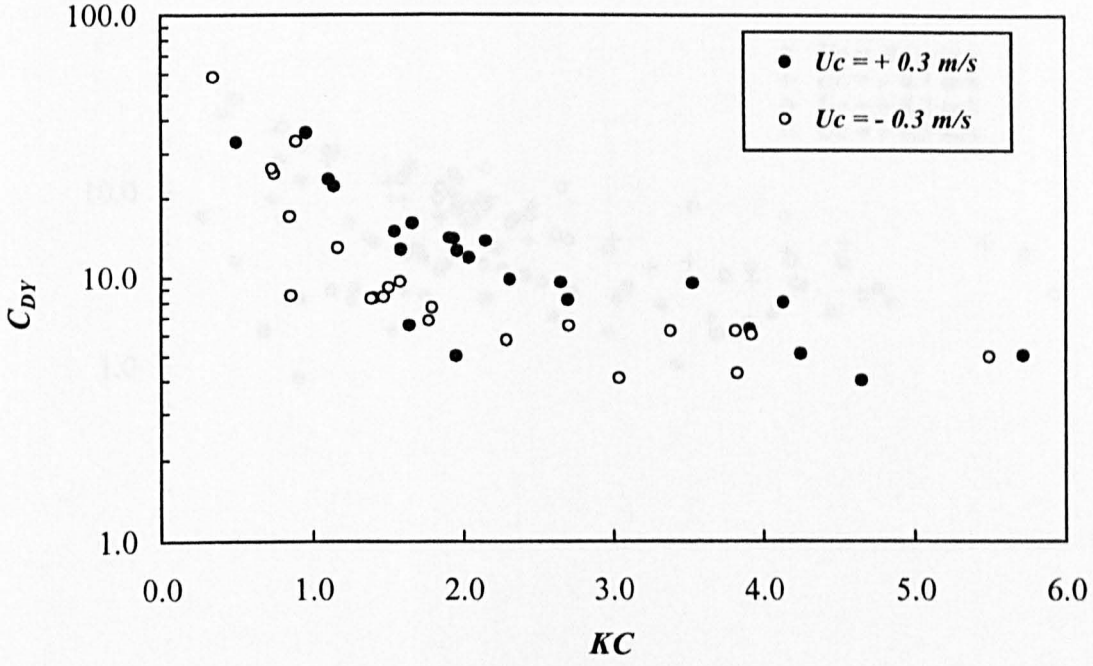

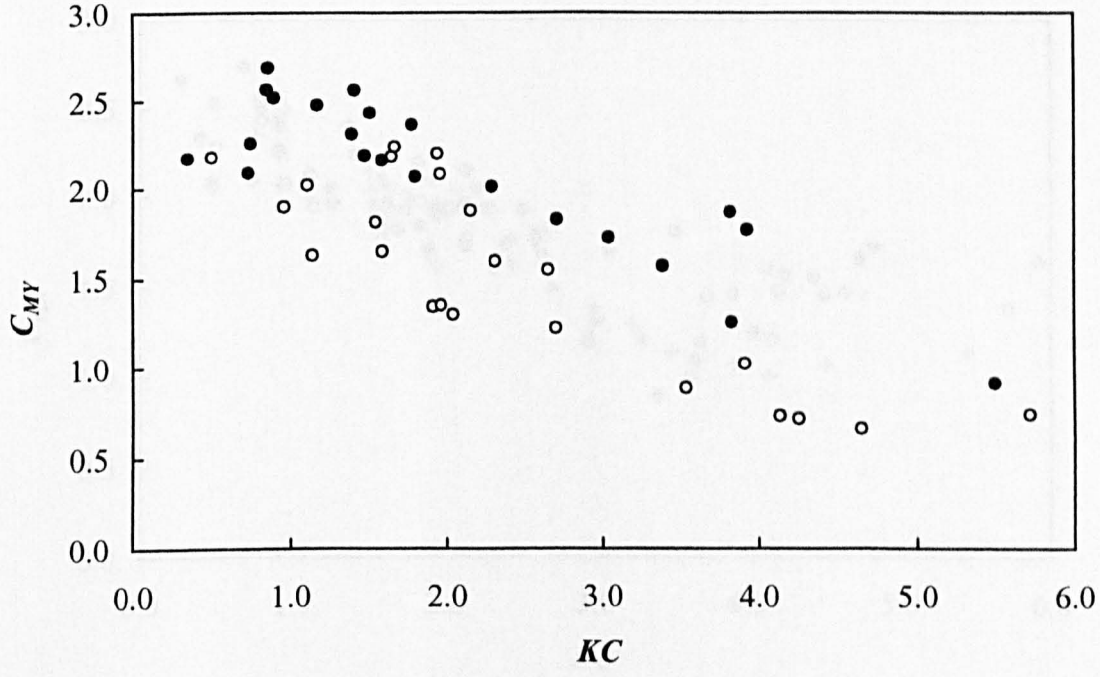

Fig. 6.202 Vertical drag and inertia coefficients for horizontal square cylinder in co-existing waves and currents for $U_c = \pm 0.3$ m/s

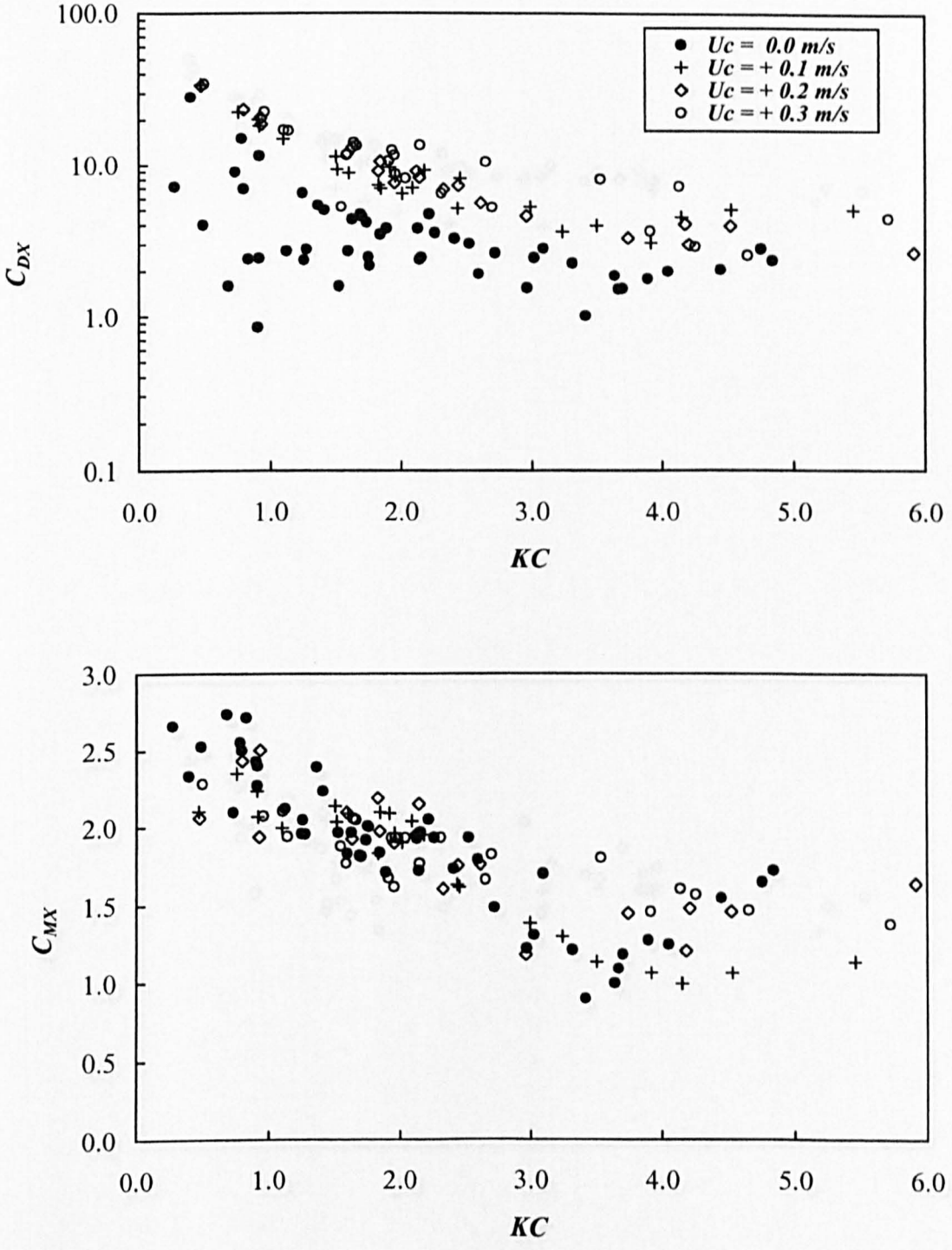

Fig. 6.203 Horizontal drag and inertia coefficients for horizontal square cylinder in co-existing waves and currents for positive currents

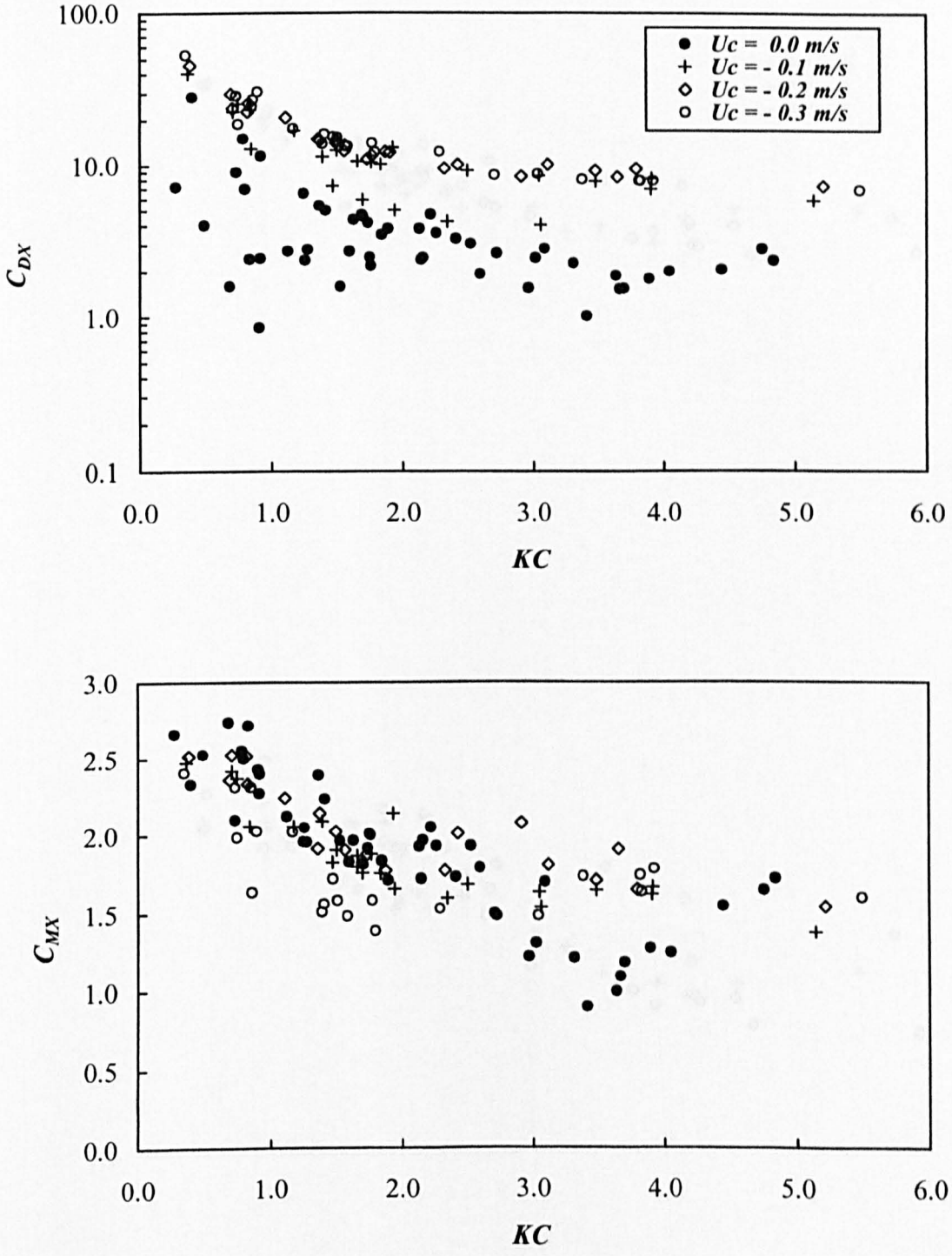

Fig. 6.204 Horizontal drag and inertia coefficients for horizontal square cylinder in co-existing waves and currents for negative currents

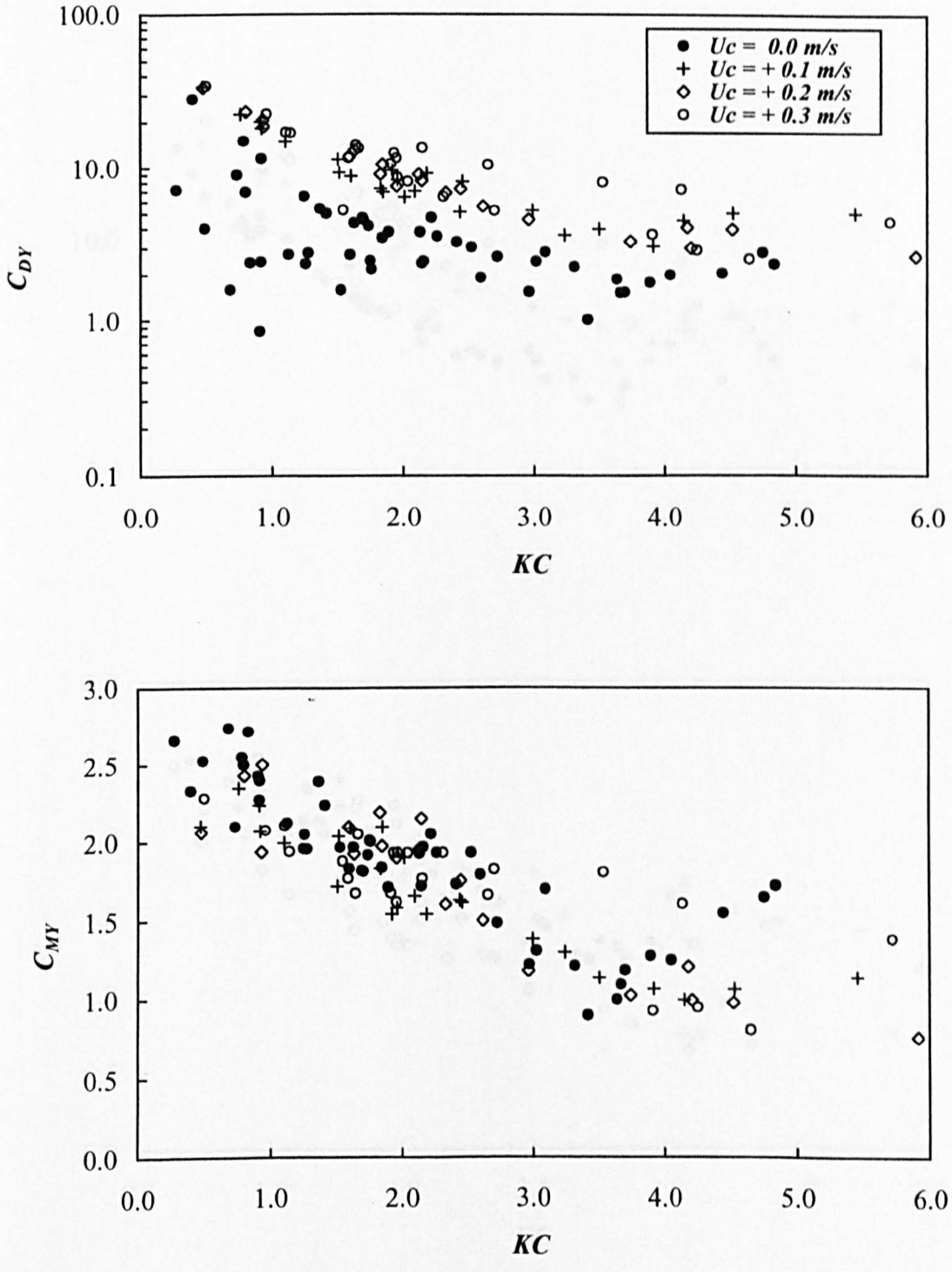

Fig. 6.205 Vertical drag and inertia coefficients for horizontal square cylinder in co-existing waves and currents for positive currents

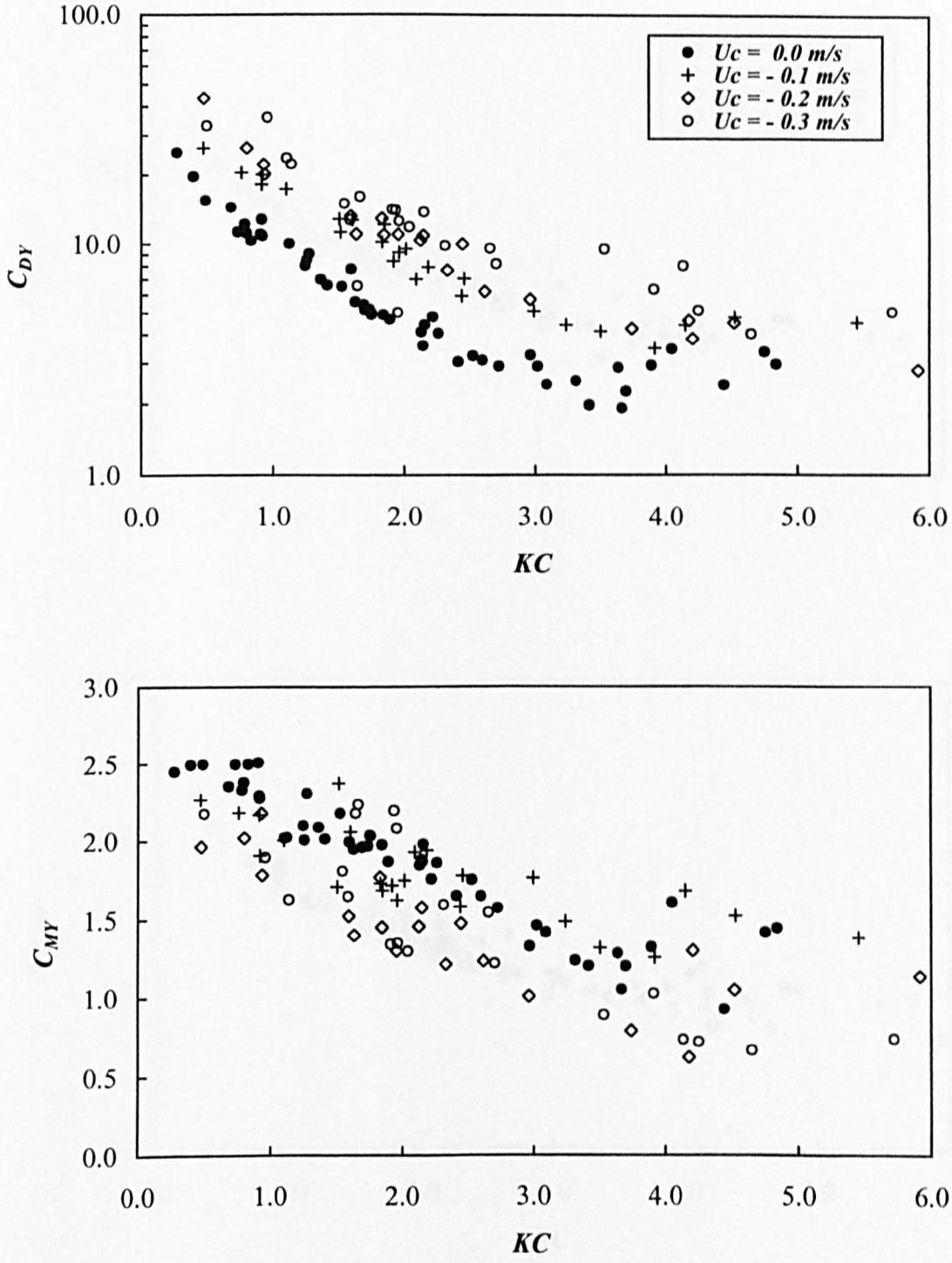

Fig. 6.206 Vertical drag and inertia coefficients for horizontal square cylinder in co-existing waves and currents for negative currents

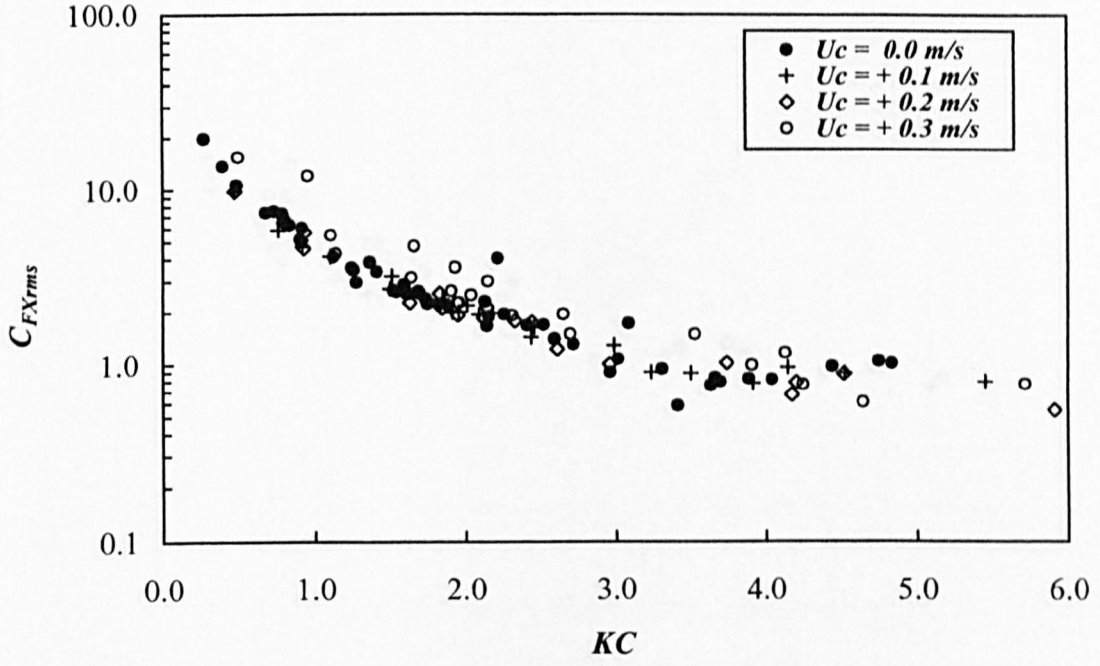

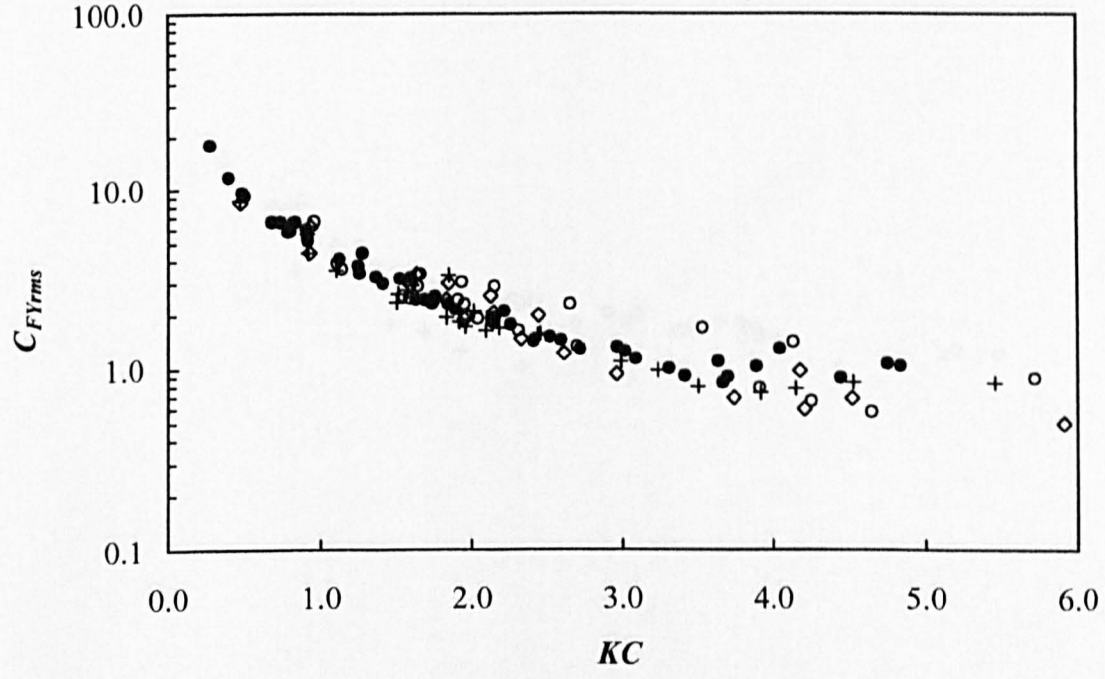

Fig. 6.207 Horizontal and vertical root mean square coefficients for horizontal square cylinder in co-existing waves and currents for positive currents

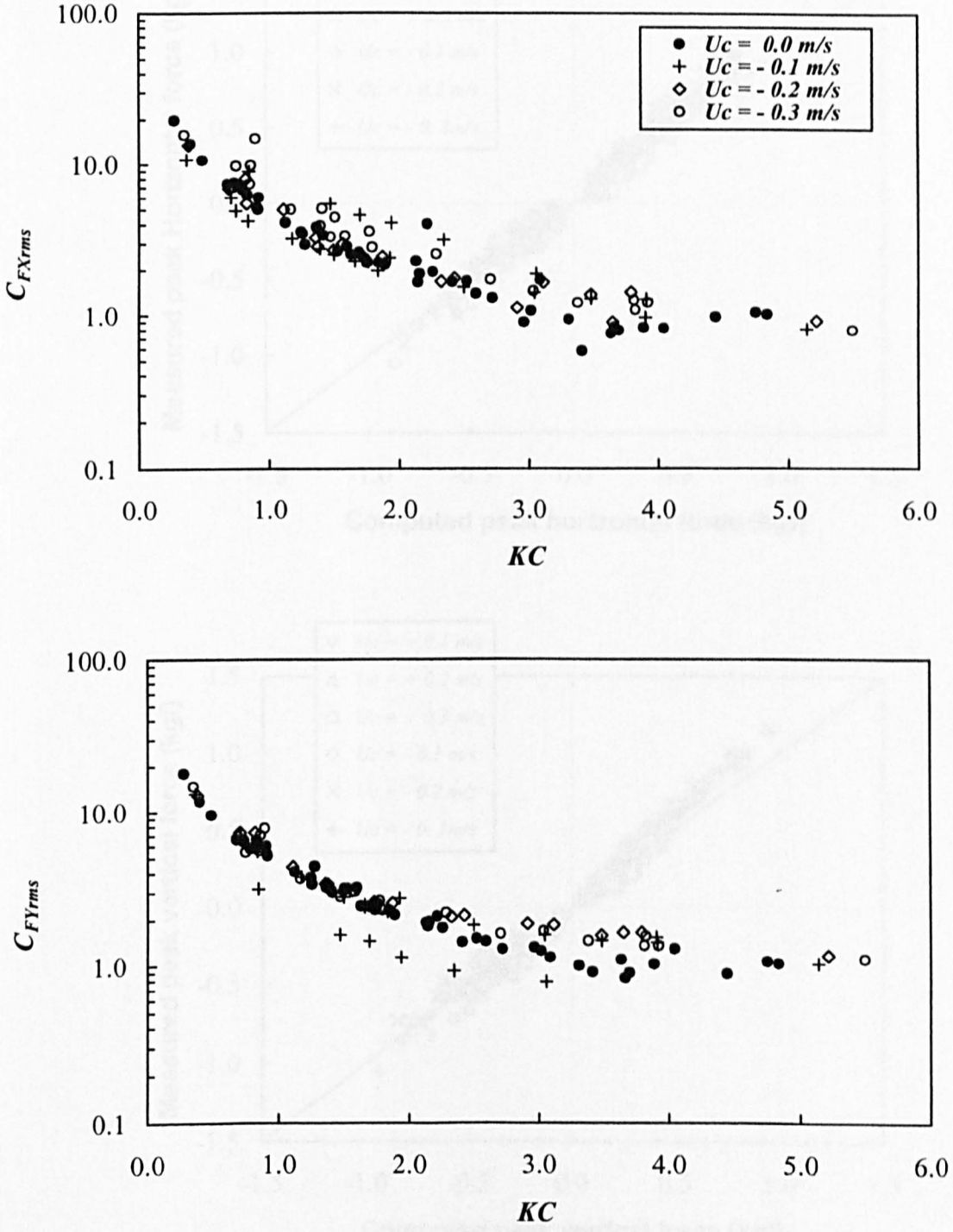

Fig. 6.208 Horizontal and vertical root mean square coefficients for horizontal square cylinder in co-existing waves and currents for negative currents

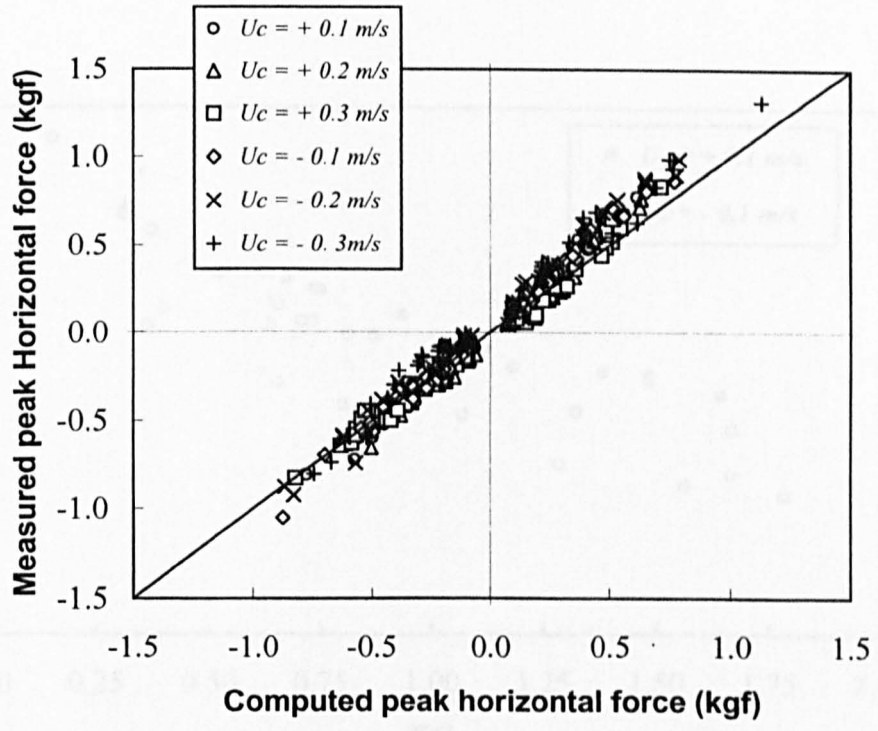

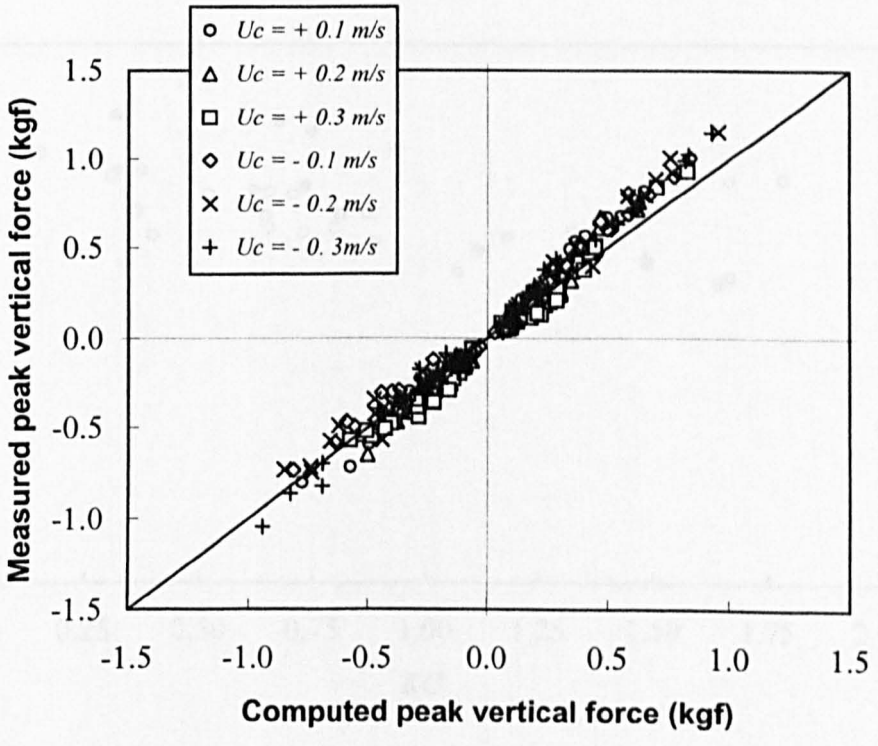

Fig. 6.209 Measured and computed peak forces for horizontal square cylinder

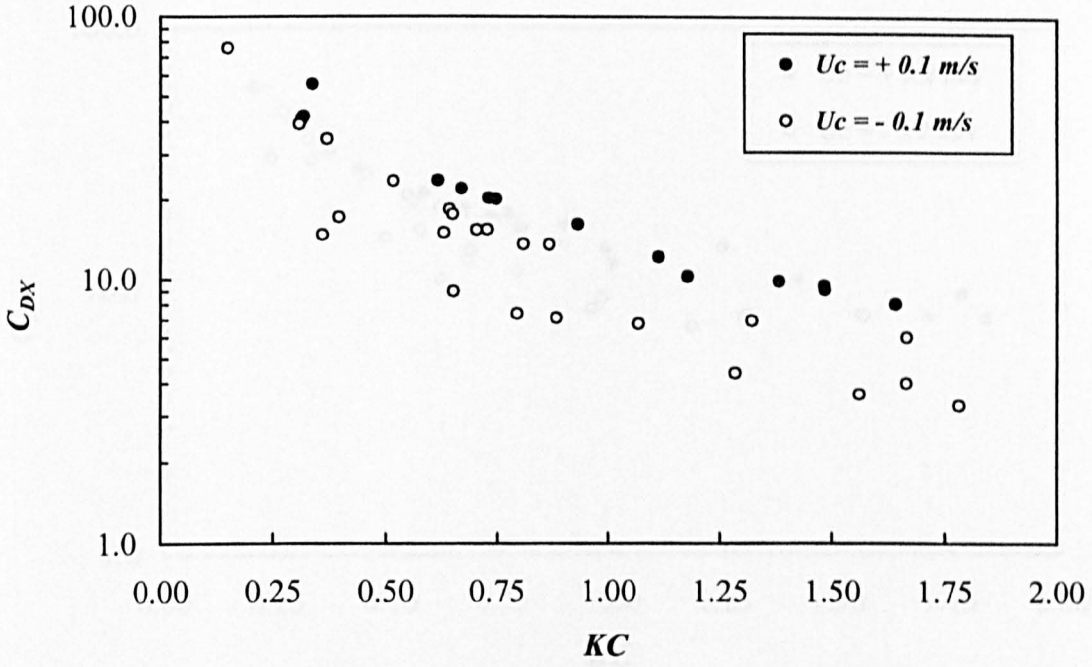

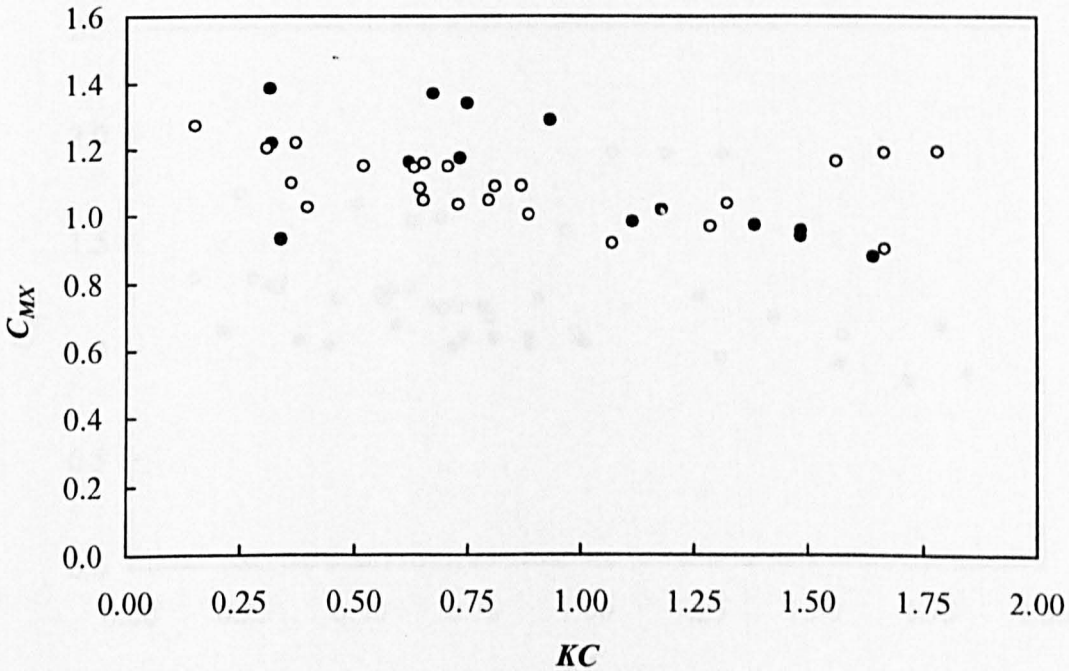

Fig. 6.210 Horizontal drag and inertia coefficients for horizontal rectangular cylinder for aspect ratio = 1/2 in co-existing waves and currents for $U_C = \pm 0.1$ m/s

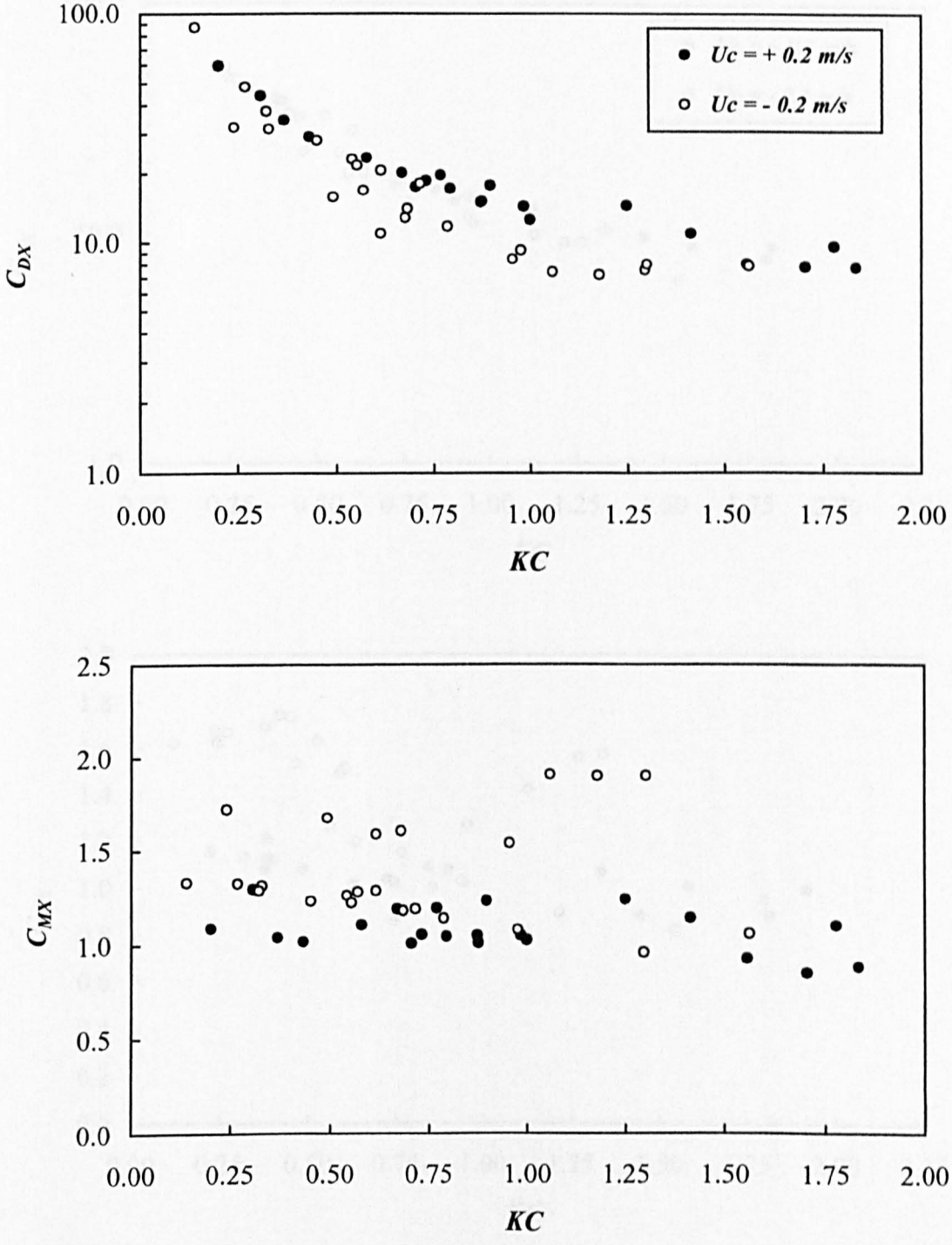

Fig. 6.211 Horizontal drag and inertia coefficients for horizontal Rectangular cylinder for aspect ratio = 1/2 in co-existing waves and currents for $U_C = \pm 0.2$ m/s

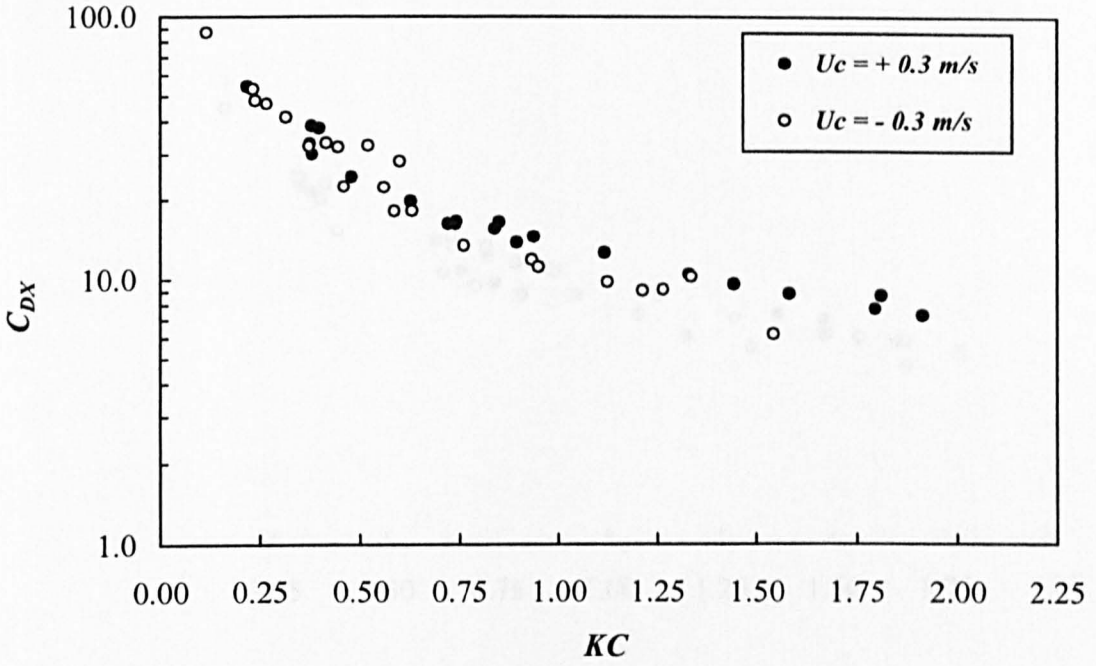

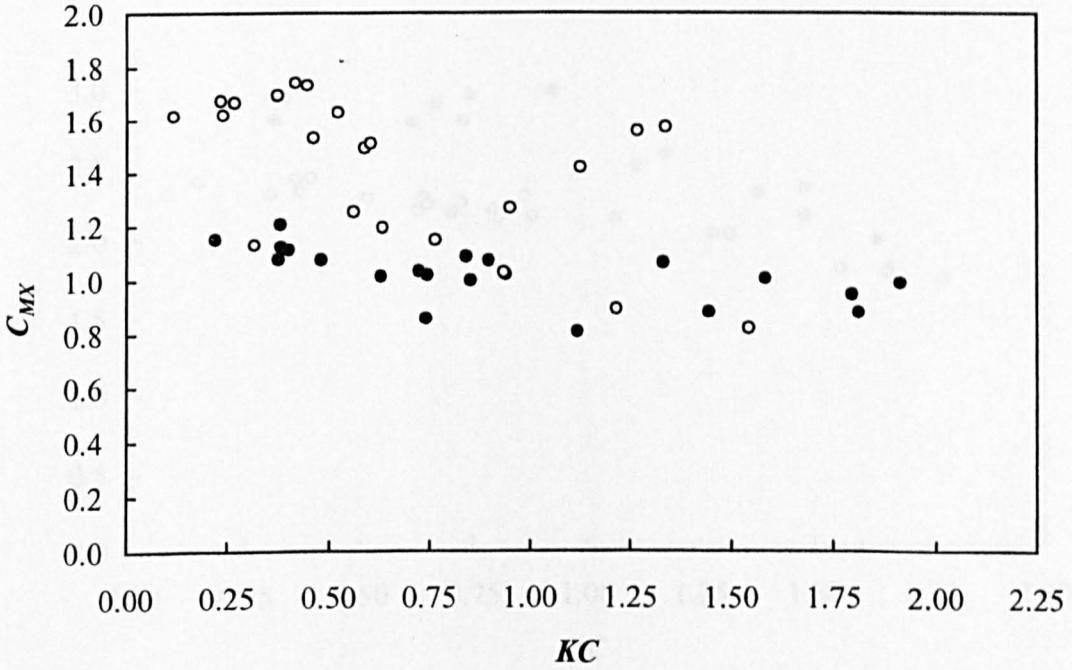

Fig. 6.212 Horizontal drag and inertia coefficients for horizontal rectangular cylinder for aspect ratio = 1/2 in co-existing waves and currents for $U_C = \pm 0.3$ m/s

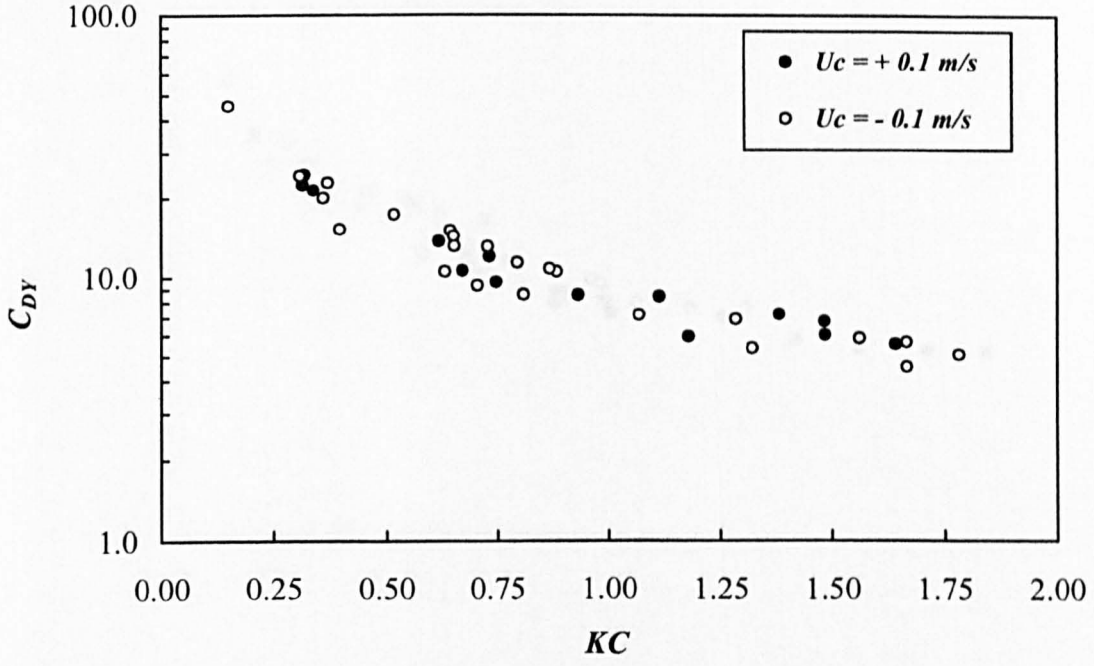

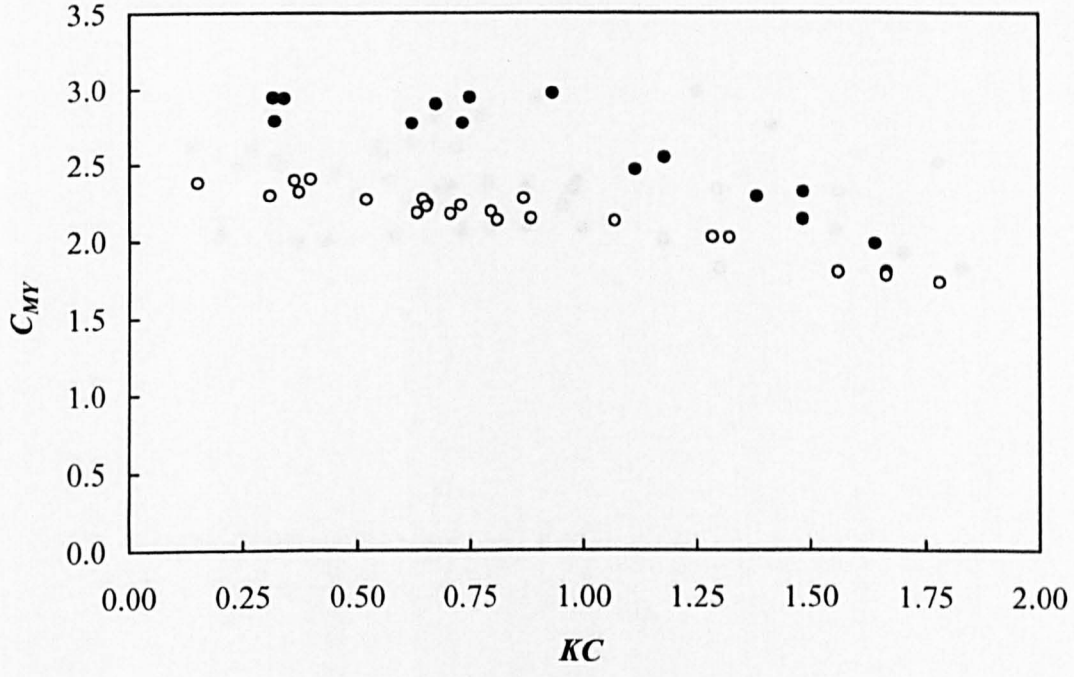

Fig. 6.213 Vertical drag and inertia coefficients for horizontal rectangular cylinder for aspect ratio = 1/2 in co-existing waves and currents for $U_C = \pm 0.1$ m/s

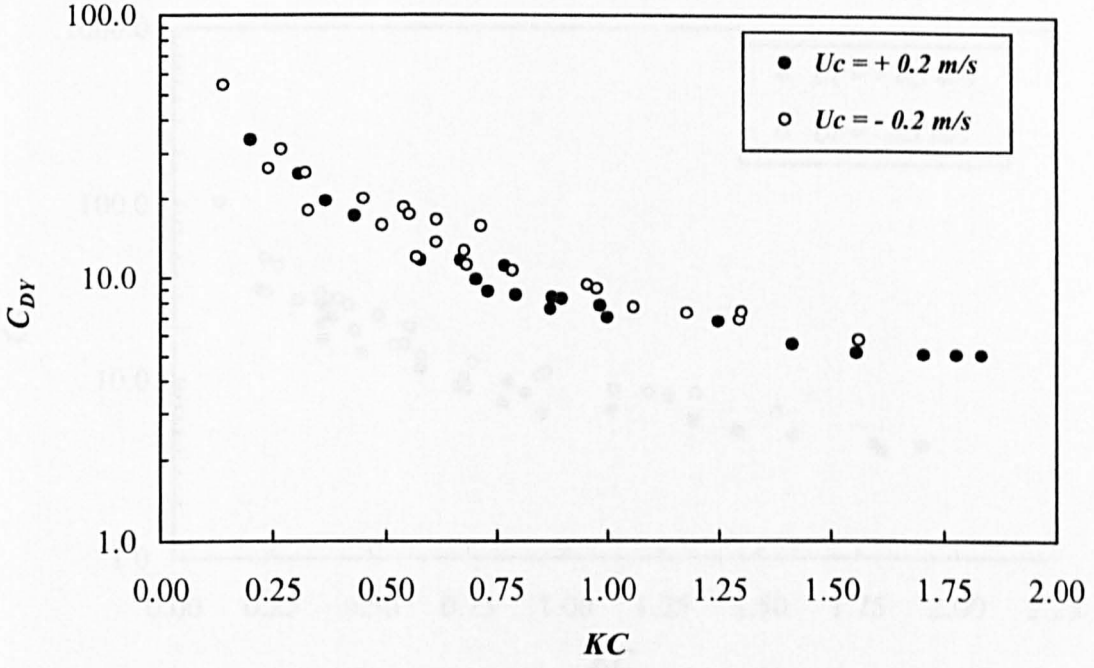

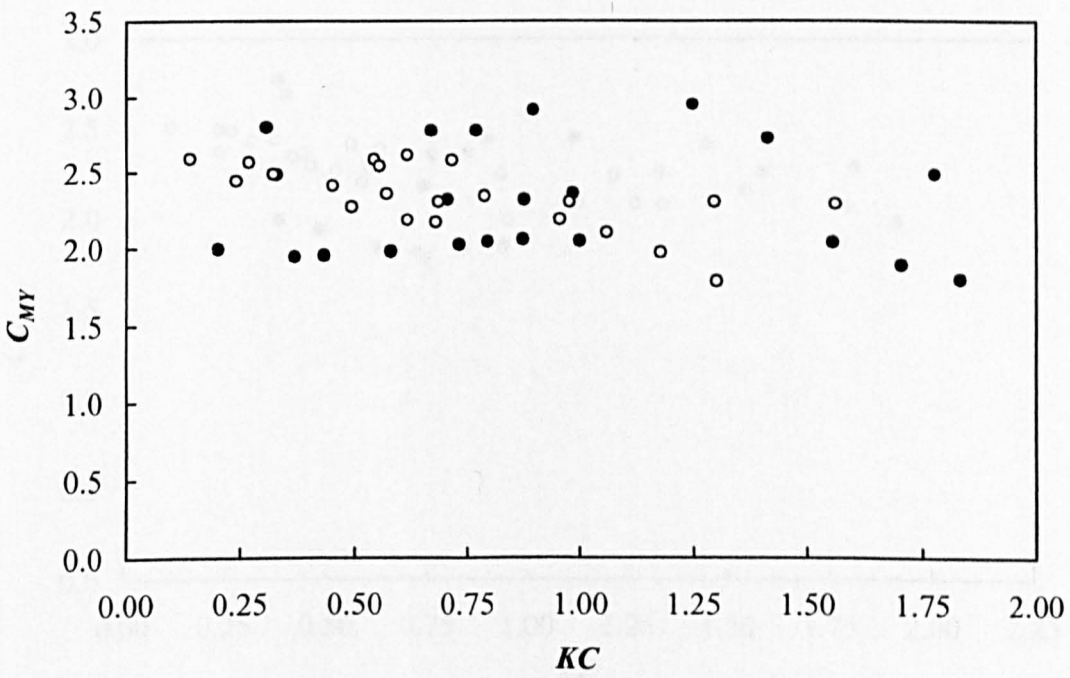

Fig. 6.214 Vertical drag and inertia coefficients for horizontal rectangular cylinder for aspect ratio = 1/2 in co-existing waves and currents for $U_C = \pm 0.2$ m/s

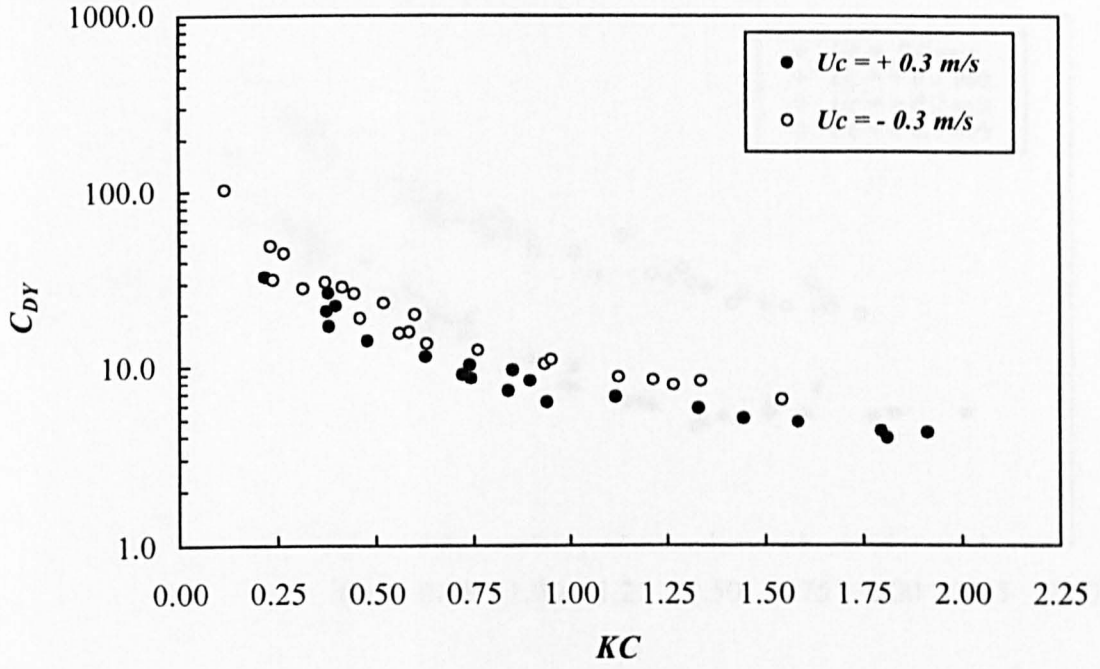

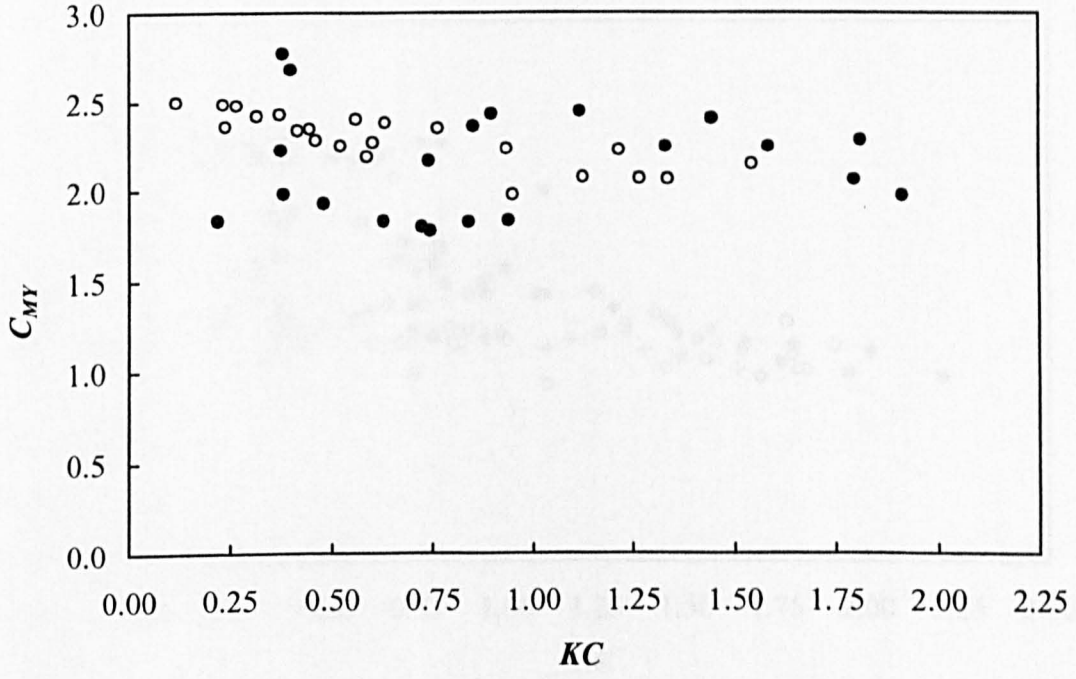

Fig. 6.215 Vertical drag and inertia coefficients for horizontal rectangular cylinder for aspect ratio = 1/2 in co-existing waves and currents for $U_C = \pm 0.3$ m/s

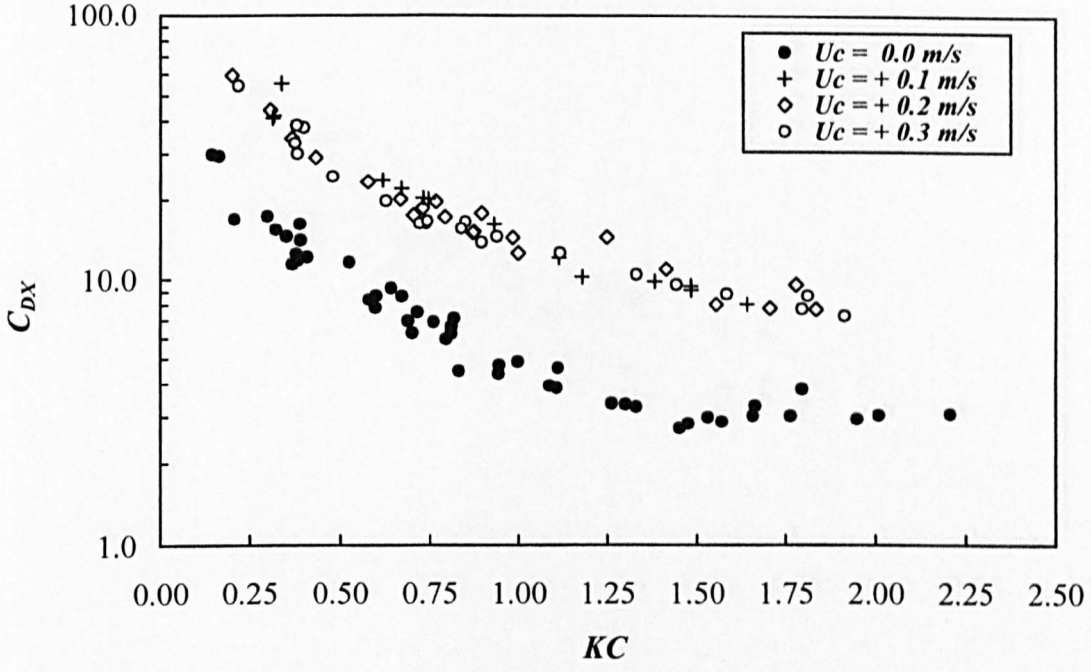

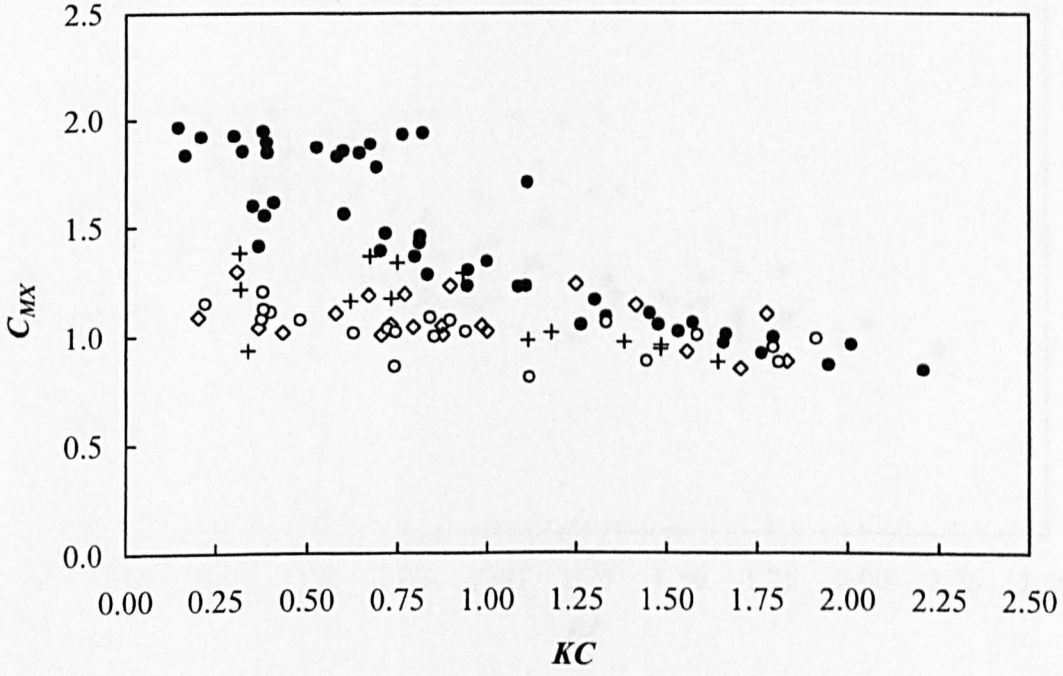

Fig. 6.216 Horizontal drag and inertia coefficients for horizontal rectangular cylinder for aspect ratio = 1/2 in co-existing waves and currents for positive currents

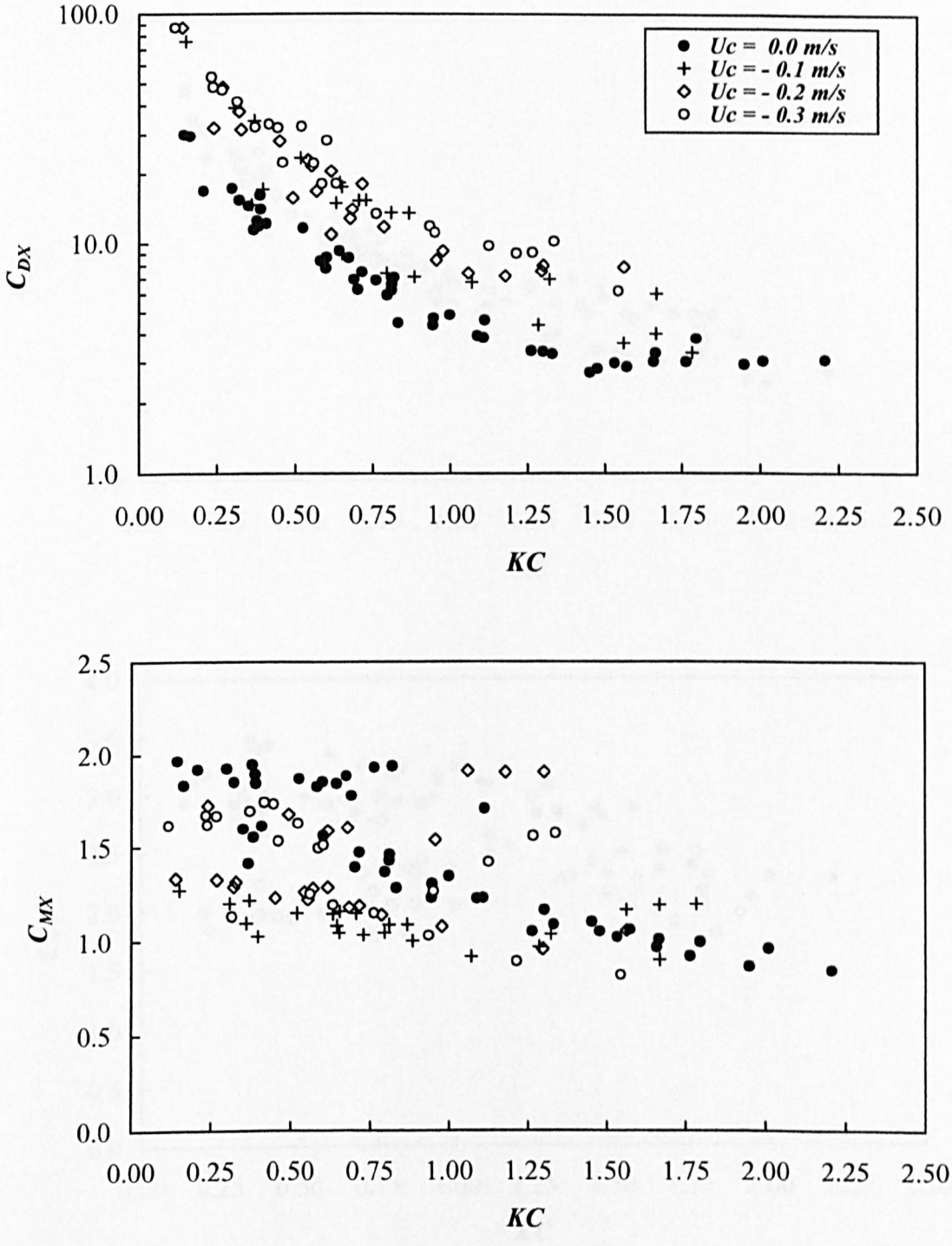

Fig. 6.217 Horizontal drag and inertia coefficients for horizontal rectangular cylinder for aspect ratio = 1/2 in co-existing waves and currents for negative currents

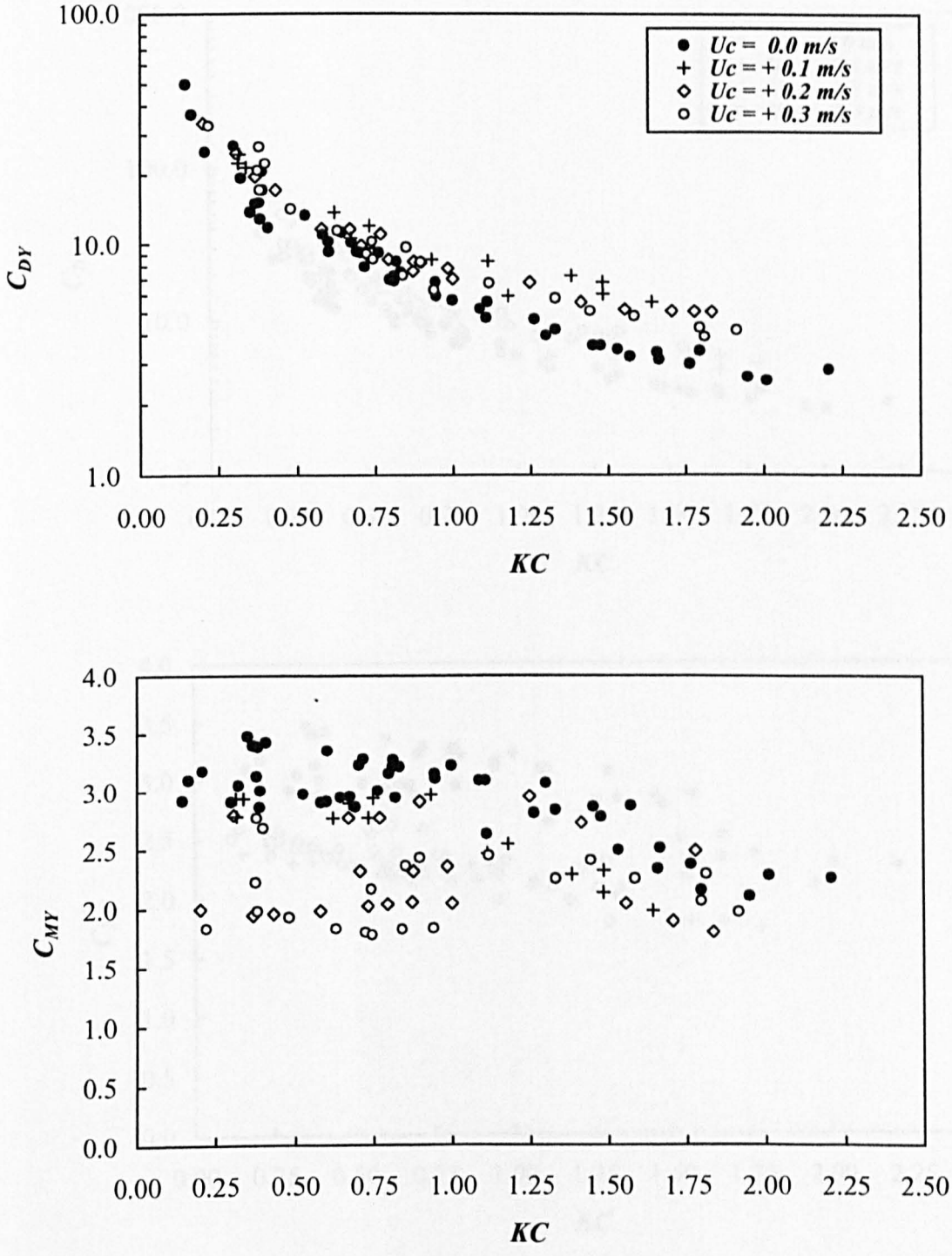

Fig. 6.218 Vertical drag and inertia coefficients for horizontal rectangular cylinder for aspect ratio = 1/2 in co-existing waves and currents for positive currents

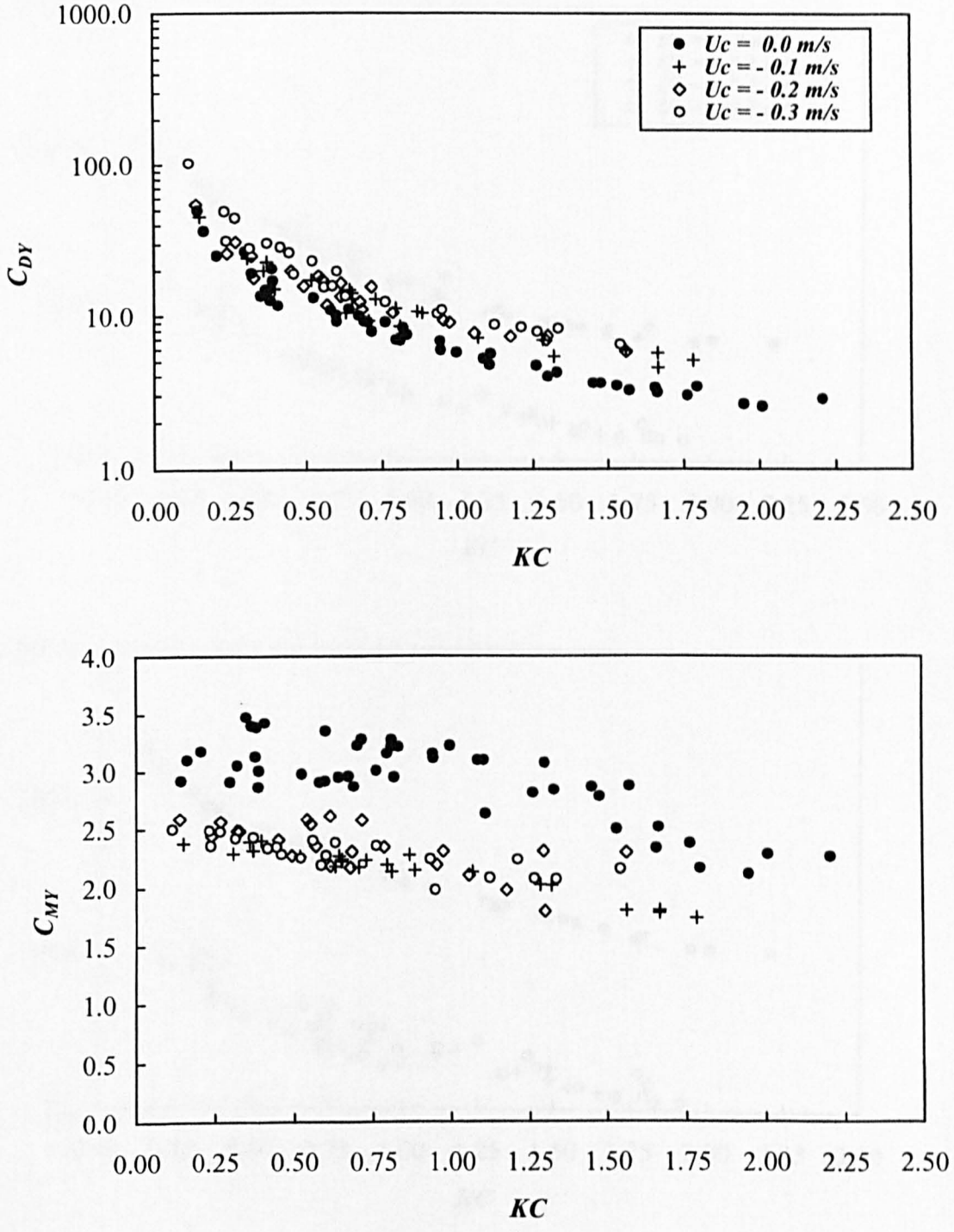

Fig. 6.219 Vertical drag and inertia coefficients for horizontal rectangular cylinder for aspect ratio = 1/2 in co-existing waves and currents for negative currents

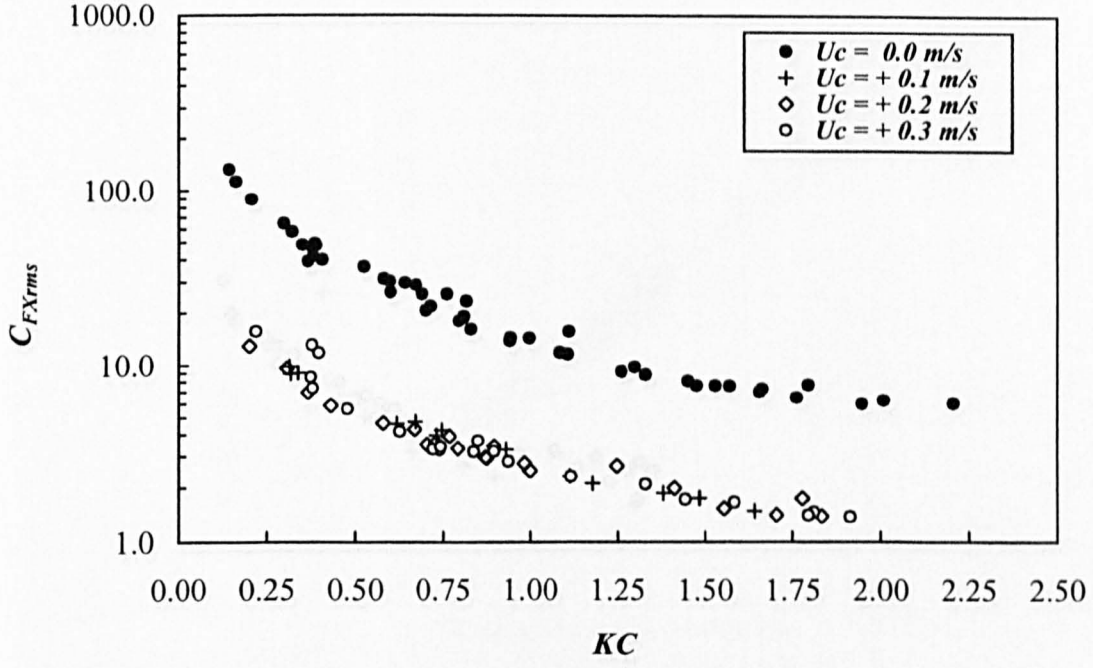

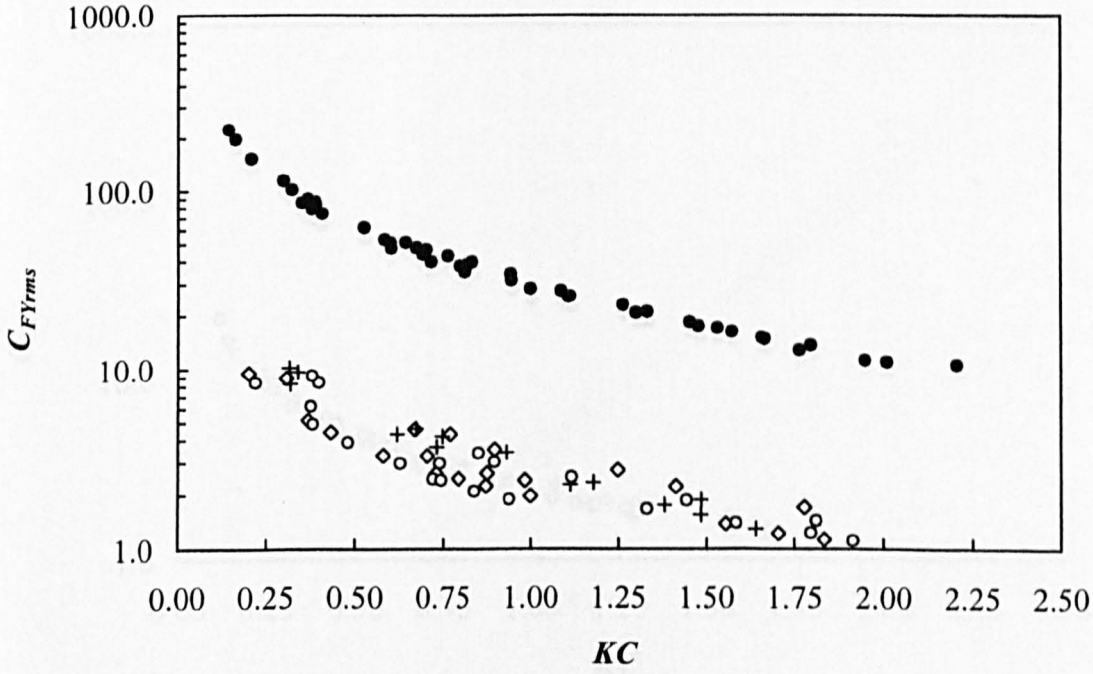

Fig. 6.220 Horizontal and vertical root mean square coefficients for horizontal rectangular cylinder for aspect ratio = 1/2 in co-existing waves and currents for positive currents

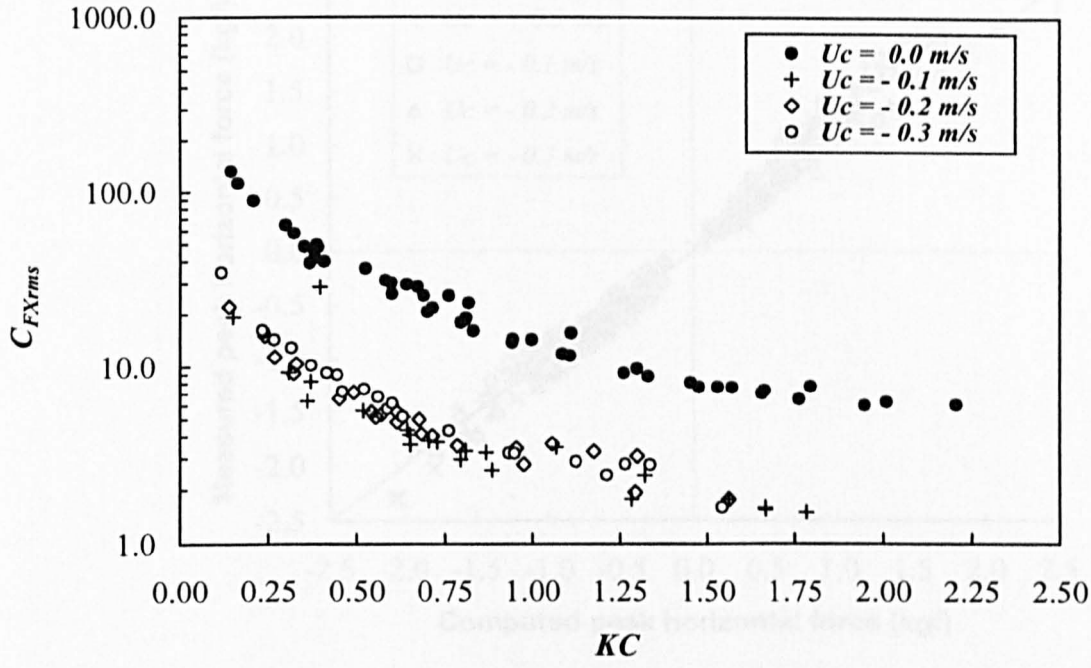

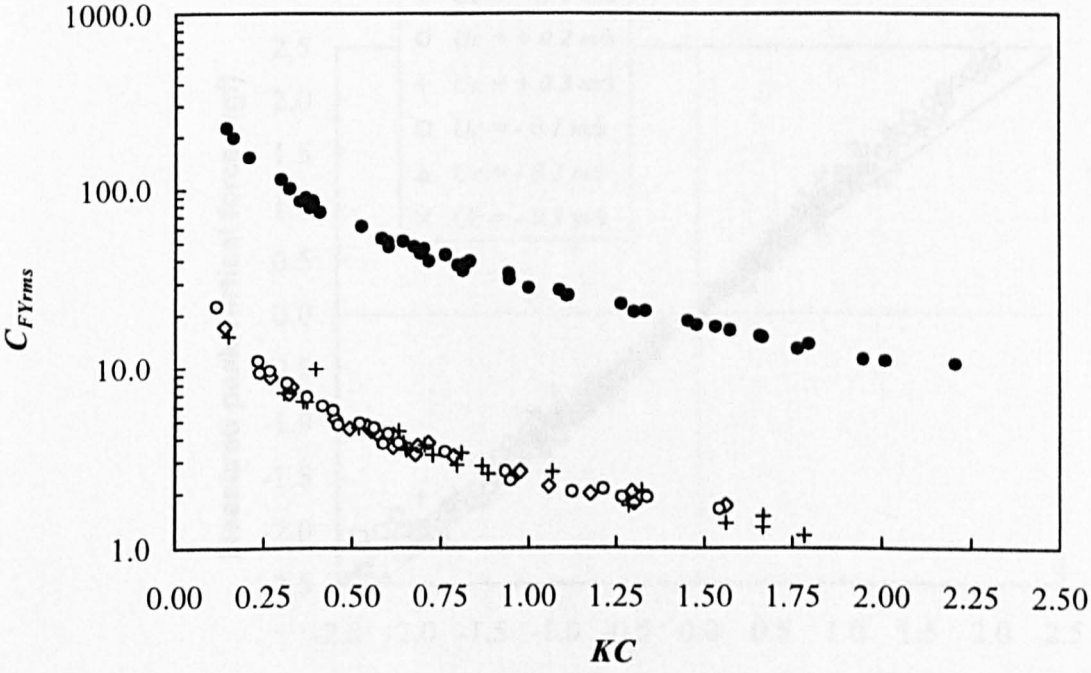

Fig. 6.221 Horizontal and vertical root mean square coefficients for horizontal rectangular cylinder for aspect ratio = 1/2 in co-existing waves and currents for negative currents

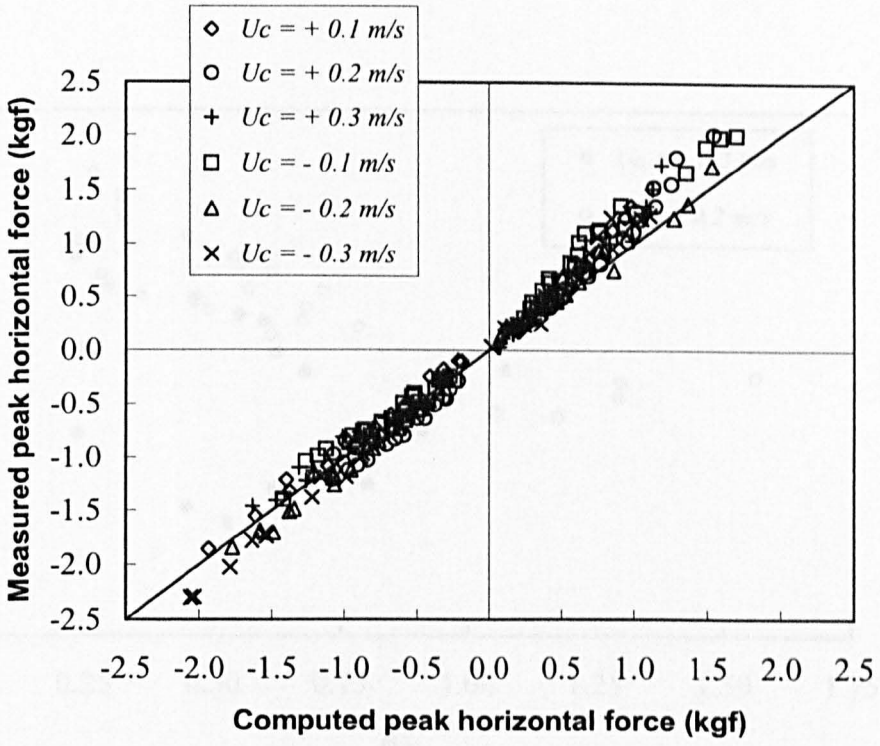

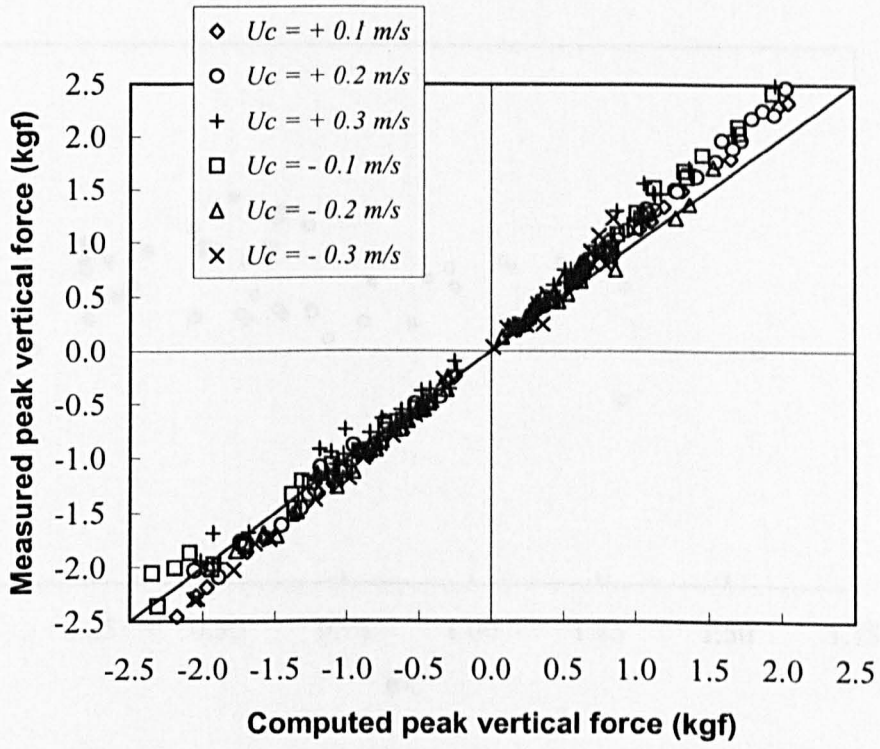

Fig. 6.222 Measured and computed peak forces for horizontal Rectangular cylinder for aspect ratio = 1/2

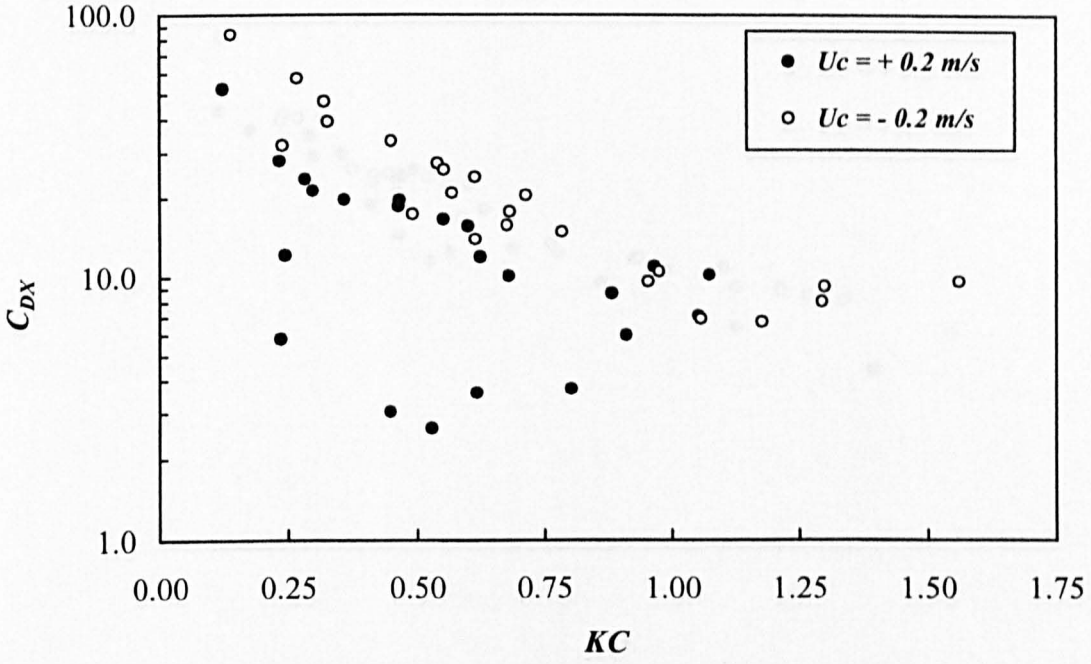

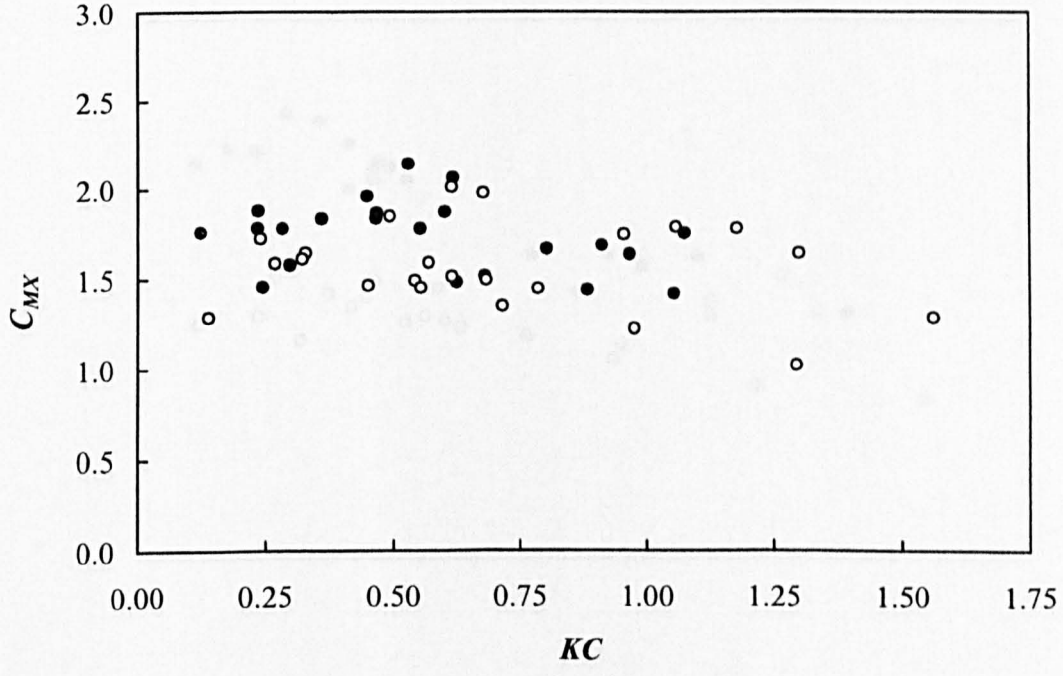

Fig. 6.223 Horizontal drag and inertia coefficients for horizontal rectangular cylinder for aspect ratio = 3/4 in co-existing waves and currents for $U_C = \pm 0.2$ m/s

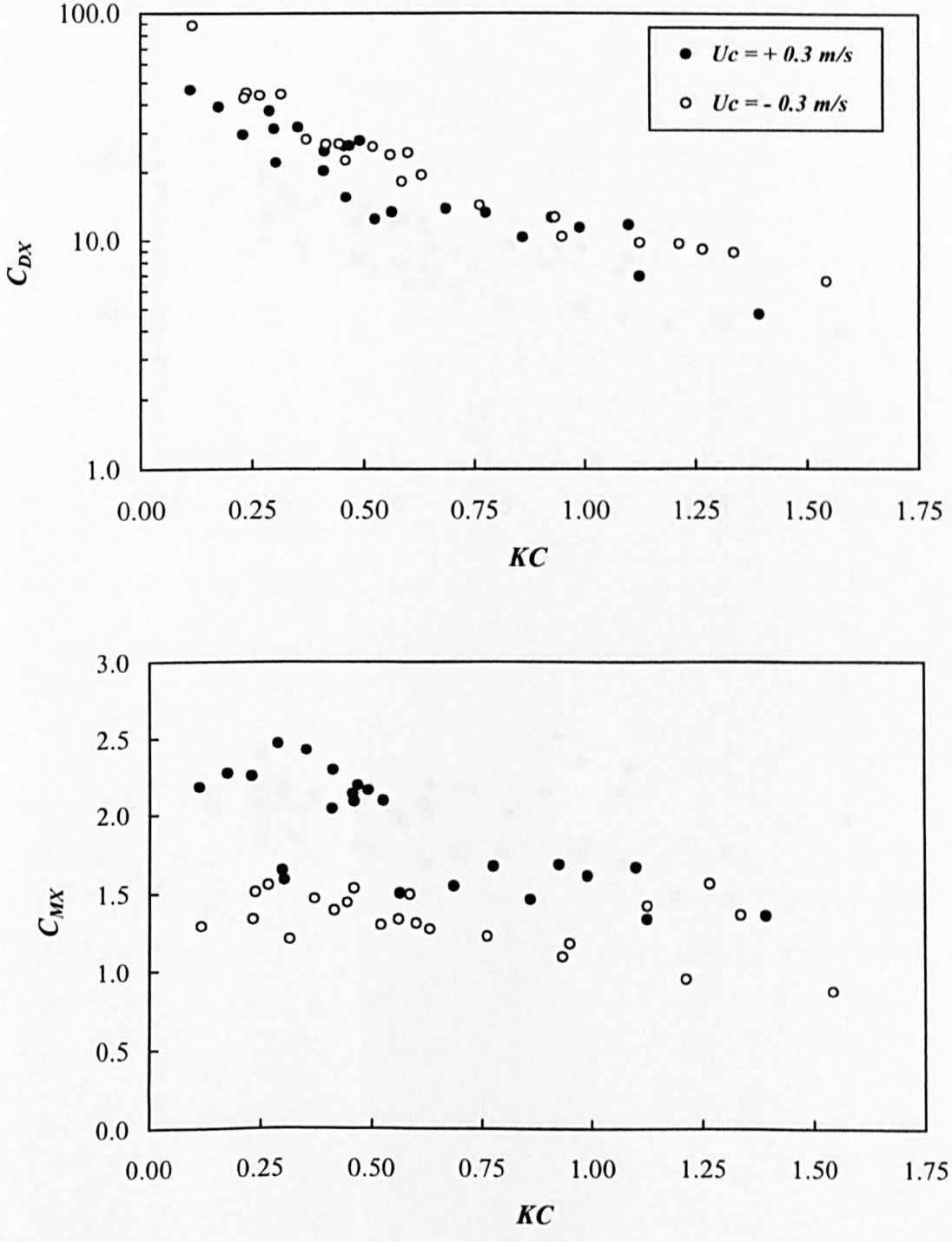

Fig. 6.224 Horizontal drag and inertia coefficients for horizontal rectangular cylinder for aspect ratio = 3/4 in co-existing waves and currents for $U_C = \pm 0.3$ m/s

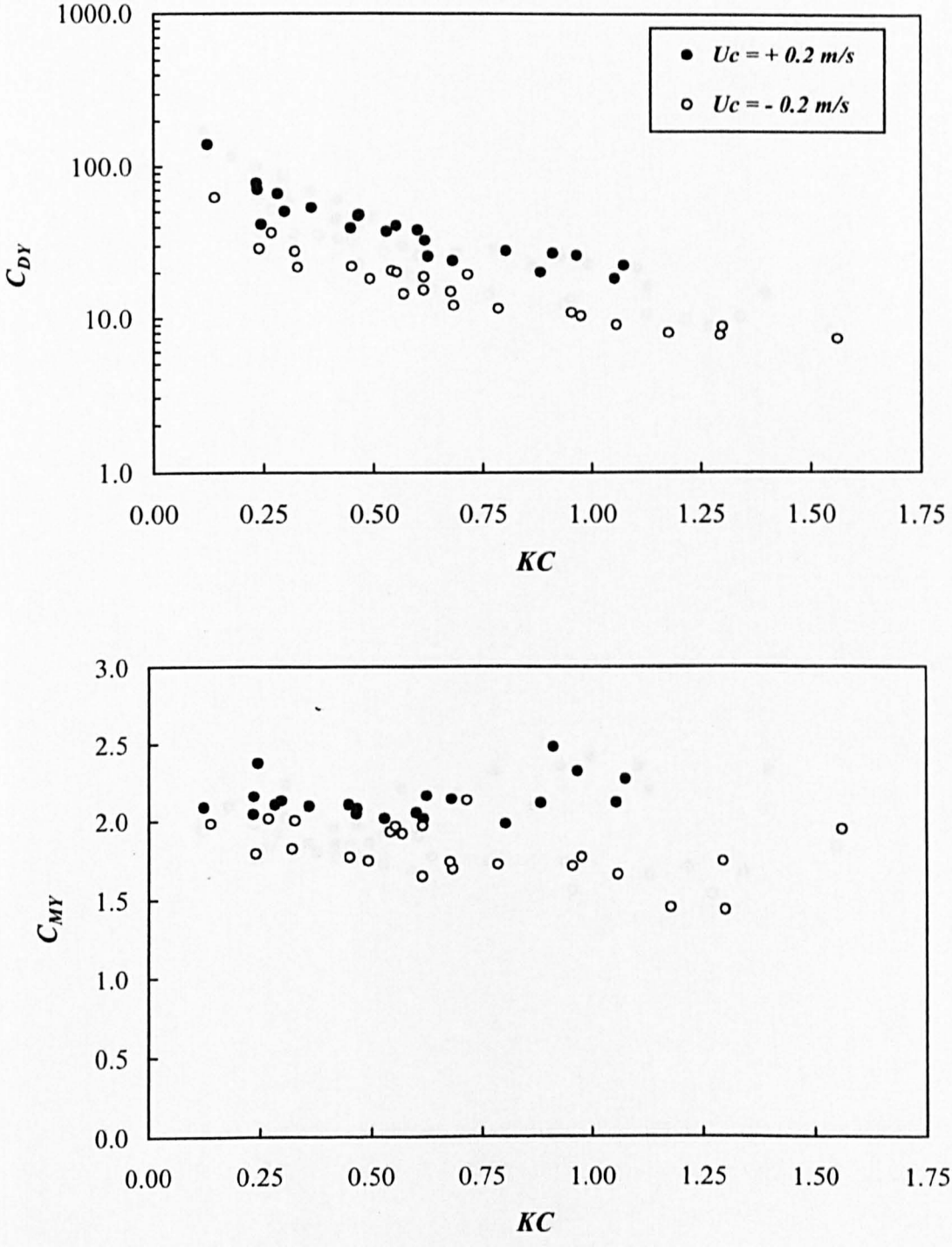

Fig. 6.225 Vertical drag and inertia coefficients for horizontal rectangular cylinder for aspect ratio = 3/4 in co-existing waves and currents for $U_C = \pm 0.2$ m/s

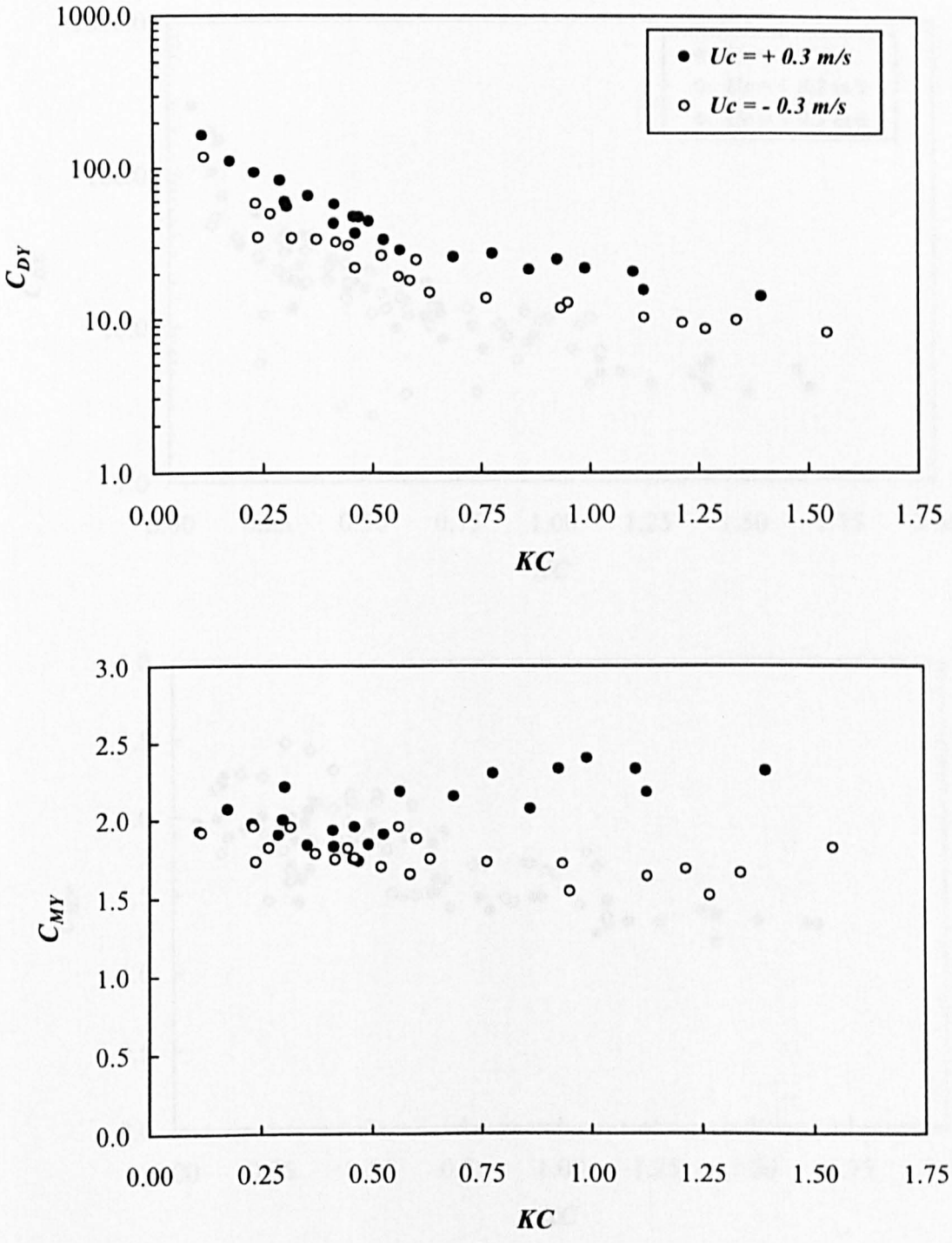

Fig. 6.226 Vertical drag and inertia coefficients for horizontal rectangular cylinder for aspect ratio = 3/4 in co-existing waves and currents for $U_C = \pm 0.3$ m/s

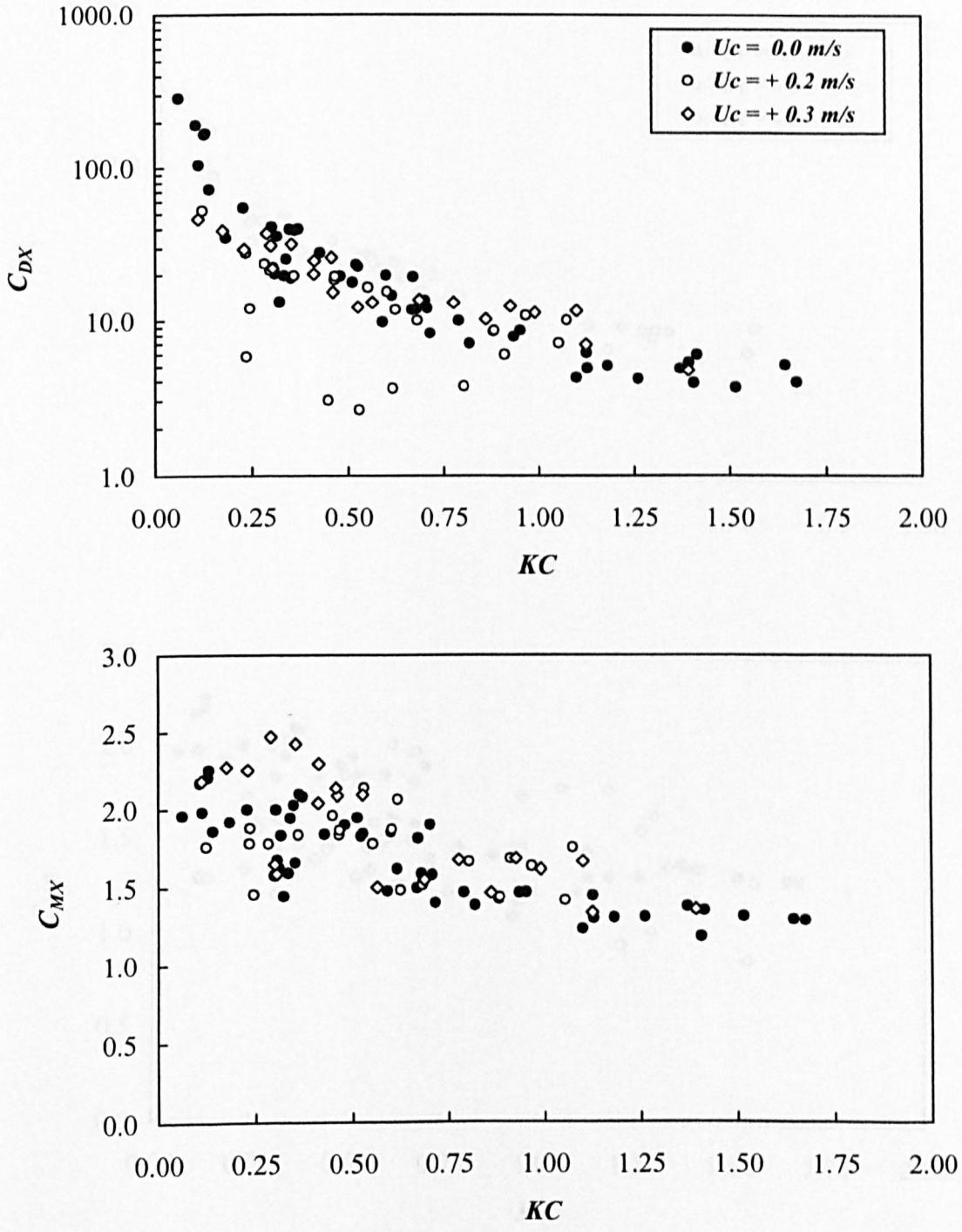

Fig. 6.227 Horizontal drag and inertia coefficients for horizontal rectangular cylinder for aspect ratio = 3/4 in co-existing waves and currents for positive currents

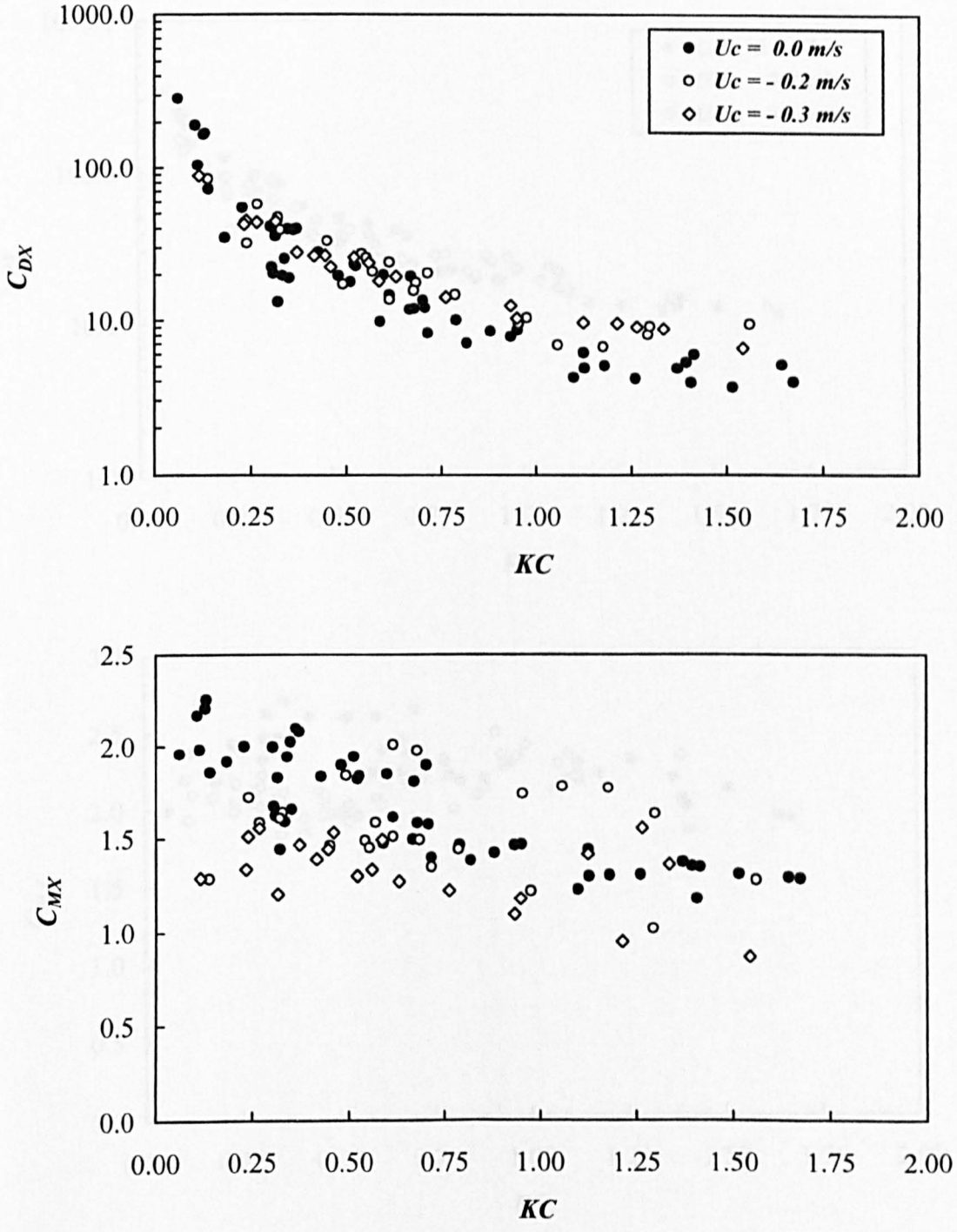

Fig. 6.228 Horizontal drag and inertia coefficients for horizontal rectangular cylinder for aspect ratio = 3/4 in co-existing waves and currents for negative currents

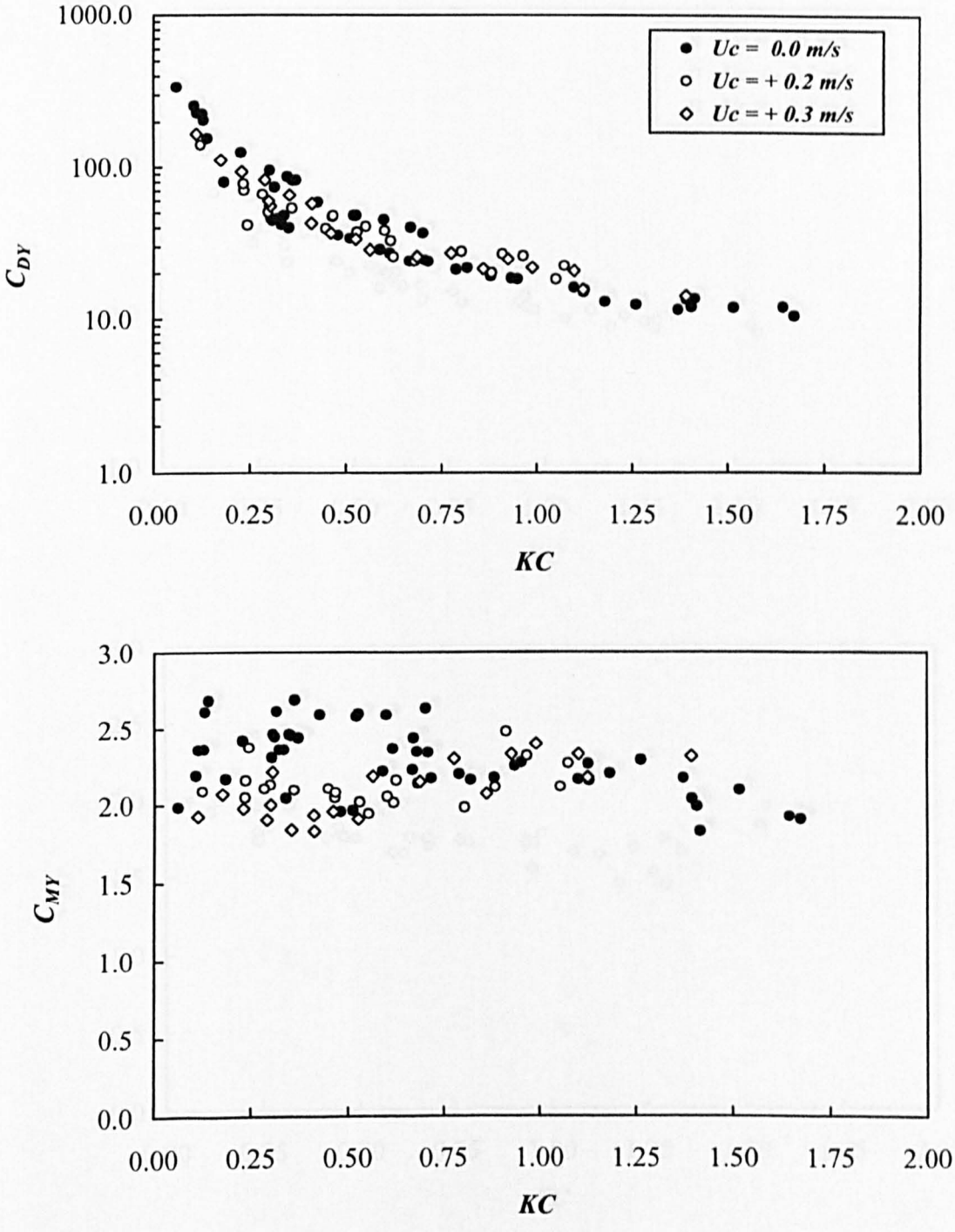

Fig. 6.229 Vertical drag and inertia coefficients for horizontal rectangular cylinder for aspect ratio = 3/4 in co-existing waves and currents for positive currents

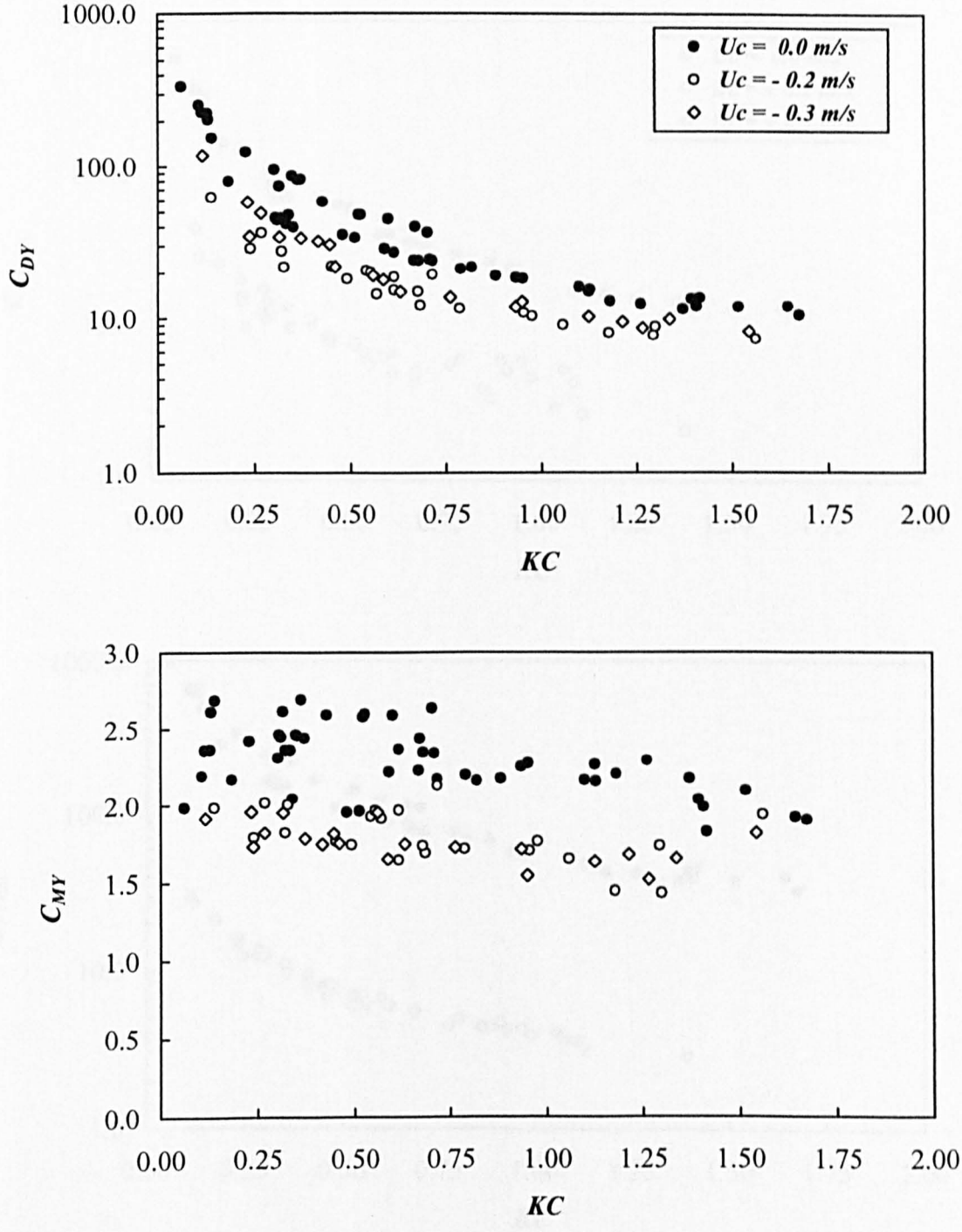

Fig. 6.230 Vertical drag and inertia coefficients for horizontal rectangular cylinder for aspect ratio = 3/4 in co-existing waves and currents for negative currents

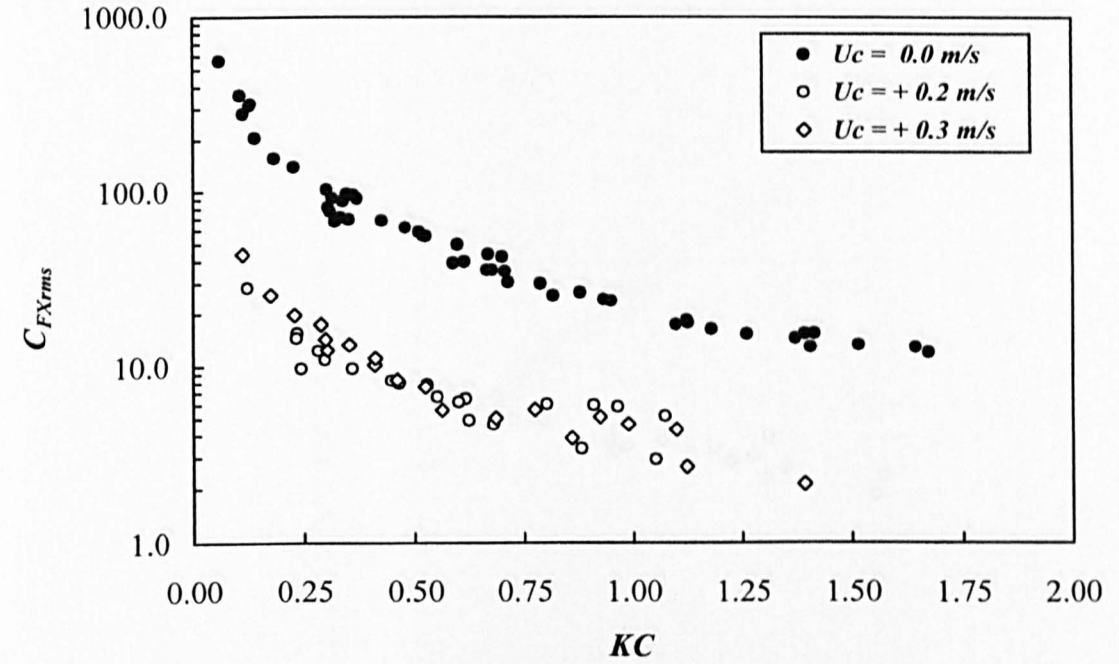

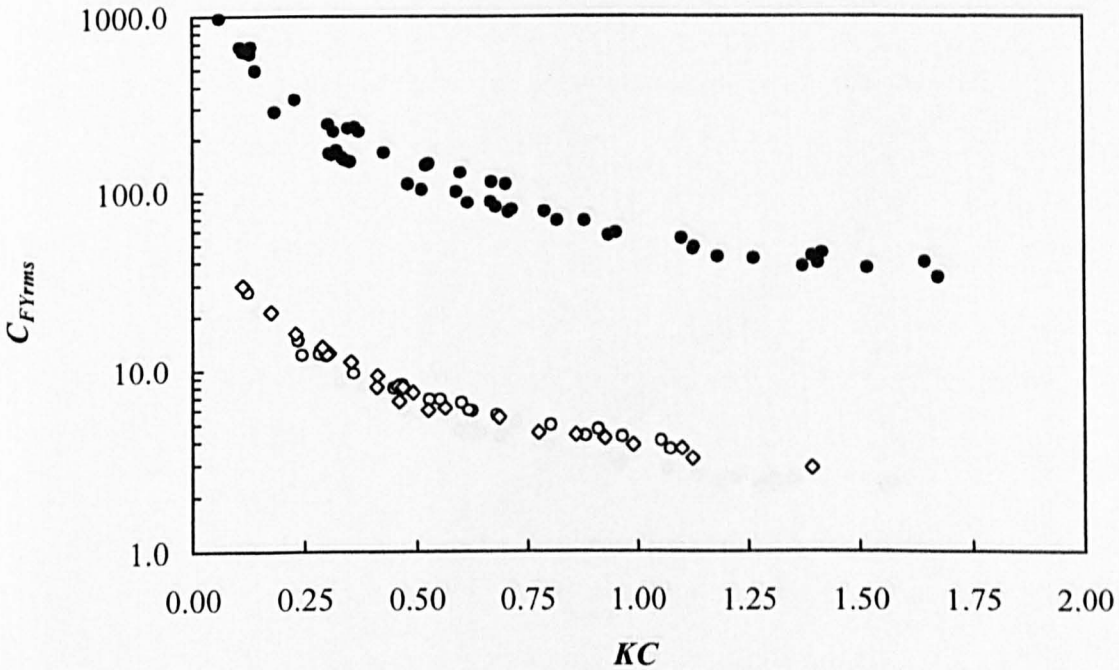

Fig. 6.231 Horizontal and vertical rms force coefficients for horizontal rectangular cylinder for aspect ratio = 3/4 in co-existing waves and currents for positive currents

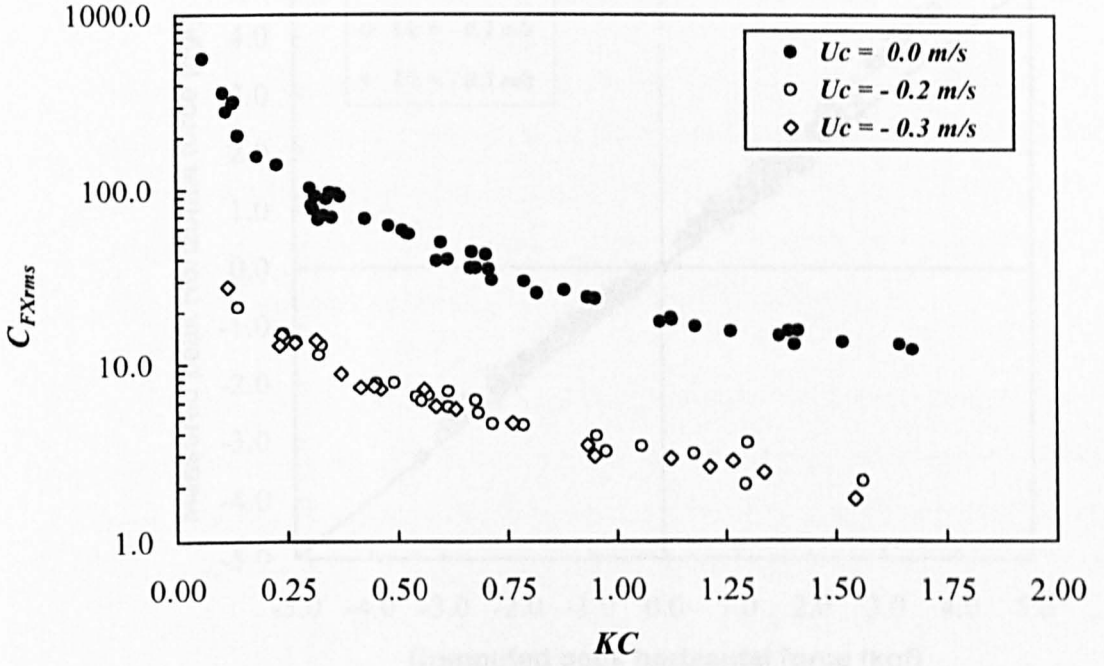

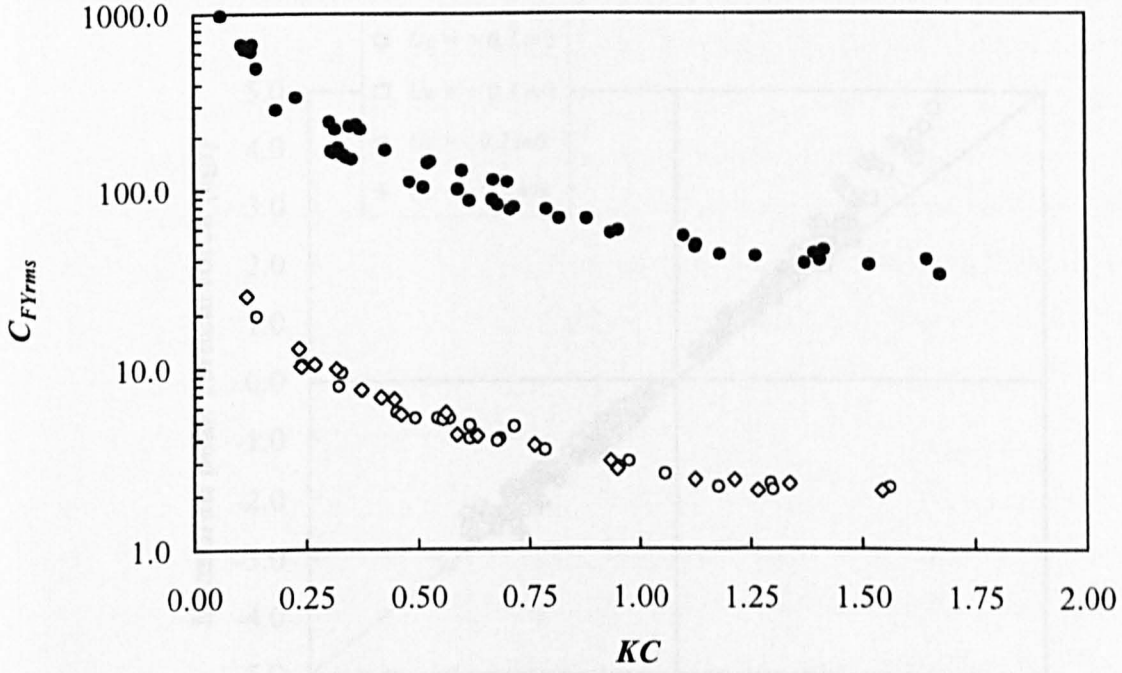

Fig. 6.232 Horizontal and vertical rms force coefficients for horizontal rectangular cylinder for aspect ratio = 3/4 in co-existing waves and currents for negative currents

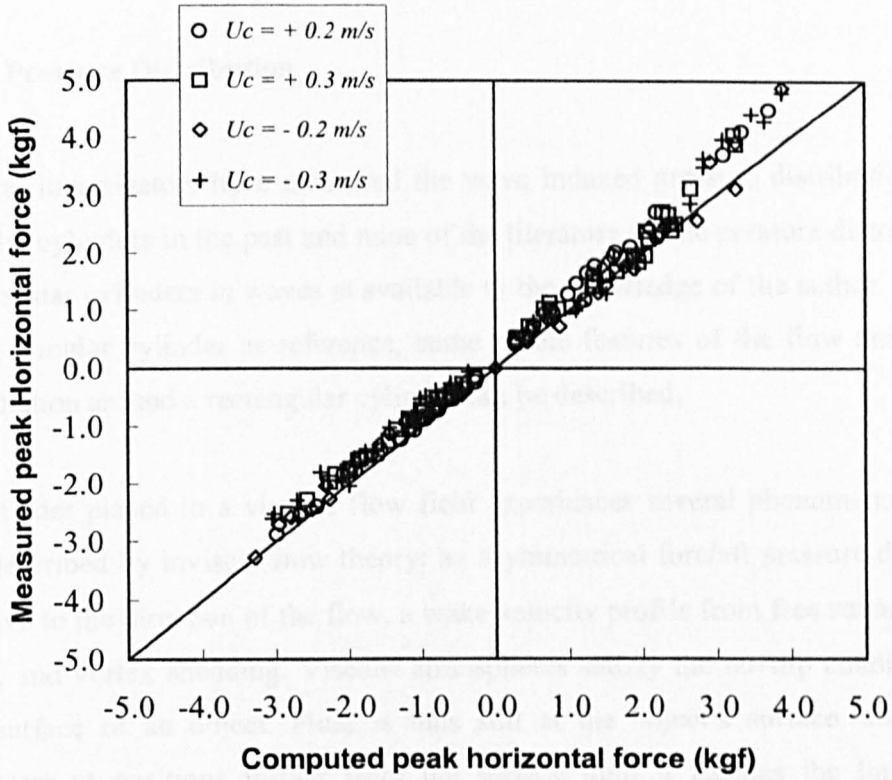

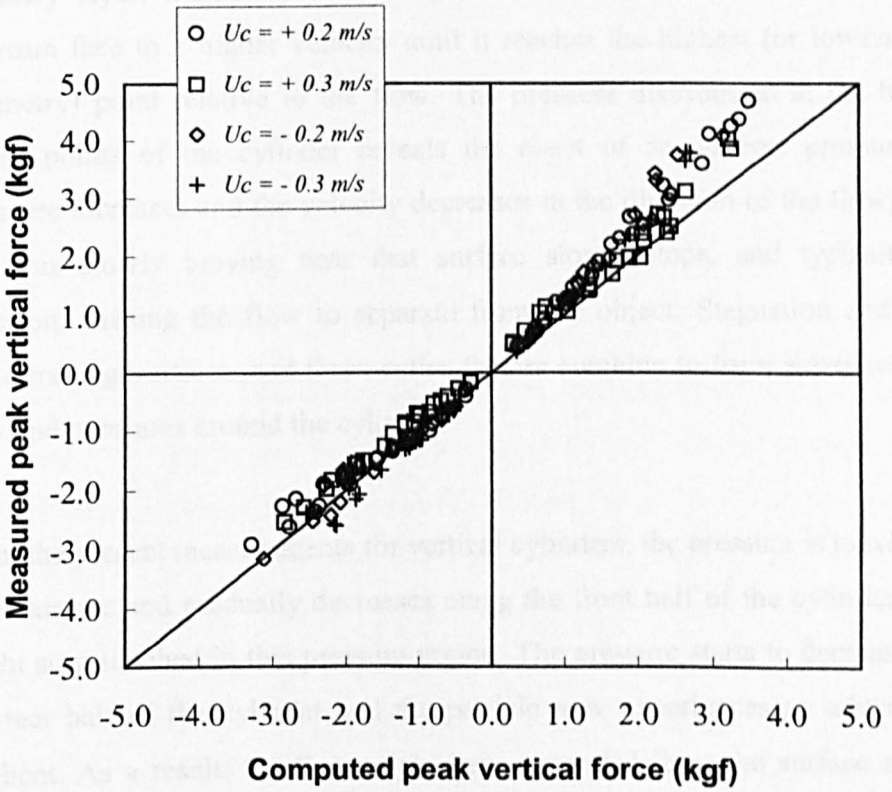

Fig. 6.233 Measured and computed peak forces for horizontal rectangular cylinder for aspect ratio = 3/4

6.4 Pressure Distribution

Several investigators have measured the wave induced pressure distribution around circular cylinders in the past and none of the literature on the pressure distribution on rectangular cylinders in waves is available to the knowledge of the author. However, using circular cylinder as reference, some of the features of the flow and pressure distribution around a rectangular cylinder can be described.

A cylinder placed in a viscous flow field experiences several phenomenon that are not described by inviscid flow theory; an asymmetrical fore/aft pressure distribution relative to the direction of the flow, a wake velocity profile from free stream uniform flow, and vortex shedding. Viscous atmospheres satisfy the no-slip condition along the surface of an object. Fluid is thus still at the object's surface, and velocity increases at positions further from the surface until it reaches the limits of the boundary layer, where the flow is again uniform. The flow expands around the upstream face to a higher velocity until it reaches the highest (or lowest, based on symmetry) point relative to the flow. The pressure distribution at the highest and lowest points of the cylinder reveals the onset of an adverse pressure gradient (pressure increases and the velocity decreases in the direction of the flow). The flow that was slowly moving near that surface slows, stops, and typically reverses direction, causing the flow to separate from the object. Stagnation and separation cause trailing vortices, and these entire factors combine to form asymmetric fore/aft flow and pressures around the cylinder.

From the present measurements for vertical cylinders, the pressure is maximum at the front surface and gradually decreases along the front half of the cylinder. The flow might stay attached in this pressure region. The pressure starts to decrease further in the rear half of the cylinder and the particle now experiences an adverse pressure gradient. As a result, the flow might have separated from the surface and create a highly turbulent region behind the cylinder, resulting the wake. The pressure inside

the wake region might have been low as the flow separates. This is more pronounced for higher *d/L* ratios. In the case of horizontal cylinders, the cylinder's surface (top side) close to the free surface experiences large pressure compared to the bottom surface. Here, the asymmetry in the pressure distribution may be attributed to the steady streaming that occurs in waves around the cylinders.

These asymmetric pressure distributions around a circular cylinder have been measured by Borthwick (1990) and are reproduced in Fig. 6.234a. The pressure distributions have been obtained for 16 positions of the wave crest relative to the cylinder axis. *KC* number and *Re* numbers are calculated at the surface. The top left hand corner plot was obtained when the crest was on the cylinder axis. This figure also includes the theoretical pressure distribution obtained from local potential theory with a symmetrical distribution. As the figure indicate the agreement between theory and measurement is poor and the pressure distribution is asymmetric. Borthwick suggested that at sub-critical Reynolds number and at very low *KC* numbers, a steady streaming may cause third and fourth order components to appear in the fluctuating pressure profiles. At *KC* higher than 5, the circumferential pressures were dominated by second harmonic drag-induced components during the maximum velocity and other times of the cycle, the first harmonic inertia component due to acceleration was dominant. The asymmetry in the pressure distribution for a vertical cylinder is also confirmed by Kato and Ohmatsu (1989).

The differences in measured and potential flow pressure distributions have also been discussed by Pearcey (1990) on circular cylinders in oscillatory flow. The author explains three situations:- (i) stagnation pressure is greater than the potential flow value; in this case the incident relative velocity is momentarily greater than the displacement velocity of the cylinder itself, (ii) stagnation pressure is less than potential flow value; in here the incident relative velocity is momentarily less than the displacement velocity of the cylinder due to a velocity decrement in the re-encountered wake and (iii) stagnation pressure is nearly equal to theory; this shows a little or no perturbation in incident flow velocity.

In the case of rectangular cylinders, due to the above-explained factors, the asymmetry in the pressure distribution is quite acceptable, as the rectangular cylinders are known to produce vortices even at low KC numbers compared to circular cylinders. It has to be kept in mind that the pressure distribution is also depending on the shape of the waves, wave depth parameter (kd) and the temporal variations of wave particle kinematics. Depending upon the position of the wave or velocity time series, the resultant force vector changes its direction, which will be different from the instantaneous velocity direction. The pressure distribution is also affected by the wake that forms in the downstream and by the vortex shed by a previous cycle.

The measured dynamic pressures are analysed and presented as dimensionless pressure, $P_{max}/(0.5\rho gH)$, where P_{max} is measured maximum pressure, H is the wave height. The location of pressure transducers around the cylinders for all test conditions is shown in Figs. 6.234b and 6.234c. Only a small number of pressure transducers were used, so the derivation of forces from the pressure measurements will not be accurate and therefore they were used only to give an idea of the flow pattern around the cylinder. The results reported are only the measurements in regular waves. The variation of dimensionless pressure for various values of relative water depth, d/L is shown in Figs. 6.235a and 6.235b for vertical cylinder of aspect ratio = 1/2. The range of wave steepness for each d/L is also given in the figures. The x-axis in the figure represents corresponding location of pressure transducers around the cylinders. It is seen from Figs. 6.235a and 6.235b that the normalised pressure does not vary much around the cylinder locations for smaller values of d/L at all H/L. For large values of d/L ($d/L > 0.794$) a large variation on the pressures around the cylinder is noticed for all H/L values. Since the water depth is retained constant, the above plots reflect the effect of wavelength. It is also observed that increase in d/L results in the reduction of magnitude of the non-dimensionalised pressure, being more pronounced for deep water conditions.

A similar observation is made for all other vertical cylinders. The results for vertical rectangular cylinder with aspect ratio = 2/1 is shown in Figs. 6.236a and 6.236b. In these plots, the pressure at the surface facing the wave is found to be higher than the pressures measured at other locations. The results for aspect ratios = 3/4 and 4/3 is shown through Figs. 6.237a, 6.237b, 6.238a and 6.238b respectively.

The normalised pressure for horizontal cylinder for aspect ratio = 1/2 with depth of submergence, d/h = 4.68 is shown in Figs. 6.239a and 6.239b. A maximum pressure is observed at *P1* and it decreases gradually up to *P3*. As expected, pressures at *P5* and *P9* are lower than pressures at *P4* and *P10* respectively. The pressures at *P6* and *P7* are found to be lower than the pressures at other locations. The above-mentioned pattern of pressure distribution is found for all values of *d/L* and for all *H/L* values. Here again the magnitude of non-dimensionalised pressure decreases with increase in *d/L* values. For large values of *d/L* the pressures at locations *P6* and *P7* (at the bottom of the cylinders) reaches a lower value of about 0.2 to 0.5. A similar trend in the pressure distribution is observed for aspect ratio = 3/4 as seen from Figs. 6.240a to 6.240b, except that the pressure at *P1* is slightly lower than the pressure at *P2*.

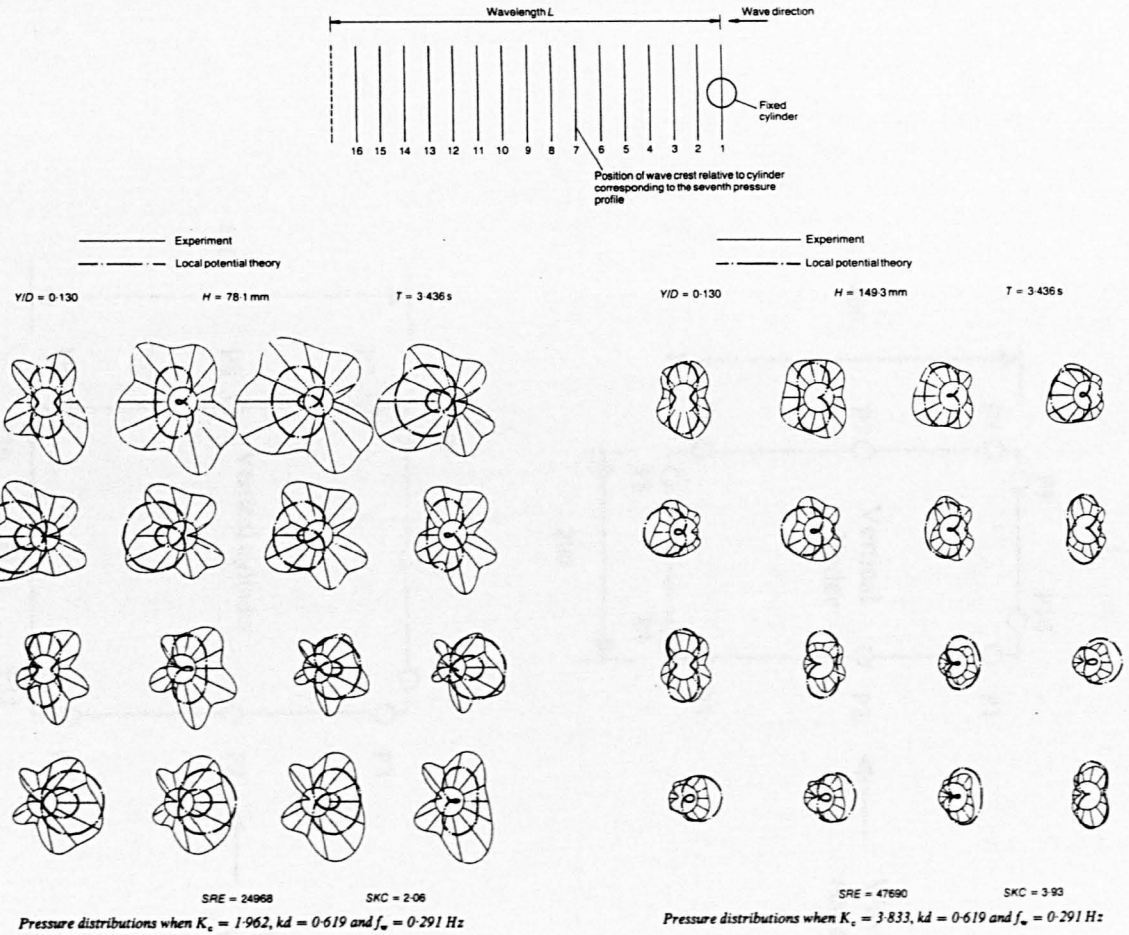

Fig. 6.234 a Pressure distribution around circular cylinders [*Borthwick (1990)*]

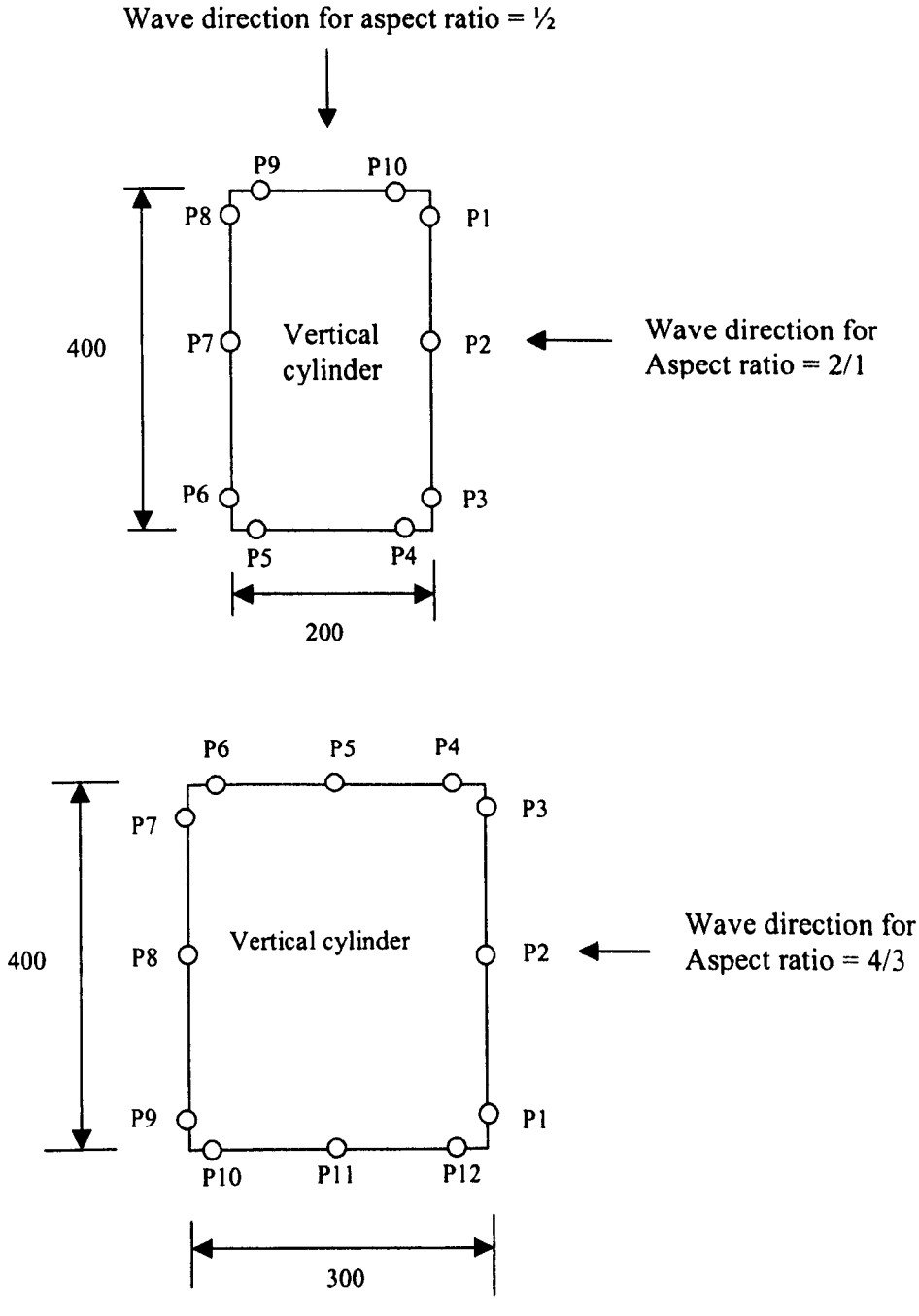

Fig. 6.234 b Location of Pressure transducers

PAGE MISSING IN ORIGINAL

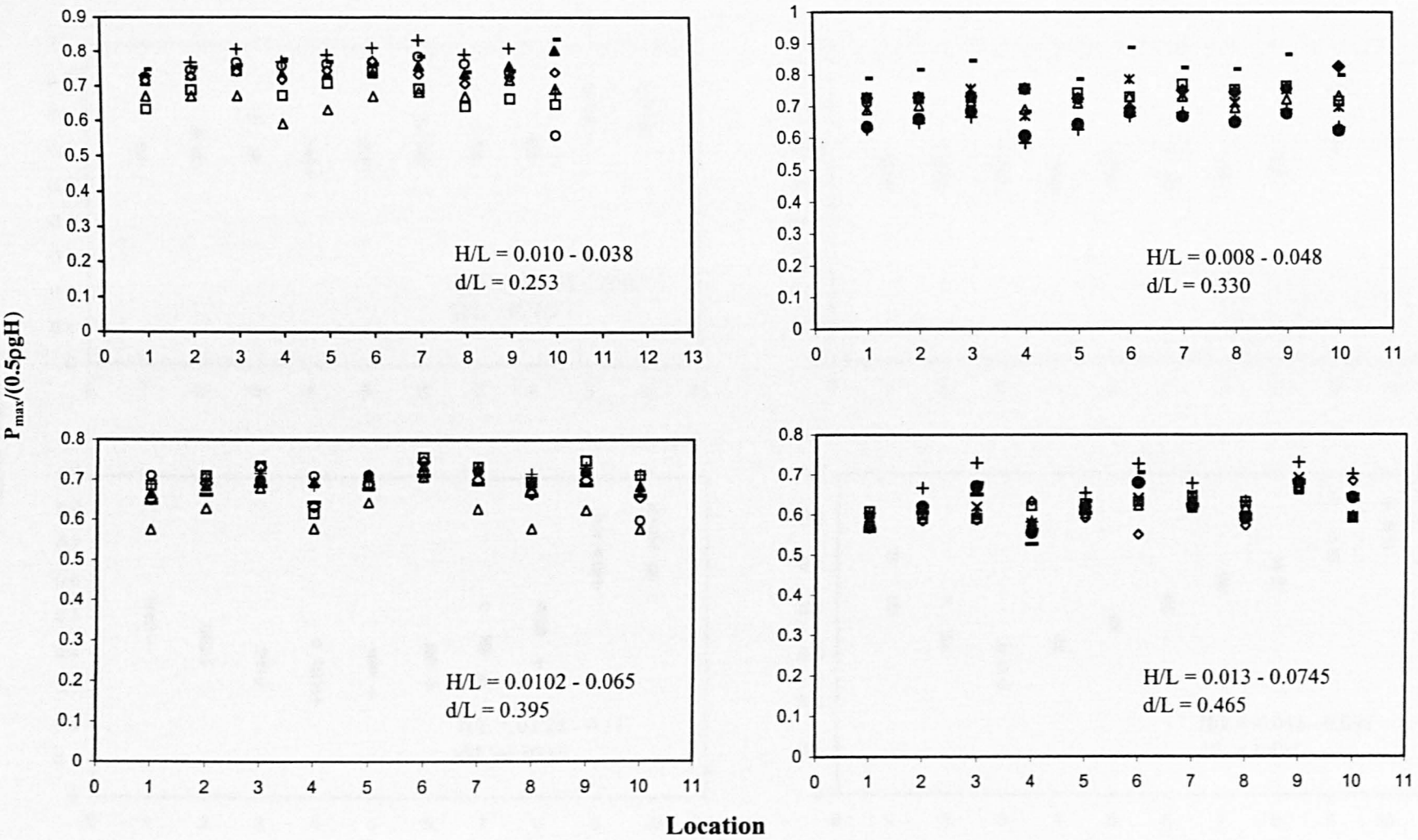

Fig. 6.235a Normalised pressure around vertical rectangular cylinder with aspect ratio = 1/2

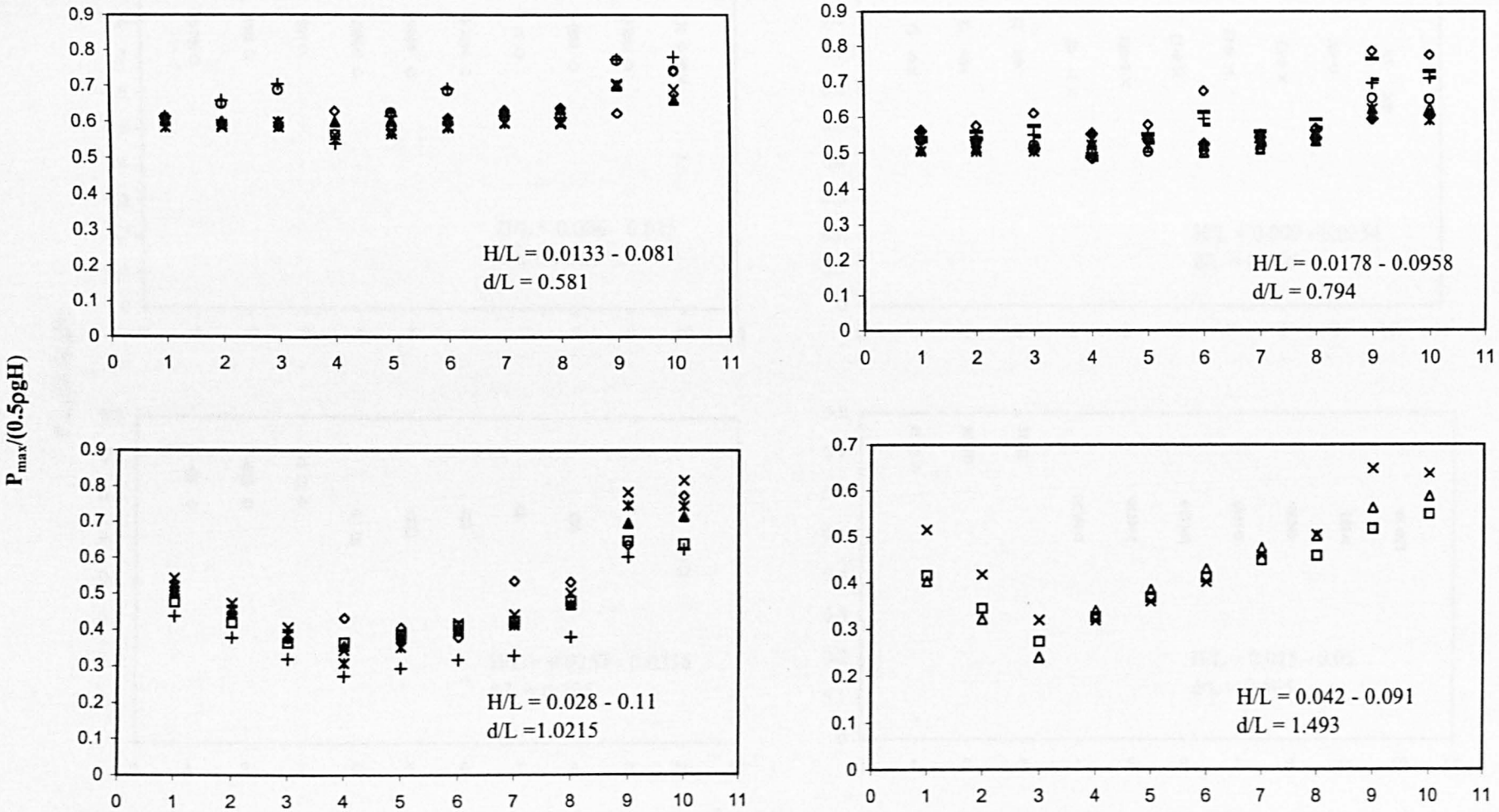

Fig. 6.235b Normalised pressure around vertical rectangular cylinder with aspect ratio = 1/2

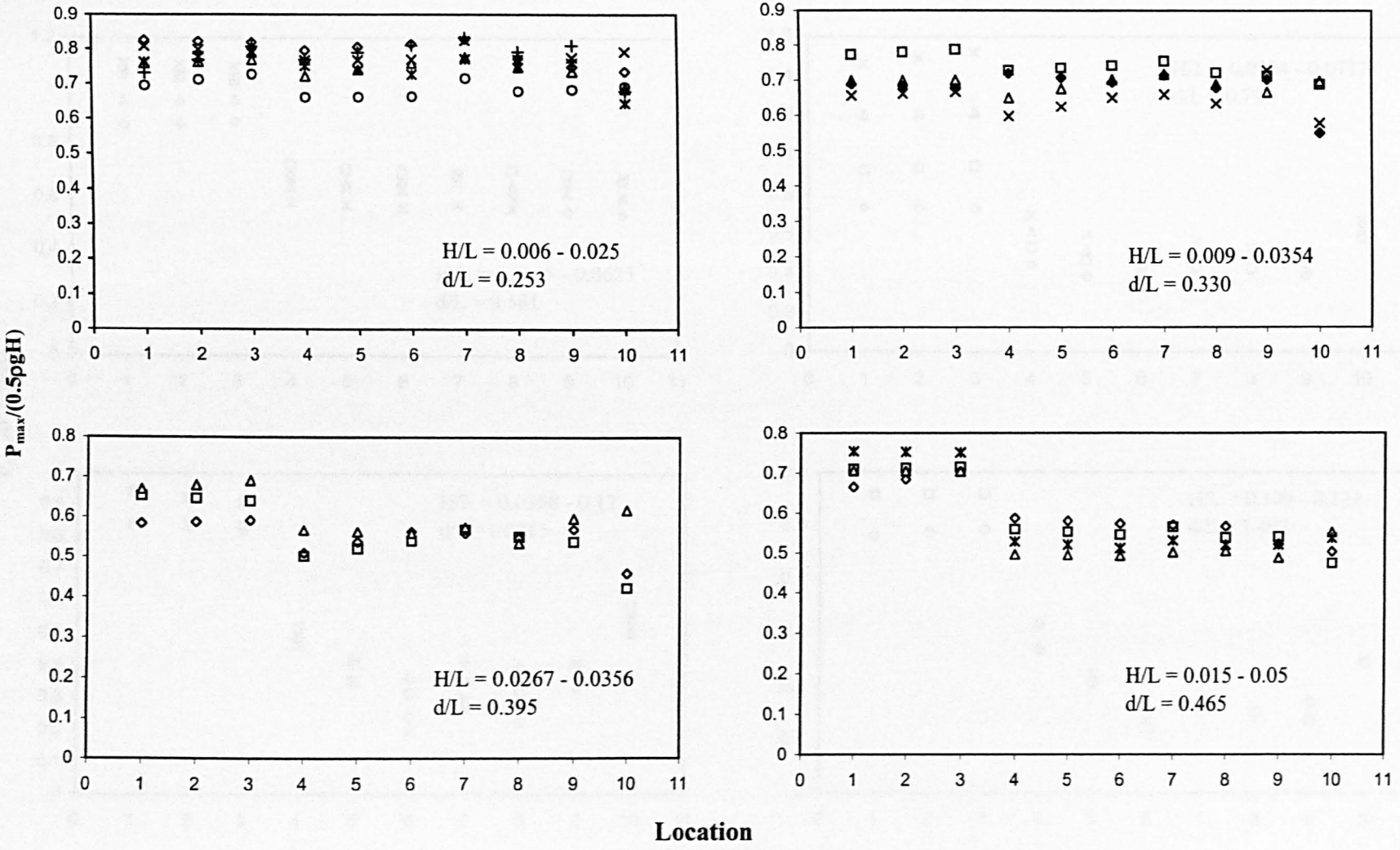

Fig. 6.236a Normalised pressure around vertical rectangular cylinder with aspect ratio = 2/1

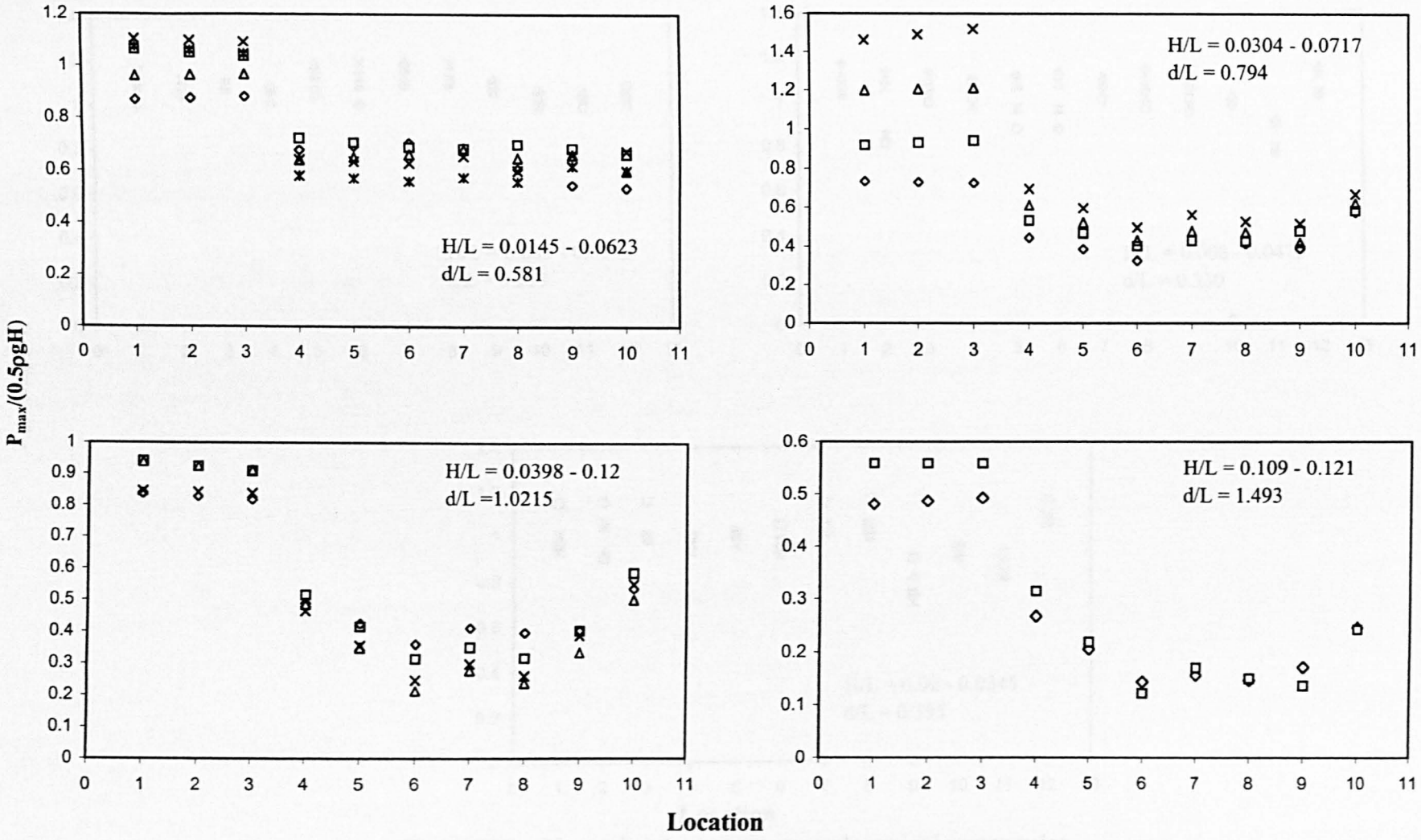

Fig. 6.236b Normalised pressure around vertical rectangular cylinder with aspect ratio = 2/1

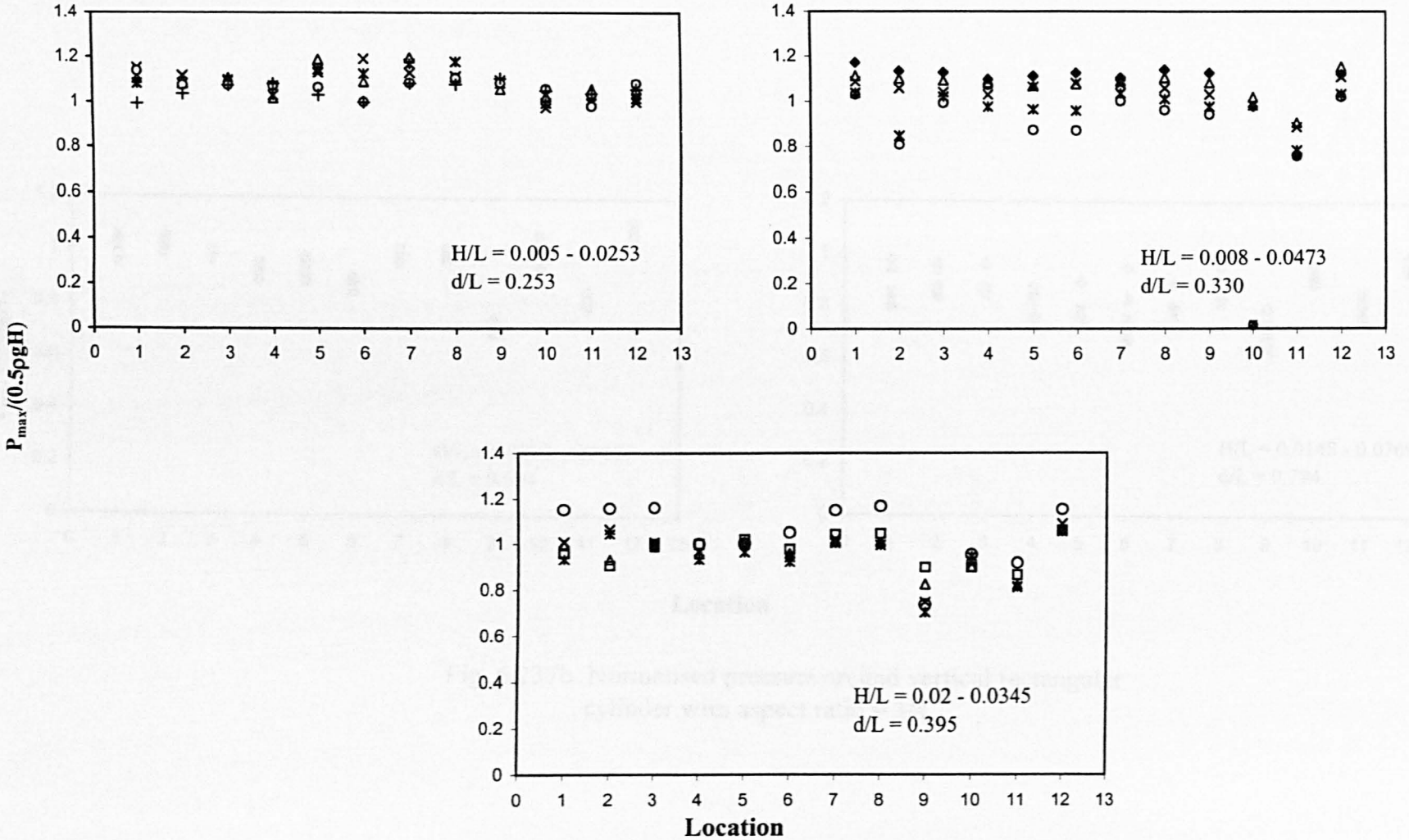

Fig. 6.237a Normalised pressure around vertical rectangular cylinder with aspect ratio = 3/4

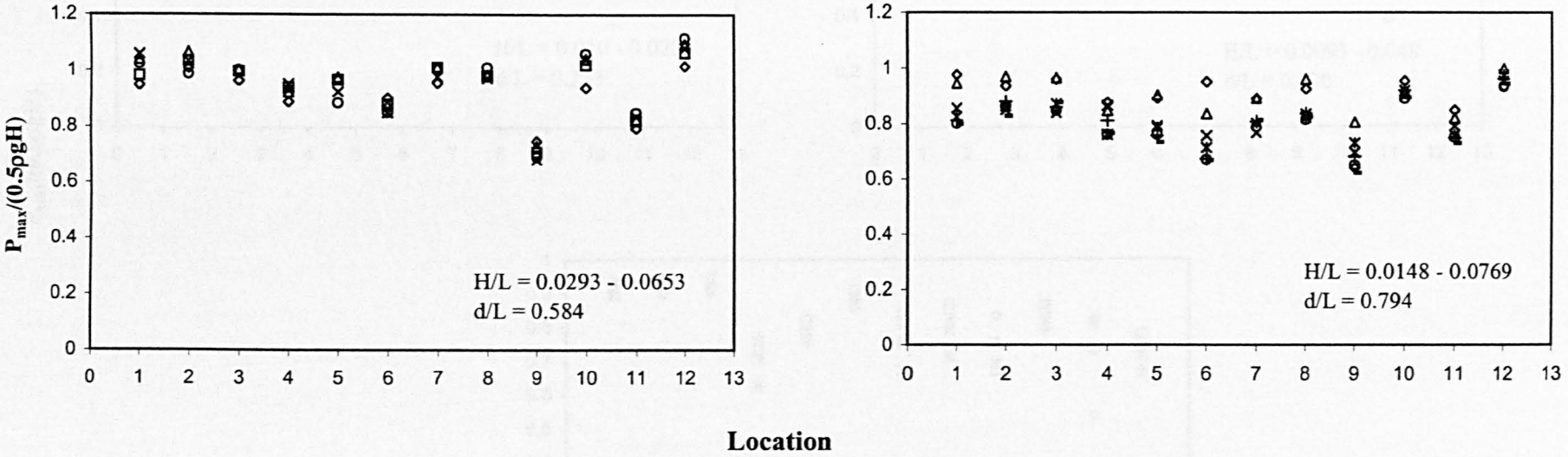

Fig. 6.237b Normalised pressure around vertical rectangular cylinder with aspect ratio = 3/4

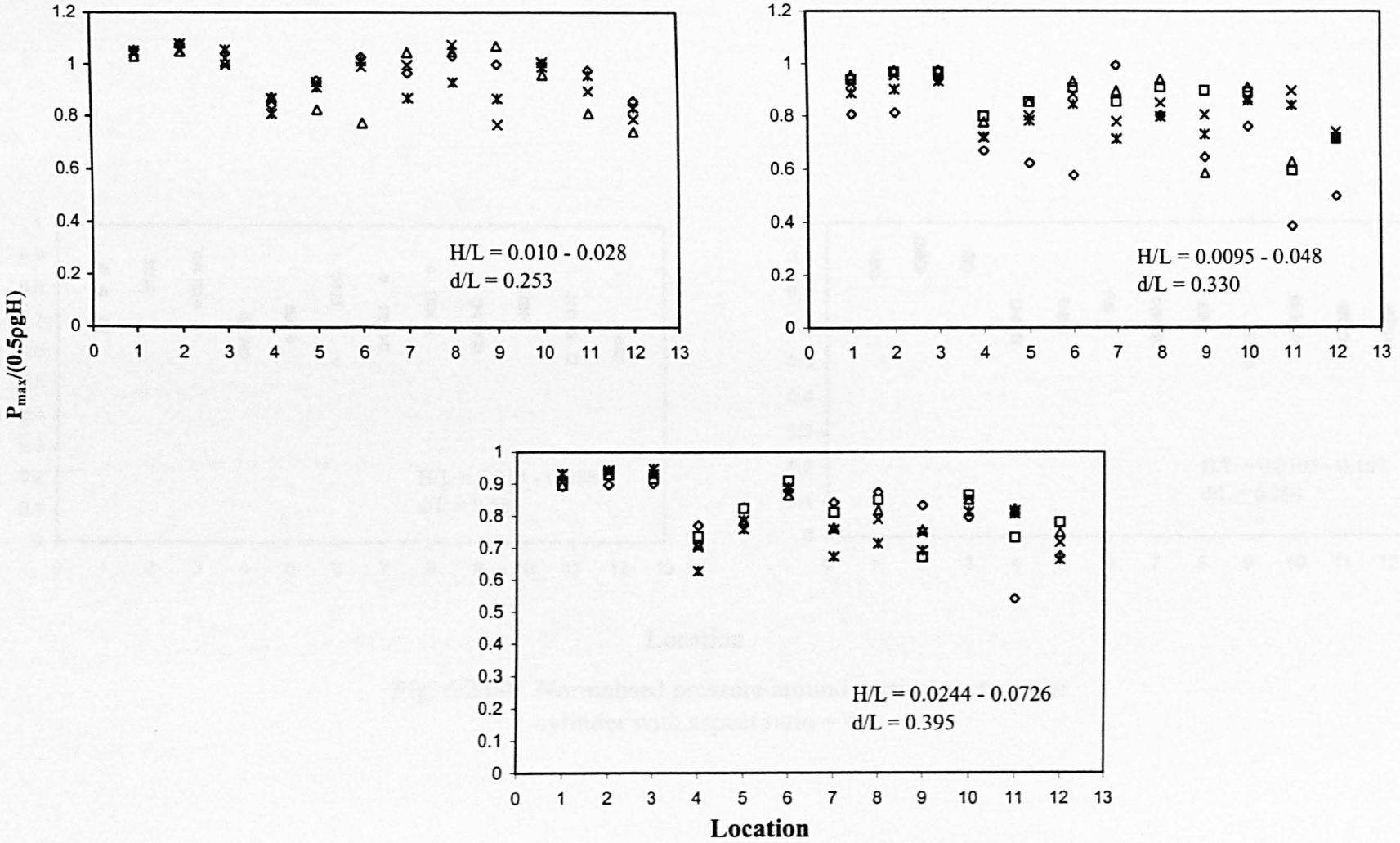

Fig. 6.238a Normalised pressure around vertical rectangular cylinder with aspect ratio = 4/3

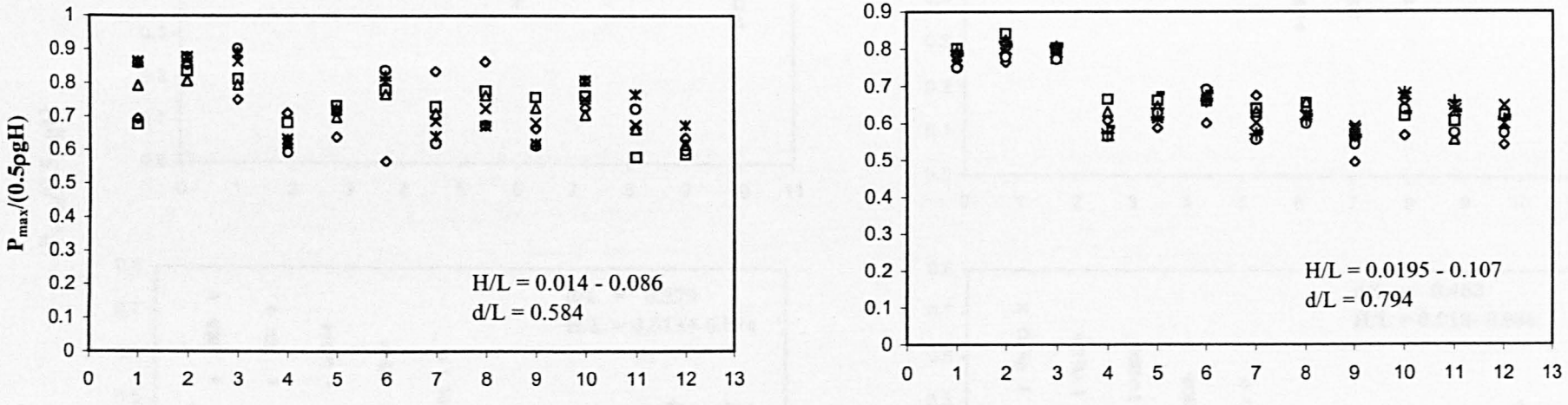

Fig. 6.238b Normalised pressure around vertical rectangular cylinder with aspect ratio = 4/3

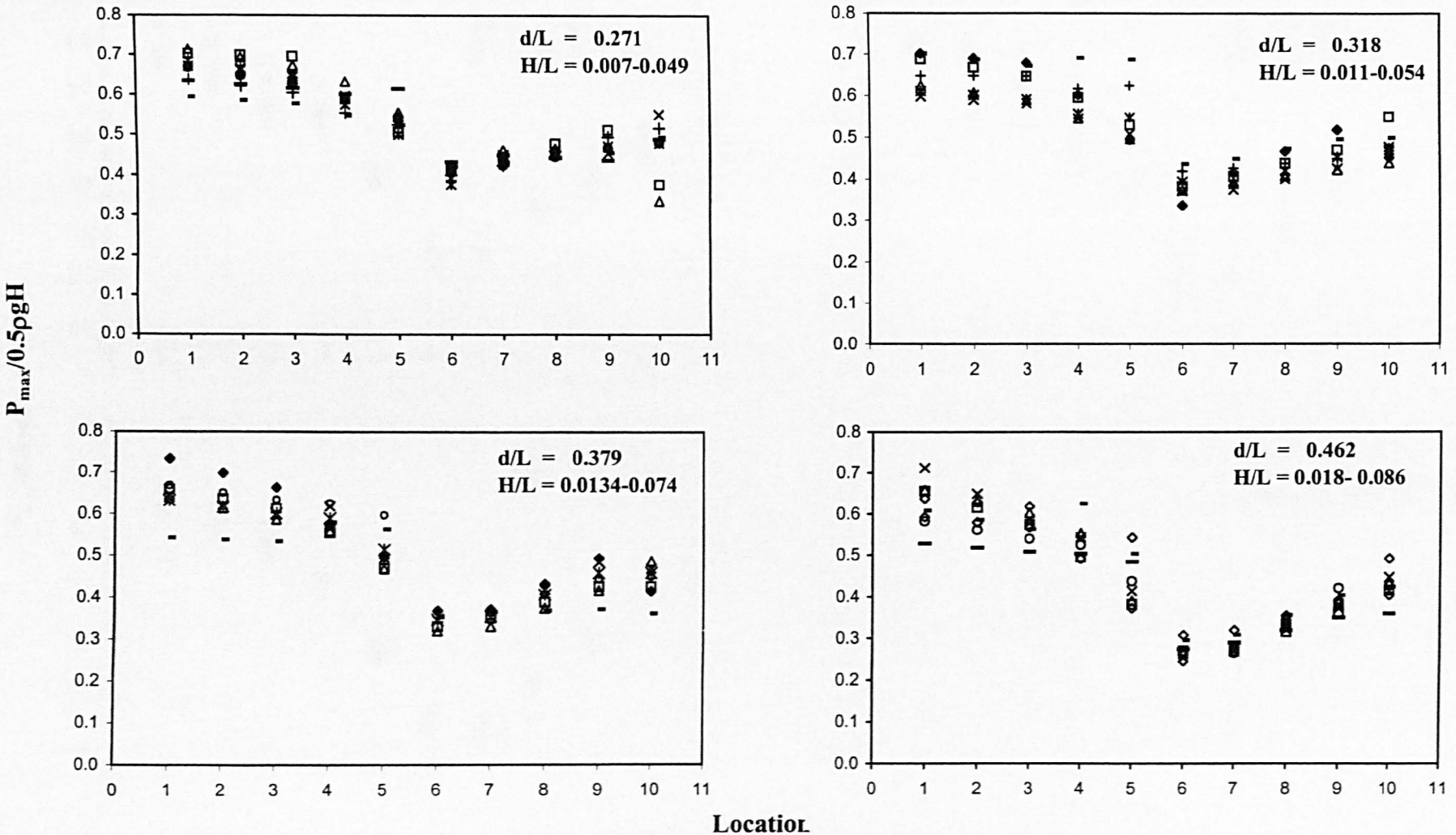

Fig. 6.239a Normalised pressure around horizontal rectangular cylinder with aspect ratio = 1/2

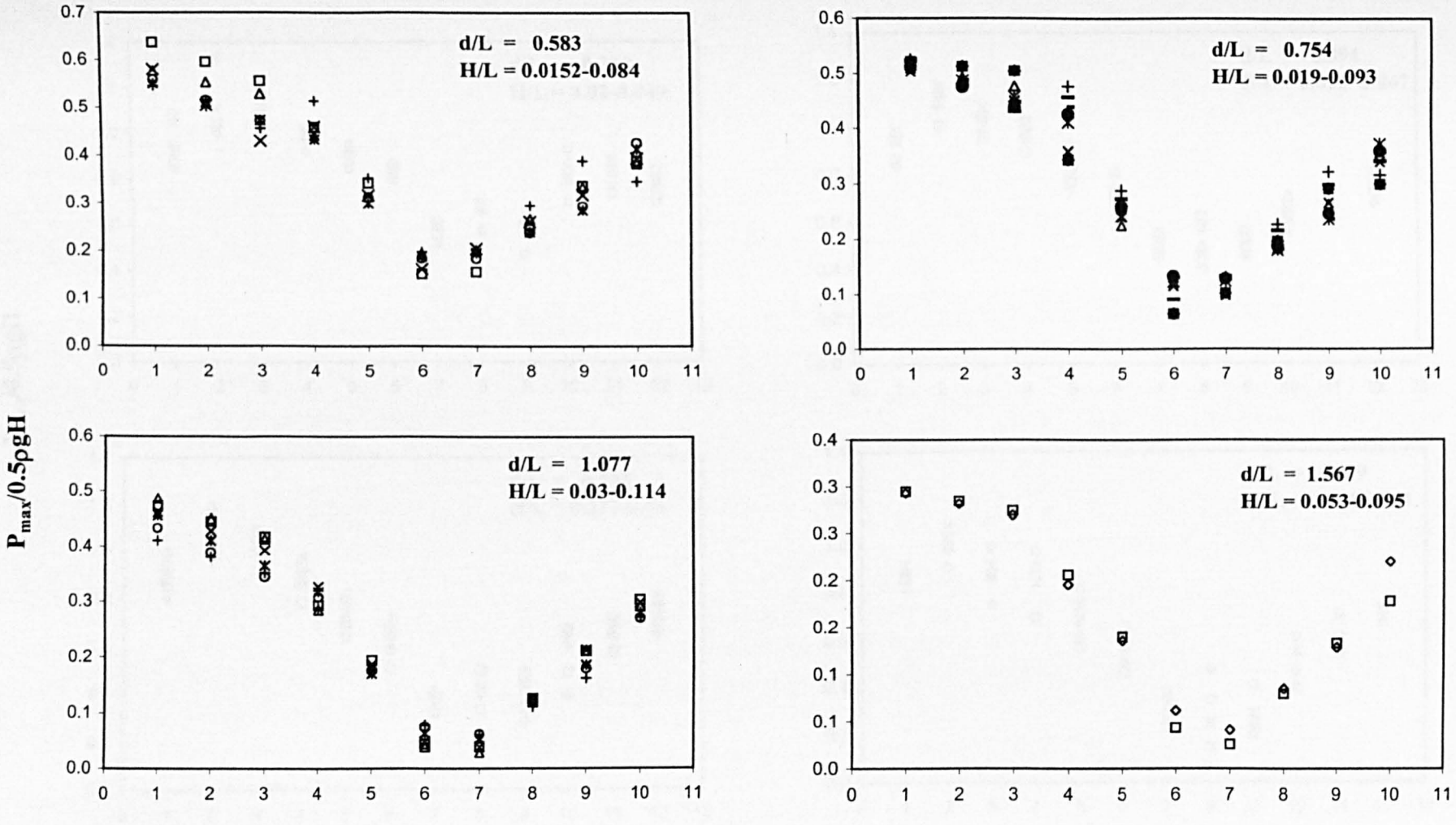

Fig. 6.239b Normalised pressure around horizontal rectangular cylinder with aspect ratio = 1/2

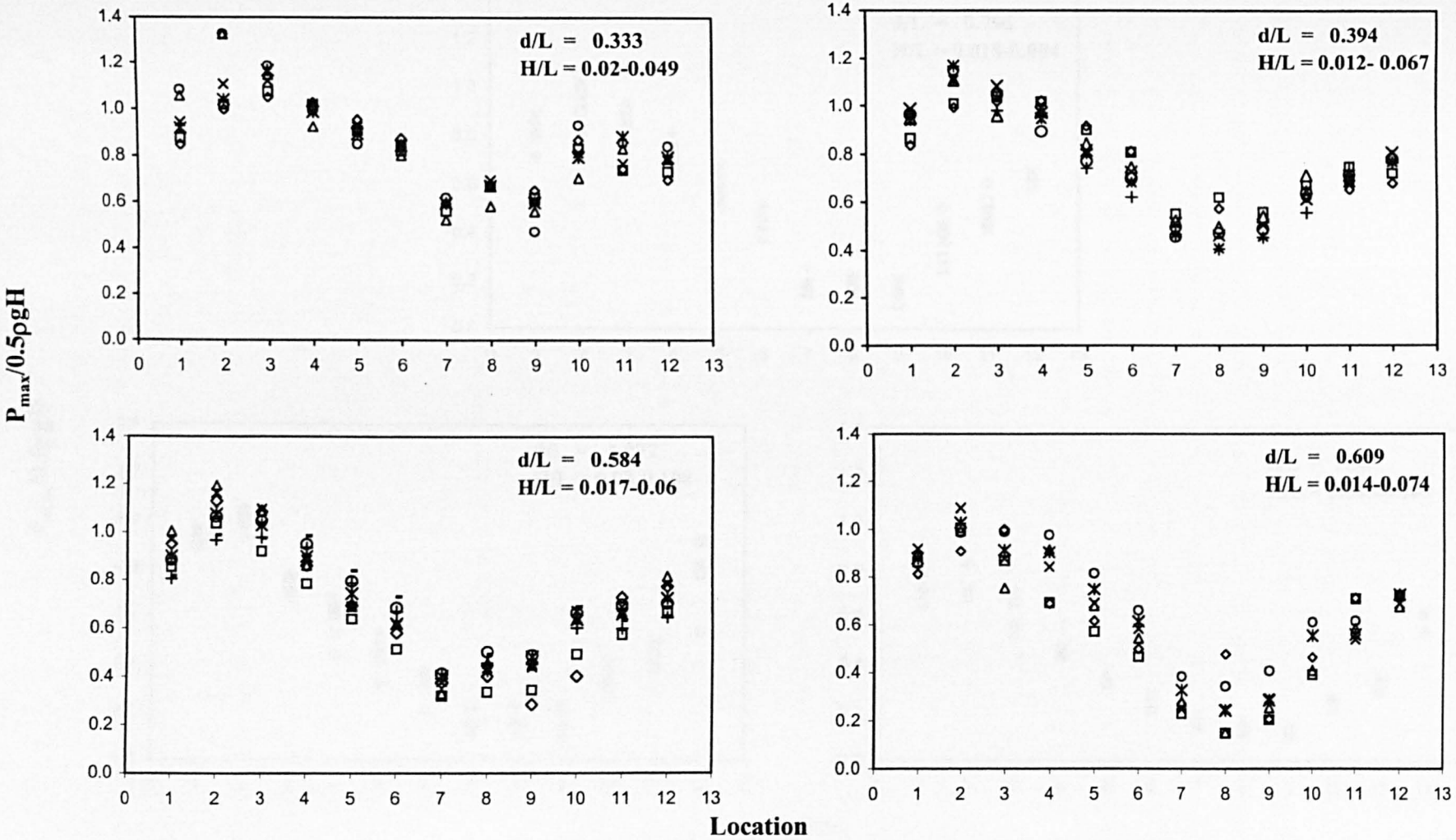

Fig. 6.240a Normalised pressure around horizontal rectangular cylinder with aspect ratio = 3/4

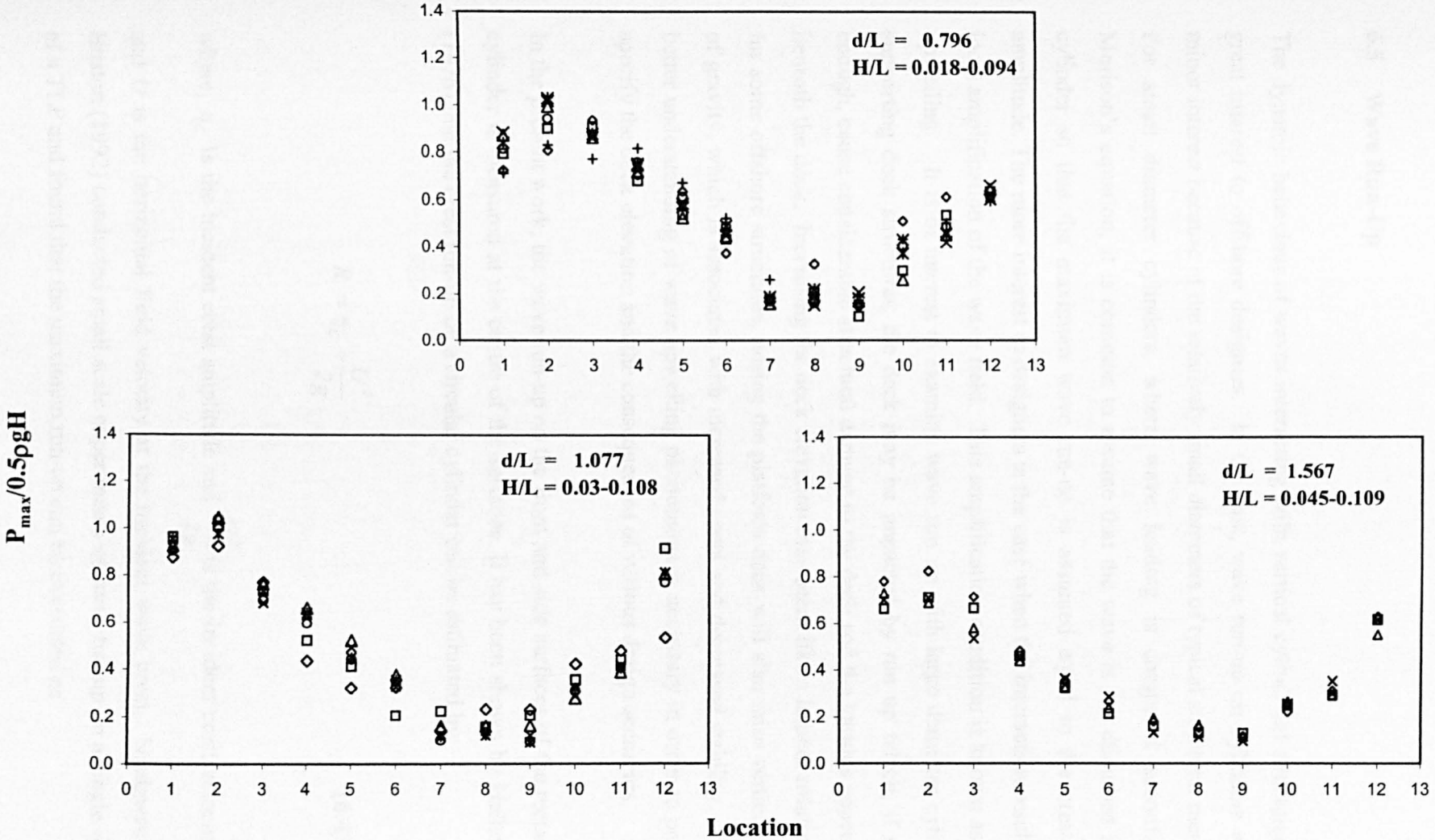

Fig. 6.240b Normalised pressure around horizontal rectangular cylinder with aspect ratio = 3/4

6.5 Wave Run-Up

The dynamic behaviour of waves interacting with vertical cylindrical structures is of great interest to offshore designers. In the past, wave run-up on cylinders was of minor interest because of the relatively small diameters of typical structural members. For small diameter cylinders, where wave loading is computed according to Morison's equation, it is common to assume that the wave is not disturbed by the cylinder so that the maximum wave run-up is assumed equal to the crest-wave amplitude. The more interest to designers is the case when the interaction results in a local amplification of the wave field. This amplification condition is known as wave upwelling. It is of interest to examine wave run up with large diameter cylinders, supporting deck structures, the deck may be impacted by run up which, if severe enough, cause considerable structural damage to the deck and the various appendages beneath the deck. Increasing the deck elevation may seem like a logical solution but, for some offshore structures, raising the platform deck will also raise vertical centre of gravity, which is associated with increased costs and decreased stability. Thus, a better understanding of wave upwelling phenomena is necessary in order to properly specify the deck elevation and the consequences of various design scenarios.

In the present work, the wave run-up on the front and side surfaces of the rectangular cylinder is measured at the centre of the surfaces. It has been shown by Hallermeier (1976) that the crest run-up on a circular cylinder can be estimated by

$$R = \eta_C + \frac{U^2}{2g} \tag{6.4}$$

where, η_C is the incident crest amplitude and $\frac{U^2}{2g}$ is the incident crest velocity head and U is the horizontal fluid velocity at the incident wave crest. Niedzwecki and Huston (1992) conducted small scale experiments of wave run-up on a single column of a TLP and found that the maximum run-up can be expressed as

$$R = 0.56H + 6.52\frac{U^2}{2g} \tag{6.5}$$

where H is the incident wave height and U is the maximum horizontal fluid velocity at the still water surface, calculated by linear wave theory. In the present study, a simple formula of the form equation (6.5) has been developed for all the cylinders. Linear wave theory has been used to calculate the maximum horizontal water velocity of the incident wave.

The variation of wave crest, measured run-up at the front and side surfaces of a square cylinder with wave steepness (H/L) for different relative water depths (d/L) is shown in Figs. 6.241 to 6.242. These results indicate that the wave crest and wave run up increase with increase in wave steepness. A critical examination of the results suggests that, given a particular value of H/L, the wave run-up at the front surface increases with increase in d/L. The rate of increase is found to be higher for higher d/L. The measured run-up at the front face is found to be more than the wave crest for all d/L and the run-up at the side face is observed to be lower than the wave crest for all d/L. The same trend is found with all other cylinders and hence they are not shown. Niedzwecki and Huston (1992) proposed that for large diameter cylinder the maximum run-up might be correlated directly to the velocity head in the form

$$R = C_1 H + C_2\left(U^2/2g\right) \tag{6.6}$$

The coefficient C_1 may generally to be assumed equal to 0.5 and the coefficient C_2 is the slope of the straight line through the data when R/H is plotted as a function of $U^2/2gH$. Fig. 6.243 shows the measured run-up in the form R_f/H plotted as a function of incident crest velocity head, $U^2/2gH$, where R_f is the measured run-up at the front face. The best fit straight line is plotted over the data points in the equation of the line is given by

$$\frac{R_f}{H} = 2.834\frac{U^2}{2gH} + 0.5088 \qquad (6.7)$$

Note that equation (6.3) is a similar form of equation (6.4) and the equation (6.4) is the linear regression formula (LRF) for the run-up on the front face. Now Fig. 6.244 is plotted with measured run-up versus the run-up (R_{LRF}) calculated by linear regression formula obtained from equation (6.4). It is evident from this plot that a good correlation is found between the measured and LRF run-up. A similar procedure is followed for all other cylinders and the results are depicted in Figs. 6.245 to 6.252. The LRF for different cylinders are given below:

$$\frac{R_f}{H} = 1.8859\frac{U^2}{2gH} + 0.5264 \qquad \text{for aspect ratio ½} \qquad (6.8)$$

$$\frac{R_f}{H} = 4.7882\frac{U^2}{2gH} + 0.4494 \qquad \text{for aspect ratio 2/1} \qquad (6.9)$$

$$\frac{R_f}{H} = 3.1659\frac{U^2}{2gH} + 0.5972 \qquad \text{for aspect ratio ¾} \qquad (6.10)$$

$$\frac{R_f}{H} = 2.0399\frac{U^2}{2gH} + 0.4401 \qquad \text{for aspect ratio 4/3} \qquad (6.11)$$

The measured run-up at the front and side surfaces is normalized with the dimension of the cylinder facing the wave (D) and is plotted as shown in Figs. 6.253 to 6.257. The data are correlated with a straight line fit and the equation of the straight line is given as

$$\frac{R_S}{D} = 0.5277\frac{R_f}{D} + 0.009 \qquad \text{for square cylinder} \qquad (6.12)$$

$$\frac{R_S}{D} = 0.7651\frac{R_f}{D} - 0.0021 \qquad \text{for aspect ratio 1/2} \qquad (6.13)$$

$$\frac{R_S}{D} = 0.2732\frac{R_f}{D} + 0.0169 \qquad \text{for aspect ratio 2/1} \qquad (6.14)$$

$$\frac{R_S}{D} = 0.5829\frac{R_f}{D} + 0.0148 \qquad \text{for aspect ratio 3/4} \qquad (6.15)$$

$$\frac{R_S}{D} = 0.453\frac{R_f}{D} + 0.0113 \qquad \text{for aspect ratio 4/3} \qquad (6.16)$$

where, R_S is the measured run up at the side. The above expressions can be used to calculate the run up on the front and sides of the rectangular cylinders.

For co-existing waves and currents, conclusive results could not be obtained as the run-up data showed large scatter with irregularity and hence the results are not presented.

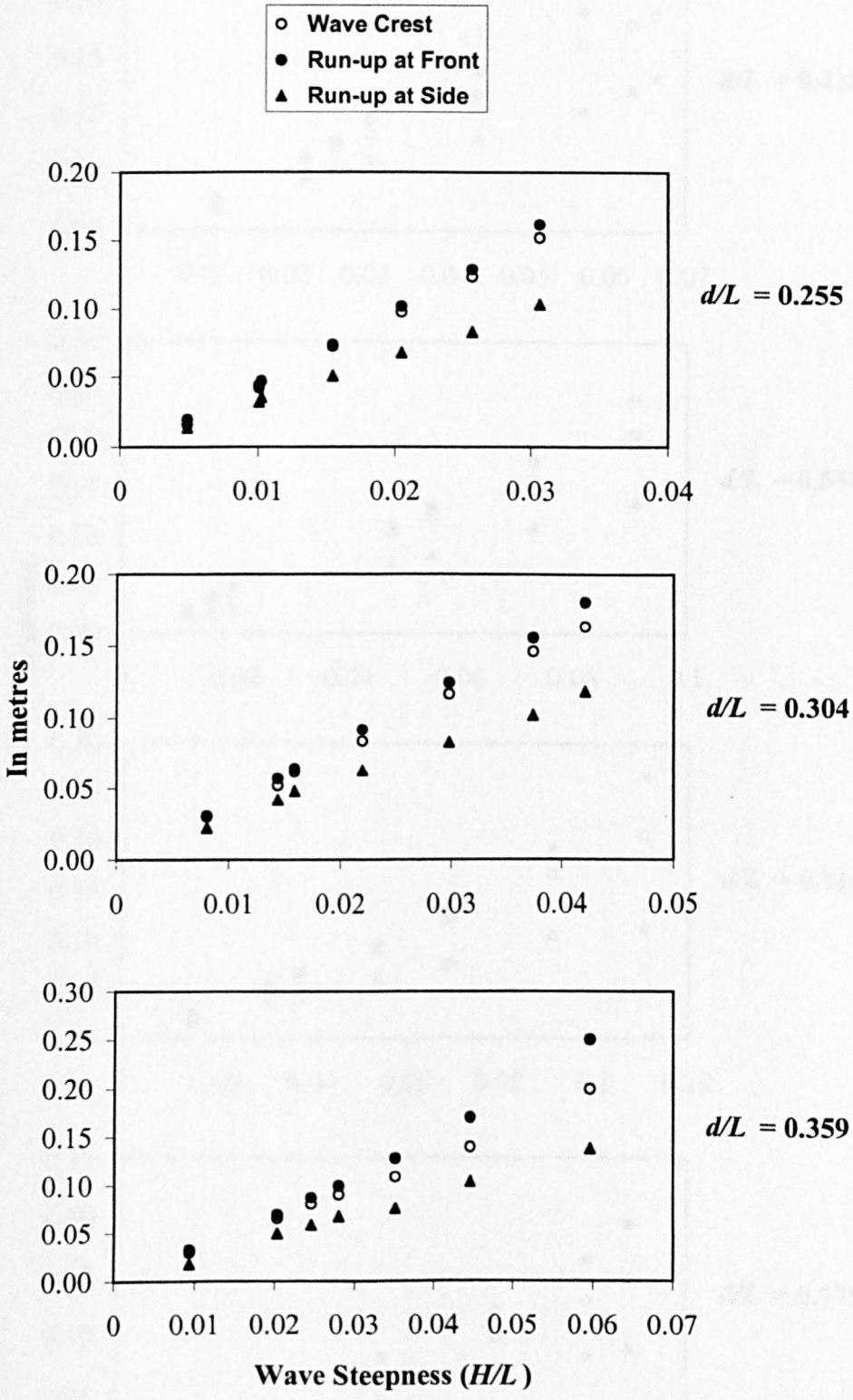

Fig. 6.241 Wave and run-up for vertical square cylinder

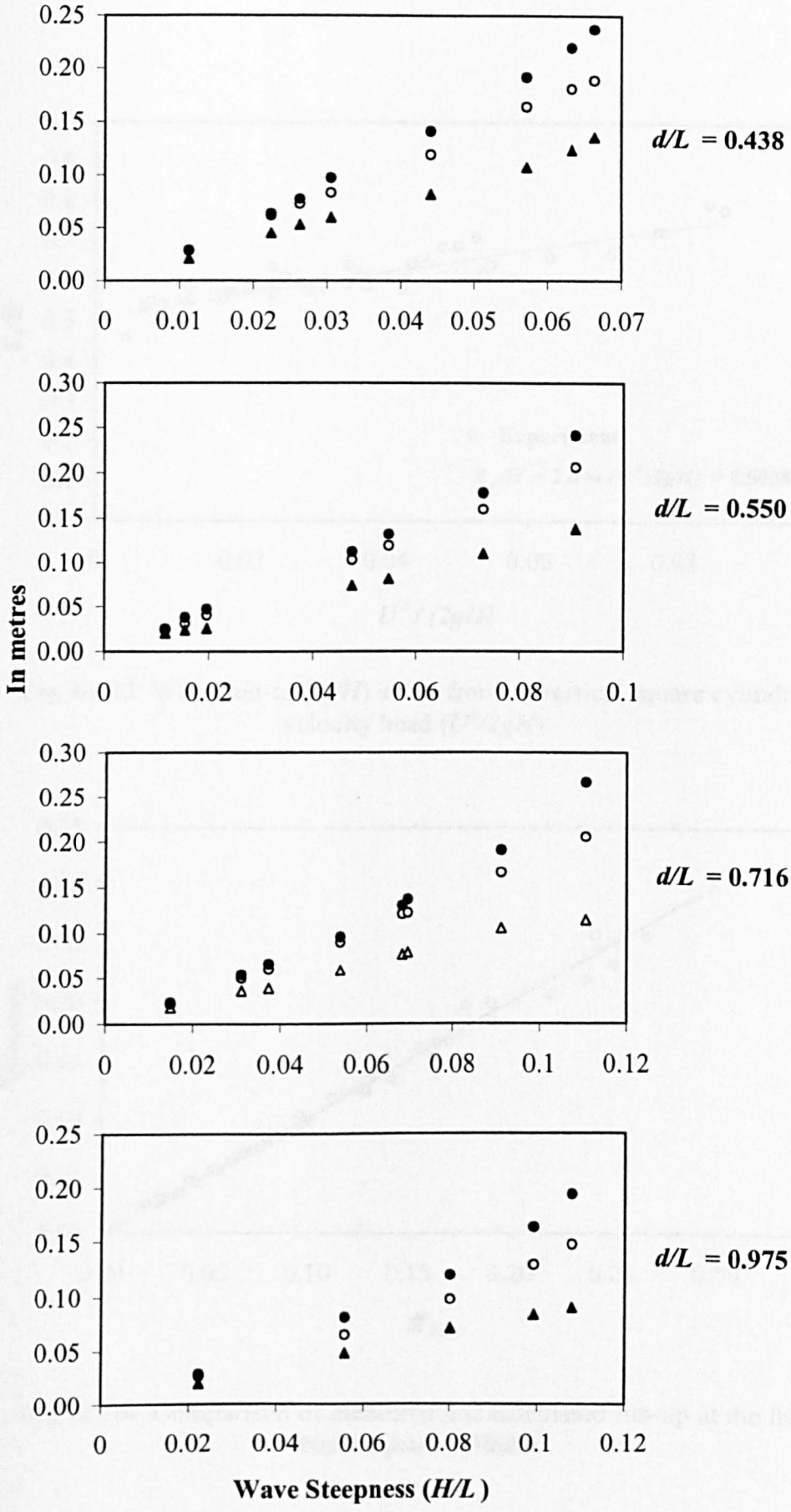

Fig. 6.242 Wave and run-up for vertical square cylinder

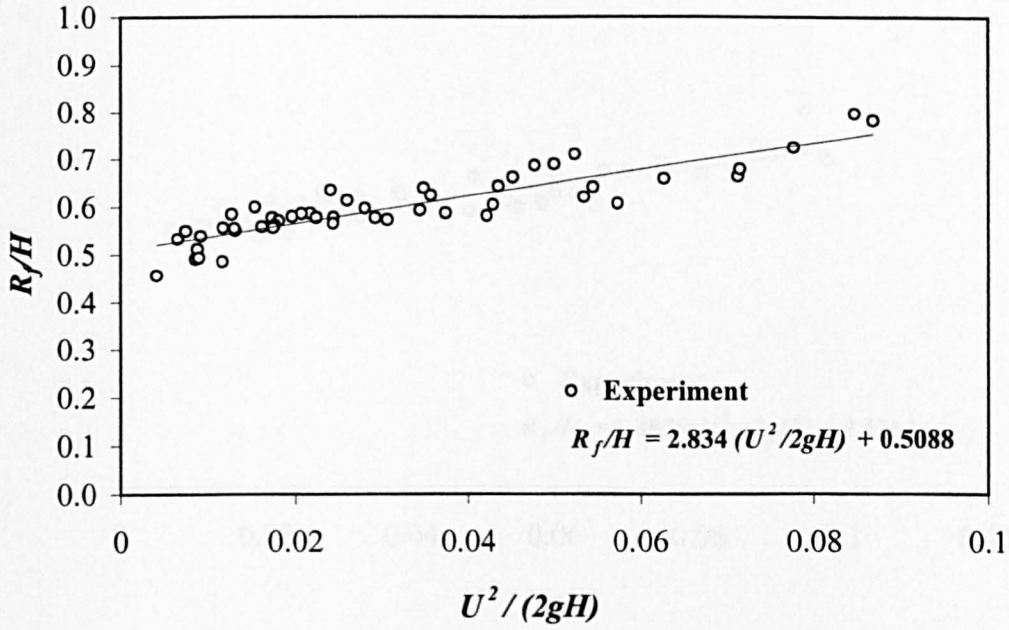

Fig. 6.243 Wave run-up(R_f/H) at the front of vertical square cylinder with velocity head ($U^2/2gH$)

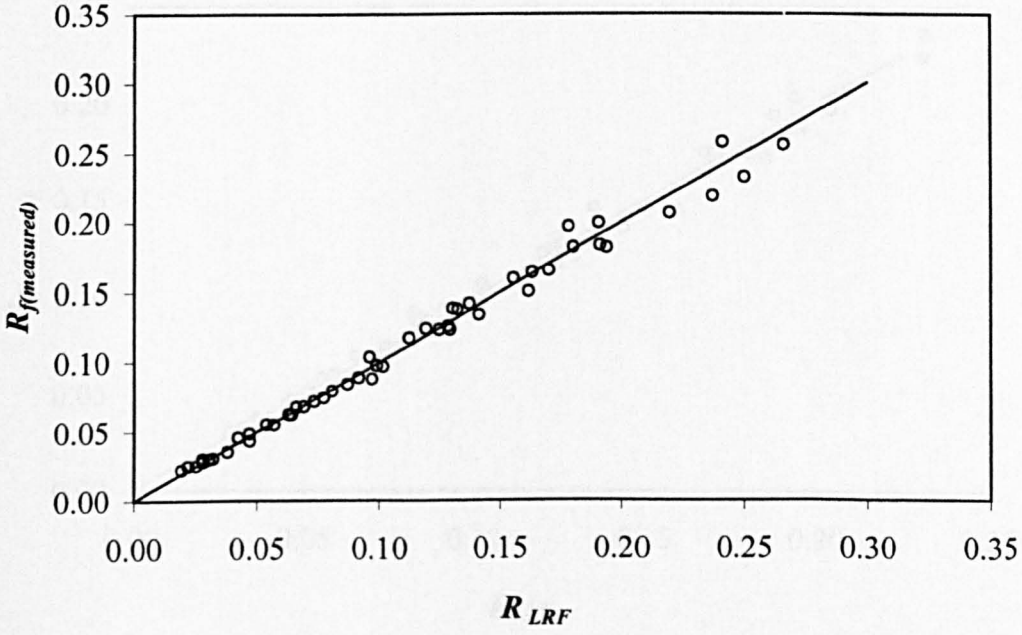

Fig. 6.244 Comparison of measured and calculated run-up at the front of vertical square cylinder

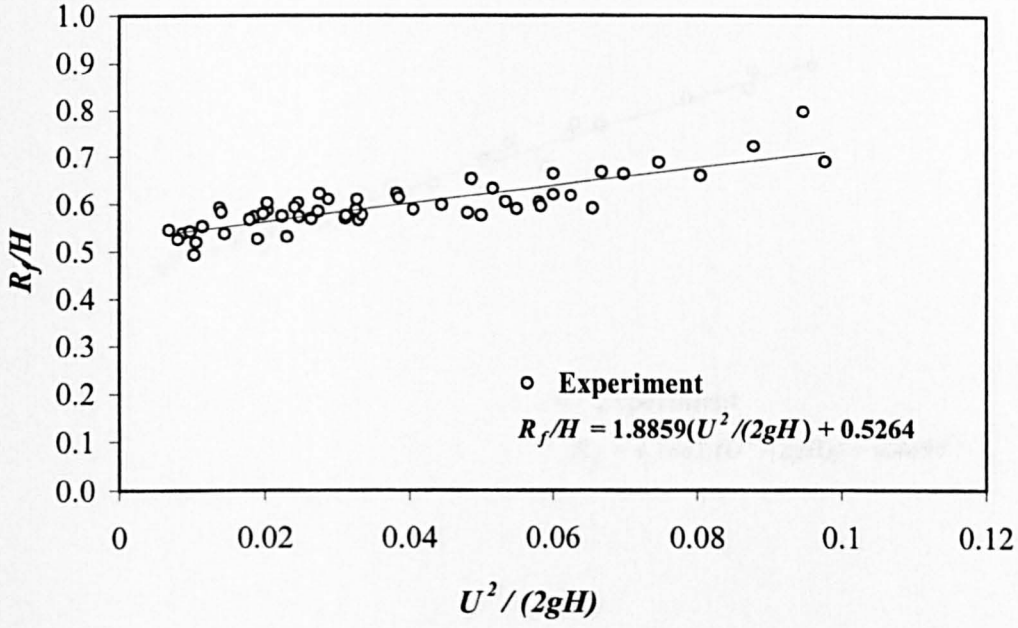

Fig. 6.245 Wave run-up(R_f/H) at the front of vertical rectangular cylinder with aspect ratio = 1/ 2 with velocity head ($U^2/2gH$)

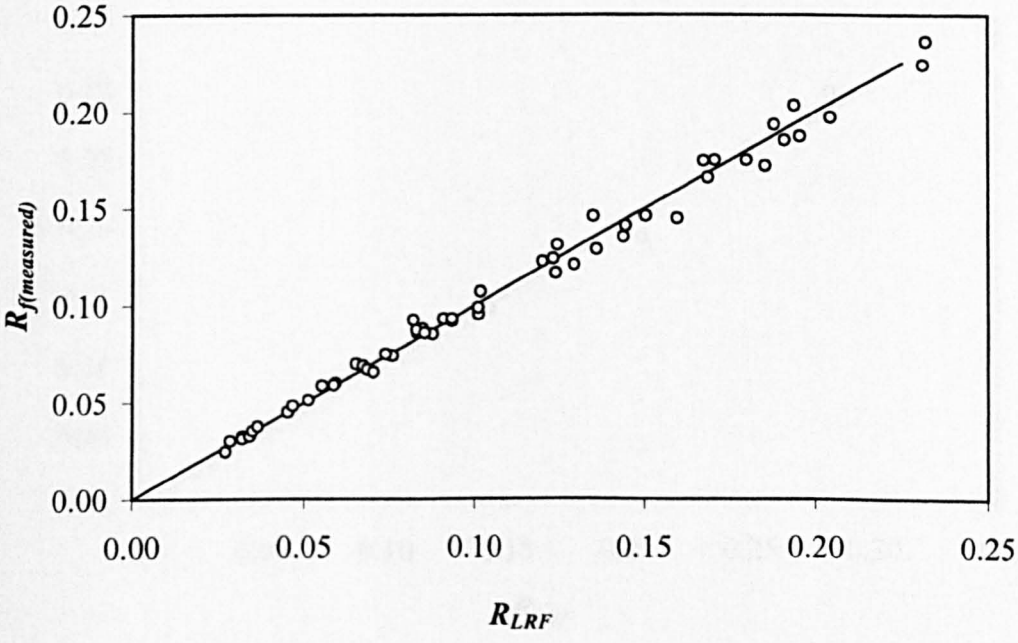

Fig. 6.246 Comparison of measured and theoretical run-up at the front of rectangular cylinder with aspect ratio = 1/2

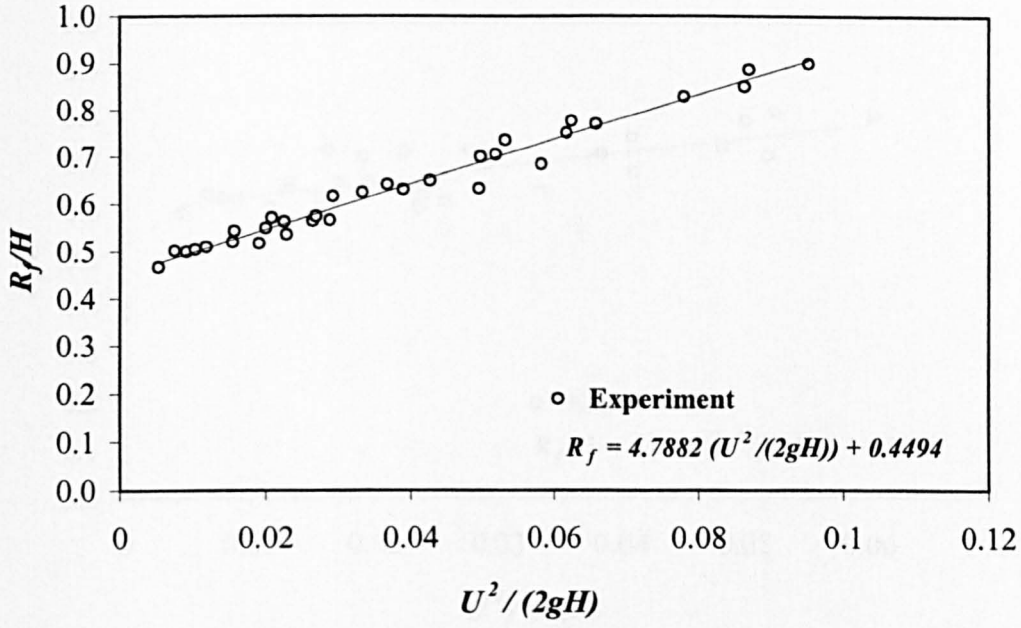

Fig. 6.247 Wave run-up(R_f/H) at the front of vertical rectangular cylinder with aspect ratio = 2/1 with velocity head ($U^2/2gH$)

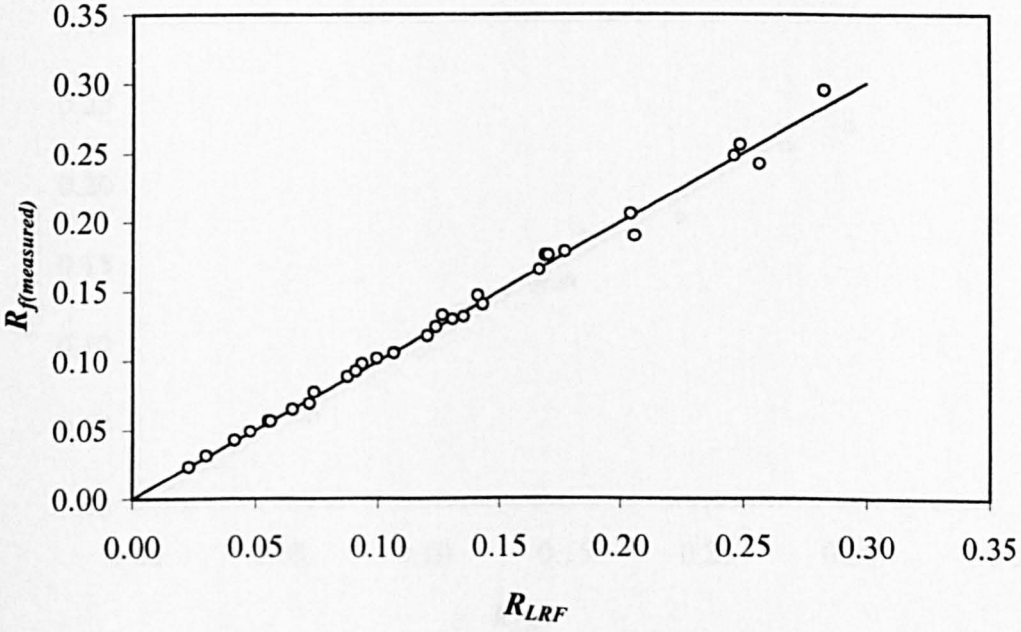

Fig. 6.248 Comparison of measured and theoretical run-up at the front of rectangular cylinder with aspect ratio = 2/1

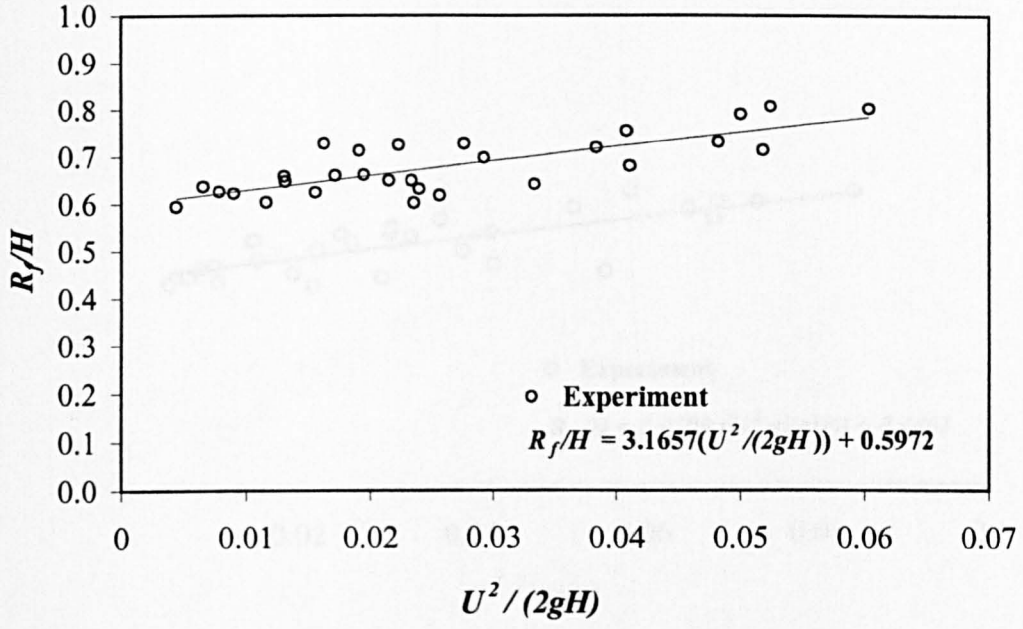

Fig. 6.249 Wave run-up(R_f/H) at the front of vertical rectangular cylinder with aspect ratio = 3/4 with velocity head ($U^2/2gH$)

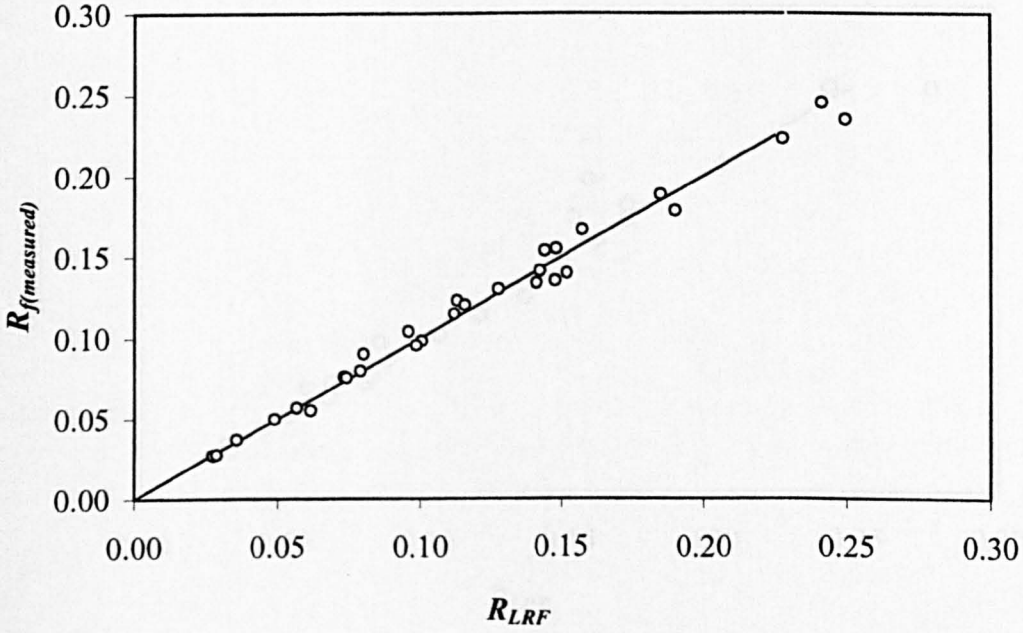

Fig. 6.250 Comparison of measured and theoretical run-up at the front of rectangular cylinder with aspect ratio = 3/4

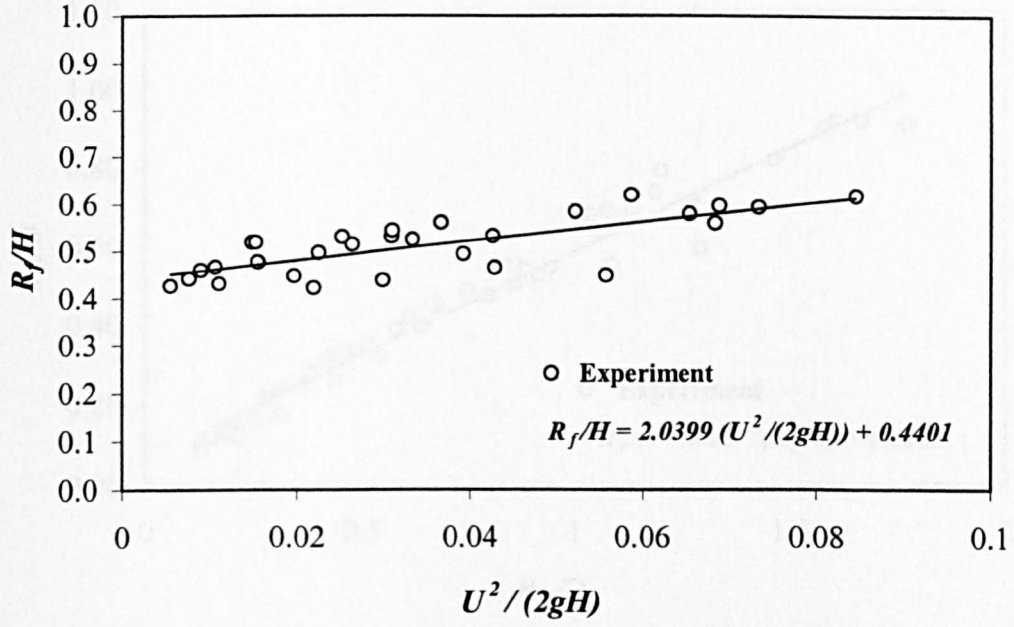

Fig. 6.251 Wave run-up(R_f/H) at the front of vertical rectangular cylinder with aspect ratio = 4/3 with velocity head ($U^2/2gH$)

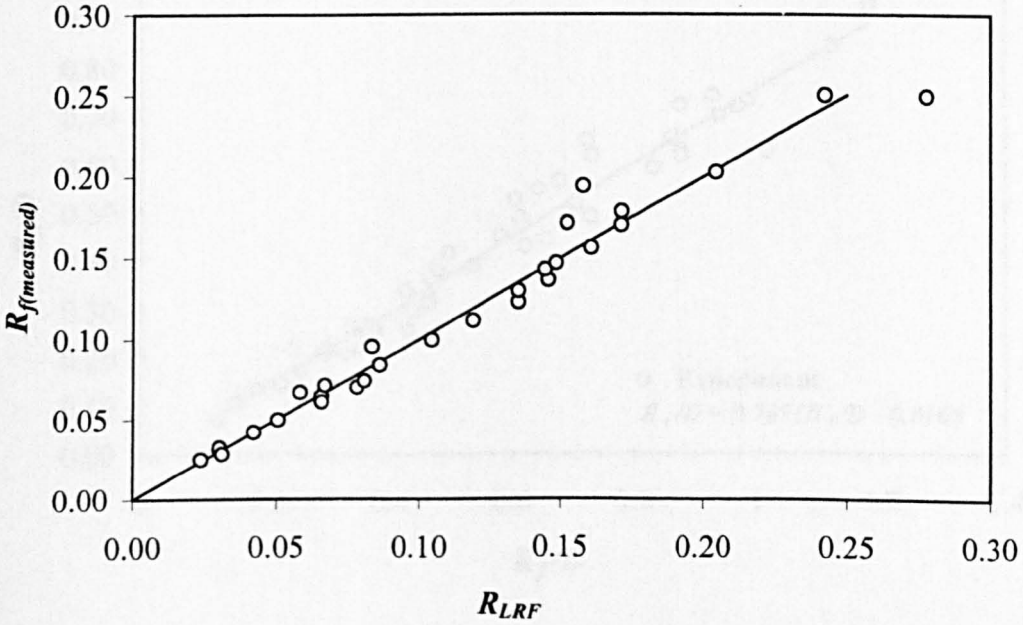

Fig. 6.252 Comparison of measured and theoretical run-up at the front of rectangular cylinder with aspect ratio = 4/3

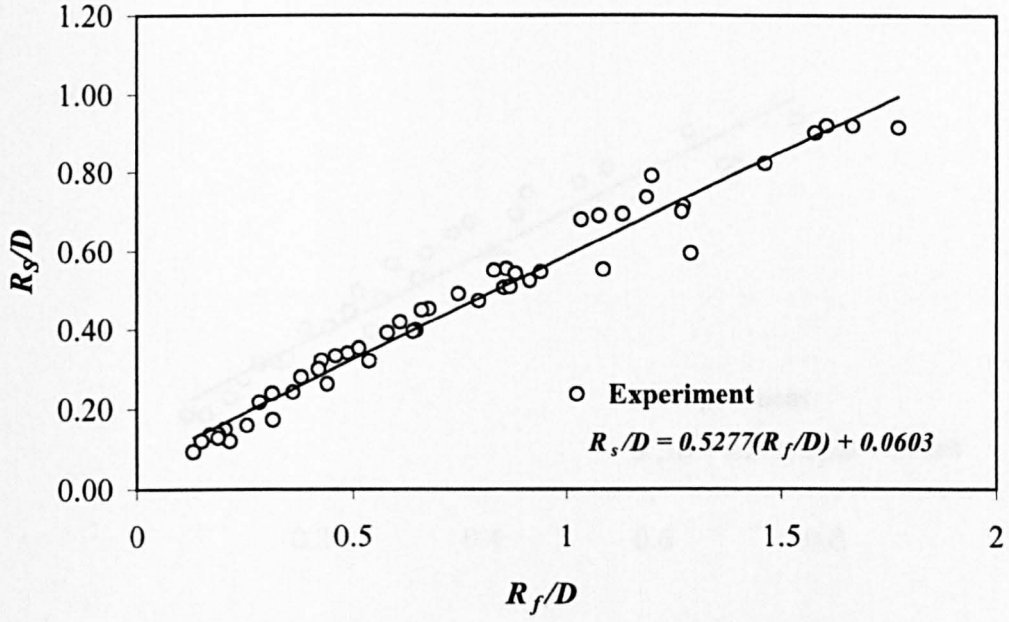

Fig. 6.253 Wave run-up at front and side surfaces of square cylinder

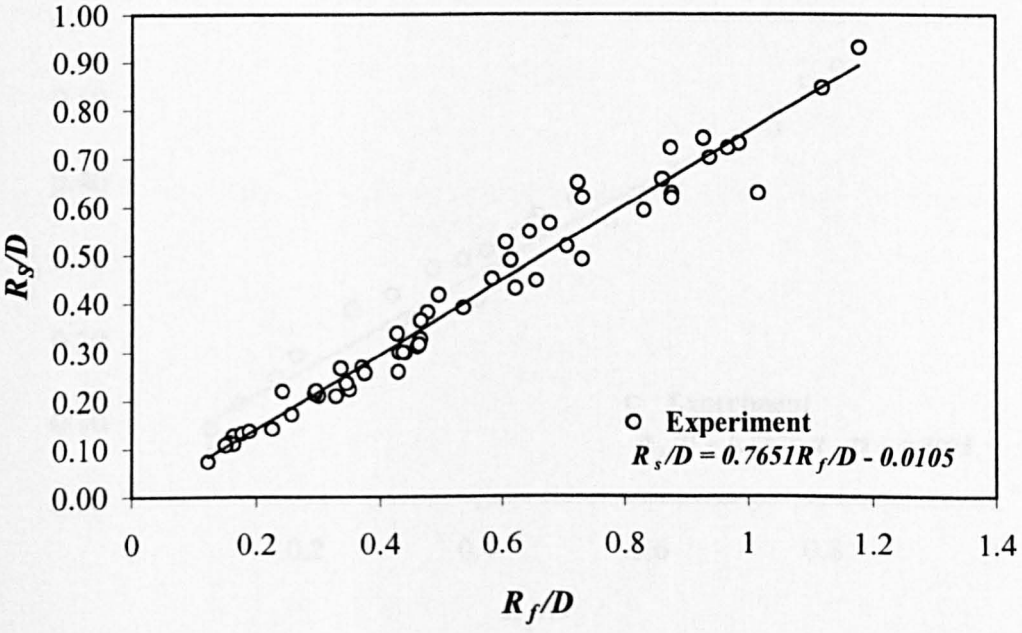

Fig. 6.254 Wave run-up at front and side surfaces of rectangular cylinder with aspect ratio = 1/2

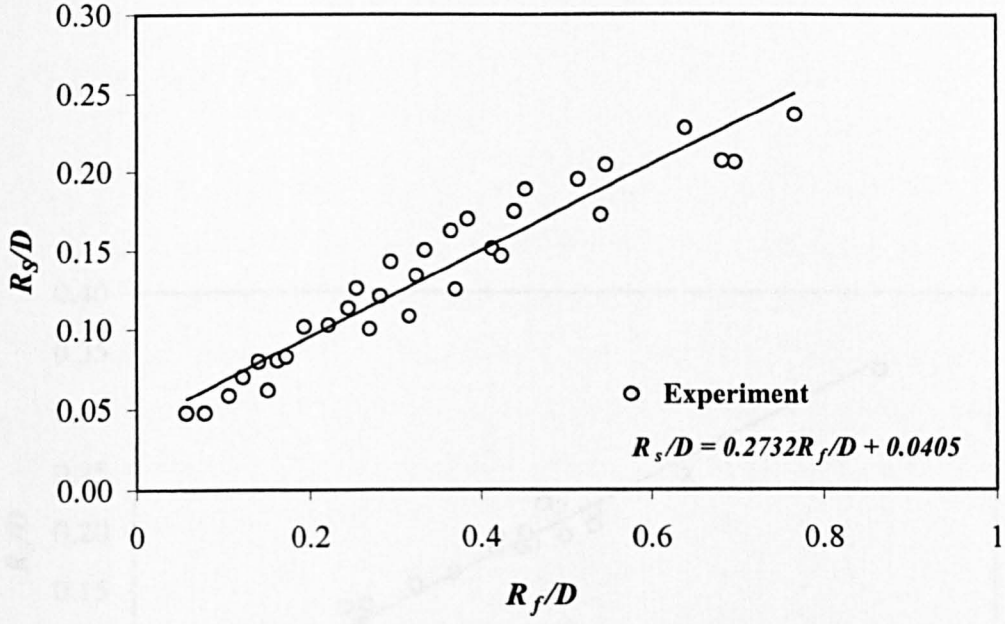

Fig. 6.255 Wave run-up at front and side surfaces of rectangular cylinder with aspect ratio = 2/1

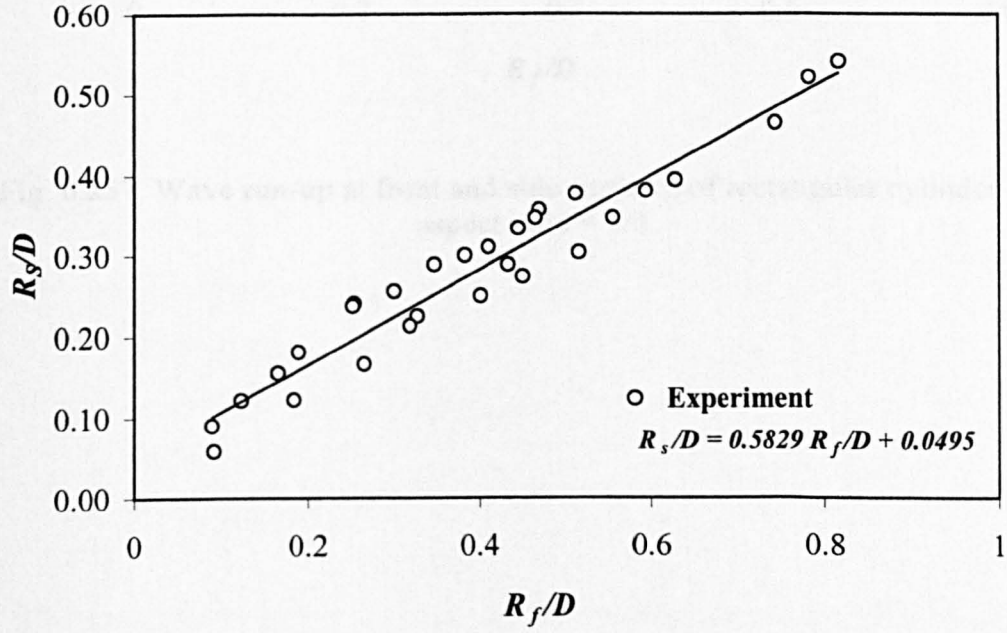

Fig. 6.256 Wave run-up at front and side surfaces of rectangular cylinder with aspect ratio = 3/4

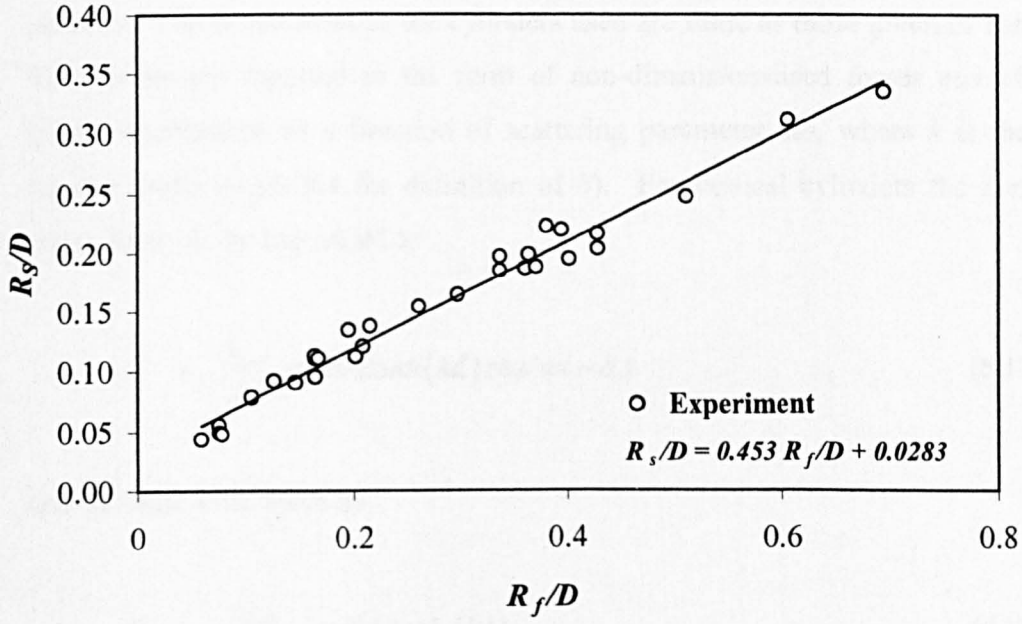

Fig. 6.257 Wave run-up at front and side surfaces of rectangular cylinder with aspect ratio = 4/3

6.6 Diffraction Force Results

6.6.1 Vertical Cylinder

The wave loading for a surface piercing vertical cylinder and for horizontally submerged cylinders are computed and the results are discussed in the following sections. The dimensions of the cylinders used are same as those given in Table 4.1. The results are reported in the form of non-dimensionalised forces and effective inertia coefficients as a function of scattering parameter, kb, where k is the wave number (refer Fig.6.264 for definition of b). For vertical cylinders the horizontal wave force can be expressed as

$$F = \frac{1}{2} C_m \rho g H A \tanh(kd) \cos(\omega t - \delta) \tag{6.17}$$

and the maximum force by,

$$F_{max} = \frac{1}{2} C_m \rho g H A \tanh(kd) \tag{6.18}$$

where,

C_m is the effective inertia coefficient
H is the wave height
A is the cross-sectional area of the cylinder
d is the water depth
δ is the phase angle

The maximum normalised force for the vertical square cylinder is shown in Fig.6.258 along with the results of Isaacson (1978). Isaacson (1978) presented another form of the normalised force on a square caisson as

$$\frac{F_{max}}{\rho g H b d (tanh(kd)/(kd))} \tag{6.19}$$

It is evident from this figure that a good comparison is found between the two curves up to kb = 2.25. However, for kb>2.25, Issacson results are found to be higher. Isaacson while comparing his results with Hogben and Standing (1975) found this divergence at larger values of kb and pointed out that this was due to the relatively large facet size to the wave length ratios used by Hogben and Standing in this range. Note that Hogben and Standing's results were based on computations involving 96 facets or area elements distributed over the immersed column surface and Isaacson used 48 segments to describe the square section and in the present study the whole cylinder surface is divided in to 226 number of panels.

The effective inertia coefficient, C_m is calculated using equation (6.18) and is compared with Isaacson results in Fig. 6.259. In the present results at $kb \approx 0$, C_m takes a value of 2.182 which is the same as the theoretical value of 2.19 for a square cylinder, whereas, Isaacson reported a value of C_m = 2.14 at $kb \rightarrow 0$ and this difference in inertia coefficient value was explained as due to the reduction in the effective sectional area associated with rounding off corners. Similar to the forces for kb > 1.43, the present results for C_m are also observed to be lower than those reported by Isaacson.

The normalised maximum resultant horizontal force can also be expressed in the form [Shankar et al. (1983)],

$$\frac{F_{max}}{\frac{1}{2}\rho g H b^2} \tag{6.20}$$

The computed force for a square cylinder is expressed in the form of equation (6.20) and is compared with results by Shankar et al. (1983) in Fig. 6.260 for two relative depth (d/b, where d is the water depth and b is same as defined above) equals to 1.0

and 2.5. The results by Shankar et al. are based on the finite element formulation of the linear diffraction problem. It is observed from Fig. 6.260, that for d/b = 1.0 and for kb < 1.92, the normalised forces reported by Shankar et al. are smaller than the present results and for 1.92 > kb < 3.67, present results are found to be lower than Shankar et al results. A similar trend is observed for d/b = 2.5, but the difference is not as significant as for d/b = 1.0.

The effect of relative depth, d/b for the square cylinder is illustrated in Fig. 6.261 for three values of d/b, 1.0, 2.5 and 5.0. In general, the normalised maximum force for a particular d/b increases as kb increase up to a certain value and then it decreases with further increase in kb. The value of scattering parameter at which the normalised force reaches its highest value is dependent on relative depth. Keeping all other parameters constant, as the value of kb is increased, a higher force results until a peak value is reached. Then, further increase in kb reduces the force.

As can be seen from the Fig. 6.261, forces on the cylinder increase with increase in relative depth d/b. For higher d/b or for deeper water conditions, any further increase in d/b is found to have less effect on the force. For kb > 1.9, the normalised force slightly decreases with increase in d/b. The corresponding inertia coefficients for three relative depths are plotted in Fig. 6.262. At lower values of kb, inertia coefficients for all d/b are found to merge together, however, for larger kb, C_m decreases with increase in d/b. The variation of phase angle for the horizontal force with kb is shown in Fig. 6.263.

The maximum normalised horizontal force and effective inertia coefficients for rectangular cylinder with aspect ratio (D/b) equal to 1/2 is shown in Figs. 6.264 and 6.265 respectively, for an angle of incidence $\alpha = 0°$. For kb< 0.82, the force on the cylinder increases with increase in the relative depth d/b and for kb > 0.82, the force coefficients corresponding to d/b = 5.0 is comparatively lower than d/b = 1.0 and 2.5 and this trend is also observed in the inertia coefficients. The inertia coefficients show a value of 1.68 at lowest kb and decrease gradually as kb increases. In Figs.6.266 and

6.267, the maximum force coefficients and respective inertia coefficients for angle of incidence $\alpha = 90^{\circ}$ is shown. This plot indicate that the force coefficients reach a maximum around kb = 0.5 to 1.5. The inertia coefficients show a value of 3.16 at lowest kb. The variation of phase angle for the horizontal force with kb is shown in Figs. 6.268 and 6.269 for both angles of incidences.

A similar trend of results is observed for another rectangular cylinder with aspect ratio = 3/4 as seen in Figs. 6.270 to 6.273 for $\alpha = 0^{\circ}$ and $\alpha = 90^{\circ}$. The inertia coefficients show a value of 1.97 and 2.53 for $\alpha = 0^{\circ}$ and $\alpha = 90^{\circ}$ respectively at lowest kb, which are nearly the same as the potential flow values. The variation of phase angle for the horizontal force with kb is shown in Figs. 6.274 and 6.275 for both angles of incidences.

6.6.2 Horizontal Cylinder

The numerical results obtained for horizontally submerged cylinders are discussed here. The aspect ratios of the cylinder chosen are 1.0, 1/2, and 3/4. Numerical results are obtained to study the effect of depth of submergence on the maximum horizontal and vertical force coefficients. The forces are computed for only two relative depths of submergence, d/h, where d is the water depth and h is the depth of cylinder axis from the still water level. These are chosen in order to compare with the experimental results for the same depth of submergence. Note that the experimental results used here for comparison include most of the tests conducted in the Morison regime. Since, the tests were conducted at low KC numbers, the contribution from drag is small so the total force can be expressed by the inertia component. Also the experimental results can be usefully compared with the numerical results.

The results for a square cylinder with aspect ratio 1.0, are shown in Figs. 6.276 and 6.277 for horizontal and vertical forces respectively for two relative depths of submergence. The forces are reported in a non-dimensional form, $F_{max}/0.5\rho gHb$.

These figures indicate that when $kb \rightarrow 0$, the normalised forces approach zero. With increase in *kb* the force coefficients in both directions increase, as the case of vertical cylinder, up to a certain value of *kb* and further increase in *kb* results in gradual decrease in force coefficients. This trend is observed for both *d/h* values. Further, the maximum force coefficients decreases with decrease in *d/h* for any given values of scattering parameter, *kb*. This result is as expected since for the given wave or wave number, *k*, the particle velocity at any fixed point in the flow field decreases with increase in water depth, and this results in smaller forces for larger depth of submergence.

Figs. 6.278 to 6.281 respectively provides a comparison of the present numerical results for the maximum horizontal and vertical force coefficients with corresponding experimental results for two values of *d/h*. The present experimental results are in reasonable agreement with numerical results. These figures indicate that the experimental results for the maximum horizontal and vertical force coefficients show similar variation with scattering parameter and relative depths of submergence as the numerical results are within the range of this parameters investigated.

The inertia coefficient in the horizontal direction, C_{mx}, and in vertical direction C_{my} are evaluated from the following equations,

$$C_{mx} = \frac{F_{X\,max}}{\rho A \dot{u}_{max}} \tag{6.21}$$

$$C_{my} = \frac{F_{Y\,max}}{\rho A \dot{w}_{max}} \tag{6.22}$$

where, A is the cross-sectional area of the cylinder, $\dot{u}$ and $\dot{w}$ are horizontal and vertical particle acceleration computed at the level of the axis of the cylinder. The variation of computed inertia coefficients in horizontal and vertical directions with scattering parameter are plotted in Figs. 6.282 and 6.283 respectively. This plot

demonstrates that for $kb \rightarrow 0$, both C_{mx} and C_{my} take identical values equal to 2.2 for both *d/h* values. Computed inertia coefficients, gradually decrease with increase in *kb* for the range of *kb* considered. For *d/h* = 2.68, inertia coefficients in both vertical and horizontal directions are lower than those calculated for *d/h* = 4.68 and for the range of *kb* considered. The phase angles at which the maximum horizontal and vertical forces occur are shown in Figs. 6.284 and 6.285 for two values of *d/h*.

The results for rectangular cylinder with aspect ratio 1/2, is shown in Figs. 6.286 and 6.287. Here again, the maximum horizontal and vertical force coefficients are plotted with *kb* for two depths of submergence. As with square cylinder the force coefficients for this rectangular cylinder show a similar variation with *kb* and *d/h*. With increase in *kb* the force coefficients in both directions increase, and reaches a peak value and further increase in *kb* results in gradual decrease in force coefficients. This trend is observed for both *d/h* values. A comparison of the present numerical results for the maximum horizontal and vertical force coefficients with corresponding experimental results for two values of *d/h* is shown in Figs. 6.288 to 6.291. The present experimental results compare reasonably well with numerically computed horizontal force, for *d/h* = 4.68, however, for vertical force coefficients, the experimental values are found to be lower than the numerical force coefficients especially for $0.5 > kb < 1.0$. For *d/h* = 2.68, the experimental horizontal force coefficients are considerably lower than the numerical values.

The variation of computed inertia coefficients in horizontal and vertical directions with scattering parameter are plotted in Figs. 6.292 and 6.293 for aspect ratio 1/2 and it is evident from this figure that for $kb \rightarrow 0$, C_{mx} = 1.68 and C_{my} = 3.1 for *d/h* = 4.68 and C_{mx} = 1.66 and C_{my} = 3.02 for *d/h* = 2.6 and these values are consistent with the potential flow values. It is further observed from this plot that C_{mx} for *d/h* = 4.68, gradually decreases with increase in *kb* for the range of *kb* considered whereas, C_{my} increases with increase in *kb* and reaches a maximum value of 3.26 at *kb* = 0.378 and then decreases for increase in *kb*. Similarly, C_{mx} for *d/h* = 2.68, gradually decreases with increase in *kb* and C_{my} increases with increase in *kb* and attains a maximum

value of 3.06 at kb = 0.279 and then decreases for increase in kb. For d/h = 2.68 and for kb < 0.83, inertia coefficients in both vertical and horizontal directions are lower than those calculated for d/h = 4.68 and for kb > 0.83, both C_{mx} and C_{my} are found to be significantly larger than the inertia coefficients obtained for d/h = 4.68 and for all values of kb. At kb = 0.83, C_{mx} takes a value of 1.58 and C_{my} takes a value of 2.84 for both d/h. The phase angles at which the maximum horizontal and vertical forces for aspect ratio = 1/2 are shown in Fig. 6.294 and 6.295 respectively for two values of d/h.

A similar trend in results for rectangular cylinder with aspect ratio 3/4, is observed. The normalised horizontal and vertical forces are presented in Figs. 6.296 and 6.297 for this aspect ratio. A comparison between the numerical and experimental results for the maximum horizontal and vertical force coefficients with kb for two values of d/h is shown in Figs. 6.298 to 6.301. The present experimental results for d/h = 4.68, compare quite well with numerically computed horizontal and vertical force coefficients. For d/h = 2.68, the horizontal force coefficients obtained from experiments are found to be smaller than the theoretical force coefficients as found for aspect ratio = 1/2.

Computed inertia coefficients in horizontal and vertical directions with scattering parameter are plotted in Fig. 6.302 and 6.303 respectively for aspect ratio 3/4 and this plot reveals that for $kb \rightarrow 0$, C_{mx} = 1.93 and C_{my} = 2.52 for d/h = 4.68 and C_{mx} = 1.89 and C_{my} = 2.43 for d/h = 2.6 and these values are again in consistent with the potential flow values. Moreover, it is observed that C_{mx} for d/h = 4.68, gradually decreases with increase in kb, whereas, C_{my} increases with increase in kb and reaches a maximum value of 2.71 at kb = 0.378 and then decreases for further increase in kb. Similarly, C_{mx} for d/h = 2.68, gradually decreases with increase in kb and C_{my} increases with increase in kb and reaches a maximum value of 2.48 at kb = 0.279 and then decreases for increase in kb. For d/h = 2.68 and for kb < 0.83, inertia coefficients in both vertical and horizontal directions are lower than those calculated for d/h = 4.68 and for kb > 0.83, both C_{mx} and C_{my} are found to be significantly larger

than the inertia coefficients obtained for d/h = 4.68 for all values of kb. At kb = 0.83, C_{mx} takes a value of 1.8 and C_{my} takes a value of 2.3 for both d/h. The phase angles at which the maximum horizontal and vertical forces occurs for aspect ratio = 3/4 are shown in Figs. 6.304 and 6.305 for two values of d/h.

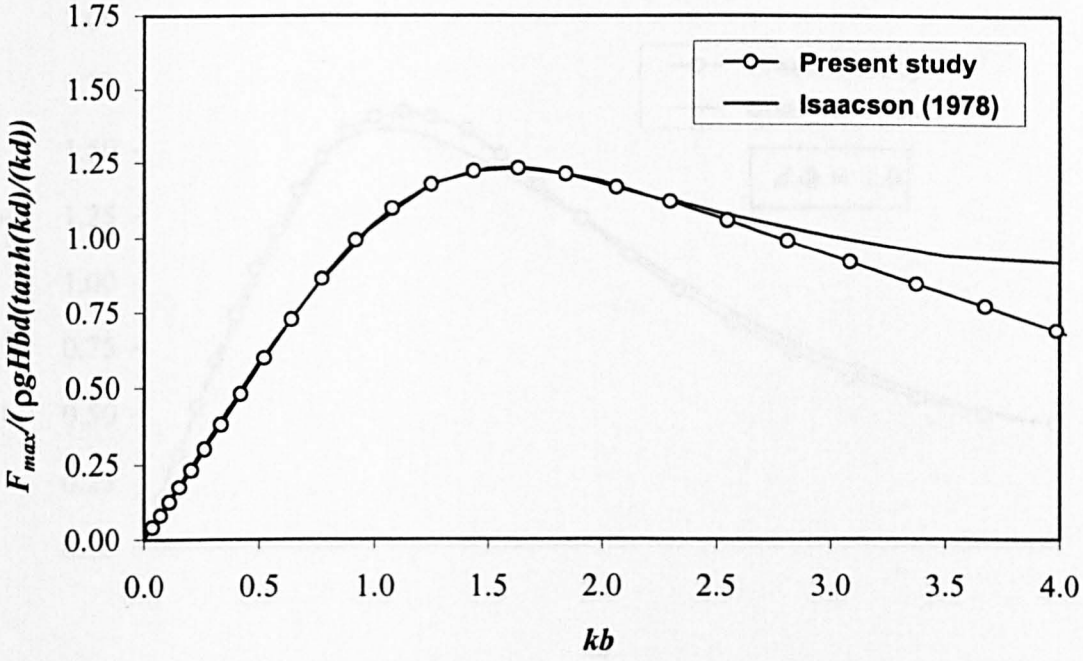

Fig. 6.258 Comparison of normalised horizontal force for vertical square Cylinder

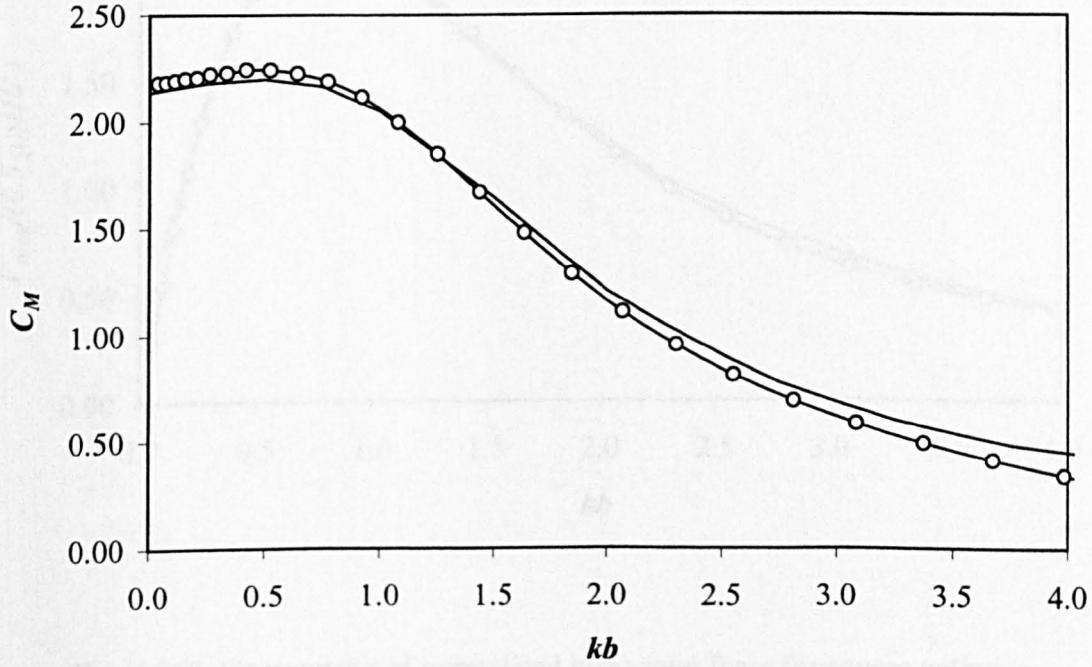

Fig. 6.259 Effective inertia coefficient for vertical square cylinder

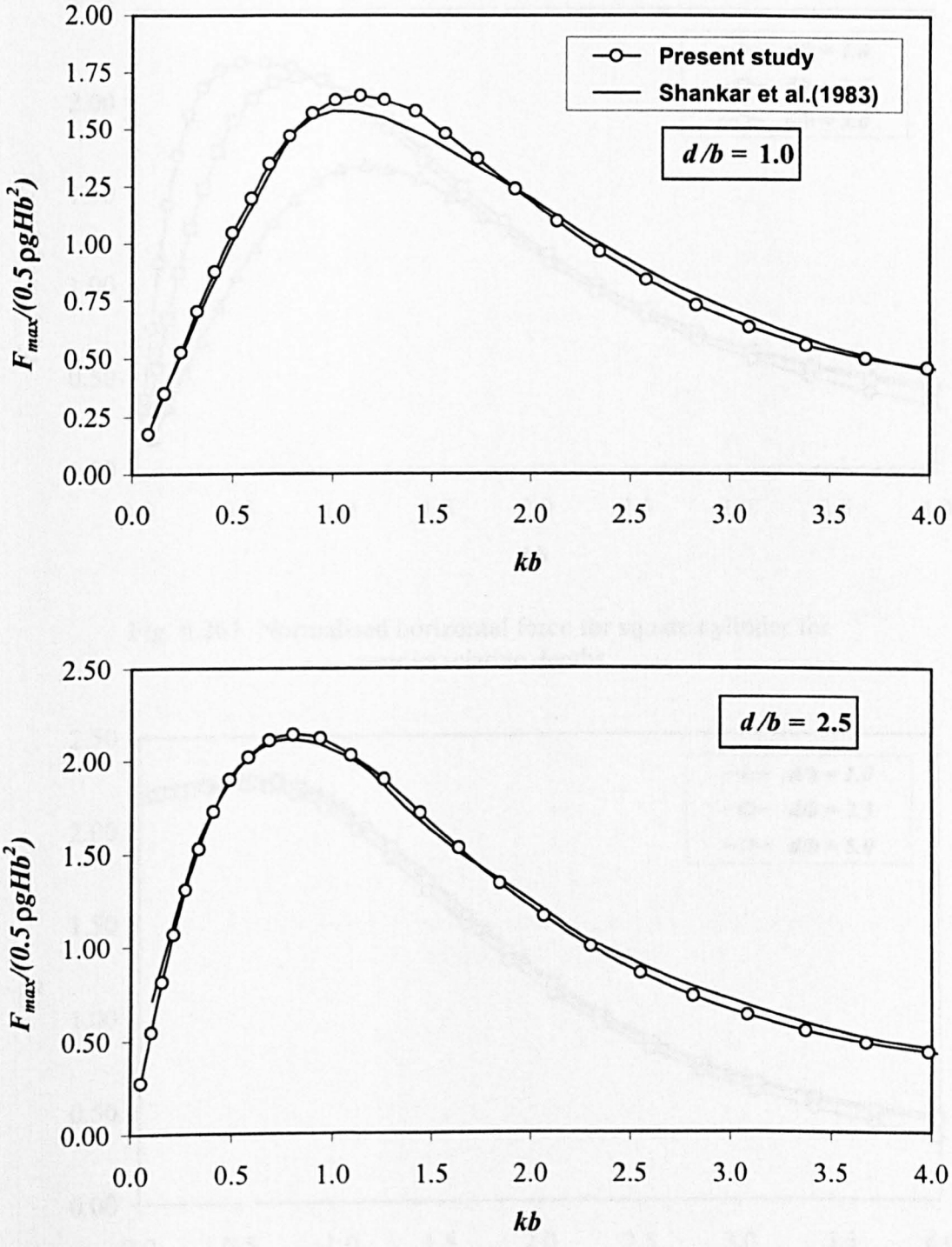

Fig. 6.260 Comparison of normalised horizontal force for square cylinder for $d/b = 1.0$ & 2.5

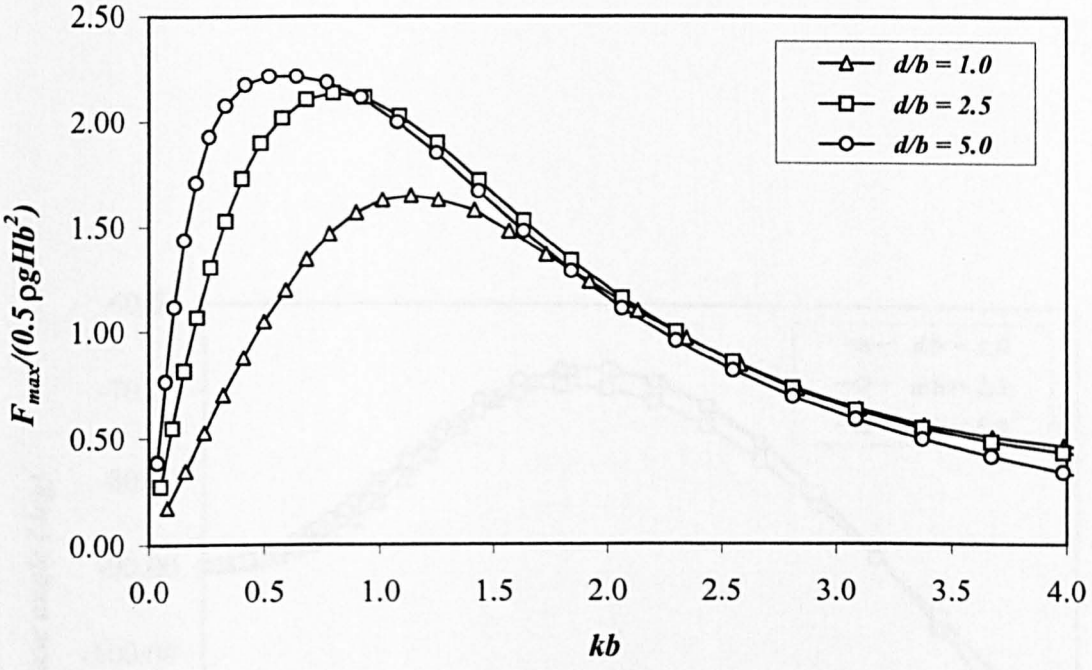

Fig. 6.261 Normalised horizontal force for square cylinder for various relative depths

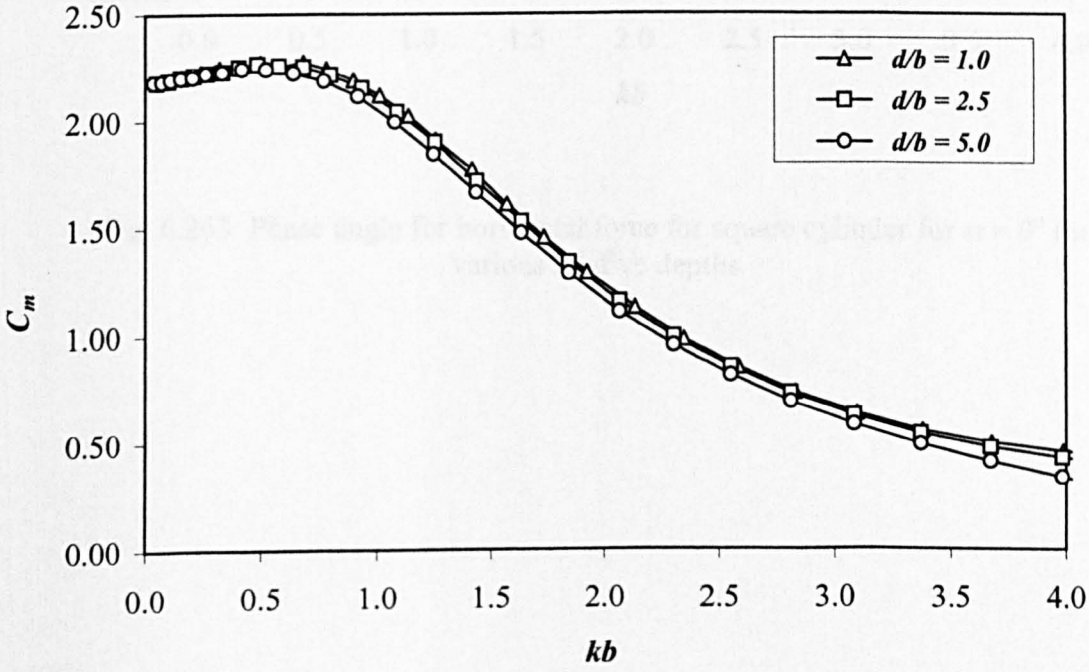

Fig. 6.262 Effective inertia coefficient for square cylinder for various relative depths

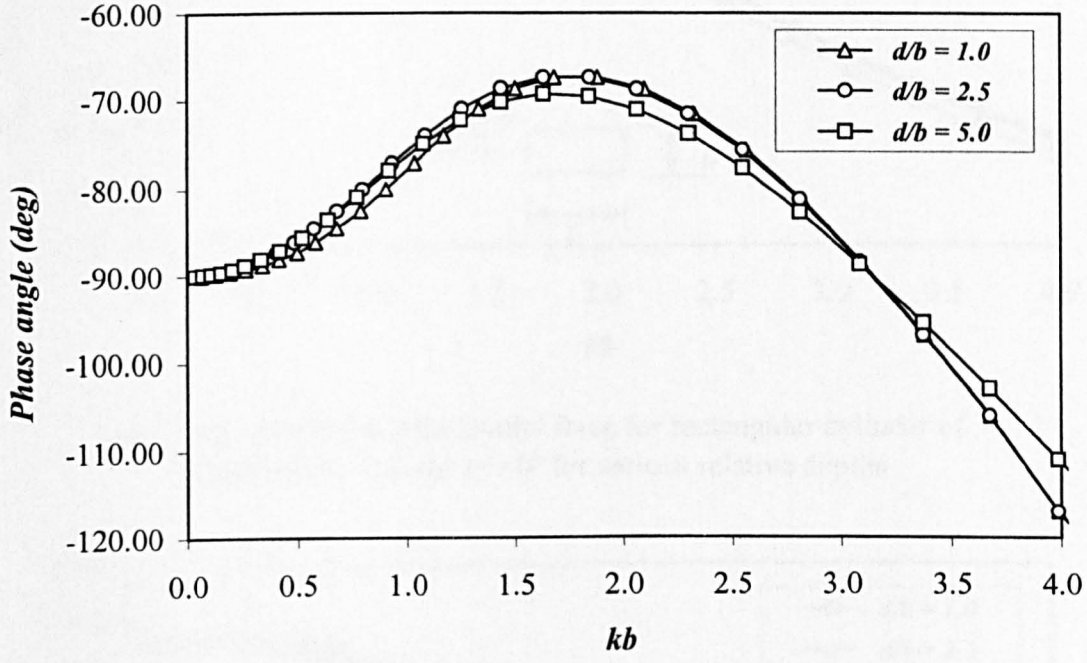

Fig. 6.263 Phase angle for horizontal force for square cylinder for $\alpha = 0^{o}$ for various relative depths

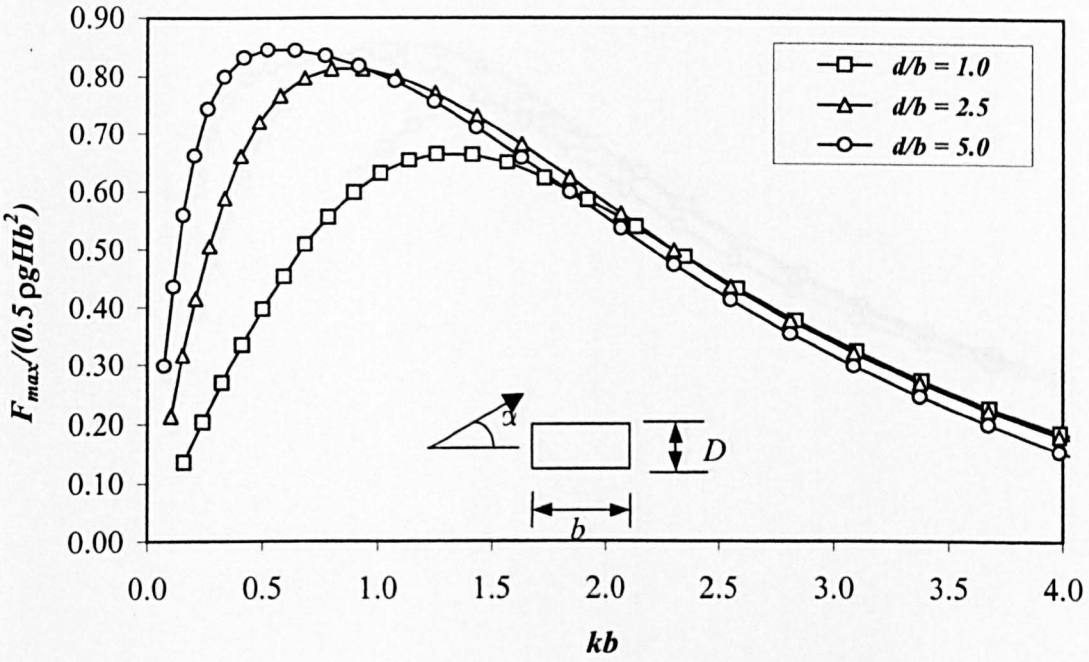

Fig. 6.264 Normalised horizontal force for rectangular cylinder of aspect ratio = 1/2 for $\alpha = 0^{\circ}$ for various relative depths

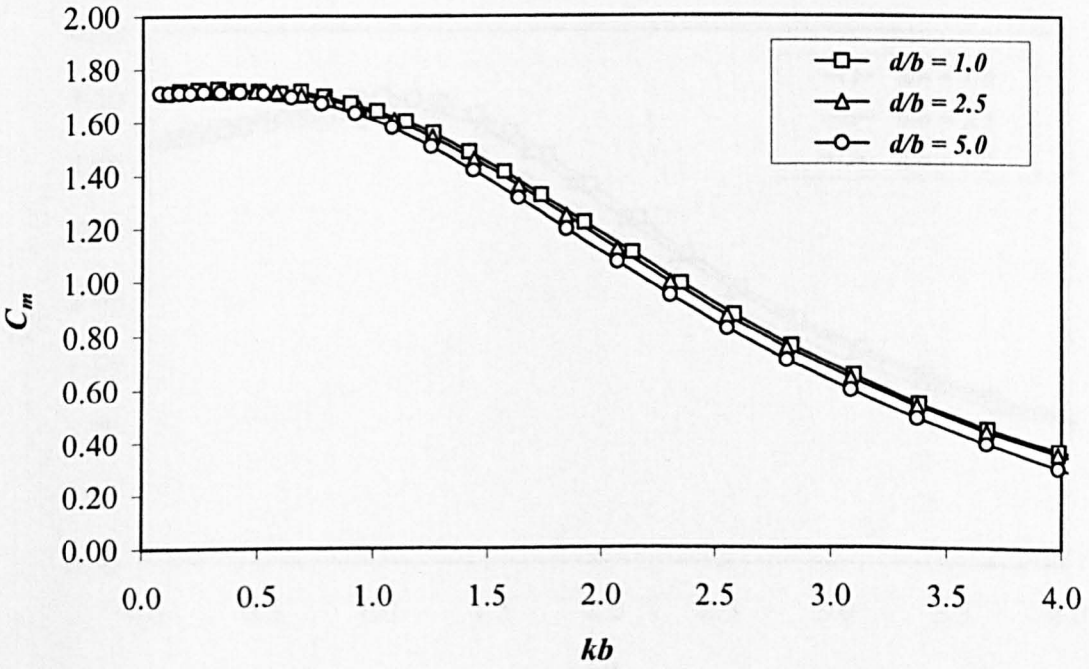

Fig. 6.265 Effective inertia coefficients for rectangular cylinder of aspect ratio = 1/2 for $\alpha = 0^{\circ}$ for various relative depths

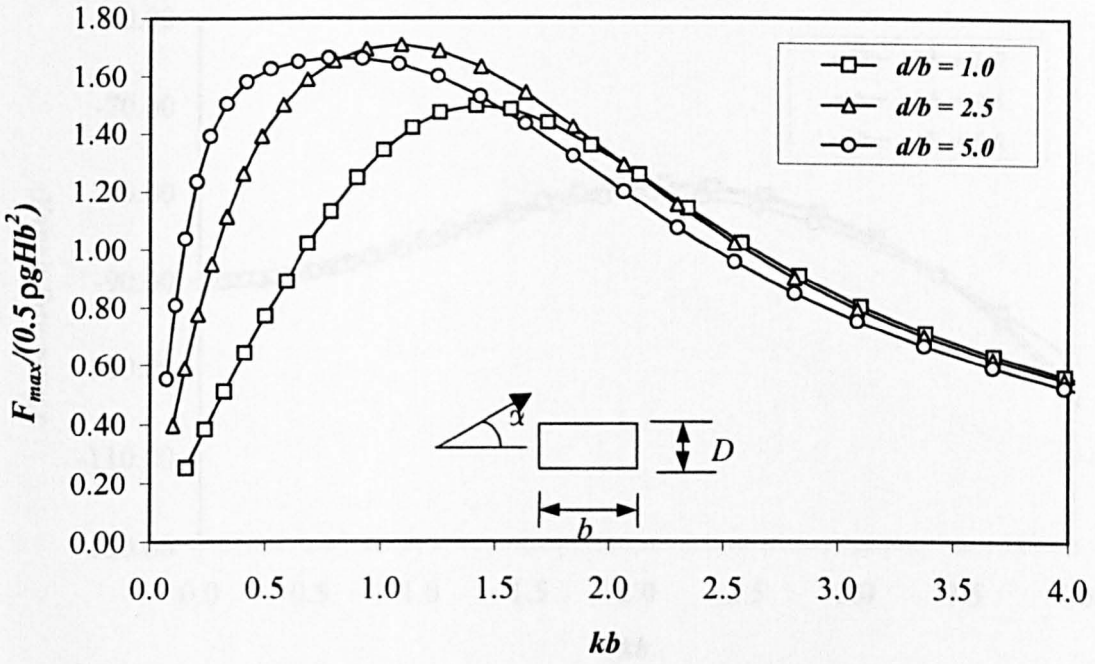

Fig. 6.266 Normalised horizontal force for rectangular cylinder of aspect ratio = 1/2 for $\alpha = 90^{\circ}$ for various relative depths

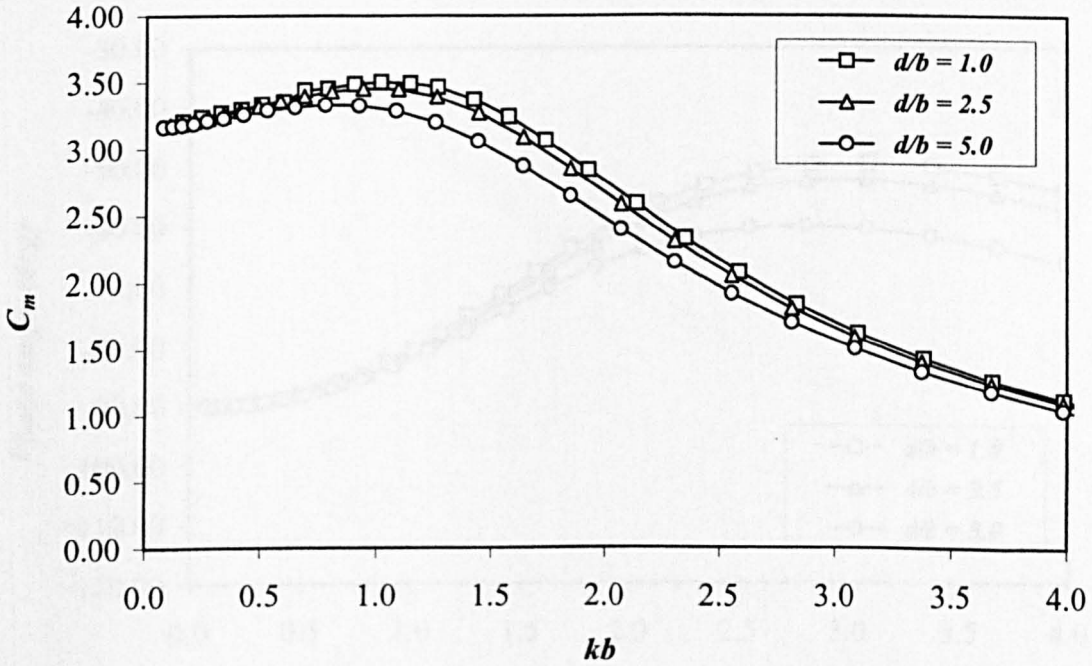

Fig. 6.267 Effective inertia coefficients for rectangular cylinder of aspect ratio = 1/2 for $\alpha = 90^{\circ}$ for various relative depths

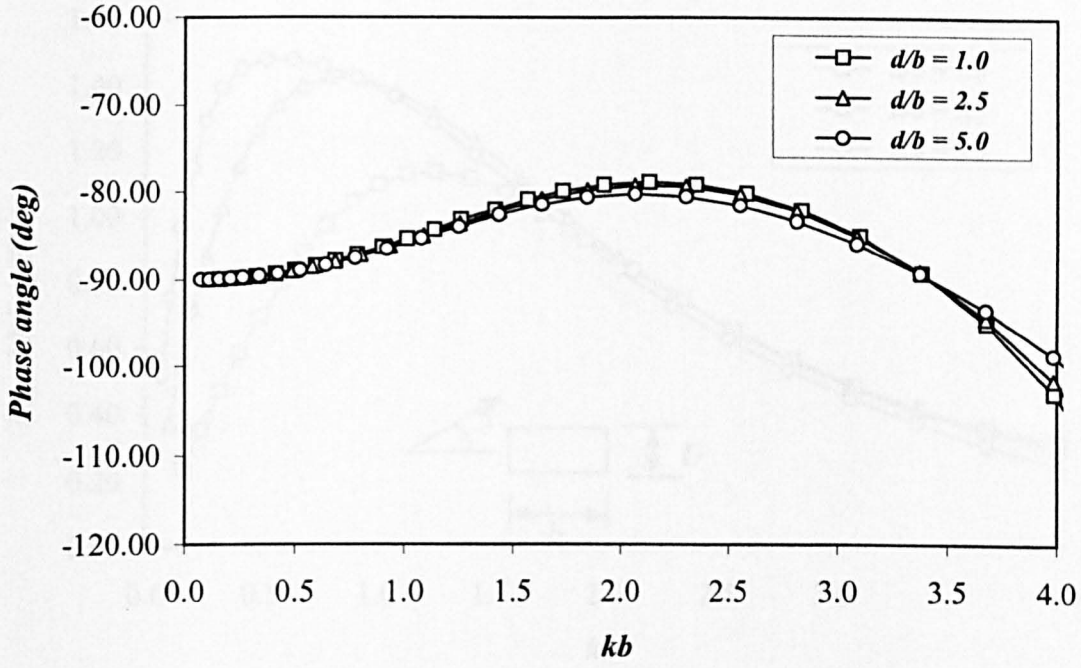

Fig. 6.268 Phase angle for horizontal force for rectangular cylinder with aspect ratio = 1/2 for $\alpha = 0^{o}$ for various relative depths

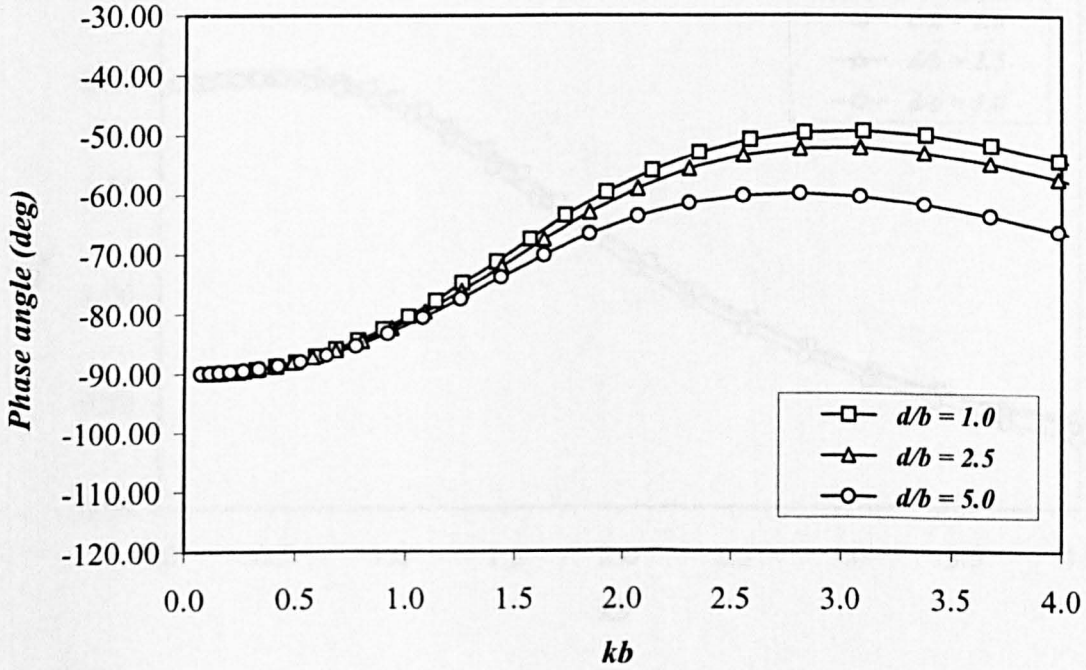

Fig. 6.269 Phase angle for horizontal force for rectangular cylinder with aspect ratio = 1/2 for $\alpha = 90^{o}$ for various relative depths

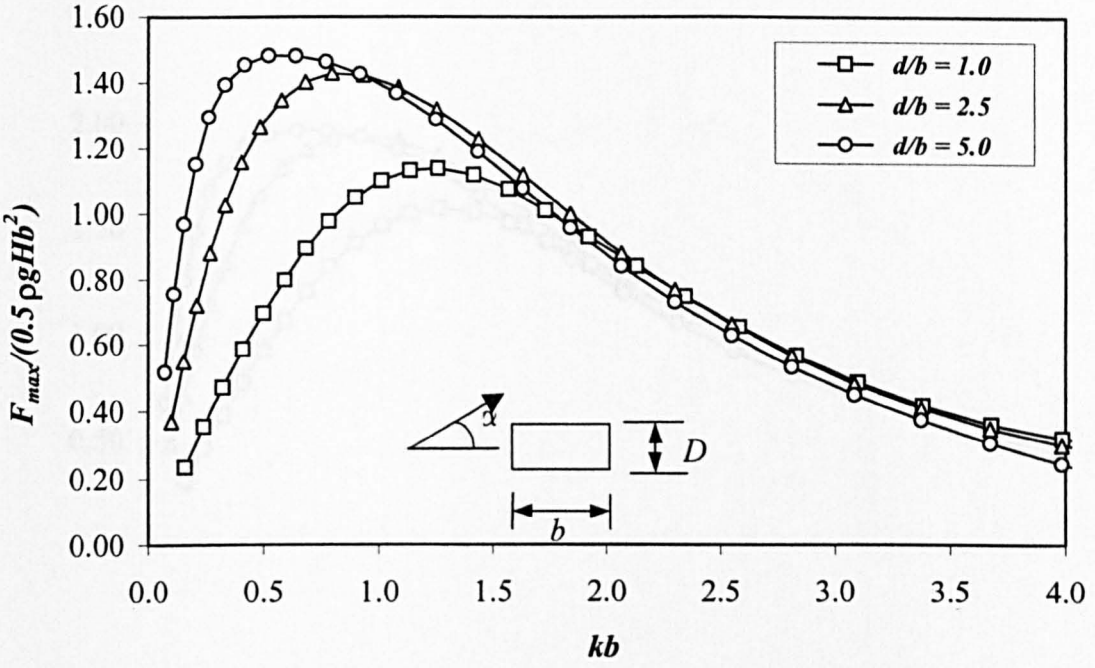

Fig. 6.270 Normalised horizontal force for rectangular cylinder of aspect ratio = 3/4 for $\alpha = 0^{\circ}$ for various relative depths

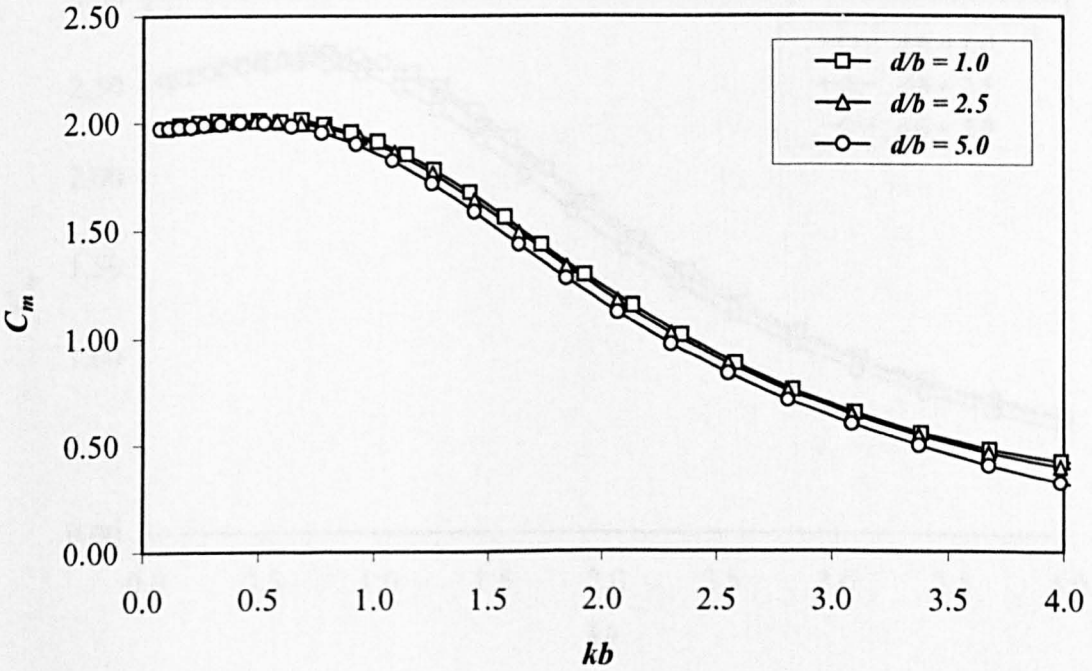

Fig. 6.271 Effective inertia coefficients for rectangular cylinder of aspect ratio = 3/4 for $\alpha = 0^{\circ}$ for various relative depths

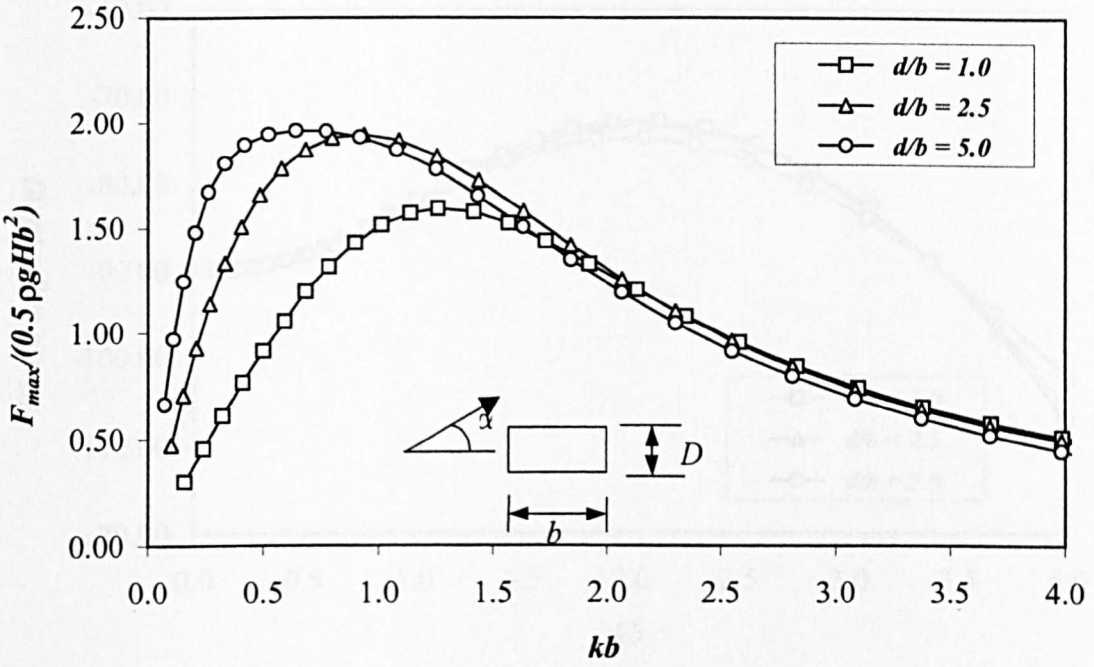

Fig. 6.272 Normalised horizontal force for rectangular cylinder of aspect ratio = 3/4 for $\alpha = 90^{\circ}$ for various relative depths

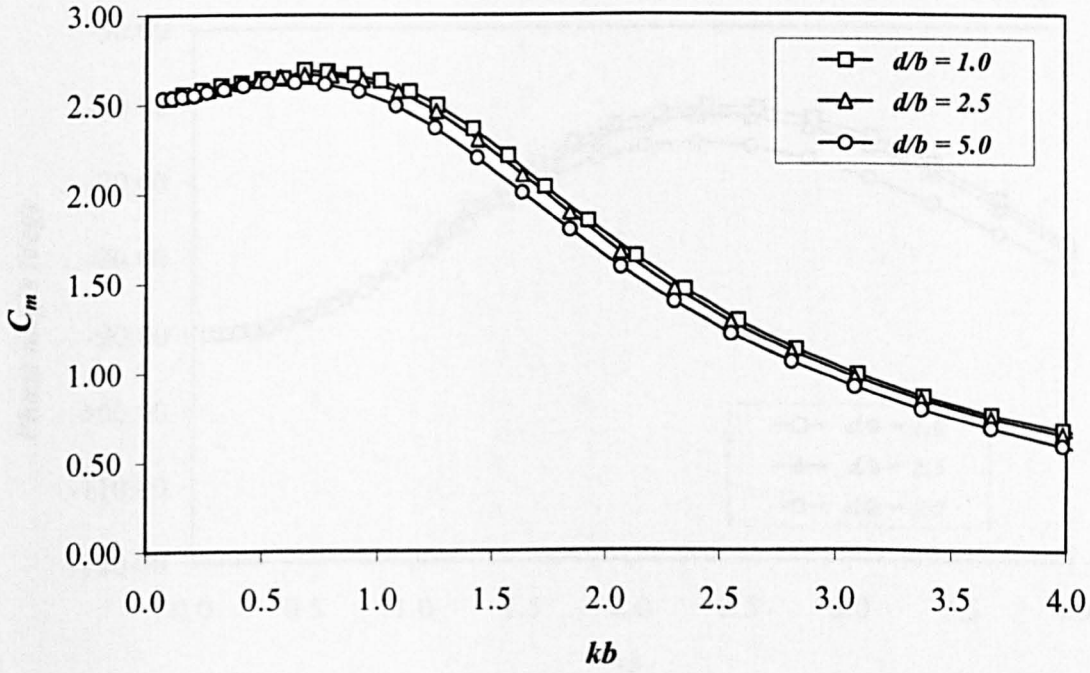

Fig. 6.273 Effective inertia coefficients for rectangular cylinder of aspect ratio = 3/4 for $\alpha = 90^{\circ}$ for various relative depths

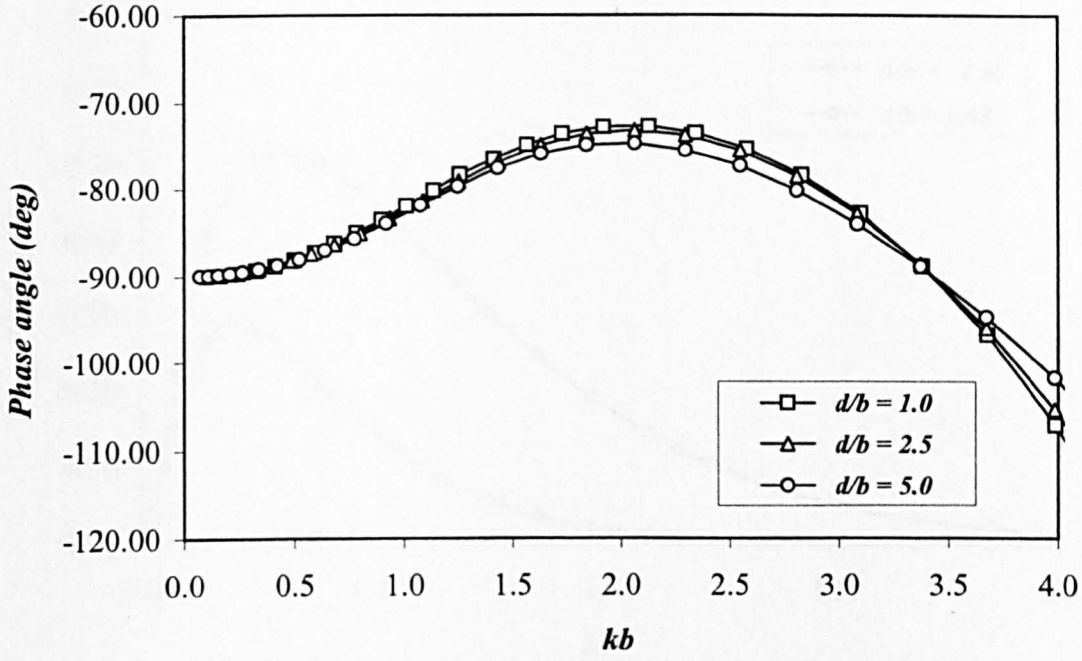

Fig. 6.274 Phase angle for horizontal force for rectangular cylinder with aspect ratio = 3/4 for $\alpha = 0^{\circ}$ for various relative depths

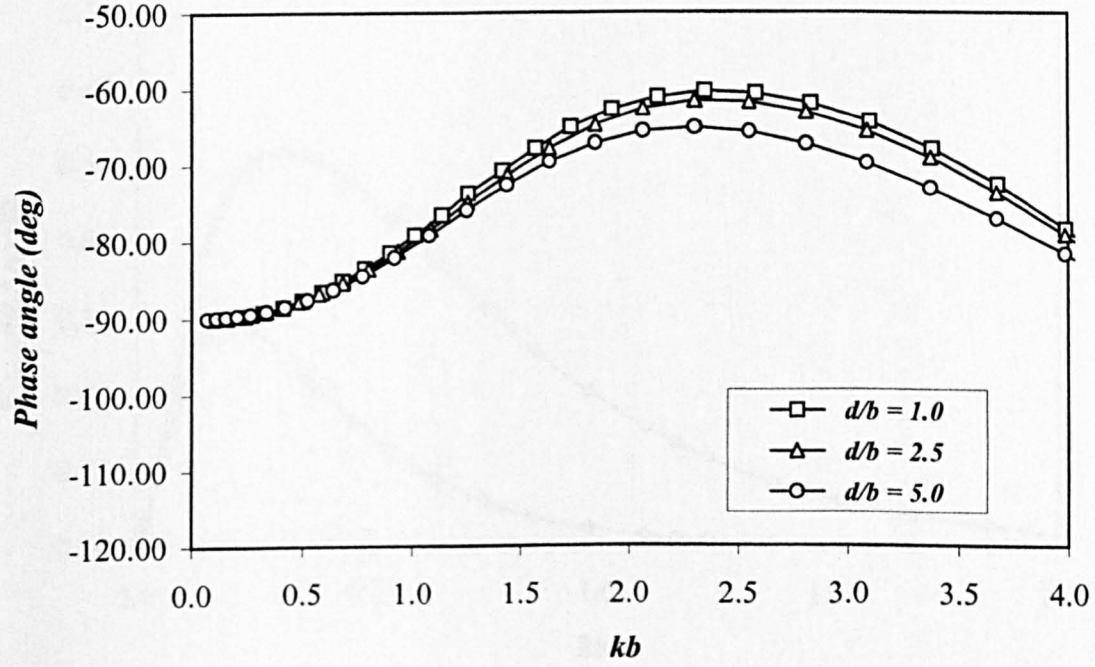

Fig. 6.275 Phase angle for horizontal force for rectangular cylinder with aspect ratio = 3/4 for $\alpha = 90^{\circ}$ for various relative depths

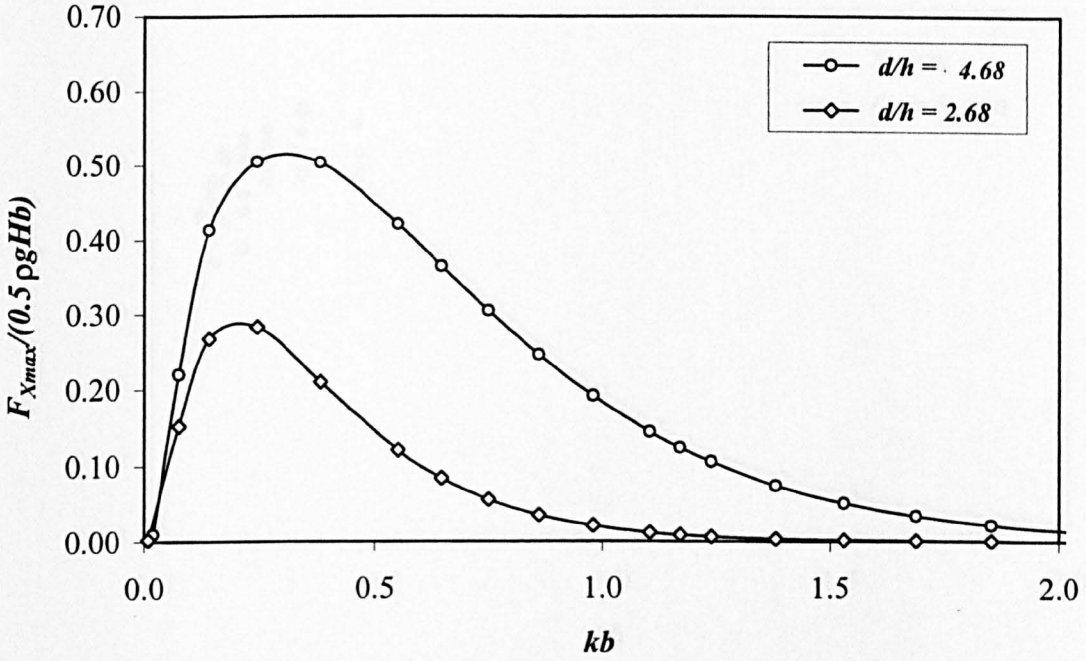

Fig. 6.276 Normalised horizontal force for square cylinder

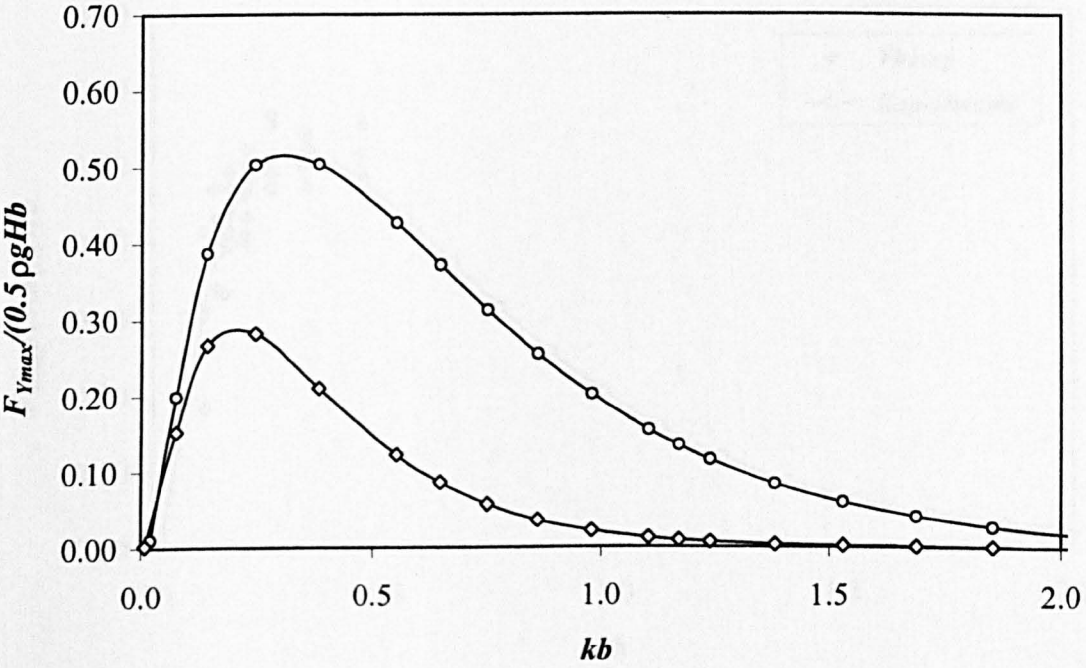

Fig. 6.277 Normalised vertical force for square cylinder

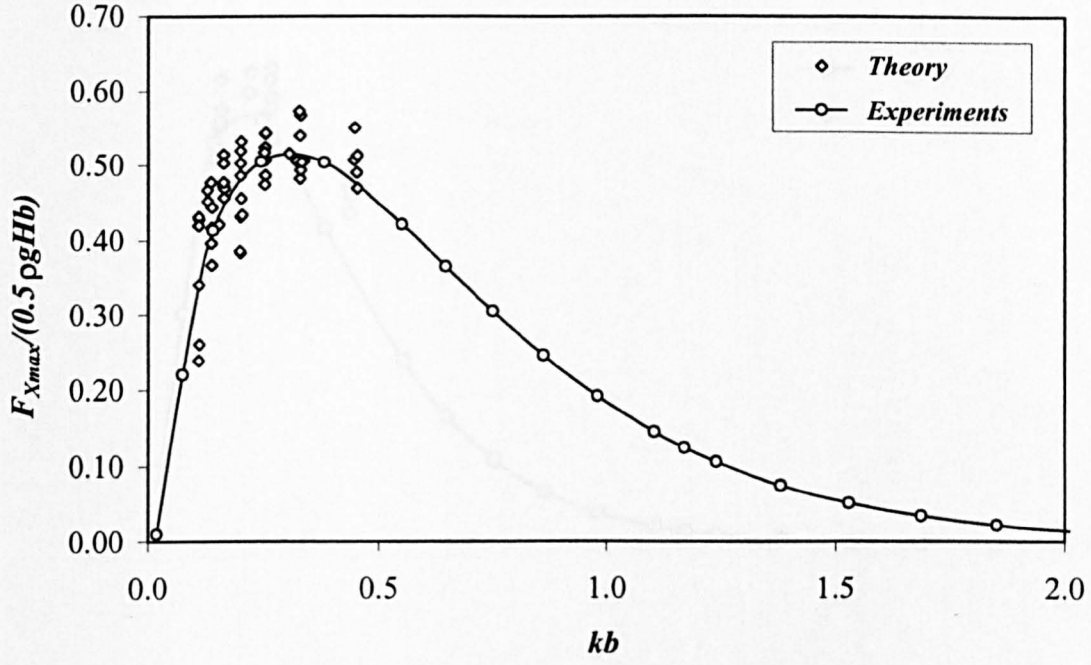

Fig. 6.278 Normalised horizontal force for square cylinder for $d/h = 4.68$

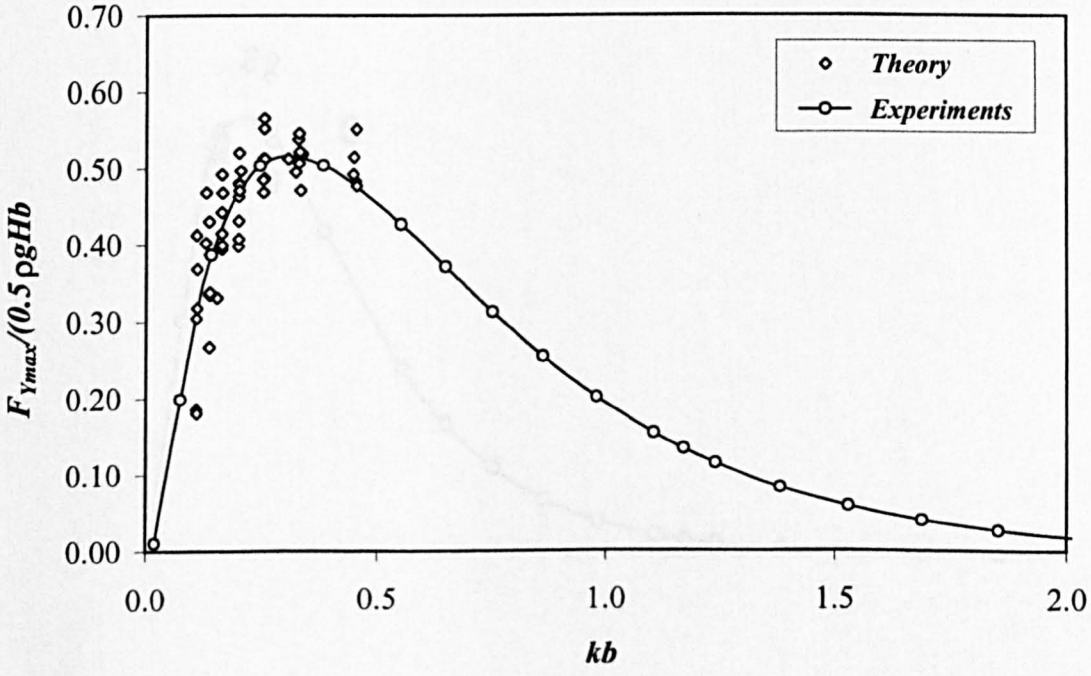

Fig. 6.279 Normalised vertical force for square cylinder for $d/h = 4.68$

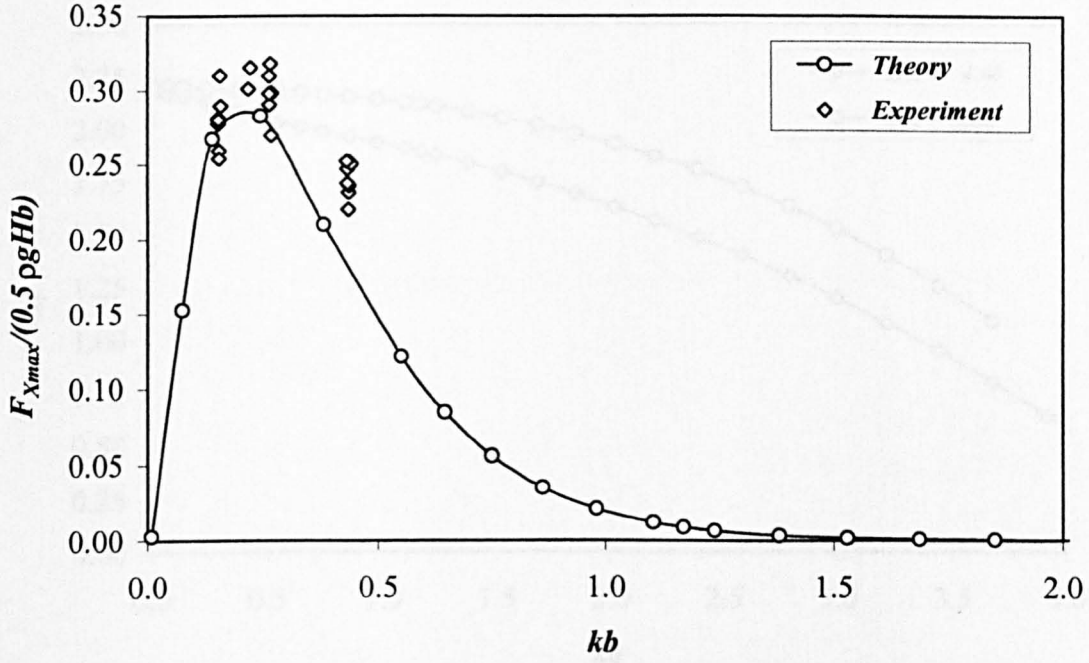

Fig. 6.280 Normalised horizontal force for square cylinder for $d/h = 2.68$

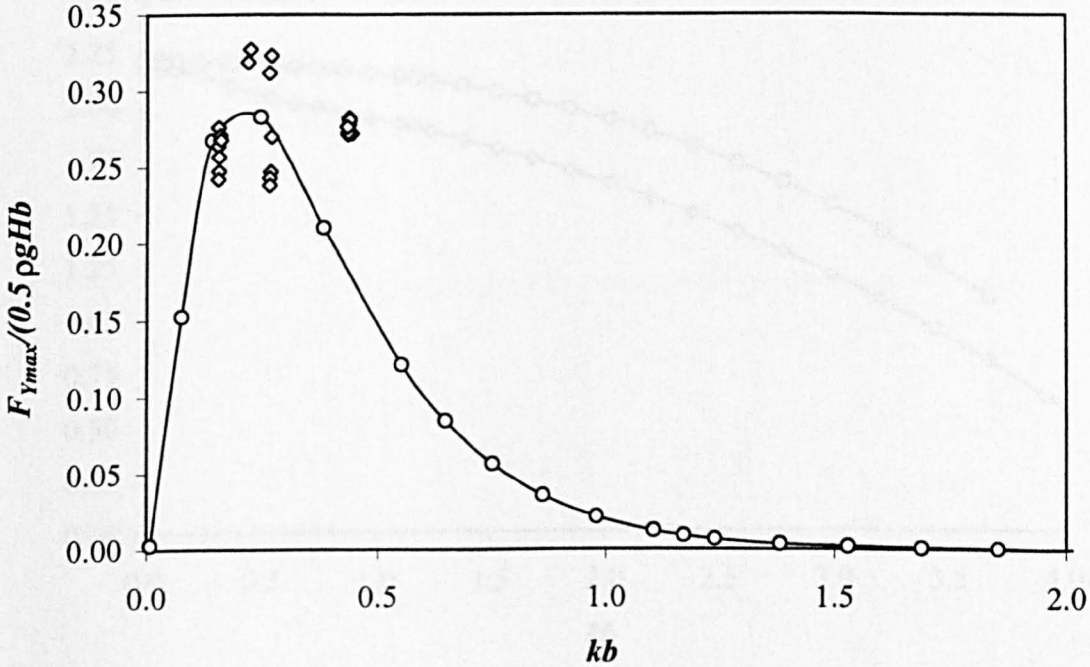

Fig. 6.281 Normalised vertical force for square cylinder for $d/h = 2.68$

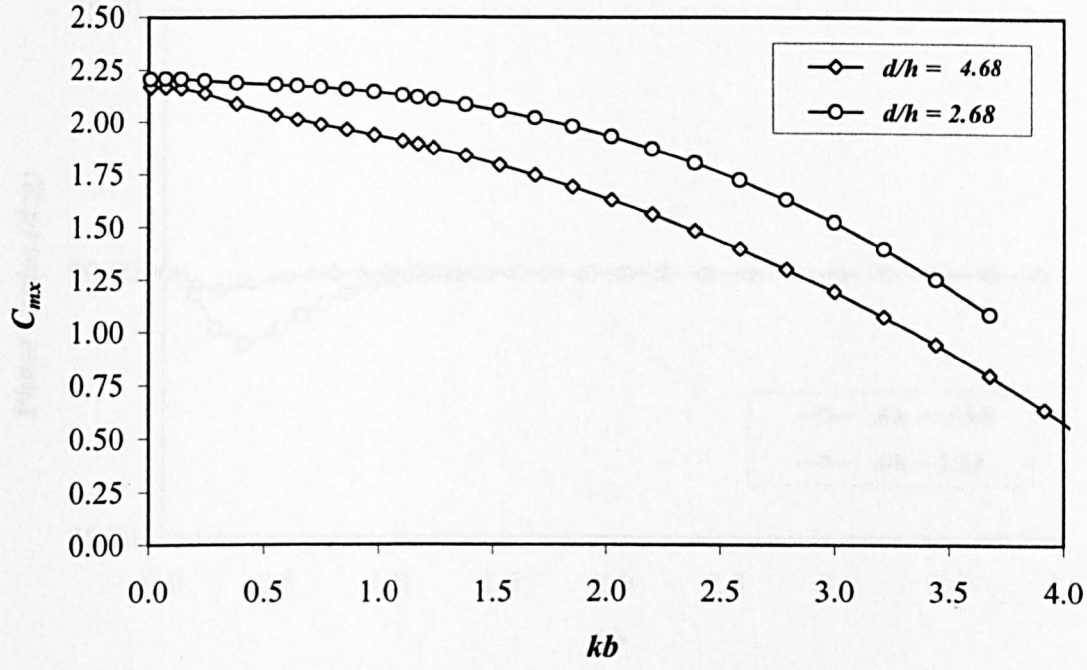

Fig. 6.282 Horizontal inertia coefficient for horizontal square cylinder

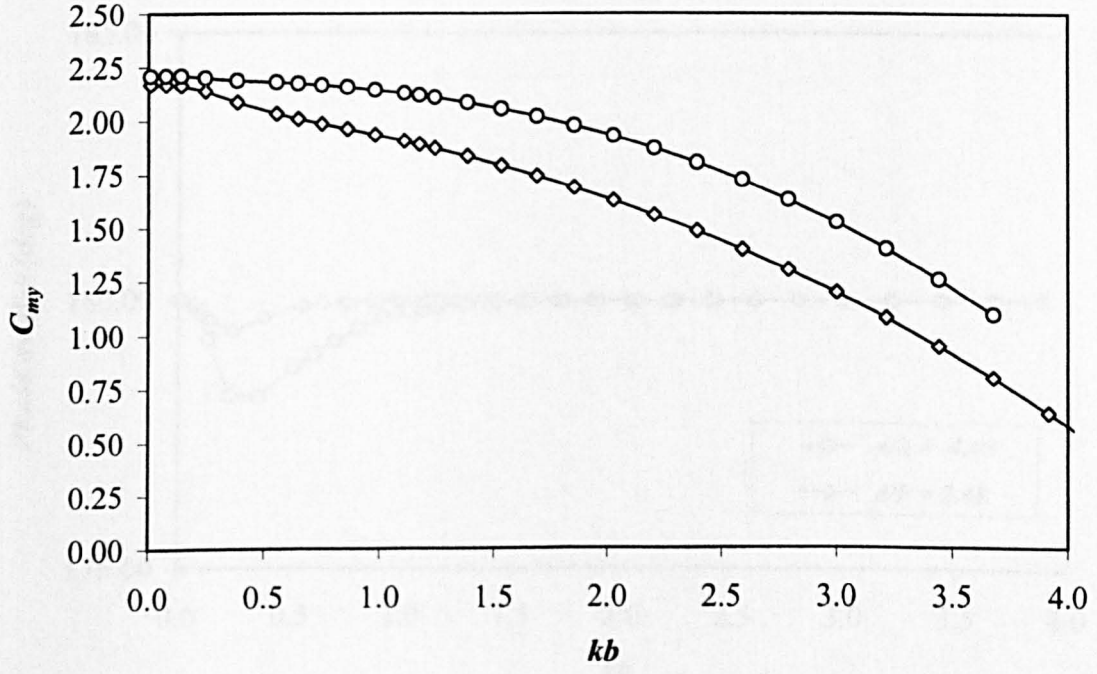

Fig. 6.283 Vertical inertia coefficient for horizontal square cylinder

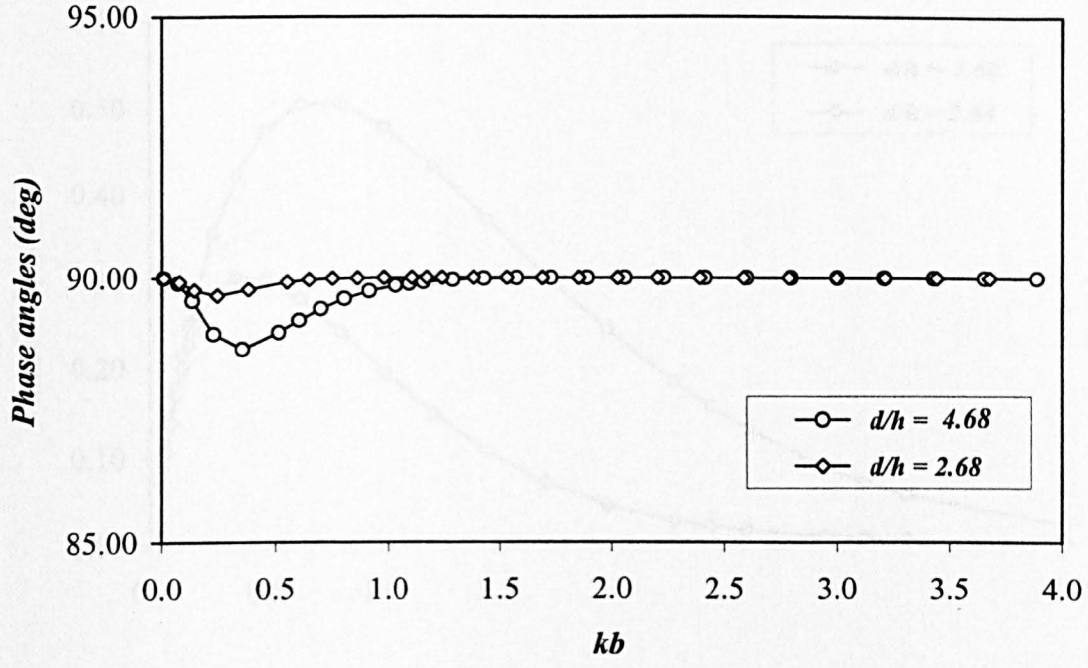

Fig. 6.284 Phase angles for horizontal force for horizontal square cylinder

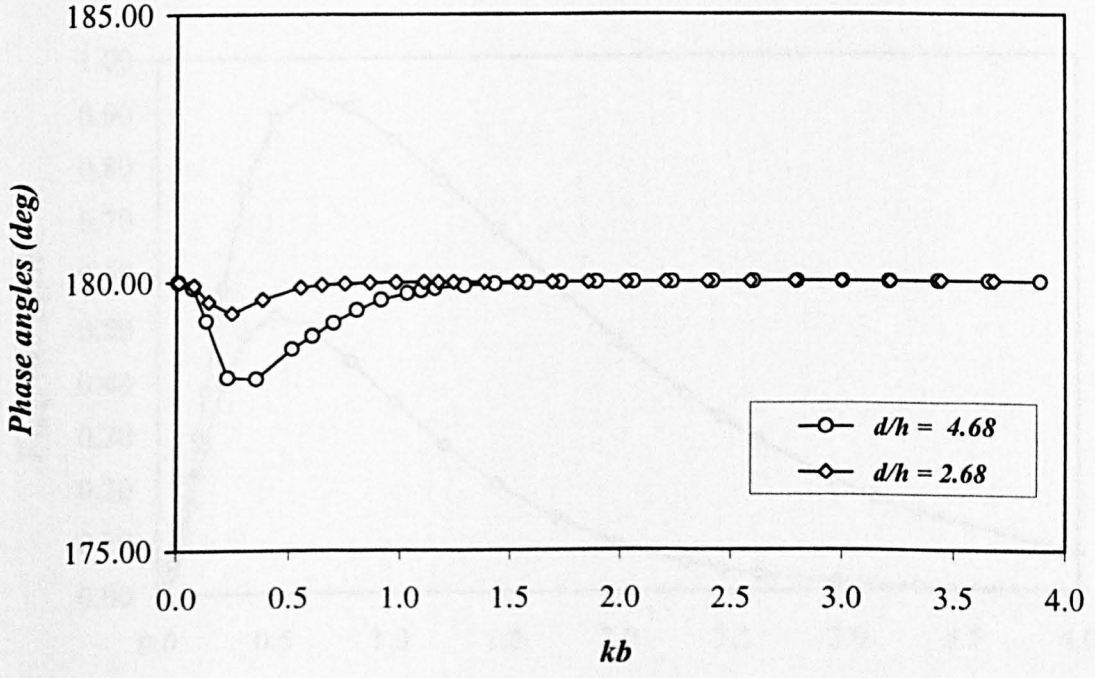

Fig. 6.285 Phase angles for vertical force for horizontal square cylinder

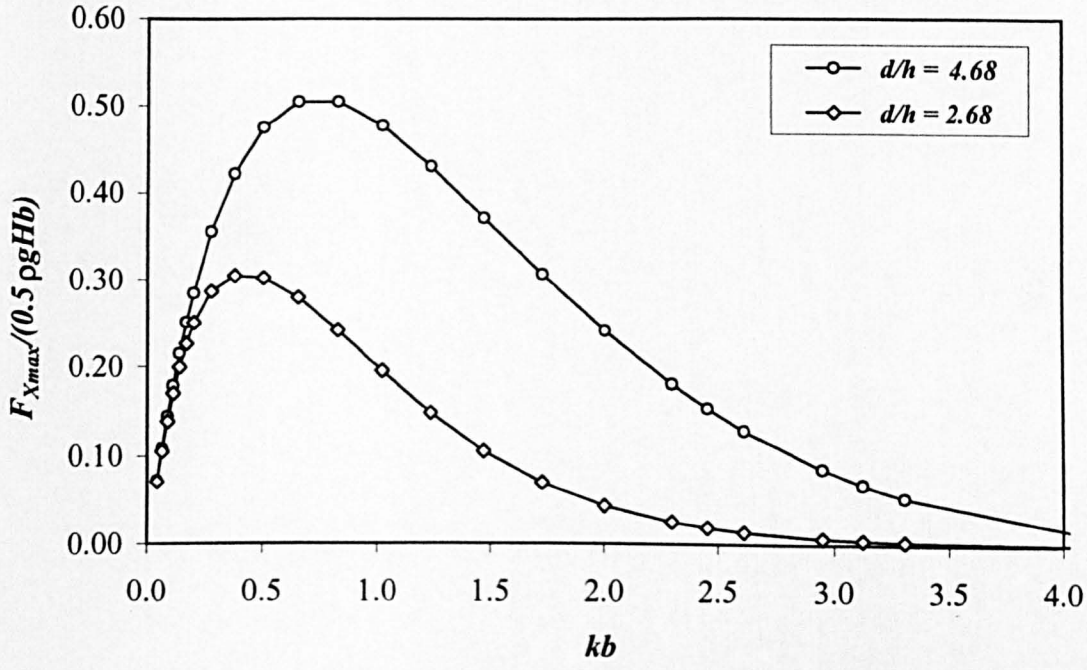

Fig. 6.286 Normalised horizontal force for horizontal rectangular cylinder of aspect ratio = 1/2

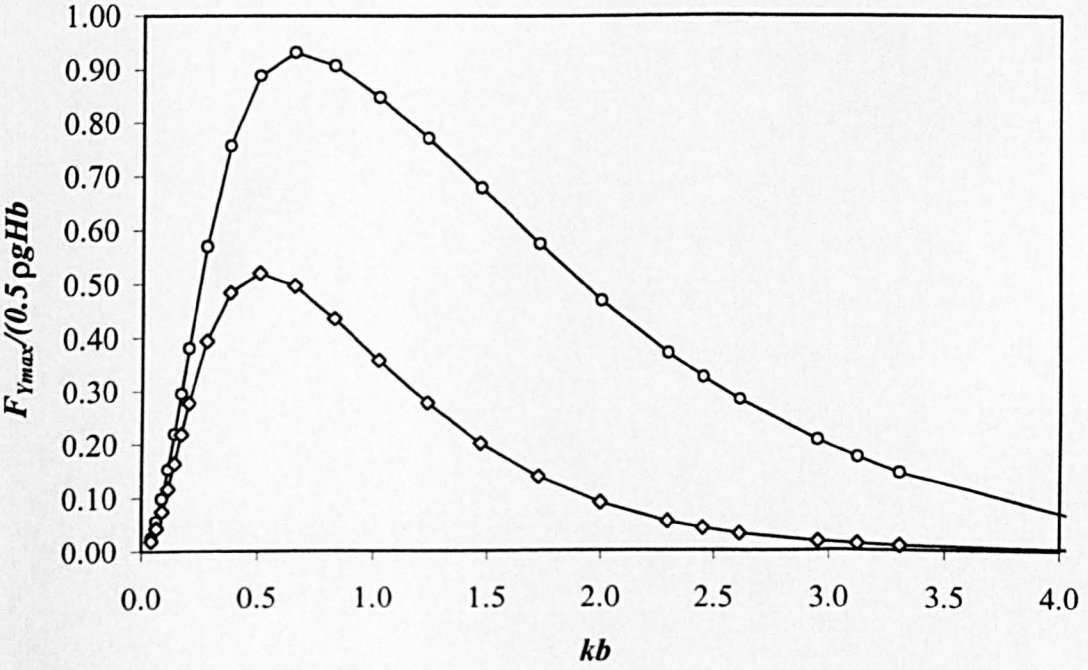

Fig. 6.287 Normalised vertical force for horizontal rectangular cylinder of aspect ratio = 1/2

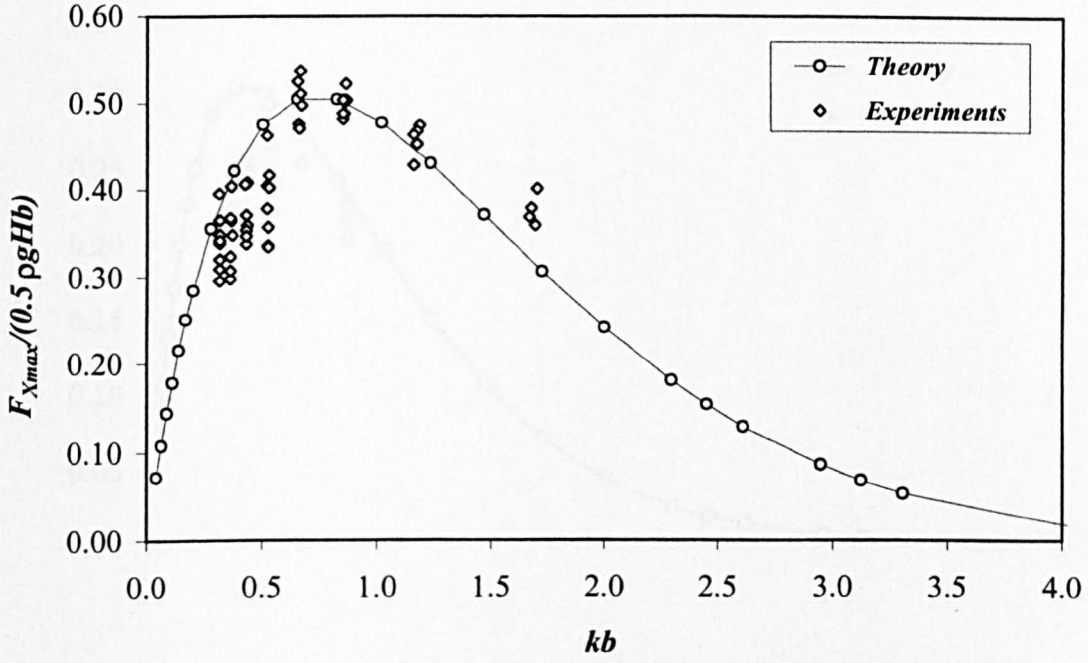

Fig. 6.288 Normalised horizontal force for horizontal rectangular cylinder of aspect ratio = 1/2 for d/h = 4.68

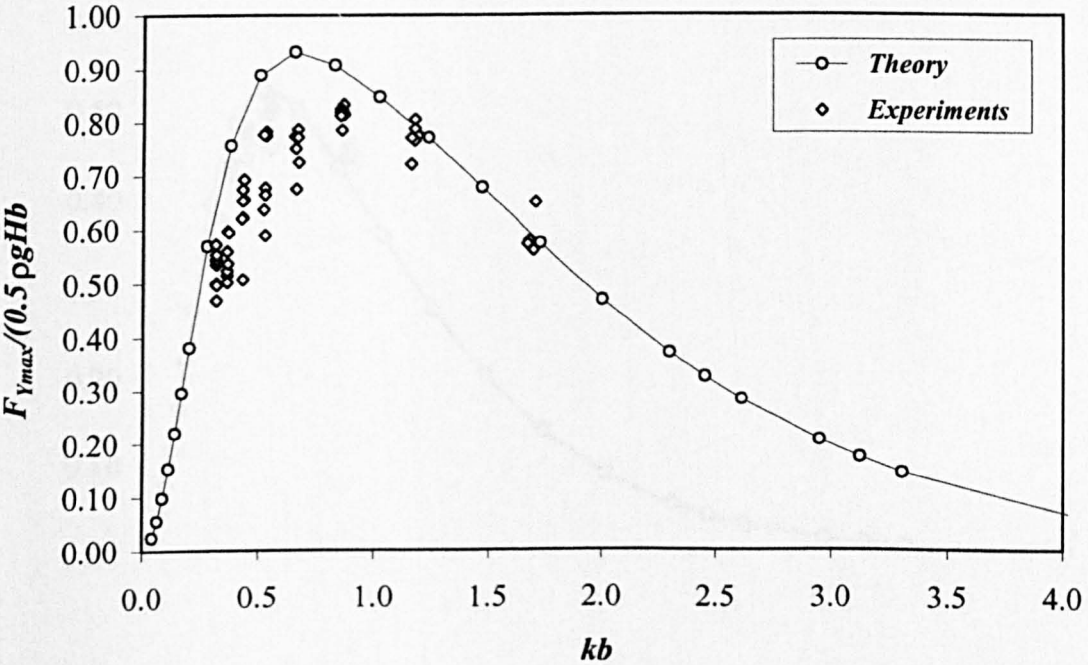

Fig. 6.289 Normalised vertical force for horizontal rectangular cylinder of aspect ratio = 1/2 for d/h = 4.68

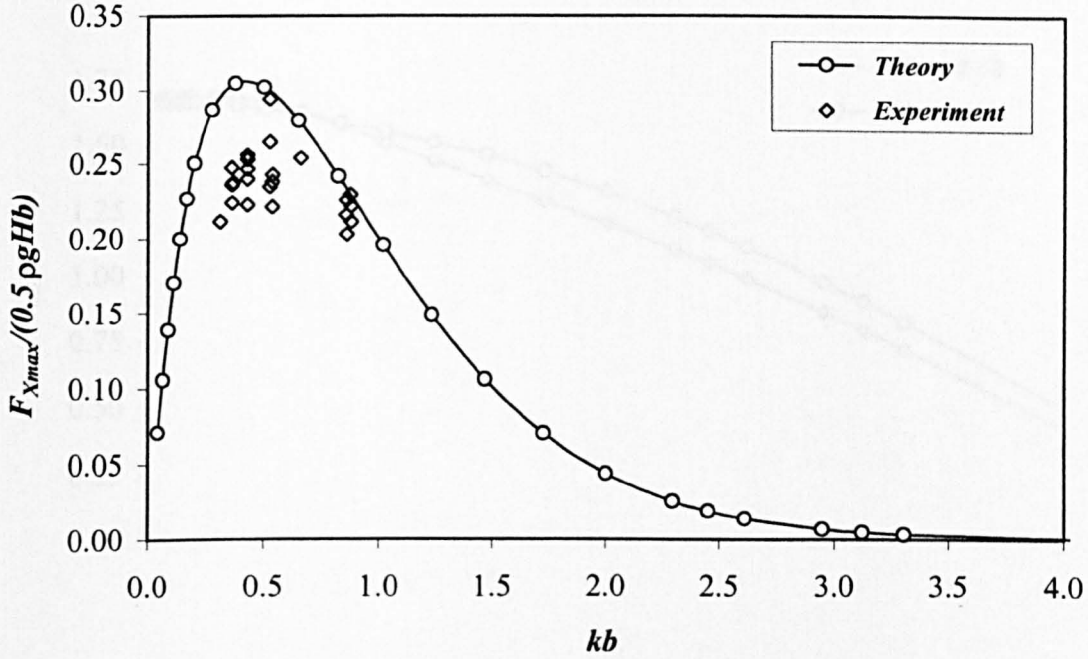

Fig. 6.290 Normalised horizontal force for horizontal rectangular cylinder of aspect ratio = 2/4 for $d/h = 2.68$

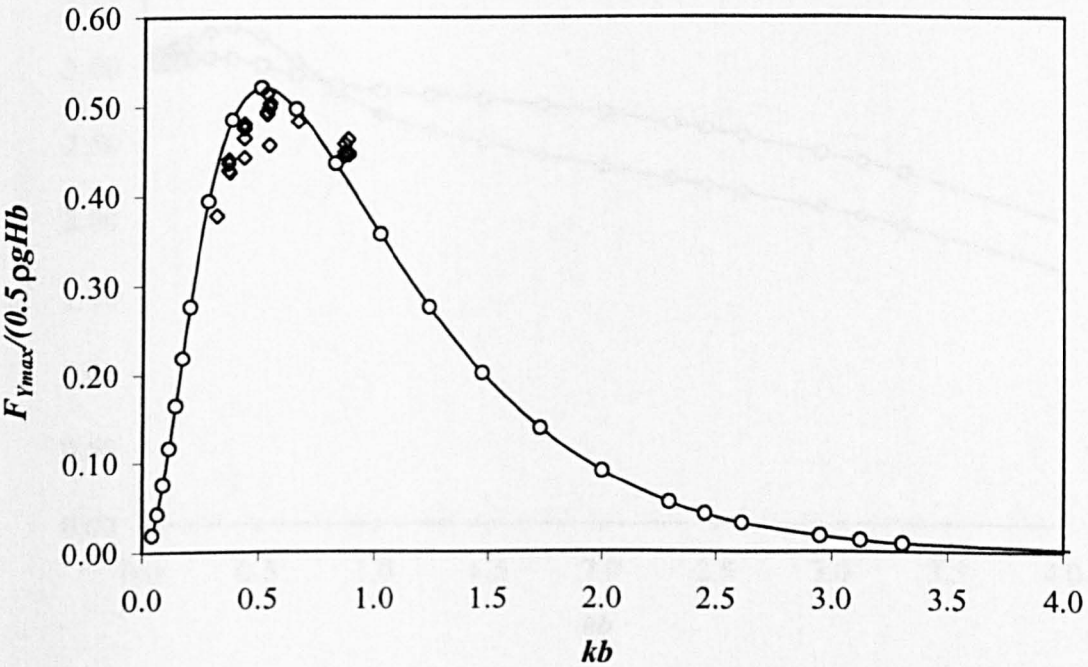

Fig. 6.291 Normalised vertical force for horizontal rectangular cylinder of aspect ratio = 2/4 for $d/h = 2.68$

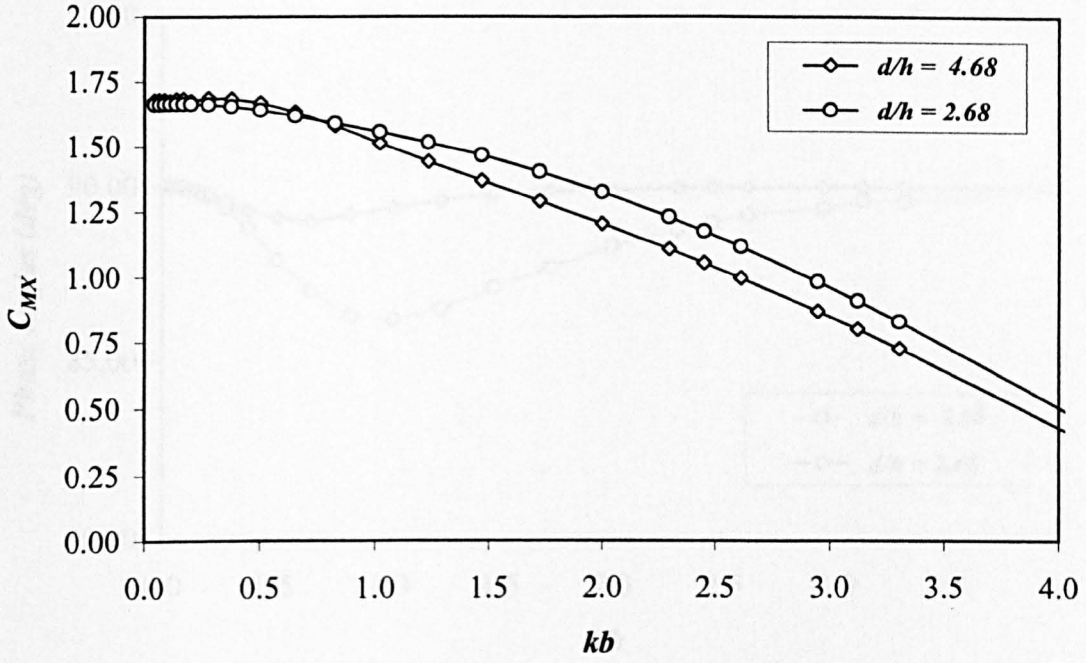

Fig. 6.292 Horizontal inertia coefficient for horizontal rectangular cylinder of aspect ratio = 1/2

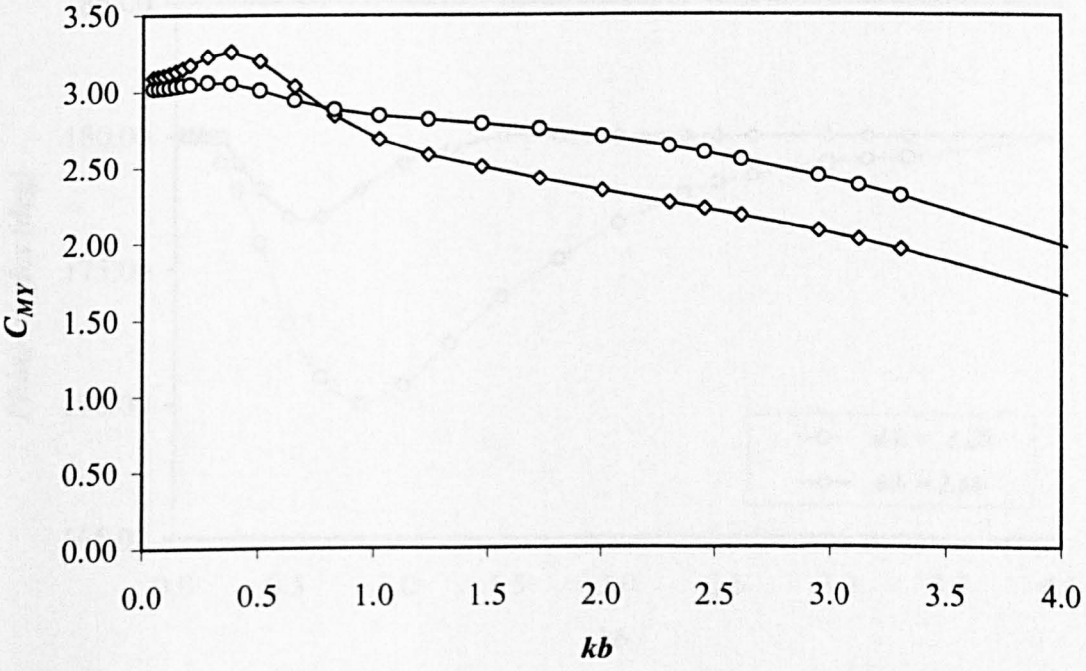

Fig. 6.293 Vertical inertia coefficient for horizontal rectangular cylinder of aspect ratio = 1/2

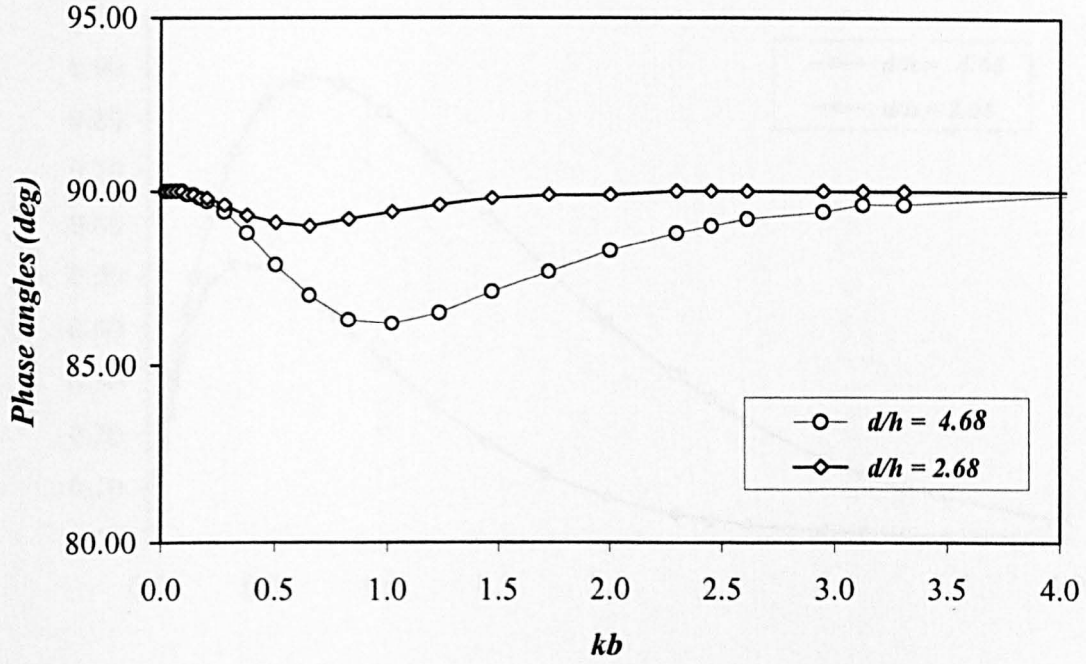

Fig. 6.294 Phase angles for horizontal force for horizontal rectangular cylinder of aspect ratio = 1/2

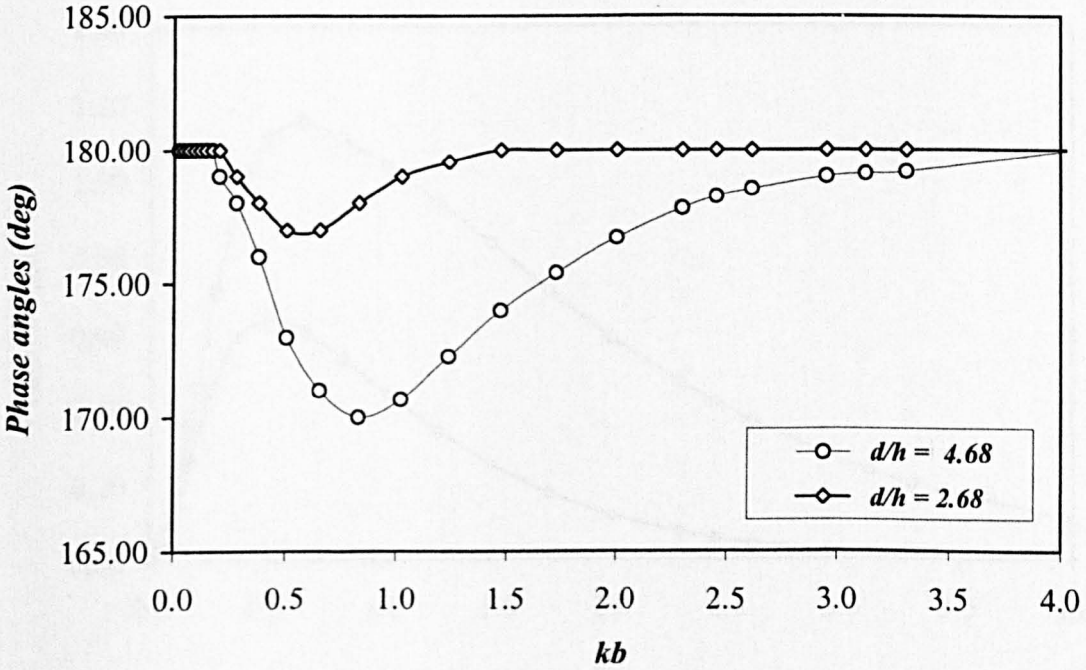

Fig. 6.295 Phase angles for vertical force for horizontal rectangular cylinder of aspect ratio = 1/2

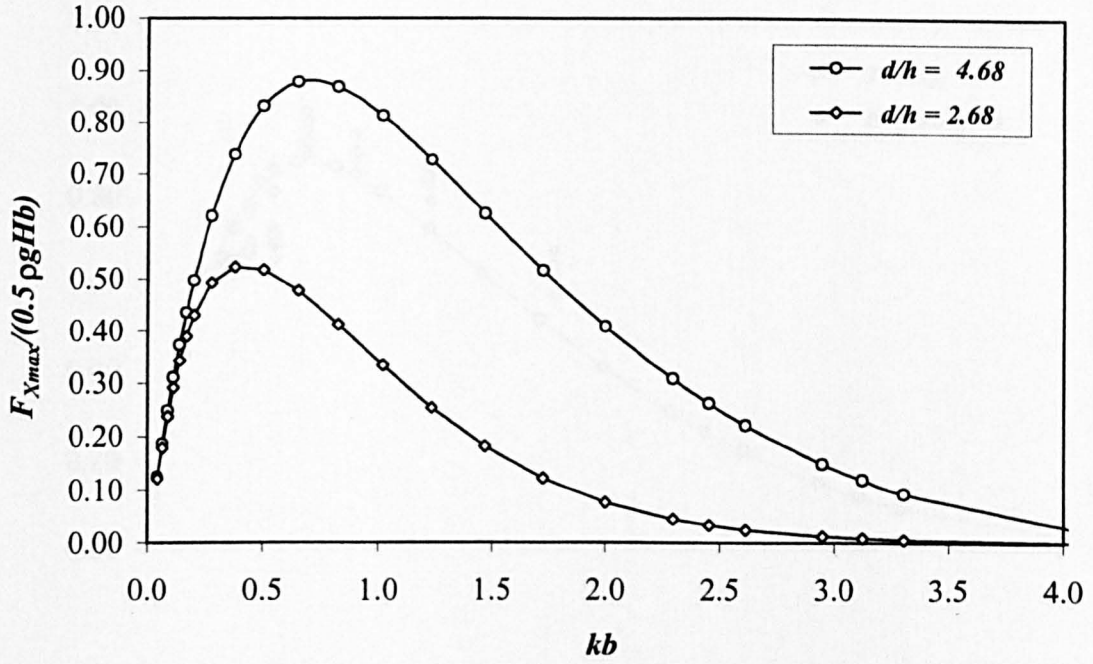

Fig. 6.296 Normalised horizontal force for horizontal rectangular cylinder of aspect ratio = 3/4

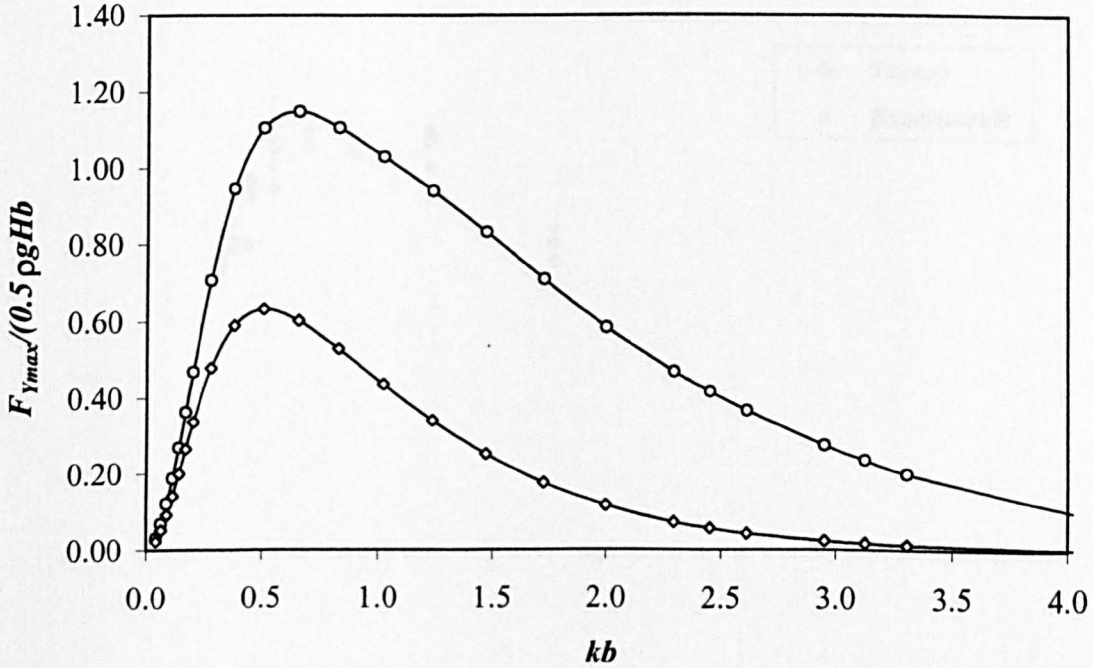

Fig. 6.297 Normalised vertical force for horizontal rectangular cylinder of aspect ratio = 3/4

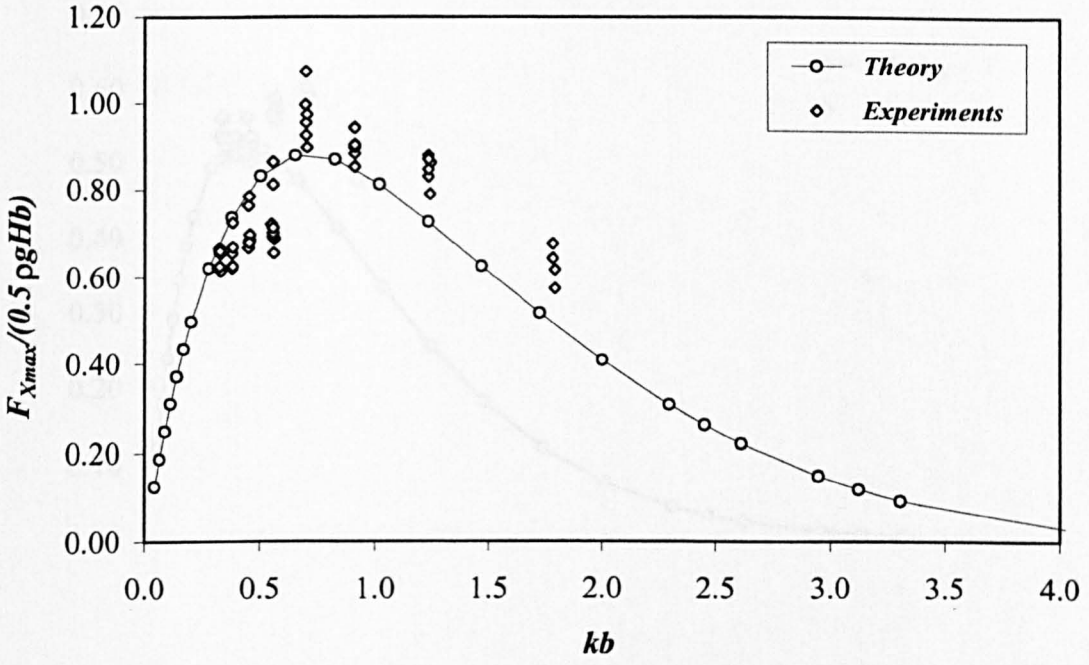

Fig. 6.298 Normalised horizontal force for horizontal rectangular cylinder of aspect ratio = 3/4 for d/h = 4.68

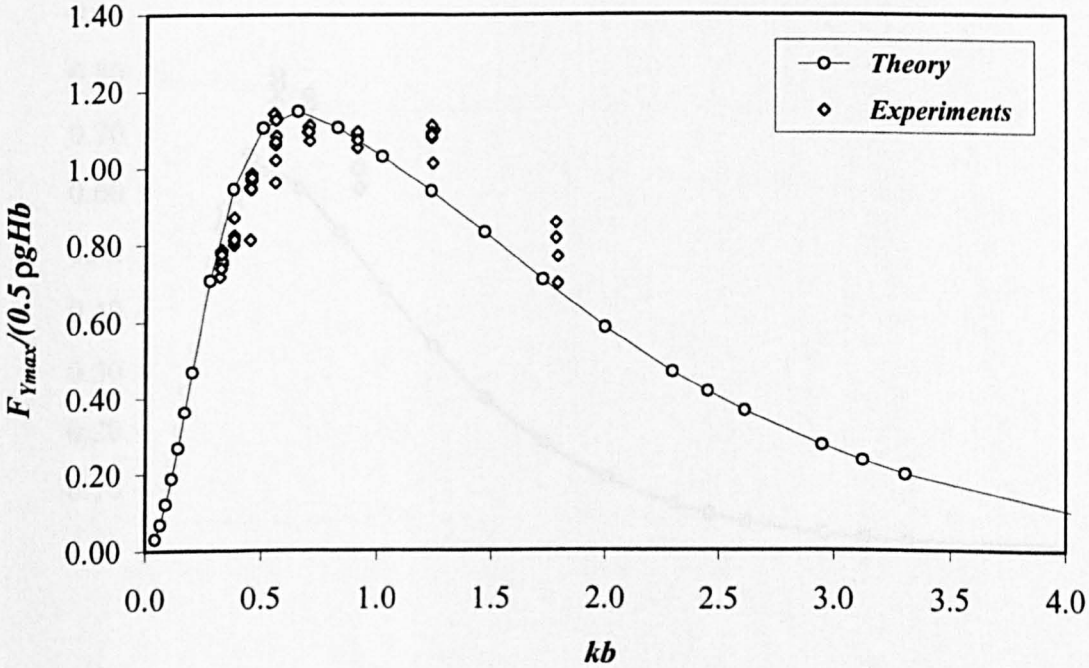

Fig. 6.299 Normalised vertical force for horizontal rectangular cylinder of aspect ratio = 3/4 for d/h = 4.68

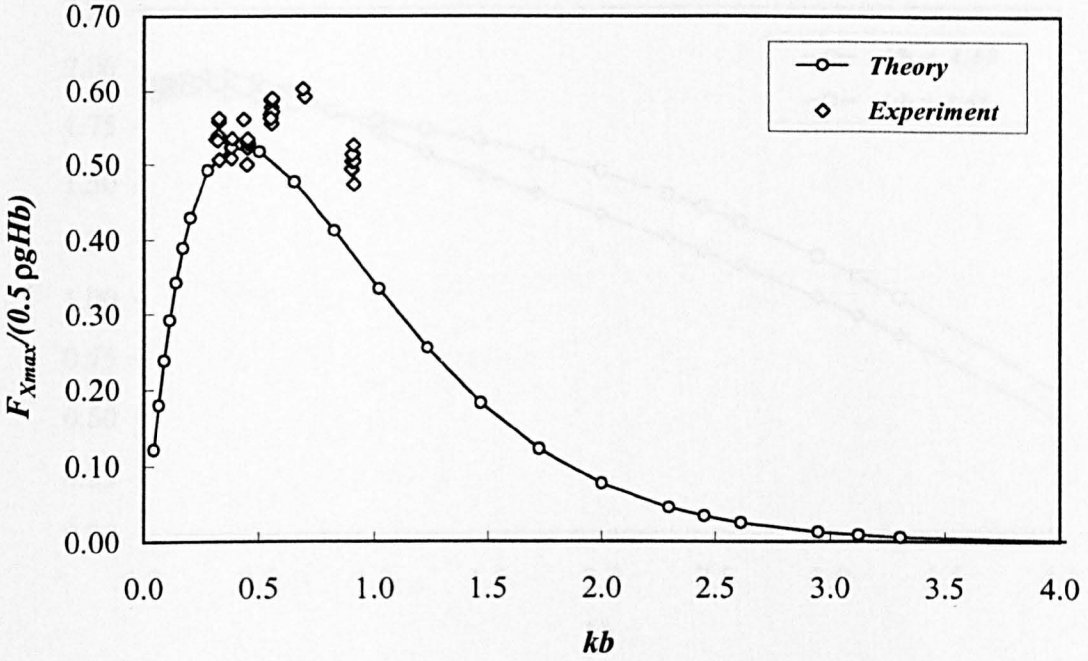

Fig. 6.300 Normalised horizontal force for horizontal rectangular cylinder of aspect ratio = ¾ for $d/h = 2.68$

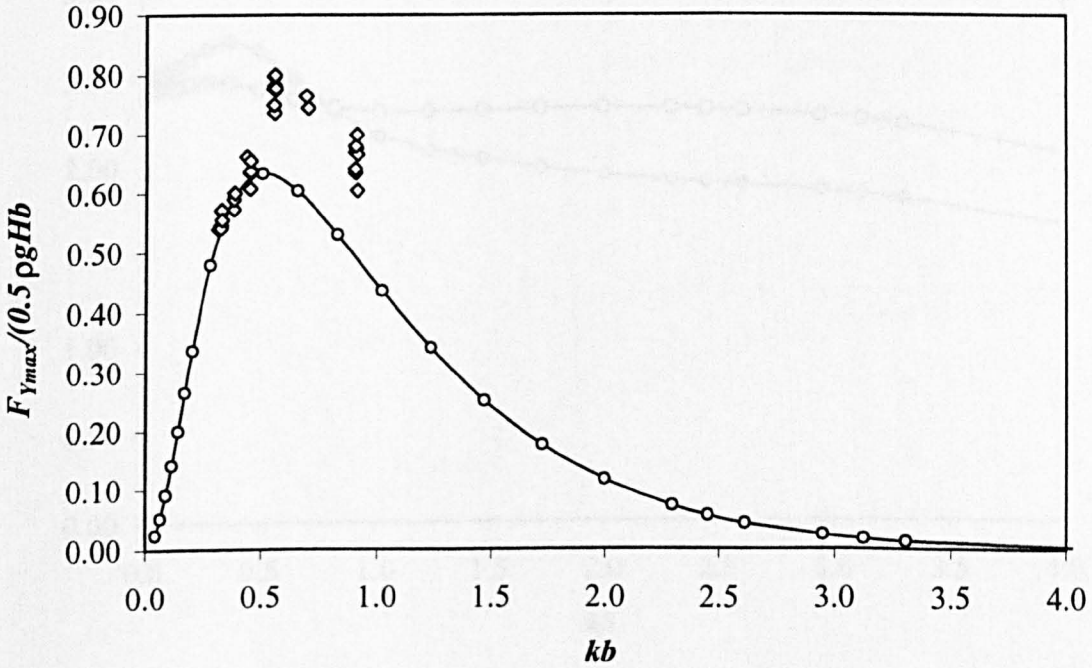

Fig. 6.301 Normalised vertical force for horizontal rectangular cylinder of aspect ratio = ¾ for $d/h = 2.68$

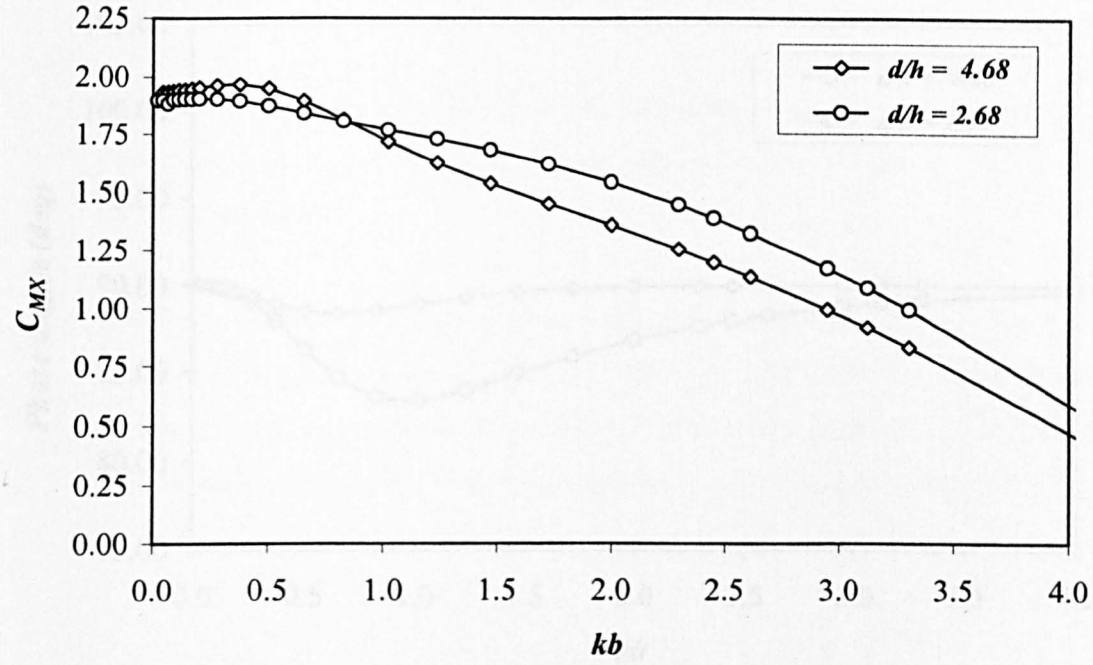

Fig. 6.302 Horizontal inertia coefficient for horizontal rectangular cylinder of aspect ratio = 3/4

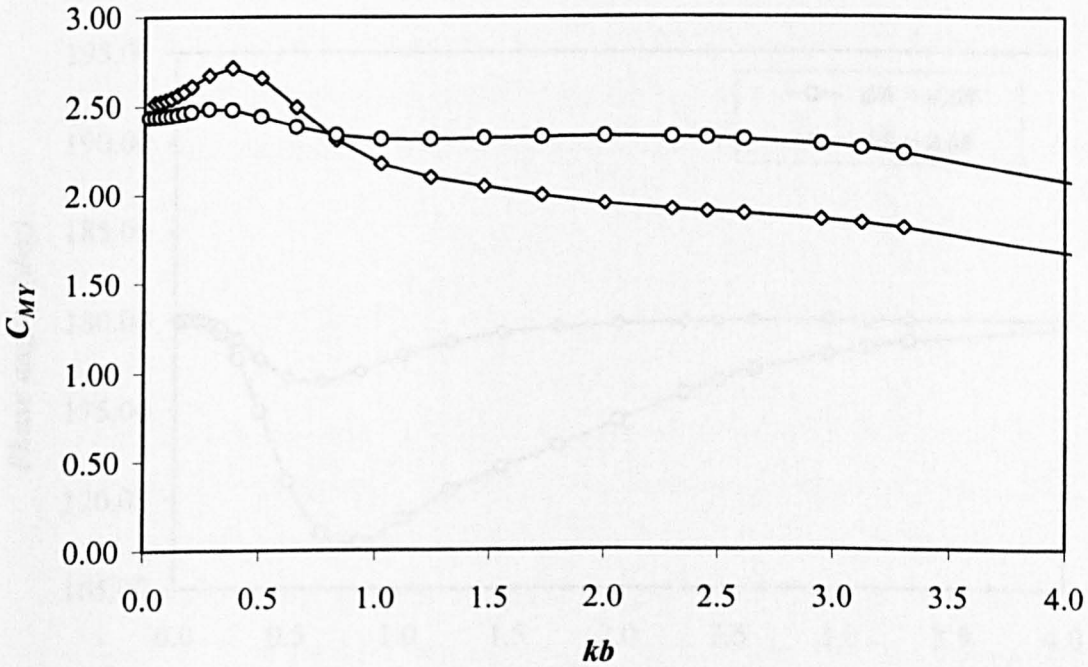

Fig. 6.303 Vertical inertia coefficient for horizontal rectangular cylinder of aspect ratio = 3/4

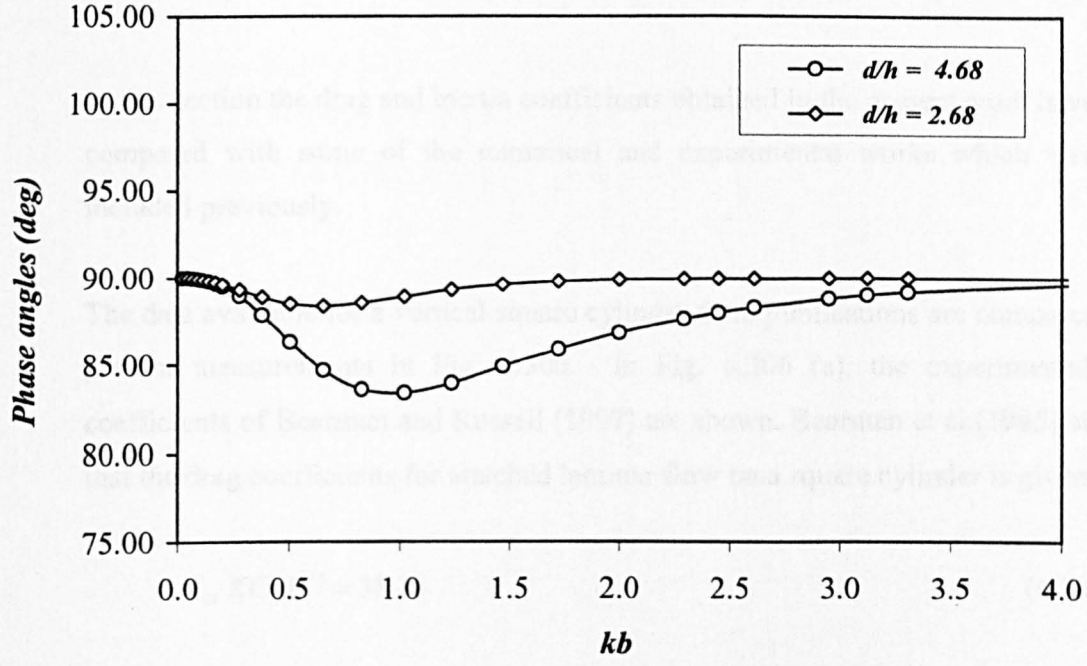

Fig. 6.304 Phase angles for horizontal force for horizontal rectangular cylinder of aspect ratio = 3/4

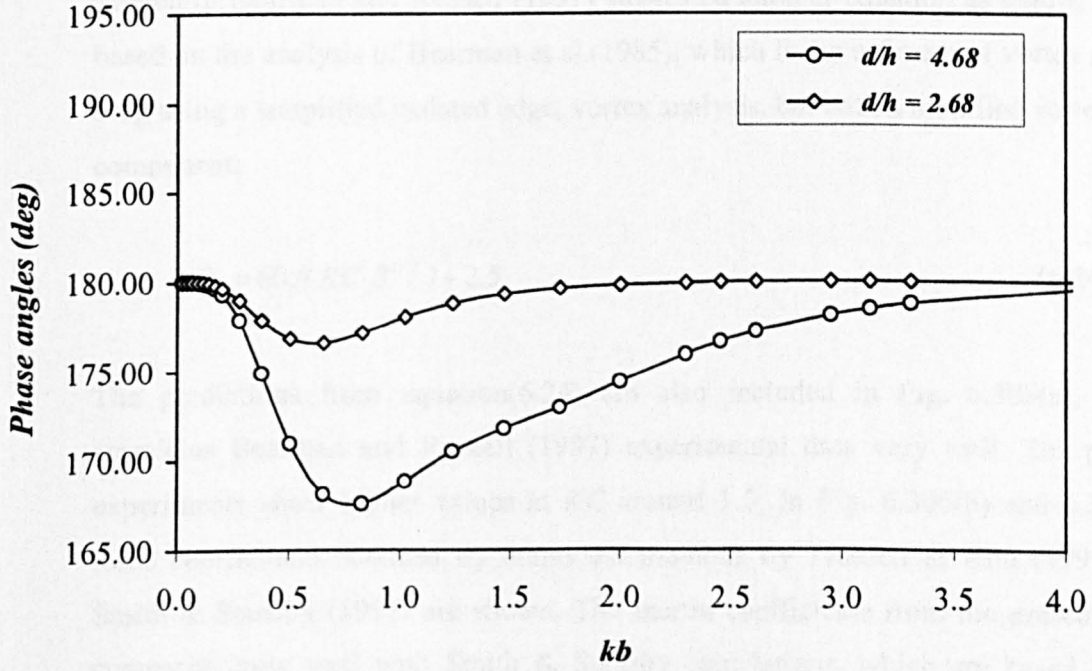

Fig. 6.305 Phase angles for vertical force for horizontal rectangular cylinder of aspect ratio = 3/4

6.7 Comparisons of force coefficients with Literature

In this section the drag and inertia coefficients obtained in the present work have been compared with some of the numerical and experimental works which were not included previously.

The data available for a vertical square cylinder from publications are compared with present measurements in Fig. 6.306. In Fig. 6.306 (a), the experimental drag coefficients of Bearman and Russell (1997) are shown. Bearman et al.(1985) showed that the drag coefficients for attached laminar flow on a square cylinder is given by

$$C_D KC \beta^{1/2} = 38.18 \tag{6.23}$$

The predictions obtained using above equation are plotted in Fig. 6.306(a) for β = 8000 and 40000. They show β dependence, but drag coefficient values are underestimated to about 50% to 60% while comparing with the measurements. Therefore Bearman and Russell (1997) suggested another equation as below, that is based on the analysis of Bearman et al.(1985), which is the estimate of vortex related drag using a simplified isolated edge, vortex analysis, but with a modified vortex drag component;

$$C_D = 60/(KC\beta^{1/2}) + 2.5 \tag{6.24}$$

The predictions from equation(6.24) are also included in Fig. 6.306(a), which correlates Bearman and Russell (1997) experimental data very well. The present experiments show higher values at KC around 1.0. In Fig. 6.306(b) and 6.306(c), force coefficients obtained by numerical methods by Troesch & Kim (1991) and Smith & Stansby (1991) are shown. The inertia coefficients from the present work compares quite well with Smith & Stansby calculations, which are based on the random-vortex method, to compute the forces in two-dimensional viscous oscillatory

flow. The numerical model by Troesch & Kim, assumes a laminar, non separating flow with the inline force has two components; one due to normal pressure stresses and one due to skin friction. The inertia coefficients from this numerical model are slightly smaller. The experimental drag coefficients appear to agree with theoretical calculations except the region of KC around 1.0.

6.8 Potential Flow values

Potential flow C_M and steady flow C_D values [Barltrop & Adams (1991), Isaacson (1978) and Shankar et al. (1984)] for square/rectangular cylinders are compared with present theoretical values in Table. 6.5. A plot of inertia coefficients values against aspect ratios taken from Barltrop & Adams (1991) is shown in Fig. 6.307. Note that for aspect ratios 3/4 and 4/3, direct values are not available and hence interpolated values are included in this table. It is evident that the present results are much similar to the values given by Barltrop & Adam (1991) and these potential flow inertia coefficient values are marked in Figs. 6.308 to 6.310, which shows the present experimental coefficients.

6.9 Comparison of Regular and Random Wave Force Coefficients

Regular and random wave force coefficients are compared for the same cylinder. The comparison for all cylinders is shown in Appendix – A, i.e., for vertical and horizontal cylinders. The results are corresponding to wave by wave method. In general, drag and inertia coefficients obtained from random wave tests are consistent with regular wave force coefficients. However, slightly higher drag coefficients are obtained through random wave tests for all horizontal cylinders. This difference could be attributed to the history effect, i.e., loading in small waves is affected by the presence of vortices generated in preceding large waves as any increase in drag coefficient is associated with an increase in the strength of vortex shedding.

6.10 Comparison of Force Coefficients with Aspect Ratio in Regular Waves

The drag and inertia coefficients for all vertical and horizontal cylinders are shown in Appendix – B. The variation of drag coefficients for vertical cylinders with KC number (Fig. B.1) follows a similar trend for all aspect ratios. In general the drag coefficients decreases rapidly from high values with increasing KC number. The drag coefficients are higher in wavy flow than in steady flow as the wake from one half wave cycle is washed back over the cylinder in the next half cycle and therefore the forces on rectangular cylinder in wave are dominated by the effects of wake re-encounter. High drag forces are associated with the shedding of strong vortices, which are prominent in the wake re-encounter. The drag coefficients are expected to reach the steady flow value only at high KC numbers as the returning wake has almost decayed. The drag coefficients of vertical cylinders are found to vary substantially with aspect ratio at low KC numbers. Drag coefficients for horizontal cylinders in horizontal and vertical directions are shown in Fig. B.3 and B.4 respectively. Horizontal drag coefficient do not show much variation with aspect ratio and the vertical drag coefficients show some variation with aspect ratio. C_{DY} for aspect ratio = 3/4 is higher than other aspect ratios. C_{DY} for square cylinder show lower values.

The inertia coefficients for all vertical cylinders (Fig. B.2) approach their potential flow values at low KC. At very low KC numbers, i.e., close to zero, there is a tendency towards an attached and undisturbed flow with vortex strength tending to zero. Inertia coefficients increase with KC up to the range of KC tested for each cylinder. Inertia coefficients are also found to increase with aspect ratio. A lower inertia coefficient is observed for lowest aspect ratio = 1/2 and a higher inertia coefficient is obtained for the highest aspect ratio = 2/1 and this is consistent with the added mass of the cylinders.

The inertia coefficients for the horizontal cylinder (Fig. B.5 & B.6) show similar trend for all aspect ratios, i.e., the values of the coefficients decrease rapidly with

increasing KC number and it is believed that this reduction is caused by the rotating separated vortices around the cylinders. The stronger the circulation of flow around the cylinder the more rapid is the reduction of inertia coefficients.

Root mean square in-line force for vertical cylinders is shown in Fig. B.7. It can be seen that rms force increases with increase in aspect ratio of the cylinder. For a given value of KC, cylinder with aspect ratio = 1/2 showed the lowest value and aspect ratio = 2/1 showed the highest rms value. This plot also shows that the square cylinder and cylinder with aspect ratio = 4/3 experience similar forces for a given value of KC number. The rms lift force coefficients for the vertical cylinder is shown in Fig.B.8, the variation of lift coefficient with aspect ratios is such that the square cylinder and the cylinder with aspect ratio = 4/3 are found to have the largest lift force coefficients.

Root mean square forces in horizontal and vertical directions, for the horizontal cylinders are shown in Fig. B.9 and B.10. The square cylinder had lowest value of rms coefficients. Aspect ratio = 3/4 had the largest value and aspect ratio = 1/2 was found to be in between the value for the square cylinder and the cylinder with aspect ratio = 3/4.

The inertia coefficients for vertical cylinders are fitted with best-fit equations and are shown in Figs. B.11 to B.12. Similarly a trail has been made to fit the inertia coefficients obtained for horizontal cylinders by the empirical equations in a form $C_M = C_{mo} - R(KC)^2$, expressed by Chaplin and Retzler (1992) and the resulting curves are shown in Figs. B.13 to B.15. The best fitting equations are given as:

For vertical cylinders:

$$C_M = 2.6711(KC)^{0.0924} \qquad \text{for aspect ratio =1.0} \qquad (6.25)$$

$$C_M = 2.1512(KC)^{0.079} \qquad \text{for aspect ratio =1/2} \qquad (6.26)$$

$$C_M = 3.433(KC)^{0.0699} \quad \text{for aspect ratio =2/1} \quad (6.27)$$

$$C_M = 2.2463(KC)^{0.0659} \quad \text{for aspect ratio =3/4} \quad (6.28)$$

$$C_M = 2.617(KC)^{0.092} \quad \text{for aspect ratio =4/3} \quad (6.29)$$

For horizontal cylinder:

For aspect ratio = 1.0

$$C_{MX} = 2.2 - 0.08(KC)^2 \quad (6.30)$$

$$C_{MY} = 2.2 - 0.08(KC)^2 \quad (6.31)$$

For aspect ratio = 1/2

$$C_{MX} = 1.67 - 0.25(KC)^2 \quad (6.32)$$

$$C_{MX} = 3.14 - 0.25(KC)^2 \quad (6.33)$$

For aspect ratio = 3/4

$$C_{MX} = 1.90 - 0.4(KC)^2 \quad (6.34)$$

$$C_{MX} = 2.40 - 0.2(KC)^2 \quad (6.35)$$

The above expressions can be used to calculate the inertia loading on vertical and horizontal cylinders within the range of KC numbers presented in this thesis.

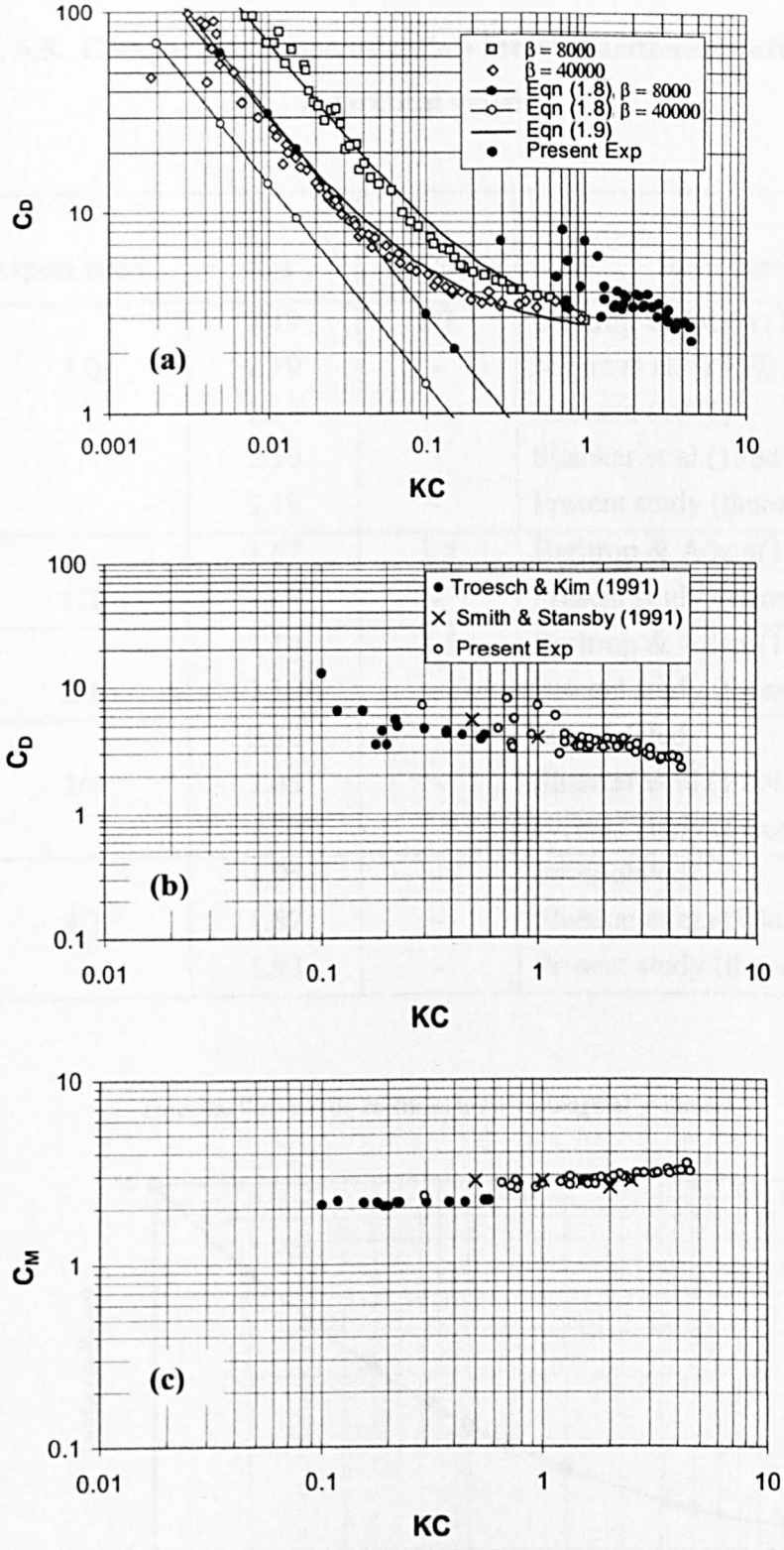

Fig. 6.306 (a) Drag coefficients for a square cylinder; experimental and predictions [Bearman and Russell (1997)], present experimental coefficients are shown by filled circles; (b) and (c) theoretical drag and inertia coefficients [Troesch & Kim (1991), $\beta = 23200$; Smith & Stansby (1991), for $\beta = 213$] and present experimental values are shown by empty circles.

Table. 6.5. Comparison of potential flow inertia coefficients with present theoretical values

Aspect ratio	C_M	C_D	Reference
1.0	2.19	2.2	Barltrop & Adam (1991)
	2.19	-	Myers et al. (1969)
	2.14	-	Issacson (1978)
	2.10	-	Shankar et al.(1984)
	2.18	-	Present study (theory)
1/2	1.67	1.5	Barltrop & Adam(1991)
	1.68	-	Present study (theory)
2/1	3.14	2.5	Barltrop & Adam(1991)
	3.10	-	Present study (theory)
3/4	2.50	-	Interpolated
	2.45	-	Shankar et al.(1984)
	2.52	-	Present study (theory)
4/3	1.95	-	Interpolated
	1.87	-	Shankar et al.(1984)
	1.93	-	Present study (theory)

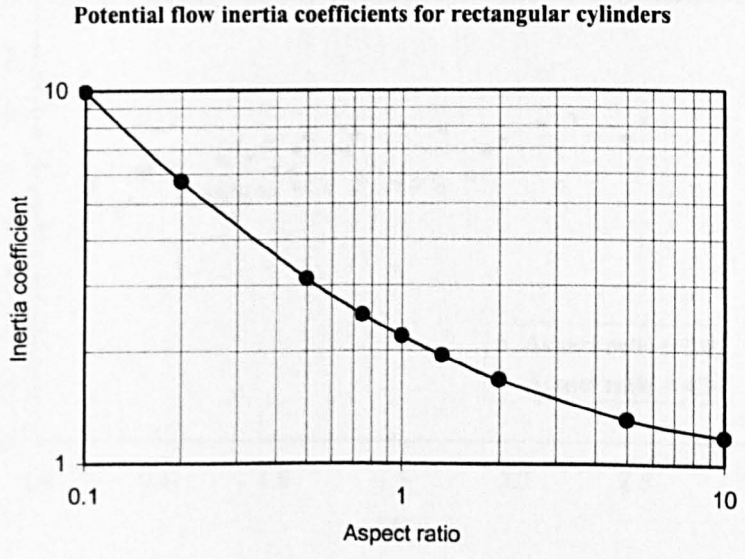

Fig. 6.307 Potential flow inertia coefficients with aspect ratio [Barltrop & Adams (1991)]

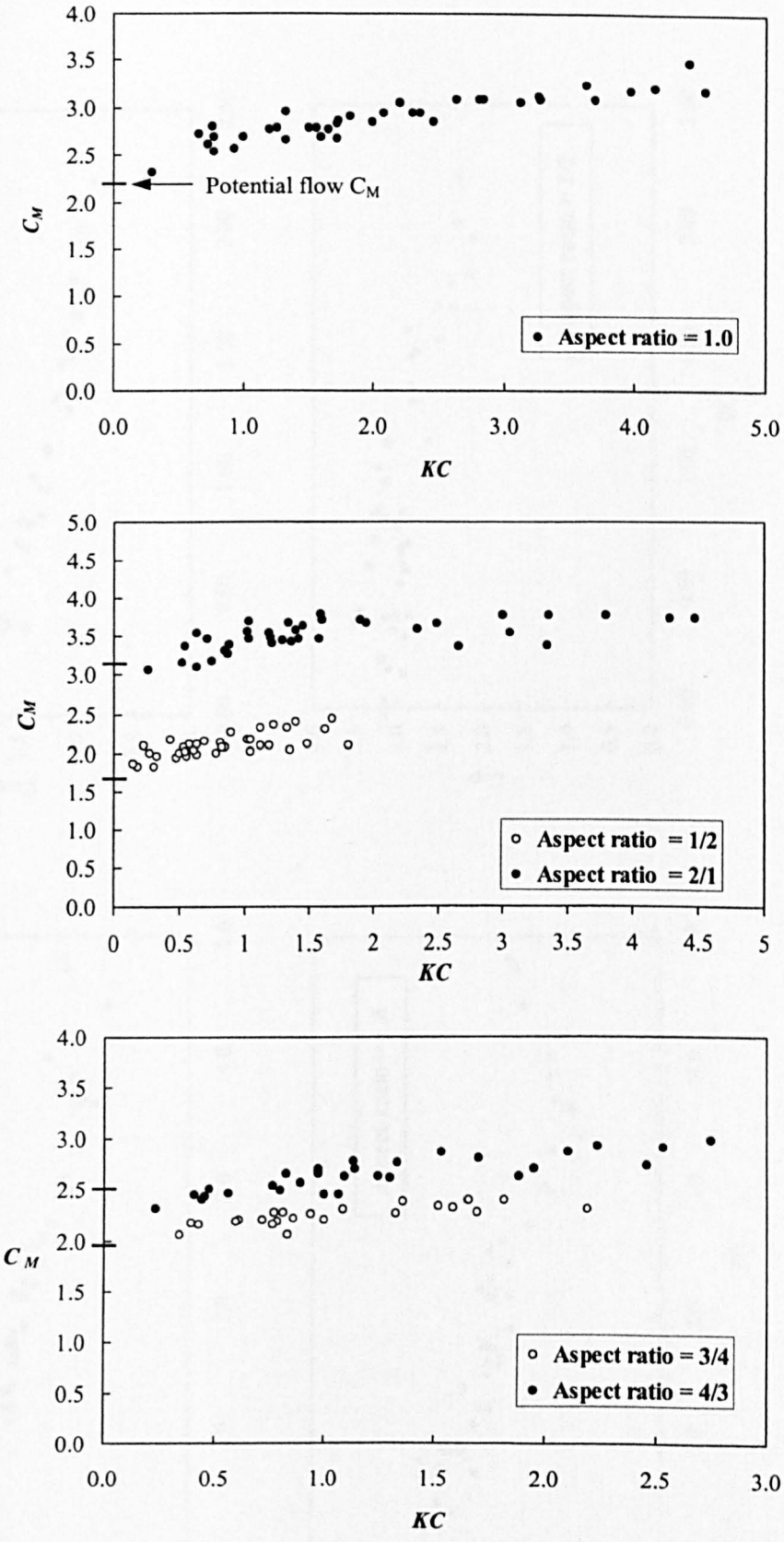

Fig. 6.308 Inertia coefficients for vertical square and rectangular cylinders: The potential flow inertia coefficients values are marked by a short horizontal line at $KC = 0.0$

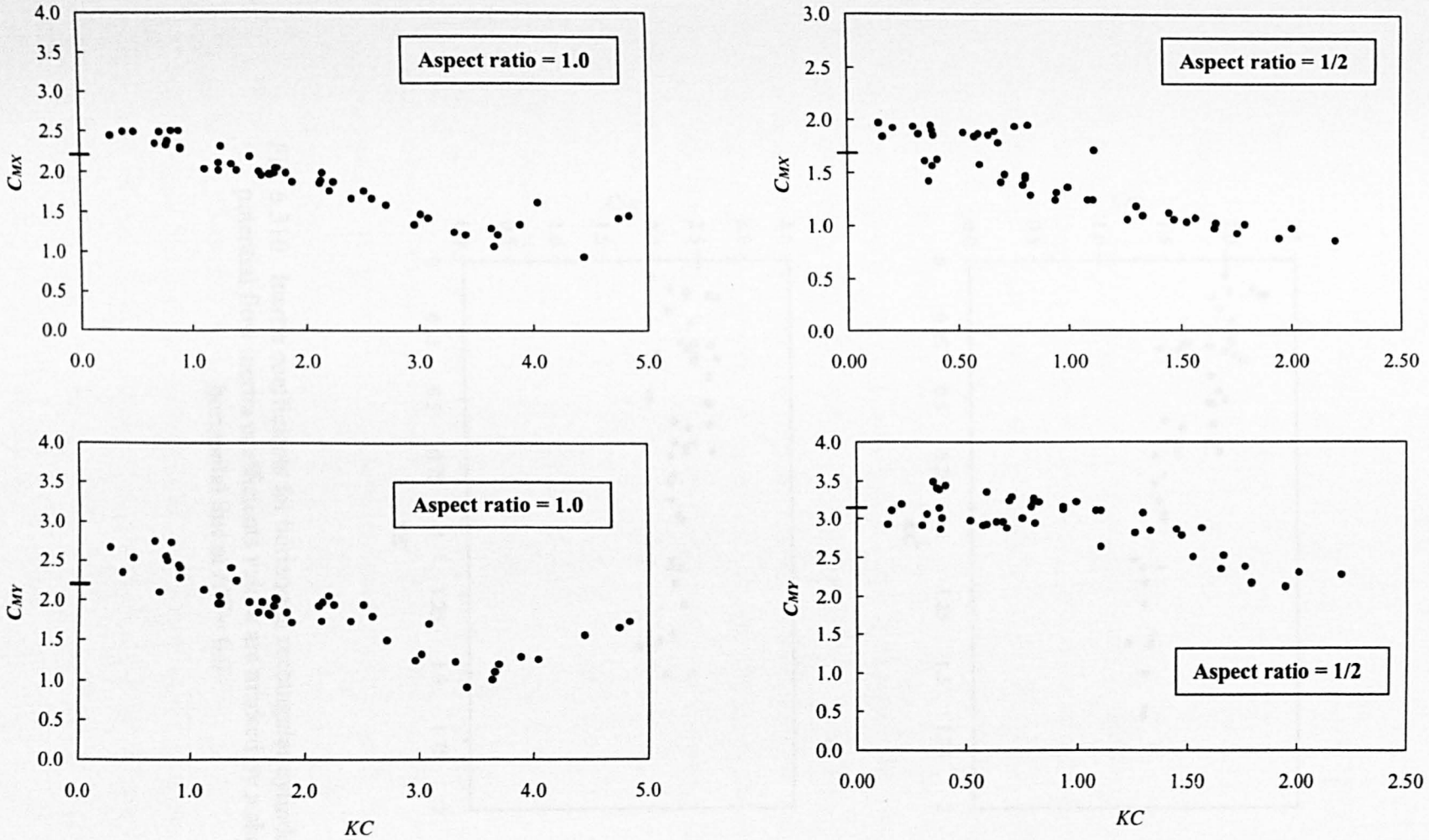

Fig. 6.309 Inertia coefficients for horizontal square and rectangular cylinders: The potential flow inertia coefficients values are marked by a short horizontal line at $KC = 0.0$

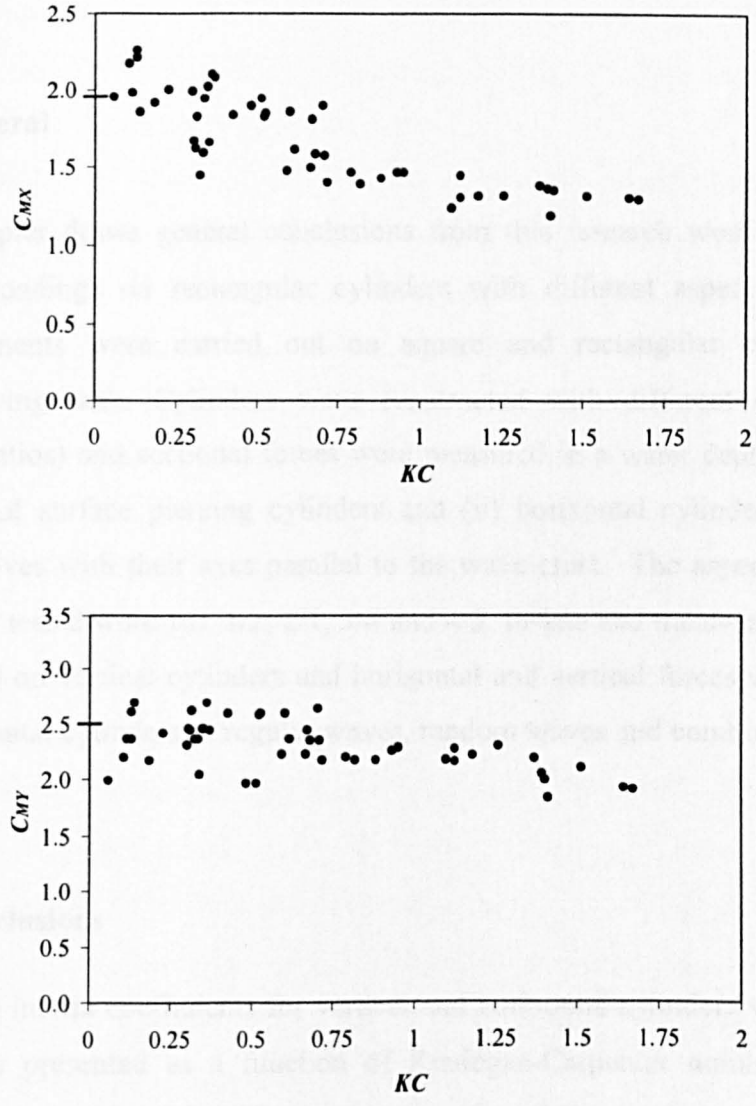

Fig. 6.310 Inertia coefficients for horizontal rectangular cylinders: the potential flow inertia coefficients values are marked by a short horizontal line at $KC = 0.0$

CHAPTER 7

CONCLUSIONS

7.1 General

This chapter draws general conclusions from this research work on wave and current loadings on rectangular cylinders with different aspect ratios. Force measurements were carried out on square and rectangular cylinders in a wave/towing tank. Cylinders were constructed with different cross sections (aspect ratios) and sectional forces were measured in a water depth of 2.2 m on (i) vertical surface piercing cylinders and (ii) horizontal cylinders, submerged under waves with their axes parallel to the wave crest. The aspect ratios of the cylinders tested were 1.0, 1/2, 2/1, 3/4 and 4/3. In-line and transverse forces were measured on vertical cylinders and horizontal and vertical forces were measured on horizontal cylinders in regular waves, random waves and combined waves and currents.

7.2 Conclusions

Drag and inertia coefficients for vertical and horizontal cylinders were evaluated and were presented as a function of Keulegan-Carpenter numbers (KC) and frequency parameter (β). The maximum value of KC number obtained is about 4.5 and the Reynolds number varied from 6.397×10^3 to 1.18×10^5. Maximum force coefficients and root mean square force coefficients were also calculated and reported. The effect of varying the depth of submergence of the cylinder on force coefficients has also been investigated for two relative depths of submergence, d/h = 4.68 and 2.68. The salient conclusions drawn from this investigation are summarized below:

(1) The drag coefficients at low KC numbers exhibited large values and these coefficients decreased sharply with increase in KC number for all cylinders. The high drag coefficients at low KC numbers are associated with the flow separation and the first appearances of vortices [Bearman et al. (1979,1984,1985)], which take place for sharp edged rectangular cylinders at very low KC numbers.

(2) At lower values of KC number, the inertia coefficients approach its potential flow values for both vertical and horizontal cylinders. Inertia coefficients obtained for vertical cylinders are substantially different from those obtained for horizontal cylinders. For vertical cylinders, inertia coefficients increased with increase in KC numbers for all aspect ratios. For horizontal cylinders, inertia coefficient decreased with increase in KC number, due to presence of a circulating flow [Chaplin (1984)] around the cylinders, up to the range of KC number tested. For the square cylinder, where a comparatively large KC number is obtained, the inertia coefficient decreased up to a value of KC number around 3.5 to 3.75, then further increase in KC resulted in an increase in the inertia coefficient. Comparisons of the inertia coefficients with similar data obtained by other investigators show good agreement. Some empirical formulae are presented for the calculation of inertia forces at low KC numbers.

(3) Frequency parameter, β did not have much effect on measured drag and inertia coefficients, suggesting that the force coefficients are free from Reynolds numbers effect.

(4) Root mean square in-line forces (for vertical cylinders) and root mean square horizontal and vertical forces (for horizontal cylinders) show a similar trend to the drag coefficients with less scatter.

(5) Larger values of lift force coefficients for vertical cylinder are observed at low KC numbers and it decreased with increase in KC numbers. The first frequency component of the lift force coefficient shows a regular trend with KC and is found to be higher than 2^{nd},3^{rd},4^{th} & 5^{th} frequency components of the lift forces.

(6) For horizontal cylinders, changing the depth of submergence of the cylinder affected the inertia coefficients, with some evidence of lower inertia coefficients at smaller relative depth of submergence.

(7) Force coefficients obtained for random wave forces are consistent with the coefficients obtained from regular wave force measurements, for both vertical and horizontal cylinders.

(8) In combined waves and currents, the inertia coefficient is strongly affected by the presence of a current and the values of inertia coefficient in waves and currents are generally smaller than the inertia coefficients obtained in waves, irrespective of current magnitude and direction. The drag coefficients in waves and currents are lower than drag coefficients derived from waves alone for vertical cylinders.

(9) The measured peak forces for all the cylinders are larger than the Morison forces at high KC numbers. The maximum under prediction of forces are observed in waves and currents. This difference may be a result of poor estimate of wave kinematics or due to a more complicated loading.

(10) Measurement of pressure distribution around the cylinder indicates that the wave-induced pressure is dependent on relative water depth and wave steepness. The pressure distribution around the vertical cylinder is different from horizontally submerged cylinder.

(11) Estimates of wave run-up on rectangular cylinders are obtained through simple empirical correlation. Wave run-up is influenced by aspect ratio of the cylinder.

(12) Normalised forces, inertia coefficients and phase angles are studied in the diffraction regime for vertical and horizontal cylinders for all the aspect ratios. Comparison of the diffraction force results with the present experiments show reasonable agreement.

(13) The phase shift analysis using the phase calculated from diffraction analysis and the measured force phase indicate a large reduction of drag coefficients. The phase shifted inertia coefficients are generally larger than the inertia coefficients derived prior to applying the phase correction.

(14) The contribution of drag coefficients to the total loading is less than 2% for vertical cylinders (aspect ratio = 1.0 & 1/2) and 5.4% for horizontal cylinder (aspect ratio = 1/2) and this indicate that although the drag coefficients appear to have large values, its contribution to the total loading is less and the inertia forces are dominant.

7.3 Suggestions for Future Research

The force coefficients presented in this study are based on the wave kinematics obtained using linear wave theory, as no instrument is available to measure the wave particle kinematics. If the ambient flow were measured directly, the obtained results would not be subjected to any additional uncertainties associated with the use of linear wave theory. Hence the future experiments may be performed with direct velocity measurements. The pattern of vortex formation and shedding of vortices around rectangular cylinders in the combination of waves and current flow are still unexplored and therefore flow visualisation studies would be useful to help us to understand the complex flow behaviour and the resulting forces. The force coefficients presented in the present study corresponding to waves approaching from only one angle to the cylinder axis and it would be interesting to investigate the various angle of wave incidence on the cylinders. Investigation on force coefficients at high *KC* numbers would also be useful.

REFERENCES

STEADY FLOW

Bearman, P.W., and Trueman, D.M., 1972, An investigation of the flow around rectangular cylinders, *The Aeronautical Quarterly*, Vol. 23, 229 – 237.

Bostock, B.R., and Mair, W.A., 1972, Pressure distributions on forces on rectangular and D-shaped cylinders, *The Aeronautical Quarterly*, Vol. 23, 1 - 6.

Courchesne, J., and Laneville, A., 1979, A comparison of correction methods used in the evaluation of drag coefficient measurements of two-dimensional rectangular cylinders, *Trans. A.S.M.E., Jl. of Fluids Engineering*, Vol. 101, 506 – 510.

Davies, R.W., Moore, E.F., and Purtell, L.P., 1984, A numerical-experimental study of confined flow around rectangular cylinders, *The Phys. of Fluids*, Vol. 27, No. 1-12, 46 – 59.

Delany, N.K., and Sorensen, N.E., 1953, Low speed drag of cylinders of various shapes, NACA TN 3038.

Fox, T.A. and West, G.S. 1990. On the use of end plates with circular cylinders, *Experiments in Fluids*, Vol.9, part 4, 237-239.

Hoshino, K., Kato, S., Saito, M and Sato, H. 1993. Hydrodynamic forces acting on finite-length circular cylinder oscillating in a uniform flow, *Proc. of the third International Offshore and Polar Engineering Conference*, Singapore, 6-11, June 1993, Vol.3, pp.242-253.

Kwok, K.C.S., 1983, Effects of turbulence on the pressure distribution around a square cylinder and possibility of reduction, *Jl. Fluids Engineering*, Vol. 105, 140 – 145.

Laneville, A., and Williams, C.D., 1979, The effect of intensity on large scale turbulence on the mean pressure and drag coefficients of 2D rectangular cylinders, *Proc. of the 5th Int. Conf. on Wind Engineering*, 397 – 404.

Laneville, A., and Yong, L.Z., 1983, Mean flow patterns around two-dimensional rectangular cylinders and their interpretation, *Jl. of Wind Engineering and Industrial Aerodynamics*, Vol. 14, 387 – 398.

Laneville, A., Gartshore, I.S., and Parkinson, G.V., 1975, An explanation of some effects of turbulence on bluff bodies, *Proc. 4th Int. Conf. on Wind Effects on Buildings and Structures*, London.

Nakaguchi, H., Hashimoto, K., and Muto, S., 1968, An experimental study on aerodynamic drag of rectangular cylinders, *Jl. of Japan Soc. for Aero and Space Sciences*, Vol. 16, 1-5.

Nakamura, Y., and Mizota, T., 1975, Unsteady lifts and wakes of oscillating rectangular prisms, *Proc. A.S.C.E., Jl. of Engineering Mechanics Div.*, Vol. 101, 855 – 871.

Obasaju, E.D., 1983, An investigation of the effects of incidence on the flow around a square section cylinder, *Aeronautical Querterly*, 243 – 259.

Okajima, A. 1982. Strouhal numbers of rectangular cylinders, *Jl. of Fluid Mechanics*, Vol. 123, pp. 479-398.

Okajima, A., 1982, Strouhal numbers of rectangular cylinders, *Jl. of Fluid Mechanics*, Vol. 123, 379 – 398.

Okajima, A., Mizota, T., and Tanida, Y., 1983, Observation of flow around rectangular cylinders, *Proc. 3rd Int. Symp. on Flow Visualisation*, Ann Arbor, U.S.A., 381 – 386.

Okamoto. S and Yagita. M. 1984. Flow past circular cylinder of finite length placed normal to ground plane in uniform shear flow, *Bulletin of JSME*, Vol.27, No.229, July 1984, pp.1454-1459.

Otsuki, Y., Washizu, K., Tomizawa, H., and Oya, A., 1974, A note on the aeroelastic instability of a prismatic bar with square section, *Jl. of Sound Vibration*, Vol. 34, 233 – 248.

Roshko, A., 1955, On the wake and drag of bluff bodies, *Jl. of Aeronautical Sciences*, 124 – 132.

Roshko, A., 1961, Experiments on the flow passed a circular cylinder at very high Reynolds number, *Jl. of Fluid Mechanics*, Vol. 10, 345 – 356.

Roshko, A., and Fiszdon, W., 1969, On the persistence of transition in the near wake, Problems of hydrodynamic and continuum mechanics, *Society of Industrial and Applied Mathematics*, Philadelphia, 606 – 616.

Sachs, P. 1978. *Wind forces in Engineering*, 2nd Edition, Pergamon Press.

Stansby, P.K. 1974. The effects of end plates on the base pressure coefficient of a circular cylinder, *Aeronautical Jl.* 78,36-37.

Taneda, S., 1963, The stability of two dimensional laminar wakes at low Reynolds numbers, *Jl. of Phys. Soc.* Japan, Vol. 18, 288.

Taneda, S.,1959, Downstream development of the wakes behind cylinders, *Jl. of Phys. Soc.* Japan, Vol. 14, 843.

Vickery, B.J., 1966, Fluctuating lift and drag on a long cylinder of square cross-section in a smooth and in a turbulent stream, *Jl. of Fluid Mechanics*, Vol. 25, 481 – 494.

PLANAR OSCILLATORY AND WAVY FLOWS

Arai, S., 1993, Forces and circulation of horizontal cylinders submerged in regular waves, *Proceedings of the Third International Offshore and Polar Engineering Conference*, Singapore, 6-11 June ,Vol.3, 288-293.

Arai, S., 1995, Forces on and flows around a horizontal rectangular cylinder submerged in regular waves, *Proceedings of the Fifth International Offshore and Polar Engineering Conference, The Hague*, The Netherlands, 6-11 June, Vol.3, 348-355.

Barltrop, N.D.P., and Adams, A.J., 1991, Dynamics of fixed marine structures, *The Marine Technology Directorate Limited*, Butterworth Heinemann.

Bea, R.G., and Lai, N.W., 1978, Hydrodynamic loading on offshore platforms, *Proceedings of the 10th Annual Offshore Technology Conference*, Vol1, OTC 3064.

Bearman, P and Russell, M. 1997. Measurements of hydrodynamic damping of bluff bodies with applications to the prediction of viscous damping of TLP hulls, *Twenty-First Symposium on Naval Hydrodynamics*, National academic press, Trondheim, Norway, pp.622-634.

Bearman, P.W., 1988, Wave loading experiments on circular cylinders at large scale, *Proc. of the International Conference on Behaviour of Offshore Structures*, Norway, 471- 487.

Bearman, P.W., Chaplin, J.R., Graham, J.M.R., Mackwood, P., Otta, A., Subbiah, K., and Wouters, J., 1994, Loading on a cylinder at large scale in irregular waves with currents, *International Symposium on Waves Physical and Numerical Modelling*, Canada, Vol.3, 1133-1142.

Bearman, P.W., Graham, J.M.R., Obasaju, E.D., and Drossopoulos, G.M., 1984, The influence of corner radius on the forces experienced by cylindrical bluff bodies in oscillatory flow, *Applied Ocean Research*, Vol.6, 83-89.

Bearman, P.W., Graham, J.M.R., Obasaju, E.D., and Drossopoulos, G.M., 1985, Forces on cylinders in viscous oscillatory flow at low kuelegan-carpenter numbers, *Jl. of Fluid Mechanics*, Vol.154, 337-365.

Bearman,P.W., Graham, J.M.R., and Singh, S., 1979, Forces on cylinders in harmonically oscillating flow, *Proc. Symp. on Mechanics of wave induced forces on cylinders*, Bristol (UK), 437-449.

Bidde, D.D., 1971, Laboratory study of lift forces on circular piles, *Jl. waterways, Harbors and Coastal Engineering Div., ASCE*, Vol.97, No. WW4, 595-614.

Borgman, L.E., 1972, Statistical models for ocean waves and wave forces, *Advances in Hydroscience*, Vol. 8, 139-181.

Borthwick, A.G.L. 1990. Circumferential pressures on fixed vertical cylinder in waves, *Proc. Instn Civ. Engrs*, Part 2, 89, June, pp.143-162.

Burrows, R., Tickell, R.G., Hames, D., and Najafian, G., 1997, Morison wave force coefficients for application to random seas, *Applied Ocean Research*, Vol.19, 183-199.

Chakrabarti, S.K., 1987, Hydrodynamics of offshore structures, *Computational Mechanics Publications*.

Chakrabarti, S.K., 1988, Forces on vertical cylinder due to random waves, *Jl. of Waterway, Port, Coastal, and Ocean Engineering, ASCE* Vol.114, No.3, 267-279.

Chakrabarti, S.K., 1988, Forces on vertical cylinder due to random waves, *Jl. of Waterway, Port, Coastal and Ocean Engineering*, Vol.114, No.3, 267-280.

Chakrabarti, S.K., 1990, Nonlinear methods in offshore engineering, *Elsevier Science Publishers*, New York.

Chan, H.S., 1990, A three-dimensional technique for predicting first and second order hydrodynamic forces on a marine vehicle advancing in waves, Ph.D. Thesis, *Department of Naval Architecture and Ocean Engineering*, University of Glasgow.

Chaplin, J.R., 1984a, Nonlinear forces on a horizontal cylinder beneath waves, *Jl. of Fluid Mechanics.*, Vol.147, 449-464.

Chaplin, J.R., 1984b, Mass transport around a horizontal cylinder beneath waves, *Jl. of Fluid Mechanics*, Vol. 140, 175-187.

Chaplin, J.R., 1985, Morison inertia coefficients in orbital flow, *Jl. of Waterway Port Coastal and Ocean Engg. Div., A.S.C.E.*, Vol.111, 201-215.

Chaplin, J.R., 1988a, Loading on a cylinder in uniform oscillatory flow: Part I – planar oscillatory flow, *Applied Ocean Research*, 1988, Vol.10, N0.3, 21-128.

Chaplin, J.R., 1988b, Loading on a cylinder in uniform oscillatory flow: Part II – elliptical orbital flow, *Applied Ocean Research*, 1988, Vol.10, N0.4, 199-206.

Chaplin, J.R., 1988c, Non linear forces on horizontal cylinders in the inertia regime in waves at high Reynolds numbers, *Proc. of BOSS Conf.*, Vol.2, 505-518.

Chaplin, J.R., 1997, Large scale horizontal cylinder forces in waves and currents, *Applied Ocean Research*, Vol.19, 211-223.

Chaplin, J.R., and Retzler, C.H., 1992, Fluid loading on pontoon sections, *Health and Safety Executive*, OTI 91 551.

Chaplin, J.R., and Retzler, C.H., 1993, Influence of waves and current on separation and forces, *Health and Safety Executive*, OTH 93 409.

Chaplin, J.R., and Subbiah. K., 1996, Wave and current loads on large scale horizontal cylinders, *International Conference in Ocean Engineering, COE'96*, IIT Madras, India, 199- 203.

Clauss, G., Lehmann, E., and Ostergaard, C., 1992, *Offshore Structures, Vol.I*, Springer-Verlag London Limited, Germnay.

Davies, M.J.S, Graham, J.M.R and Bearman, P.W. 1990. In-line forces on fixed cylinders in regular and random waves, *Environmental Forces on Offshore Structures and their Predictions*, Advances in Underwater Technology, Ocean Science and Offshore Engineering, Vol. 26, pp.113-136.

Davies, M.J.S., Graham, J.M.R., and Bearman, P.W., 1990, In-line forces on fixed cylinders in regular and random waves, Environmental forces on offshore structures and their predictions, Vol.26, *Society for Underwater Technology, Kluwer Academic Publishers*, 113-136.

Dean, R.G., 1976, Methodology for evaluating suitability of wave and wave force data for determining drag and inertia coefficients, *Proc. of 1st the International Conference on Behaviour of Off-shore Structures, BOSS'76*, 40- 64.

Dean, R.G., and Dalrymple, R. A., 1992, Water wave mechanics for engineers and scientists, *Advanced Series on Ocean Engineering*, Vol. 2, World Scientific.

Garrison, C.J., Field, J.B., and May, M.D., 1977, Drag and inertia forces on a cylinder in periodic flow, *Jl. of Waterway, Port Coastal and Ocean Division., Proc. A.S.C.E.*, Vol.103, No.WW2.

Graham, J.M.R., 1979, Forces on cylindrical bodies on oscillatory flow at low Keulegan-Carpenter numbers, *Pro.Symp.on mechanics of wave Induced Forces on cylinders*, Bristol (UK), 461-474.

Graham, J.M.R., 1980, The forces on sharp edged cylinders in oscillatory flow at low Keulegan-Carpenter numbers, *Jl. Fluid Mech.*, Vol.97, 331-346.

Hallermeier, R.J., 1976, Nonlinear flow of wave crests past a thin pile, *Jl. of Waterway, Harbours Coastal Engg Div., ASCE* 102, 365-377.

Hamel-Derouich, D., 1992, Forces on vertical rectangular cylinders in wavy flow and in combined wave and current flow at low Keulegan-Carpenter numbers, *Pro. Int, Symp. Offshore Mech. and Arctic Engg., A.S.M.E.*, 79-86.

Hayashi, K., and Chaplin, J.R., 1989, Lift forces on a rigid vertical cylinder in waves, *Pro. of 8th International conference on Offshore Mechanics and Arctic Engg.*, The Hague, 279-287.

Ikeda, Y., Otsuka, K., and KiKu, T., 1990, Wave forces acting on a horizontal circular cylinder moving at a constant speed, *Proc. of the first Pacific Asia Offshore Technology Conference*, 307-316.

Ikeda, Y., Otsuka, K., and Tanaka, N., 1988a, Wave forces acting on horizontally submerged cylinders in regular waves at low kc number, *Report of Department of Naval Architecture, University of Osaka Prefecture*, Japan, Report No. 00410.

Ikeda, Y., Otsuka, K., and Tanaka, N., 1988b, Viscous forces acting on a semi submersible, *Seventh International Conference on Offshore Mechanics and Arctic Engineering,* Houstan, Texas, Feb 7-12, 101-108.

Isaacson, M., 1979, Wave forces on rectangular caissons, *Proc. Civil Engg. Oceans IV, ASCE,* San Francisco, Vol.I, 518-530.

Isaacson, M., and Maull, D.J., 1976, Transverse forces on vertical cylinders in waves, *ASCE*, Vol.102, WW1, paper no. 11934, 49-60.

Isaacson, M., Baldwin, J., and Niwinski, C., 1991, Estimation of drag and inertia coefficients from random wave data, *Jl. of Offshore Mechanics and Arctic Engineering,* Vol.113, 128-136.

Iwagaki, Y., and Asano, T., 1984, Hydrodynamic forces on a circular cylinder due to combined wave and current loading, *Coastal Engineering*, 2857-2874.

Jothi Shankar, N., Cheong, H.F., and Subbiah, K., 1987, Forces on a smooth submarine pipeline in random waves – a comparative study, *Coastal Engineering,* Vol.11, 1987, 89-218.

Kasahara, Y., Keterayama, W., and Shimazaki, K., 1987, Wave forces acting on rough circular cylinders at high Reynolds numbers, *19th Offshore Technology Conference,* 153-160.

Keulegan, G.H., and Carpenter, L.H., 1958, Forces on cylinders and plates in an oscillating fluid, *Jl. of Research of the National Bureau of Standards,* Vol.60, 423-440.

Koterayama, W., 1984, Wave forces acting on a circular cylinder with a constant forward velocity, *Ocean Engineering*, Vol.11, No.4, 363-379.

Koterayama, W., and Hu, C., 1995, Wave forces on horizontal cylinders at low Keulegan-Carpenter and Reynolds numbers, *Proc. of the 5th International Offshore and Polar Engineering Conference,* The Hague, The Netherlands, 189-195.

Koterayama, W., and Nakamura, M., 1992, Drag and inertia force coefficients derived from field tests, *Proc. of the second International Offshore and Polar Engineering Conference,* San Francisco, 398-405.

Kriebel, D., 1992a, Non linear wave interaction with a vertical circular cylinder. Part II : wave runup, *Ocean Engineering,* Vol.19, No.1, 75-99.

Kriebel, D., 1992b, Non linear wave runup on large circular cylinders, *Proc. of Civil Engg. in the Oceans,* ASCE, 173-187.

Li, Y., and He, M., 1995, The in-line wave forces on small square cylinder, *Proc. of the Fifth International Offshore and Polar Engineering Conference*, The Hague, The Netherlands, 289-296.

Li, Y., and Ye, Z., 1990, Random wave and current force on vertical cylinder, *Applied Ocean Research,* Vol.12, No.3, 126-133.

Li, Y.C., and Kang, H.G., 1992, Wave current forces on slender circular cylinder, *Proc. Int. Symp. Offshore Mech. and Arctic Engg.*, A.S.M.E., 117-125.

Lighthill, M.J., 1979, Waves and hydrodynamic loading, *Second Int. Conf. on Behaviour of Offshore Structures,* Imperial College, London, 1- 40.

Marine Research Review 11, 1997, Drag and Inertia Coefficient Data for Cylinders, Marine Technology Directorate, Edited by Sharon J. Clark, MTD Ltd, London, 1997.

Maull, D.J., and Milliner, M.G., 1978, Sinusoidal flow past a circular cylinder, *Coastal Engg.* Vol.2, No.2, Oct'78.

Maull, D.J., and Norman, S.G., 1979, A horizontal circular cylinder under waves, *Proc. Symp. on Mechanics of Wave Induced Forces on Cylinders*, Bristol (UK), 359-378.

Moe, G., and Verley, R., 1980, Hydrodynamic damping of offshore structures in waves and current, *Proc. of the Offshore technology Conference*, 37-44.

Morison, J.R., O'Brien, M.P., Johnson, J.W., and Schaaf, S.A., 1950, The force exerted by surface waves on piles, *Petroleum Transactions*, AIME, 189, 149 –154.

Nakamura. M, Koterayama. W and Hoshino. K. 1991. Three dimensional effects on hydrodynamic forces acting on an oscillating finite-length circular cylinder, *Proc. of the First International Offshore and Polar Engineering Conference*, United Kingdom, 11-16 August, 1991.

Niedzwecki, J.M., and Huston, J.R., 1992, Wave interaction with Tension Leg Platforms, *Jl. of Ocean Engg.*, Vol.19. No.1, 21-37.

Okajima, A, Matsumoto,T and Kimura, S. 1998. Force measurements and flow visualization of circular and square cylinders in oscillatory flow, *JSME International Journal, Series B*, Vol.41, No.4, pp. 796-805.

Pearcey, H.H., 1979, Some observations on fundamental features of wave-induced viscous flows past cylinder, *Proc. Symp. on Mechanics of Wave Induced Forces on Cylinders*, Bristol (UK), 1-54.

Pearcey, H.H., 1990, On the effects of wake re-encounter for wave forces on cylinder, *Soc.for Underwater Technology Conference*, 2091-2101.

Rahman, M., 1987, A design method of predicting second order wave diffraction caused by large offshore structures, *Jl. of Ocean Engg.*, Vol. 14, No. 1, 1 – 18.

Ramberg, S.E., and Niedzwecki, J.M., 1979, Some uncertainties and errors on wave force computations, *Proc. of Offshore Technology Conference*, 2091-2101.

Sarpkaya, T., 1975, Forces on cylinders and spheres in an oscillating fluid, *Jl of Applied Mechanics*, ASME, Vol.42, 32-37.

Sarpkaya, T., 1976a, Vortex shedding and resistance in harmonic flow about smooth and rough circular cylinders at high Reynolds numbers, *Naval Postgraduate School*, Monterey, California, NPS – 59SL 76021, Feb 1976.

Sarpkaya, T., 1976b, In-line and transverse forces on smooth and sand roughened cylinders in oscillatory flow at high Reynolds numbers, *Naval Postgraduate School*, Monterey, California, NPS – 69SL 76062, June 1976.

Sarpkaya, T., and Isaacson, M., 1981, Mechanics of wave forces on offshore structures, *Van Nostrand Reinhold Company*.

Sarpkaya, T., and Storm, M., 1985, In-line force on a cylinder translating in oscillatory flow, *Applied Ocean Research*, Vol.7, No.5, 188-196.

Sarpkaya, T., Bakmis, C., and Storm. M., 1984, Hydrodynamic forces from combined wave and current flow on smooth and rough circular cylinders at high Reynolds numbers, *OTC* 4830, Vol.3, May 1984, 455-462.

Shankar, N.J., Balendra, T., and Soon, C.E., 1983, Wave forces on large vertical cylinders of square and rectangular sections, *Civil Engineering Transactions*, The Institution of Engineers, Australia.

Singh, S., 1979, Forces on bodies in oscillatory flow, *Ph.D. Thesis*, Imperial College, University of London.

Smith, P.A. and Stansby, P.K. 1991. Viscous oscillatory flows around cylindrical bodies at low Keulegan-Carpeneter numbers using the vortex method, *Jl. of Fluids and Structures*, 5, pp.339-361.

Svendsen, I.A., and Jonsson, I.G., 1976, Hydrodynamics of coastal regions, *Technical University of Denmark*, 282.

Tanaka, N., Ikeda,Y., and Nishino, K., 1982, Hydrodynamic viscous force acting on oscillating cylinders with various shapes, *Proc.6th Symp. Marine Technology,* Soc. Naval Arch. of Japan.

Tanaka, N., Ikeda,Y., Himeno, Y., and Fukutomi, Y. 1980, Experimental study on hydrodynamic viscous force acting on oscillating bluff body, *Jl. of the Kansai Soc. of Naval Architects,* Vol.179, 35-43.

Teng, B., and Li.Y., 1990, Wave-current force coefficients on inclined cylinder and a new estimation method, *China Ocean Engineering,* Vol.4, No.3, 283-296.

Teng, C.C., and Nath, J.H., 1985, Forces on horizontal cylinder towed in waves, *Jl. Waterway Port Coastal and Ocean Engg. Div.,* A.S.C.E., Vol.111, No.6, 1022-1040.

Troesch, A.W. and Kim, S.K. 1991. Hydrodynamic forces acting on cylinders oscillating at small amplitudes, *Jl. of Fluids and Structures*, 5, pp. 111-124.

Vugts, J.H., 1979, A review of hydrodynamic loads on offshore structures and their formulation, BOSS'79, 693-708.

Yu, Y., and Miso, X., 1989, Transverse forces on vertical pile in regular and irregular waves, *Pro. of 8th International conference on Offshore Mechanics and Arctic Engg.*, The Hague, 229-236.

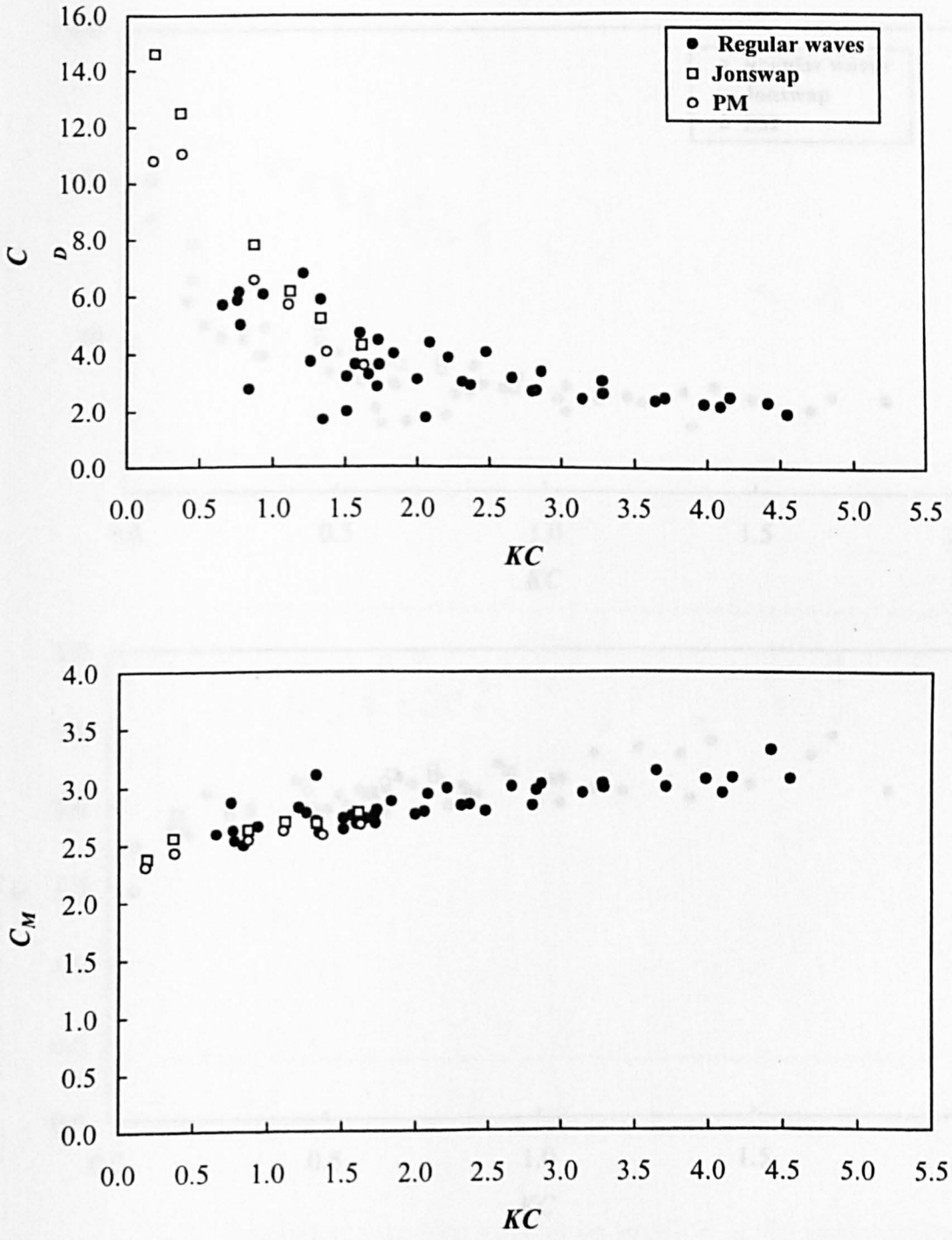

Fig. A. 1 Regular and random wave force coefficients for vertical square cylinder

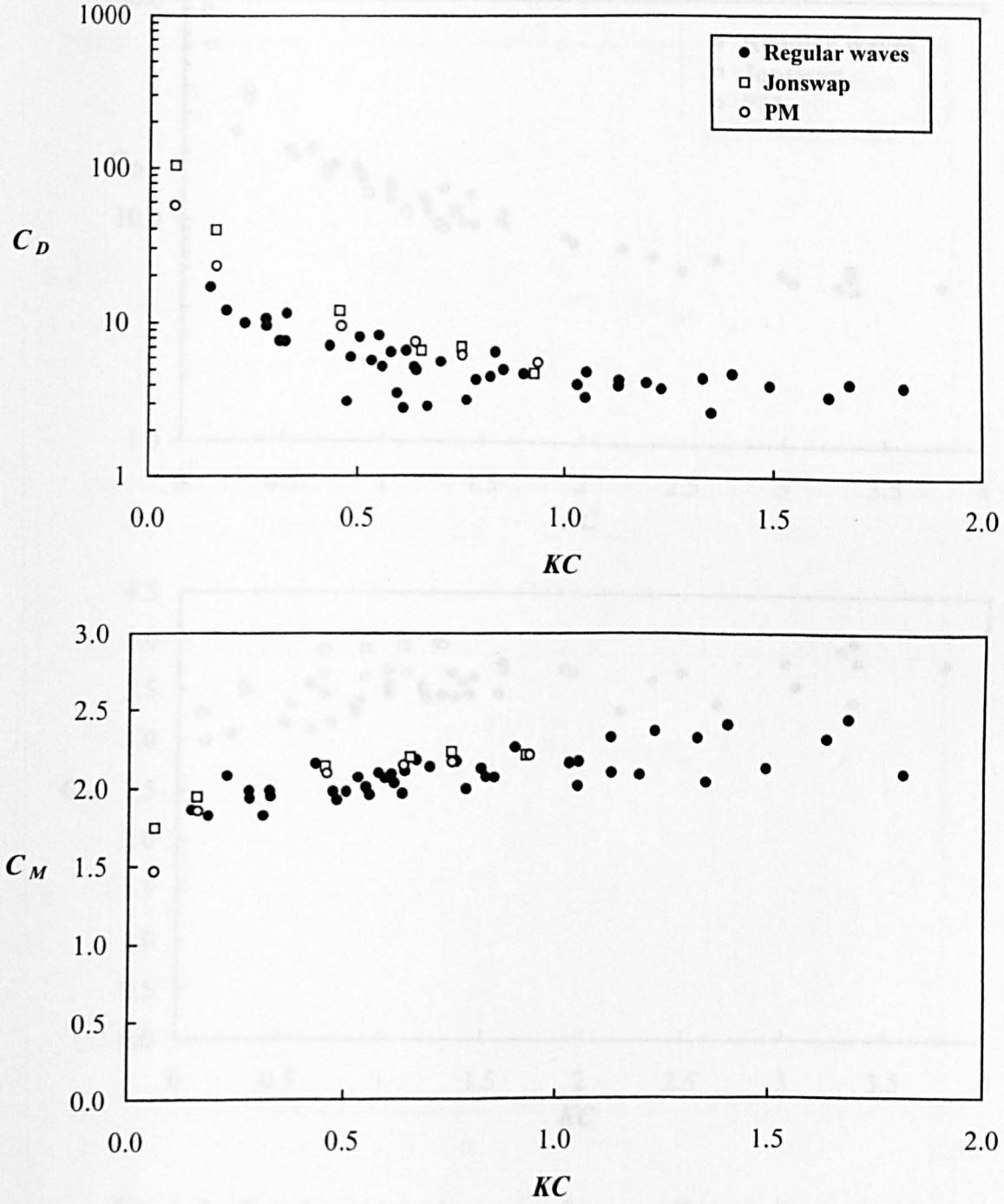

Fig. A. 2 Regular and random wave force coefficients for vertical rectangular cylinder with aspect ratio = ½

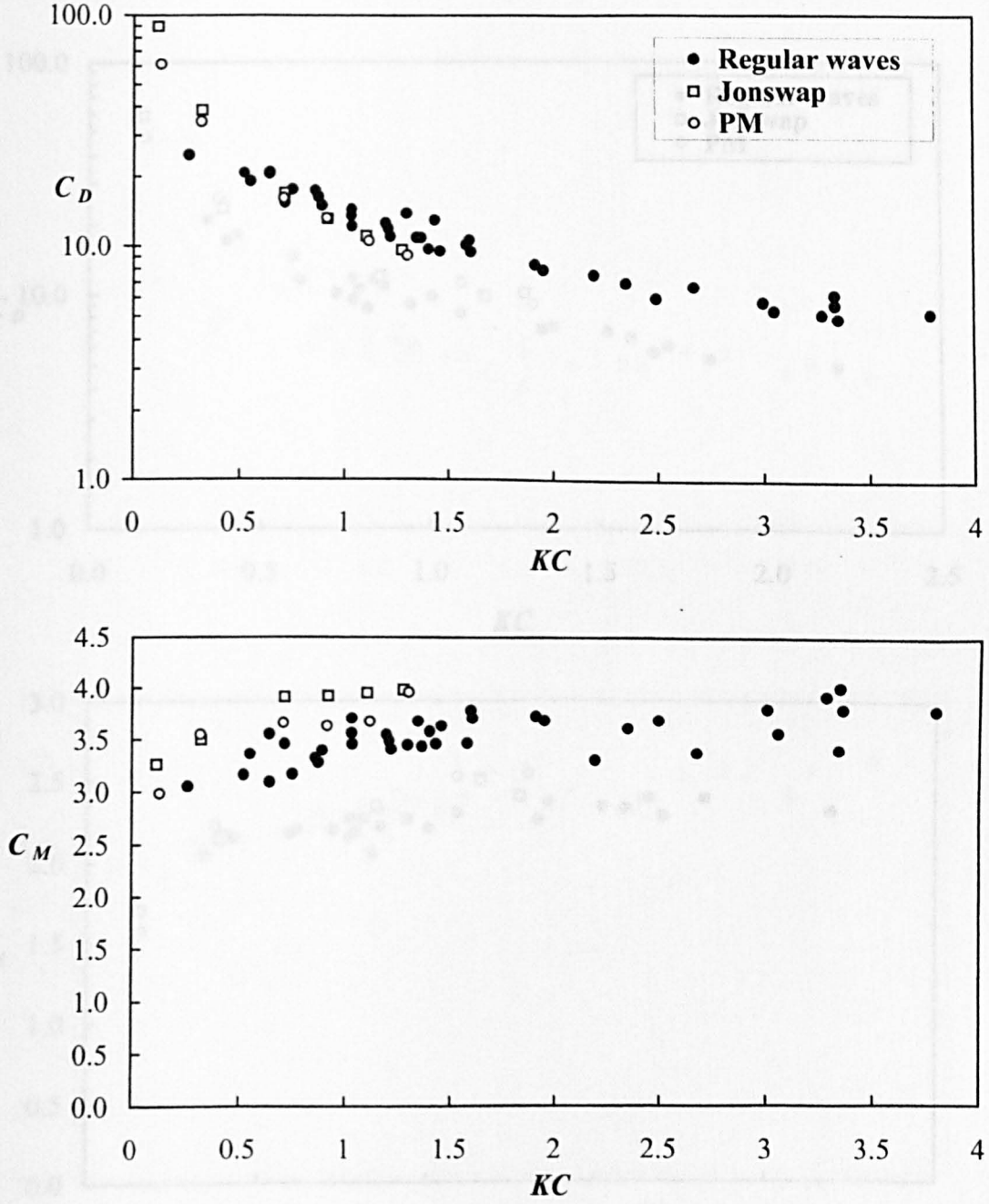

Fig. A. 3 Regular and random wave force coefficients for vertical rectangular cylinder with aspect ratio = 2/1

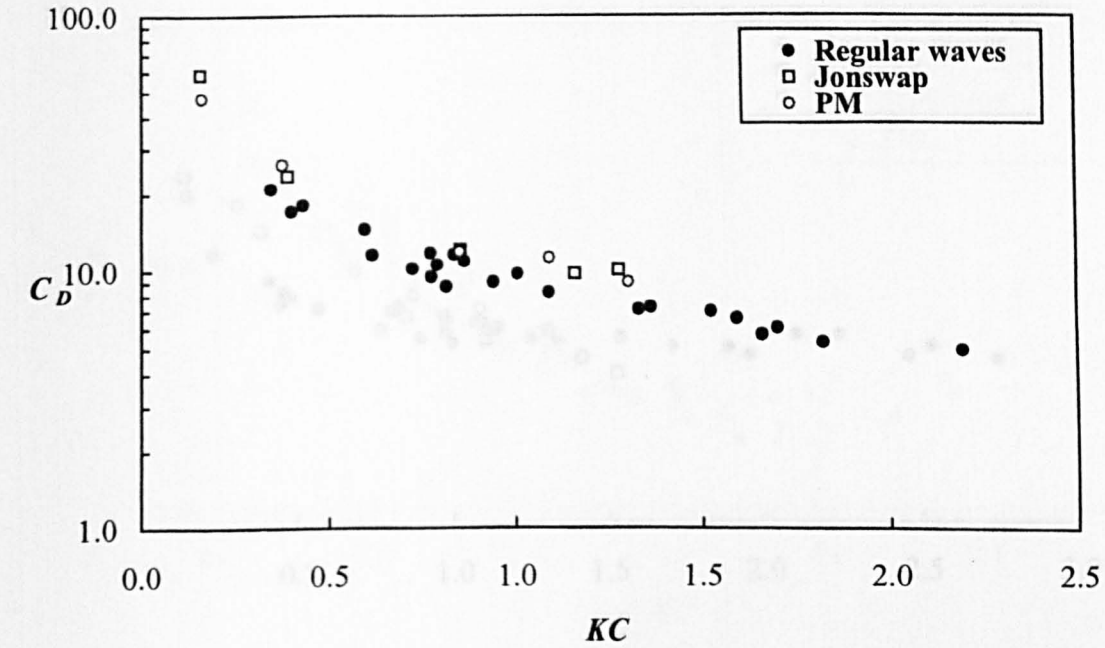

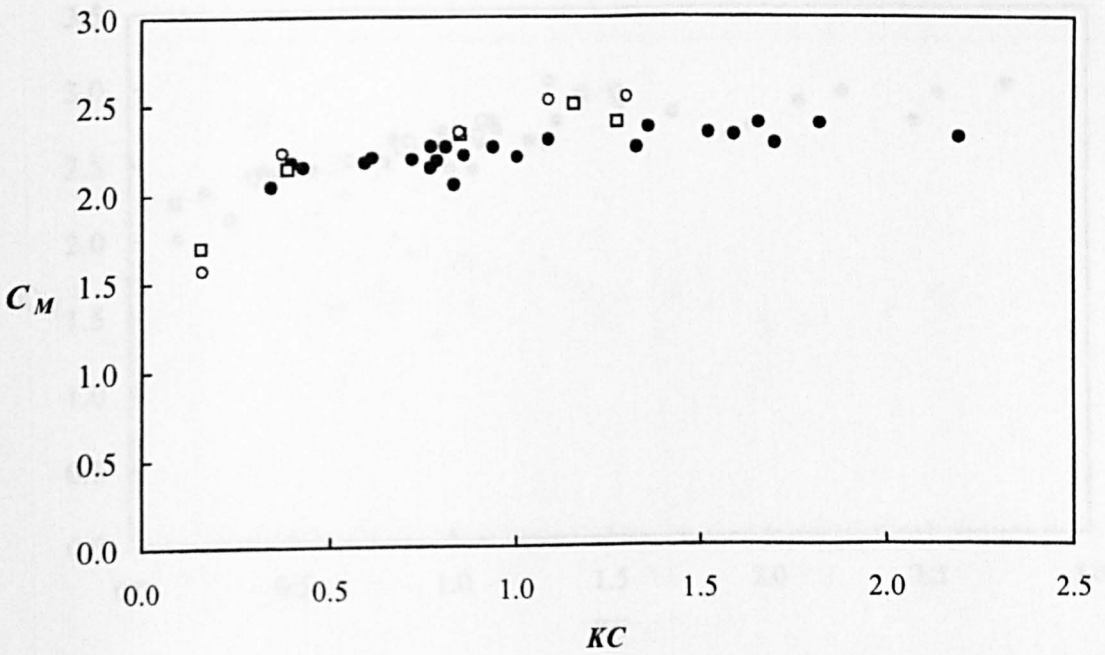

Fig. A. 4 Regular and random wave force coefficients for vertical rectangular cylinder with aspect ratio = 3/4

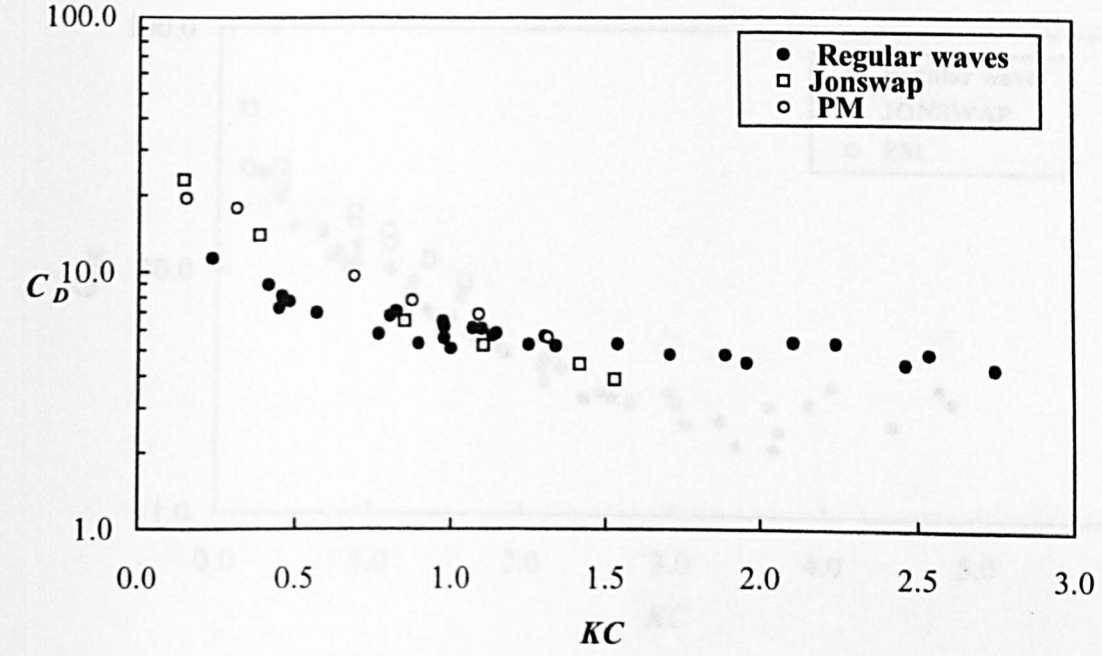

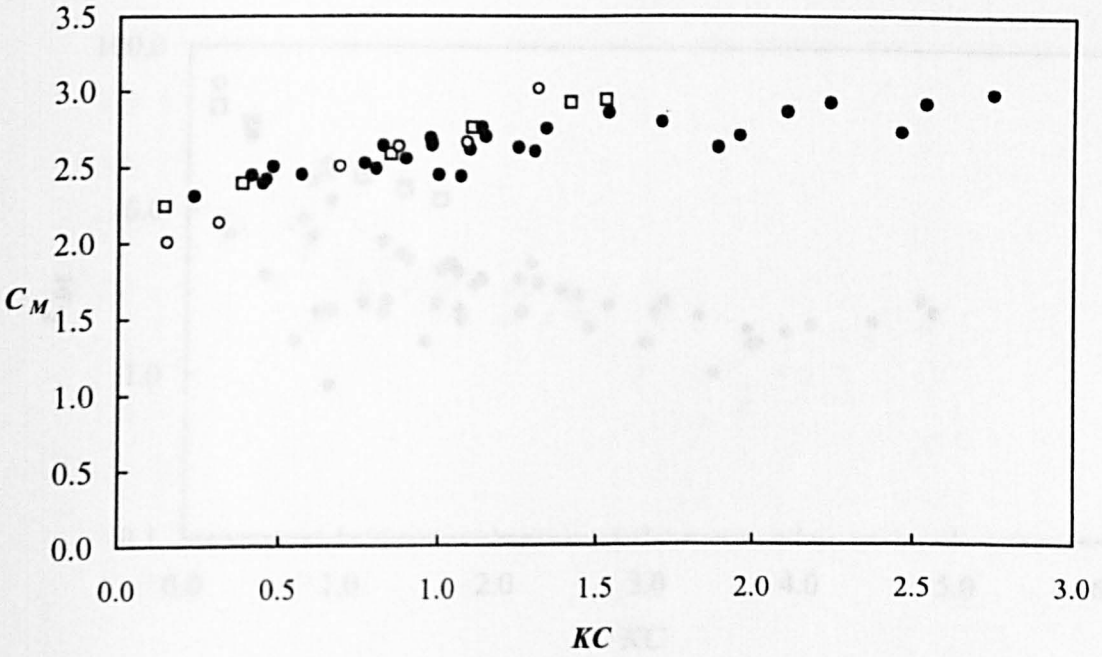

Fig. A. 5 Regular and random wave force coefficients for vertical rectangular cylinder with aspect ratio = 4/3

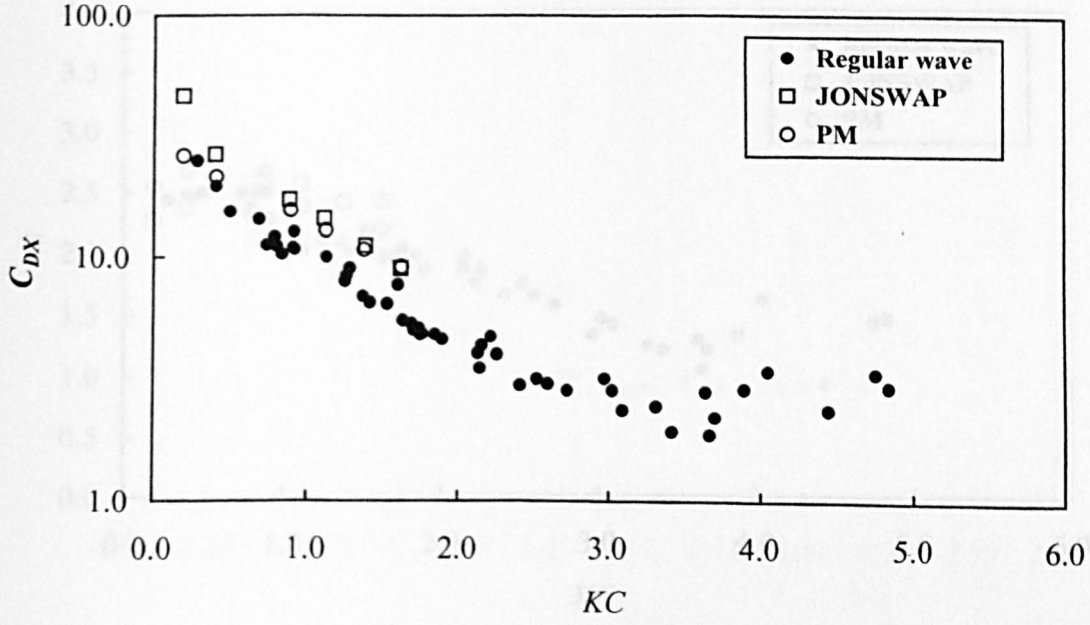

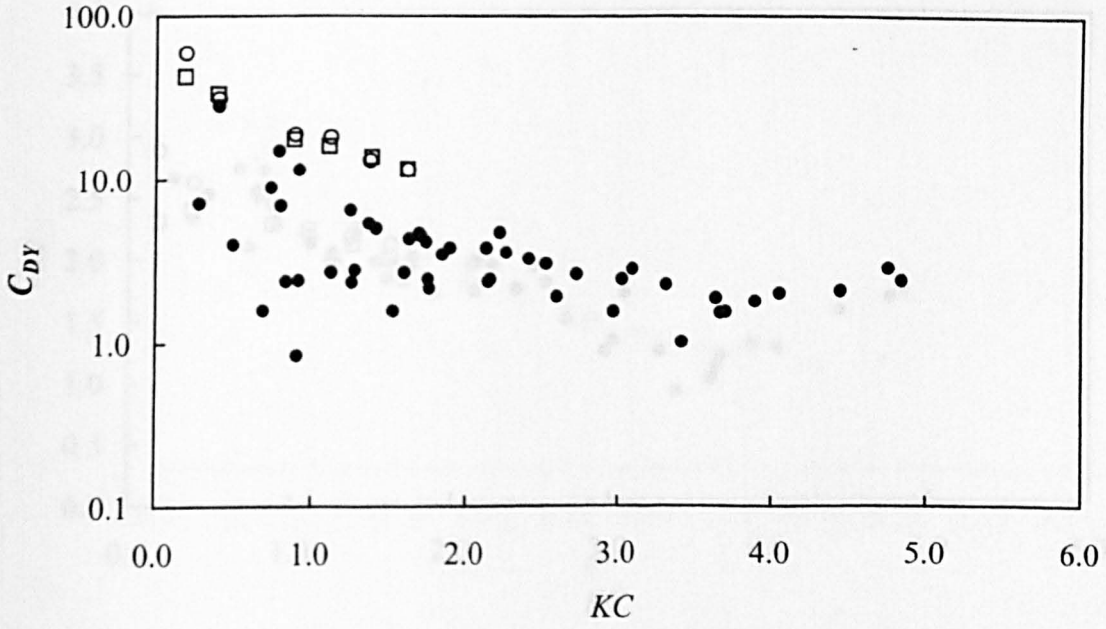

Fig. A. 6 Drag coefficients in regular and random wave for horizontal square cylinder

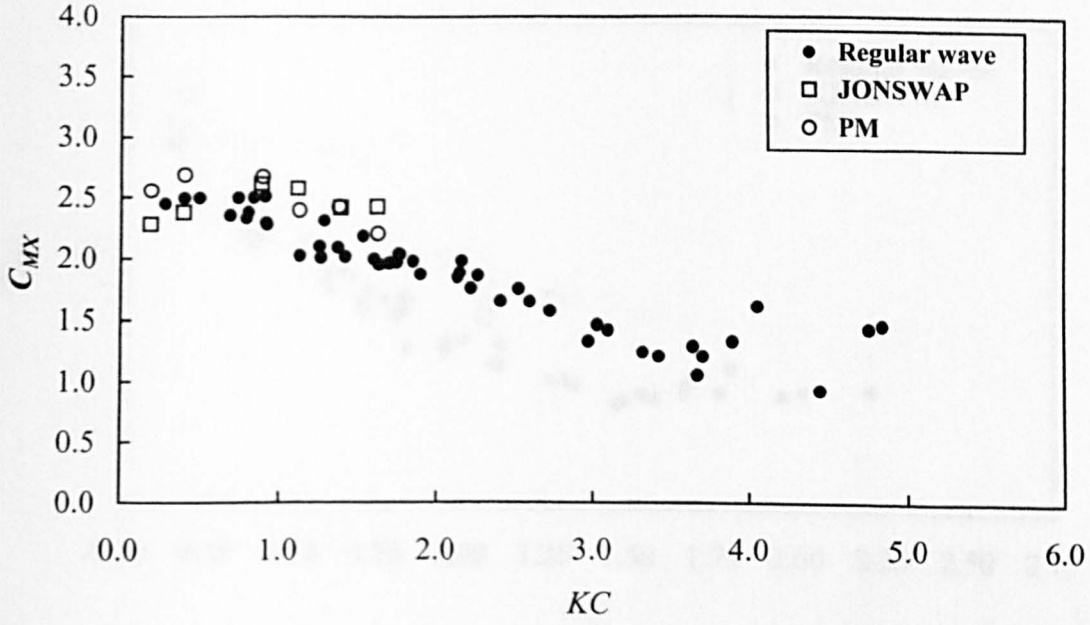

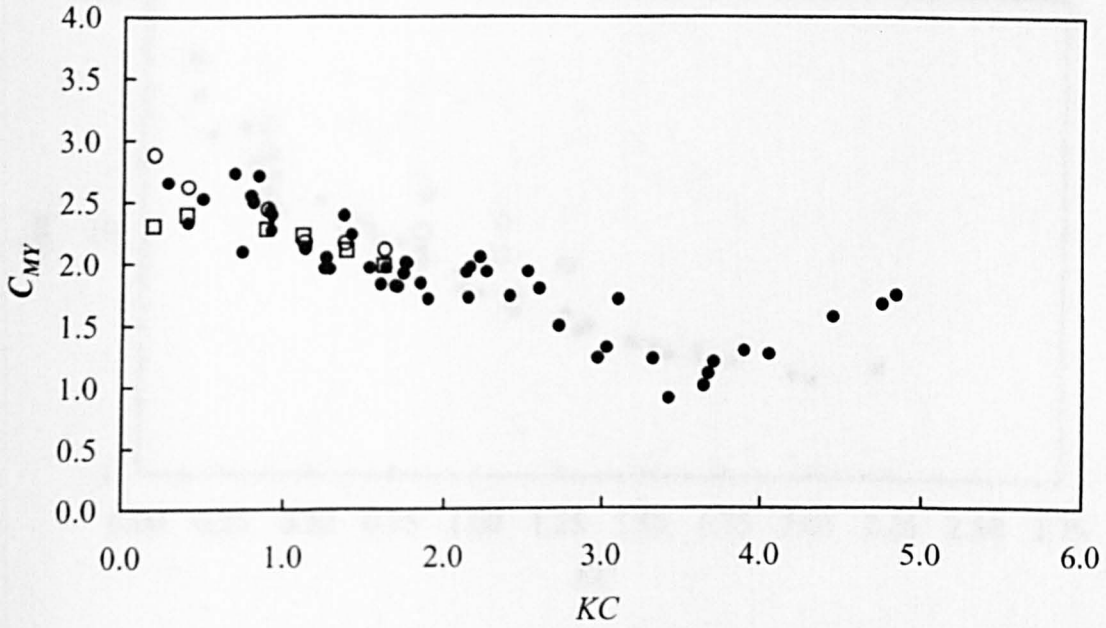

Fig. A. 7 Inertia coefficients in regular and random wave for horizontal square cylinder

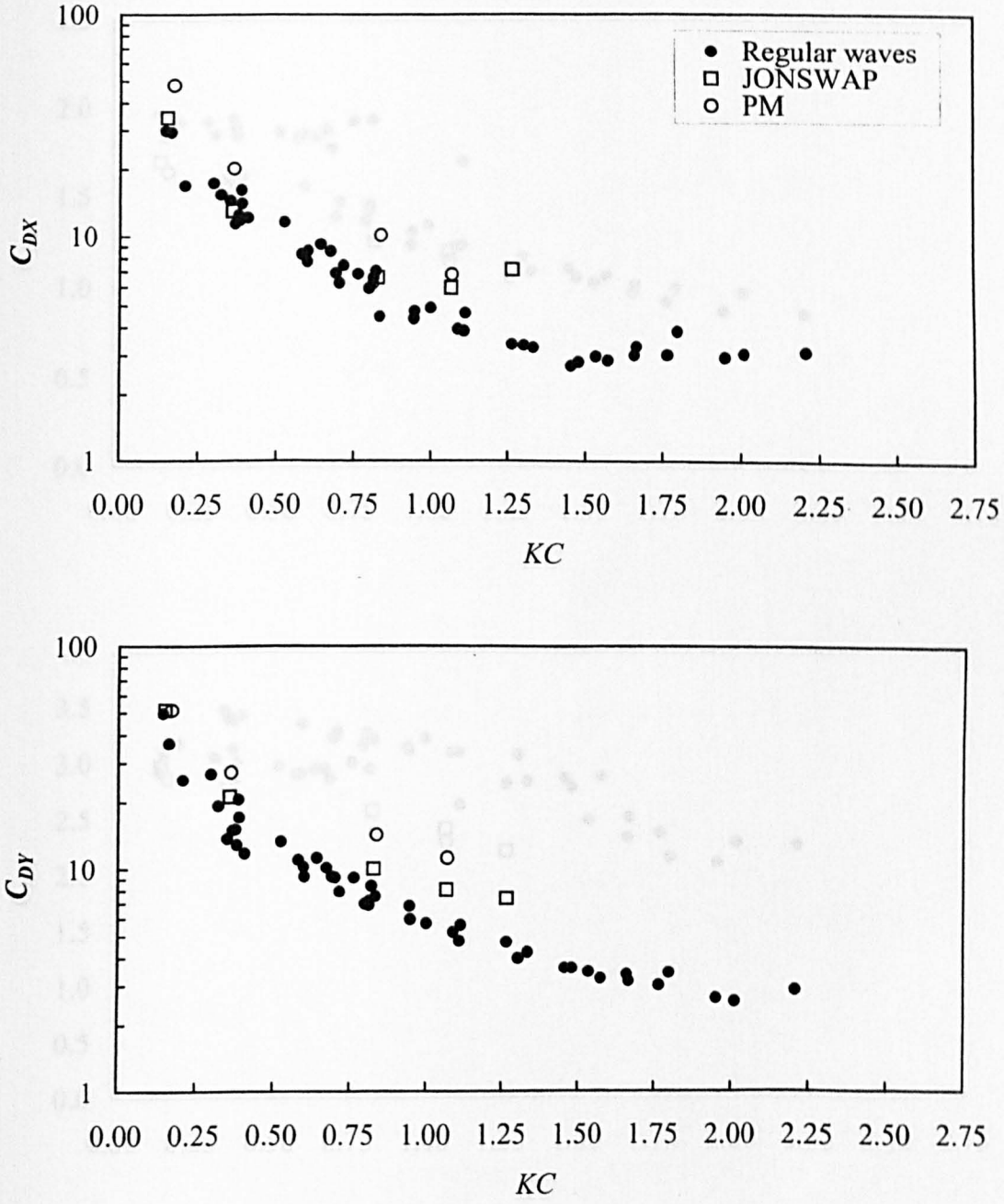

Fig. A. 8 Drag coefficients in regular and random waves for horizontal rectangular cylinder with aspect ratio = 1/2

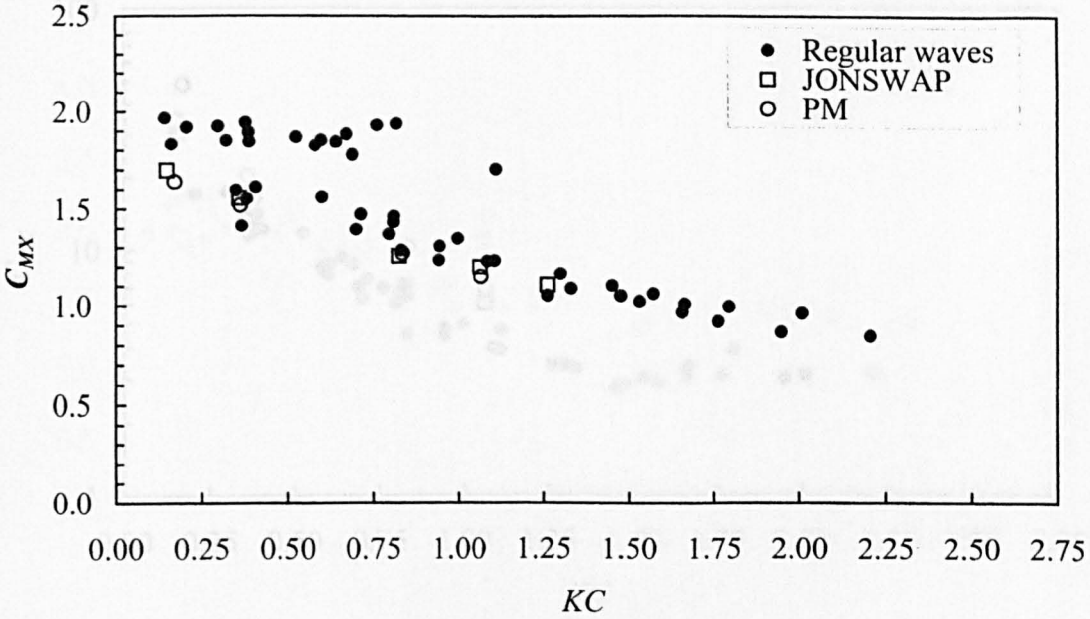

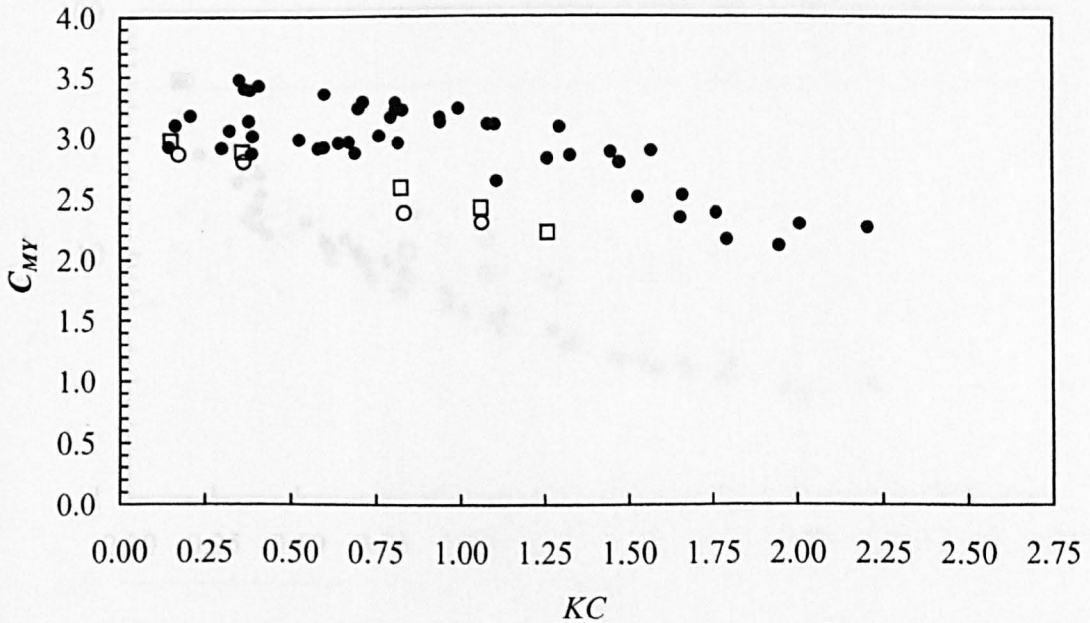

Fig. A. 9 Inertia coefficients in regular and random waves for horizontal rectangular cylinder with aspect ratio = 1/2

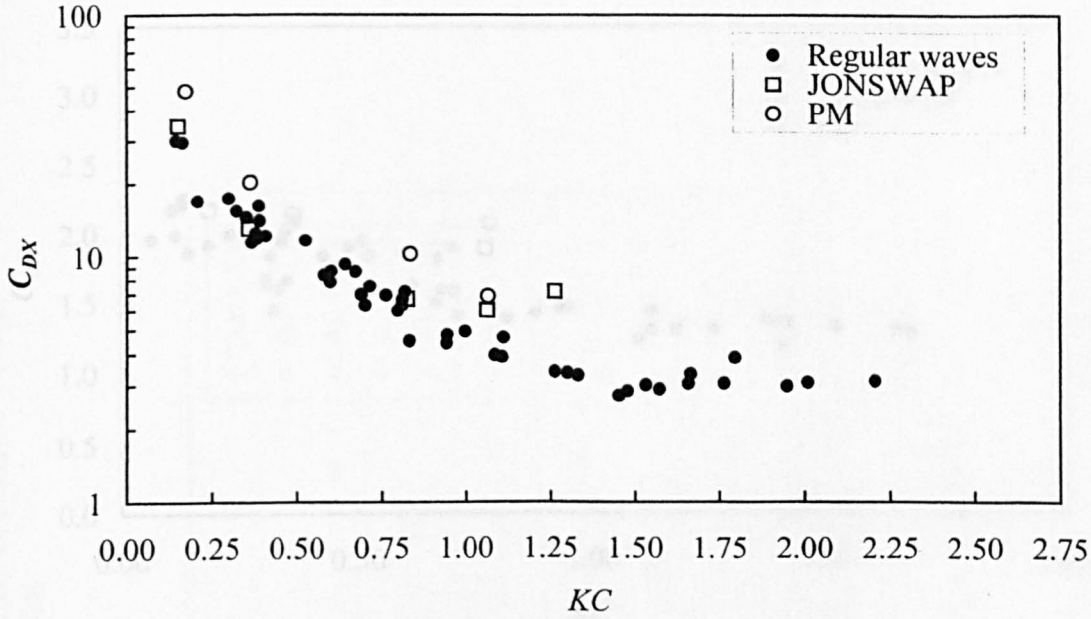

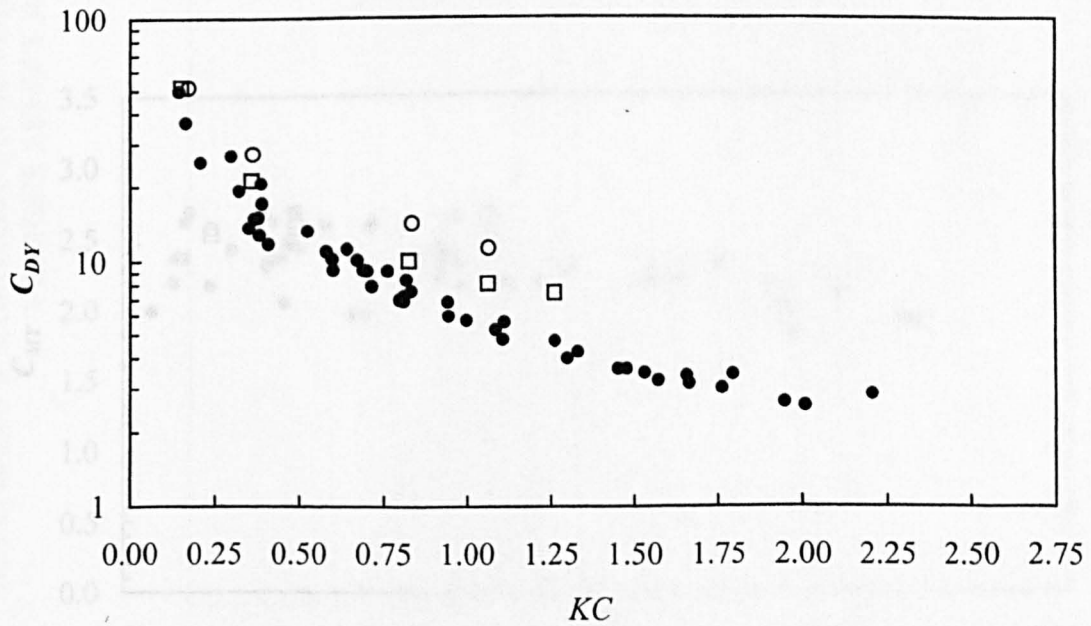

Fig. A. 10 Drag coefficients in regular and random waves for horizontal rectangular cylinder with aspect ratio = 3/4

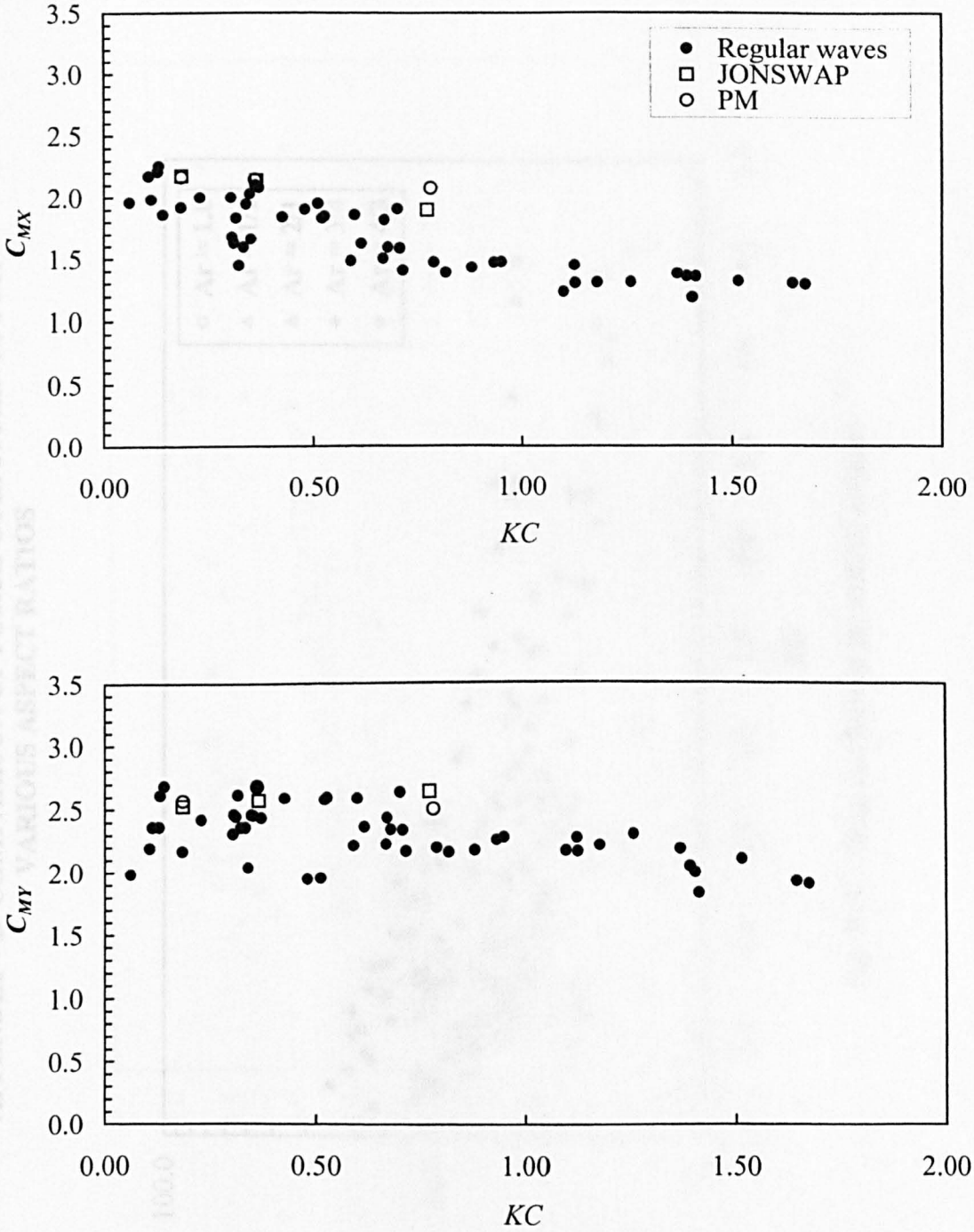

Fig. A. 11 Inertia coefficients in regular and random wave for horizontal rectangular cylinder with aspect ratio = 3/4

APPENDIX – B COMPARISON OF FORCE COEFFICIENTS FOR VARIOUS ASPECT RATIOS

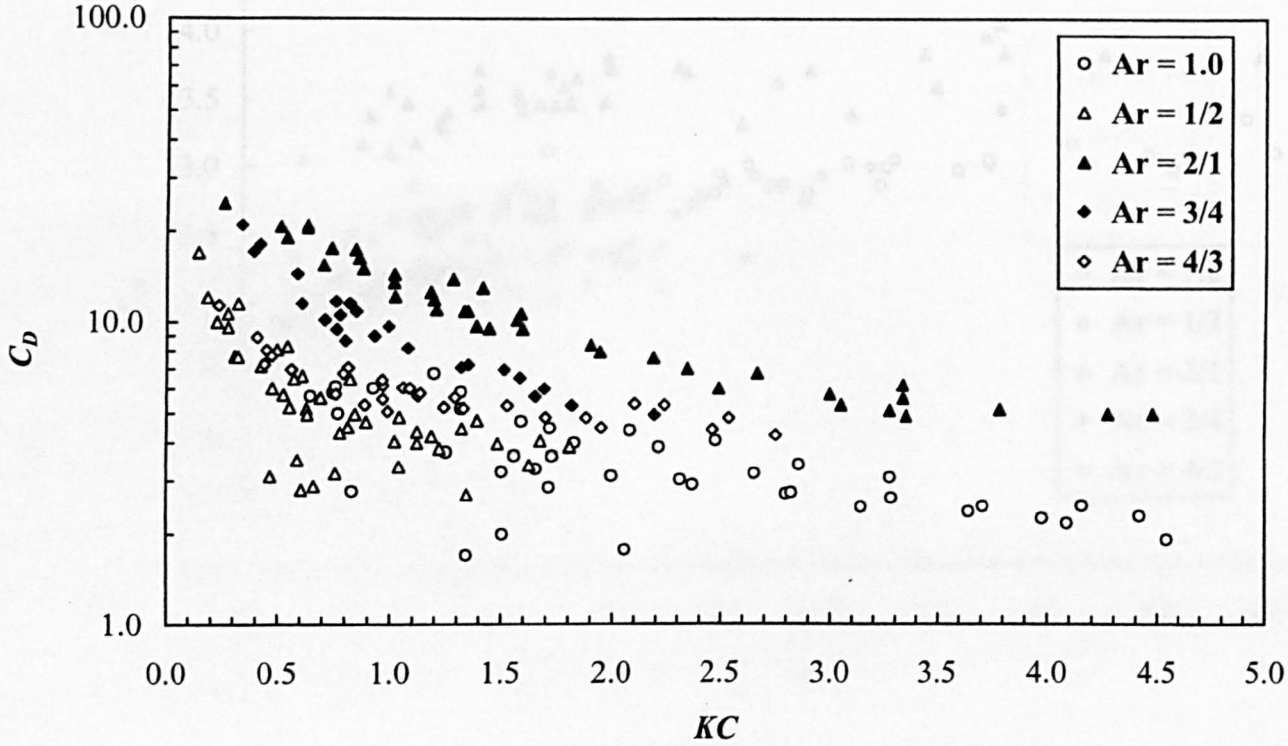

Fig. B. 1 Drag coefficients for vertical cylinder

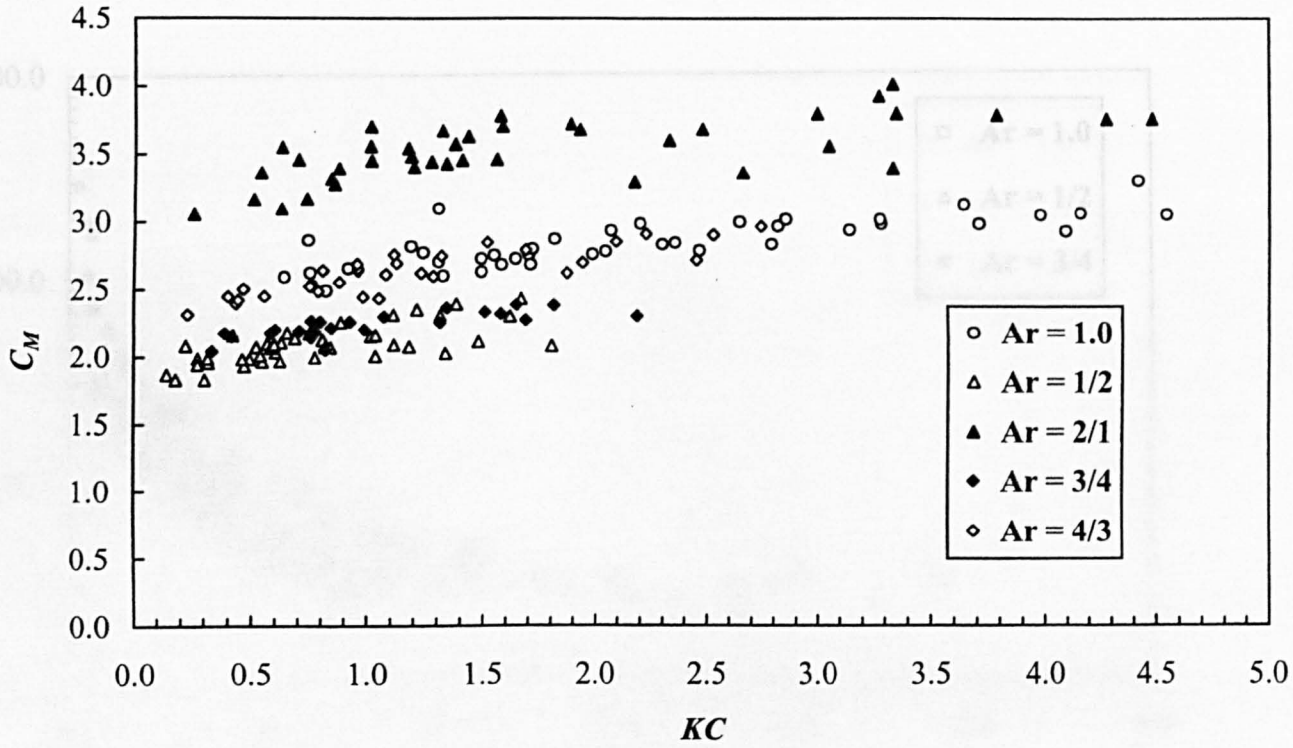

Fig. B. 2 Inertia coefficients for vertical cylinders

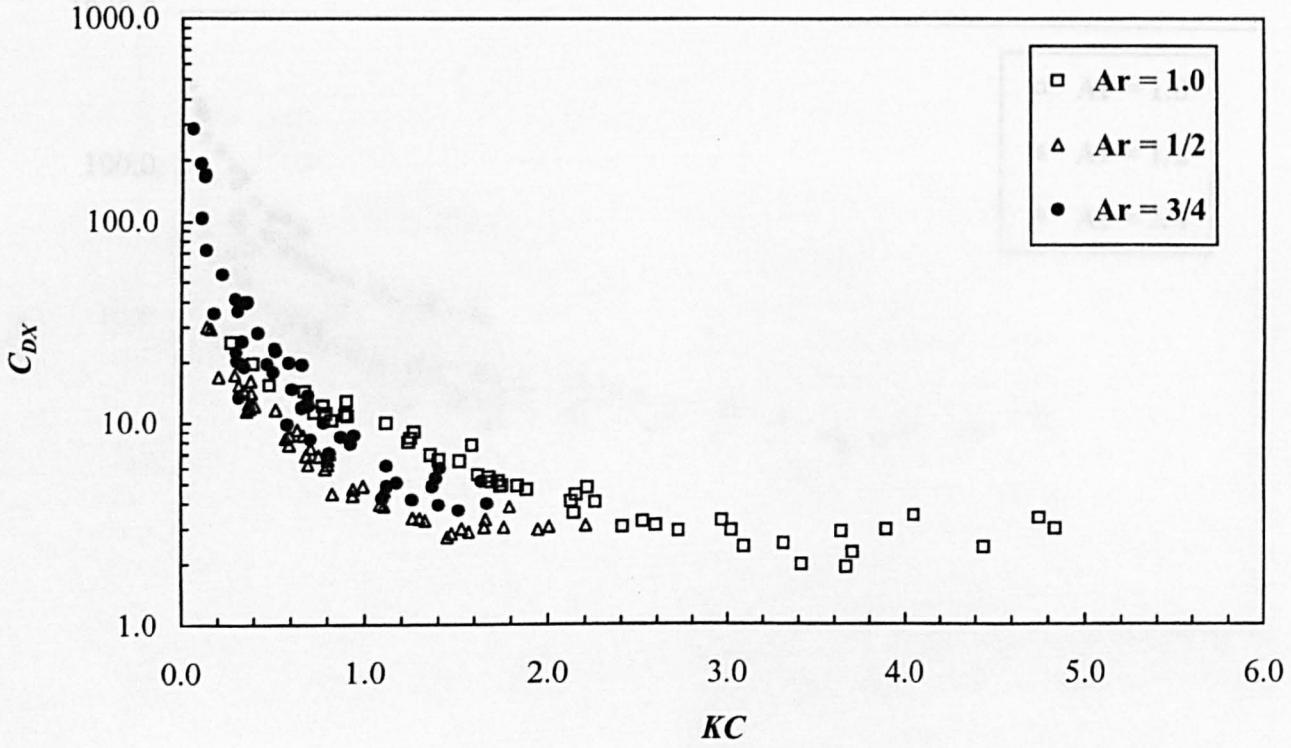

Fig. B. 3 Horizontal drag coefficients for horizontal cylinders

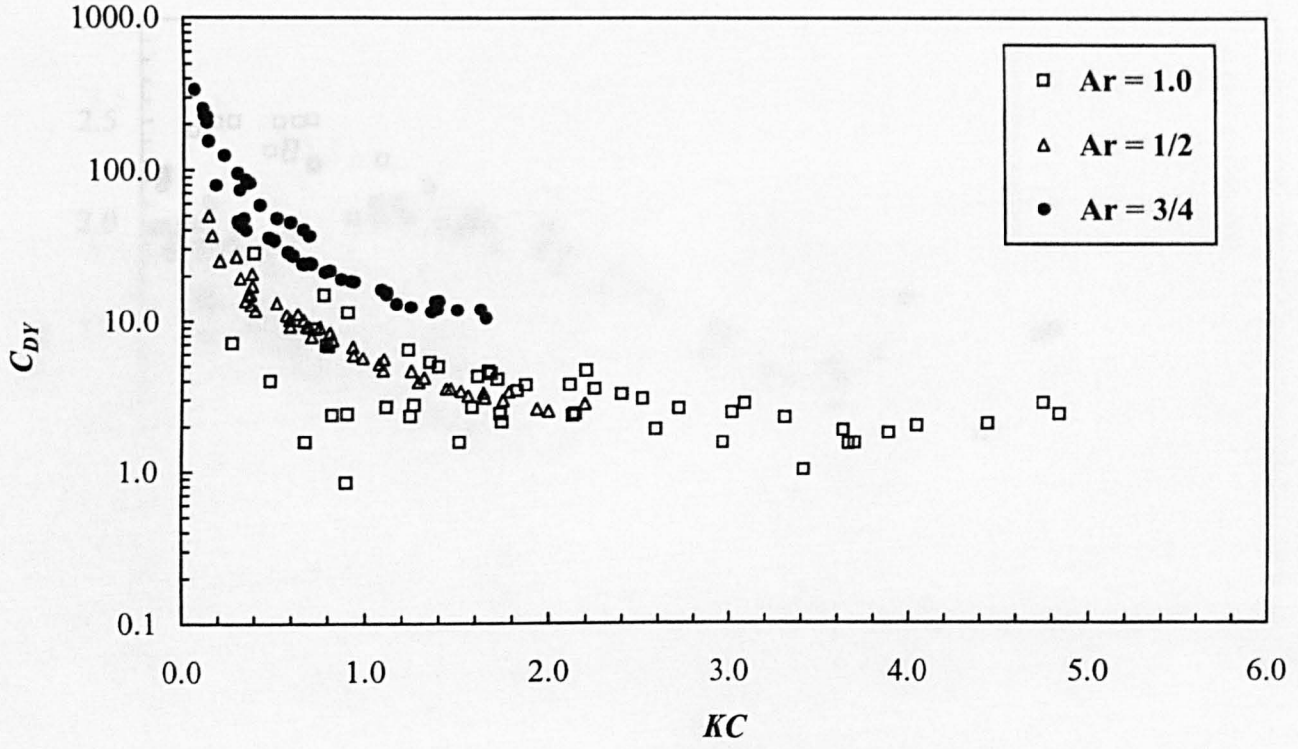

Fig. B. 4 Vertical drag coefficients for horizontal cylinders

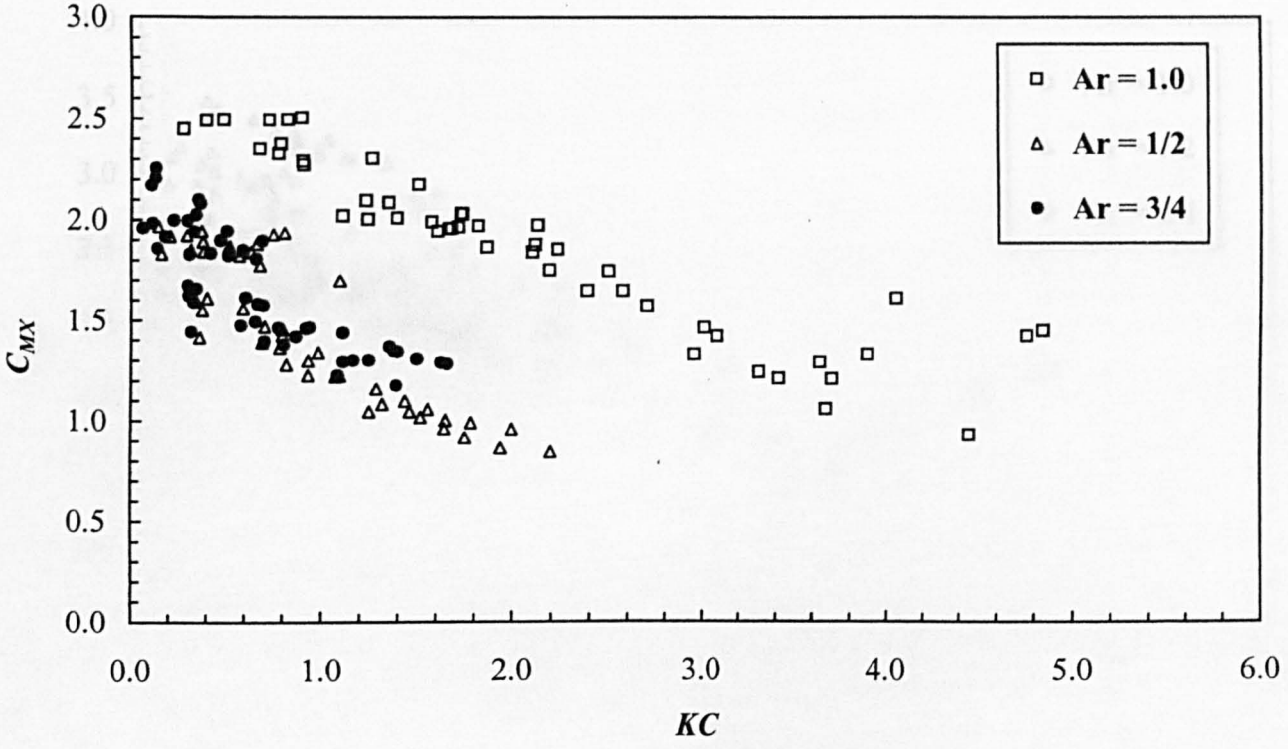

Fig. B. 5 Horizontal inertia coefficients for horizontal cylinders

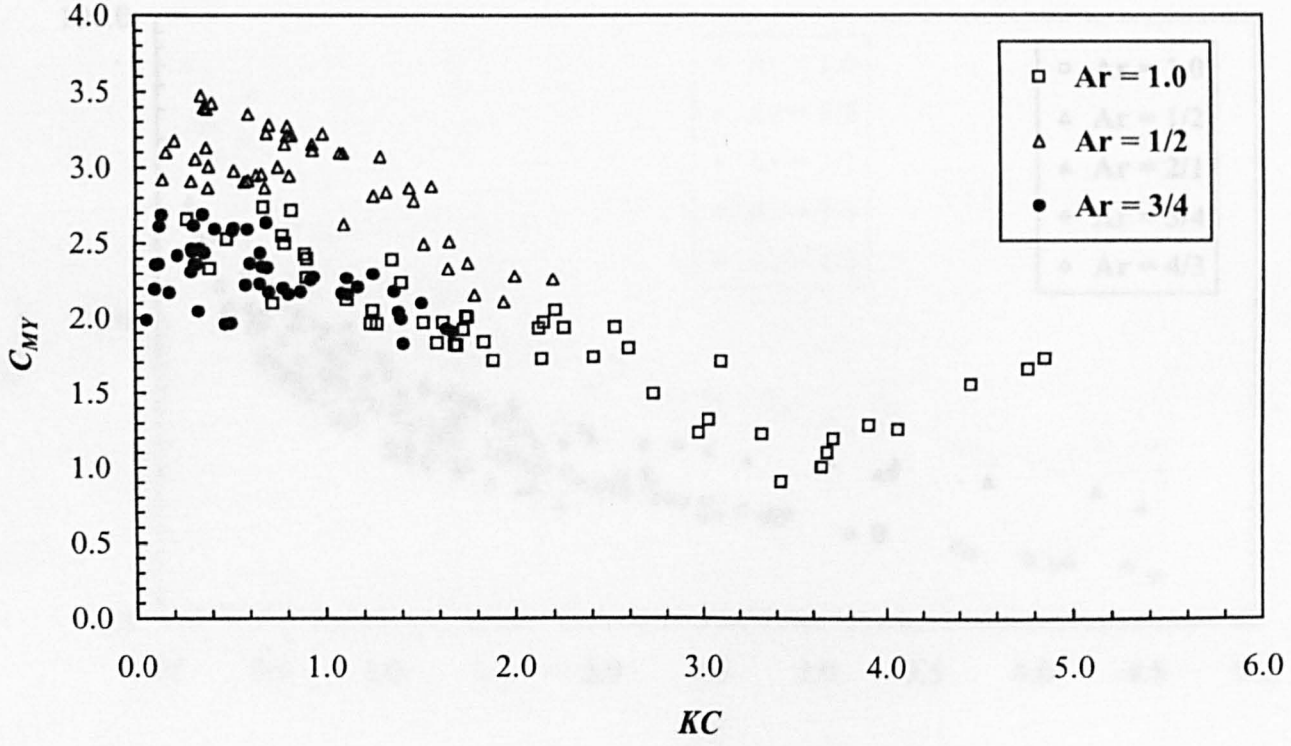

Fig. B. 6 Vertical inertia coefficients for horizontal cylinders

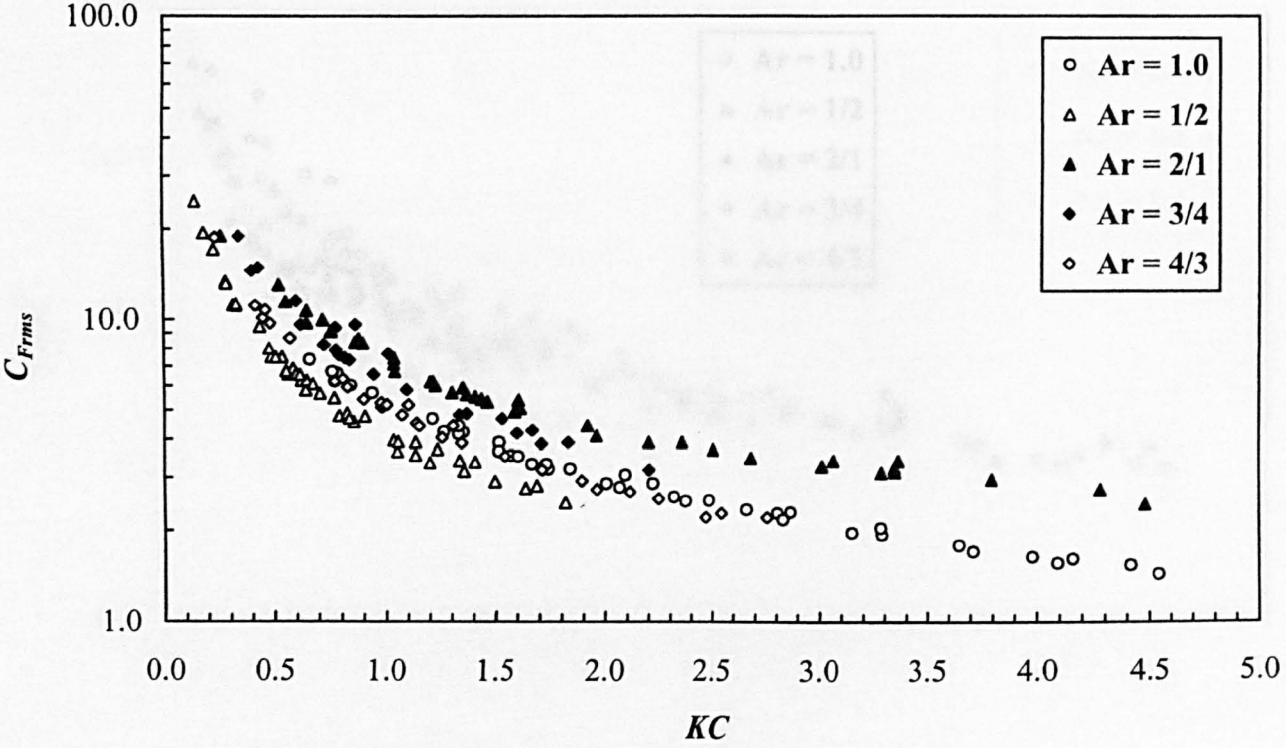

Fig. B. 7 Rms in-line force coefficients for vertical cylinders

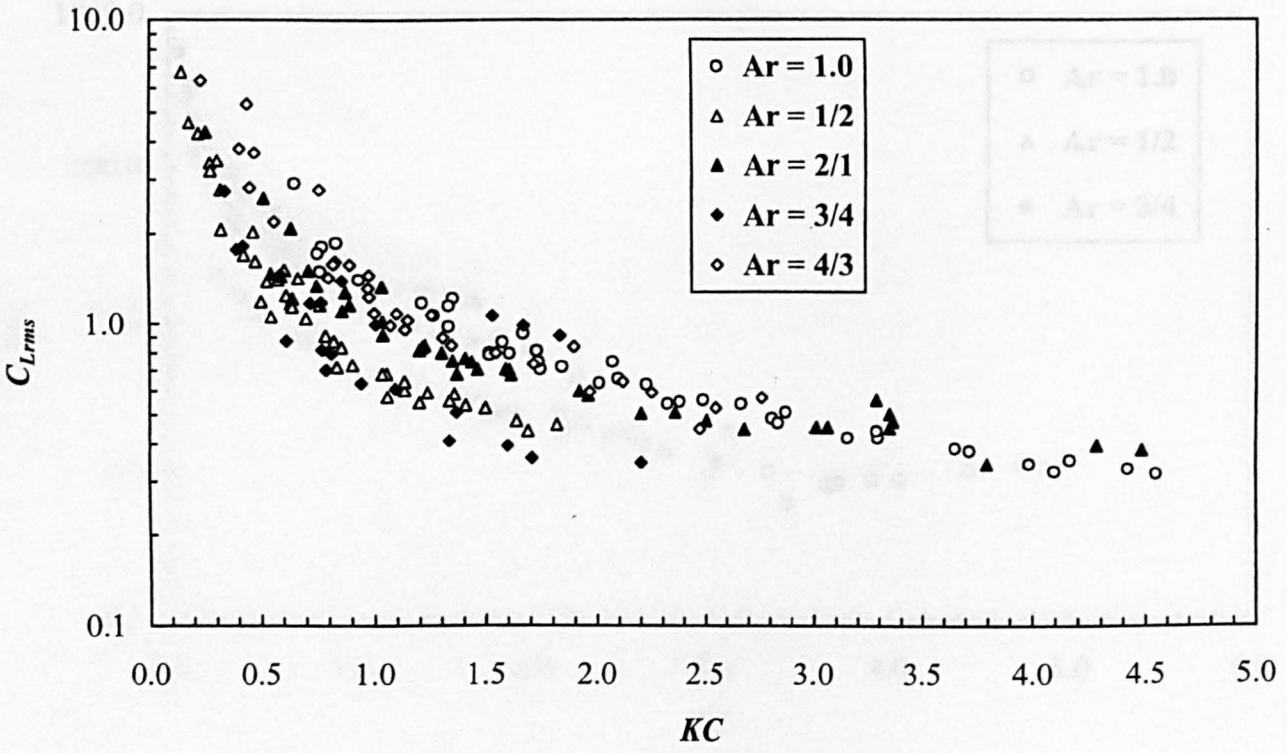

Fig. B. 8 Rms lift force coefficients for vertical cylinders

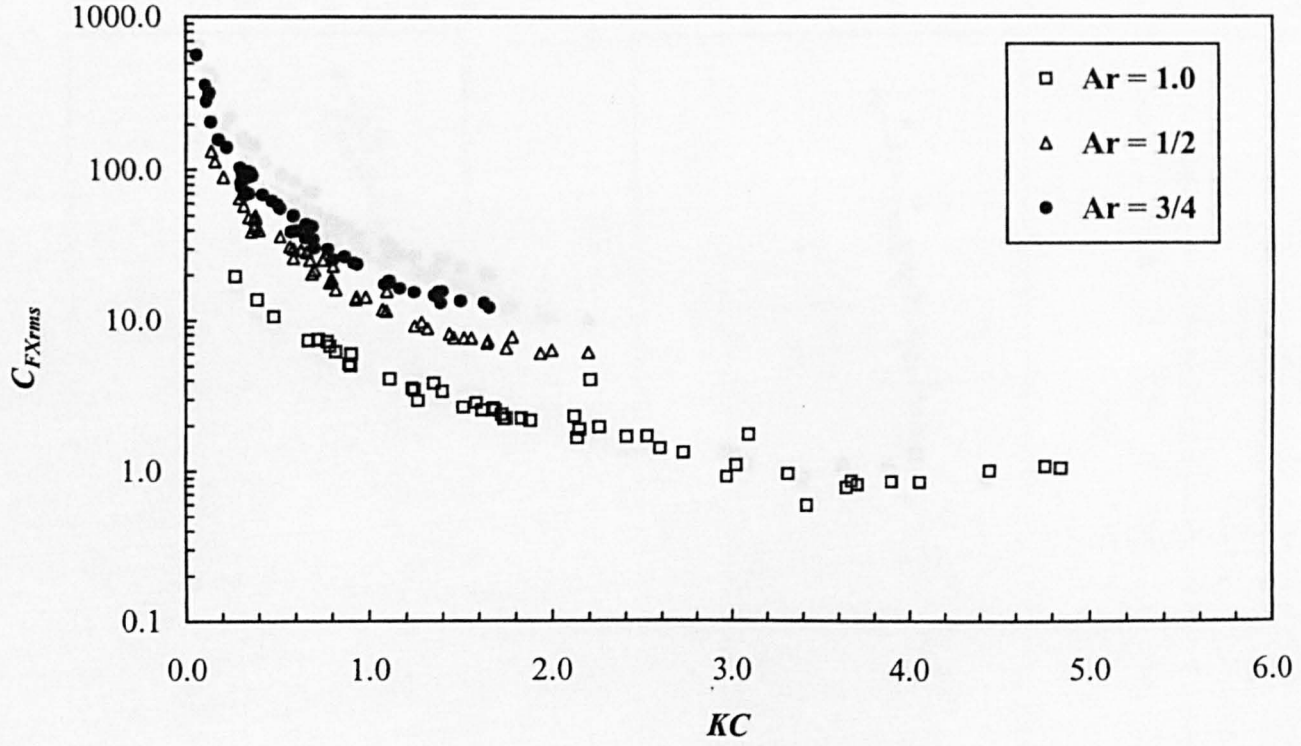

Fig. B. 9 Horizontal rms force coefficients for horizontal cylinders

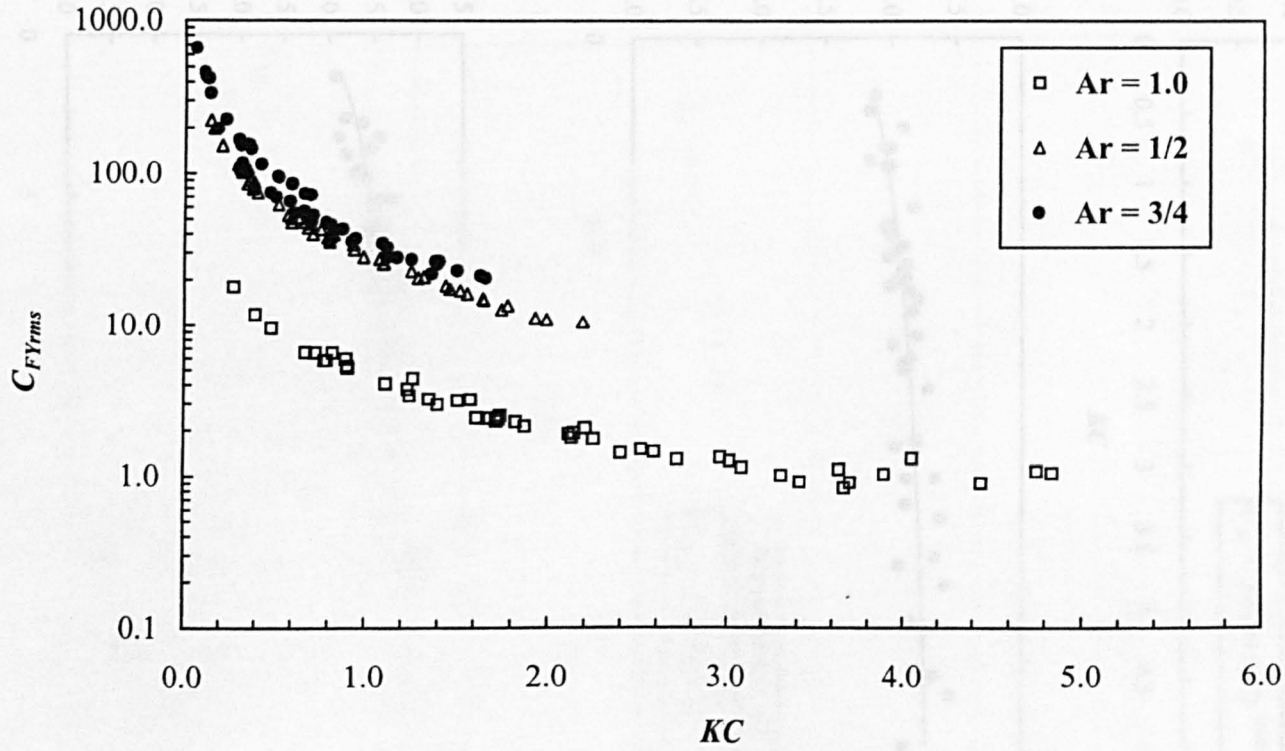

Fig. B. 10 Vertical rms force coefficients for horizontal cylinders

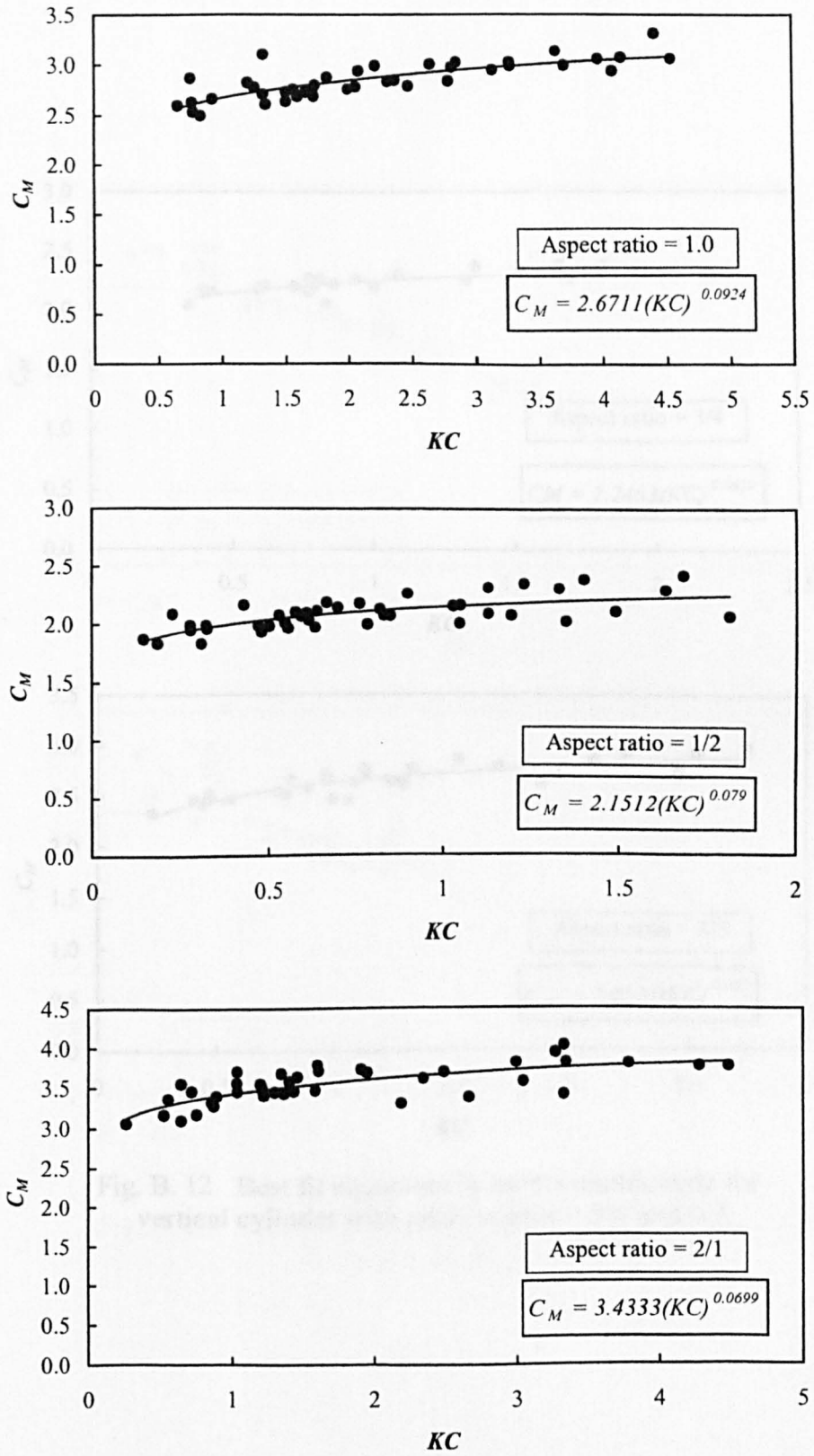

Fig. B. 11 Best fit equations to inertia coefficients for vertical cylinder with aspect ratios = 1.0,1/2 and 2/1

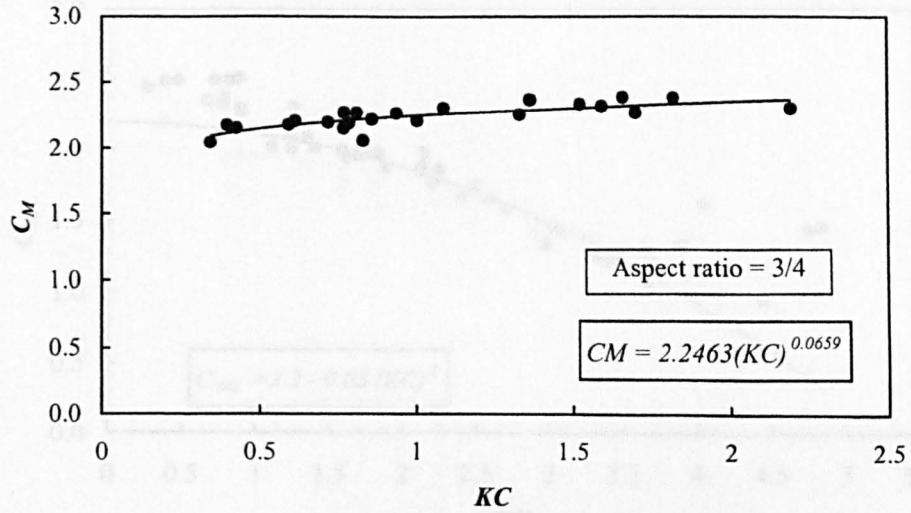

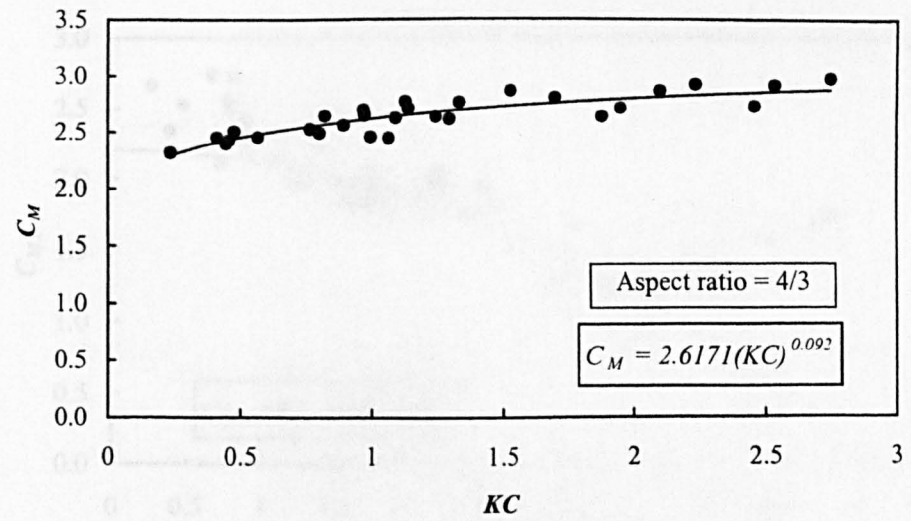

Fig. B. 12 Best fit equations to inertia coefficients for vertical cylinder with aspect ratios = 3/4 and 4/3

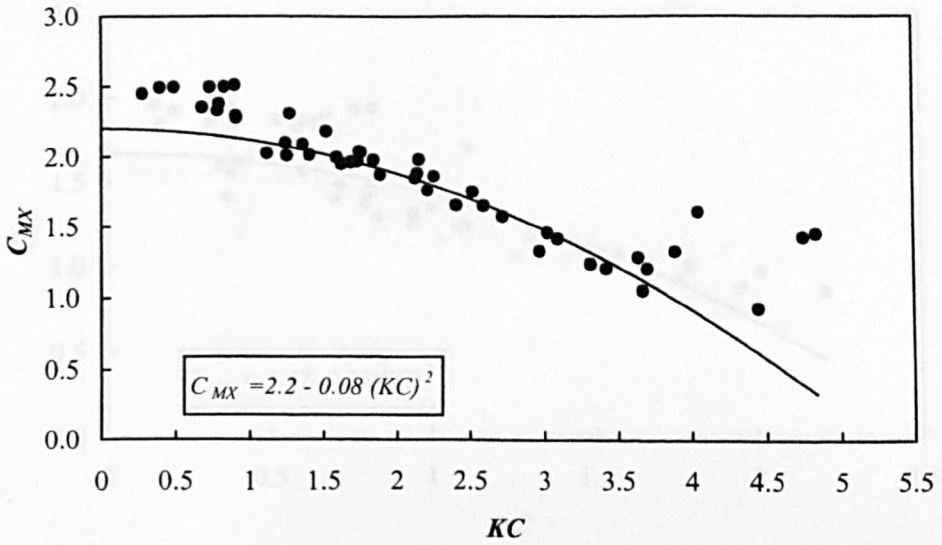

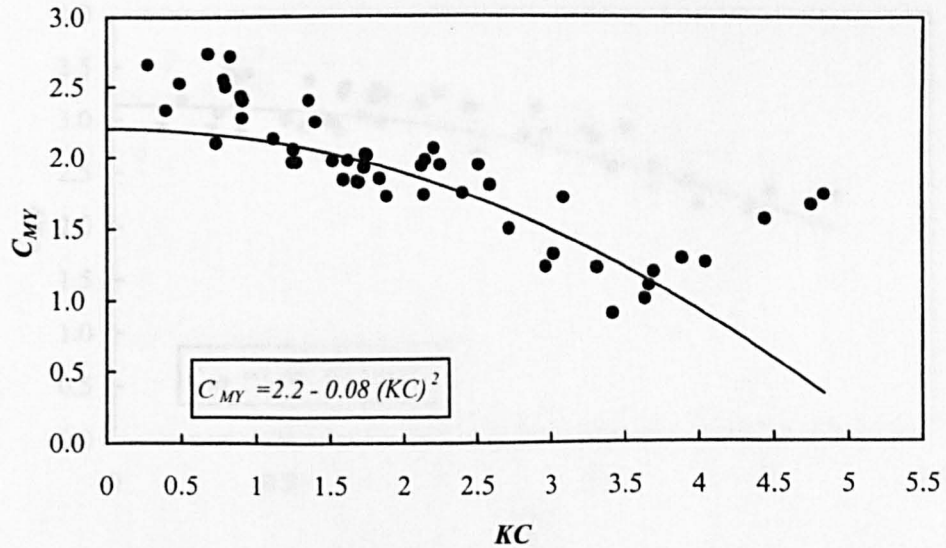

Fig. B. 13 Empirical equation fit to inertia coefficients for horizontal square cylinder

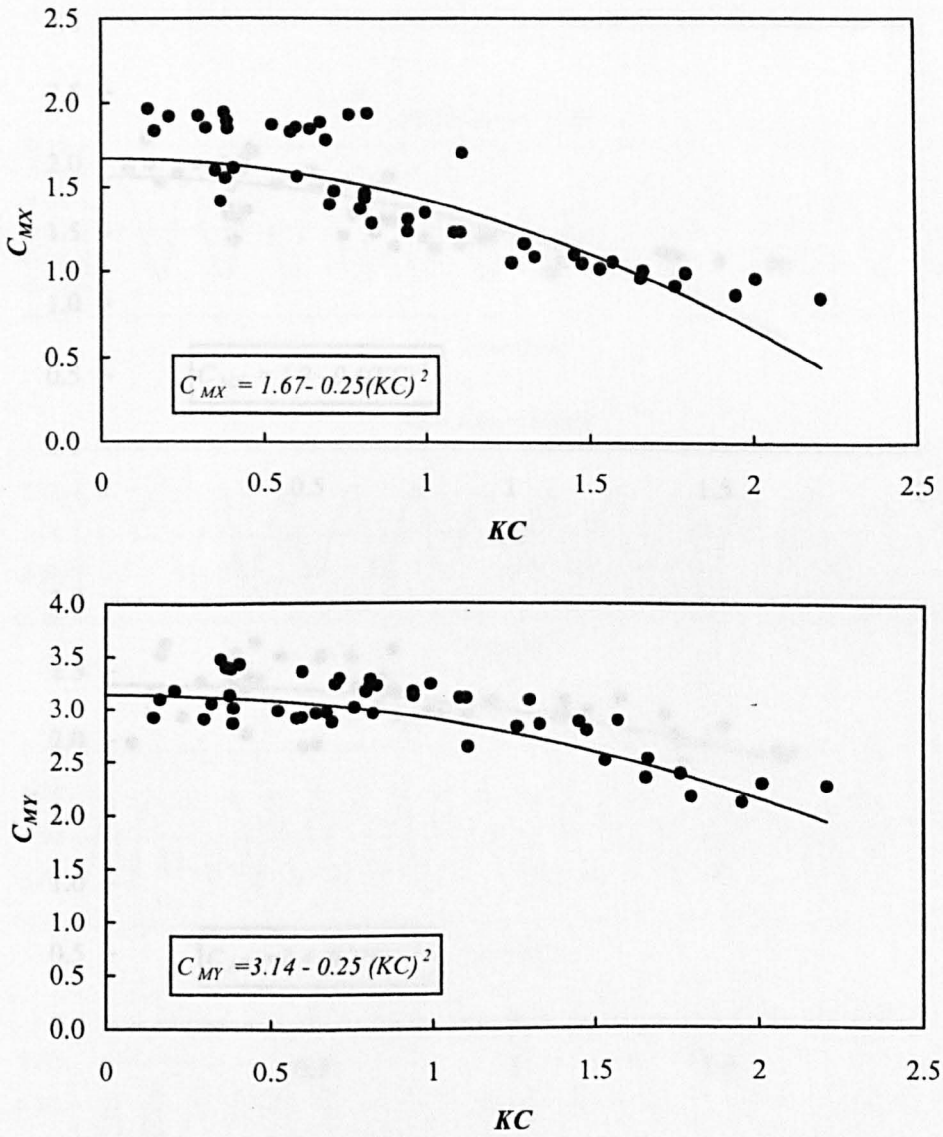

Fig. B. 14 Empirical equation fit to inertia coefficients for horizontal cylinder with aspect ratio = 1/2

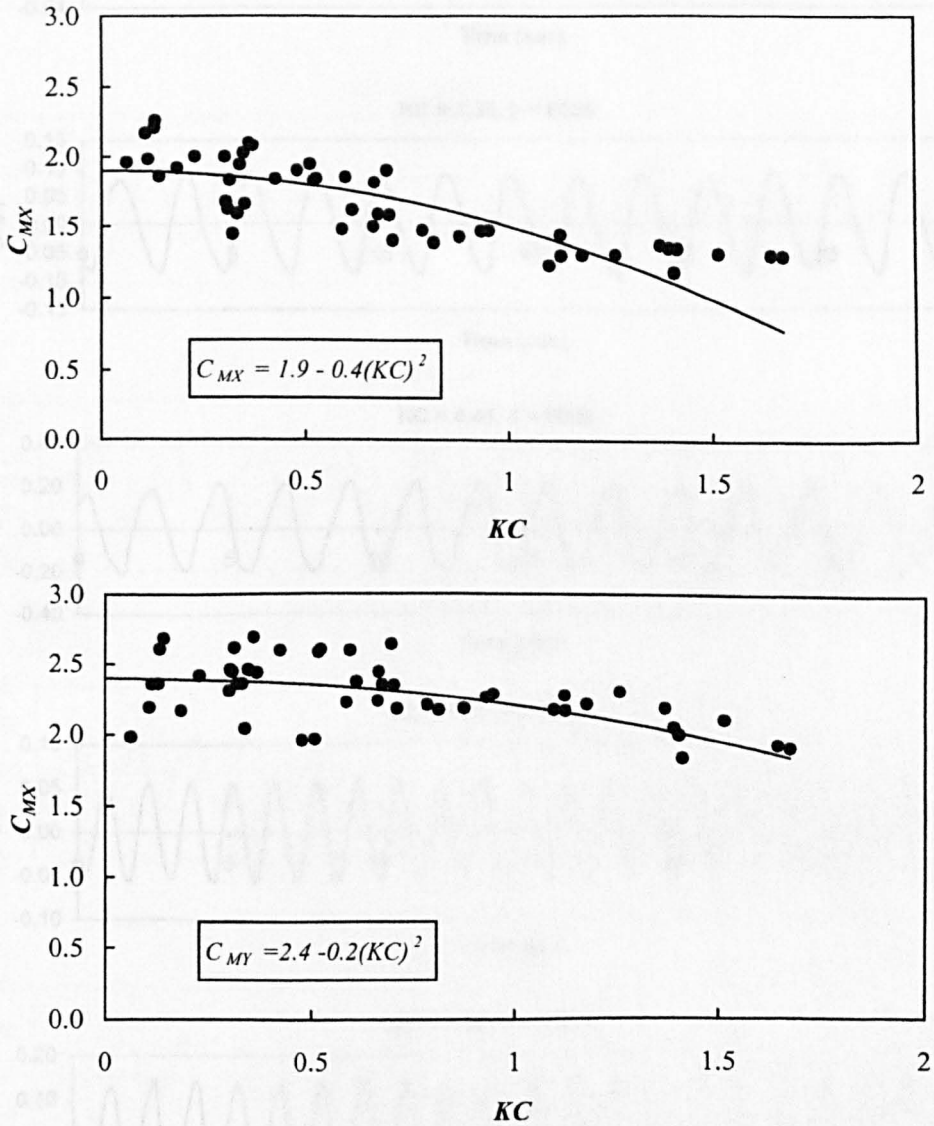

Fig. B. 15 Empirical equation fit to inertia coefficients for horizontal cylinder with aspect ratio = 3/4

APPENDIX – C TRANSVERSE FORCES

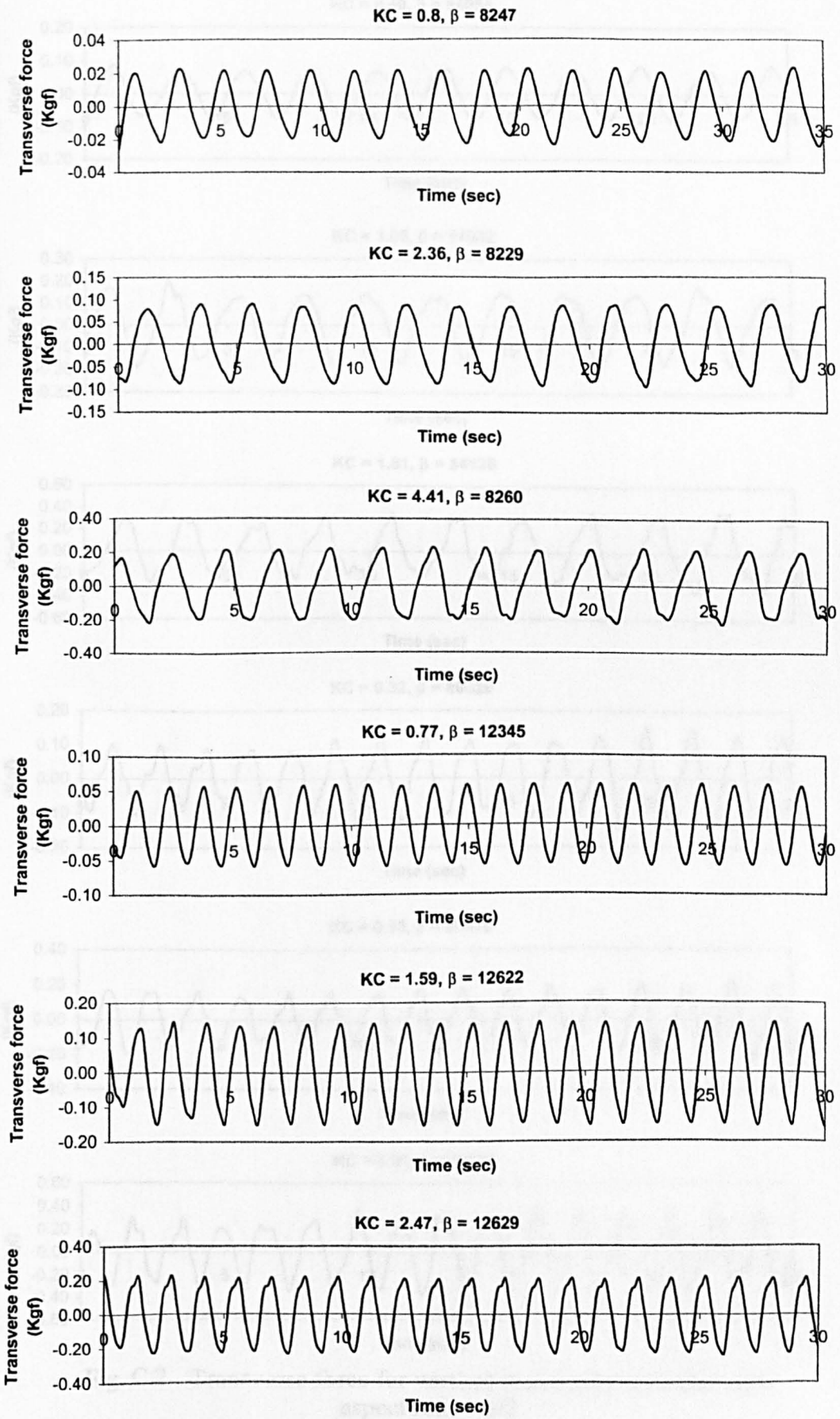

Fig. C.1 Transverse force for vertical square cylinder

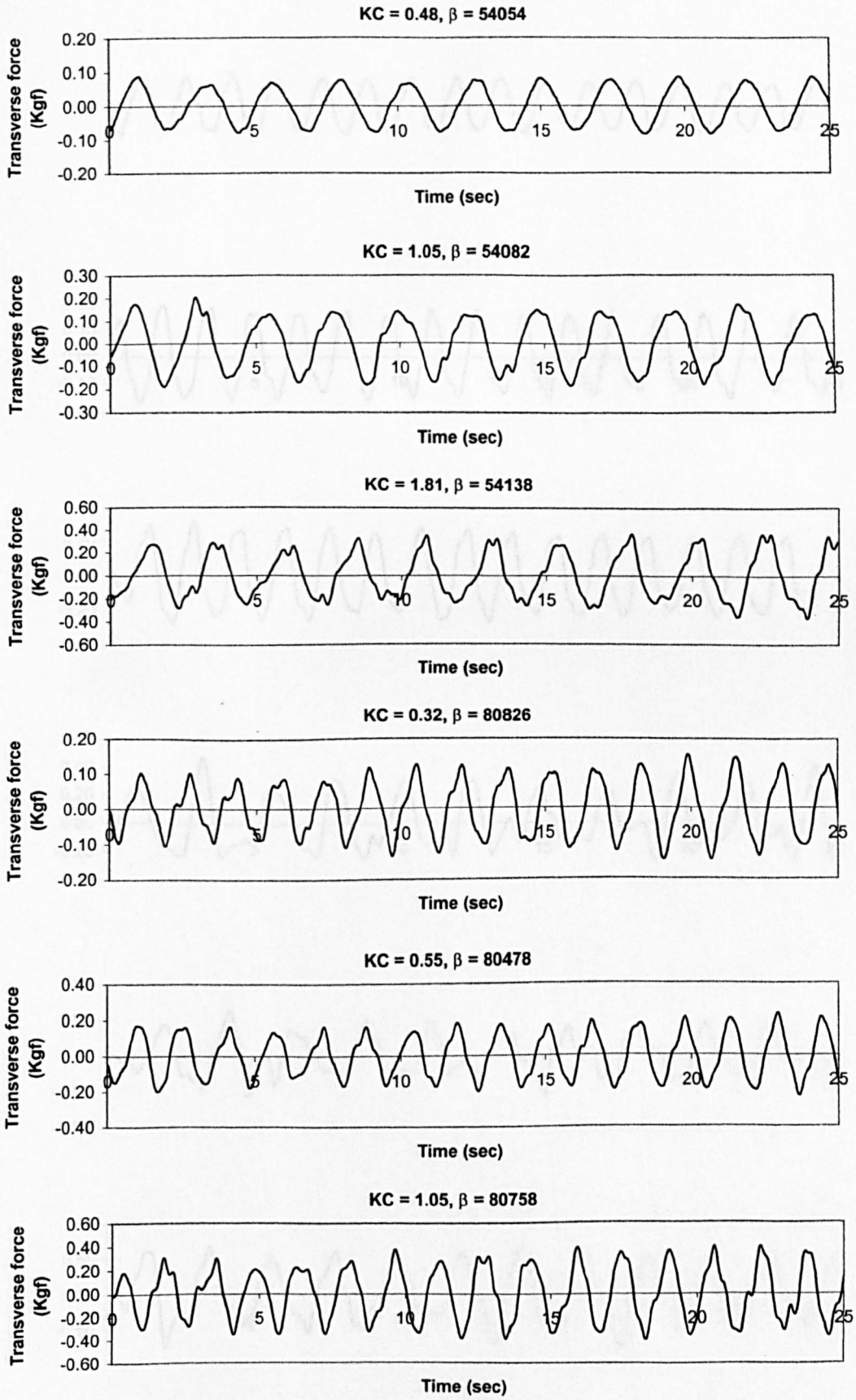

Fig. C.2 Transverse force for vertical rectangular cylinder with aspect ratio =1/2

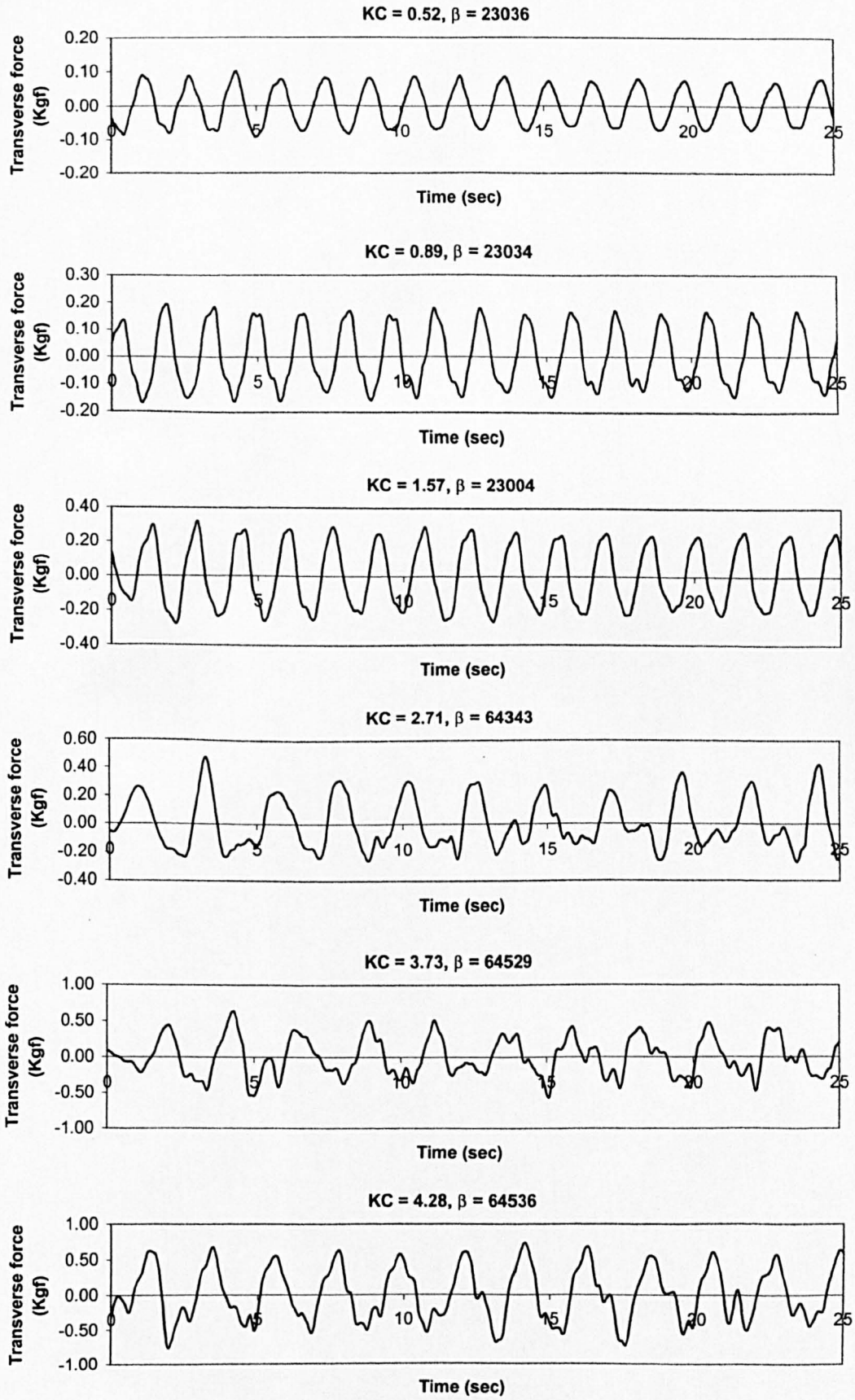

Fig. C.3 Transverse force for vertical rectangular cylinder with aspect ratio =2/1